H24/3655

MONASH UNIVERSITY
THESIS ACCEPTED IN SATISFACTION OF THE
REQUIREMENTS FOR THE DEGREE OF
DOCTOR OF PHILOSOPHY
ON..... 1 April 2003 .....
.....[redacted].....
Sec. Research Graduate School Committee

SUBDUCTION ROLLBACK, ARC FORMATION AND BACK-ARC EXTENSION

by

Wouter Pieter Schellart (MSc)

A thesis submitted for the
Degree of Doctor of Philosophy
in the School of Geosciences,
Faculty of Science,
Monash University,
Melbourne, Australia

January 2003

The senses had for ages declared the earth to be at rest, until the astronomer taught that it was carried through space with inconceivable rapidity. In like manner was the surface of this planet regarded as having remained unaltered since its creation, until the geologist proved that it had been the theatre of reiterated change, and was still the subject of slow but never ending fluctuations.

Charles Lyell

TABLE OF CONTENTS

SUMMARY

An enigmatic feature of the Earth is that most subduction zones and mountain belts are not straight but show arc-shaped features. In addition, numerous of such arc-shaped convergent zones are accompanied by a basin on their concave side (e.g. back-arc basin or marginal basin). These basins have often originated from extension (e.g. back-arc extension). For the past 30 years it has become evident that these arcuate features are not static initial geometries, but that they develop from initially more rectilinear geometries, accompanied by extension in the back-arc region. Several mechanisms have been proposed to be the main driving mechanism behind arc formation and back-arc extension, including slab rollback, gravitational collapse, lateral escape/extrusion and oroclinal bending. Slab rollback is the most promising mechanism to explain these arc back-arc systems, since it can be applied to both ocean-ocean subduction settings and ocean-continent subduction settings. The other mechanisms are either only partly applicable to a limited number of arc - back-arc settings or physically unsound. In this thesis I have investigated the process of subduction rollback and its role in arc formation and back-arc extension. These investigations involved both theoretical research and research applied to several natural arc systems. The processes have been investigated with analogue experiments (scaled physical laboratory experiments).

The first part of the thesis focuses on the structural evolution of the overriding plate during arc formation and back-arc extension. In the first place, these investigations were concerned with determining the influence of different modes of hinge-line migration (radial, unidirectional and asymmetrical) on the structural evolution of the back-arc region, which were found to be critical in determining the structural evolution of the back-arc region. In the second place, the influence of the overriding plate rheology and potential energy were investigated. It was found that with an increase in brittle integrated strength to buoyancy force ratio, deformation tends to localise close to the retreating boundary in discrete graben-like structures. With a relatively low brittle integrated strength to buoyancy force ratio, deformation is more diffuse over a wide area and is preferentially accommodated by (transtensional) strike-slip faults and to a lesser extent by normal faults. Third, two regional studies were conducted, in which the asymmetrical model was applied to explain the asymmetric structures found in the back-arc region of the Kuril arc and New Hebrides arc. The results demonstrated that the structures can indeed be explained to have resulted from asymmetric slab rollback. Fourth, the role of the East Asian active margin in driving wide-spread deformation in East Asia has been investigated. Analogue models were used to investigate physical factors that influence the amount of inboard propagation of the deformation front in the overriding plate. It was found that for conditions scaled to represent East Asia, the East Asian subduction zone can explain the large-scale structures observed in East Asia as far west as the Baikal rift zone.

The second part of the thesis focuses on lithospheric subduction and slab rollback. I have investigated the influence of several physical parameters (including slab density and slab width) and boundary conditions (fixed, free and pushed trailing edge) on the geometric, kinematic and dynamic behaviour of the subducting slab during its descent into the upper mantle and on the hinge-migration rate. It was found that an increase in slab density promotes slab rollback. The highest slab retreat velocity is observed with a slab width to thickness ratio of 7.7. Slab retreat is promoted with a fixed trailing edge and steadily decreases with increasing applied velocity to the trailing edge. A free trailing edge also slows down the

retreat velocity. Slab rollback induces mantle convection with lateral flow from underneath the slab around the slab edges towards the mantle wedge. No flow is observed underneath the slab tip. The predominance of lateral flow might explain why a large number of short subduction zones with a relatively short trench-parallel extent are presently actively retreating (Hellenic arc, Calabrian arc, Scotia arc, Ryukyu arc, Mariana arc, New Hebrides arc, Tonga arc) while long subduction zones are not (e.g. South America, Sunda arc, Aleutian arc). The lateral flow forces the slab to attain a convex shape towards the direction of retreat, which results in an arc-shaped trench at the surface. During its descent in the upper mantle, the slab pulls the horizontal part of the subducting lithosphere into the subduction zone (slab pull force). This force increases with increasing slab length and slab dip and constitutes up to ~ 8% of the total negative buoyancy force of the slab in a late stage of subduction. In a late stage of subduction, most of the total negative buoyancy force is dissipated in the mantle due to slab rollback induced mantle convection (~ 54%). The rest is dissipated in shear forces between the slab and the mantle (~ 10%) and in bending forces to bend the subducting plate into the subduction zone (~ 28%).

STATEMENT

This thesis contains no material, which has been accepted for the award of any other degree or diploma in any other university or institution. To the best of my knowledge, the thesis contains no material previously published or written by others, except where due reference is made in the text.

Wouter Pieter Schellart
January 2003

ACKNOWLEDGEMENTS

There is only so much one can achieve in three years and eight months time, and this is what I have achieved. Given more time, I would have been able to include more, but time was running short, and money even shorter. As my fiancé put it: "It's time to get a job and earn some real money". So I decided to finish the PhD, get a job, earn a living, be a good citizen and pay tax. It was about time as well, since I have spent the last nine years of my life as a university student. *Hora est.*

First of all, I would like to thank my supervisors, Professor Gordon Lister and Dr Mark Jessell for their support and inspiration during my PhD. I would especially like to acknowledge the freedom they have given me to decide what I find interesting to investigate and to let me stumble my way into becoming a self-thinking, independent scientist. At least now I have the feeling that I can not only try and attack a geological problem and have a throw at trying to solve it, but also, and more importantly, that I can come up with an interesting geological problem itself in the first place. Many thanks for that.

I like to thank several people from the Vrije Universiteit in Amsterdam, including Cees Bierman, Randell Stephenson and Dick Nieuwland for supporting me during my application for a PhD at Monash University and also Paul Bons, who was then at Monash University and helped me during my application as well. Without their help I wouldn't have been here doing the things that I have done. I would also like to thank Ritske Huismans and Randell Stephenson for initially inspiring me to do a PhD in a foreign country.

Furthermore, I would like to thank numerous people from Monash University and elsewhere for stimulating discussions about subduction, rollback, arc formation, back-arc extension, collapse, convection and other large-scale tectonic processes, including Patrice Rey, Terrence Barr, Gideon Rosenbaum, Maarten Krabbendam, Greg Houseman, Peter Betts, David Giles, Dave Gray, Louis Moresi, Laurent Allièrres, Mike Sandiford, Steve Boger, Kurt Stüwe, Mike Raetz, Ivo Vos, Marnie Forster, Hans-Peter Bunge, Guust Nolet, Janos Urai, Ross Griffiths, Chris Kincaid and Jean Braun. Furthermore, I would like to thank lots of people at Monash for help with all these very important things that come with a PhD (especially Florita Henricus, Kirsten Wholt, Megan Hough and Meaghan McDougall) and everyone in the ACRC and in the department who made my time here very enjoyable. Special thanks go to Megan Hough for proof-reading chapters 1-4, 8 and 10. I would also like to acknowledge the contribution of Andrew Chryss, who conducted the viscosity measurement for the silicone putty.

I would like to thank several people who have helped me with suggestions for doing the actual experimental work, mainly Andrew Kos, Patrice Rey, Claudio Faccenna, Myra Keep and Peter Cobbold. Also, I would like to thank the people from the physics workshop who have actually built most of the models with which I have done my experimental research.

Many thanks go to all the people who made my stay in Australia very enjoyable, especially Cameron, Anthony, Sue, Kate, Gideon, Arava, Tamra, Tali, Sigrid, Maree, Dennis, Ivo, Dunja, Sika, Doug, Biliana, Claus, Maarten, Kitty and everyone else I might have forgotten for making my stay in Australia a very pleasant one.

I would also like to thank all the friends and family in the Netherlands for keeping in touch and coming over to visit. Also I would show my gratitude to all of Gerda's friends for allowing me to let her join me to come to Australia to do my PhD and not hating me for it (or

at least not showing it). I would especially like to thank my parents and parents in law for supporting me to go to Australia (at least for the last months before departure) and showing their support during my stay. In addition, I would like to thank my father for teaching me the principles of how to handle tools, something that proved very handy indeed when working on physical models in the lab.

Coming to an end here, I would like to thank Sierra and Samson for all the excellent times we spent together during the five years prior to my departure to Australia. Out of everything, I've certainly missed you two the most.

Finally, I would like to thank the love of my life and future wife for all the support I could have only wished for. All the love, enjoyment and happiness that comes out of your presence is amazing. And yes, you can now leave the vacuum cleaning to me again. Love, forever,

Wouter

CHAPTER 1

Introduction

Abstract

This thesis investigates the role of hinge-line retreat of the subducting lithosphere (i.e. rollback) as a mechanism for arc formation and back-arc extension, as well as its influence on the overriding plate and the subducting slab itself. Since this investigation involves ideas of large-scale geologic and tectonic processes, I will start with a brief historic outline of the evolution of theories about geologic and tectonic processes that have shaped the large-scale features of the Earth. This will be followed by an overview of arc formation, back-arc extension and possible mechanisms responsible for these geological phenomena such as rollback, gravitational collapse and oroclinal bending, viewed from the perspective of the plate tectonic theory. Subsequently, the scope of the thesis will be presented, followed by the working hypotheses, which took a central place in this PhD research-project. This is followed by the modelling philosophy, in which the technique will be discussed that has been used throughout the thesis in an attempt to solve arc-related problems such as outlined in the hypotheses. Finally, this chapter is concluded with an outline of the thesis, summarising the contents of each individual chapter.

1.1. Historic outline

The mobilist view of the Earth, which culminated in the theory of plate tectonics in the 1960's, was preceded by a long history of geological data collection and development of geological theories. Probably the most important advance in understanding the Earth was the appreciation by mankind that the Earth is spherical rather than flat. This idea was already proposed in the 4th century B.C. by the Greek philosopher Aristotle. In his book "On the Heavens", Aristotle put forward two arguments to support the hypothesis that the Earth would have a spherical shape rather than being flat. First, he realised that lunar eclipses were caused by the Earth moving between the Sun and the Moon. Since the shadow of the Earth on the Moon was always round, this could only be explained if the Earth would be spherical. Second, it was known from travelling that the North Star appeared lower in the sky when viewed from the south than it did when viewed in more northerly regions. Again, this could only be explained if the Earth was spherical.

In the second century A.D. Ptolemy incorporated the hypothesis of a spherical earth into his geocentric model for the universe. Much later, in the 16th century A.D., several European scientists, such as Copernicus, Kepler and Galileo, adopted the hypothesis of a spherical earth in their heliocentric model of the universe. From this century onwards it was generally accepted that the Earth has a spherical shape. During this century, cartography of the Earth's landmasses was revived due to exploration of the Dutch, Spanish, Portuguese, English and French. From the moment of compilation of geographical maps of Europe, Africa and the Americas, people have been intrigued by the similarity of the coastlines of Africa and Europe on one side and the Americas on the other. Possibly the first person who noticed this similarity and proposed an ancient separation between these continents was the Dutch

cartographer Abraham Ortelius in 1596 [*Rom*, 1994]. This hypothesis would imply a mobilist view of the Earth with large horizontal displacements between the different landmasses in the order of thousands of kilometres.

In that same century, theories were developed to explain the occurrence of mountain belts. One theory proposed to explain mountain building was the contracting earth theory due to cooling of the earth, from which the Italian philosopher Giordano Bruno (1548-1600) was one of the early founders [*Dennis*, 1982]. This theory was later expanded by the French philosopher *Descartes* [1644] in his book "Principia Philosophiae". Much later, in the 18th century, James Hutton [*Hutton*, 1788] proposed another idea for the formation of elevations including mountain belts, continental platforms, and most folding of rocks. Hutton proposed that thermal expansion of the Earth was the cause for such elevations observed around the globe.

An important insight into mountain building then came from *de Saussure* [1784-1796, 1796], in which he proposed that lateral forces were the cause for shortening, tilting and folding of originally horizontal strata. The original ideas of *de Saussure* [1784-1796, 1796] gained more ground in the 19th century as it was convincingly demonstrated that the internal structure of the Alps had resulted from large scale horizontal shortening, involving northward overthrusting of the whole range [*Suess*, 1875]. At the same time, these ideas were experimentally investigated with analogue models (small-scale physical laboratory experiments), which provided valuable new insights into structures of the Earth. The results verified that folding and thrusting of rocks, as well as mountain formation resulted from lateral compression [*Hall*, 1815; *Favre*, 1878; *Daubre*, 1879; *Schard*, 1884; *Cadell*, 1889; *Willis*, 1893]. However, Suess continued to explain this shortening with the contracting earth theory [*Suess*, 1875, 1885].

Near the end of the 19th century and the start of the 20th century, geologist started to place doubt with the contraction theory as a mechanism for orogenesis. *Fisher* [1881] expressed his doubts about the ability of a cooling and contracting Earth to produce large amounts of crustal shortening as observed in the Alps. *Dutton* [1889] raised further doubt about the contracting Earth theory by reasoning that a contracting Earth would result in shortening of the Earth's crust in each direction equally and would not explain the occurrence of long narrow belts of parallel folds.

In 1912 Alfred Wegener proposed his theory of continental drift [*Wegener*, 1912], in which a large amount of data was put forward from various disciplines to support the hypothesis that North and South America were once connected to Europe and Africa and formed the supercontinent Pangea. The continents were later separated from each other due to divergent motion between these landmasses. Wegener compiled much of the pre-drift geological data to show that the continuity of older structures, formations and fossil floras and faunas located along the shorelines of many continents could be explained on a pre-drift reconstruction of Pangea. The geoscience community received the continental drift theory with disbelief, since the theory broke with established orthodoxy of a static Earth. Furthermore, many geoscientists found fault in detail in the geological and geophysical data and interpretations outlined in Wegener's work to support his theory. Finally, most of the geophysical community at that time rejected the theory, since Wegener, as he realised himself, did not propose a reasonable mechanism for continental movements. Wegener had suggested that continental drift was powered by the centripetal force, which would cause high standing continents to move due to rotation of the Earth. However, it was soon realised that this force was much too small to drive continental movement.

In 1928, help came along from Holmes [*Holmes*, 1928], who proposed that continental drift could be driven by convection currents from deep within the earth, which in turn were powered by the heat in the interior of the Earth generated by radioactive decay. The idea of sub-crustal convection in the Earth's mantle was not new and had already been proposed a century earlier [*Hopkins*, 1839; *Fisher*, 1881]. In the beginning of the twentieth century it was proposed by several geoscientists that these mantle convection currents could also drive the formation of mountain belts and their associated fold and thrust structures [*Ampferer*, 1906; *Schwinner*, 1920; *Vening Meinesz*, 1934]. These theories were later supported by results of analogue experiments [*Griggs*, 1939], which showed that convection in a fluid substratum can cause shortening in an overlying plastic crust.

After the publication of Wegener's drift theory [*Wegener*, 1912, 1915], the geoscience community was divided into two schools of thought, the drifters and the non-drifters. In the thirty years or so following the publication of Holmes' convection model, very little was written about the continental drift theory. However, this was about to change when in the 1950s and 1960s a wealth of geological and geophysical techniques and data were acquired. These included radiometric dating, seafloor topography mapping, the discovery of magnetic reversals patterns and oceanic spreading centres, paleomagnetic data and magnetic polar wandering. The interpretation of these new data sets in the 1960s resulted in a revolution in geology, which led to the development of the theory of plate tectonics.

First of all, in the early 1960's, Harry Hess and Robert Dietz [*Hess*, 1962; *Dietz*, 1961] proposed the concept of seafloor spreading, which stated that seafloor comes into being at mid-oceanic ridges to fill the cracks or voids that are being created by the surrounding seafloor that is moving away in opposite direction on either side of the ocean ridge. This model provided a viable mechanism for the supposed continental drift of continents as proposed by Wegener [*Wegener*, 1912, 1915], where the continents were split up and pushed apart during the formation of new oceanic crust instead of continents moving through the oceans like icebreakers move through frozen sea.

This theory elegantly explained the relatively young age of the ocean basins, which was found to be no more than ~ 200 Ma, as well as the observation that the age of the ocean floor increases away from midoceanic ridges. The theory also provided explanations for various geological observations such as the topography of the ocean floor [*Menard*, 1965], normal faulting on the top of mid-oceanic ridges [*Ewing and Heezen*, 1956] and linear magnetic anomalies on the seafloor [*Vine and Matthews*, 1963]. The magnetic anomalies were discovered in the 1950s and were shown to be remarkably linear and continuous, running roughly parallel to the mid-oceanic ridges. Vine and Matthews suggested that these magnetic lineations might be explained in terms of seafloor spreading and paleomagnetism, where the oceanic crust that is continuously formed along midoceanic ridges records the reversal history of the Earth's magnetic field. The theory of seafloor spreading would require either expansion of the earth or destruction of ocean floor away from ridges. It was soon realised that any expansion hypothesis would require an extremely high rate of expansion of the Earth since the Jurassic, since no ocean floor on Earth is older than Jurassic. Thus, it was more logical to pursue the hypothesis of seafloor destruction.

It was already proposed much earlier by Vening Meinesz that trenches were the sites of seafloor destruction, based on gravity measurements along deep sea trenches in the East Indies [*Vening Meinesz*, 1934, 1962]. This idea was further supported by small-scale analogue models [*Kuenen*, 1936], in which lateral compression of a plastic layer overlying a viscous substratum initially caused downbuckling of the plastic layer and finally resulted in

some sort of primitive subduction in a more advanced stage. The most convincing evidence for destruction of seafloor came from earthquake seismology, where it was shown that ocean floor is thrusted underneath continents or island arcs along trenches [*Plafker*, 1965; *Sykes*, 1966]. At the same time, *Wilson* [1965] stated the basic assumptions of plate tectonic theory, realising the importance of rigidity of rocks in aseismic areas. Furthermore, Wilson recognised a new class of faults named transform faults, which connect linear belts of tectonic activity and along which motion is parallel and horizontal. The geometrical basis of the theory of plate tectonics was soon established by *McKenzie and Parker* [1967], *Morgan* [1968] and *Le Pichon* [1968]. By this time, the Earth was viewed as a mosaic of six major and several minor lithospheric plates in relative motion to each other and bound by divergent, convergent or transform plate boundaries. The geometrical outline of these plates was confirmed by earthquake seismology work of *Isacks et al.* [1968] showing that the majority of seismic activity occurs along the boundaries of these plates.

From several hundred years of observations and geological interpretations of the Earth, a general acceptance of the theory of plate tectonics was achieved in the late 1960s. However, it was soon realised that although the theory worked well for describing the structures and movements of the oceanic plates, it did not serve the same function for the continental lithosphere [*Isacks et al.*, 1968]. Deformation in oceanic lithosphere is observed along narrow strips of some 10 km along the plate boundaries, while deformation in continental lithosphere is more diffuse and can take place hundreds to thousands of kilometres away from plate boundaries [*McKenzie*, 1969]. The difference in behaviour of continental lithosphere has been ascribed to its greater buoyancy force and lesser strength compared to oceanic lithosphere, resulting from the thicker crust in continental lithosphere [*McKenzie*, 1969].

The plate tectonic theory is basically only a kinematic theory and does not provide any clues as to what the actual driving mechanism(s) of the plates are. Two different types of driving mechanisms have been proposed [*Forsyth and Uyeda*, 1975; *Kearey and Vine*, 1996]: the mantle drag mechanism and the edge force mechanism.

The mantle drag mechanism was proposed by *Holmes* [1928] in order to explain the continental drift theory proposed by *Wegener* [1912, 1915], but has been discussed by numerous others including *Ampferer* [1906], *Schwinner* [1920], *Vening Meinesz* [1934], *Griggs* [1939], *Runcorn* [1962], *Morgan* [1972] and *Turcotte and Oxburgh* [1972]. In this mechanism, the upper cool boundary layer of the convective system is located in the upper part of the asthenosphere, where the lithospheric plates are driven by the viscous drag exerted by the asthenosphere on their base.

Several objections have been raised against this mechanism. One problem is that aspect ratios of convection cells in the asthenosphere are expected to be close to one, indicating the horizontal dimensions of such cells are significantly smaller than that of typical plates [*Forsyth and Uyeda*, 1975]. The cumulative force that numerous small convection cells would apply to an overlying lithosphere would then add up to a negligible contribution, indicating that they are incapable of driving plates [*Richter*, 1973]. Also, the relatively low viscosity of the asthenosphere compared to the rapidity of convection would inhibit it from transmitting any significant stresses on the base of lithospheric plates [*Artyushkov*, 1973]. Another argument against the viability of the mantle drag mechanism is that one would expect the larger plates to have a larger velocity compared to the smaller plates, which is not in agreement with observations [*Forsyth and Uyeda*, 1975; *Turcotte*, 1983]. In conclusion, it is more likely that the mantle drag force acts as a resistive force rather than a driving force in tectonic plate movement [*Forsyth and Uyeda*, 1975].

The edge force mechanism proposes that the plates are driven by the forces exerted to the margins of these plates. Here, the lithosphere itself is recognised as being part of the convection cells. The main driving forces are thought to be the ridge push force and the slab pull force [*Forsyth and Uyeda*, 1975]. A third force, the trench suction force [*Elsasser*, 1971] is thought to be of less importance [*Forsyth and Uyeda*, 1975]. The ridge push force is a driving force exerted by the mid-oceanic ridge on the surrounding lithosphere. It can simply be explained as resulting from the excess potential energy of the ridge compared to the surrounding lower-lying ocean and acts perpendicular to the ridge axis [*Forsyth and Uyeda*, 1975]. The magnitude of this force is in the order of $\sim 3 \times 10^{12}$ N/m of ridge boundary [*Harper*, 1975; *Lister*, 1975; *Parsons and Richter*, 1980]. The slab pull force results from the negative buoyancy of the subducting slab compared with the surrounding sub-lithospheric mantle, which is supposed to be transferred to the horizontal part of the subducting plate. This stress transfer would be possible if the lithosphere can act as a stress guide, where tensional stresses can be transmitted from the slab across the hinge towards the horizontal part of the subducting lithosphere [*Elsasser*, 1967, 1969, 1971]. The total magnitude of the slab pull force is an order of magnitude larger than the ridge push force, but part of the slab pull force is thought to be consumed by shear forces in the mantle resisting subduction of the slab [*Forsyth and Uyeda*, 1975]. Also, it is not immediately clear how much of this force can actually be transmitted across a non-stationary subduction hinge. However, empirical data indicate that plates, attached for a large part of their circumference to old (and thus dense) segments of slab, have a relatively high velocity [*Forsyth and Uyeda*, 1975], underlining the importance of the slab pull force in driving tectonic plates. At present, it seems to be generally agreed upon that the ridge push force and the slab pull force are of comparable importance as driving mechanisms of tectonic plates, while collisional resistance and basal drag are the main forces resisting plate motion.

1.2. Rollback, arc formation and back-arc extension

A striking feature of Earth is that most active subduction zones and collision zones, as well as ancient convergent zones display arc-shaped features. Present day examples of such arc-shaped features are numerous (Fig. 1-1). Some examples from the Pacific region are the Aleutian arc, the Kuril arc, the Japan arc, the Mariana arc, the Ryukyu arc, the New Hebrides arc and the Tonga arc. Examples from the Mediterranean region are the Betic/Rif arc, the Calabrian arc, the Carpathian arc, the Hellenic arc and the Cyprus arc. Other examples include the Java arc and the Banda arc in southeast Asia, the Lesser Antilles arc from the Caribbean Sea and the Scotia arc, located between South America and Antarctica.

One of the first people who tried to explain why these zones are arc-shaped and not simply rectilinear from a plate tectonic perspective was *Frank* [1968]. In *Frank*'s [1968] model the curvature of an arc is explained to be a mere consequence of the sphericity of the Earth. In this model, subduction zones are viewed as dents on an elastic sphere (compare with dents on a ping pong ball). The slab follows a path in the asthenosphere, which is defined by a sphere segment with a similar radius as the earth and intersecting with the earth but with an opposite flexure (Fig. 1-2). The intersection between the two spheres defines a small circle on the Earth, along which the subduction zone would be aligned. This model would imply that there would be a direct relationship between slab dip angle (α), central vortex angle (β) and arc radius (r):

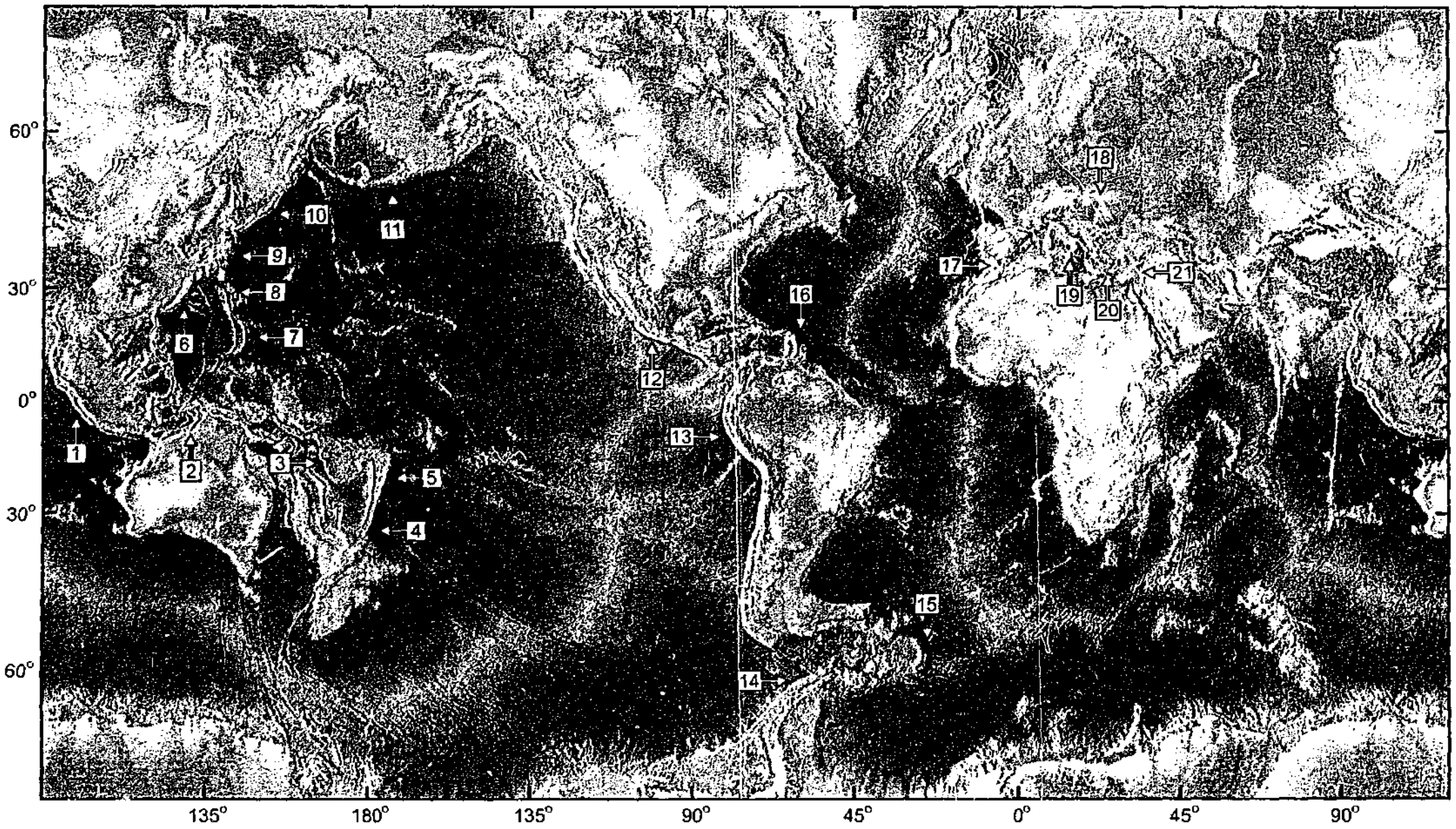

Fig. 1-1. Topography and bathymetry of the world indicating the location of several arc - back-arc systems. 1-Sunda arc; 2-Banda arc; 3-New Hebrides arc; 4-Kermadec arc; 5-Tonga arc; 6-Ruykyu arc; 7-Mariana arc; 8-Izu-Bonin arc; 9-Japan arc; 10-Kuril arc; 11-Aleutian arc; 12-Trans Mexican arc; 13-North Andean arc; 14-South Shetland arc; 15-Scotia arc; 16-Lesser Antilles arc; 17-Betic-Rif arc; 18-Carpathian arc; 19-Calabrian arc; 20-Hellinic arc; 21-Cyprus arc.

$$\alpha = 2\beta = 360(r/\pi R) \qquad (1\text{-}1)$$

where R is the radius of the Earth (≈ 6350 km). Equation (1-1) indicates that slab dip should increase with increasing central vortex angle. Also, arcs with a small central vortex angle, such as the Mariana, Scotia, Banda and Hellenic arc, should have an extremely shallow slab dip, while this is not observed (Table 1-1). Furthermore, *Frank*'s [1968] model would imply that subducted slabs should have concave upward shapes with shallowing dips from top to bottom, while the opposite is observed. Most subducting slabs become steeper with depth for depths down to ~ 500 km [*Isacks and Barazangi*, 1977]. Finally, the model would imply that the slab dip would remain constant along the length of the arc, another requirement which is not met by numerous natural examples [e.g. *Yokokura*, 1981]. Based on these criteria it can be concluded that the model can not account for arcuate subduction zones around the globe as has been suggested previously by other authors [*De Fazio*, 1974; *Tovish and Schubert*, 1978].

Frank's [1968] so called "ping pong" model would also imply that arcs are incipient static features, where the subduction zone initially forms as an arc-shaped subduction zone and remains static in time. However, there are several lines of evidence from different disciplines in geology, which suggest that most arcs are not initial static geometries but evolve through time from more rectilinear geometries. First of all, the wide range of arcuate shapes with varying curvature angles and back-arc geometries support this idea. Second, data for paleomagnetic rotations along some arcs point to comparable or different magnitudes of rotation along the arc and/or opposite sense rotations on either side of the arc (Betic/Rif Arc and Calabrian arc [*Lonergan and White*, 1997], Hellenic arc [*Walcott and White*, 1998], Carpathian arc [*Marton and Fodor*, 1995], Mariana arc [*McCabe*, 1984], New Hebrides arc [*Musgrave and Firth*, 1999], Japan arc [*Otofuji et al.*, 1991], Ryukyu arc [*Kamata and Kodama*, 1994]). Third, evidence from GPS data along some arcs indicates that different segments of arcs have different velocities and/or orientations compared to the "fixed" hinterland, indicating that arcs are not static geometries but evolve through time (e.g. Tonga

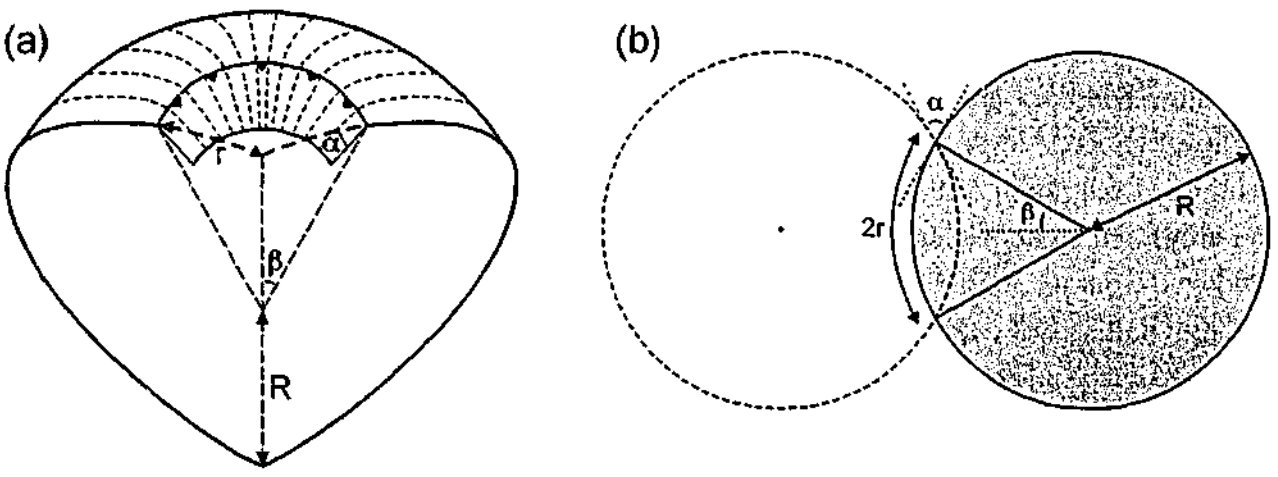

Fig. 1-2. Schematic diagrams illustrating the equal-sphere intersection model of *Frank* [1968]. (a) 3D cut-away view of Earth at an island arc showing the descending slab (modified from *Tovish and Schubert* [1978]). (b) 2D cross-sectional view showing intersection of two spheres with an equal radius. With decreasing distance between the two spheres the central vortex angle increases. α = slab dip angle; β = central vortex angle; r = arc radius; R = radius Earth.

Arc	Central vortex angle (α)	Arc radius (r)	Predicted slab dip angle (β)	Observed slab dip angle (β')	Reference observed slab dip angle
Mariana arc	7°	~ 780 km	14°	~ 80-90°	1,2
Banda arc	3°	~ 330 km	6°	~ 60-80°	3
Hellenic arc	~ 4°	~ 440 km	8°	~ 55°	4
Scotia arc	3°	~ 330 km	6°	~ 70°	2

Table 1-1. Slab dip angle as predicted from *Frank*'s [1968] equal sphere intersection model and slab dip angle as observed from seismology and tomography for several arc - back-arc systems with a relatively small central vortex angle. Clearly, observed slab dip angle is much greater than predicted slab dip angle. References: 1—*Katsumata and Sykes* [1969]; 2—*Yamaoka et al.* [1986]; 3—*Widiyantoro and van der Hilst* [1996] and *Hafkenscheid et al.* [2001]; 4—*Spakman et al.* [1988], *Meulenkamp et al.* [1988] and *Wortel and Spakman* [1992].

arc [*Bevis et al.*, 1995], Hellenic arc [*Kahle et al.*, 1998], New Hebrides arc [*Taylor et al.*, 1995]). Fourth, most arcs are bordered by back-arc regions on their concave side, which have often experienced extension for an extensive period (i.e. back-arc extension). This indicates that the geometry of these arcs must have changed during such extension. Thus, following these arguments, it is most probable that these arcs progressively develop and become more arc-shaped through time, as has been suggested earlier by *Vogt* [1973].

It should be mentioned, however, that not all arc-shaped convergent zones necessarily have to have evolved from initially straighter geometries. For example, the arc-shaped northern Andean subduction zone (from ~ 06° north to ~ 18° south) is most likely a mere consequence of the incipient shape of the western border of the South American plate. The Aleutian arc, located in the Northern Pacific, is another example. The arc is bordered to the north by the Bering Sea back-arc basin. This back-arc basin is most likely a trapped piece of oceanic lithosphere [*Cooper et al.*, 1992], which does not seem to possess any structures that could be related to the formation of the arcuate shape of the Aleutian arc. Magnetic lineations from the Bering Sea strike ~ N-S and increase in age from west to east [*Cooper et al.*, 1992]. One would expect them to strike ~ E-W and to increase in age from some former spreading ridge located in the centre of the basin, if the Bering sea were to be the result of southward arc migration and back-arc opening. In addition, the back-arc basin is older (Cretaceous) than the arc itself (Eocene to Present), indicating that the back-arc basin can not have developed from southward migration of the Aleutian arc. This arc is actually one of the few examples (if not the only), which does seem to fit *Frank*'s [1968] model with a slab dip angle close to the one predicted from its central vortex angle.

The hypothesis of evolving arcs is also supported by palinspastic and evolutionary diagrams proposed previously for numerous arcs around the globe (e.g. New Hebrides arc and Tonga arc [*Auzende et al.*, 1988; *Hathway*, 1993], Hellenic arc [*Kissel and Laj*, 1988; *Walcott and White*, 1998], Calabrian arc [*Faccenna et al.*, 1996]; Cyprus arc [*Payne and Robertson*, 1995]).

Since most arcs are likely to have evolved through time, one can wonder what drives the formation of arcs. The formation of arcuate subduction zones in combination with back-arc extension has been ascribed to several driving mechanisms such as rollback of the hinge-line of the subducting slab [*Royden et al.*, 1983, 1987; *Hsui and Younquist*, 1985; *Viallon et al.*, 1986; *Malinverno and Ryan*, 1986; *Wortel and Spakman*, 1992, 2000; *Shemenda*, 1994; *Lonergan and White*, 1997], gravitational/extensional collapse [*Dewey*, 1988; *Platt and Vissers*, 1989; *Platt and England*, 1994], lateral escape/extrusion [*McKenzie*, 1972; *Ratschbacher et al.*, 1991a,b] and oroclinal bending [*Mantovani et al.*, 1997, 2000]. From these, rollback seems to be the most favoured mechanisms and has been suggested for the development of numerous arc - back-arc systems, including: the Mariana arc [*Hsui and Younquist*, 1985; *Fryer*, 1996], the Kuril arc [*Jolivet*, 1987; *Maeda*, 1990], the Japan arc [*Jolivet*, 1987], the Ryukyu arc [*Viallon et al.*, 1986], the Izu-Bonin arc [*van der Hilst and Seno*, 1993], the New Hebrides arc [*Schellart et al.*, 2002], the Tonga arc [*Bevis et al.*, 1995], the Kermadec arc [*Molnar and Atwater*, 1978; *Gamble and Wright*, 1995], the Banda arc [*Hamilton*, 1979], the Scotia arc [*Alvarez*, 1982; *Barker*, 1995], the South Shetland arc [*Lawver et al.*, 1995], the Trans Mexican arc [*Ferrari et al.*, 2001], the Lesser Antilles arc [*Alvarez*, 1982], the Betic/Rif arc [*Royden*, 1993; *Lonergan and White*, 1997], the Carpathian arc [*Royden*, 1983, 1993], the Calabrian arc [*Malinverno and Ryan*, 1986; *Royden et al.*, 1987; *Faccenna et al.*, 2001a,b], the Hellenic arc [*Le Pichon*, 1982; *Meijer and Wortel*, 1997; *ten Veen and Meijer*, 1998] and the Cyprus arc [*Payne and Robertson*, 1995].

Rollback is a process related to subduction of lithosphere, where the hinge-line of the subduction zone is not fixed in time, but progressively retreats oceanwards in a hot spot reference frame (Fig. 1-3). Hinge-line retreat was first proposed and discussed by *Elsasser* [1971], but was already suggested in schematic diagrams several years earlier [*Elsasser*, 1967, 1969]. Rollback is commonly related to the negative buoyancy of the subducting plate compared to the surrounding asthenosphere [*Elsasser*, 1971; *Molnar and Atwater*, 1978; *Malinverno and Ryan*, 1986; *Lonergan and White*, 1997], which pulls the subducting plate downwards and results in the regressive hinge-line retreat of this plate.

It is often thought that for slab rollback to occur, the subducting lithosphere should be relatively old (> 50 Ma) [e.g. *Molnar and Atwater*, 1978]. However, rollback as a driving mechanism for back-arc extension has been suggested for several arcs along which very young oceanic lithosphere is being subducted. Examples include extension in the Trans-Mexican Volcanic Belt, located in western Central America behind the Middle America Trench [*Ferrari et al.*, 2001; *Suter et al.*, 2001], along which ~ 4-15 Ma oceanic lithosphere is being subducted [*Madsen et al.*, 1992; *Lonsdale*, 1995]. Another example is the South Shetland arc in Antarctica, where northwest directed rollback of a southeast directed subducting slab has resulted in back-arc opening of the Bransfield Strait [*Lawver et al.*, 1995]. The subducting lithosphere close to the trench has an age of ~ 14 Ma in the southwest

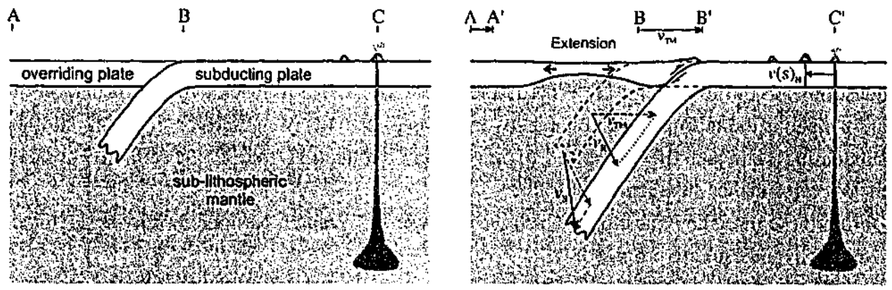

Fig. 1-3. Simple kinematic model for subduction rollback, where the advancing rate (AC - A'C' = AA') is slower than the trench migration rate (BC - B'C' = BB') in a hot spot reference frame. This trench migration (v_{TM}) could be related to the sinking of the slab, as indicated by the vector v_R. Horizontal

velocity of subducting plate is indicated by $v(s)_H$. Final kinematic behaviour of the slab (v_s) results from v_R and $v(s)_H$.

to ~ 23 Ma in the northeast [*Barker*, 1982]. Calculations from *Le Pichon* [1982] have shown that oceanic lithosphere older than ~ 8 Ma is already gravitationally unstable with respect to the asthenosphere, implying that rollback can already occur during subduction of very young oceanic lithosphere.

An important consequence of the dynamic interpretation of arc formation (contrary to the interpretation that arcs are static features) is that it should have a profound influence on the structural development of the subducting slab and the overriding plate. From a geometrical point of view, one would expect this to have a major influence on the structural evolution of both the overriding plate and the subducting slab. One would expect the overriding plate to experience space problems in both the arc-parallel as well as the arc-perpendicular orientation, and the slab to experience space problems in the orientation parallel to the slab and perpendicular to the slab dip. The extent of these space problems would depend on the style of hinge-line migration of the subducting lithosphere.

1.3. Scope of thesis

In this thesis, the kinematics and dynamics of subduction rollback, arc formation and back-arc extension are analysed. These processes have been investigated with scaled analogue models (physical laboratory experiments) to gain better insights into the three-dimensional geometric, structural, kinematic and dynamic evolution of arc - back-arc systems, and into the processes which drive their formation and structural evolution. The main goal in this thesis is to provide new insights into these processes by doing the experiments in three-dimensional space. Geoscientists, who have modelled these processes previously either with analogue or numerical models, have mainly done so with models in two-dimensional space in sections perpendicular to the hinge [e.g. *Kincaid and Olson*, 1987; *Shemenda*, 1993; *Giunchi et al.*, 1994; *Griffiths at al.*, 1995; *Guillou-Frottier et al.*, 1995; *Marotta and Sabadini*, 1995; *Faccenna et al.*, 1996, 1999; *Becker et al.*, 1999]. Since I have argued that slab rollback, arc formation, back-arc extension and slab-induced mantle convection are processes, which operate in three-dimensional space that vary significantly along the strike of the arc, the tectonic modelling described in this thesis has been done in three-dimensional space.

1.4. Formulation of key questions and working hypotheses

In this thesis, three questions have played a central part in the research undertaken. These questions are the following: (1) What is the influence of slab rollback and the formation of arc-shaped subduction zones on the overriding plate? (2) What drives rollback of the subducting slab and the formation of arc-shaped subduction zones? (3) Which physical factors can enhance subduction rollback?

From these three key questions, which have driven the research outlined in this thesis, three working hypotheses are proposed:

1. The formation of arc-shaped subduction zones imposes significant strain on the overriding plate (back-arc extension) where the style and localisation of deformation depend to a large extent on the kinematic evolution of the subduction zone interface.

2. Rollback can be driven by the negative buoyancy of the slab compared to the asthenosphere and is resisted by the resistance of the slab to tear and by the asthenosphere to flow from underneath the slab towards the mantle wedge. Arc-shaped subduction zones can evolve from rectilinear subduction zones due to density anomalies in the subducting slab in a direction parallel to the trench. This leads to faster rollback of the denser part of the slab, compared to the less dense regions.
3. Slab rollback is enhanced by (1) an increase in density contrast between slab and sub-lithospheric mantle, (2) the possibility of sub-lithospheric mantle material to flow laterally around slab edges and (3) the decrease in effective viscosity of lithosphere and/or sub-lithospheric mantle.

1.5. Modelling philosophy

Conceptual models of subduction, slab rollback, arc formation and back-arc extension will be tested with physical experiments (small-scale physical laboratory experiments or analogue experiments) simulating these processes. An advantage of analogue modelling is that it can be done in four dimensions (3-dimensional space + time), which is a requisite for modelling of rollback, arc formation and back-arc extension, since these processes show a strong non-linear behaviour in the direction parallel to the trench.

It should be kept in mind that the models described in this thesis are dynamic models, in which the thermal component is not taken into account. This is a major simplification with respect to numerical modelling, in which thermal components are often incorporated but where the experiments are often executed in two-dimensional space. For the processes investigated in this thesis, I consider the addition of a third dimension of primary importance and the addition of a thermal component of secondary importance, and therefore, the physical modelling technique was preferred above the numerical modelling technique. Physical models provide a means of investigating the interaction of several processes that might be responsible for the formation of a specific geological structure and can also be used to investigate qualitatively and quantitatively the effect of change in a relevant parameter. Furthermore, physical models can provide insights into the physical feasibility of a specific conceptual model. Finally, physical models, as any dynamical model, are more process oriented than kinematic models and can therefore help in providing new insights into specific geological processes.

The theory for analogue or physical modelling, applied to geological processes, was first introduced by *Hubbert* [1937] and was later discussed by *Horsfield* [1977] and *Davy and Cobbold* [1991], among others. According to these rules a model is representative of a natural prototype if both systems have similar distributions of stresses, densities and rheologies. When analogue experiments are executed in a normal field of gravity, stresses and cohesion should be scaled down as the product of density and length scale down [*Horsfield*, 1977; *Davy and Cobbold*, 1991].

The scaling rule implies that only specific materials will be suitable to use in analogue models. Furthermore, apart from being properly scaled, the price and availability of a modelling material also plays a significant role. For analogue modelling of plate-tectonic processes both brittle and ductile rheologies should be considered. Layer-cake models have been built in order to simulate the stratified rheology of the Earth's lithosphere and asthenosphere [cf. *Davy and Cobbold*, 1991]. For brittle materials, different types of granular

material have been investigated to find the material that is best scaled for cohesion and coefficient of internal friction, when compared to nature [*Schellart*, 2000; Appendix III]. For ductile material different materials have been investigated to find which material is properly scaled for viscosity and density. In the analogue models discussed in the following chapters, three different materials have been used: (1) glass microspheres to model brittle deformation of rocks (e.g. upper lithosphere); (2) silicone putty to model high viscosity material (e.g. lower lithosphere); and (3) glucose syrup to model the low viscosity asthenosphere or sub-lithospheric mantle.

1.6. Outline of thesis

As mentioned above, the main goals of this thesis are to investigate if rollback is a process that can drive the formation of arcuate subduction zones and back-arc basins, and to test its influence on the 3D geometrical, structural and kinematic evolution of the overriding plate, the slab and their interface. This chapter is followed by two introductory chapters (Chapters 2 and 3) outlining the modelling technique and conceptual models of arc formation and back-arc extension. These are followed by five chapters (Chapters 4-8) focusing on the 3D geometrical and structural development of the overriding plate for various kinematic boundary conditions and varying rheological profiles. Three chapters follow (Chapters 9-11), which focus on the kinematic and dynamic evolution of the slab during subduction and on the three-dimensional convection pattern in the sub-lithospheric upper mantle resulting from slab subduction and rollback. The final conclusions are described in Chapter 12, which are concluded with some suggestions for future research into arc-related tectonic processes. The last chapter is followed by four appendices. Appendix I deals with the scaling theory for analogue modelling. Appendix II elaborates on some rheological equations that are dealt with throughout the thesis. Appendix III describes results of shear test experiments to obtain a quantitative insight into the physical properties of various granular materials. Appendix IV describes the rheological properties of the viscous materials used in the analogue models.

Chapter 2 gives a brief historical outline of the analytical technique (analogue modelling) which has been used to investigate the tectonic processes mentioned above. Furthermore, the technique itself is briefly described, where some of the most important scaling relationships are discussed. Finally, the materials used in the experiments described in this thesis are briefly discussed.

Chapter 3 describes several important tectonic models, which have been proposed as driving mechanisms for the formation coupled shortening-extension systems, such as of arc – back-arc systems. These systems are characterised by shortening along the convex side of the arc (trench region) contemporaneously with extension on the concave side of the arc (back-arc region). The driving mechanisms include rollback of the subducting slab (also known as hinge-line migration or trench-line migration), gravitational collapse (also known as orogenic, extensional, late-orogenic or post-orogenic collapse), extrusion tectonics (also known as escape tectonics) and oroclinal bending.

Chapter 4 describes experiments carried out to investigate the geometrical and structural evolution of the overriding plate during rollback of the subducting lithosphere. Conceptual

models of the kinematic evolution of arcs are presented which have been deduced from a number of natural examples. The influence of different styles of hinge-line migration on the structural and geometrical development of the overriding plate is investigated through a series of model experiments with three different boundaries conditions (e.g. radial spreading model, unidirectional spreading model and asymmetrical spreading model). These three different models simulate different modes of arc formation and back-arc spreading as observed in nature (e.g. radial model: Hellenic arc, Carpathian arc; unidirectional model: Scotia arc, Mariana arc, South Shetland arc; asymmetrical model: Tonga arc, New Hebrides arc, Kuril arc). The experimental results are briefly compared with several natural arc – back-arc systems.

Chapter 5 presents the general findings of models simulating asymmetrical back-arc deformation. Results of experiments will be presented with varying initial brittle strength to viscous strength ratio (BS/VS) and varying integrated strength to buoyancy force ratio (IS/BF). One of the important findings from the experiments is that with increasing BS/VS and IS/BF the fault density and surface extent of the deformed area decrease, while the degree of asymmetry in the strain pattern increases. Finally, the experimental results will be compared with two natural arc - back-arc systems, which are interpreted to have originated for a large part from asymmetric hinge-line retreat of the subducting lithosphere.

In *Chapter 6* the experimental results of several experiments discussed in Chapter 5 are discussed and interpreted in more detail and are applied to structures observed in the Kuril arc, Kuril back-arc Basin and Sea of Okhotsk, located in the Northwest Pacific region. The results demonstrate that the Eocene to Middle/Late Miocene back-arc deformation could have resulted from asymmetric spreading in the overriding plate due to asymmetric anticlockwise rollback of the Pacific plate. This asymmetric rollback could be explained by the increase in age (and therefore density) of the Pacific plate along the trench from the northeast to the southwest.

Chapter 7 presents the results of a more complicated analogue model to simulate asymmetrical back-arc extension and arc deformation in the North Fiji back-arc Basin and the New Hebrides arc, located in the Southwest Pacific region. The modelling results indicate that the complex pattern of faults and spreading axes observed in the North Fiji back-arc Basin can be explained to a large extent by asymmetric hinge-line retreat of the subducting Australian plate and subsequent collision of the North D'Entrecasteaux Ridge and West Torres Plateau, located on the Australian plate, with the New Hebrides arc.

Chapter 8 presents some speculations on the far field effect of subduction rollback on the interior of the continental overriding plate adjacent to the subduction zone. Some empirical data for several arc systems are provided for the correlation between arc width, slab retreat, overriding plate rheology and inboard propagation of the deformation front. These data are compared with results from analogue experiments presented in Chapters 4, 5 and 6. This finally leads to the proposal of a new tectonic model, in which slab rollback along the entire East Asian active margin (~ 7000 km long) could explain the large-scale structures observed in East Asia, as an alternative model to the extrusion tectonics model.

Chapter 9 presents the results of fluid dynamical experiments, which investigate the three-dimensional kinematic behaviour of a viscous slab subducting in a low viscosity upper mantle. The model results indicate that slab rollback is a transient process, which naturally accompanies subduction. The rate of slab retreat is influenced by the density contrast between slab and surrounding material as well as the slab width.

Chapter 10 discusses the influence of an applied horizontal velocity to the subducting lithosphere on the hinge-line migration rate. With increasing applied velocity, hinge-line retreat is increasingly retarded, which can result in intermittent periods of hinge retreat and hinge advance.

Chapter 11 presents the results of quantitative calculations of the effective slab pull force in relation to the total negative buoyancy force of the slab for fluid dynamical experiments presented in chapter 9. The results show that the lithosphere acts as a stress guide, where tensional stresses are transmitted from the slab to the horizontal surface part of the subducting lithosphere. These stresses, however, constitute only up to 8% of the total negative buoyancy force of the slab.

In *Chapter 12* the findings of the previous chapters are summarised and integrated, and placed in a broader context of conceptual models describing large-scale tectonic processes including subduction, slab rollback, arc formation and back-arc extension. The shortcomings of the analogue models and some suggestions are presented for directions of future research in subduction rollback, arc formation and back-arc extension.

Chapters 2, 3, 4, 5, 6, 7, 8, 9, 10 and 11 and Appendix III are written as self-standing entities, published or intended to be published as papers in scientific journals. As a result, some repetition is unavoidable.

FOREWORD CHAPTER 2

This chapter discusses the analogue modelling technique, which was applied to investigate the processes of subduction rollback, arc formation and back-arc extension. The discussion on the history of the modelling technique, the various sub-techniques of analogue modelling and the materials used in these models followed from an extensive literature review.

Part of the contents of this chapter has been published in the *Journal of the Virtual Explorer*. A full reference can be found at the end of the thesis in the bibliography.

CHAPTER 2

Introduction Analogue Modelling

Abstract

Analogue modelling has been applied to study geological processes since the beginning of the 19th century to provide qualitative and quantitative insights into specific geological problems. The advantage of analogue models is that they offer the opportunity to investigate the individual influence of different parameters on geological processes. Furthermore, boundary conditions can be set according to the needs of the experimenter. Also, they offer the opportunity to study the three-dimensional structural evolution of a specific model, thus supplying a clear coherent kinematic picture, which can help with the interpretation of natural prototypes. Analogue models are representative of a natural prototype if they are properly scaled and if the materials used show a similar rheological behaviour as the natural prototype. For mechanical modelling, this requires the proper scaling of surface forces (stresses) in relation to body forces (due to gravity). Other parameters that need to be properly scaled are cohesion, viscosity, time, density and length. Due to these scaling rules, only specific materials are appropriate for usage in analogue models simulating geological processes. This choice mainly depends on the length and time scale ratio between the natural prototype and the model. For the analogue modelling presented in this thesis, certain materials have been used. These include glass microspheres to simulate the brittle behaviour of rocks (e.g. upper lithosphere), silicone putty to simulate the viscous behaviour of highly viscous rocks (e.g. lower lithosphere), and glucose syrup to simulate the viscous behaviour of low-viscosity rocks (e.g. asthenosphere/sub-lithospheric mantle).

2.1. History of analogue modelling

Probably the first documentation of an analogue experiment to simulate a geological process was presented in the *Transactions of the Royal Society of Edinburgh* by Sir James Hall [*Hall*, 1815]. Here, he described his first attempts to model folding in geological strata, as he had observed in a belt of deformed Silurian clastic rocks that run across the southern Uplands of Scotland from Galloway to Berwickshire. Two experiments were performed. In the first experiment, several pieces of cloth, linen and woollen fabric were spread out on a table, one above the other. A flat door was put on top of the layered stack, being loaded with weights, to confine the stack. Next, two boards were applied to the sides of the stratified mass and were subsequently forced towards each other. This resulted in the gradual uplift of the heavy door, while the strata were constrained and adopted upward and downward bending folds. In the second experiment, beds of clay confined in a box were subjected to lateral compression due to movement of movable ends driven by screw jacks, which is basically the same experimental design as is still in use today for fold and thrust type experiments. This experiment resulted in the generation of folds in the strata. The similarity between the folds reproduced in the experiments and folds observed in natural strata led the author to conclude that folds observed in nature must have a similar origin as in the experiment and therefore are

the result of horizontal compression. This hypothesis had already been proposed by *de Saussure* [1796], where he spoke of a lateral push as the cause for shortening and folding of rocks in the Alps. This experiment illustrated over almost two centuries ago the potential of analogue modelling techniques to understand geological structures.

Since the pioneering experiments in the early 1800's, several other modellers followed in the late 1800's studying fractures, folds and thrusts [e.g. *Favre*, 1878; *Daubre*, 1879; *Schardt*, 1884; *Cadell*, 1889; *Willis*, 1893]. In the 20th century, analogue modellers started to investigate a wider range of geological problems with similar modelling techniques [*Mead*, 1920; *Link*, 1930; *Escher and Kuenen*, 1929; *Kuenen and de Sitter*, 1938; *Nettleton and Elkins*, 1947; *Hubbert*, 1951; *Cloos*, 1955; *Parker and McDowell*, 1955; *Ramberg*, 1955; *Oertel*, 1962].

A major step forward in analogue modelling came with the advent of a well-founded scaling theory for analogue modelling of geological processes, provided by *Hubbert* [1937]. This theory revolutionised analogue modelling by changing it from a descriptive tool to a quantitative technique, thus making it an efficient and reliable tool to study geological processes at various scales (e.g. from microstructure analysis to large-scale tectonic processes) [*Koyi*, 1997]. According to *Hubbert* [1937] an analogue model is a good representative of a natural prototype, if it follows the three aspects of similarity: geometric, kinematic and dynamic. Since *Hubbert* [1937] several other papers have been published on scaling of analogue models applied to geological processes [*Hubbert*, 1951; *Horsfield*, 1977; *Shemenda*, 1983; *Richard*, 1991; *Davy and cobbold*, 1991, *Cobbold and Jackson*, 1992].

Another major step forward in analogue modelling, especially for modelling of large-scale tectonic processes, came in the 1980's, when realistic models were build to simulate crustal and lithospheric-scale processes [*Faugere and Brun*, 1984; *Davy and Cobbold*, 1988]. Here, different types of material (brittle and viscous) were combined in one model to simulate a rheologically stratified crust and mantle, e.g. conform to the predicted strength profiles for the Earth's crust and lithospheric mantle [*Davy and Cobbold*, 1988, 1991]. In these experiments, the materials were chosen as such, that the experiments were properly scaled when executed in the normal field of gravity. However, one limitation of such models is that they are unable to take into account the rheological modifications due to temperature variations during crustal or lithospheric scale deformation [*Brun*, 1999], such as occur during subduction and rifting. Some attempts have been made to find appropriate analogue materials to be used in thermomechanical modelling [*Cobbold and Jackson*, 1992; *Rossetti et al.*, 1999] and has, for instance, proven to be useful in modelling the thermomechanical development of orogenic wedges [*Rossetti et al.*, 2000]. Some initial attempts have been made to build thermomechanical models to simulate crustal and lithospheric scale processes such as continental collision and subduction [*Boutelier and Chemenda*, 2002].

2.2. Modelling techniques

Several different techniques have been used to construct analogue models of large-scale tectonic processes, such as subduction, rifting, gravity spreading, indenter tectonics, escape tectonics and convection. A first division can be made between models, which are designed as such to be used in the normal field of gravity and models constructed for the usage in an artificially high field of gravity.

The latter of these two groups are performed in a centrifuge, where the centrifugal force plays the same role in the models as the force of gravity does in geological processes. The advantage of this technique is that the analogue materials used for centrifuge experiments have a relatively high strength and are therefore relatively easy to work with during construction and analysis of the model. The obvious disadvantage is that an entire (expensive) centrifuge is needed to conduct an experiment. Furthermore, every time an intermittent stage in the structural evolution of an experiment needs to be examined, the machine has to be turned of. Centrifuge modelling was first introduced to analogue modelling of geological processes by *Bucky* [1931]. The centrifuge modelling technique took a great step forward in the early 1960's due to the work of Hans Ramberg, who build an entire analogue lab around a centrifuge at the University of Uppsala in Sweden. His work led to a better understanding of the role of gravity in deformation of the earth's crust and lithosphere [*Ramberg*, 1967, 1981]. From this time onwards, centrifuge modelling has been widely used to investigate geological processes [*Ramberg*, 1970; *Dixon*, 1974, 1975; *Talbot*, 1977; *Dixon and Summers*, 1985; *Koyi*, 1988; *Liu and Dixon*, 1991; *Koyi and Skelton*, 2001]. The centrifuge technique has dominated analogue modelling for some three decades, but has now largely been replaced by analogue models deformed in the normal field of gravity, in which much weaker materials are used [*Koyi*, 1997].

Experiments performed in the normal field of gravity should be made of extremely weak materials, in order to be properly scaled for gravity. The advantage of this approach is that it does not require an (expensive) centrifuge in order to run an experiment and that the evolution of an experiment can be recorded continuously. Furthermore, most materials used in these type of experiments (such as granular material and syrups) are relatively cheap and easy to obtain (except for silicone putties). A disadvantage of this approach is that the construction of models is more difficult, especially for experiments with inverted density profiles (e.g. a dense oceanic lithosphere overlying a less dense sub-lithospheric mantle). Several different modelling approaches exist, which are mainly related to the rheological approximation of the lithosphere and sub-lithospheric mantle.

(1) The first approach has been developed by the analogue modelling group in Rennes (France). In this approach, analogue models are constructed of materials with different rheologies (brittle and viscous), to incorporate the different behaviour of rocks at different depths in the crust and mantle. Brittle behaviour in rocks is modelled by granular material (such as sand), which deforms conform a Mohr-Coulomb type behaviour [*Mandl*, 1977]. The viscous behaviour of rocks is simulated with viscous material such as silicone putty, honey and glucose syrup. These models have been used to investigate a wide variety of geological phenomena, including extrusion tectonics, subduction, rollback, back-arc extension, gravity spreading and continental collision [*Faugere and Brun*, 1984; *Davy and Cobbold*, 1988, 1991; *Ratschbacher et al.*, 1991; *Brun et al.*, 1994; *Faccenna et al.*, 1996, 1999; *Hatzfeld et al.*, 1997; *Brun*, 1999; *Diraison et al.*, 2000; *Keep*, 2000; *Martinod et al.*, 2000; *Schellart et al.*, 2002a,b,c; *Burg et al.*, 2002].

(2) In a second approach, plastic materials are used to model the deformation of rocks. This approach has been used to model the India-Eurasia collision [*Tapponnier et al.*, 1982]. This approach has also been applied by Alexander Chemenda, with models primarily constructed of plastic and viscoplastic hydrocarbon waxes to simulate the lithosphere and water to simulate the asthenosphere. These models have been build to investigate processes such as subduction, extension, slab rollback and back-arc deformation [*Shemenda*, 1992, 1993, 1994; *Shemenda and Grocholsky*, 1992, 1994; *Chemenda et al.*, 1995, 1996, 1997, 2000, 2001].

(3) In a third approach, the lithosphere and sub-lithospheric mantle are modelled with viscous rheologies only. Each layer is represented by a material with a homogeneous viscous rheology. Thus, these experimental designs are effectively the same as those used in numerical models using the thin viscous sheet approximation to simulate the lithosphere [e.g. *Bird and Piper*, 1980; *England and McKenzie*, 1982, 1983; *Vilotte et al.*, 1982; *Houseman and England*, 1986]. With such an analogue set-up, modellers have investigated slab kinematics and dynamics during subduction [*Olson and Kincaid*, 1991; *Griffiths et al.*, 1995; *Guillou-Frottier et al.*, 1995; *Funiciello et al.*, 2000, 2002; *Faccenna et al.*, 2001b].

(4) In a fourth approach, the lithosphere and sub-lithospheric mantle are modelled with temperature dependent viscous or plastic rheologies. An appropriate vertical temperature gradient is applied to the experiment, simulating the geothermal gradient in the Earth's lithosphere and sub-lithospheric mantle, thus influencing the rheological behaviour of the analogue materials during deformation. These models have been build to investigate various geological processes such as rifting [*Brune and Ellis*, 1997], subduction [*Kincaid and Olson*, 1987] and the thermomechanical development of orogenic wedges [*Rossetti et al.*, 2000].

All the analogue experiments described in this thesis were performed in the normal field of gravity. I have followed the first approach described above (brittle-viscous layered models) to model the processes of arc and back-arc deformation in order to get an understanding of the surficial deformation patterns observed in arc - back-arc regions. I have followed the third approach described above (thin viscous sheet models) to model the processes of subduction, slab rollback and mantle convection.

2.3. Scaling

In analogue or physical modelling of geological processes certain scaling rules should be followed in order to make the model a good analogue of the natural prototype. The theory of these rules was first introduced by *Hubbert* [1937] and was later discussed by *Hubbert* [1951], *Horsfield* [1977], *Shemenda* [1983], *Richard* [1991], *Davy and Cobbold* [1991] and *Cobbold and Jackson* [1992]. For a thorough discussion of these rules, the reader is referred these authors or to Appendix I.

According to *Hubbert* [1937], a model is properly scaled to its natural counterpart if it is geometrically, kinematically and dynamically similar. An analogue model and a natural prototype are geometrically similar if all the corresponding lengths are proportional and all the corresponding angles within the bodies are equal. For kinematic similarity, the geometrically similar model and prototype have to undergo similar changes of shape and/or position, where the time required for any change in the model is proportional for the corresponding change in the prototype [*Ramberg*, 1967]. Finally, for dynamical similarity between a geometrically and kinematically similar model and prototype, the two bodies have to have similar ratios and distributions of different kinds of forces (gravitational, frictional and viscous) acting on the different particles of the body.

In mechanical analogue modelling, the most important relationship is the one that relates body forces (due to gravity) to surface forces (stresses) [*Davy and Cobbold*, 1991]. This relationship can be found in Cauchy's equation of motion for a continuous medium, describing the balance of linear momentum:

$$\rho\frac{D^2x_i}{Dt^2}=\frac{\partial\sigma_{ij}}{\partial x_j}+\rho g_i \qquad (i,j=1,2,3) \qquad (2\text{-}1)$$

where ρ is the density, x_i and x_j are position vectors, t is the time, σ_{ij} is Cauchy's stress tensor and g_i is the acceleration due to gravity. The suffixes refer to Cartesian vector and tensor components in a fixed spatial frame.

For slow motions, the only forces to be considered are body forces and surface forces. Therefore, it is reasonable to neglect inertial forces [*Davy and Cobbold*, 1991] and thus the left-hand term in equation (2-1) can be removed. Rearrangement of equation (2-1) leads to:

$$\partial\sigma_{ij}=-\rho g_i\partial x_j \qquad (2\text{-}2)$$

When the experiments are executed in a normal field of gravity, then gravity is the same for both model and nature. Integrating equation (2-2) with the condition that normal and shear stresses at the Earth's surface are negligible compared to stresses at depth and rewriting for both the analogue model (superscript a) and the natural prototype (superscript n), and dividing the first by the last results in (see also Appendix I):

$$\frac{\sigma_{ij}^a}{\sigma_{ij}^a}=\frac{\rho^a x_j^a}{\rho^a x_j^a} \qquad (2\text{-}3)$$

From equation (2-3) it can be concluded that stresses should scale down in a similar way that the product of density and length scale down.

Furthermore, for brittle material, cohesion has the dimension of Pascal (Pa) and therefore should be scaled down in a similar way that stresses scale down [*Horsfield*, 1977; *Davy and Cobbold*, 1988; *Cobbold and Jackson*, 1992]. Since the cohesion of rocks can range up to ~ 110 MPa (see *Schellart* [2000] and references therein), the maximum appropriate cohesion of the analogue material with a scale ratio of, for example, 10^{-6} and a density ratio of 0.5 is ~ 55 Pa. Furthermore, non-dimensional quantities such as the friction coefficient should be similar in both model and nature for proper scaling.

Viscosity has the dimensions of Pa·s and therefore scales down as the product of stresses and time scales down [*Cobbold and Jackson*, 1992]. For example, with a time ratio of 1.14×10^{-11} (1 hour in experiment corresponds to 10 Myr in nature) and a stress ratio of 10^{-7}, upper mantle rocks with a viscosity of ~ 10^{20} Pa·s should be simulated with an analogue material with a viscosity of ~ 114 Pa·s.

2.4. Materials

A wide variety of materials have been used in analogue modelling of geological processes. Since *Hall*'s [1815] pioneering analogue experiments, using cloth, linen, woollen fabric and clay, modellers have sought and used a wide variety of materials in their models to properly scale the variety in rheological behaviour of rocks, such as brittle, viscous and plastic behaviour. These materials include various sorts of cohesive and non-cohesive materials. Examples of cohesive materials used in analogue models include clay [*Riedel*, 1929; *Ramberg*, 1967; *Wilcox et al.*, 1973; *Rixon*, 1978], wax [*Ramberg*, 1967; *Brune and Ellis*, 1997], plasticine [*Cobbold*, 1975; *Tapponnier et al.*, 1982] hydrocarbons [*Shemenda*, 1993,

1994; *Chemenda et al.*, 2000], silicone putty [*Ramberg*, 1967; *Davy and Cobbold*, 1988, 1991; *Faccenna et al.*, 1996, 1999; *Brun*, 1999; *Diraison et al.*, 2000; *Schellart et al.*, 2002a,b,c], bouncing putty [*Ramberg*, 1967], honey [*Diraison et al.*, 2000], glucose syrup [*Davy and Cobbold*, 1988; *Griffiths et al.*, 1995; *Faccenna et al.*, 1996, 1999; *Schellart et al.*, 2002a,b,c], golden syrup [*Griffiths et al.*, 1995], corn syrup [*Guillou-Frottier et al.*, 1995], gum rosin [*Cobbold and Jackson*, 1992], sugar solution [*Davy and Cobbold*, 1991; *Kincaid and Olson*, 1987; *Buttles and Olson*, 1998] and water [*Shemenda*, 1993, 1994; *Chemenda et al.*, 2000]. Examples of non-cohesive materials used in analogue models include sand [*Hubbert*, 1951; *Horsfield*, 1977; *Davy and Cobbold*, 1988, 1991; *Brun*, 1999; *Faccenna et al.*, 1996, 1999; *Diraison et al.*, 2000], glass microspheres [*Schellart et al.*, 2002a,b,c], hollow microspheres [*Schellart et al.*, 2002a,b,c; *Rossi*, 2002], sugar [*Keep*, 2000], and other granular materials [*Krantz*, 1991; *Schellart*, 2000]). From the cohesive materials, several materials are more suitable to model plastic and viscoplastic behaviour (wax, plaster, clay, turpentine, asphalt, heavy oil, hydrocarbons), while others are more appropriate to model viscous behaviour (silicone putty, bouncing putty, honey, glucose syrup, sugar solution, water). The non-cohesive or granular materials are most suitable to model brittle deformation in rocks, since these materials deform according to the Mohr-Coulomb fracture theory [*Mandl et al.*, 1977; *Mandl*, 1988; *Krantz*, 1991, *Schellart*, 2000], in which clear defined localised shear bands develop during deformation, bounding relatively undeformed blocks.

Below, the materials that were used in the analogue experiments presented in this thesis will briefly be described. For a thorough discussion of the physical properties and the suitability of these brittle and viscous materials the reader is referred to Appendix III and IV respectively.

2.4.1. Brittle materials

In analogue modelling of large scale tectonic processes, granular material such as sand has often been used to simulate brittle deformation of rocks [*Hubbert*, 1951; *Horsfield*, 1977; *Davy and Cobbold*, 1988, 1991; *Ratschbacher et al.*, 1991; *Brun et al.*, 1994; *Faccenna et al.*, 1996, 1999; *Hatzfeld et al.*, 1997; *Keep*, 2000; *Martinod et al.*, 2000; *Schellart et al.*, 2002a,b,c; Burg et al., 2002]. The philosophy behind the suitability was that granular material displays a Mohr-Coulomb type behaviour, where its strength increases with increasing confining pressure. Granular material tends to localise deformation in relatively narrow shear zones or faults, comparable to the formation of faults and shear zones in brittle rocks. Sand is also characterised by a drop in stress during formation of faults, due to a loss of cohesion of the material [*Krantz*, 1991]. Furthermore, granular material has a friction coefficient which is comparable to the friction coefficient of rocks and was assumed to have a negligible cohesion, which would therefore make it a suitable analogue, especially when used in experiments with a small scale ratio (and therefore a small stress ratio), such as crustal and lithospheric scale models (scale ratio ~ 10^{-7}-10^{-6}). However, shear test results for various granular materials demonstrated that sand in particular can have cohesion values of up to ~ 500 Pa for normal stresses greater than ~ 600 Pa [*Krantz*, 1991], which would lead to an up-scaled cohesion of 500 - 5000 MPa for rocks in nature, when scale ratios of 10^{-7}-10^{-6} are applied. Values for cohesion of rocks are much lower (up to ~ 110 MPa). However, the shear test results of *Krantz* [1991], suggested that well-rounded spherical granular material might have a smaller cohesion, which would make it a better analogue to be used in analogue models. Therefore, I have conducted numerous shear test experiments for different types of

granular material with different roundness and sphericity values (sand, sugar, glass microspheres) to investigate which granular material would be most suitable to be used in analogue modelling of large-scale tectonic processes (see Appendix III and also *Schellart* [2000]). From these shear test experiments it was clear that finegrained glass microspheres are most suitable, since they have the smallest cohesion and a friction coefficient which comes closest to the friction coefficient of rocks in nature.

One disadvantage of granular material is that the width of shear zones in granular materials is relatively large in comparison to the width of shear zones in nature. The width increase with increasing grain size and therefore it is best to use granular material with a relatively small grain size (~ 50-100 μm). However, a decrease in grain size results in an increase in "van der Waals bonding" (an electrostatic force) between individual particles, which increases the overall cohesion of the material and therefore places a lower limit on the grain size for granular material in analogue modelling. Furthermore, it should be kept in mind that initiation of faulting in granular material occurs after more strain than in rocks. For example, dry sand can absorb up to 10 % of diffuse plastic deformation [*Benes and Davy*, 1996] before localisation of strain occurs in narrow fault zones or shear zones, while rocks commonly start to rupture after ~ 2 % of strain [*Davis*, 1984]). Thus, granular material can absorb a considerable amount of diffuse strain before faulting, probably because of the reorganisation of individual grains in the granular pack prior to faulting.

2.4.2. Viscous materials

In analogue modelling of large-scale tectonic processes basically two types of viscous materials have been used which both have an approximately Newtonian viscosity: a silicone putty or silicone oil (relatively high viscosity) and any kind of sugar solution (honey, glucose syrup, corn syrup, golden syrup, sugar solution, sucrose solution) (relatively low viscosity). In the experiments described in this thesis, I have used a silicone putty (Rhodorsil Gum FB, manufactured by Rhodia, France) as a relatively high viscosity material and glucose syrup (manufactured by Colonial Farms, Australia) as a relatively low viscosity material.

The silicone putty has a viscosity of ~ 2×10^4 Pa·s (at room temperature), is transparent and has a density of 970 kg/m^3. This density can be changed by mixing the putty with a dense filler. I have used finegrained iron powder as filler (grainsize of 0-150 μm). With this method, the density of the silicone putty has been increased to 1200 – 1600 kg/m^3 without changing the viscosity of the material significantly. However, the addition of filler to the silicone putty makes the mix opaque. An advantage of this material is that it is relatively easy and clean to work with, and its density can be varied according to needs without changing its mechanical properties significantly. Furthermore, the material can be moulded into sheets with a desired geometry, it can be recycled and it is harmless to work with in experiments. Although the price at which this material has been obtained in Australia was relatively cheap (AU$ 13.- per kg), these prices may vary significantly in different countries (up to ~ AU$ 50.- per kg). Furthermore, the material (as any other high viscosity silicone putty) is not easily obtainable, since several main producers of silicone putties stopped the production some years ago [*P.R. Cobbold*, pers. comm.].

The glucose syrup has a viscosity of ~ 100 Pa·s (at room temperature), but this can be changed significantly by changing its water content (addition of water will decrease its viscosity) or by changing its temperature (decreasing the temperature will increase its viscosity). It has a density of ~ 1420 kg/m^3. An advantage of glucose syrup is that its viscosity

is a factor of ~ 200 smaller than that of the silicone putty (which is similar to factors between lithosphere and sub-lithospheric mantle as proposed by *Houseman and Gubbins* [1997] (~ 200) and *Faccenna et al.* [2001a] (~ 100 - 500). Furthermore, it is relatively transparent, it is a harmless chemical, cheap and easily available in large quantities (~ AU$ 50.- for a 25 kg drum). Although the syrup is relatively sticky, it can be relatively easily rinsed of with warm water. One disadvantage of the material is that it can attract large quantities of ants, which means that after every experiment, the lab has to be thoroughly cleaned.

2.5. Discussion

Results of analogue experiments will be described in the following chapters to test conceptual models of subduction, slab rollback, arc formation and back-arc extension. The analogue modelling technique was preferred above the numerical modelling technique, since the former can be better applied in four dimensions (three-dimensional space + time). Modelling in three-dimensional space is required when investigating the processes of rollback, arc formation and back-arc extension, since these processes show a strong non-linear behaviour in the direction parallel to the trench.

Analogue models to investigate back-arc deformation will be discussed in Chapter 4,5,6,7 and 8. These models have been built with a stratified brittle-high viscous-low viscous layer set-up to model the brittle upper lithosphere, the viscous lower lithosphere and the asthenosphere, respectively. The brittle top-layer was incorporated in the models, because it was of main interest in these studies to investigate the structural evolution in the models and compare such structures with structures observed in natural arc - back-arc systems. The low-viscosity lower layer was incorporated to scale the experiments for gravity. Similar type models have been constructed before and have been applied to investigate back-arc deformation in the Aegean Sea region [*Hatzfeld et al.*, 1997; *Gautier et al.*, 1999]. In this thesis, the investigation will be more quantitative, to get insights into parameters of importance in controlling the structural and geometrical evolution of arc -back-arc systems. In addition, the results will be compared with a number of natural examples of arc - back-arc systems.

Fluid dynamical models to investigate subduction, slab rollback and slab induced convection will be discussed in Chapter 9, 10 and 11. These models have been built with a stratified high viscous-low viscous layer set-up to model the lithosphere and the sub-lithospheric upper mantle. Analogue models with a similar model design have been constructed previously to model subduction and slab rollback in the mantle [*Jacoby*, 1973; *Kincaid and Olson*, 1987; *Funiciello et al.*, 2000, 2002; *Faccenna et al.*, 2001b]. The choice to model the lithosphere with a homogenous viscous sheet is a simplification that has been adopted before [*Bird and Piper*, 1980; *England and McKenzie*, 1982, 1983; *Vilotte et al.*, 1982; *Houseman and England*, 1986; *Griffiths et al.*, 1995; *Guillou-Frottier et al.*, 1995; *Funiciello et al.*, 2000, 2002; *Faccenna et al.*, 2001b]. Naturally, for many lithospheric phenomena a pure viscous rheology would not apply. However, for the long-term interaction between the subducting lithosphere and surrounding mantle, a viscous rheology would provide a good analogue [e.g. *Faccenna et al.*, 2001b]. In choosing boundary conditions of the model and the rheological parameters for the materials it was taken into consideration that it is intended to do similar simulations in three-dimensional space with the numerical modelling method in future research.

FOREWORD CHAPTER 3

In this chapter, four tectonic models are discussed, which attempt to explain the formation of arcs and back-arc basins. These four models are widely discussed in the literature and have been applied to numerous arc – back-arc systems. This chapter summarises these tectonic models and discusses the pros and cons of each of these individual models.

The ideas presented in this chapter are primarily the work of the author. The development of the ideas concerning collapse, potential energy and rollback benefited from discussions with Patrice Rey, Maarten Krabbendam, Mike Sandiford, Kurt Stüwe, Gordon Lister, Mark Jessell and Greg Houseman. A modified version of this chapter has been submitted for publication to *Special Paper - Geological Society of America.* A reference can be found at the end of the thesis in the bibliography.

CHAPTER 3

Tectonic models for the formation of arc-shaped convergent zones and back-arc basins

Abstract

In this chapter four popular tectonic models will be discussed that attempt to explain the formation of arc – back-arc systems. These systems develop in an overall convergent setting with shortening in the fore-arc region and extension in the back-arc region. The four models are the gravitational collapse model, the rollback model, the extrusion tectonics model and the oroclinal bending model. For the first model the internal buoyancy force and the strength of the lithosphere are the most important parameters to be considered, while for the last three models the lithospheric strength and plate boundary forces are the most important parameters. The rollback model can explain most arcs, such as those found in the Western Pacific and the Mediterranean, in combination with back-arc extension driven by retreat of the subducting plate. Slab rollback ultimately is a consequence of the negative buoyancy of the slab. Collapse models can explain extensional structures in high-standing mountain belts such as the Andes and Tibet, since these regions involve large potential energy contrasts between mountain range and foreland. However these models cannot explain the development of Western Pacific and Mediterranean style arcs. The extending regions have a thin crust and therefore relatively small potential energy, which cannot drive back-arc extension and arc formation. The extrusion tectonics model can explain strike-slip structures such as observed in the Eastern Alps, Anatolia and East Asia, but fails to explain back-arc extension. The extrusion of a wedge cannot produce shortening at its leading edge contemporaneously with extension in the middle of the wedge. Oroclinal bending may result from different processes, but this mechanism provides no driving forces, and thus physically does not explain the formation of arc - back-arc systems. Of the mechanisms considered, slab rollback is the only concept based on sound physical principles that explains all of the observed geometries, and which can be simulated and modelled in numerical and analogue experiments.

3.1. Introduction

3.1.1. Contemporaneous shortening and extension

The synchronous occurrence of shortening and extension in close spatial arrangement has been noted for many convergent tectonic settings. These include arc – back-arc systems, which develop in an overall convergent tectonic setting, with shortening in the overriding plate close to the subduction interface and extension on the concave side of the arc (back-arc region). Numerous examples have been documented in the Western Pacific region and the Mediterranean region (Fig. 1-1). Arc – back-arc systems from the Mediterranean region are especially interesting, since they involve large amounts of shortening in the overriding plate close to the subduction zone, synchronously with extension in the back-arc region. Examples from the Mediterranean region include the Hellenic region, with extension in the Aegean Sea

and shortening in the surrounding outer Hellenic arc [*McKenzie*, 1978; *Le Pichon*, 1982], and the Alboran region with extension in the Alboran Sea and shortening in the surrounding Betic-Rif arc [*Platt and Vissers*, 1989; *Lonergan and White*, 1997]. Two other examples include the Tyrrhenian domain with extension in the Tyrrhenian Sea and shortening in the Maghebrides – Calabria – Apennines region [*Malinverno and Ryan*, 1986; *Channel*, 1986; *Carmignani and Kligfield*, 1990], and the Pannonian region with extension in the Pannonian Basin and shortening in the surrounding Carpathian arc [*Royden et al.*, 1983].

Similar observations of shortening and extension have been made for several orogenic systems, with shortening at the edge of the mountain range and extension in its interior. Examples include the Central Andes [*Mercier*, 1981; *Sébrier et al.*, 1985], the Himalayas [*Molnar and Tapponnier*, 1975; *Ni and York*, 1978] and the Alps [*Ratschbacher et al.*, 1989]. The controversy of these discoveries is that shortening (σ_1 horizontal) is active at the same time that extension (σ_1 vertical) is active in relatively close proximity (tens to hundreds of kilometres). Shortening at the edge of the mountain belt is oriented perpendicular to the axis of the orogen and extension in the interior of mountain belts is often oriented parallel to the axis of the orogen (such as in the Eastern Alps and Tibet). In arc - back-arc systems, shortening at the convex side of the arc is oriented perpendicular to the arc and extension at the concave side of the arc is generally also oriented perpendicular to the arc.

3.1.2. Tectonic models

Different types of conceptual tectonic models have been proposed to explain the contemporaneous shortening-extension regimes, such as occur in arc – back-arc settings. Here, I will discuss four popular models. The first model is related to plate interior body forces (gravitational collapse model) and the latter three are related to plate boundary forces (rollback model, extrusion tectonics model and oroclinal bending model).

Gravitational collapse: In this model, shortening and extension are initiated and driven by the potential energy difference between the extending region and the surrounding shortening region (Fig. 3-1a) [*Sonder et al.*, 1987; *Dewey*, 1988; *Molnar and Lyon-Caen*, 1988; *England and Houseman*, 1988, 1989; *Platt and Vissers*, 1989; *Platt and England*, 1994].

Slab rollback: In this model, deformation results from retreat of the subducting slab, with extension in the overriding plate due to slab retreat and shortening in the overriding plate close to the trench due to friction along the subduction interface and accretion of material to the overriding plate (Fig. 3-1b) [*Malinverno and Ryan*, 1986; *Lonergan and White*, 1997].

Extrusion tectonics: In this model, arc formation and back-arc extension result from sideways escape of continental fragments away from a continent-continent collision zone (Fig. 3-1c) [*McKenzie*, 1972; *Ratschbacher et al.*, 1991].

Oroclinal bending: In this model, compression oriented parallel to the axis of an orogen would lead to outward bending of this orogen with the formation of a back-arc region on the concave side of the orocline and shortening on the convex side (Fig. 3-1d) [*Ghisetti and Vezzani*, 1982; *Van der Linden*, 1985; *Mantovani et al.*, 1997a,b; *Mantovani et al.*, 2000; *Gelabert et al.*, 2002].

In this chapter, the case for and against each tectonic model will be discussed, supported by some argumentation, empirical (geological) data and some analytical calculations. It will be argued that subduction rollback is the most likely candidate for the formation of arc – back-arc systems and can also play a significant role in extension in the interior of mountain belts.

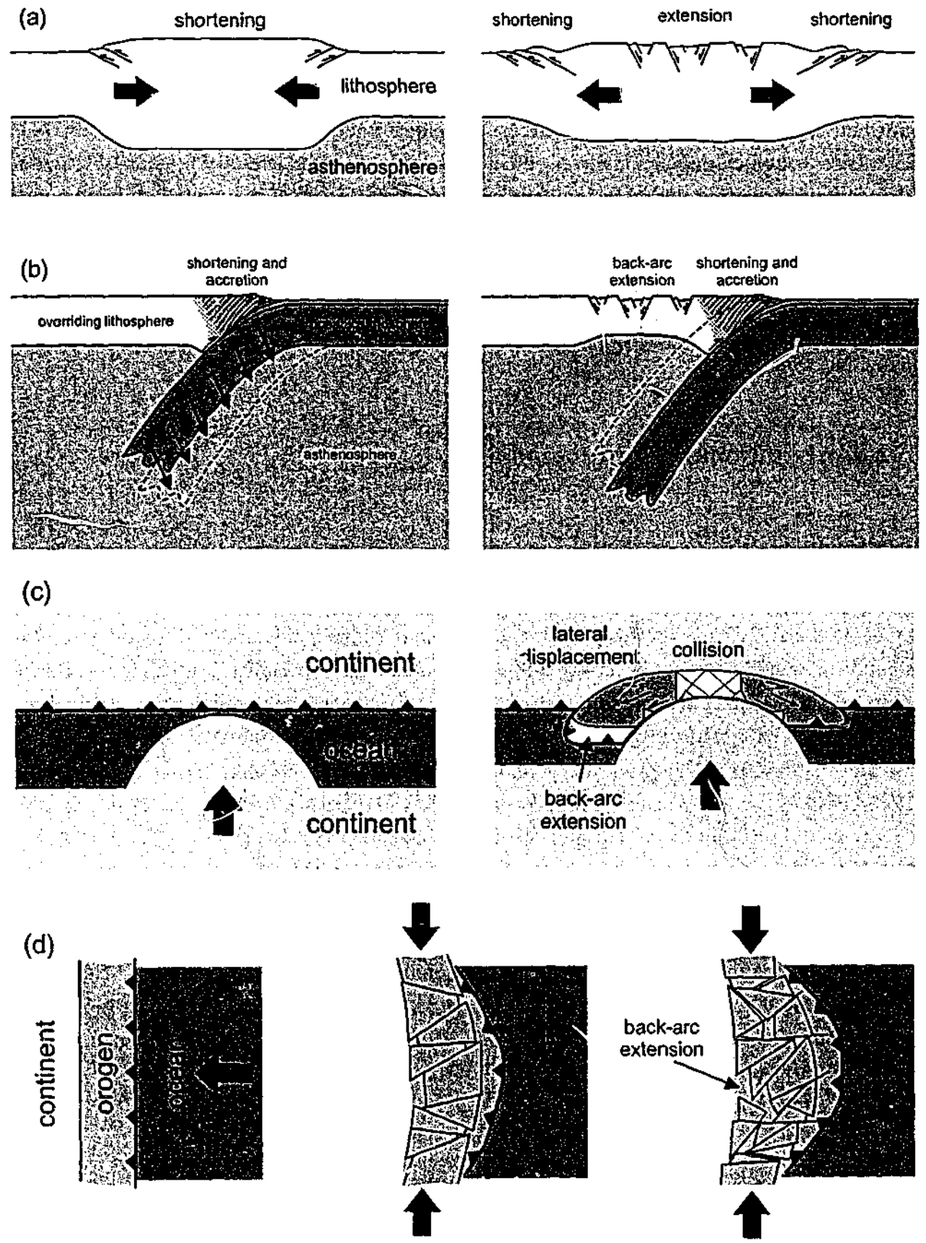

Fig. 3-1. Four possible mechanisms for the formation of arc – back-arc systems, with shortening in the fore-arc region and extension in the back-arc region. (a) Cross-section illustrating gravitational collapse resulting from the potential energy difference between the thickened lithosphere and the surrounding lithosphere, with extension in the thickened lithosphere and shortening in the foreland region (based on *Platt and Vissers* [1989]). (b) Cross-section illustrating collapse and extension of an overriding lithosphere resulting from rollback of a subducting oceanic lithosphere, which provides space for the thickened lithosphere to collapses into. Shortening occurs along the subduction interface due to friction and possible accretion of sediments from the subducting lithosphere to the overriding lithosphere (based on *Malinverno and Ryan* [1986]). (c) Top view sequence of extrusion tectonics of continental wedges away from a continent-continent collision zone, resulting in extension in between the leading and trailing edge of the wedge and shortening at the leading edge of the extruding wedge (redrawn from *McKenzie* [1972]). (d) Top view sequence showing oroclinal bending due to orogen-parallel compression resulting in outward bending of the orogen towards the oceanic side of the orogen, accompanied by shortening along the convex side and extension on the concave side of the orocline (redrawn from *Mantovani et al.* [2000]).

The role of the buoyancy force in gravitational collapse might be of significant importance in driving extension of thickened crust in orogenic belts, but in this scenario one has to take into account the strength of the surrounding foreland, which is often neglected, if one wants to attribute the collapse only to the excess potential energy stored in the mountain belt. Extrusion tectonics only seems to occur in orogens, which are laterally bounded by a zone that can retreat during the extrusion. It is not immediately clear if this boundary is retreating on its own or is actively being pushed back by the extruding orogenic wedge. If the latter is true, then this would contradict the presence of a zone of extension in between the leading and trailing edge of the extruded wedge. Finally, it will be argued that the oroclinal bending mechanism is not a sound physical mechanism to explain arc – back-arc related structures for numerous reasons.

3.2. Gravitational collapse model

3.2.1. Introduction

The gravitational collapse model has been mainly applied to presently high-standing mountain belts (Himalayas, Andes, Alps) and regions which were supposed to have been the sight of mountain belts in the geological past (Alboran Sea, Tyrrhenian Sea, Pannonian Basin, Aegean Sea). In this conceptual model, collapse of a mountain belt is initiated and driven by the potential energy difference between the mountain belt and the surrounding lowlands [*Sonder et al.*, 1987; *Dewey*, 1988; *Molnar and Lyon-Caen*, 1988; *England and Houseman*, 1988, 1989; *Platt and Vissers*, 1989; *Platt and England*, 1994]. The difference in potential energy would result in the collapse of the mountainous region and shortening in the lowlands (Fig. 3-1a), leading to regions with extensional structures in the centre, encircled by a radial pattern of shortening [*Dewey*, 1988; *Platt and Vissers*, 1989; *Platt and England*, 1994].

Following the concept outlined above, the potential energy difference is the driving force behind extension in the higher regions and shortening in the surrounding regions. The origin of this potential energy difference has been related to either a thickened crust only [*Molnar and Tapponnier*, 1978; *Molnar and Lyon-Caen*, 1988; *Dewey*, 1988] or to a thickened crust in combination with the convective removal of the lower part of the lithospheric mantle [*England and Houseman*, 1989; *Platt and England*, 1994, *Houseman and Molnar*, 1997]. This removal would occur because the protrusion of a cold lithospheric root in the asthenosphere should create lateral temperature gradients that drive convection, which could remove at least the lower (weak) part of the thickened lithosphere [*Houseman et al.*, 1981]. This sudden removal would lead to a rapid increase in potential energy which would trigger the collapse of the lithosphere [*Platt and England*, 1994].

Previous authors [*Dewey*, 1988; *Platt and Vissers*, 1989; *Platt and England*, 1994; *Liu and Shen*, 1998] have mentioned that extension in the interior of a mountain belt is accommodated by shortening in the surrounding lowlands, but have not considered the integrated strength of the surrounding lithosphere as a possible factor that could prevent collapse. Other authors do not specifically mention that extension in one place needs to be absorbed by shortening elsewhere [*Sonder et al.*, 1987; *England*, 1987; *Molnar and Lyon-Caen*, 1988; *England and Houseman*, 1988, 1989; *Liu and Furlong*, 1993; *Mareschal*, 1994; *Houseman and Molnar*, 1997]. But, as has been mentioned by *Platt and England* [1994], on a globe of constant radius, extension in the thickened zone must be accommodated by shortening elsewhere,

unless there is a retreating boundary (as in rollback) surrounding the thickened region that provides the space into which the thickened lithosphere can extend. Since this shortening requires energy, the integrated strength (for shortening) of the foreland must be incorporated in the calculations as well.

The collapse problem can be compared with the "cup of tea" analogy. Take a foam-board cup and fill it with tea. Place this cup of tea on the ground (simply for a reference level). Here, the tea could represent Tibet, the cup (made of foam-board) could represent the strong foreland immediately surrounding Tibet and the region surrounding the cup of tea represents the remainder of East Asia. In this analogy, the potential energy difference between the tea and the cup, as well as between the tea and the area surrounding the cup is great enough to let the tea collapse instantaneously. However, this does not happen, simply because the cup surrounding the tea is too strong to let the tea collapse. Is that not handy? Otherwise it would be very difficult to enjoy our cup of tea! Thus, without taking into consideration the strength of the cup (foreland), one would reach very wrong conclusions about the behaviour of the tea (Tibet).

In many numerical models simulating processes of lithosphere thickening and subsequent collapse, a thin viscous sheet approximation has been used to model the lithosphere [e.g. *Sonder and England*, 1986; *England*, 1987; *England and Houseman*, 1986, 1988, 1989; *Houseman and England*, 1993]. One of the problems with these models is that the lithosphere has the same strength for both extension and shortening, since it is approximated with a viscous sheet. However, more realistic lithospheric strength profiles [*Goetze and Evans*, 1979; *Brace and Kohlstedt*, 1980; *Kirby*, 1983; *Ranalli and Murphy*, 1987; *Stephenson and Cloetingh*, 1991] tell us that lithospheric strength for shortening can be as much as ~ three times greater than for extension. Therefore, collapse in such models might not be opposed by surrounding lithosphere in an appropriate manner.

In the following three sections, it will be discussed how potential energy and integrated strength are usually calculated and brought together to explain how the collapse model works. The potential flaws of the assumptions applied in these calculations are also discussed.

3.2.2. Potential energy calculations

For obtaining the driving force of gravitational collapse, one usually calculates the potential energy difference per unit area (ΔE_p) between a thickened (T) and reference (R) lithospheric column. This is done by integrating the lithostatic pressure difference between these columns from the Earth's surface to the isostatic compensation depth (z_c) [*Molnar and Lyon-Caen*, 1988, *Stüwe and Barr*, 2000]:

$$\Delta E_p = \int_0^{z_c}\int_0^{z} (\rho(z)g)_T \mathrm{d}z\mathrm{d}z - \int_0^{z_c}\int_0^{z} (\rho(z)g)_R \mathrm{d}z\mathrm{d}z \qquad (3\text{-}1)$$

where z is the depth below the surface ($z = 0$ is the surface of the highest column); $\rho(z)$ is the depth-dependent density; g is the acceleration due to gravity; and subscripts T and R denote thickened and reference column, respectively.

The density of crust and lithospheric mantle can be assumed to be constant or temperature dependent. For simplicity, the density has been assumed to be temperature independent, since I am only interested in the approximate potential energy difference between a thickened and

reference lithosphere. In Fig. 3-2a, two lithospheric columns have been plotted (T and R) for a temperature independent density of the lithosphere. The reference crust has a thickness H and the thickened crust has a thickness $h + H + \Delta H$, where h is the difference in topographic elevation between both columns and ΔH is the crustal root of the thickened column. Since the lithostatic pressure at depth $z = h + H + \Delta H$ is the same for both columns, integration is only necessary for $z = 0$ to $z_c = h + H + \Delta H$. The potential energy difference can be calculated by integrating equation (3-1), which results in [*Molnar and Lyon-Caen*, 1988]:

$$\Delta E_p = \tfrac{1}{2}\rho_{cr} g h^2 + \rho_{cr} g h H + \tfrac{1}{2}\rho_{cr} g h \Delta H \qquad (3\text{-}2a)$$

where ρ_{cr} is the density of the crust. This ΔE_p has been graphically illustrated in Fig. 3-2b, where the lithostatic pressure for both columns has been plotted. The area underneath each curve represents the potential energy of each column. The difference between the two areas is the ΔE_p between the two columns. Rewriting ΔE_p in terms of h and H, with:

$$\Delta H = \frac{\rho_{cr} h}{(\rho_m - \rho_{cr})} \qquad (3\text{-}2b)$$

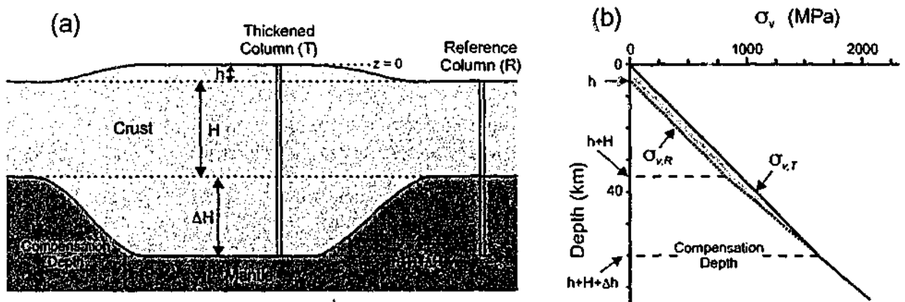

Fig. 3-2. (a) Diagram showing reference crust with thickness H and a thickened crust with a thickness $h + H + \Delta H$, which are both in isostatic equilibrium. (b) Vertical pressure for thickened (T) and reference (R) column, and the potential energy difference (ΔE_p) between the two columns (shaded grey region). (c) Relationship between thickening factor (T_F), elevation (h) and ΔE_p for a reference crust with $H = 30$ km. $T_F < 1$ indicates thinning and $T_F > 1$ indicates thickening.

results in:

$$\Delta E_p = \tfrac{1}{2}\rho_{cr} g h^2 + \rho_{cr} g h H + \frac{\rho_{cr}^2 g h^2}{2(\rho_m - \rho_{cr})} \qquad (3\text{-}2c)$$

One can now plot h as well as plot the thickening factor (F_T) against ΔE_p for a given H value. Here, F_T can be expressed as:

$$F_T = \frac{h + H + \Delta H}{H} = 1 + \frac{\rho_m h}{(\rho_m - \rho_{cr})H} \qquad (3\text{-}2d)$$

This has been done in Fig. 3-2c. Here one can observe that ΔE_p is quadratically dependent on h and therefore also on F_T. In this plot, I have chosen the reference crust to be 30 km thick, which has subsequently been homogeneously thickened by a factor F_T. Furthermore, I assume total isostatic compensation at the base of the thickened crust and I have chosen $\rho_{cr} = 2750$ kg/m^3 and $\rho_m = 3300$ kg/m^3. For example, if $F_T = 1$ (no thickening), then $h = 0$ km, $\Delta H = 0$ km and $\Delta E_p = 0$ N/m. If $F_T = 2$, this results in $h = 5$ km, $\Delta H = 25$ km, and a total ΔE_p between T and R of ~ 6.1 x 10^{12} N/m.

3.2.3. Integrated strength

The integrated strength of the lithosphere is a factor that resists deformation. The integrated strength is a combination of the brittle resistance of the upper lithosphere and the viscous resistance of the lower lithosphere to deformation. The brittle strength of pre-fractured rocks can be expressed using Byerlee's law [*Byerlee*, 1978]:

$$\tau = \mu\sigma_n \qquad (\mu = 0.85) \qquad (\sigma_n < 200 \text{ MPa}) \qquad (3\text{-}3a)$$

$$\tau = \mu\sigma_n + C \qquad (\mu = 0.6,\ C = 60 \text{ MPa}) \qquad (200 < \sigma_n \leq 1700 \text{ MPa}) \qquad (3\text{-}3b)$$

where τ is the shear stress; μ is the coefficient of internal friction; σ_n is the normal stress; and C is the cohesion. Equations (3-3a) and (3-3b) can be rewritten in terms of principal stresses by using the following equations:

$$\sigma_1 - \sigma_3 = \frac{(K-1)}{K}\rho g z(1-\lambda) + \frac{S}{K} \qquad \text{(extension)} \qquad (3\text{-}4a)$$

$$\sigma_1 - \sigma_3 = (K-1)\rho g z(1-\lambda) + S \qquad \text{(shortening)} \qquad (3\text{-}4b)$$

(see Appendix II for a derivation of equation (3-4a) and (3-4b))
with:

$$S = \frac{2C\sin 2\theta_f}{1+\cos 2\theta_f} \qquad K = \frac{1-\cos 2\theta_f}{1+\cos 2\theta_f} \qquad 2\theta_f = 90 + \phi \qquad \mu = \tan\phi \qquad (3\text{-}4c)$$

where σ_1 and σ_3 are the maximum and minimum principal stress, respectively; λ is the pore fluid factor; K is a parameter depending on the fracture angle; S is the fracture strength under uniaxial compression with zero confining pressure; θ_f is the fracture angle; and ϕ is the angle of internal friction. Combining equation (3-3) and (3-4) results in:

$$\sigma_1 - \sigma_3 = 0.79\rho g z(1-\lambda) \qquad \sigma_1 - \sigma_3 < 500 \text{ MPa} \qquad \text{(extension)} \qquad (3\text{-}5ai)$$

$$\sigma_1 - \sigma_3 = 0.68\rho g z(1-\lambda) + 68 \text{ MPa} \qquad \sigma_1 - \sigma_3 > 500 \text{ MPa} \qquad \text{(extension)} \qquad (3\text{-}5aii)$$

$$\sigma_1 - \sigma_3 = 3.68\rho g z(1-\lambda) \qquad \sigma_1 - \sigma_3 < 500 \text{ MPa} \qquad \text{(shortening)} \qquad (3\text{-}5bi)$$

$$\sigma_1 - \sigma_3 = 2.12\rho g z(1-\lambda) + 212 \text{ MPa} \qquad \sigma_1 - \sigma_3 > 500 \text{ MPa} \qquad \text{(shortening)} \qquad (3\text{-}5bii)$$

The viscous strength of rocks, deforming at a specific strain rate, can be calculated by the following power law [*Kirby*, 1983]:

$$\sigma_1 - \sigma_3 = \left|\frac{\dot{\varepsilon}}{A}\right|^{\frac{1}{n}} e^{\frac{Q}{nRT}} \qquad (3\text{-}6)$$

where $\dot{\varepsilon}$ is the strain rate; A, n and Q are material constants; and R is the gas constant. *Brace and Kohlstedt* [1980] have used the following flow laws for the viscous strength of olivine:

$$\sigma_1 - \sigma_3 = \left|\frac{\dot{\varepsilon}}{A}\right|^{\frac{1}{n}} e^{\frac{Q}{nRT}} \qquad \sigma_1 - \sigma_3 < 200 \text{ MPa} \qquad (3\text{-}7a)$$

$$\sigma_1 - \sigma_3 = \sigma_D\left\{1 - \left[\frac{RT}{Q_D}\ln\left(\frac{\dot{\varepsilon}_D}{\dot{\varepsilon}}\right)\right]^{1/2}\right\} \qquad \sigma_1 - \sigma_3 > 200 \text{ MPa} \qquad (3\text{-}7b)$$

where $\dot{\varepsilon}_D$ is the pre-exponential constant for Dorn law creep; Q_D is the activation energy for Dorn law creep; and σ_D is the threshold stress for Dorn law creep. Combining equation (3-5) for the brittle strength of rocks and equation (3-6) and/or (3-7) for the viscous strength of rocks leads to the well known strength profiles for lithospheric columns [*Goetze and Evans*, 1979; *Brace and Kohlstedt*, 1980; *Kirby*, 1983; *Ranalli and Murphy*, 1987; *Stephenson and Cloetingh*, 1991]. The integrated strength of the lithosphere at a specific strain rate can then be calculated by integrating the differential stress over its depth range [*Sonder and England*, 1986; *Ranalli*, 1987]:

$$\text{Integrated Strength} = \int_0^{z_l} (\sigma_1 - \sigma_3)\,dz \qquad (3\text{-}8)$$

where z_l is the base of the lithosphere.

3.2.4. Why gravitational collapse?

The possibility of gravitational collapse of a thickened lithosphere is investigated for different stages in the thermal evolution of the thickened (T) and reference (R) lithosphere (Fig. 3-3). Let us consider a 120 km thick lithosphere with a crust with an original thickness of 30 km, a crustal density of 2750 kg/m^3 (granite) and a mantle density of 3300 kg/m^3 (olivine) (Fig. 3-3a). For the temperature, a linear geotherm has been used for the crust, where the temperature increases from T_0 = 273 °K at the surface to T_{Moho} at Moho depth (598°K, 673°K, 773°K, 873°K and 973°K) and a linear geotherm for the lithospheric mantle which

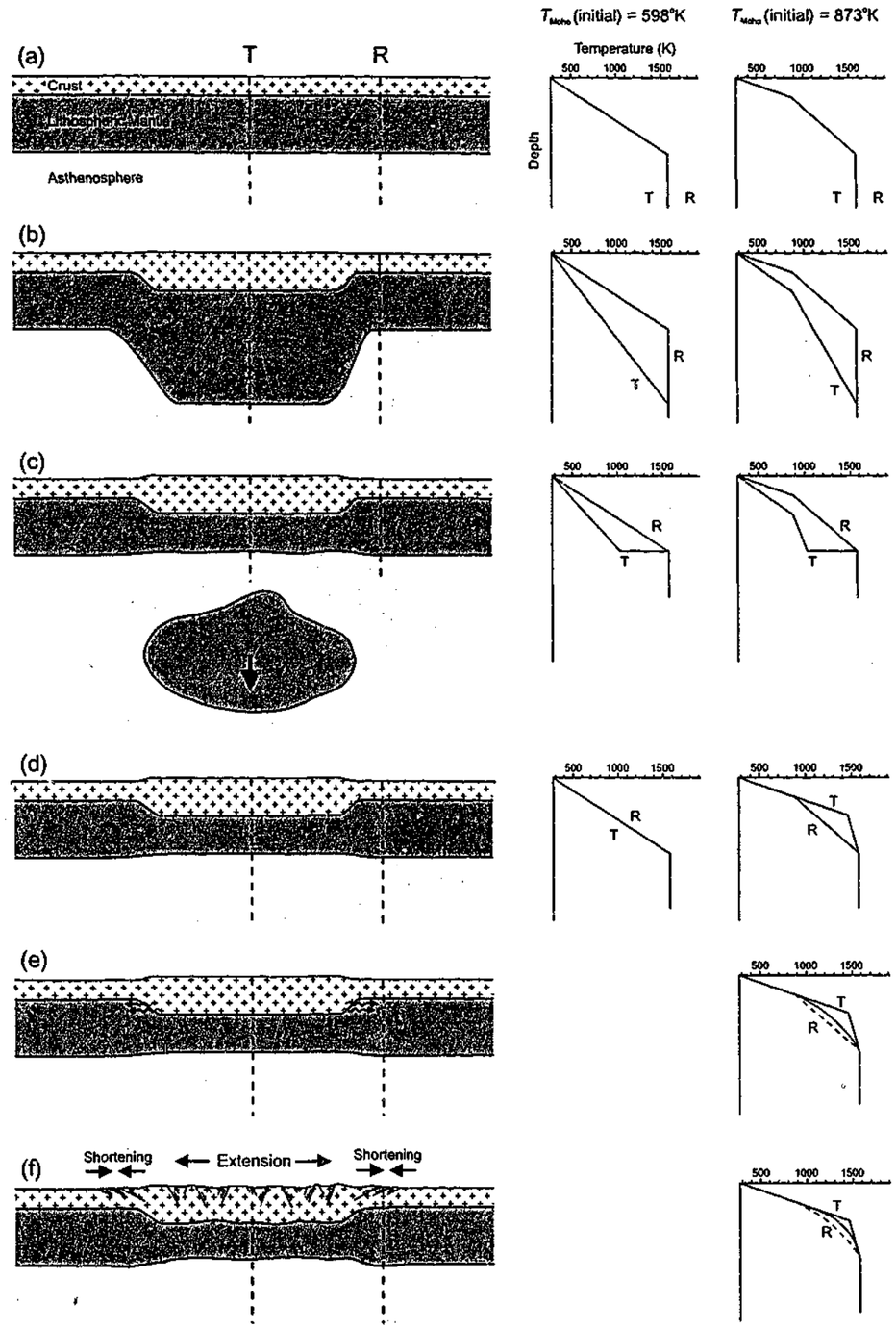

Fig.3-3. Thermal evolution of a lithosphere experiencing shortening and thickening (T) and the lithosphere surrounding the thickened lithosphere (R). Evolution is for two different initial geotherms with a different initial Moho temperature. (a) initial stage, (b) thickening by a factor of two, (c) convective thinning, (d) thermal relaxation of T, (e) lateral heat flow from the lower crust of T to the upper mantle of R, (f) extensional collapse in T and shortening in R. Integrated strengths of T and R for five different initial Moho temperatures have been plotted in Fig. 3-4a (entire lithosphere) and Fig. 3-4b (crust only) for stages (a), (c), (d) and (e).

increases from T_{Moho} to T_1 = 1573°K at the base of the lithosphere. The temperature in the asthenosphere is constant and equals 1573°K. At some stage, part of this lithosphere is thickened homogeneously by a factor of two (Fig. 3-3b). Thermal advection during shortening is assumed to be dominant over thermal relaxation. This assumption is valid for strain rates of ~ ≥ 10^{-15}, where deformation of lithosphere occurs practically isothermally [*England*, 1987] but might be an oversimplification if it is compared with the Tibetan Plateau, for which it has been suggested that it has been thickened at a strain rate of ~ 3-5 x 10^{-16} s^{-1} during the last 45 Myr [*England and Houseman*, 1989]. After thickening, the lower 120 km of the lithospheric mantle of T is convectively removed before significant thermal relaxation has occurred (Fig. 3-3c). When total isostatic compensation is assumed (at the base of the crust), this leads to an elevation h = 5 km for T. After some amount of time, T has reached thermal equilibrium (Fig. 3-3d). For the lithospheric columns with a relatively high Moho temperature it can be observed in Fig. 3-3d that T has a warmer geotherm than R due to the thicker crust. This will result in lateral heat flow from T to R (Fig. 3-3e), which will result in thermal weakening of R. Here, lateral heat flow is greatest for high initial Moho temperatures. This lateral heat flow may lead to such a decrease in strength of R that it is not capable to prevent collapse in T, which may finally lead to gravitational collapse (Fig. 3-3f).

Total integrated strengths for the thickened and reference lithosphere and crust with different initial Moho temperatures have been plotted in Fig. 3-4 during different stages in the evolution of the system. For the brittle strength, equation (3-5) has been used and for the viscous strength of granite (dry), equation (3-6) has been used. For the viscous strength of olivine, equation (3-7) has been used as a lower limit of the strength of the lithospheric mantle. In all plots and calculations the pore fluid pressure was zero. A relatively low strain rate of 10^{-16} s^{-1} (compared with the present E-W extensional strain rate of ~ 2 x 10^{-16} in the Tibetan Plateau [*Molnar and Qidong*, 1984; *England*, 1987] and the present extensional strain rate in the Basin and Range of ~ 3.5 x 10^{-16} [*Sonder et al.*, 1987]) has been used as a lower bound of geologically significant strain rates. Data for the material constants A, n, and Q have been obtained from *Ranalli and Murphy* [1987]. Data for the material constants σ_D, Q_D and $\dot{\varepsilon}_D$ have been obtained from *Sonder and England* [1986]. Below follows a description of three different types of collapse that have been proposed in the literature. The three types of collapse are lithospheric scale collapse [e.g. *Platt and England*, 1994], crustal scale collapse [e.g. *Liu and Shen*, 1998] and lower crustal collapse (or flow) [e.g. *Bird*, 1991]. The lithospheric and crustal collapse models follow the scenario outlined above and some integrated strength calculations are plotted in Fig. 3-4.

3.2.4.1. Lithospheric collapse and crustal collapse

In the lithospheric and crustal collapse models it has generally been assumed [e.g. *Platt and England*, 1994] that collapse will occur when the potential energy difference between a thickened column and foreland column (equation (3-2a)) is larger than the integrated strength of the thickened column (equation (3-8)), which can be expressed as follows:

$$\Delta E_p > \int_0^{z_l} (\sigma_1 - \sigma_3)_T \, dz \qquad \text{(lithosphere)} \qquad (3\text{-}9a)$$

$$\Delta E_p > \int_0^{z_{cr}} (\sigma_1 - \sigma_3)_T \, dz \qquad \text{(crust)} \qquad (3\text{-}9b)$$

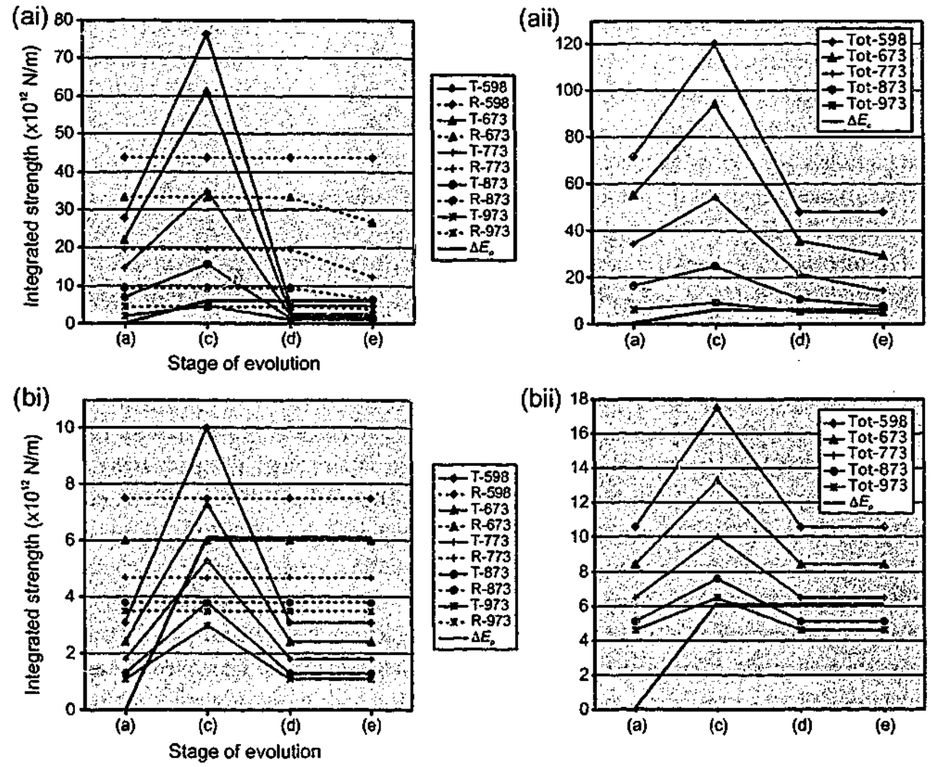

Fig. 3-4. Evolution of the integrated strength of (ai) the thickened lithosphere (T) and the reference lithosphere (R), (aii) the sum of T and R, (bi) the thickened crust (T) and the reference crust (R) and (bii) the sum of T and R for different initial Moho temperatures during different stages of evolution of the mountain belt. Here, stage (a), (c), (d) and (e) correspond to the stages of the same name in Fig. 3-3. Also plotted is the potential energy difference (ΔE_p) between T and R, as has been calculated in section 3.2.2.

However, in these equations, the strength of the surrounding foreland is entirely neglected, which will resist collapse of the thickened region. Thus it is more likely that the relations expressed above should be modified to incorporate this resistive factor, which is dependent on the strength of the surrounding lithosphere:

$$\Delta E_p > \int_0^{z_l} (\sigma_1 - \sigma_3)_T \, dz + F \int_0^{z_l} (\sigma_1 - \sigma_3)_R \, dz \qquad \text{(lithosphere)} \qquad (3\text{-}10a)$$

$$\Delta E_p > \int_0^{z_{cr}} (\sigma_1 - \sigma_3)_T \, dz + F \int_0^{z_{cr}} (\sigma_1 - \sigma_3)_R \, dz \qquad \text{(crust)} \qquad (3\text{-}10b)$$

where F is an undefined constant expressing the relative resistance of the surrounding foreland to inhibit collapse, with $0 < F \leq 1$. In equation (3-9) and (3-10), the integrated strength for T and R are for extension and shortening respectively.

In Fig. 3-4 the integrated strengths of T and R (Fig. 3-4ai and 3-4bi) and the sum of T and R (for F = 1) (Fig. 3-4aii and 3-4bii) are given for the stages (a), (c), (d) and (e) plotted in Fig.

3-3 for five different initial geotherms. Stage (a) gives the integrated strength for T and R before deformation. Stage (c) gives the integrated strength after thickening of T, for which the strength has significantly increased since it has been assumed that during thickening advection was dominant over thermal relaxation. In stage (d), after thermal relaxation of T, its strength has been reduced compared to stage (a), related to the thickened crust. Finally, in stage (e) the strength of the sub-lithospheric mantle of R has been reduced due to lateral heat flow from T to R.

For lithospheric collapse, comparison of the values of the sums of the integrated strengths for both T and R (for $F = 1$) with the ΔE_p of 6.1 x 10^{12} N/m (calculated in section 3.2.2), demonstrates that for a relatively cold geotherm with a low initial Moho temperature (598°K, 673°K and 773°K) gravitational collapse is probably not possible (Fig. 3-4aii)), at least for strain rates of $\geq 10^{-16}$ s^{-1}. This is mainly related to the strength of the reference lithosphere, which is up to eight times too strong to let the excess potential energy be released. However, for high initial Moho temperature (873°K, 973°K) the sum of the integrated strengths of T and R during stage (e) is of the same order as the ΔE_p (IS ≈ 7.7 x 10^{12} N/m (873°K) and IS ≈ 5.0 x 10^{12} N/m (973°K)), which may result in collapse of the thickened lithosphere and shortening of the reference lithosphere (Fig. 3-4aii). Furthermore, it can be concluded from Fig. 3-4ai that without incorporating the strength of R and after thermal relaxation of T (stage (d)), collapse would look plausible for all of the initial geothermal gradients.

For crustal collapse, comparison of the values of the sums of the integrated strengths for both T and R (for $F = 1$) with the ΔE_p of 6.1 x 10^{12} N/m (calculated in section 3.2.2), shows that for a relatively cold geotherm with a low initial Moho temperature (598°K and 673°K) gravitational collapse is not likely, because the sum of the integrated strengths is greater than the ΔE_p (Fig. 3-4bii). However, for a relatively hot geotherm with a high initial Moho temperature (873°K and 973°K) the sum of the integrated strengths for stage (d) is smaller than the ΔE_p (IS ≈ 5.1 x 10^{12} N/m (873°K) and IS ≈ 4.6 x 10^{12} N/m (973°K)). This may result in collapse of the thickened crust and shortening in the reference crust (Fig. 3-4bii). Note that after thermal relaxation of the thickened column (Fig. 3-3d) there is no difference between the geotherms of T and R for the uppermost 30 km, thus there is no lateral heat flow in this upper region and therefore no thermal weakening of the reference crust will take place.

It should be noted that the calculations presented above are hypothetical, since the major unknown, F, has been arbitrarily assumed to be 1.00, without justification. Experimental work is required to determine this value.

3.2.4.2. Lower crustal flow

It has been suggested that lower crustal flow or lower crustal collapse can occur from a region with a relatively high potential energy (orogen) to a region of relatively low potential energy (foreland) [*Kusznir and Matthews*, 1988; *Bird*, 1991; *Royden et al.*, 1997; *McQuarrie and Chase*, 2000]. In this scenario, flow occurs in the lower (ductile) part of the crust due to a lateral pressure gradient between the orogen and the foreland region (Fig. 3-5). Viscous flow velocities can be obtained by determining pressure gradients along possible travel paths and combining these with flow laws and possible crustal rheologies [*Bird*, 1991].

Fig. 3-5 indicates that crustal flow from T to R is possible between some ill-defined point in the middle crust (largely dependant on the temperature profile) down to P_1. In this region, the differential pressure between T and R is maximum ($\Delta\sigma_v \approx \rho g h$). In addition, there is an

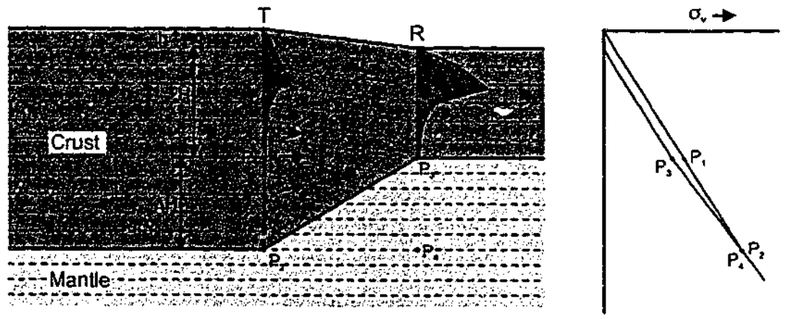

Fig. 3-5. Diagram illustrating lower crustal flow from orogen to foreland due to horizontal pressure gradient. Thickened crust (T) and reference crust (R) are plotted with strength profiles and lithostatic pressure curves (right) for a low initial Moho temperature (598°K). Strength envelopes and pressure differences have been drawn at the same scale. Dashed strength envelope is for the stage after thickening (Fig. 3-3b) and continuous strength envelope is for the stage after thermal relaxation (Fig. 3-3d). Dashed (sub)horizontal lines indicate isobars.

effective pressure difference of $\rho g h$ between the crustal root of T and P_3 [*Bird*, 1991]. Thus, crustal flow in T would extend for a depth range from P_1 to P_2. The fastest crustal flow could be located near the base of the Moho, because the effective viscosity there is the lowest related to the highest temperature. However, this might be somewhat suppressed because the effective pressure gradient is greater between P_1 and P_3 than between P_2 and P_3, because the path is longer for the latter. Further, the lowermost part of the crust might be composed of more mafic rocks (e.g. feldspar/diorite/diabase), which have higher viscosity/yield strength, leading to a higher resistance to lower crustal flow.

The process of middle to lower crustal flow leads to a gradually thinning orogenic crustal root, a gradual thickening of the foreland crust and a decrease of the ΔE_p. However, this localised flow would not result in extension of the entire crust or lithosphere of the thickened column and shortening of the entire crust or lithosphere of the reference column, and thus it would not result in deformation at the surface. Therefore, this process is not of much interest here, because the topic of the thesis focuses on arc – back-arc systems, which are characterised by extensive surface deformation on the back-arc side.

3.2.5. Discussion

Lonergan and White [1997] proposed several problems for the gravitational collapse model as a driving mechanism for extension in an orogen and shortening in the foreland: Firstly, patterns of shortening, surrounding regions of extension, are never truly radial (for a full 360°). Secondly, it is not clear why some regions which are argued to have formed by gravitational collapse continue to extend when the surface submerges beneath sea level (e.g. Alboran Sea). Third, some of the areas bordering the regions, which supposedly formed due to gravitational collapse, have experienced considerable rotations, as indicated by paleomagnetic data, which can not be easily explained by radial spreading.

Other problems come from the supposedly short time span between thickening and collapse of the lithosphere. *England and Thompson* [1984] argued that the thermal time constant for re-establishment of a normal thermal gradient for a 125 km thick lithosphere, which is thickened by a factor of two, is ~ 240 Myr. This is much too long to explain collapse in

mountain belts, since it occurs millions to several tens of millions of years after lithospheric thickening has ceased (see *Houseman and Molnar* [1997] and references therein). *Platt and England* [1994] argued that before considerable thermal relaxation by thermal diffusion can occur, the lower (mechanically weak part) of the lithosphere is removed by convection, leading to a step in the thermal gradient at the boundary between the lithosphere and the asthenosphere. Calculations showed that the time necessary to restore the thermal gradient by conduction would still be ~ 60 my for a 120 km thick lithosphere. Therefore they argued that extensional collapse results very soon after convective thinning of the lithosphere, solely as a result of an increase in potential energy of this lithosphere, and before significant thermal weakening of the thickened lithosphere can occur. However, the calculations done in the section 3.2.4.1 have shown that gravitational collapse is not possible without thermal relaxation of the thickened lithosphere (crust only) and considerable thermal heating of the surrounding lithosphere (entire lithosphere), even for relatively hot initial geotherms and weak rheologies. The time-lapse for thermal relaxation could be significantly reduced if radiogenic heat production in the crust was incorporated in calculations of geothermal gradient evolution [e.g. *Glazner and Bartley*; 1985].

According to *England and Houseman* [1989] there is no obvious geological process that would accomplish a reduction in strength of lithosphere surrounding a mountain range. However, in a situation where the lithosphere has an initially high Moho temperature, the higher temperature of the thickened crust of the thickened lithosphere after thermal re-adjustment, compared to the lower temperature of the upper mantle of the surrounding lithosphere results in a thermal gradient between the two regions (Fig. 3-3d). This gradient results in lateral heat flow from the thickened lithosphere towards the surrounding lithosphere, which leads to an increase in temperature of the upper mantle of the surrounding lithosphere and finally to a reduction in strength of this lithosphere. The amount of heating of the reference lithosphere probably increases when the transition zone between orogen and lowland is relatively narrow.

The concept of lateral heat transfer between orogens and surrounding lowlands has been proposed previously by *Gaudemer et al.* [1988]. They focussed on the concept that lowlands lithosphere has a cooling effect on the orogenic lithosphere it surrounds. Here, a relatively narrow orogenic belt would be significantly cooled by the surrounding lowlands lithosphere, which would therefore remain too strong to collapse under its own gravity. On the other hand, a relatively wide orogenic belt would retain a hotter geotherm, especially in the more interior regions of the orogen, and would therefore be more likely to collapse. However, from a different point of view, it can also be argued that orogenic lithosphere has a warming effect on the surrounding lowlands lithosphere. Thus, in relatively wide orogenic belts (e.g. Himalayas, Variscan, Basin and Range) there could be enough heat production to lead to thermal weakening of the surrounding lowlands to initiate collapse in the orogen and shortening in the surrounding lowlands, while in relatively narrow orogenic belts there is not (e.g. Urals, Pyrenees, Western Alps).

To conclude, the gravitational collapse model might work for orogenic regions with a thick crust and therefore high potential energy, such as the Tibetan Plateau and the Altiplano in the Andes. However, plate boundary forces can not be ruled out as having an effect on extension in these regions. For example, E-W extension in Tibet could also be influenced by the East Asian active margin located to the east. Gravitational collapse can not account for Western Pacific style arc - back-arc systems, since gravitational collapse, unaided by plate boundary forces, will proceed only until a reduced elevation of ~ 3 km can no longer drive the

extension [*Dewey*, 1988]. Most arc - back-arc systems around the world have a considerably lower elevation and the back-arc region is often several kilometres below sea level.

3.3. Rollback model

3.3.1. Introduction

In the rollback model, extension in the overriding plate is triggered by rollback of the adjacent subducting plate, leading to the formation of a potential vacant region at the contact between the subducting and overriding plate [*Elsasser*, 1971]. This vacant region will not arise, but will be filled by the overriding plate, which collapses towards the retreating hinge of the subducting plate (Fig. 3-1b), because it is not strong enough to sustain such a potential vacant region at the plate boundary [*Elsasser*, 1971; *Shemenda*, 1993]. Extension in the overriding plate will be dominantly oriented in the direction perpendicular to the trench. Along the subduction boundary, shortening will be the dominant deformation type, related to friction at the subduction zone interface, which might result in accretion of ocean sediments to the overriding plate. Furthermore, collapse is most likely to occur at places where the lithosphere has a relatively high potential energy and a relatively low integrated strength, such as a volcanic arc [*Molnar and Atwater*, 1978; *Dewey*, 1980].

Several driving mechanisms have been proposed for retreat of the hinge-line of the subducting lithosphere:

(1) Hinge-line retreat is driven by the negative buoyancy of the slab with respect to the sub-lithospheric mantle through which it sinks (Fig. 3-6a) [*Elsasser*, 1971; *Molnar and Atwater*, 1978; *Malinverno and Ryan*, 1986; *Royden*, 1993; *Shemenda*, 1993; *Lonergan and White*, 1997]. This model applies when the subducting lithosphere is of oceanic nature. Oceanic lithosphere has the same mineralogical composition as the surrounding mantle (except for its thin (~ 6 km) crust), but is much colder and therefore it is denser than the surrounding mantle. The thermal expansion coefficient ($\alpha \approx 2.4 \times 10^{-5}$ °K^{-1}) for mantle material [*Turcotte and Schubert*, 2002] indicates that for a 1000 °K temperature increase, the density decreases with 2.4% (assuming density is not effected by change in pressure). Since oceanic lithosphere grows with age due to conductive cooling of sub-crustal mantle, its average density increases with increasing age, because the thickness ratio of (buoyant) crust to lithosphere (T_{CR}/T_L) decreases with age (from 1 at 0 Ma ($T_{CR} = T_L \approx 6$ km) to 0.06 at ~ 100 Ma ($T_{CR} \approx 6$ km, $T_L \approx$ 100 km)). Therefore, the thin oceanic crust (~ 2950 kg/m^3 (basalt) for the crust compared to ~ 3250 kg/m^3 (peridotite) for the mantle [*Turcotte and Schubert*, 2002]) places a lower limit on the age of oceanic lithosphere, which is negatively buoyant and therefore will have a tendency to roll back. Calculations from *Le Pichon* [1982] place this lower limit at ~ 8 Ma and calculations of *Cloos* [1993] place this at 10 Ma, while *Molnar and Atwater* [1978] place this lower limit at ~ 30 Ma. However, once subducted, subduction zone metamorphism causes the crustal layer of basalt/gabbro to transform into more dense amphibolite (~ 3.15 kg/m^3) and eclogite (~ 3.40 kg/m^3), further increasing the negative buoyancy force of the slab [*Cloos*, 1993]. Upward displacement of the olivine-spinel phase boundary in the subducting slab also increases the buoyancy contrast between slab and surrounding mantle [*Turcotte and Schubert*, 1971]. This additional downward body force on the subducting lithosphere is of the same

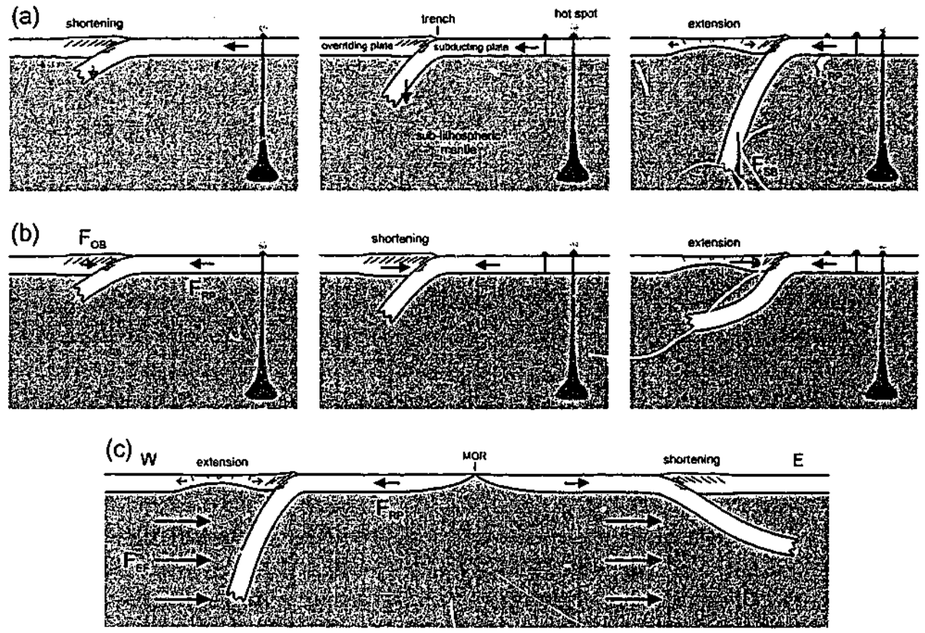

Fig. 3-6. Three possible driving mechanisms for hinge-line migration of a subducting slab. (a) Migration due to sinking of the slab, resulting from the negative buoyancy of the slab with respect to the surrounding mantle. (b) Migration due to push exerted from the overriding plate to the hinge-line. (c) Migration of west-dipping subduction zones due to global east-directed asthenosphere flow. F_{SB} = slab buoyancy force; F_{RP} = ridge push force; F_{OB} = overriding plate buoyancy force; F_{EF} = eastward asthenosphere flow force.

magnitude as the body force due to thermal contraction [*Turcotte and Schubert*, 1971]. The fact that numerous arc cusps are defined by buoyant irregularities on the subducting slab (such as aseismic ridges, oceanic plateaux and continental fragments) further supports the concept of density driven slab rollback (e.g. Marcus-Necker Ridge and Caroline Plateau for Mariana arc, Melanesian Border Plateau and Louisville ridge for Tonga arc, Emperor Seamount Chain for Kuril-Aleutian cusp).

(2) Hinge-line retreat is driven by the push exerted on the hinge-line of the subducting lithosphere by the overriding plate (Fig. 3-6b) [*Davies et al.*, 1997; *Hatzfeld et al.*, 1997; *ten Veen and Meijer*, 1998; *Gautier et al.*, 1999]. This push force is either caused by the excess potential energy in the overriding plate with respect to the subducting plate or by a tectonic force. In the former case, the model is actually similar to the gravitational collapse model discussed in section 3.2. Thus, the excess potential energy drives extension in the overriding plate as well as pushes back the hinge-line of the retreating slab. In the latter case, the model is similar to the extrusion tectonics model and the oroclinal bending model, which will be discussed in section 3.4 and 3.5 Therefore, this type of driving force for hinge-line retreat will not be extensively discussed here. I will mention, however, that if this would be the driving mechanism, then one would expect the retreating slabs bordering arc – back-arc systems to be shallowly dipping and concave upward (Fig. 3-6b), because this push back force is only exerted on the hinge of the subducting lithosphere and not on the remainder of the slab. This implication is in stark contrast with the observed dip angles for slabs bordering actively

extending back-arc regions, which are generally steeper than dip angles for slabs that do not border such regions (Table 3-1). This push back mechanism has been proposed for the Andean subduction zone [*Uyeda and Kanamori*, 1979], which is retreating westward at a rate of ~ 1.5-3.0 cm/yr [*Jarrard*, 1986] and is supposedly being pushed back by the ridge push force from the South Atlantic mid-oceanic ridge [*Meijer and Wortel*, 1992]. This, however, results in high compressional stresses and mountain building (e.g. the Andes) close to the subduction interface and not in the formation of a back-arc basin.

(3) Hinge-line retreat is driven by an overall east-directed flow in the asthenosphere or a net westward rotation of the lithosphere towards the west (Fig. 3-6c) [*Nelson and Temple*, 1972; *Moore*, 1973; *Alvarez*, 1982; *Shemenda*, 1994; *Doglioni et al.*, 1999a,b]. This asthenosphere flow or lithosphere motion itself would in some way be related to the rotation of the Earth and/or tidal effects [*Moore*, 1973]. The model has been proposed to explain the preference of west-directed subduction zones to be relatively steep and of low compressive nature (e.g. Mariana type) compared to east-directed subduction zones (Chilean type) [*Uyeda and Kanamori*, 1979], which are relatively shallow dipping and of high compressive nature. Therefore, west-directed subduction zones would preferentially be bordered by back-arc basins, while east-directed subduction zones would not. Thus, east-directed asthenosphere flow would push west-dipping slabs eastward, increase the slab dip angle and cause a deviatoric tension along the subduction interface. Although this might seem an appealing mechanism at first, there are several subduction zones, which do not fit this model. The most important example is the New Hebrides arc in the Southwest Pacific, which is dipping eastward, has an actively opening back-arc basin (North Fiji Basin) and is the second most fastest retreating subduction zone on Earth. GPS measurements indicate that the southernmost part is retreating westward at ~ 12 cm/yr [*Taylor et al.*, 1995]. Another example is the Hellenic arc in the Eastern Mediterranean with a northeast dipping subduction zone, which is retreating southwestward at a rate of ~ 3.5 cm/yr, accompanied by extension in the Aegean Sea [*Kahle et al.*, 1998]. Two other examples involve the South Shetland arc in the Southeast Pacific and the Trans Mexican arc in the East Pacific, the former a southeast dipping subduction zone retreating northwestward [*Lawver et al.*, 1995] and the latter a northeast

Subduction zone	Slab dip angle (°)	Reference	Back-arc basin	Active extension / spreading in back-arc	Active shortening in back-arc
Chile	16-31	1	No	No	Yes
Peru	15-32	1	No	No	Yes
Kuril	42-47	1	Yes	No*	No
Japan	26	1	Yes	No	Yes
Izu-Bonin	40-60	1	Yes	Yes#	No
Mariana	45-85	1	Yes	Yes	No
Ryukyu	36-40	1	Yes	Yes	No
New Hebrides	64	1	Yes	Yes	No
Tonga	35-50	1	Yes	Yes	No
Kermadec	47-60	1	Yes	Yes	No
Hellenic	~ 55	2	Yes	Yes	No
Calabrian	~ 70	3	Yes	Yes	No

Table 3-1. Slab dip data in comparison with active extension in back-arc region. References: 1—*Yokokura* [1981], 2—*Spakman et al.* [1988], 3—*Wortel and Spakman* [2000]. *Except active extension in Kamchatka (Central Kamchatka graben). #Active intra-arc extension.

dipping subduction zone retreating southwestward [*Ferrari et al.*, 2001]. Also, several west-dipping subduction zones (the Philippine and Japan subduction zones) are not bordered by actively opening back-arc basins, and are therefore not retreating eastward with respect of the overriding plate, which further undermines the model. Another argument against this model is that if retreat would be driven by such a flow, then one would expect the slab to be concave towards the direction of retreat (and thus back-arc basins to be located on the convex side of the arc). This, because in order to be the driving mechanism, the east-directed flow would have to be faster than the slab retreat and would therefore flow around the edges of the slab, which would force the slab into such a geometry. However, for all arc - back-arc systems it is observed that back-arc basins occur on the concave side of the arc (Fig. 1-1).

From discussion of the three above mentioned possible mechanisms to drive hinge-line migration it can be concluded that slab rollback is most likely caused by the negative buoyancy force resulting from the higher average density of the slab compared to the sub-lithospheric mantle through which it sinks. The concept behind the mechanism is simple and physically sound, and has been supported by numerous analogue and numerical experiments, in which slab rollback is driven by the negative buoyancy of the slab [*Kincaid and Olson*, 1987; *Olson and Kincaid*, 1991; *Guillou-Frottier et al.*, 1995; *Griffiths et al.*, 1995; *Christensen*, 1996; *Houseman and Gubbins*, 1997; *Faccenna et al.*, 1996, 1999; *Becker et al.*, 1999; *Faccenna et al.*, 2001b]. Although it is argued that the buoyancy force is the main driving mechanism for rollback, it should be kept in mind that numerous other factors influence slab retreat and back-arc formation, including the slab width, viscosity of the slab and sub-lithospheric mantle, horizontal velocity of the subducting plate, horizontal velocity of the overriding plate, irregularities on the subducting plate, tearability of the subducting lithosphere, etc. Finally, it should be mentioned that even though the horizontal buoyancy force resulting from the potential energy difference between the overriding and subducting plate is a magnitude smaller than the force resulting from the sinking slab [*Faccenna et al.*, 1996], it still exerts a net force from the overriding plate to the subducting plate. This force is important, since it forces the overriding plate to follow the hinge-line of the subducting lithosphere during slab retreat.

3.3.2. Why rollback?

I will now expand on some simple arguments as to why the rollback model is a good candidate to explain extension in the overriding plate. First of all, it is assumed that every slab with an average higher density than the surrounding mantle will have the tendency to sink due to its negative buoyancy and therefore roll back. It has indeed been shown that most subduction zones are presently retreating [*Garfunkel et al.*, 1986], therefore supporting the assumption. Secondly, if the subducting plate rolls back, the upper plate has no other option but to simply follow the migrating hinge. If this was not the case, the retreating slab would simply create a lithospheric-scale gap. Of course, no such lithospheric-scale gaps are found along subduction zones. However, as a thought experiment, consider the extreme case, where a retreating slab would roll back instantaneously with respect to the overriding plate for a short distance, creating a narrow lithospheric-scale gap. Then, the potential energy difference between the overriding plate and this gap would simply be the potential energy of the overriding lithosphere from the surface to its base. Collapse of the overriding plate towards this potential gap would occur if its potential energy difference compared to the gap is greater than its own integrated strength (for extension). This can be written as follows:

$$\Delta E_p = \int_0^{z_c}\int_0^{z}(\rho g)\,dz\,dz = \int_0^{z_c}(\rho g z)\,dz > \int_0^{z_c}(\sigma_1 - \sigma_3)\,dz \qquad (3\text{-}11)$$

In equation (3-11) the upper limit of the strength of a lithospheric column (for extension) can be given by equation (3-5ai). From this it follows that the (extensional) integrated strength of a column of lithosphere is always smaller than its potential energy at any strain rate, since $0.79\rho gz(1-\lambda) < \rho gz$ (with $0 \le \lambda \le 1$). Thus, no matter how fast a subducting slab is rolling back, the upper plate will always follow the retreating hinge instantaneously, simply because it is not capable to support a potential lithospheric-scale gap that would otherwise arise at the plate contact. The locus of extension is most likely to occur at places with a relatively low integrated strength and relatively high potential energy.

3.3.3. Discussion

Several problems have been identified for the subduction rollback model, as a mechanism for arc formation and back-arc extension. It has been argued that it is difficult for the slab to move in a direction perpendicular to its own surface, because it would require a large volume of surrounding mantle to be displaced. Therefore, the anchored slab model has been proposed, in which the slab is fixed to the lower mantle and does not move laterally [*Uyeda and Kanamori*, 1979]. In this model, back-arc opening is explained by retreat of the overriding plate from the trench (Fig. 3-7). However, simple kinematic arguments can be put forward against this model, since it cannot explain the lateral discontinuity of back-arc basins [*Hsui*, 1988], the variation in arc-perpendicular opening rate parallel to the trench and the irregular arc-shaped nature of many subduction interfaces. An illustration of these difficulties can be found in Fig. 3-8, using the example of the Izu-Boni-Mariana subduction system. It seems hard to explain the opening of the Parece-Vela basin due to westward migration of the overriding Philippine plate, since the shape of the Palau-Kyushu Ridge and the Izu-Bonin - West Marian Ridge are very dissimilar. The ridges testify to a variation in the amount of opening of the basin in the E-W direction. In addition, westward retreat would not be able to explain the recent opening of the Mariana Trough without similar amounts of opening along the Izu-Bonin ridge and the Yap Ridge. In conclusion, overriding plate retreat cannot explain the formation of back-arc basins.

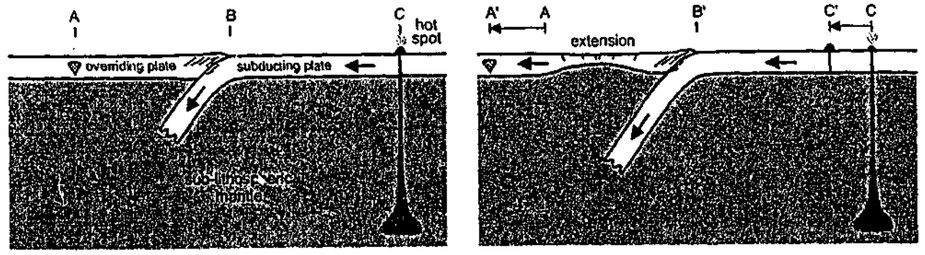

Fig. 3-7. Illustration of the anchored slab model, where trench (B/B') is stationary with respect to hot spot and slab only moves parallel to its dip-angle. Subducting plate moves towards left over a distance C-C' with respect to hot spot. Overriding plate moves towards left (A-A') with respect to hot spot (C) and therefore also with respect to trench (B/B'). As a result of overriding plate movement and stationary trench, overriding plate is extended.

Another problem with rollback and back-arc extension has been proposed by *Hsui* [1988], who argued that it is not clear why the overriding and subducting plate do not simply separate along the subduction interface letting the less viscous mantle material fill the gap created by rollback. This is simply explained by the horizontal buoyancy force exerted on the subducting lithosphere by the overriding plate, resulting from the higher potential energy of the overriding plate with respect to the subducting lithosphere. The subducting oceanic lithosphere always has a lower potential energy than the overriding plate. If the overriding plate is of continental nature with normal crustal thickness (~ 35 km, ρ(crust) = 2750 kg/m^3, ρ(mantle) = 3300 kg/m^3), then the $\Delta E_P \approx 2.0 \times 10^{12}$ N/m. If the overriding plate is of oceanic nature with an arc with a 20 km thick crust (ρ(crust) = 2750 kg/m^3, ρ(mantle) = 3300 kg/m^3), then $\Delta E_P \approx 9.0 \times 10^{11}$ N/m. This buoyancy force will push the fore-arc sliver towards the trench and will therefore not allow separation along the subduction interface. In addition, subduction induced return flow in the mantle wedge will always provide a net drag force on the overriding lithosphere towards the trench [*McKenzie*, 1978], although the magnitude of this force is probably relatively small.

The overriding plate does not simply break up along or close to this contact because it also has a relatively strong extensional strength near this contact related to the subduction of cool

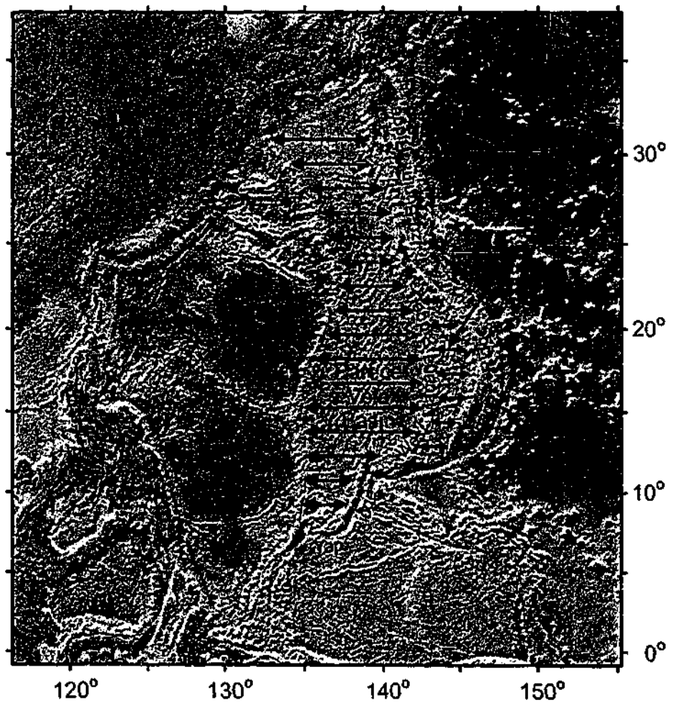

Fig. 3-8. Topography and bathymetry of the Philippine Sea region (from *Smith and Sandwell* [1997]). Arrows illustrate separation between Palau-Kyushu Ridge and Yap-West Mariana-Izu-Bonin Ridge, and between West Mariana Ridge and Mariana Ridge. Since the amount of E-W separation is highly variable in the N-S direction, this implies opening up of the Parece-Vela Basin and Mariana Trough can not have resulted from ~ westward retreat of the Philippine Sea plate. Otherwise, the width of the Parece-Vela Basin should be continuous and the Mariana Trough should extend along the entire eastern margin of the Philippine Sea plate.

lithosphere and subsequent cooling of the overriding plate near the subduction interface (see for instance *Hsui* [1988] Fig. 2). The overriding plate is more likely to extend at places with relatively low integrated strength and high potential energy. For instance, this has been observed at several subduction zones in the Western Pacific (e.g. Mariana arc, Tonga-Kermadec arc, Izu-Bonin arc). Here, local rollback of the Pacific plate led to extension of the upper plate along a volcanic arc adjacent to the subduction zone, resulting in the formation of a back-arc basin in between a remnant arc and a new volcanic arc [*Karig*, 1970; *Kobayashi and Nakada*, 1979; *Fryer and Hussong*, 1981]. This suggests that a volcanic arc is a fundamental line of weakness [*Molnar and Atwater*, 1978; *Dewey*, 1980], resulting from a thicker crust and a higher geothermal gradient than surrounding regions. Also, the higher potential energy of the arc compared to surrounding ocean floor will favour extension to initiate in the arc region.

3.4. Extrusion tectonics model

In the extrusion tectonics model, arc formation and back-arc extension occurs due to sideways escape of continental fragments away from a continent-continent collision zone towards regions of low compression or low confinement (Fig. 3-1c). This model was first proposed by *McKenzie* [1972] for the formation of the Hellenic arc and the Aegean Sea back-arc region, which supposedly formed due to the Arabia-Eurasia collision and escape of the Anatolian plate towards the west. This model was later applied to the India-Eurasia collision zone and the wide-spread deformation found in East Asia and along the East Asian active margin [*Molnar and* , 1975; *et al.*, 1982]. In this model, the indentation of the Indian continent into Eurasia would have led to thickening in front of the indenter (Himalayas, Tibet), the eastward escape of continental blocks (such as the Indo-China block) and widespread deformation in East Asia, with strike-slip faulting and opening of several basins in a pull apart fashion (Baikal rift, Shanxi graben, South China Sea). More recently, this model has been applied to the Eastern Alps, Pannonian Basin and Carpathian arc [*Ratschbacher et al.*, 1991]. In this example, indentation of Adria into Europe would have led to eastward escape of continental blocks in the Eastern Alps, formation of the Pannonian Basin and the Carpathian arc.

The extrusion tectonics model has been supported by various analogue models, such as plain strain models [*Tapponnier et al.*, 1982] and 3D models scaled for gravity [*Davy and Cobbold*, 1988; *Peltzer*, 1988; *Jolivet et al.*, 1990; *Ratschbacher et al.*, 1991; *Martinod et al.*, 2000]. In these models a rigid indenter collided with a homogeneous or stratified layer representing the lithosphere. The requirement for eastward extrusion of lithospheric blocks was the presence of a "free boundary" to the side of such a collision zone [*Tapponnier et al.*, 1982; *Davy and Cobbold*, 1988; *Ratschbacher et al.*, 1991], simulating a subduction zone, supposedly a zone of low compressional stresses. The role of such a "free boundary" in the analogue models was to give the lithosphere lateral isostatic support, where it was unable to apply or support any lateral deviatoric stresses. Alternatively, one could consider the subduction margin to play an active role in the extensional back-arc deformation (i.e. rollback), instead of being passively pushed back.

The model is probably not far from the truth concerning extrusion of crustal or lithospheric wedges located inside and close to the collision zone, but it seems mechanically unsound to justify that during extrusion of a wedge, the push from the rear of the wedge can be

transmitted to the leading edge of the wedge (arc), while at the same time producing extension in the middle of the wedge (back-arc). For example, how can extrusion of orogenic wedges in the Eastern Alps produce shortening along the Carpathians simultaneously with extension in the Pannonian Basin?

Additionally, timing can be invoked as a problem when one wants to hold extrusion tectonics responsible for some arc and back-arc deformation. For the Hellenic arc – back-arc system, extension in the Aegean region had already started in the latest Oligocene (~ 25 Ma [*Lister et al.*, 1984]) or Early Miocene, while collision between Arabia and the Eurasian continent only started in the Middle to Late Miocene [*Gautier et al.*, 1999]. In East Asia, the South China Sea region had already started extending in the latest Cretaceous [*Northrup et al.*, 1995; *Ren et al.*, 2002], while the India-Eurasia collision only started in the Early Eocene [*Searle et al.*, 1987; *Beck et al.*, 1995]. Thus, there is evidently need for another mechanism to account for the extension observed in these regions.

3.5. Oroclinal bending model

In the oroclinal bending model, compression oriented parallel to the axis of an orogen would lead to outward bending of this orogen with the formation of an extensional back-arc basin on the concave side of the orocline (Fig. 3-1d) and shortening on the convex side of the orogen. This model has been proposed for several arcs in the Mediterranean, such as the Apennines - Calabria arc [*Ghisetti and Vezzani*, 1982; *Van der Linden*, 1985; *Mantovani et al.*, 1997a,b], the Hellenic arc [*Mantovani et al.*, 2000], the Betic-Rif-Maghebrides-Calabria-Apennines system [*Gelabert et al.*, 2002] and the entire West Pacific arc – back-arc system [*Mantovani*, 2001]. A number of conceptual oroclinal bending models have been proposed, which mainly differ on the grounds of structural geometries expected to result from orogen-parallel compression (Fig. 3-1d and 3-9).

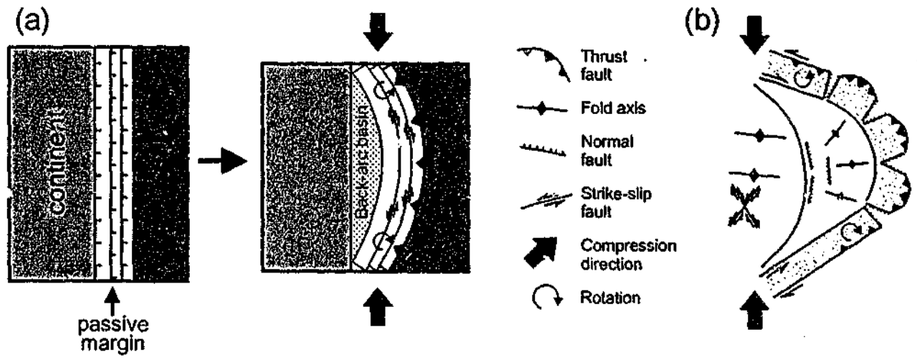

Fig. 3-9. Two conceptual models for oroclinal bending showing different structures. (a) Horizontal compression of a passive margin parallel to the margin, resulting in reactivation of normal faults as strike-slip faults, outward bending of the passive margin towards the ocean-side, with compression in the fore-arc region and extension in the back-arc region (from *Gelabert et al.* [2002]). (b) Horizontal orogen-parallel compression resulting in various structures in the back-arc region, opposite-side rotation on either side of the arc and arc-perpendicular faults close to the arc (from *van Dijk and Okkes* [1990]). For third conceptual model of oroclinal bending see Fig. 3-1d.

The oroclinal bending mechanism is not a sound physical mechanism to explain arc – back-arc related structures for several reasons. Firstly, it is hard to explain why only an orogen would be compressed parallel to its longer side and not the lithosphere surrounding each side of the orogen, as proposed by *Mantovani et al.* [2000]. *Gelabert et al.* [2002] do show that the surrounding lithosphere is shortened in the direction parallel to the orogen, but do not offer any solution as to where such shortening is actually absorbed (e.g. local crustal thickening or subduction). Secondly, the model would require the orogen to behave elastically, while an orogen is generally a region with relatively low integrated strength and high potential energy, due to its thick crust and warm average thermal gradient. This would imply that the orogen would behave elastically only on a small length scale (~ 100 km). The oroclinal bending model would require the orogen to behave elastically with a characteristic half wavelength of some thousand kilometres or more.

Flexural modelling studies of the lithosphere indicate that the characteristic flexural half wavelength is only in the order of 250 km in the case of old, and therefore strong, oceanic lithosphere. Examples include the flexure of the 80 - 120 Ma Pacific plate due to the Emperor - Hawaiian Chain [*Watts et al.*, 1980] and the flexure of the 80 Ma oceanic lithosphere of the northeastern Atlantic due to the Great Meteor Seamount [*Watts et al.*, 1975]. For example, *Mantovani et al.* [1997a,b] and *Gelabert et al.* [2002] have suggested that orogen-parallel compression of the Oligocene orogenic belt, striking NE-SW and running from the Betics to the Western Alps, resulted in the formation of the arcuate Betic-Rif-Maghebrides-Calabrian-Apennines belt. The length of the Oligocene structure is ~ 1500 km which is almost an order of magnitude larger than the characteristic flexural half wavelength of strong oceanic lithosphere. To continue, in this particular example, the amount of orogen-parallel convergence from the Late Oligocene to the present between Africa and Europe near the Betic-Rif arc is < 200 km [*Rosenbaum et al.*, 2002a], which is much smaller than the maximum amount of arc migration of ~ 800 km during the same time interval [*Faccenna et al.*, 2001a,b, *Rosenbaum et al.*, 2002b]. To finalise, it does not seem mechanically sound to assume that a linear orogen, embedded in a lithospheric plate, would behave elastically in the plane of the lithosphere. Rather, one would only expect bending to occur only in the direction perpendicular to the lithospheric plane.

From the above mentioned arguments and possibly many others not mentioned, it is concluded that the oroclinal bending model is not a physically sound mechanism on the scale (~ 1000 km and over) for which it has been proposed to explain the formation of arc – back-arc structures.

3.6. Conclusions

In this chapter, the pros and cons for four tectonic models have been discussed, which attempt to explain the formation of arc back-arc systems. These models are the gravitational collapse model, the rollback model, the extrusion tectonics model and the oroclinal bending model.

It has been argued that subduction rollback is the most likely candidate for the formation of arc – back-arc systems in which shortening and extension occur simultaneously in relatively close proximity (tens to hundreds of kilometres). The physical concept behind the slab rollback mechanism is simple: the slab is on average more dense than its surrounding mantle and will therefore sink not only in a direction parallel to its dip but also perpendicular to it. At

the surface, this will necessitate the oceanward migration of its hinge-line, resulting in extension of the overriding plate (i.e. back-arc extension). Continued subduction will result in shortening at the subduction interface and possible accretion of material from the subducting to the overriding plate synchronously with back-arc extension. This buoyancy driven rollback is a physically sound mechanism as demonstrated by several physical and numerical experimental investigations [*Kincaid and Olson*, 1987; *Olson and Kincaid*, 1991; *Guillou-Frottier et al.*, 1995; *Griffiths et al.*, 1995; *Christensen*, 1996; *Houseman and Gubbins*, 1997; *Faccenna et al.*, 1996, 1999; *Becker et al.*, 1999; *Faccenna et al.*, 2001b].

The role of the buoyancy force in gravitational collapse might also be of significant importance in driving extension of thickened crust in orogenic belts, as these have a relatively high potential energy. However, in this scenario one has to take into account the strength of the surrounding foreland as a factor inhibiting collapse, which is often neglected. For gravitational collapse to occur, the extending lithosphere has to be relatively thick and weak (warm), while the surrounding foreland has to be relatively weak. Collapse and extension in an arc – back-arc setting can better be viewed as an effect of slab rollback rather then causing slab rollback (e.g. push back).

Extrusion tectonics only seems to occur in orogens, which are laterally bounded by a zone, which can retreat during the extrusion. It is not immediately clear if this boundary is retreating on its own or is actively being pushed back by the extruding orogenic wedges. If the latter is true, then this would not explain the presence of a zone of extension in between the leading and trailing edge of the extruded wedge.

The oroclinal bending mechanism is not a sound physical mechanism to explain arc – back-arc related structures because orogenic lithosphere is relatively weak due to its thick crust and warm geotherm, making it unfit to behave elastically on the scale for which it has been proposed ($\geq$ 1000 km). Also, it is entirely unclear why an orogen would bend in the plane of the lithosphere while subjected to compression parallel to its axis. Normally, bending of lithosphere is only considered to occur in the direction perpendicular to the plane of the lithosphere.

FOREWORD CHAPTER 4

This chapter discusses the formation of arcs and back-arc basins, and attempts to classify the kinematic evolution of these systems in three separate models: the radial model, the unidirectional model and the asymmetrical model. These conceptual kinematic models have been inspired by the geometry and structure of numerous arc - back-arc systems around the globe, published tectonic reconstructions of such systems and published data on paleomagnetism and geodesy of various arc regions.

The ideas and interpretations presented in this chapter are the sole work of the author. All the experimental work presented in this chapter is the sole work of the author. Construction of the radial spreading model was inspired by a paper from *Hatzfeld et al.* [1997]. The clarity of ideas presented in this chapter benefited from discussions with Mark Jessell and Gordon Lister. Reviews of earlier versions of this chapter by Peter Betts, Gideon Rosenbaum, Laurent Aillères and David Giles are also acknowledged. Part of the contents of this chapter has been published in *Bollettino di Geofisica Teorica ed Applicata*. A full reference can be found at the end of the thesis in the bibliography.

CHAPTER 4

Analogue modelling of back-arc extension

Abstract

The structural evolution in the back-arc region of the overriding plate depends to a large extent on the mode of migration of the hinge-line of the adjacent retreating slab. Three-dimensional analogue experiments have been conducted to simulate the process of arc formation and back-arc extension. Three models have been built, which simulate different modes of hinge-line migration, to investigate the structural and kinematic evolution of the overriding lithosphere for a particular subduction zone configuration. The models have been built for two types of rheological stratification, one with a two-layered brittle-viscous system and the other with a three-layered brittle-high viscous-low viscous system. The latter is an improved version of the former, since in these experiments, the uppermost two layers (representing the lithosphere) are isostatically supported by the bottom layer (representing the asthenosphere). For both stratified set-ups, the uppermost two layers are comprised in a box, to model the overriding lithosphere. Part of one of the four side-walls is removable and upon removal, the uppermost two layers flow through the resulting opening. In the first model back-arc extension is unconstrained and the outward flow is allowed in all directions, to simulate radial hinge-line migration (e.g. Hellenic arc, Carpathian arc). In the second model the outward flow is allowed in one direction, perpendicular to the gate, modelling unidirectional hinge-line migration (e.g. Scotia arc, Mariana arc, South Shetland arc). In the third model the outward flow is asymmetrical and rotates around a hinge-point, where the opening of the gate is analogous to an opening door, modelling asymmetric hinge-line migration (e.g. New Hebrides arc, Tonga arc, Kuril arc). The resulting strain patterns of these models are significantly different. The first model is characterised by radial spreading, arc-parallel and arc-perpendicular extension close to the arc, conjugate strike-slip faulting to oblique faulting in the interior of the box, and opposite sense rotation on either side of the spreading sheet. The deformation pattern in the second model is similar to the first model, except that spreading only occurs in the direction perpendicular to the gate, leading to reduced rotation and arc-parallel extension, but considerable shear rotation. In the third model an asymmetrical strain pattern develops, where the local extension direction is generally focussed on a point at the far end of the rotating boundary. Most rotation is in accordance with rotation of the boundary, but opposite sense rotation is observed near the non-hinge side of the gate. No arc-parallel extension is observed in this model.

4.1. Introduction

A striking feature of the Earth is that most of the active subduction zones and convergent boundaries, as well as ancient mountain belts are not straight but display arc-shaped features (Fig. 1-1). Present day examples of such arcs are numerous. In the Mediterranean region examples are the Calabrian arc, the Hellenic arc, the Betic/Rif arc, the Cyprus arc and the Carpathian arc. Examples from the Pacific region include the Mariana arc, the Aleutian arc, the Japan arc, the Ryukyu arc, the Kuril arc, the Sunda arc, the New Hebrides arc, the Tonga

arc and the Banda arc. Other examples include the Scotia arc and the South Shetland arc in the Southern Atlantic and the Lesser Antilles arc in the Caribbean Sea.

The wide range of arcuate shapes with varying curvature angles and back-arc geometries suggests that these arcs are not initial static geometries, as, for example, the equal sphere intersection model of *Frank* [1968] would suggest. Rather, the curvature of many arcs appears to have evolved gradually from initially straighter geometries. Evidence that supports this idea comes from data for paleomagnetic rotations along some arcs (Betic/Rif arc and Calabrian arc [*Lonergan and White*, 1997], Hellenic arc [*Walcott and White*, 1998], Carpathian arc [*Marton and Fodor*, 1995], Mariana arc [*McCabe*, 1984], New Hebrides arc [*Musgrave and Firth*, 1999], Japan arc [*Otofuji et al.*, 1991], Ryukyu arc [*Kamata and Kodama*, 1994]). These rotations can point to comparable or different magnitudes of rotation along the arc and/or opposite sense rotations on either side of the arc. These rotations are often coeval with deformation in the back-arc region, supporting the hypothesis of a dynamic origin of arcs. Also, evidence from GPS data along some arcs indicates that different segments of arcs have different velocities and/or orientations compared to the "fixed" hinterland, indicating that arcs are not static geometries but evolve through time (e.g. Tonga arc [*Bevis et al.*, 1995], Hellenic arc [*Kahle et al.*, 1998], New Hebrides arc [*Taylor et al.*, 1995]). Thus, following these arguments, it is most probable that these arcs progressively develop and become more arc-shaped through time, as has been suggested earlier by *Vogt* [1973].

The hypothesis of evolving arcs is also supported by palinspastic and evolutionary diagrams (e.g. New Hebrides arc and Tonga arc [*Auzende et al.*, 1988; *Hathway*, 1993], Hellenic arc [*Kissel and Laj*, 1988; *Walcott and White*, 1998], Calabrian arc [*Faccenna et al.*, 1996]; Cyprus arc [*Payne and Robertson*, 1995]; Scotia arc [*Barker*, 2001]). In Figs. 4-1, 4-2 and 4-3 evolutionary diagrams have been plotted for the Hellenic arc in the Eastern Mediterranean, the Scotia arc from the Southern Atlantic, and the New Hebrides and Tonga arc in the Western Pacific, respectively. Fig. 4-1a shows the Hellenic arc as an initially almost rectilinear subduction zone, which evolved into a curved subduction zone with radial spreading in the overriding plate and opposite sense rotations on either side of the arc (Fig. 4-1b). Finally a curved subduction zone developed, bounded in the east by a transform fault zone, suggesting some sort of asymmetrical spreading (Fig. 4-1c). Fig. 4-2 shows the evolution of the Scotia arc – back-arc system, which seems to have developed mainly due to

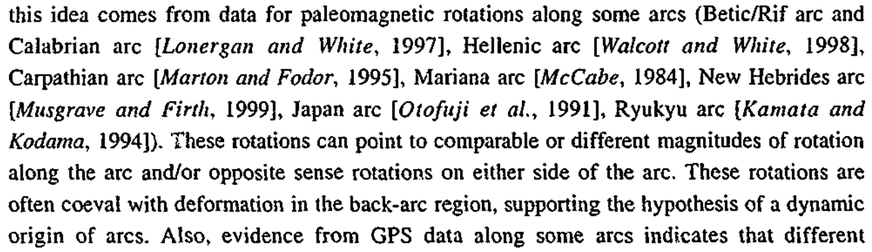

Fig. 4-1. Evolution of the curvature of the Aegean Arc from the Oligocene - Present (modified from *Kissel and Laj* [1988], *Walcott and White* [1998] and *Angelier et al.* [1982]). Curved arrows with numbers indicate sense and amount of rotation. Arrows indicate direction of arc migration. The original arc was approximately rectilinear and trending ~ E-W. Cr = Crete, Ka = Karpathos, Ky = Kythira, PT = Pliny Trench, Rh = Rhodos, ST = Strabo Trench.

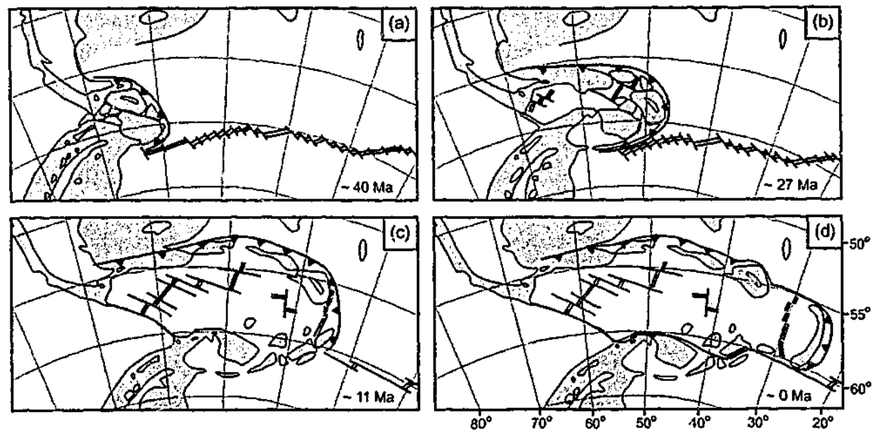

Fig. 4-2. Schematic sketches showing the evolution of the Scotia arc - back-arc system since ~ 40 Ma (modified from *Barker* [2001]). System is dominated by the eastward migration of the trench.

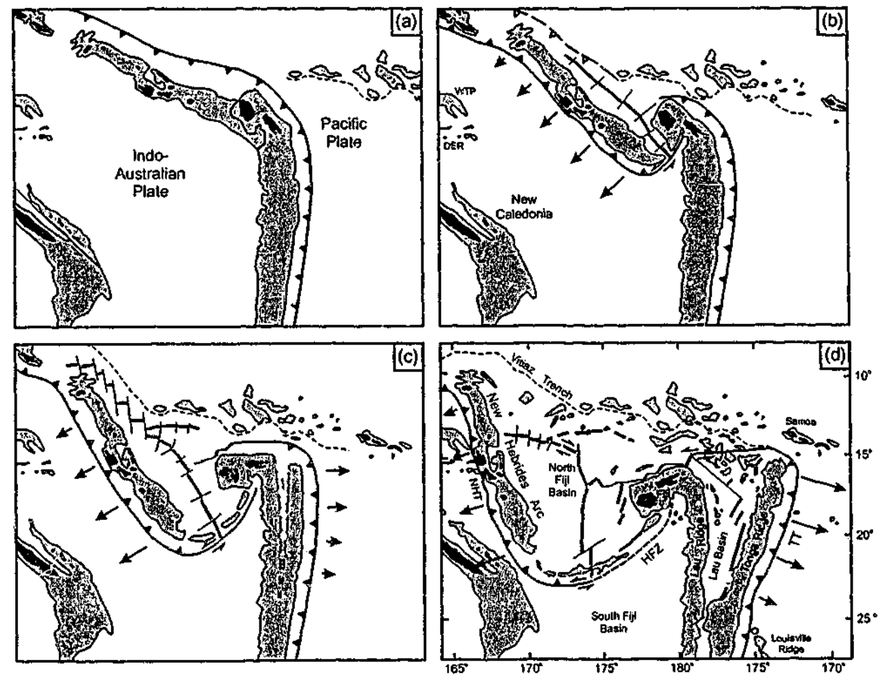

Fig. 4-3. Tectonic reconstruction of the New Hebrides - Tonga region (modified and interpreted from *Auzende et al.* [1988], *Pelletier et al.* [1993] and *Hathway* [1993]) at (a) ~ 13 Ma, (b) ~ 9 Ma, (c) 5 Ma and (d) Present. The Indo-Australian plate is fixed. DER = d'Entrecasteaux Ridge, HFZ = Hunter Fracture Zone, NHT = New Hebrides Trench, TT = Tonga Trench, WTP = West Torres Plateau. Arrows indicate direction of arc migration. During opening of the North Fiji Basin, the New Hebrides block has rotated some 40-50° clockwise [*Musgrave and Firth*, 1999], while the Fiji Plateau has rotated some 70-115° anticlockwise [*Malahoff et al.*, 1982]. During opening of the Lau Basin, the Tonga Ridge has rotated ~ 20° clockwise [*Sager et al.*, 1994].

eastward migration of the trench. Fig. 4-3 shows the evolution of the New Hebrides arc and the Tonga arc. Both systems have developed by clockwise rotation of the arc and formation of a wedge shaped back-arc basin.

In this paper, three schematic kinematic models are proposed for the evolution of arcs and back-arc basins, which are designed to simulate radial (e.g. Hellenic arc (Fig. 4-1)), unidirectional (e.g. Scotia arc (Fig. 4-2)) and asymmetrical (e.g. New Hebrides and Tonga arc (Fig. 4-3)) retreat of the hinge-line of the subducting slab. These models have been deduced from the range of data for arcs and back-arc regions discussed above (e.g. structural data, paleomagnetic data, GPS data, evolutionary diagrams). The structural development to be expected in the overriding plate of these models has been investigated with analogue experiments, which provide a self-consistent coherent framework for better understanding the characteristic structures and the kinematic evolution of such arcs and back-arc regions. Finally, the experimental results will be compared briefly with several natural examples of arc - back-arc systems to test the applicability of the models.

4.2. Rollback and the formation of arcs

The formation of arcuate subduction zones in combination with back-arc extension has been ascribed to several driving mechanisms such as rollback of the hinge-line of the subducting slab [*Royden et al.*, 1983; *Hsui and Younquist*, 1985; *Viallon et al.*, 1986; *Malinverno and Ryan*, 1986; *Royden et al.*, 1987; *Wortel and Spakman*, 1992; *Shemenda*, 1994; *Lonergan and White*, 1997], gravitational/extensional collapse [*Dewey*, 1988; *Platt and Vissers*, 1989; *Platt and England*, 1994], lateral escape/extrusion [*Ratschbacher et al.*, 1991a,b] and oroclinal bending [*Mantovani et al.*, 1997, 2000] (see Chapter 3 for a discussion). Rollback seems to be the most favoured mechanism, especially for arcs and back-arc basins in the Western Pacific. Here, most arcs and adjacent back-arc basins in the overriding plate are bound on one side by an oceanic lithosphere subducting underneath the overriding plate, which might be responsible for rollback. The trace of the subducting slab is well defined by seismological and tomographic data. For the Mediterranean region, the mechanism responsible for the formation of its arcs and back-arc basins remains more controversial. This is partly related to the fact that seismological and tomographic data provide a more dispersed image of slabs and slab remnants (e.g. Betic/Rif arc, Carpathian arc), which might be responsible for slab rollback. Also, there is no general agreement about the nature of the lithosphere that is being or has been subducted along these arcs (e.g. oceanic or thinned continental lithosphere). However, a recent tomographic study of the Mediterranean region [*Wortel and Spakman*, 2000] indicates that the back-arc basins in this region are underlain by slab remnants at the upper-lower mantle transition zone, suggesting that these slab remnants have been draped over the transition zone during slab rollback, accompanied by back-arc extension.

In subduction rollback (or retreating subduction boundaries [*Royden*, 1993a]) the advancing rate (the rate at which the overriding plate advances ocean-ward in a hot-spot reference frame) is slower than the trench migration rate (the rate at which the hinge of the subducting plate retreats ocean-ward in a hot-spot reference frame), which results in extension of the overriding plate (Fig. 1-2) [*Dewey*, 1980; *Royden*, 1993a]. The following mechanisms have been proposed to be the cause of hinge migration of the subducting slab and back-arc extension (see also Chapter 3): (1) the negative buoyancy of the subducting slab, which would cause it to sink, resulting in the regressive motion of the hinge-line [*Elsasser*, 1971; *Molnar and Atwater*, 1978; *Malinverno and Ryan*, 1986; *Royden*, 1993b; *Shemenda*, 1993; *Lonergan and White*, 1997]; (2) the horizontal buoyancy force of the overriding plate exerted on the hinge-line of the subducting plate, which would cause it to migrate ocean-ward [*Davies et al.*, 1997; *Hatzfeld et al.*, 1997; *ten Veen and Meijer*, 1998; *Gautier et al.*, 1999]; (3) flow in the asthenosphere, where a subducting slab would experience an asthenospheric counterflow, which would result in a steeply dipping slab and retreat of the hinge-line [*Nelson and Temple*, 1972; *Moore*, 1973; *Alvarez*, 1982; *Shemenda*, 1994; *Doglioni et al.*, 1999a,b]. With the first mechanism, the subducting plate dictates in which direction the overriding plate is allowed to extend. The overriding plate is forced to follow the retreating hinge, since it is not strong enough to sustain a potentially vacant region along the subduction zone [*Elsasser*, 1971; *Shemenda*, 1993; *Lonergan and White*, 1997]. With the second mechanism, the asthenosphere dictates in which direction the hinge of the subducting plate migrates, which again dictates in which direction the overriding plate is allowed to spread. Finally, with the third mechanism, the overriding plate (its excess potential energy) dictates in which direction it is allowed to spread. Extension is most likely to occur at places with the steepest potential energy gradient.

4.3. Kinematic models for the formation of arcuate subduction zones

Irrespective of which of the above mentioned mechanisms is the (main) contributor to rollback and hinge-line migration, from natural examples it is clear that: (1) migration of the hinge-line as well as arc and back-arc formation and evolution occur in different manners (e.g. compare Figs. 4-1, 4-2 and 4-3); (2) the pattern of hinge-line migration must exhibit a great deal of control on the style and pattern of deformation in the overriding plate. Three simple kinematic models are proposed to describe the boundary constraints on the overriding plate, which are critical in the formation and evolution of arcs and back-arc basins:

(1) Arc formation by radial hinge-line migration of the subducting slab and radial spreading in the overriding plate (radial model, Fig. 4-4a). This model has been proposed for the Hellenic arc and the Aegean Sea, where spreading in the overriding plate along the arc is oriented perpendicular to the arc and where opposite sense rotations of similar magnitude occur on either side of the arc (Fig. 4-1a,b) [*Hatzfeld et al.*, 1997; *Meijer and Wortel*, 1997; *ten Veen and Meijer*, 1998; *Gautier et al.*, 1999]. In terms of dynamics, this model could be explained by the third mechanism, where the hinge-line is actively pushed backwards by the overriding plate collapsing in a radial fashion or by the first mechanism, where the subducting plate is actively rolling back in a radial fashion. This, however, would lead to large in-plane slab-dip-perpendicular extension in the slab, which could be resolved by formation of large vertical tears in the slab (Fig. 4-4a). The second mechanism is not capable of explaining this spreading model, since it would require a radial asthenosphere flow. Other natural examples of this configuration could be the Carpathian arc [*Royden et al.*, 1983], the Calabrian arc [*Malinverno and Ryan*, 1986; *Royden et al.*, 1987] and the Ryukyu arc [*Viallon et al.*, 1986; *Kamata and Kodama*, 1994], which all have opposite sense rotations of comparable magnitude on either side of the arc.

(2) Arc formation by unidirectional hinge-line migration of the slab and unidirectional spreading in the overriding plate (unidirectional model, Fig. 4-4b). This model seems to be applicable to the Scotia arc (Fig. 4-2) [*Shemenda*, 1994; *Barker*, 2001], the Mariana arc [*Hsui*

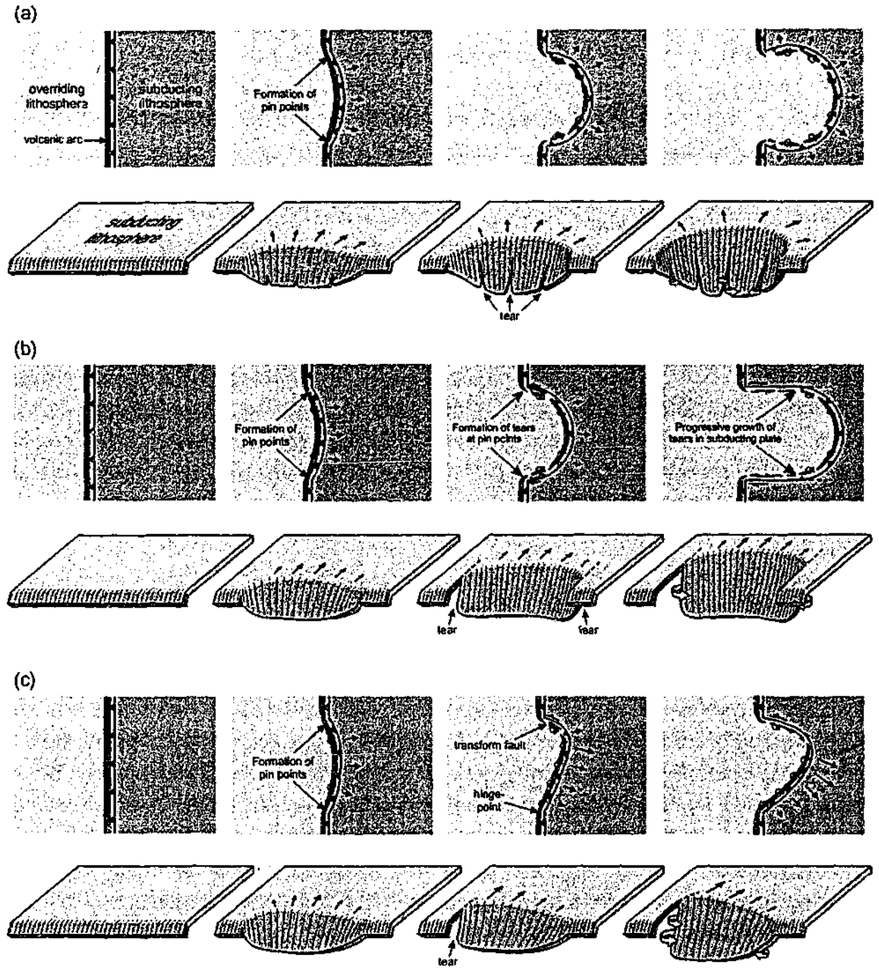

Fig. 4-4. Schematic sketches of development of arc during rollback of subducting slab in plan view (top) and three-dimensional view (bottom) for (a) radial rollback, (b) unidirectional rollback and (c) asymmetrical rollback. Black arrows indicate direction of hinge-line migration. Thick arrows indicate direction of asthenosphere flow to accommodate slab retreat.

and Younquist, 1985], the Lesser Antilles arc [*Burke*, 1988] and the South Shetland arc [*Lawver et al.*, 1995], where arc migration and spreading in the back-arc region is operative in one direction. In a later stage, this spreading is confined on either side by two major transform fault systems (e.g. Scotia arc, Lesser Antilles arc). This model could be explained by either the first or second mechanism, where the formation of tears in the slab on either side of the arc is a requirement for the subducting plate to be able to roll back (Fig. 4-4b). The third mechanism cannot explain this type of back-arc spreading, since the style of rollback of the slab is mainly dependent on the structural configuration of the slab itself.

(3) Arc formation by asymmetrical hinge-line migration of the slab and asymmetrical spreading in the overriding plate (asymmetrical model, Fig. 4-4c). This has been observed for the New Hebrides arc and the Tonga arc (Fig. 4-3) [*Auzende et al.*, 1988; *Hathway*, 1993;

Schellart et al., 2002], as well as the Kuril arc [*Maeda*, 1990]. Spreading of the arc occurs around a hinge-point on one side of the arc and is accommodated on the other side by a transform fault separating the overriding plate and subducting plate. Furthermore, rotation along the arc would be expected to be similar in orientation and magnitude. This model would predict a gradual increase in spreading velocity along the arc from the hinge-point towards the other end, as has been observed along the Tonga arc [*Bevis et al.*, 1995]. This model can probably only be explained by the first mechanism, where asymmetric slab retreat is accommodated by the formation of a vertical tear in the subducting slab on one end of the arc during rotation around a hinge-point on the other end of the arc (Fig. 4-4c). Such a tear would relax in-plane slab-dip-perpendicular tensional stresses in the subducting slab. The hinge-point could be defined by a buoyant ridge on the subducting plate (e.g. the Louisville Ridge on the Pacific plate for the Tonga arc).

I argue that the main contributor to hinge-line migration is the negative buoyancy of the subducting plate, since it can explain all three types of arc formation and back-arc extension mentioned above and is also a physically sound and feasible mechanism (see also Chapter 3). The second mechanism is less feasible since the horizontal buoyancy force of the horizontal plate alone is not great enough to overcome both the resistance of the overriding plate to collapse, as well as the shear resistance of the subduction fault and the resistance of the flexure of the subducting plate to migrate backwards [e.g. *Meijer and Wortel*, 1997]. Furthermore, from this push back mechanism one would expect subduction zones bounding extending back-arc regions to be shallow dipping, while the opposite is observed (Table 3-1). Also, most back-arc regions, which are currently or have recently been extending do not have a high topography (down to several kilometres below sea level) and therefore do not have a very high potential energy to drive extension and push back the hinge-line of the subducting slab (e.g. Alboran Sea, Tyrrhenian Sea, Aegean Sea, Pannonian Basin, Mariana Trough, Okinawa Trough, North Fiji Basin, Lau Basin, Bransfield Strait).

The asthenosphere counterflow mechanism might be a likely mechanism for some arcs (e.g. Lesser Antilles arc, Scotia arc [*Alvarez*, 1982]), but the consequences of this mechanism for the overriding plate are the same as for the first mechanism, since it passively follows the migration of the slab hinge. A global west-directed asthenosphere flow might seem a likely candidate at first to explain the eastward opening up of several back-arc basins [e.g. *Doglioni et al.*, 1999a,b]. However, a thorough investigation of all active arc – back-arc systems indicates that several arcs are currently retreating in a ~ westward direction (e.g. New Hebrides arc [*Schellart et al.*, 2002], Hellenic arc [*Le Pichon*, 1982], South Shetland arc [*Lawver*, 1995], Trans Mexican arc [*Ferrari et al.*, 2001]) or have recently done so (Betic/Rif arc [*Lonergan and White*, 1997]).

Following the reasoning mentioned above and outlined more extensively in Chapter 3, it will be assumed that it is the subducting plate that dictates in which direction the overriding plate is allowed to spread. The models will be built to simulate back-arc extension in the overriding plate from this plausible assumption. From the three proposed scenarios of rollback, arc formation and back-arc extension mentioned above (Fig. 4-4), three simple analogue models have been deduced to investigate the internal structural evolution in the back-arc region of the overriding plate resulting from different boundary conditions along the plate boundary.

4.4. Analogue models

4.4.1. Scaling

In analogue or physical modelling of geological processes, certain scaling rules should be followed in order to make the model a good analogue of the natural prototype. The theory of these rules was first introduced by *Hubbert* [1937]. For a thorough discussion of these rules the reader is referred to previous authors [*Horsfield*, 1977; *Davy and Cobbold*, 1991; *Cobbold and Jackson*, 1992] and to Appendix I. The most important relationship in analogue modelling is the one that relates body forces (due to gravity) to surface forces (stresses). This relationship can be found in Cauchy's equation of motion for a continuous medium, describing the balance of linear momentum:

$$\rho\frac{D^2x_i}{Dt^2}=\frac{\partial\sigma_{ij}}{\partial x_j}+\rho g_i \qquad (i,j=1,2,3) \qquad (4\text{-}1)$$

where ρ is the density, x is the position vector, t is the time, σ is Cauchy's stress tensor and g is the acceleration due to gravity. The suffixes refer to Cartesian vector and tensor components in a fixed spatial frame.

For slow motions, the only forces to be considered are body forces and surface forces. Therefore, it is reasonable to neglect inertial forces [*Davy and Cobbold*, 1991] and the left-hand term in equation (4-1) can be removed. Rearrangement of equation (4-1) leads to:

$$\partial\sigma_{ij}=-\rho g_i\partial x_j \qquad (4\text{-}2)$$

When the experiments are executed in a normal field of gravity, then gravity is the same for both model and nature. Integrating equation (4-2) with the condition that normal and shear stresses at the Earth's surface are negligible compared to stresses at depth for lithospheric scale processes and rewriting for both the analogue model (superscript *a*) and the natural prototype (superscript *n*), and dividing the first by the last results in (see also Appendix I):

$$\frac{\sigma_{ij}^a}{\sigma_{ij}^n}=\frac{\rho^a x_j^a}{\rho^n x_j^n} \qquad (4\text{-}3)$$

Thus, equation (4-3) indicates that stresses should scale down in a similar way that the product of density and length scale down. Viscosity has the dimensions of Pa·s, and therefore scales down as the product of stresses and time scales down [*Cobbold and Jackson*, 1992] (see also Appendix I):

$$\frac{\eta^a}{\eta^n}=\frac{\sigma_{ij}^a t^a}{\sigma_{ij}^n t^n} \qquad (4\text{-}4)$$

where η is the dynamic viscosity and t is time.

In the following experiments, a length scaling factor of 2.5 - 5.0 × 10^{-7} (1 cm in the model represents 20 - 40 km in nature) and a density scaling factor of ~ 0.5 is applied. From

equation (4-3) this leads to stresses, which should be scaled down by a factor 1.25 - 2.5 × 10^{-7}. For brittle material, cohesion should be properly scaled as well. Cohesion has the dimension of Pascal (Pa) and therefore should be scaled down in a similar way that stresses scale down [*Horsfield*, 1977; *Davy and Cobbold*, 1988; *Cobbold and Jackson*, 1992]. Since the cohesion of rocks can range up to ~ 110 MPa (*Schellart* [2000], Appendix III), the cohesion of the analogue material should range up to a maximum of ~ 14 - 28 Pa.

4.4.2. Model set-up

4.4.2.1. Rheology

Two sets of experiments have been executed with a different rheological stratification. In the first set, the model lithosphere consists of a two-layered brittle-ductile system, which lies on top of a flat rigid basement (the perspex bottom of the model box), and is therefore not isostatically supported (Fig. 4-5a). In addition, the overriding plate collapsed into open space

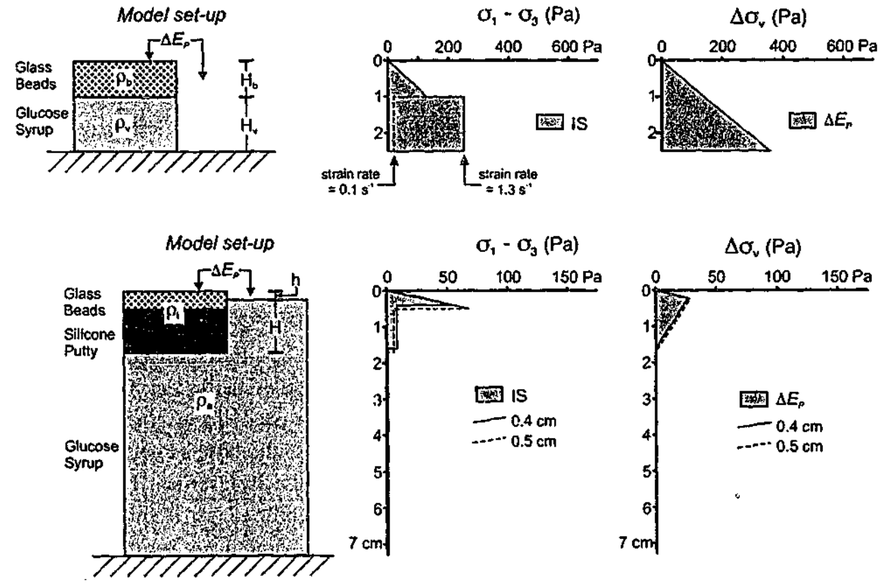

Fig. 4-5. Plots for integrated strength (IS) and potential energy difference (ΔE_p) for two-layered and three-layered models. (a) Two-layered model showing cross-sectional view of experimental set-up (left), integrated strength for extension (middle) for an average strain rate (~ 0.1 s^{-1}, dashed line) and calculated strain rate (1.3 s^{-1}, continuous line) and potential energy difference (right). (b) Three-layered model showing cross-sectional view of model set-up (left), integrated strength (middle) for calculated strain rate for two brittle layer thicknesses (4.4 × 10^{-4} s^{-1} (0.4 cm) and 3.1 × 10^{-4} s^{-1} (0.5 cm) and potential energy difference (right). Integrated strength of the brittle top-layer was calculated from shear test results reported by *Schellart* [2000] (see also Appendix III). Calculated strain rate has been determined by assuming that total integrated strength (brittle integrated strength + viscous integrated strength) is equal to potential energy difference. For two-layered model, this results in very high initial strain rate because potential energy difference is very high in beginning of experiment. For two-layered models, strain rate will decrease rapidly in first seconds of experiment to < 0.1 s^{-1}.

during spreading and therefore the buoyancy forces were not properly scaled. The potential energy difference between the overriding plate and the open space for these experiments can be expressed as follows (see Fig. 4-5a):

$$\Delta E_p = \tfrac{1}{2}\rho_b g(H_b)^2 + \rho_b g H_b(H_v - H_b) + \tfrac{1}{2}\rho_v g(H_v)^2 \qquad (4\text{-}5)$$

where ρ_b and H_b are the density and the thickness of the brittle layer, respectively, and ρ_v and H_v are the density and thickness of the viscous layer, respectively. Also, the results of these two-layered experiments were influenced by the boundaries of the box (especially for larger strains). Therefore another set of experiments was conducted, with a two-layered brittle-ductile system (representing the lithosphere), isostatically supported by an underlying low-viscosity layer (representing the asthenosphere) (Fig. 4-5b). Therefore, the ratio between the buoyancy forces (a driving force) and the integrated strength of overriding plate (a resistive force) were better scaled in the three-layered experiments. For these three-layered experiments, the potential energy difference between the overriding plate and a column of model asthenosphere can be expressed as follows (see Fig. 4-5b):

$$\Delta E_p = \tfrac{1}{2}(\rho_l g h)(h + H) \qquad (4\text{-}6)$$

with:

$$h = \frac{H(\rho_a - \rho_l)}{\rho_l} \qquad (4\text{-}7)$$

where ρ_l is the density of the model lithosphere, h is the elevation difference between the model lithosphere and the model asthenosphere, $h + H$ is the thickness of the model lithosphere, and ρ_a is the density of the asthenosphere.

In the two-layered experiments, the layered system consists of a brittle upper layer and a viscous lower layer. The two-layered system is laid on top of a rigid flat basement, which has been lubricated to reduce friction between the basement and the overlying layer (e.g. conform with *Faugère and Brun* [1984] and *Brun et al.* [1994]). The brittle layer is ~ 1.0 cm thick, simulating a 20 - 40 km thick brittle upper lithosphere. The viscous layer is ~ 1.5 cm thick, simulating a 30 - 60 km thick ductile lower lithosphere. The brittle layer is simulated with fine-grained dry glass microspheres (90 - 180 μm), which show a Mohr-Coulomb type behaviour with an angle of internal friction, $\phi \approx 33°$, and a minimal cohesion [*Schellart*, 2000]. This material is reasonably scaled to model brittle rocks in crustal and lithospheric scale experiments, although its cohesion is still slightly too large. The viscous lower crust is simulated with glucose syrup with a viscosity of ~ 50 - 400 Pa·s. On top of the brittle upper layer, a passive grid of black glass microspheres is laid, where the individual lines have a spacing of 3 cm. Each experiment normally lasted ~ 10 minutes until the spreading arc front would reach the boundary of the box (radial model + unidirectional model) or after 90° of rotation of the boundary (asymmetrical model). In the two-layered experiments, 20 s resembles ~ 1 Ma in nature. With a model material viscosity of 400 Pa·s and a stress ratio of 1.25 - 2.5 × 10^{-7}, one can calculate the apparent viscosity for the natural prototype with equation (4-4). This results in a viscosity of ~ 2.5 × 10^{21} - 5.0 × 10^{21} Pa·s for the viscous lower lithosphere in the natural prototype. These values are close to real values for the lower

lithosphere, but might be somewhat too low, since the sub-lithospheric mantle already has a viscosity of ~ 10^{20} - 10^{21} Pa·s [*Ranalli*, 1995]. In total, 15 experiments have been conducted with the two-layered configuration. The parameters for the two-layered experiments discussed in the text are given in Table 4-1.

The three-layer experiments consist of a brittle upper layer, a high-viscosity middle layer and a low-viscosity lower layer. The uppermost two layers represent the lithosphere and the lowermost layer represents the asthenosphere. The brittle layer is ~ 0.5 cm thick, simulating a 10 - 20 km thick brittle upper lithosphere. The high-viscosity layer is ~ 1.2 cm thick, simulating a 20 - 40 km thick ductile lower lithosphere. The low-viscosity layer is 5.5 cm thick and represents the low-viscosity asthenosphere, and gives the overlying model lithosphere isostatic support. The brittle layer is simulated with fine-grained dry glass microspheres (90 - 180 μm). The lower lithosphere is simulated with silicone putty with a viscosity of ~ 2 × 10^4 Pa·s. The asthenosphere is simulated with glucose syrup with a viscosity of ~ 100 Pa·s. On top of the brittle upper layer, a passive grid of black glass microspheres is laid, where the individual lines have a spacing of 3 cm. Each experiment normally lasted ~ 20 hours. In the three-layered experiments, 1 hr resembles ~ 1 Ma in nature. With a model material viscosity of 100 Pa·s and a stress ratio of 1.25 - 2.5 × 10^{-7}, this is equivalent to a viscosity of ~ 1.1 × 10^{19} - 2.2 × 10^{19} Pa·s, in the natural prototype, which is equivalent to the viscosity of the asthenosphere (~ 10^{19} - 10^{20} Pa·s [*Artyushkov*, 1983]). In total, 10 experiments have been conducted with a three-layered configuration. The parameters for the three-layered experiments discussed in the text are given in Table 4-2.

All the experiments have been recorded in plan view with a camera under oblique lighting of the top surface of the experiment from the back to enhance visualisation of the faults and fault escarpments. After each experiment, the images have been analysed in terms of the type of deformation and on the amount of displacement, strain and rotation.

4.4.2.2. Boundary conditions

The model apparatus consists of a rectangular box (60 by 40 cm), which is filled by a two- or three-layered system. At one of the long sides of this box there is a 34 cm wide gate, in which a removable side-wall can be positioned (radial model + unidirectional model) or a

Experiment number	Model type	Material	Density (kg/m^3)	Layer thickness (cm)	Viscosity (Pa·s)
2	Radial	Microspheres	1.48 x 10^3	1.0	-
		Glucose syrup	1.42 x 10^3	1.5	± 50
5	Radial	Microspheres	1.48 x 10^3	1.0	-
		Glucose syrup	1.42 x 10^3	1.5	± 100
9	Asymmetrical	Microspheres	1.48 x 10^3	1.0	-
		Glucose syrup	1.42 x 10^3	1.7	± 100
12	Asymmetrical	Microspheres	1.48 x 10^3	1.0	-
		Glucose syrup	1.42 x 10^3	1.6	± 100
13	Unidirectional	Microspheres	1.48 x 10^3	1.0	-
		Glucose syrup	1.42 x 10^3	1.6	± 100
15	Radial	Microspheres	1.48 x 10^3	1.0	-
		Glucose syrup	1.42 x 10^3	1.7	± 400

Table 4-1. Physical properties of modelling materials and experimental set-up for two-layered experiments discussed in the text.

Experiment number	Model type	Material	Density (kg/m³)	Layer thickness (cm)	Viscosity (Pa·s)
		Microspheres	1.22×10^3	0.5	-
3	Asymmetrical	Silicone Putty	1.22×10^3	1.2	2×10^4
		Glucose syrup	1.42×10^3	5.5	± 100
		Microspheres	1.22×10^3	0.5	-
4	Radial	Silicone Putty	1.22×10^3	1.2	2×10^4
		Glucose syrup	1.42×10^3	5.5	± 100
		Microspheres	1.22×10^3	0.5	-
5	Unidirectional	Silicone Putty	1.22×10^3	1.2	2×10^4
		Glucose syrup	1.42×10^3	5.5	± 100
		Microspheres	1.22×10^3	0.4	-
6	Unidirectional	Silicone Putty	1.22×10^3	1.2	2×10^4
		Glucose syrup	1.42×10^3	5.5	± 100
		Microspheres	1.22×10^3	0.6	-
7	Unidirectional	Silicone Putty	1.22×10^3	1.2	2×10^4
		Glucose syrup	1.42×10^3	5.5	± 100
		Microspheres	1.22×10^3	0.7	-
8	Unidirectional	Silicone Putty	1.22×10^3	1.2	2×10^4
		Glucose syrup	1.42×10^3	5.5	± 100
		Microspheres	1.22×10^3	0.3	-
9	Unidirectional	Silicone Putty	1.22×10^3	1.2	2×10^4
		Glucose syrup	1.42×10^3	5.5	± 100
		Microspheres	1.22×10^3	0.8	-
10	Unidirectional	Silicone Putty	1.22×10^3	1.2	2×10^4
		Glucose syrup	1.42×10^3	5.5	± 100

Table 4-2. Physical properties of modelling materials and experimental set-up for three-layered experiments discussed in the text.

side-wall, which can be rotated outwards progressively, analogous to an opening door (asymmetrical model). After removal or rotation of this side-wall, the layered system flows outward through the gate, because of its excess potential energy. In the radial model, the outward flow is not restricted in any direction (Fig. 4-6a) and shows similarity to the models made by *Merle* [1989], *Hatzfeld et al.* [1997] and *Gautier et al.* [1999]. In the unidirectional model, the outward flow is restricted by two parallel side-walls, which originate at the edges of the gate (Fig. 4-6b). The boundary conditions of this model are similar to the ones of the analytical model proposed by *Hsui and Youngquist* [1985] for the Mariana arc, where a Newtonian viscous fluid with a linear front moves over two stationary obstacle points. In the

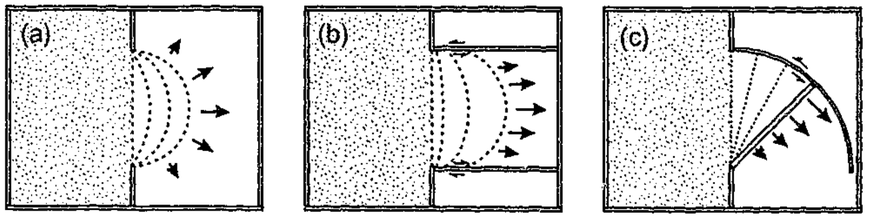

Fig. 4-6. Three basic models to investigate back-arc extension with (a) radial spreading model, (b) unidirectional spreading model with spreading perpendicular to the gate opening and (c) asymmetrical spreading model.

asymmetrical model, a rotational side-wall is positioned in the gate, which rotates around a hinge-point located at one of the edges of the gate (Fig. 4-6c). This rotating side-wall is straight and does not deform during rotation. In the two-layered experiments this side-wall was pushed open by the spreading sheet itself, while in the three-layered experiments the opening was driven by a motor.

The three models simulate the three different types of arc and back-arc formation related to the three different modes of slab rollback, as described in section 4.3 (Fig. 4-4). The simulations are best modelled by the three-layered asymmetrical model, in which retreat of the boundary is controlled by a motor. Thus, the rate of retreat and amount of provided space into which the layered system is allowed to collapse is controlled externally. The radial and unidirectional model are less realistic, since they have free boundaries and there is no external moving boundary, which dictates the direction and the rate at which the system is allowed to spread. However, the stationary boundary conditions in these models force the whole system to spread in such a way as needed to mimic the types of arc formation in the radial and unidirectional model as described in section 4.3 (Fig. 4-4). Therefore, the resulting back-arc strain patterns observed in these two models should give a good indication of strain patterns to be expected behind these types of arcs, even though the retreating hinge-line has been effectively removed from the analogue models. Another limitation of the radial and unidirectional model, as well as the two-layered asymmetrical model, is that the rate at which the deformation occurs is entirely determined by the rate at which the overriding plate collapses, simply because there is no retreating hinge involved in the model. The collapse rate itself is dependent on the integrated strength of the layered system and the potential energy difference (Fig. 4-5). In the two-layered experiments, this leads to very a high strain rate in the initial stage of deformation, which then decreases due to a decrease in potential energy gradient. In nature, the extensional strain rate is influenced (if not determined) by the rate at which the slab retreats. Although these limitations are acknowledged, the experiments will still provide valuable insights into the structural evolution of arc – back-arc systems for different boundary conditions along the arc.

4.5. Results of two-layered experiments

4.5.1. General results

All the experiments show a decrease in spreading velocity of the arc through time. Deformation starts in a region, close to the free boundary (up to ~ 3-4 cm behind the free boundary). As the experiment continues, the deformation front rapidly propagates backward, while deformation continues to take place close to the arc. Moreover, with a relatively high viscosity lower layer, the deformation takes place over a larger area and is facilitated along many small faults with minor displacement, while a relatively low viscosity lower layer results in deformation along fewer, larger faults, along which displacement is greater (Fig. 4-7). The radial and unidirectional model give symmetrical deformation patterns, while deformation patterns in the asymmetrical model are asymmetric. Also, the radial and unidirectional model give a much more diffuse spreading pattern, while deformation in the asymmetrical model results in the formation of several clearly defined fault blocks that remain rigid and only show translation and rotation. Finally, in the three models, the zone of deformation in the interior of the box is of comparable size to the dimensions of the gate.

However, the two-layered models show that the boundaries in the interior of the box influence the deformation pattern inside the box in the later stages of deformation.

For convenience in the following descriptions, it is assumed that the filled box is situated west of the gate, that the gate is oriented N-S and that the spreading sheet is situated east of the gate.

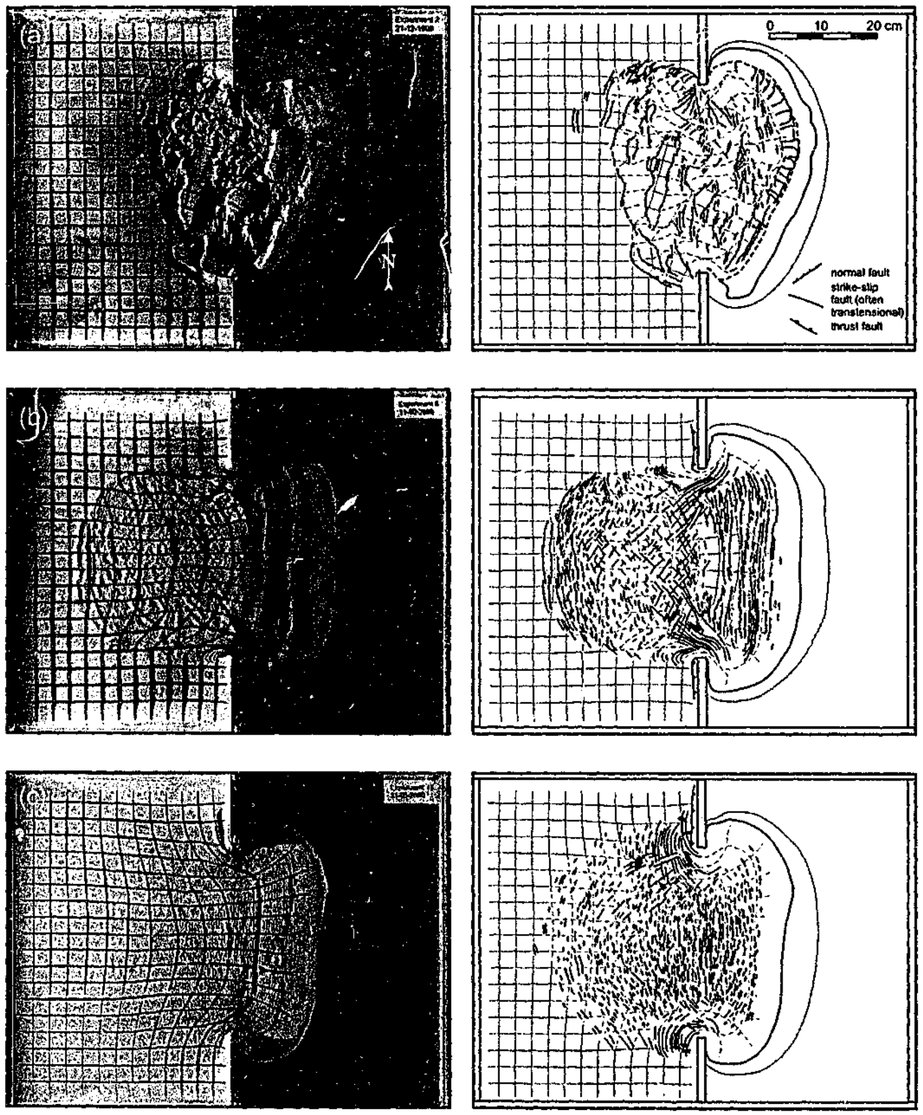

Fig. 4-7. Top view photographs (left) and interpretation (right) of three two-layered experiments with the radial model configuration and different bottom layer viscosity. (a) Experiment 2 ($\eta \sim 50$ Pa s) after 240 s, (b) experiment 5 ($\eta \sim 100$ Pa s) after 120 s and (c) experiment 15 ($\eta \sim 400$ Pa s) after 88 s.

4.5.1.1. Radial model

The results described here are from experiment 5 (Fig. 4-8). In this model, the free boundary becomes progressively more convex towards the direction of spreading. Deformation starts with formation of a straight graben bounded by several normal faults located a few centimetres behind the free boundary, more or less parallel to the free boundary (Fig. 4-8a). This structure develops from two individual grabens at the edges of the gate, which later connect in the centre. Contemporaneous with graben formation is the development of conjugate strike-slip faults near the corners of the gate behind the graben. Here, individual faults start to propagate towards the centre and west. This results in a large zone of conjugate strike-slip faults and normal oblique-slip faults in the box interior, which is separated from the graben in the east by a large undeformed fault bound block (Fig. 4-8b). In a later stage, the strike-slip faults start to accommodate normal dip-slip movement as well. At the edge of the major conjugate strike-slip and oblique-slip fault zone, normal faults start to develop in the west and normal oblique-slip faults to the north and south (Fig. 4-8c). Arc-parallel extension takes place along the arc (at the outermost marker line near the arc, arc-parallel extension ranges between 50 and 150%). In a late stage of the experiment, a new graben develops in the undeformed block, striking parallel to the arc and is followed by the development of several arc-perpendicular normal faults (Fig. 4-8d). Rotation of up to ~ 90° takes place on both sides of the gate, with clockwise rotation in the south and anticlockwise rotation in the north. Shear rotation of up to 60 - 70° occurs predominantly in the inside of the box with dextral shearing in the south and sinistral shearing in the north.

4.5.1.2. Unidirectional model

The results described here are from experiment 13 (Fig. 4-9). During the experiment, the free boundary becomes progressively more arc-shaped, convex towards the direction of spreading. Extension starts close behind the free boundary, forming a normal fault zone, with faults parallel to the free boundary (Fig. 4-9a). This zone of extension rapidly migrates towards the west, where at ~ 6 - 8 cm behind the free boundary a localised zone of extension starts to form. This zone quickly starts to accommodate most of the arc-perpendicular extension (Fig. 4-9b) and becomes convex towards the direction of spreading. Behind the normal fault zone, a zone of conjugate strike-slip faults forms, similar to that in the radial model (Fig. 4-9c). This zone of conjugate strike-slip faults progressively migrates towards the west. With ongoing deformation, shearing takes place in the spreading sheet along the two side-walls with dextral shearing along the southern side-wall and sinistral shearing along the northern side-wall. Rotation is small with up to 20° of clockwise rotation in the south and anticlockwise rotation in the north. In contrast, shear rotation is very large with up to 80° of dextral shearing in the south and sinistral shearing in the north. In a late stage, normal faults at the western end and oblique normal faults at the northern and southern side of the conjugate strike-slip zone start to develop (Fig. 4-9d), although not as clearly defined as in the radial model. Arc-parallel extension is less prominent in this model, when compared to the radial model (at the easternmost marker line near the arc, arc-parallel extension ranges between 5 and 15%).

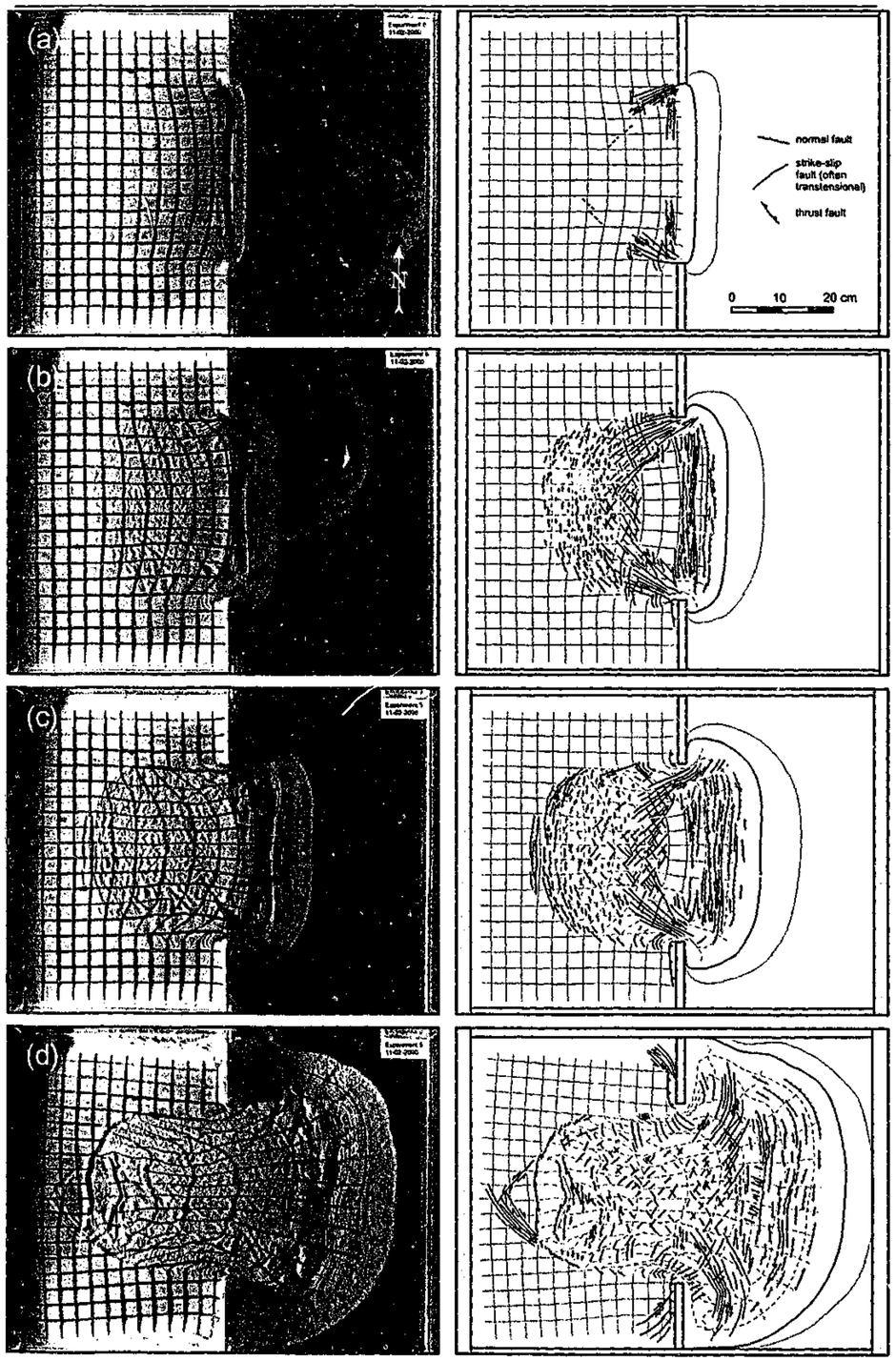

Fig. 4-8. Top view photographs (left) and interpretation (right) of two-layered experiment 5 (radial model) during different stages of deformation, with (a) after 10 s, (b) after 35 s, (c) after 90 s and (d) after 420 s.

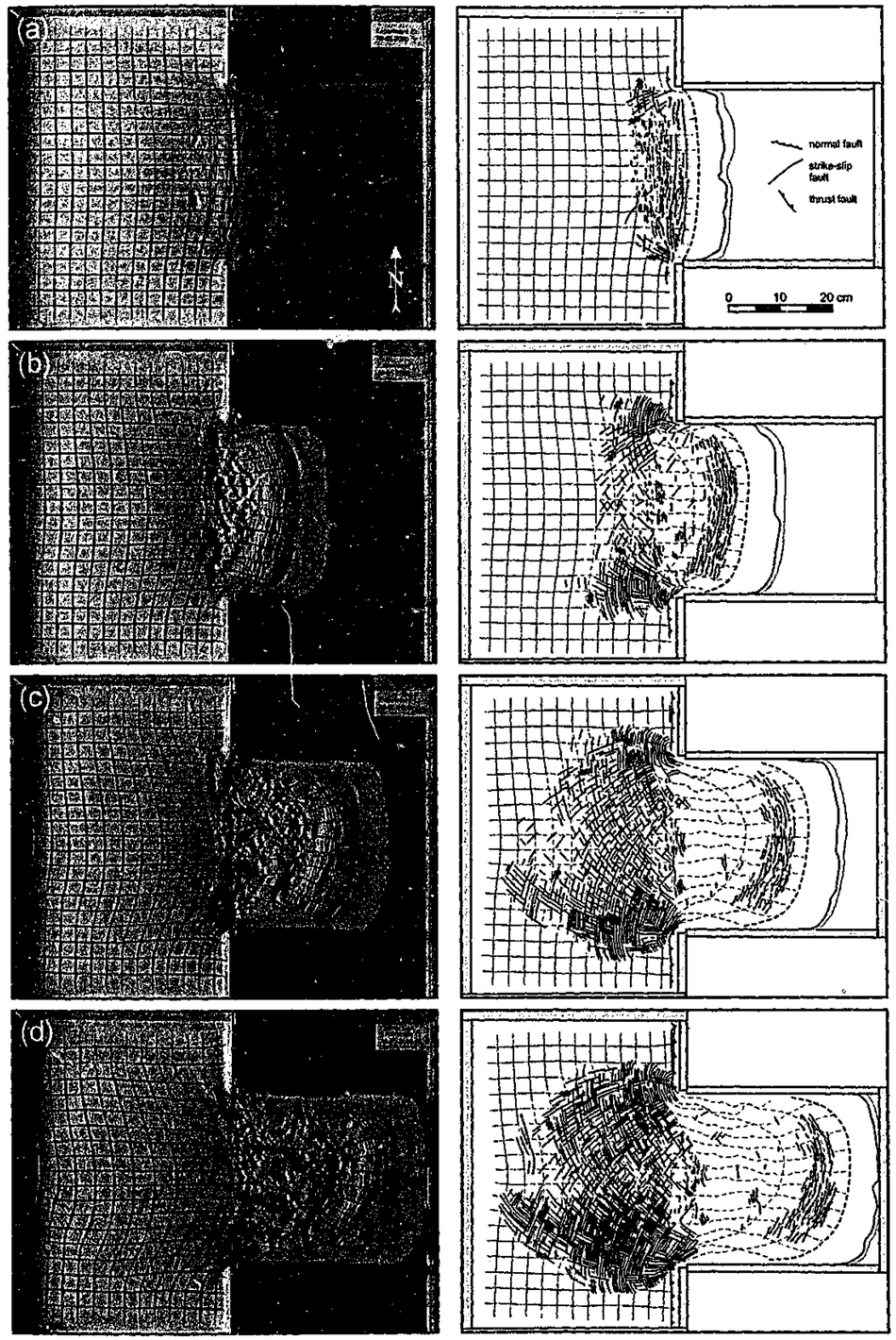

Fig. 4-9. Top view photographs (left) and interpretation (right) of two-layered experiment 13 (unidirectional model) during different stages of deformation, with (a) after 45 s, (b) after 150 s, (c) after 390 s and (d) after 540 s.

4.5.1.3. Asymmetrical model

The results described here are from experiment 12 (Fig. 4-10). Deformation starts with extension located in a zone a few centimetres behind the rotating wall along the northern side of this wall, followed by development of strike-slip faults in the northern corner of the gate (Fig. 4-10a). With ongoing deformation, the strike-slip faults progressively propagate towards the centre of the box, where a wide zone of deformation develops, with (oblique) normal faults striking parallel (in the north) to oblique (in the south) (up to ~ 45°) to the gate (Fig. 4-10b). In the southern corner of the gate, a graben develops, striking approximately E-W, which curves northward in the west to connect with the oblique-extension zone. From this stage onward, a major individual fault block develops which is bounded in the south by the E-W striking graben, to the west by the oblique-extension zone, in the north by the strike-slip zone and in the east by the rotating boundary. This fault block rotates clockwise, according to the rotation of the rotating boundary, without much internal deformation. With ongoing rotation, new grabens and strike-slip zones develop in the west and north, leading to four new individual fault blocks (Fig. 4-10c). Continued rotation of the boundary results in the lateral displacement of three fault blocks in the west towards the east with only minor rotation (up to 30°) (Fig. 4-10d). The large fault block in the east continues to rotate clockwise. In contrast, the northernmost fault block rotates anticlockwise (up to 100°). During the clockwise rotation of the eastern fault block, sinistral shearing along the curved boundary leads to the formation of right-stepping en echelon sinistral strike-slip faults and left-stepping en echelon folds (Fig. 4-10d).

4.5.2. Displacement

The displacement fields of the three models is shown in Fig. 4-11 (experiment 15, 13 and 12) for individual points located on the top surface of the model, between different stages of deformation. Each model shows its own distinct displacement field pattern. In all three experiments, the displacement (and thus spreading velocity) is greatest along the arc and decreases progressively towards the west. The spreading velocity is greatest in the radial model and smallest in the asymmetrical model, resulting from the frictional resistance along the boundaries in the unidirectional and asymmetrical model.

Displacement in the radial model initially shows parallel spreading vectors near the free boundary, which are perpendicular to the gate (Fig. 4-11a), resulting in the formation of arc-perpendicular extension with arc-parallel grabens. Inside the box, further away from the gate, the displacement vectors show a converging pattern towards the gate. This converging component, together with the overall displacement towards the east results in the formation of conjugate strike-slip faults and oblique-slip faults, accommodating shortening in the N-S direction, as well as extension in the E-W direction. In a later stage during spreading, when a significant part of the sheet is outside the box, the sheet shows a diverging or radial pattern of displacement vectors, thus combining both N-S and E-W extension. This results in continued arc-perpendicular extension combined with arc-parallel extension near the free boundary.

The unidirectional model shows a similar displacement pattern in the initial stages of deformation, compared to the radial model, with parallel spreading vectors near the free boundary, perpendicular to the gate and a converging pattern inside the box (Fig. 4-11b). However, in a more advanced stage, the spreading sheet, (the part located to the east of the

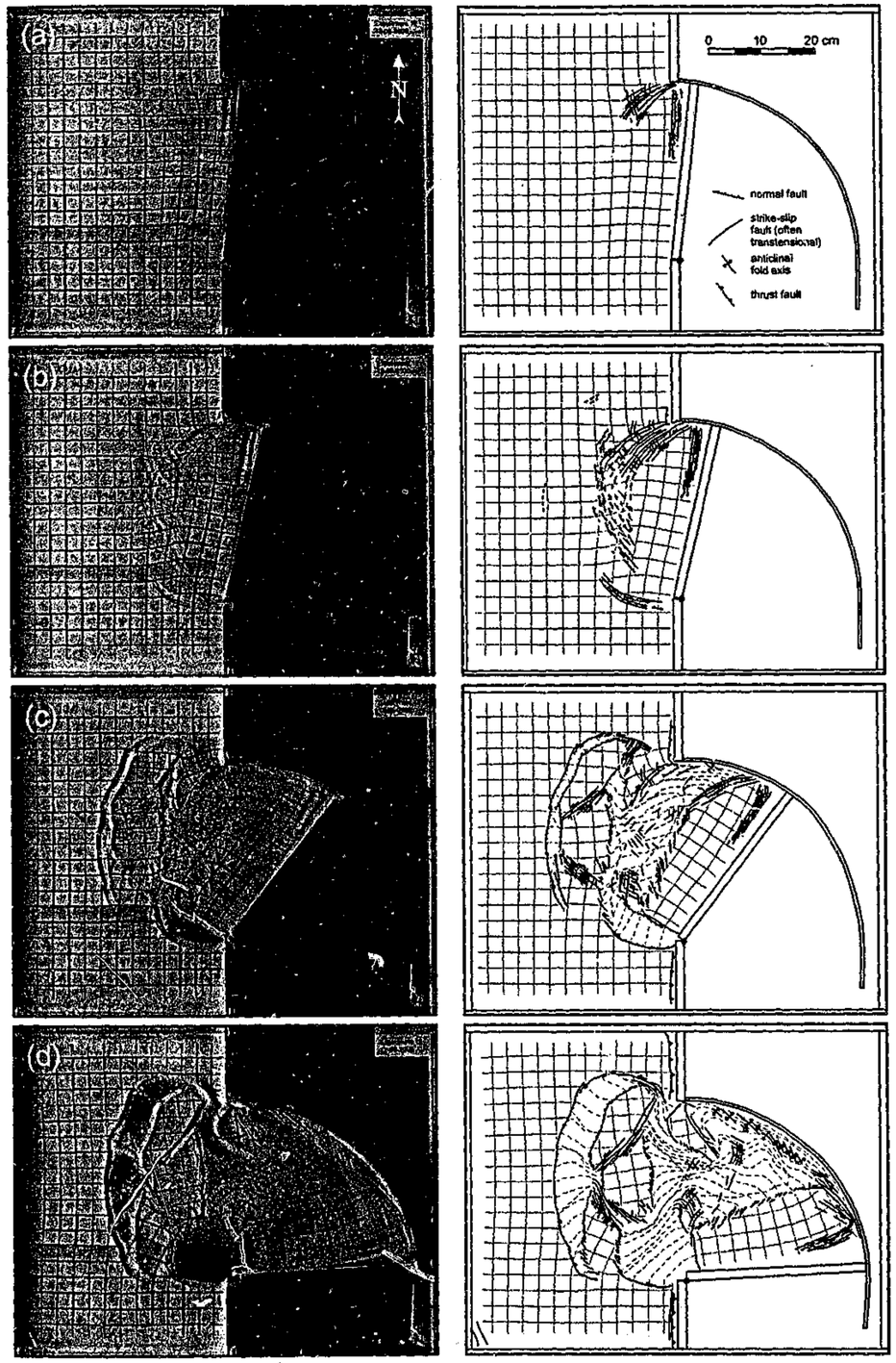

Fig. 4-10. Top view photographs (left) and interpretation (right) of two-layered experiment 12 (asymmetrical model) during different stages of rotation of the boundary, with (a)after ~ 20 s (6°), (b) after ~ 60 s (13°), (c) after ~ 300 s (38°) and (d) after ~ 780 s (87°).

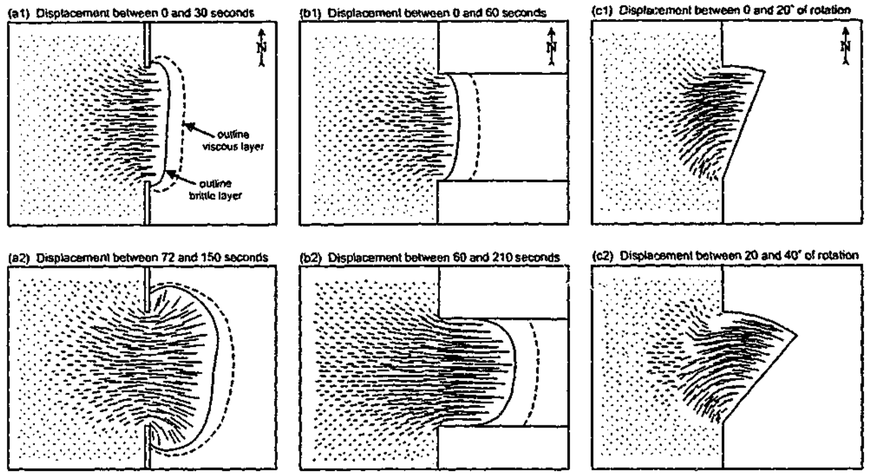

Fig. 4-11. Displacement fields for the three different two-layered models during different stages of their structural evolution, with (a) radial model (experiment 15), (b) unidirectional model (experiment 13) and (c) asymmetrical model (experiment 12).

gate) shows displacement vectors, which are approximately parallel to each other and oriented perpendicular to the gate. Displacement is faster in the centre than on the sides due to friction along the side-walls, resulting in sinistral shearing in the north and dextral shearing in the south. Since there is hardly any displacement in the spreading sheet in the N-S direction, arc-parallel extension is hardly evident in this model.

The asymmetrical model shows an asymmetrical displacement pattern (Fig. 4-11c), as opposed to the displacement patterns observed in the radial and unidirectional model. There is an overall convergent pattern of displacement vectors towards the gate. However, there is an asymmetry in this convergent pattern with displacement vectors oriented more towards the far end of the rotating boundary. This is related to the faster opening of the gate near the far end of the rotating boundary, when compared with the region close to the hinge. Some regions have similar displacement vectors, related to the formation of individual fault blocks, where all points on a fault block show a common history of displacement. This behaviour is not as obvious for the fault block adjacent to the rotating boundary, because of its major clockwise rotation, which results in a curved pattern of displacement vectors.

4.5.3. Rotation and simple shear

Fig. 4-12 shows the rotation fields of the three models (experiment 15, 13 and 12) at four stages during deformation. In these plots, the intersection points of the N-S and E-W grid lines have been plotted. For each intersection point which has experienced only rigid body rotation only the originally E-W oriented grid line has been plotted. For each intersection point, which has experienced shear rotation (with or without rigid body rotation), both N-S and E-W grid lines have been plotted.

In the radial model, shear rotation is dominant in the inside of the box with dextral shearing in the south and sinistral shearing in the north of up to 60 - 70°. This shear rotation starts close to the gate boundaries (Fig. 4-12a1) and migrates towards the west (Fig. 4-12a2-4).

Rotation is only apparent for the spreading sheet located east of the gate (Fig. 4-12a2-4). It shows clockwise rotation in the south and anticlockwise rotation in the north, which can be as large as ~ 90° (Fig. 4-12a3-4).

Rotation in the unidirectional model is small (< 20°) and is only present in the spreading sheet located east of the gate, with clockwise rotation in the south and anticlockwise rotation in the north (Fig. 4-12b). Most apparent rotation of the N-S grid lines is related to simple shear, with dextral shear in the south and sinistral shear in the north. It can also be observed that this shearing is best developed on either side of the out-flowing sheet near the corners of the gate. Shear rotation originates close to the gate boundaries and progressively migrates towards the west. The maximum shear angle can be as large as 80°.

Rotation in the asymmetrical model is mostly in accordance with the clockwise rotation of the rotating boundary, (Fig. 4-12c), especially for the fault block adjacent to this boundary. For the most part, this rotation is not larger than the amount of rotation of the opening door. However, an individual fault block, located in the region immediately west of the northern boundary of the gate, shows anticlockwise rotation of up to 100° after 90° of rotation of the door. In experiment 9, an individual fault block located in an equivalent position as in experiment 12, had even rotated some 80-100° anticlockwise after some 60° of clockwise rotation of the door.

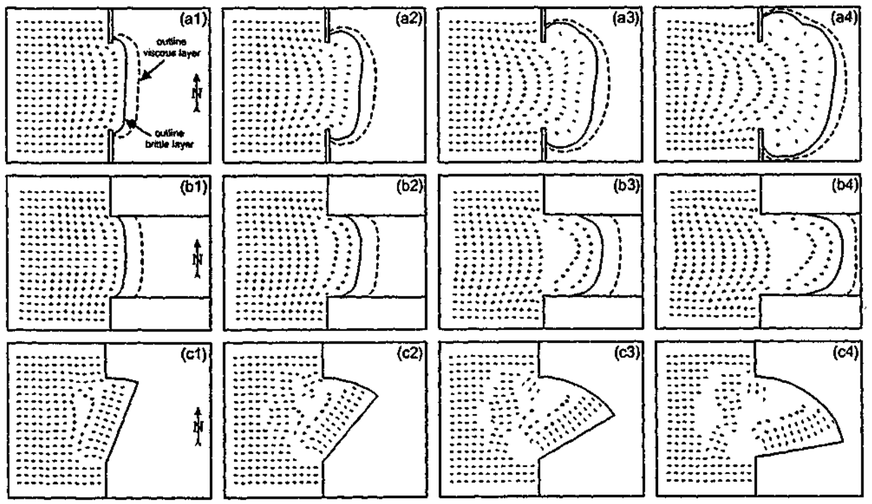

Fig. 4-12. Rotation fields for the two-layered experiments with the three model configurations. (a) For the radial model (experiment 15), with (a1) after 30 s, (a2) after 72 s, (a3) after 150 s and (a4) after 300 s. (b) For the unidirectional model (experiment 13), with (b1) after 60 s, (b2) after 90 s, (b3) after 210 s and (b4) after 600 s. (c) for the asymmetrical model (experiment 12), with (c1) after ~ 120 s (20°), (c2) after ~ 315 s (40°), (c3) after ~ 500 s (60°) and (c4) after ~ 700 s (80°) of rotation. Rigid block rotation is indicated by lines, while rotation involving simple shear is indicated by crosses.

4.6. Results of three-layered experiments

4.6.1. General Results

The experiments with a free boundary (radial and unidirectional model) show a decrease in spreading velocity of the arc through time (for the asymmetrical model the spreading rate is controlled by the retreating door, which is driven by a motor). Deformation starts in a region, close to the free boundary (up to ~ 3-4 cm behind the free boundary) and with ongoing deformation, the deformation front slowly propagates backward, while deformation continues to take place close to the arc. Moreover, with a relatively thin brittle top layer, the deformation takes place over a larger area and is facilitated along many small faults with minor displacement, while a relatively thick brittle top layer results in deformation along fewer, larger faults, along which displacement is larger. The radial and unidirectional model give symmetric deformation patterns, while deformation patterns in the asymmetrical model are asymmetric. Finally, in the three models, the zone of deformation in the interior of the box is of comparable size to the dimensions of the gate.

The results of the three-layered experiments are qualitatively and semi-quantitatively similar to the results of the two-layered experiments. The same types of faults develop at similar places with similar orientations for the three models. Also, the extent of deformation inside the box is of similar magnitude for each model in the two- and three-layered case. The major difference is the time-scale, since the two-layered experiments last up to ~ 15 minutes while the three-layered experiments last up to ~ 24 hours. Also, the side-walls do not influence the experimental results in the three-layered experiments, as was observed in the two-layered experiments.

4.6.1.1. Radial model

In the radial model (experiment 4 (Fig. 4-13a)) deformation starts with arc-perpendicular extension (arc-parallel grabens) close to the free boundary and strike-slip faults at the corners of the gate (sinistral in the north and dextral in the south). New grabens develop progressively further away from the retreating boundary and the strike-slip faults grow progressively towards the west. In an advanced stage, arc-perpendicular faults form close to the retreating boundary to accommodate arc-parallel extension. Rotation of up to 50° is observed in the spreading sheet with clockwise rotation in the south and anticlockwise rotation in the north.

4.6.1.2. Unidirectional model

In the unidirectional model (experiment 5 (Fig. 4-13b)), deformation is similar to the radial model (Fig. 4-13a), but the arc-parallel extension is less evident and the strike-slip faults are more developed. The influence of the thickness of the brittle top layer on the deformation in the overriding plate is shown in Fig. 4-14. With a thin brittle top layer, deformation is accommodated over a large area and is absorbed by many small faults. With increasing thickness of the brittle top layer, relatively large undeformed plate segments develop, bounded by normal and strike-slip faults, which might be translated and rotated during the experiment, but do not experience any significant internal deformation. Also, the relative importance of normal faults to absorb deformation with respect to strike-slip faults increases with increasing brittle layer thickness. In experiment 9 (Fig. 4-14a), deformation is mainly

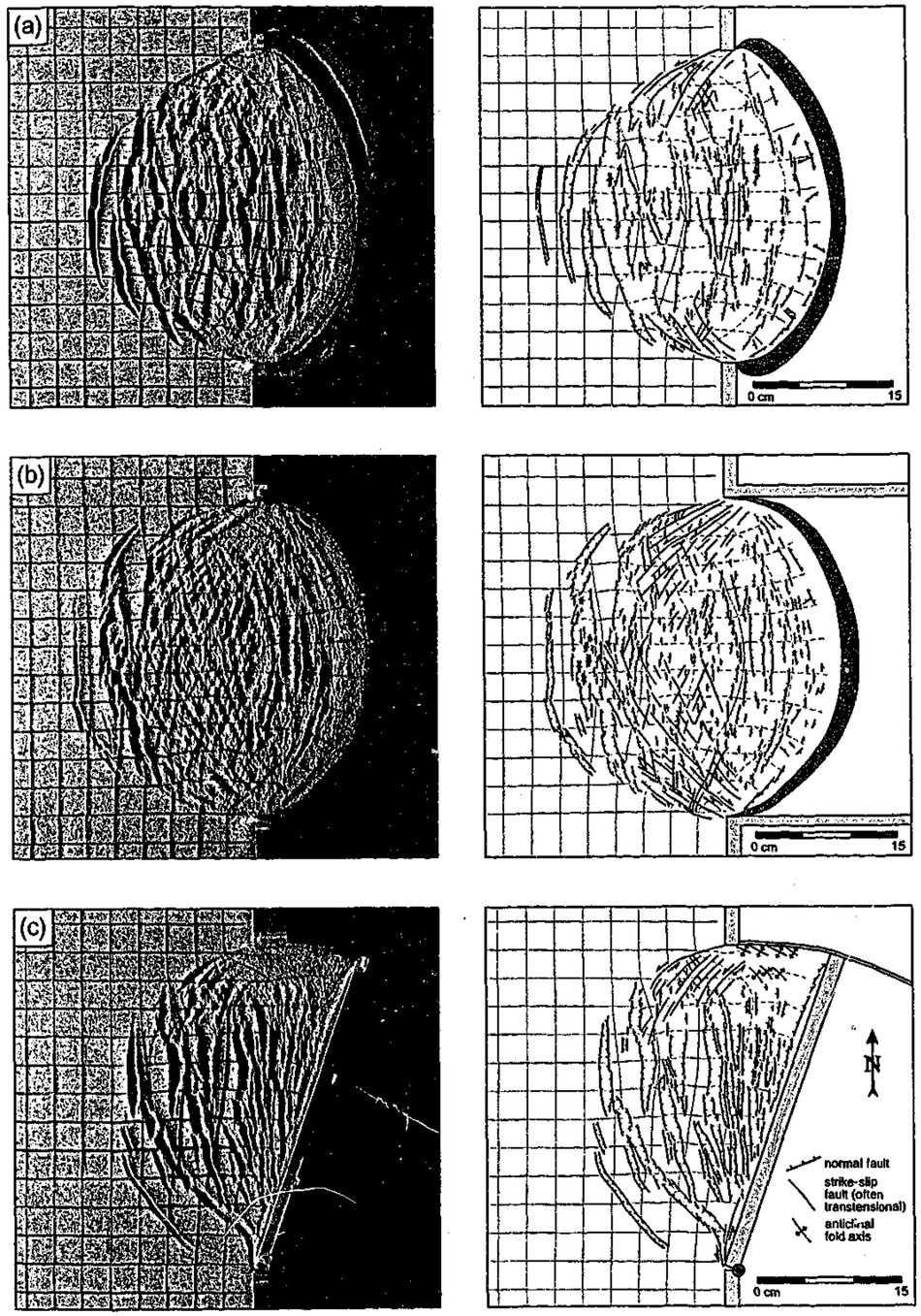

Fig. 4-13. Top view photographs (left) and interpretation (right) of three-layered experiments for the three different model configurations. (a) Experiment 4 after 5 hr (radial model), (b) experiment 6 after 3 1/2 hr (unidirectional model) and (c) experiment 3 after 5 hr (asymmetrical model). All three experiments have a 0.5 cm brittle top-layer, a 1.2 cm high-viscosity layer and a 5.5 cm low-viscosity layer.

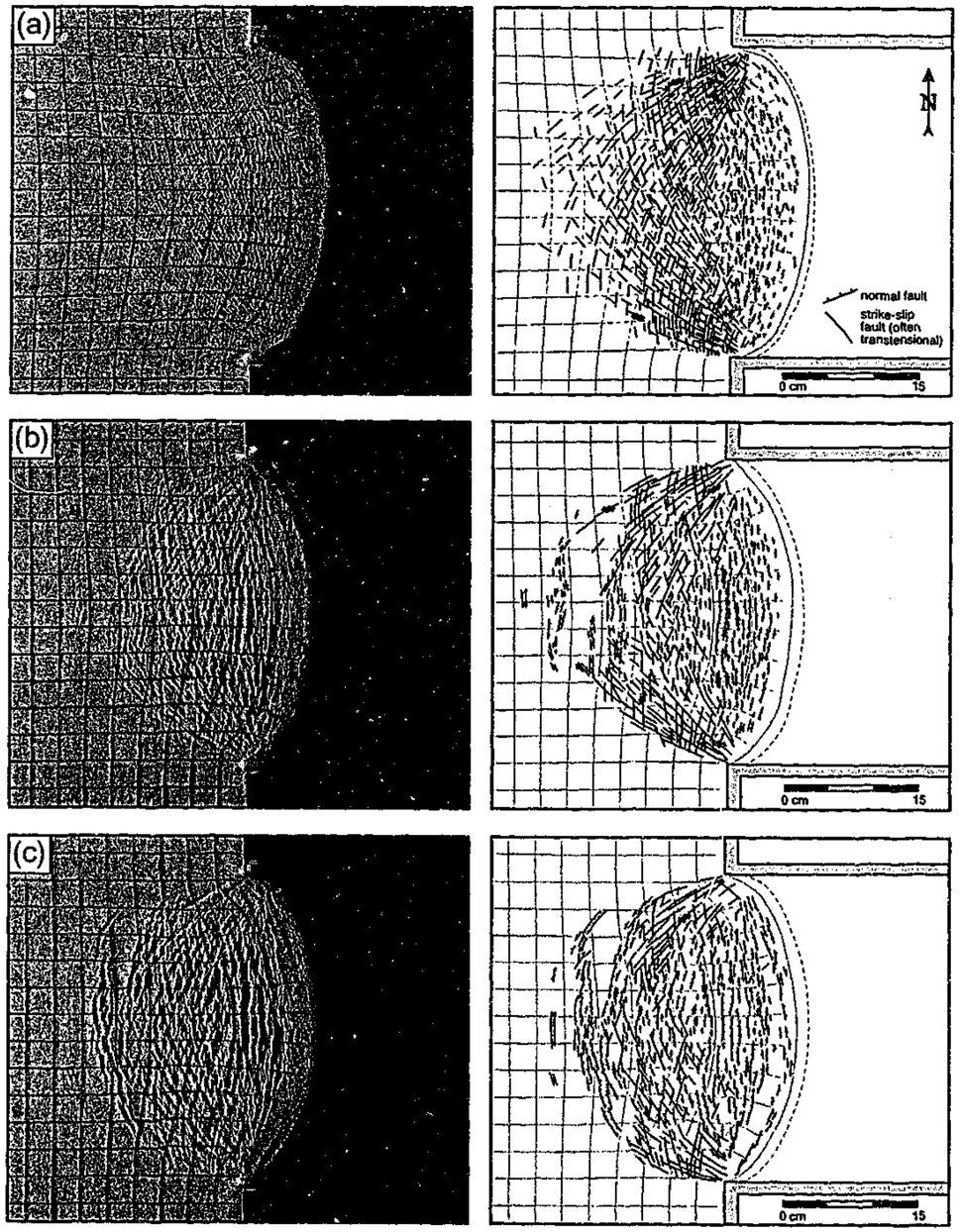

Fig. 4-14. Top view photographs (left) and interpretation (right) of three-layered experiments with unidirectional model set up for various brittle top layer thicknesses. (a) Experiment 9 (3 mm) after 1 1/4 hr, (b) experiment 5 (4 mm) after 2 1/2 hr, (c) experiment 6 (5 mm) after 2 hr.

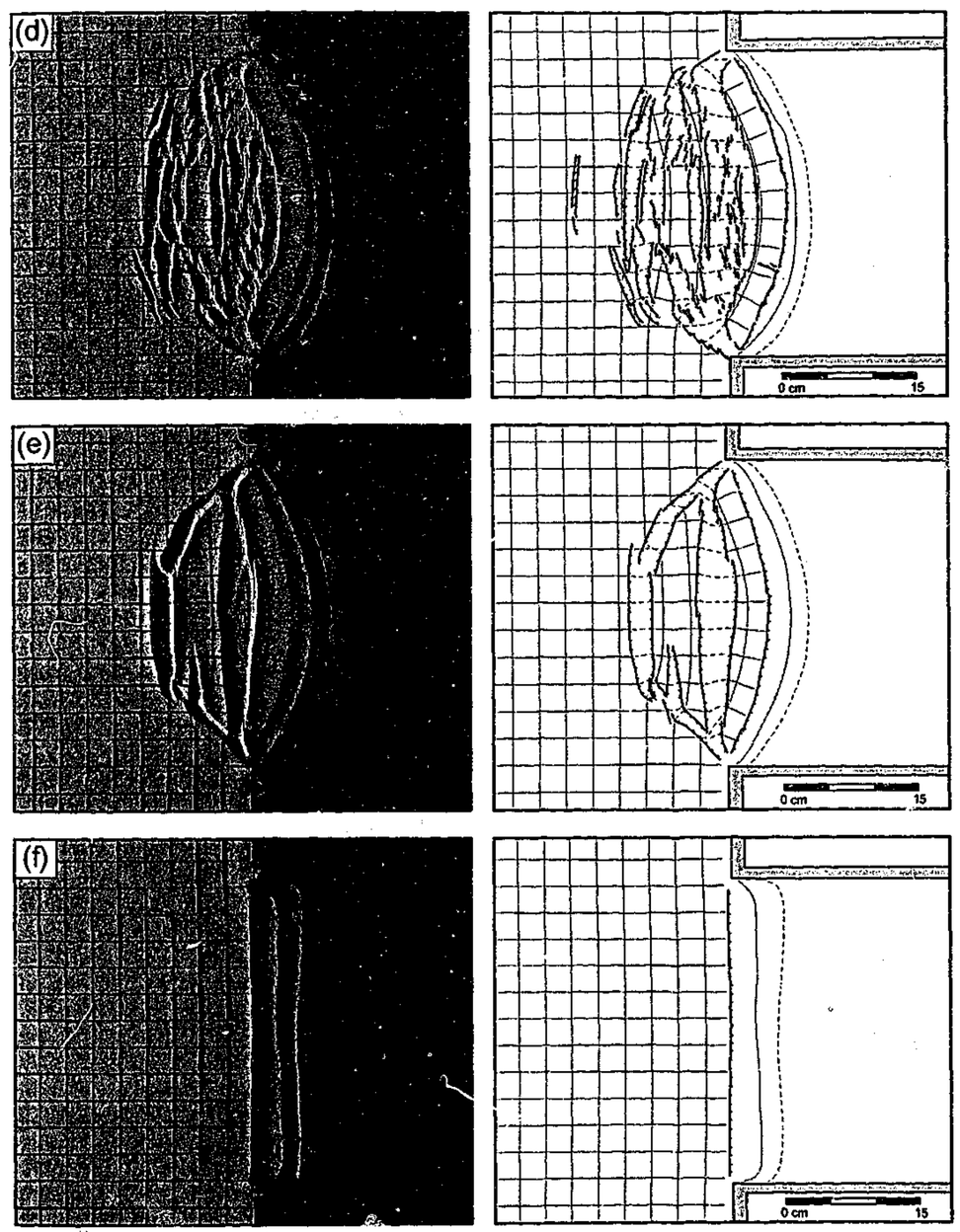

Fig. 4-14 (continued). Top view photographs (left) and interpretation (right) of three-layered experiments with unidirectional model set up for various brittle top layer thicknesses. (d) Experiment 7 (6 mm) after 4 hr, (e) experiment 8 (7 mm) after 5 hr and (f) experiment 10 (8 mm) after 7 hr.

accommodated by strike-slip faults, while in experiment 8 (Fig. 4-14e), deformation is almost entirely accommodated by normal faults. For experiment 10, the brittle integrated strength was significantly greater (~ 0.43 N/m) than the buoyancy force of the overriding plate with respect to the glucose syrup (0.377 N/m). Therefore, no deformation occurred in the brittle top layer, but viscous spreading of the high-viscosity layer towards the low-viscosity front did occur (Fig. 4-14f). The evolution of experiment 7 with a 6 mm thick brittle top layer is shown in Fig. 4-15. As in the two-layer experiments, deformation starts close to the retreating boundary and progressively migrates away from the retreating boundary. Deformation starts with arc-perpendicular extension (arc-parallel grabens) close to the free boundary (Fig. 4-15a). New grabens develop progressively further away from the retreating boundary (Fig. 4-15b). In an advanced stage, a small number of distinct arc-perpendicular faults form close to the retreating boundary to accommodate arc-parallel extension (Fig. 4-15c,d). Rotation can be up to 40° in an advanced stage of deformation, with clockwise rotation in the south and anticlockwise rotation in the north.

4.6.1.3. Asymmetrical model

In the asymmetrical model (Experiment 3 (Fig. 4-13c)), deformation starts with arc-perpendicular extension (arc-parallel grabens) close to the retreating boundary in the north and sinistral strike-slip faults in the northern corner of the gate. New grabens develop progressively further away from the retreating boundary and towards the hinge-point at progressively more oblique angles to the retreating boundary. Strike-slip faults progressively grow towards the centre of the box. In an advanced stage, en echelon left-stepping folds develop near the curved boundary due to shearing of the spreading sheet along this boundary. Also, individual grabens develop close to the hinge-point striking almost perpendicular to the retreating boundary. Rotation is in accordance with rotation of the boundary and decreases from close to the retreating boundary towards the west.

4.7. Discussion

4.7.1. Structural styles

The radial and unidirectional model both show symmetrical deformation patterns, while in the asymmetrical model, the deformation pattern is asymmetrical, reflecting the boundary conditions of the three models. In both the radial and unidirectional model, arc-perpendicular extension (with arc-parallel grabens) takes place. This is related to the stretching of the layered system perpendicular to the free boundary resulting from arc-perpendicular spreading. The arc-parallel grabens rotate as the free boundary becomes progressively more arcuate. Arc-parallel extension (with arc-perpendicular grabens) is best developed in the radial model and is related to the progressive lengthening of the free boundary itself, in a direction parallel to the arc. Due to the outward spreading of the arc, the first arc-parallel extension commences along the arc front and progressively propagates towards the centre. In the unidirectional model, arc-parallel extension is less defined and part of the increase in length of the free boundary is related to the shearing of the spreading system along the two parallel side-walls. This leads to slower spreading of the system near the sides compared to the central part. The difference in velocity leads to the development of the arc-shaped free boundary.

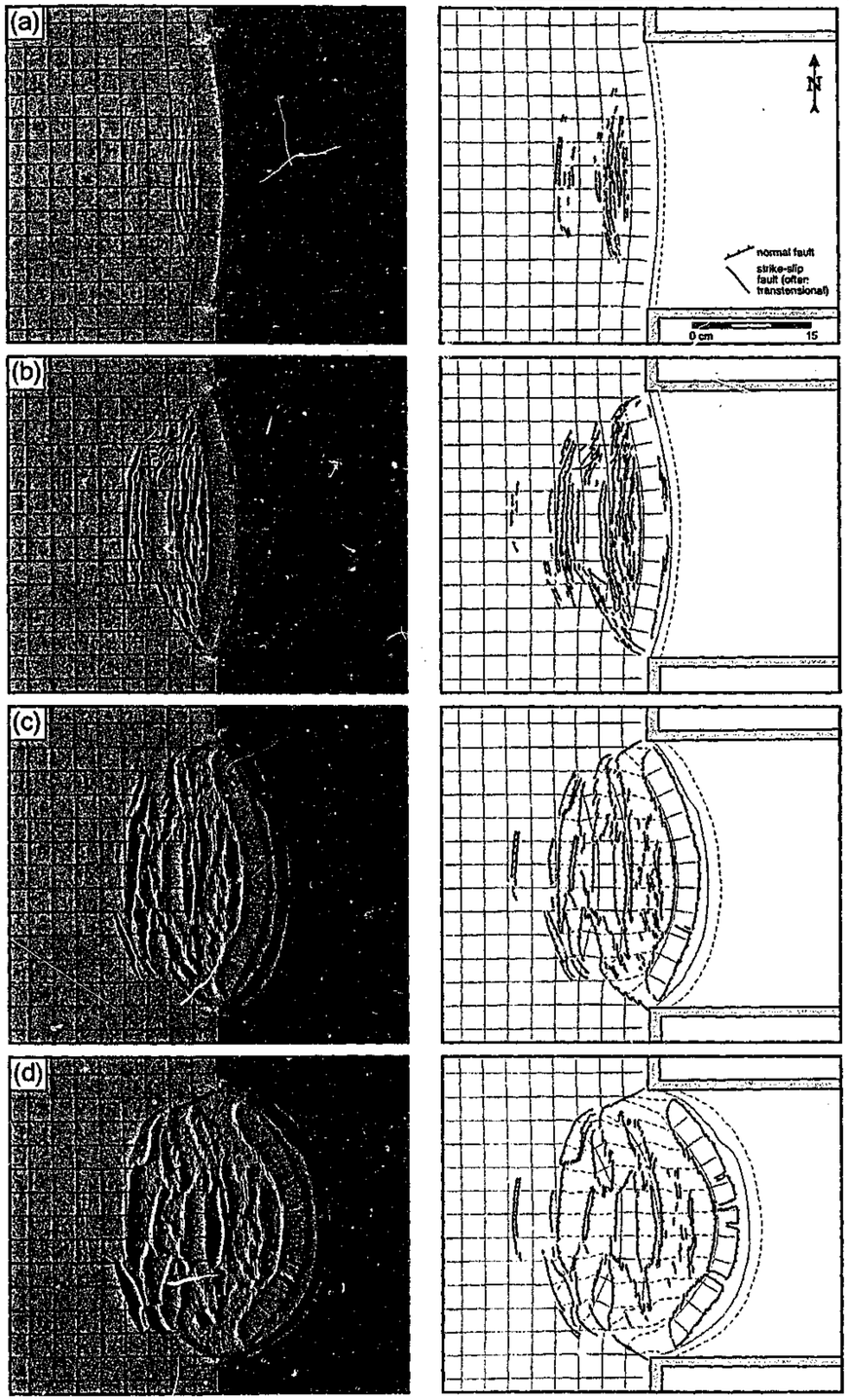

Fig. 4-15. Top view photographs (left) and interpretation (right) of three-layered experiment 7 (unidirectional model) with (a) after 3/4 hr, (b) after 1 1/2 hr, (c) after 4 hr and (d) after 10 hr.

The sets of conjugate (transtensional) strike-slip faults that develop to the west of the gate in both the radial and unidirectional model indicate that the maximum principal stress is oriented horizontal and parallel to the gate in this region. This is in contrast with the local stress field along and close to the arc, where the maximum principal stress is vertical, resulting in the formation of normal faults (Fig. 4-16). This difference in stress field is related to the material in the centre of the box, which flows outward, leading to a smaller potential energy in this region compared to the regions to the north and south. Therefore, these side regions start to flow toward the centre, leading to compression parallel to the gate, which results in the strike-slip faults in this region to accommodate E-W extension and N-S shortening (thus σ_1 oriented N-S, σ_2 oriented vertical and σ_3 oriented E-W). These conjugate transtensional strike-slip faults are well developed in experiments with a relatively thin brittle top layer, while they are not (very well) developed in experiments with a relatively thick brittle top layer (Fig. 4-14). This can be explained by the low resistance of these side regions to deform for a relatively thin brittle top layer, which results in a relatively low plate rigidity. Thus, inward N-S oriented flow is not resisted because the buoyancy force is relatively large compared to the integrated strength for experiments with a relatively thin brittle top layer, resulting in N-S oriented compression in conjunction with E-W tension.

In the asymmetrical model, extension starts close to the rotating boundary and is the result of lengthening of the layered system perpendicular to the rotating boundary. This extension starts near the northern edge of this boundary since lengthening is greatest near this end. In a later stage, this extension migrates towards the west and south where normal faults in the north are oriented more parallel (striking N-S) to the rotating boundary but become more

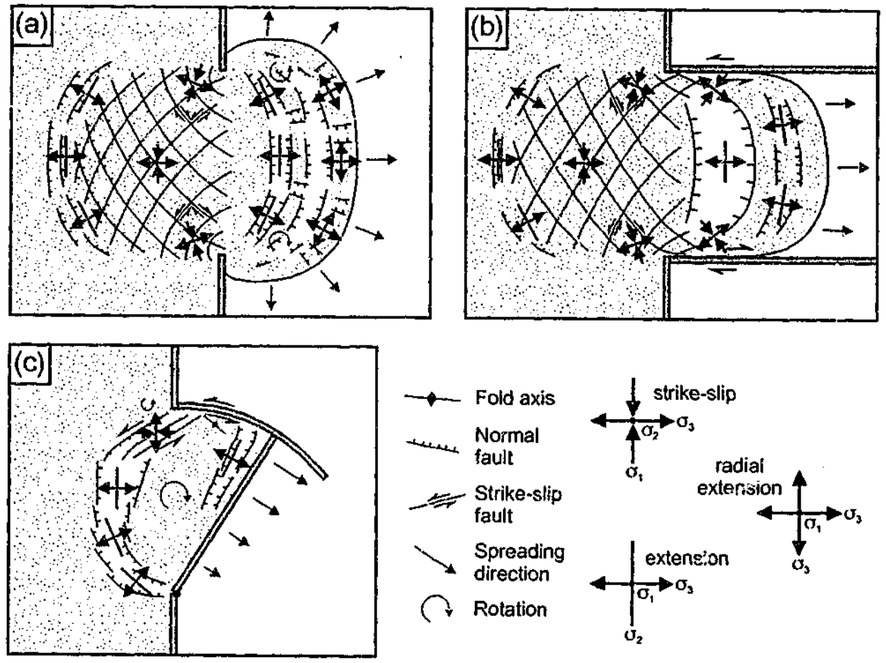

Fig. 4-16. Schematic representation of structures observed in models together with associated stress field, with (a) radial model, (b) unidirectional model and (c) asymmetrical model.

oblique (striking NW-SE) towards the south and strike ~ E-W close to the hinge-point. This asymmetry is related to the faster opening of the free boundary in the north compared to the slower opening in the south. This leads to a component of spreading not only in a direction perpendicular to the rotating boundary, but also a component of spreading towards the arc corner near the northern end of the rotating boundary.

4.7.2. Comparison with other experiments and conceptual models

2D physical experiments of gravity spreading have been executed by *Faugère and Brun* [1984] and *Brun et al.* [1994]. The general conclusion of these experiments was that spreading of a homogeneous sand layer overlying a viscous lower layer would lead to the formation of rotated fault blocks, while the sand-silicone interface remained planar, thus without any localisation of deformation and local rising of the ductile layer [*Faugère and Brun*, 1984]. The addition of a local low viscosity layer between the two layers led to localisation of extension and the local rise of viscous material in these regions [*Brun et al.*, 1994]. The experiments described here show localisation of deformation (especially the asymmetrical model) and regions with local rise of the ductile lower layer. This localisation of strain is probably related to the three-dimensional approach to simulate gravity spreading, where boundary conditions force the sheet to spread in different directions and at different velocities along the boundary, resulting in inhomogeneous internal deformation.

Three-dimensional physical experiments of gravity spreading have been performed by *Merle* [1989], *Hatzfeld et al.* [1997] and *Gautier et al.* [1999], which show similarities with the results of the radial model. The results of *Hatzfeld et al.* [1997] and *Gautier et al.* [1999], who used brittle-ductile rheologies, show qualitatively similar results for strain, displacement and rotation. For example, *Hatzfeld et al.* [1997] describe experiments with arc-parallel extension along the arc and arc-perpendicular extension further behind the arc, separated from a broad zone of strike-slip and oblique-slip faulting in the box interior by a relatively undeformed zone. This shows a good agreement with the structures observed in the radial model. Furthermore, the experimental results of *Gautier et al.* [1999] and *Hatzfeld et al.* [1997] show that deformation initiates close to the free boundary and quickly propagates towards the box interior, where the final zone of deformation is comparable in size to the dimensions of the gate. This has also been observed in the radial model.

Results of experiments executed with a different viscosity for the lower ductile layer revealed that a relatively high viscosity results in distributed deformation along small faults with minor displacement along the faults, while a relatively low viscosity results in localised deformation along fewer larger faults, which absorb more displacement. This phenomenon has been reported earlier by *Buck* [1991], *Benes and Davy* [1996] and *Brune and Ellis* [1997]. According to *Brune and Ellis* [1997], localised extension occurs when the brittle layer is relatively thick (or strong), because failure in such a layer will reduce the strength of the brittle-viscous system significantly, leading to model-scale strain softening. In contrast, for extension in a brittle-viscous system with a relatively thin (or weak) brittle layer, this will not lead to significant strain softening at places where this brittle layer is extended, thus resulting in more distributed deformation.

Simple kinematic models have been proposed for the formation of arcs previously. An overview of such models, as have been proposed for the Calabrian arc, has been given by *van Dijk and Okkes* [1991] (Fig. 4-17). They describe four models, from which three have

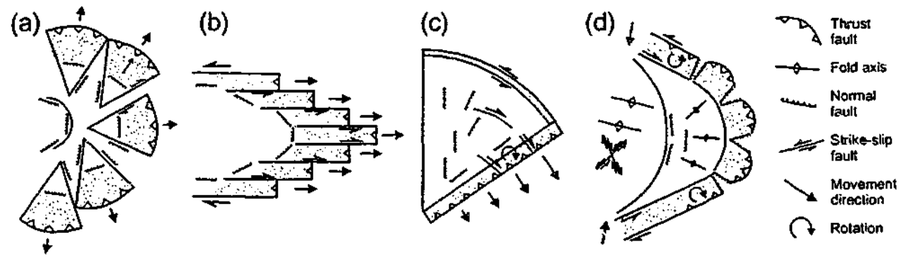

Fig. 4-17. Schematic sketches of kinematic models for arc formation and back-arc structures, (modified from *van Dijk and Okkes* [1991]). (a) Radial drift model, (b) translation model, (c) sphenochasm model and (d) bending model.

kinematic boundary conditions similar to the three models presented in this chapter: the radial drift model (compare with the radial model); the translation model (compare with the unidirectional model); and the sphenochasm model (compare with the asymmetrical model). It is interesting to see that most of the predicted structures in the back-arc region, schematically sketched for these kinematic models do not resemble the results of the experiments (compare Fig. 4-16 and Fig. 4-17). Interestingly enough, some of the predicted structures in the so-called bending model (Fig. 4-17d) show more resemblance with the results of the radial spreading model (Fig. 4-16a) than the radial drift model does (Fig. 4-17a). This includes arc-parallel extension with grabens widening towards the arc front, arc-perpendicular extension behind the arc and conjugate strike-slip faulting in the back. However, geodynamic models for these bending models vary greatly from the radial spreading model. For example, *Mantovani et al.* [1997, 2000] proposed that several arcs in the Mediterranean region (Betic/Rif arc, Apennines-Calabrian arc, Carpathian arc, Hellenic arc) are the result of oroclinal bending and lateral escape due to orogen parallel compression with strike-slip faults in the back-arc region (Fig. 3-1d). However, the modelling results presented in this paper indicate that qualitatively similar strike-slip structures can be reproduced during rollback of the subducting plate and radial spreading in the overriding plate, without any orogen parallel compression. Thus, it might be difficult to differentiate between geodynamic models, responsible for arc formation and back-arc deformation, on structural data alone. In such a case, analogue models might provide new insights into the plausibility of certain geodynamic models.

4.7.3. Comparison between models and nature

The three basic models show similarities with natural arcs and related back-arc basins. I will briefly describe some similarities observed between the radial model and the Carpathian arc - back-arc system and the Hellenic arc - back-arc system. The unidirectional model will be compared with the Mariana arc system and the South Shetland arc system. The analogue results of the asymmetrical model will not be compared with natural examples, since this will be done in more detail in the following three chapters.

4.7.3.1. Radial model

4.7.3.1.1. Carpathian arc

The Carpathian arc formed mainly during late Cainozoic time [*Linzer*, 1996] by continental collision between Europe and smaller continental fragments following southward and westward subduction of oceanic lithosphere [*Royden et al.*, 1983], which was probably of Jurassic age [*Linzer*, 1996]. It has been argued that the following mechanisms have contributed to the formation of the Carpathian arc and the Pannonian Basin: lateral escape / extrusion from the Eastern Alps [*Ratschbacher et al.*, 1991a,b], gravitational / extensional collapse of a pre-thickened orogenic region [*Horváth*, 1993] and rollback of a subducting lithosphere towards the east [*Royden et al.*, 1983]. The relative importance of each mechanism is still a matter of debate and the co-operation between these mechanisms in the formation of the Carpathian arc and the Pannonian Basin has been discussed by several authors [*Linzer et al.*, 1998; *Frisch et al.*, 1998; *Bada et al.*, 1999]. However, *Royden et al.* [1983] have argued that the dominant control on the basin formation and geometry is slab rollback. Here, rollback of European oceanic lithosphere towards the east, located in a continental embayment of the Bohemian Massif, the Ukraine Platform and the Moesian Platform, would have enabled lateral extrusion of crustal wedges from the Eastern and Southern Alps [*Linzer et al.*, 1998].

A simplified tectonic map of the Carpathian arc and the Pannonian Basin is shown in Fig. 4-18, in which Neogene faults active in the Pannonian region have been plotted. Many of these faults are strike-slip faults, which accommodate a considerable amount of lateral displacement and a smaller component of dip-slip. It is argued that the strike-slip faults in the Western Pannonian Region could be explained by rollback and related back-arc extension, similar to the development of conjugate strike-slip and oblique-slip faults in the back-arc region of the radial model (Fig. 4-8, 4-13a). Thus, the strike-slip faults are not necessarily the result of escape tectonics from the Eastern Alps, as has been proposed by *Ratschbacher et al.* [1991a,b] and *Horváth* [1993]. On top of the tectonic map of Fig. 4-18, a schematic pattern of conjugate strike-slip faults (as has been observed in the radial model) was plotted. The approximate location of the two gate boundaries have also been plotted, simulating the relatively stable buttresses of the Moesian Platform and the Bohemian Massif. This overlay shows that some of the major faults in the western part of the Pannonian Basin have a similar orientation and sense of shear as the strike-slip faults observed in the radial model. Furthermore, the shape of the Carpathian arc is similar to the shape of the arc, observed in the radial model, where the original strike of the subduction zone was probably oriented ~ NW-SE [e.g. *Wortel and Spakman*, 2000]. Further data in support of the rollback + back-arc extension hypothesis come from paleomagnetic declinations, which indicate anticlockwise rotations in the Northern Carpathians and clockwise rotations in the Eastern and Southern Carpathians (Fig. 1, *Marton and Fodor* [1995]; Fig. 1b, *Csontos and Nagymarosy* [1998]) and a roughly radial pattern of transport vectors along the arc (Fig. 10, *Csontos et al.* [1991]). Similar rotations and spreading patterns have also been observed in the radial model. Finally, transport vectors given for the Pannonian Basin (Fig. 7d, *Royden et al.* [1983]) clearly indicate a decrease in amount of eastward displacement from the arc towards the back-arc region, as has been observed in the radial model (Fig. 4-11a).

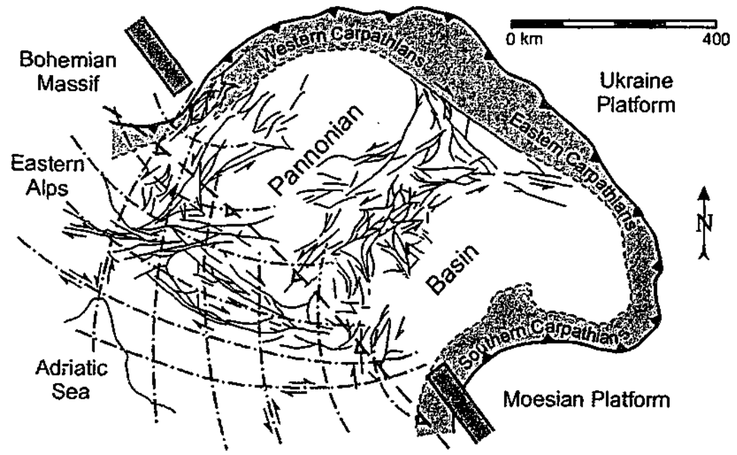

Fig. 4-18. Structural map of Neogene faults (continuous lines) in the intra-Carpathian region (modified from *Royden et al.* [1983]). Dash-dot lines represent generalised pattern of conjugate strike-slip faults, as observed in the radial model. Dashed line with white teeth indicates approximate location of thrust front prior to rollback. Approximate locations of the gate boundaries have also been indicated.

4.7.3.1.2. Hellenic arc

In the Hellenic region, it has been argued that southward rollback of the African plate led to the formation of the Hellenic arc and the Aegean Sea (Fig. 4-1) [*Le Pichon*, 1982; *Meulenkamp et al.*, 1988; *Wortel and Spakman*, 1992]. It has been proposed that the Ionian lithosphere subducting northeastward along the Hellenic trench is of oceanic nature and is of Late Jurassic – Early Cretaceous age [*Catalano et al.*, 2001] and therefore relatively dense and likely to roll back. The Aegean back-arc region has some similar major deformation patterns as observed in the radial model (Fig. 4-19). Most normal faults along and away from the arc and in the Aegean are subparallel to the Hellenic trench (Fig. 4-19b) [*Angelier et al.*, 1982] (compare with arc-perpendicular extension near the free boundary and more towards the back in the model (Fig. 4-19d)). Faults striking oblique to perpendicular to the trench occur mainly along the arc (Fig. 4-19b) [*Angelier et al.*, 1982] (compare with arc-parallel extension near the free boundary in the model (Fig. 4-19d)). The amount of extension in the Aegean decreases from south to north (Fig. 4-19c), as is also observed in the model (Fig. 4-19d). Such a strain gradient would imply a tensional boundary condition along the Hellenic arc.

Clockwise rotation in the West Aegean of ~ 25-30° and anticlockwise rotation of ~ 19-30° in the East Aegean during the Middle - Late Miocene have been reported (Fig. 4-1b) [*Kissel and Laj*, 1988; *Walcott and White*, 1998]. These opposite sense rotations of comparable size on either side of the Hellenic arc are reproduced in the radial model. In the West Aegean, clockwise rotation of ~ 15-25° took place from Pliocene - Present times, while the East Aegean shows no rotation for this time span [*Kissel and Laj*, 1988; *Walcott and White*, 1998]. However, local anticlockwise block rotations did occur on Crete during the Pliocene-Present, related to localised sinistral shear [*Duermeijer et al.*, 1998]. This change in rotation style could be related to the change in structural setting along the southeastern boundary of the

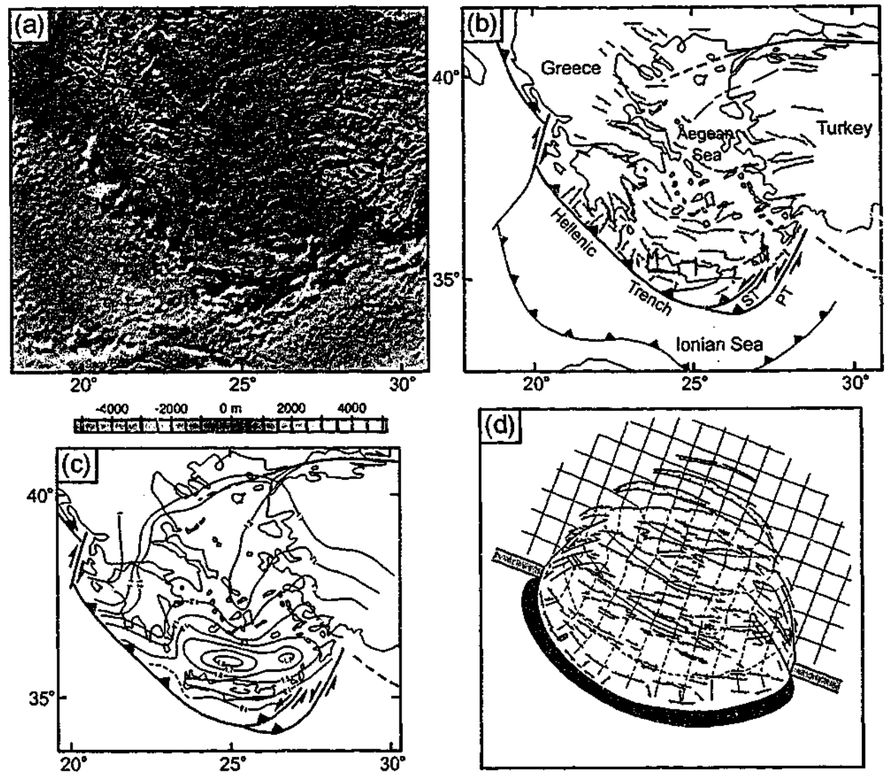

Fig. 4-19. (a) Topography and bathymetry of Aegean region (from *Smith and Sandwell* [1997]). (b) Tectonic map of (a) compiled after *Angelier* [1982], *Armijo et al.* [1996] and *ten Veen and Meijer* [1998] (c) Map showing stretching factor β ($\beta = L_N / L_O$, where L_N is new length and L_O is original length) of Aegean region (from *Angelier* [1982]). (d) Top view interpretation of experiment 4 (three-layered radial model) after 5 hr.

Hellenic trench, which changed from a subduction boundary to a sinistral transform fault system at the end of the Miocene (e.g. Strabo and Pliny Trench) (Fig. 4-1c). Thus one might conclude that only the Middle - Late Miocene stage of development of the Hellenic arc can be compared with the radial model, while the Pliocene - Present stage is more compatible with the asymmetrical model. The formation of such a sinistral transform fault system could be the result of the formation of a vertical tear along the eastern boundary of the subducting plate. This tearing could be related to in-plane extension at one of the corners of the arc, due to initial radial rollback of the slab (e.g. Fig. 4-4a).

In the radial model (Fig. 4-8, Fig. 4-19d), extension along the arc started with arc-perpendicular extension (arc-parallel normal faults), and was later followed by arc-parallel and arc-perpendicular extension (arc-perpendicular and arc-parallel normal faults). A similar deformation pattern has also been observed close to the Hellenic arc in Crete. The first extension that took place in the early Late Miocene was oriented NNE-SSW (arc-perpendicular extension), and was followed by extension in both the N-S (arc-perpendicular extension) and the E-W (arc-parallel extension) direction [*ten Veen and Meijer*, 1998].

4.7.3.2. Unidirectional model

4.7.3.2.1. Mariana arc

The Mariana arc is situated along the convergent boundary of the Philippine plate in the west and the subducting Pacific plate in the east (Fig. 4-20). It has been argued by *Hsui and Younquist* [1985] that the curvature of the Mariana arc is related to rollback of the Pacific plate to the east in between the roughly parallel Marcus-Necker Ridge in the north and the Caroline Ridge in the south. The oceanic lithosphere in between is probably relatively dense, because it is of Jurassic age [*Molnar and Atwater*, 1978]. Thus, the Mariana arc might be a natural example of the unidirectional model, where the buoyant ridges act as a retardant to rollback and spreading in the overriding plate similar to the parallel boundaries in the unidirectional model, while retreat and spreading continues in between the parallel ridges. When the strain pattern of the unidirectional model is compared with the Mariana arc, some superficial similarities are evident (Fig. 4-20). First of all, the shape of both arcs is similar. Second, the zone of major extension in the Mariana arc, the Mariana Trough is convex shaped towards the direction of spreading and is wide in the centre (with true seafloor spreading) and narrows towards the north and south [*Fryer*, 1996]. This is in agreement with the zone of major extension in the model. The relatively undeformed zone between the arc front and the zone of major extension in the model could be compared with the Mariana Ridge.

Despite the curvature of the Mariana Trough, it has been argued that the spreading-rifting direction is oriented nearly E-W along its entire length [*Fryer*, 1995] (i.e. (sub) parallel to the Marcus-Necker Ridge and Caroline Ridge). This implies that the spreading rate (and thus rollback rate) is faster in the centre of the arc, when compared to the north and the south. This has also been observed in the model, where spreading is more rapid in the centre than on either side of the spreading sheet and displacement vectors in the spreading sheet are nearly parallel to the two parallel confining boundaries. More recently, however, *Martínez et al.* [2000] have suggested that in the southern most part of the Mariana Trough, spreading is more radial, resulting in arc-parallel extension close to the trench and arc-perpendicular extension in the more interior parts. This is also evident in the unidirectional model, where some arc-parallel extension with arc-perpendicular grabens also developed in a late stage of deformation.

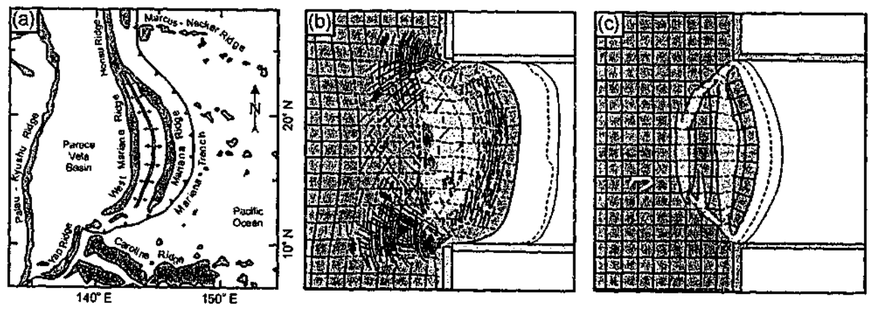

Fig. 4-20. (a) Sketch map of the Mariana Arc as a possible natural prototype of the unidirectional model. (b) Interpretation of two-layered experiment 13 (unidirectional model) after 210 s of spreading. (c) Interpretation of three-layered experiment 8 (unidirectional model) after 5 hr of spreading. Light grey region in the middle of (b) and (c) represents the region which has experienced major extension and thinning.

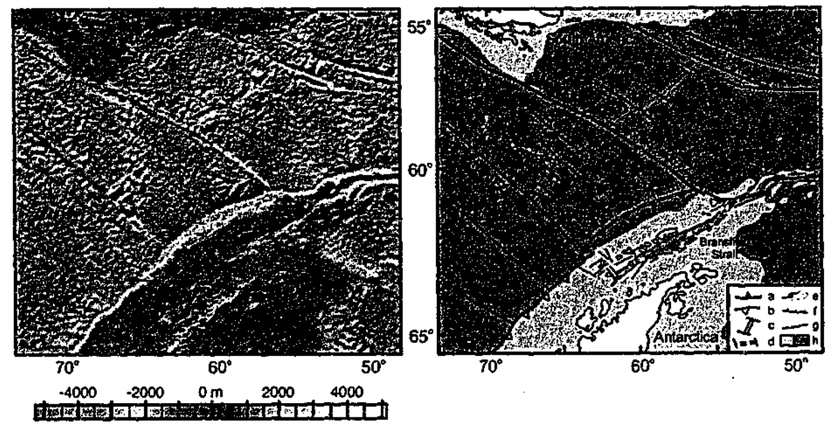

Fig. 4-21. (a) Topography and bathymetry of South Shetland arc and surrounding (from *Smith and Sandwell* [1997]). (b) Tectonic map of (a) (modified from *Lawver et al.* [1995] and *Barker* [1995]). The location of the northeastern and southwestern cusp of the South Shetland arc seem to be controlled by the Shackleton fracture zone and Hero fracture zone. Arrows indicate direction of hinge-line migration. a, trench (triangles on upper plate); b, inactive trench; c, active spreading ridge and transforms; d, inactive spreading ridge and transforms; e, transform fault with shear direction; f, normal fault; g, fault/lineament (undifferentiated); h, continental shelf (left) and continental slope / (ocean) basin (right).

4.7.3.2.2. South Shetland arc

The unidirectional model can also be compared with the South Shetland arc, where deformation is dominated by arc-parallel normal faults. The South Shetland arc (Fig. 4-21) is a relatively young arc with back-arc extension starting at ~ 4 Ma [*Lawver et al.*, 1995]. The extent of the arc is controlled by two parallel running fracture zones on the subducting plate, which are connected to the eastern and western cusp of the arc. Extension in the back-arc region is mainly confined to the Bransfield Strait, with normal faults striking sub-parallel to the arc. This is also observed in the analogue models of the unidirectional model, where normal faults are mainly oriented parallel to the arc. The length of the back-arc basin is of similar magnitude as the arc itself. The western and eastern extremities of the basin are linked to the western and eastern cusp of the arc by strike-slip faults, in a similar fashion as in the model (Fig. 4-14).

4.8. Conclusions

In this chapter, scaled lithospheric experiments have been described to simulate back-arc formation and deformation. Three different models have been tested with different boundary conditions that model three different types of arc formation and back-arc extension in the overriding plate. In the first model, radial arc formation and back-arc extension are modelled, where extension is allowed in all directions. In the second model, unidirectional arc formation and back-arc extension are modelled, and spreading is allowed only in one direction. In the third model, asymmetrical back-arc extension is modelled, where back-arc opening is analogous to an opening door. The models show the progressive development of an arc,

which is convex towards the direction of spreading. In the models, initiation of deformation starts close to the free boundary. Migration of the deformation front towards the back is rapid in the beginning and slows down in a later stage. Experiments with different brittle strength versus viscous strength have been executed. The results indicate that with increasing brittle strength, deformation is increasingly localised and the surface extent of deformation inside the box decreases. The radial model and the unidirectional model show symmetrical deformation patterns, while the asymmetrical model shows an asymmetrical deformation pattern. The strain patterns, displacement patterns and rotation patterns of these models are significantly different (Fig. 4-16).

The general pattern of deformation of the radial model has been compared with the Carpathian - Pannonian arc – back-arc system and the Hellenic - Aegean arc – back-arc system. The general pattern of deformation in the unidirectional model has been compared with the Mariana arc – back-arc system and the South Shetland - Bransfield arc – back-arc system. The models show similar structural, rotational and displacement patterns as observed in the natural examples, supporting the idea that these systems have a dynamic origin and developed from initially more rectilinear structures into arc-shaped structures due to rollback of the hinge-line of the subducting lithosphere. The model results can best be compared with back-arc deformation in continental lithosphere. This is partly because the rheology of the analogue models is a better representation of the rheology of continental lithosphere, which favours distributed deformation more than oceanic lithosphere. Also, back-arc spreading is not modelled in the experiments, since these are mechanical models and not thermomechanical models.

The asymmetrical model will be discussed more extensively in Chapter 5, 6 and 7, in which the analogue results will be compared with several arc – back-arc systems (Tonga arc, Ryukyu arc, New Hebrides arc, Kuril arc), which testify to asymmetric deformation.

FOREWORD CHAPTER 5

This chapter discusses the formation of asymmetric arcs and back-arc basins. The conceptual kinematic model of asymmetric arc formation and back-arc extension was inspired by the geometry and structure of several arc back-arc systems including the New Hebrides arc - back-arc system and the Tonga arc - back-arc system. A reconstruction of the New Hebrides - Tonga region from *Hathway* [1993] and published GPS data of the Tonga region from *Bevis et al.* [1995] inspired the conceptual model as well.

The ideas and interpretations presented in this chapter are the sole work of the author. All the experimental work presented in this chapter is the sole work of the author. The clarity of ideas presented in this chapter benefited from discussions with Mark Jessell and Gordon Lister. Reviews of earlier versions of this chapter by Robert Hall and Gideon Rosenbaum are also acknowledged. The contents of this entire chapter has been published in the *Journal of the Virtual Explorer*. A full reference can be found at the end of the thesis in the bibliography. Minor changes have been made to the text of the original paper in order to make the layout and spelling of this chapter consistent with the rest of the thesis.

CHAPTER 5

Analogue modelling of asymmetrical back-arc extension

Abstract

Back-arc extension takes place in the overriding plate in an overall convergent setting during retreat of the hinge-line of the subducting slab. A large number of back-arc basins display an asymmetric geometry and internal structure, associated with an increasing amount of extension from one side of the arc to the other. Results of 3-dimensional analogue modelling are presented simulating asymmetric back-arc extension of an overriding lithosphere with a varying initial rheology. The results show that with increasing lithospheric brittle to viscous strength (BS/VS), the fault density decreases in magnitude, while the asymmetry in deformation pattern in the back-arc region increases. The area extent of deformation is mainly dependent on the ratio of brittle strength to buoyancy force (BS/BF), i.e. the larger the ratio, the smaller the area of deformation. The experimental results have been compared with several arc - back-arc systems, which display a relatively large amount of structural asymmetry (Tonga arc, Ryukyu arc, Kuril arc, New Hebrides arc) but a varying style of tectonic deformation. These differences are mainly the result of the stage of opening up of the back-arc basin, the subduction setting (ocean-ocean or ocean-continent) and difference in rheology of the overriding lithosphere.

5.1. Introduction

Back-arc basins are enigmatic geological features, which form in the overriding plate in overall convergent plate tectonic settings on the concave side of the arc. Back-arc basins occur in two different tectonic regimes: ocean-ocean subduction and ocean-continent subduction. In the former regime, the back-arc basin is commonly found in between a remnant volcanic arc and the active volcanic arc, which were separated during back-arc opening [*Karig*, 1970, 1971a,b; *Kobayashi and Nakada*, 1979]. In ocean-ocean subduction settings extension is often localised along narrow rift segments or along clear defined spreading ridges. Some examples include the Mariana arc, the Izu-Bonin arc, the Tonga arc, the Kermadec arc, the New Hebrides arc, the Scotia arc and the Lesser Antilles arc. In the latter regime, the back-arc basin is located on the continental lithosphere. This often results in more diffuse extension over a large area, as has been observed behind the Hellenic arc [*Angelier et al.*, 1982; *Le Pichon*, 1982] and the Kuril arc [*Worrall et al.*, 1996; *Schellart et al.*, in review]. Other examples include the Japan arc, the Ryukyu arc, the Banda arc, the Calabrian arc, the Betic-Rif arc and the Carpathian arc.

Back-arc extension involves regressive (oceanward) hinge-line (or trench axis) migration of the subducting plate (i.e. rollback). Whether this regressive movement is the cause or the effect of back-arc extension remains a debate, but presently the majority of geoscientists favour the former view [*Taylor*, 1995]. In this sense, rollback is driven by the negative buoyancy of the subducting slab compared with the asthenosphere [*Elsasser*, 1971; *Molnar and Atwater*, 1978]. Hence, rollback provides space along the plate boundary. This space is

filled by the overriding plate, which passively follows the retreating hinge of the subducting slab.

Slab rollback is primarily driven by its negative buoyancy compared with the asthenosphere, which is often related to the age of the oceanic lithosphere (i.e. older, colder, denser). However, the actual retreat velocity depends on a variety of factors, including the negative buoyancy of the slab, the ease with which the slab tears, the ability of asthenosphere material underneath the slab to migrate towards the slab corner and viscosity of the asthenosphere.

From geological, structural, geomorphological, magnetic lineation and paleomagnetic data it is clear that different arc - back-arc systems evolve quite differently [*Schellart et al.*, 2002c]. For instance, several arcs seems to have formed by radial spreading, resulting in symmetrical arc development with arc-parallel and arc-perpendicular extension in the overriding plate and equal amounts of block rotation on each side of the arc. Examples could be the Hellenic arc and Aegean Sea, the Ryukyu arc and Okinawa Trough, and the Carpathian arc and Pannonian Basin. Another group of arcs seems to have developed due to asymmetrical spreading. Two examples for this type of spreading are the New Hebrides arc [*Schellart et al.*, 2002a] and the Tonga arc, located in the southwest Pacific (Fig. 5-1). For each of these two arcs, its back-arc basin has opened up in a wedge shaped manner, with an increasing opening rate from one side of the arc to the other. Development of such arc systems involves asymmetrical back-arc spreading with similar magnitude and sense of rotation along the arc and shearing (with possible related block rotations) at the side of the arc (Fig. 5-2). Other examples of this arc configuration could include the Kuril arc and Sea of Okhotsk + Kuril Basin [*Schellart et al.*, in review], the Japan arc and Japan Sea, the Calabria – Apennines arc and Tyrrhenian Sea, and rotation of the Corsica-Sardinia block and opening of the Ligurian Sea. Also, the late stage development of both the Hellenic arc and the Ryukyu arc could have resulted from asymmetrical spreading.

This chapter will focus on arc - back-arc systems which form by asymmetrical spreading. This type of asymmetrical deformation will be investigated by means of small-scale analogue experiments. In these experiments the model apparatus configuration remains unaltered, but the rheology of the overriding plate is varied systematically for different experiments. The model results will be compared with natural examples of arc - back-arc systems, which display structural features, which could testify to a development resulting from asymmetrical spreading.

5.2. Analogue model

The scaling theory for analogue modelling of geologic processes has first been described by *Hubbert* [1937] and has later also been discussed by *Horsfield* [1977], *Davy and Cobbold* [1991] and *Cobbold and Jackson* [1992]. Here, the most important relationship is the one that relates surface forces (stresses) to body forces (gravity). When the experiments are executed in a normal field of gravity, stresses should be scaled down as the product of density and length scales down [*Horsfield*, 1977; *Davy and Cobbold*, 1991]. In the experiments described here a scale factor of ~ 1-2.5 $\times$ 10^{-7} (1 cm in experiment resembles ~ 40-100 km in nature) and a density factor of ~ 0.5 have been applied, thus stresses should be scaled down by ~ 1.25 $\times$ 10^{-7} – 5 $\times$ 10^{-8}. For brittle rocks, their cohesion and friction coefficient are the most

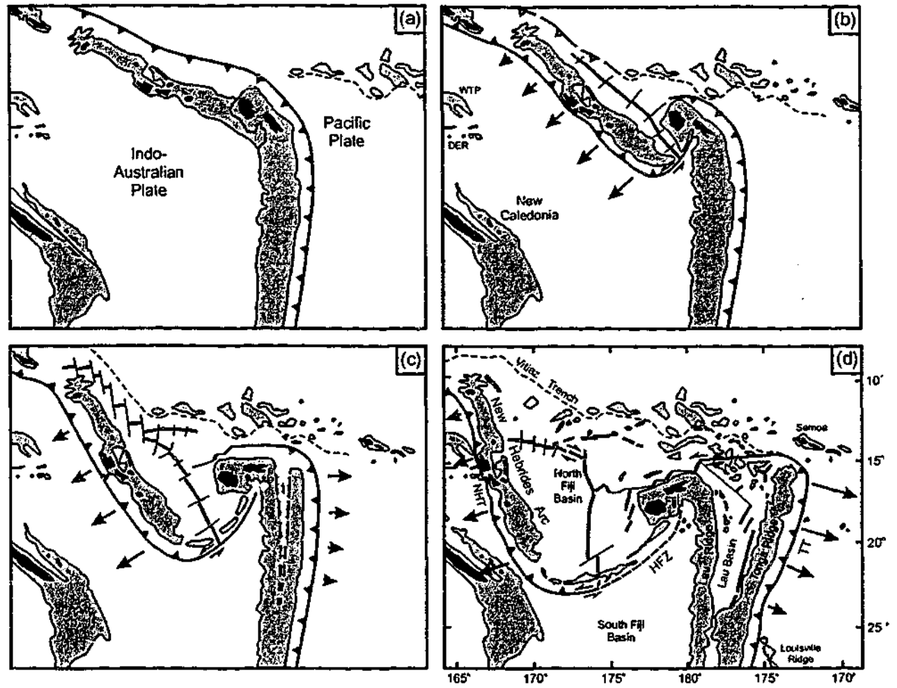

Fig. 5-1. Tectonic reconstruction of the New Hebrides - Tonga region (modified and interpreted from *Auzende et al.* [1988], *Pelletier et al.* [1993], *Hathway* [1993] and *Schellart et al.* [2002a]) at (a) ~ 13 Ma, (b) ~ 9 Ma, (c) ~ 5 Ma and (d) Present. The Indo-Australian plate is fixed in the sketch. DER = d'Entrecasteaux Ridge, HFZ = Hunter Fracture Zone, NHT = New Hebrides Trench, TT = Tonga Trench, WTP = West Torres Plateau. Arrows indicate direction of arc migration. During opening of the North Fiji Basin, the New Hebrides block has rotated some 40-50° clockwise [*Musgrave and Firth*, 1999], while the Fiji Plateau has rotated some 70-115° anticlockwise [*Malahoff et al.*, 1982]. During opening of the Lau Basin, the Tonga Ridge has rotated ~ 20° clockwise [*Sager et al.*, 1994].

important parameters, as described by Coulomb's fracture criterion [*Coulomb*, 1776]. Since cohesion has the dimensions of Pascal (Pa), it should be scaled down in a similar fashion as stresses [*Davy and Cobbold*, 1991; *Cobbold and Jackson*, 1992]. The friction coefficient is dimensionless, thus it should have similar values in both model and nature. Finally, for viscous material, viscosity should scale down as the product of stresses and time scales down [*Davy and Cobbold*, 1991]. The experiments described here are executed in the normal field of gravity and the materials used in the experiments have been chosen as such, that they have been properly scaled to model the deformation of rocks.

A model has been constructed to simulate back-arc extension in the overriding plate due to asymmetrical rollback. The model consists of only three layers in order to preserve the simplicity of the experiment (e.g. conform *Hatzfeld et al.* [1997], *Gautier et al.* [1999] and *Martinod et al.* [2000]). The layered system is confined in a 60 by 40 cm box. On one side of the box a rotational sidewall is situated, which can rotate outwards in an anticlockwise fashion (Fig. 5-3), simulating the progressive anticlockwise retreat of the hinge-line of the subducting plate. The uppermost two layers represent the overriding lithosphere. The

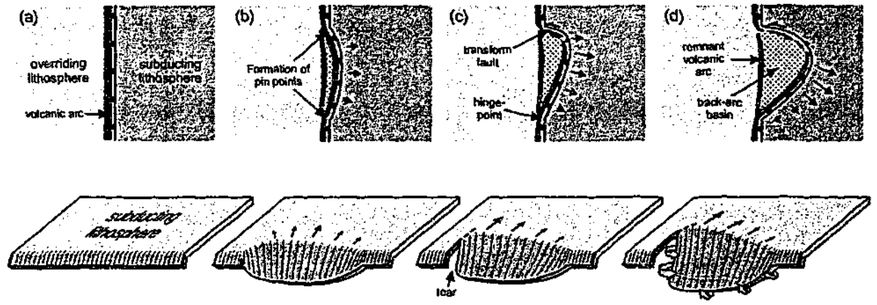

Fig. 5-2. Schematic sketches of development of asymmetrical arc during asymmetrical rollback of subducting slab in plan view (top) and three-dimensional view (bottom). (a) Initial state with rectilinear subduction zone; (b) initiation of rollback with formation of pin points or cusps (points where subducting slab is resisting to roll back); (c) one pin point evolves into transform plate boundary due to formation of vertical tear in subducting slab, while other becomes a hinge-point along which the arc rotates; (d) progressive growth of tear and continued rotation around hinge-point. Black arrows indicate direction of hinge-line migration. Thick arrows in (d) indicate direction of asthenosphere flow to accommodate slab retreat.

lowermost layer represents the asthenosphere and gives the overlying lithosphere isostatic support. The uppermost brittle layer is made of fine-grained glass microspheres simulating the brittle upper lithosphere in nature, which are properly scaled to model brittle behaviour of rocks, especially when used for extension related experiments [*Schellart*, 2000]. The high viscosity middle layer is made of silicone putty (mixed with a dense filler) with a viscosity of ~ 2×10^4 Pa·s, simulating the viscous lower lithosphere in nature. The lowermost viscous layer is made of glucose syrup with a viscosity of ~ 100 Pa·s. The experimental properties of the individual experiments discussed in the text are given in Table 6-1. The progressive opening of the sidewall is driven by a motor. A passive grid (line spacing = 3 cm) and marker

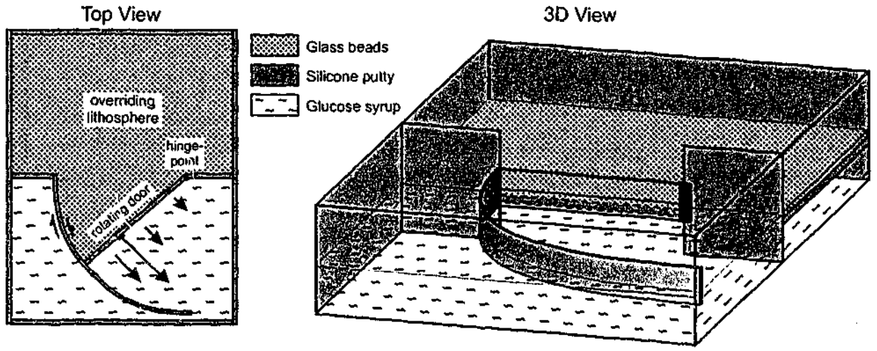

Fig. 5-3. Schematic sketch of experimental apparatus to investigate asymmetrical back-arc spreading of a two-layered brittle/ductile plate simulating the overriding lithosphere. Asymmetric hinge-line retreat of the subducting lithosphere is simulated with asymmetrical opening of a door. The model lithosphere is underlain by glucose syrup, simulating the asthenosphere, which gives the lithosphere isostatic support.

Experiment	Material	Rheology	Layer Thickness (cm)	Opening rate (°/hr)	Density ($\times 10^3$ kg/m^3)
	Microspheres	Brittle	0.4		1.22
1	Silicone	Viscous (high)	1.2	21	1.22
	Glucose	Viscous (low)	5.5		1.42
	Microspheres	Brittle	0.4		1.22
2	Silicone	Viscous (high)	1.2	12	1.22
	Glucose	Viscous (low)	5.5		1.42
	Microspheres	Brittle	0.6		1.22
3	Silicone	Viscous (high)	1.2	12	1.22
	Glucose	Viscous (low)	5.5		1.42
	Microspheres	Brittle	0.6		1.22
4	Silicone + sand	Viscoplastic	0.2		1.22
	Silicone	Viscous (high)	1.0	12	1.22
	Glucose	Viscous (low)	5.5		1.42
	Microspheres	Brittle	0.6		1.22
5	Silicone	Viscous (high)	0	36	-
	Glucose	Viscous (low)	5.5		1.42
	Microspheres	Brittle	0.5		1.22
6	Silicone	Viscous (high)	1.2	12	1.22
	Glucose	Viscous (low)	5.5		1.42
	Microspheres	Brittle	0.6		1.22
7	Silicone	Viscous (high)	0	12	-
	Glucose	Viscous (low)	5.5		1.42
	Microspheres	Brittle	0.5		1.22
8	Silicone	Viscous (high)	1.2	4	1.22
	Glucose	Viscous (low)	5.5		1.42
	Microspheres	Brittle	0.8		1.32
9	Silicone	Viscous (high)	1.0	21	1.32
	Glucose	Viscous (low)	5.5		1.42

Table 6-1. Some physical properties of experiments discussed in the text.

spheres have been laid on top of the brittle layer to monitor displacement and deformation. The progressive development of the model has been recorded by a digital camera from above, under oblique lightning of the top surface of the experiment.

5.3. Results

5.3.1. General results

Experiments with different ratios of brittle to viscous layer thickness (and therefore strength) have been executed. The results demonstrate that with increasing brittle strength to viscous strength ratio (BS/VS), deformation becomes more localised with fewer faults absorbing more deformation. In other words, the fault density decreases with increasing BS/VS ratio. This can be observed in Fig. 5-4, where the resulting strain patterns and interpretations of 9 experiments have been plotted (some of the physical properties for the experiments are given in Table 6-1 and 6-2). Furthermore, the surface extent of deformation inside the box decreases with increasing brittle strength to buoyancy force ratio (BS/BF)

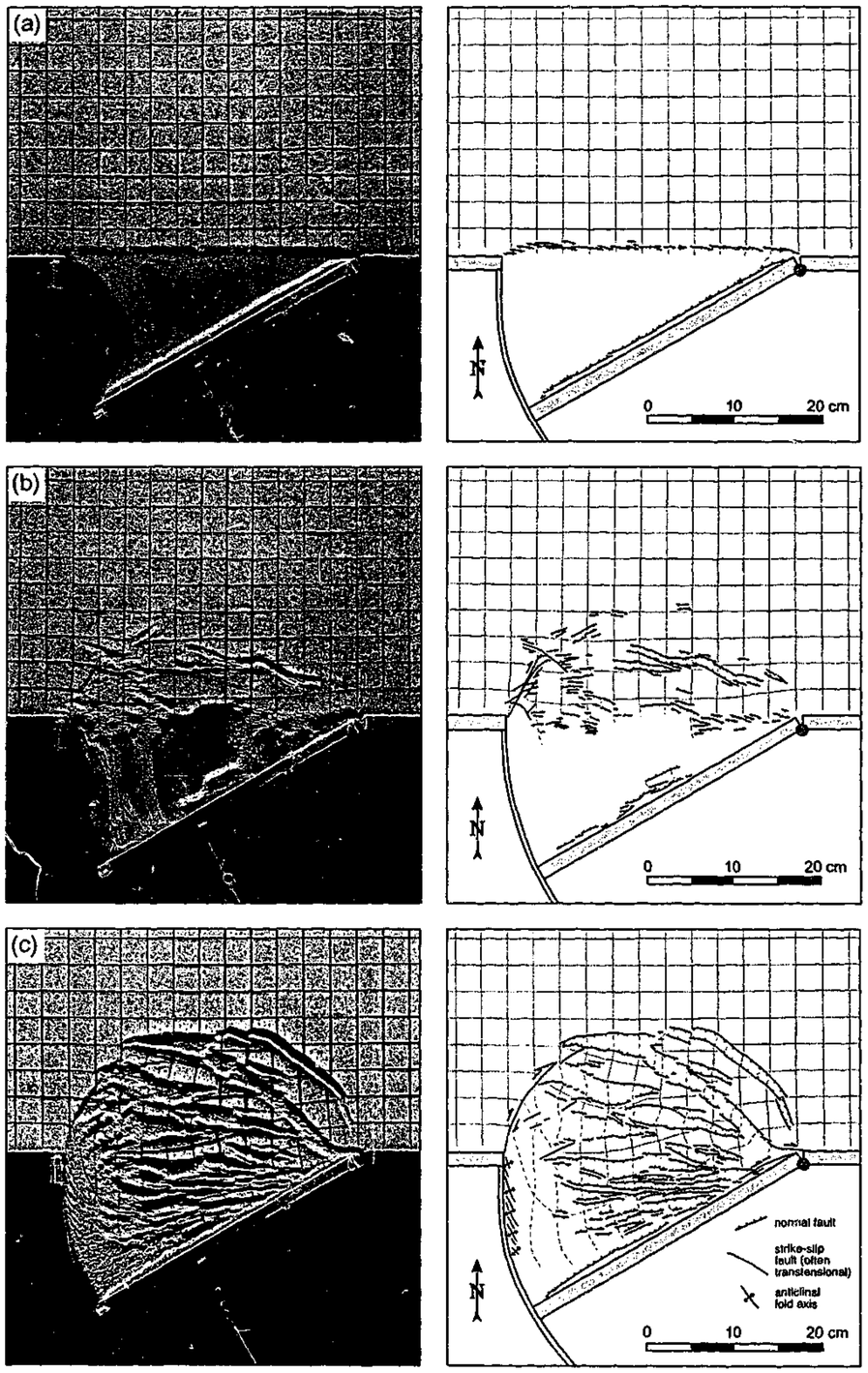

Fig. 4. Photographs (left) and interpretation (right) of experiments with different styles of extension for different ratios of brittle strength versus viscous strength (BS/VS) and different buoyancy force of the lithosphere. (a) BS/VS > 25 (exp. 7), (b) BS/VS ~ 25 (exp. 5), (c) BS/VS ~ 18 (exp. 8). All of the images are after 30° of rotation.

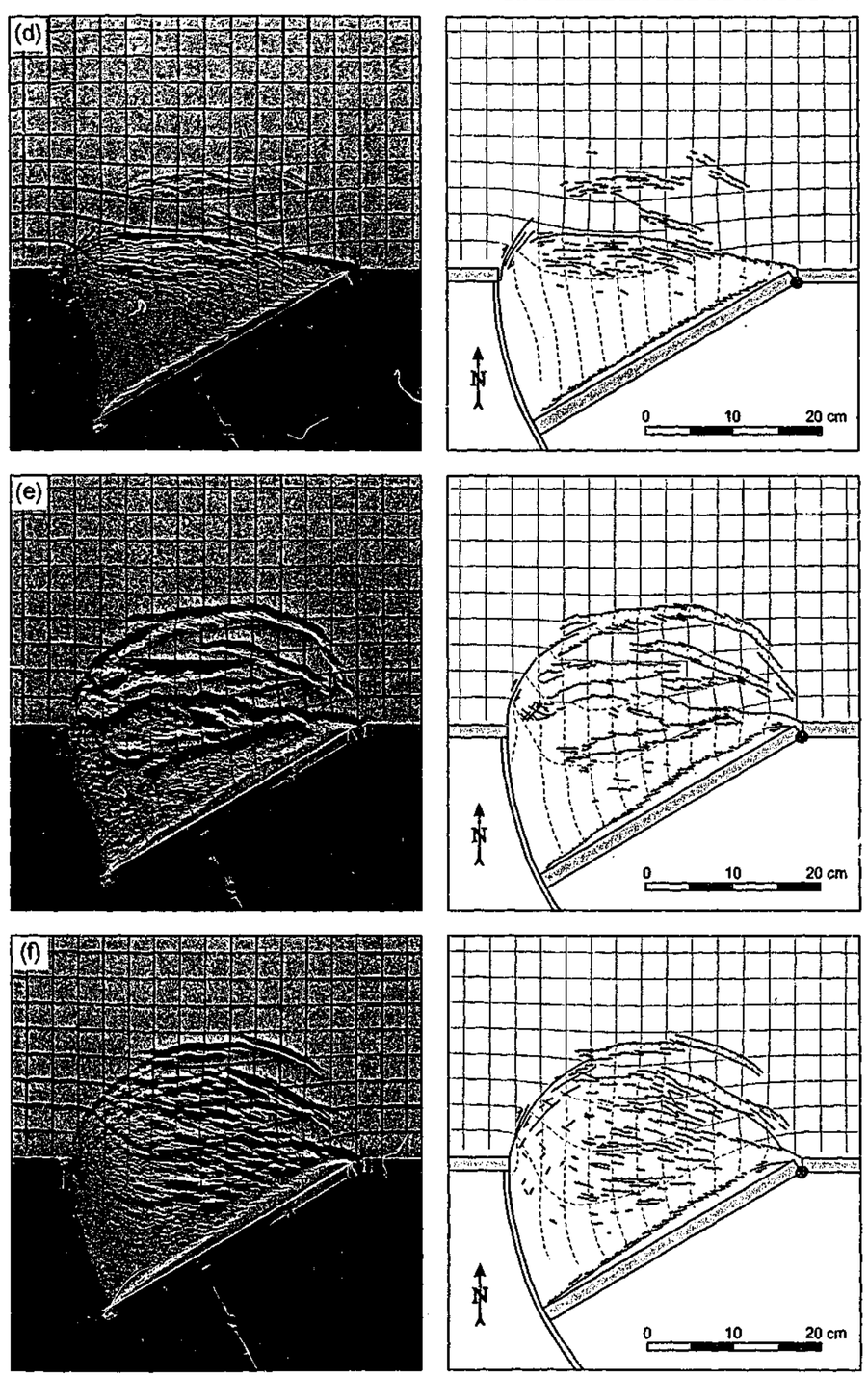

Fig. 4 (continued). (d) BS/VS ~ 8 (exp. 9) (e) BS/VS ~ 6 (exp. 4) and (f) BS/VS ~ 4 (exp. 3).

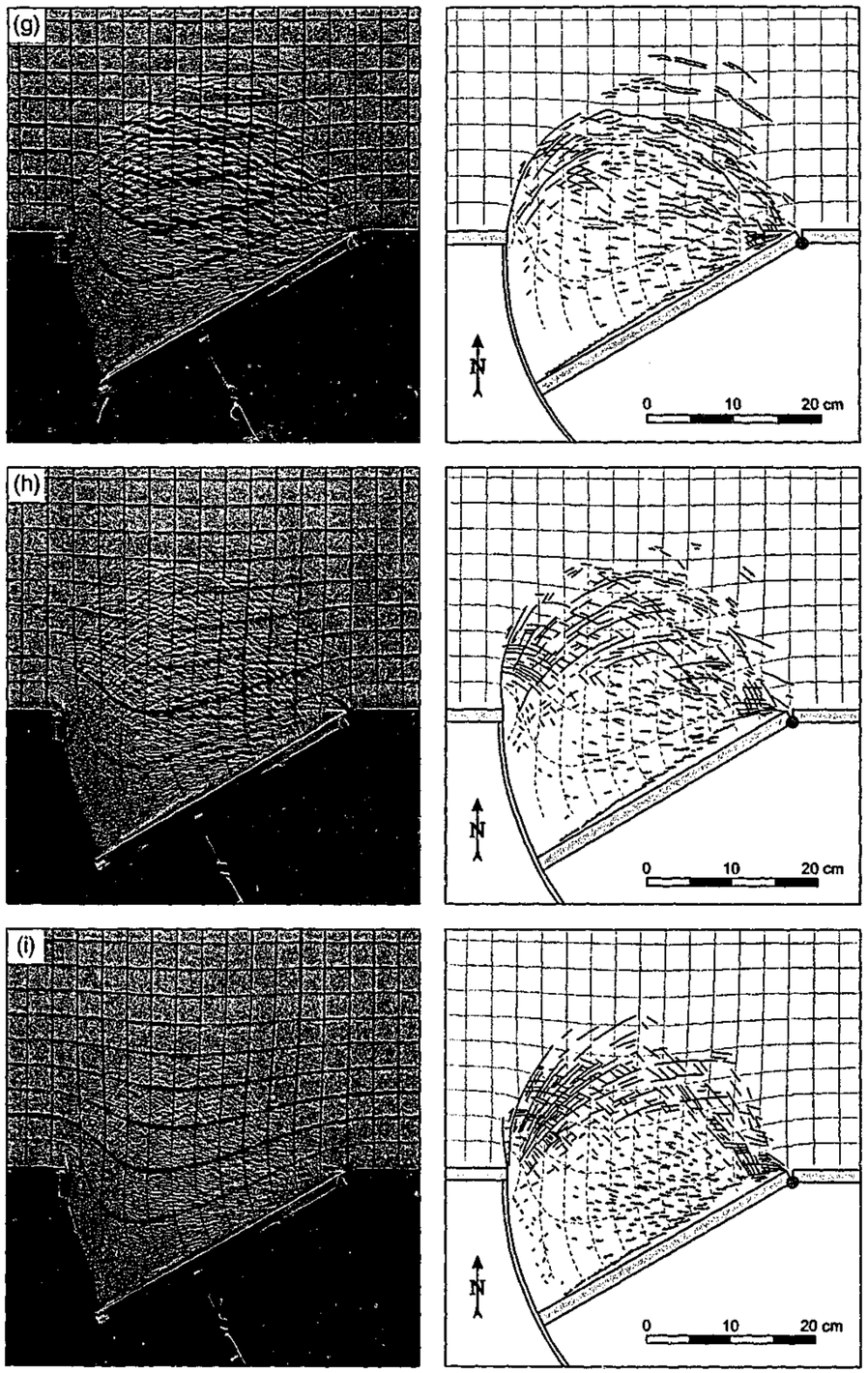

Fig.4 (continued). (g) BS/VS ~ 3, (exp.6), (h) BS/VS ~ 2 (exp.2) and (i) BS/VS ~ 1 (exp.1).

Experiment	Layer thickness ratio (B/V) (cm / cm)	BS/VS (N/m / N/m)	Buoyancy Force (N/m)	BS/BF	IS/BF
1	0.4 / 1.2	0.12 / 0.10	0.21	0.57	1.05
2	0.4 / 1.2	0.12 / 0.06	0.21	0.57	0.86
3	0.6 / 1.2	0.25 / 0.06	0.27	0.93	1.15
4	0.6 / 1.0	~0.25 / ~0.04	0.27	0.93	1.07
5	0.6 / 0.0	0.25 / ~ 0.01	0.03	8.33	8.67
6	0.5 / 1.2	0.18 / 0.06	0.24	0.75	1.00
7	0.6 / 0.0	0.25 / ~ 0.00	0.03	8.33	8.33
8	0.5 / 1.2	0.18 / 0.01	0.24	0.75	0.79
9	0.8 / 1.0	0.48 / 0.06	0.09	5.33	5.67

Table 6-2. Various experimental ratios for different experiments. B = brittle, V = viscous, BS = brittle integrated strength, VS = viscous integrated strength, IS = total integrated strength, BF = buoyancy force. For an opening rate of 12°/h the average strain rate was estimated at ~ 10^{-4} s^{-1}. It should be noted that the strain rate is highly variable in an experiment, due to the asymmetrical opening in the experiment as well as the decrease in strain rate away from the retreating boundary.

(Fig. 5-5). For all the experiments, the extent of the deformed area rapidly increases in magnitude in the first 10-30° of rotation and then slows down until it stagnates (except for experiment 1) (Fig. 5-5). For relatively high BS/VS ratios, the rapid increase takes place in the first ~ 10° (experiments 5, 7 and 8), while for relatively low BS/VS ratios, this occurs in the first ~ 30° (experiments 1, 2, 3, 6 and 9).

For the two-layer lithosphere experiments (experiments 1-4, 6, 8 and 9), the asymmetry in the deformation pattern is more pronounced in the northern part of the deformed zone with increasing BS/VS ratio. Here, most deformation is accommodated by normal faults, which increase in strike angle relative to the retreating door towards the north and east (Fig. 5-4c-f). In contrast, with a relatively low BS/VS ratio, deformation in the north is absorbed by

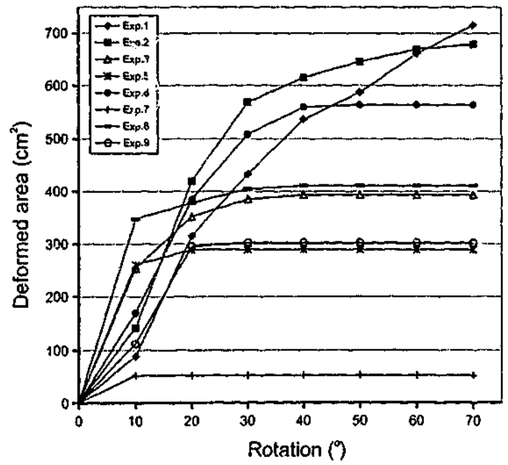

Fig. 5-5. Diagram showing the increase in deformed area inside the box (i.e. north of the gate) for every 10° increment of rotation of the door for different experiments.

conjugate strike-slip faults (with a component of transtension) (Fig. 5-4h,i). All of the experiments (except experiment 5) showed the formation of a relatively undeformed continuous strip of model lithosphere along the boundary of the retreating door, behind which extension was greatest.

For experiments in which rift systems were well developed, rift shoulder uplift was observed, resulting from the isostatic support of the lithosphere provided by the underlying glucose syrup.

5.3.2. Individual experiments

In this section the results of experiments 1 to 9 will be described individually (see Fig. 5-4).

Experiment 7 (Fig. 5-4a): In this experiment, the brittle top layer (0.6 cm) was directly superposed on top of the glucose syrup. This resulted in a very localised deformation pattern close to the gate, which was established within the first ~ 5° of rotation. Faulting was restricted to a rift system striking parallel to the door with normal faults striking slightly oblique to the rift axis. However, slight amounts of stretching of the brittle layer north of the rift zone were evident from the curvature of the east-west oriented grid lines. In between the rift system and the retreating door a narrow ridge developed, which remained attached to the door during progressive rotation.

Experiment 5 (Fig. 5-4b): In this experiment, the brittle top layer (0.6 cm) was directly superposed on top of the glucose syrup and the rate of opening was three times faster than in experiment 7. This resulted in a very localised and irregular deformation pattern, which rapidly migrated towards the north within the first ~ 10° of rotation but then stopped migrating and formed a through-going irregular rift structure parallel and closely behind the retreating door. This structure absorbed all of the continued extension. Most deformation in this experiment was accommodated by normal faults. A small number of strike-slip faults developed near the western corner of the gate.

Experiment 8 (Fig. 5-4c): In this experiment, the brittle layer (0.5 cm) was superposed on the silicone layer (1.2 cm), overlying the glucose syrup, and the opening rate of the door was relatively slow (4°/h). This resulted in a relatively localised strain pattern, although less irregular compared with experiment 5. The deformation front migrated towards the north within the first ~ 15° of rotation and then stopped migrating. From this time onwards, the extension was limited to the deformed zone. In between the extending zone and the retreating door a relatively undeformed thin strip of material developed. In this experiment most deformation was absorbed by normal faults, while a small number of strike-slip faults developed along the western side of the deformed zone striking north to northeast. The normal faults obtained a strike oriented E-W in the west but progressively more NNW-SSE towards the east.

Experiment 9 (Fig. 5-4d): In this experiment, the brittle layer (0.8 cm) was superposed on the silicone layer (1.0 cm), overlying the glucose syrup. Again, this resulted in a relatively localised strain pattern. The deformation front rapidly migrated towards the north within the first 20° of rotation and then stopped migrating. From this time onwards, the extension was localised along a through going extending zone located just north of the retreating boundary, with in between a relatively undeformed strip of material. In this experiment most deformation was absorbed by normal faults, while a small number of strike-slip faults developed near the western corner of the gate striking northeast to north-northeast. The

normal faults obtained a strike oriented E-W in the west but progressively more WNW-ESE towards the east.

Experiment 4 (Fig. 5-4e): In this experiment, a viscoplastic layer (0.2 cm) was inserted in between the brittle layer (0.6 cm) and the viscous layer (1.0 cm). This resulted in a localised deformation with well-defined elongated rift structures bounding relatively undeformed microplate-like segments. The deformation front migrated towards the north up to ~ 20° of rotation. Soon after, extension was mainly focussed along a through going extending zone located just north of the retreating boundary. As in most other experiments, a relatively undeformed strip of material developed in between the extending zone and the retreating door. Most deformation was absorbed by normal faults, while a small number of dextral strike-slip faults developed near the western corner of the gate striking northeast to north-northeast. The normal faults obtained a strike oriented E-W in the west, which became oriented progressively more NNW-SSE towards the east.

Experiment 3 (Fig. 5-4f): Here, a brittle layer (0.6 cm) was superposed on top of a viscous layer (1.2 cm), overlying glucose syrup. This resulted in a deformation pattern similar to that of experiment 4, although more diffuse with less defined graben structures close to the retreating boundary. The deformation front migrated towards the north up to ~ 25° of rotation. Extension continued in the entire deformed region, but the amount of extension absorbed by the region close to the retreating boundary increased.

Experiment 6 (Fig. 5-4g): In this experiment, a brittle layer (0.5 cm) was superposed on top of a viscous layer (1.2 cm), overlying glucose syrup. This resulted in a more diffuse deformation pattern compared with experiment 3. The deformation front migrated towards the north up to ~ 35° of rotation. Extension continued in the entire deformed region, but the amount of extension absorbed by the region close to the retreating boundary increased. As in most experiments, a relatively undeformed strip of material developed in between the extending zone and the retreating door. Close to the retreating boundary normal faulting was the dominant type of deformation, while near the corners and further to the north deformation was mainly absorbed by conjugate (transtensional) strike-slip faults.

Experiment 2 (Fig. 5-4h): In this experiment, a brittle layer (0.4 cm) was superposed on top of a viscous layer (1.2 cm), overlying glucose syrup. This resulted in a diffuse deformation pattern. The deformation front migrated towards the north up to ~ 55° of rotation. Extension continued in the entire deformed region, but the amount of extension absorbed by the region close to the retreating boundary increased. Again, a relatively undeformed strip of material developed in between the extending zone and the retreating door. Close to the retreating boundary normal faulting is the dominant type of deformation, while near the corners and further to the north deformation is mainly absorbed by conjugate (transtensional) strike-slip faults.

Experiment 1 (Fig. 5-4i): In experiment 1, a brittle layer (0.4 cm) was superposed on top of a viscous layer (1.2 cm), overlying glucose syrup. The resulting deformation pattern is similar to that of experiment 2, although it is more diffuse with a higher fault density, owing to the higher strain rate in this experiment compared with experiment 2. The deformation front continued migrating towards the north until the end of the experiment. Extension continued in the entire deformed region, but the amount of extension absorbed by the region close to the retreating boundary increased.

5.4. Discussion

5.4.1. General discussion

5.4.1.1. Slab deformation

Asymmetrical retreat of a subducting slab requires less work to deform the slab compared with other types of slab retreat (e.g. radial and unidirectional slab retreat [*Schellart et al.*, 2002c]), simply because it does not involve extensive internal slab deformation. To allow for asymmetrical slab retreat, the only permanent large-scale deformation the subducting plate has to undergo is the formation of a lithospheric-scale vertical tear on one side of the slab segment (Fig. 5-2). Examples of such tears can be observed in several arcs such as the Tonga arc and the Ryukyu arc. The formation of a tear could be facilitated by the presence of a pre-existing weak zone in the subducting lithosphere such as a transform fault, striking at high angle to the arc. The presence of a vertical tear at one cusp of the arc would further facilitate asymmetrical rollback, since it would allow lateral asthenosphere flow around the slab in addition to possible flow underneath the slab tip (Fig. 5-2c,d). A continuity of the slab across the other cusp would retard rollback of the slab in the proximity of this cusp, since the asthenosphere would only be allowed to flow underneath the slab tip. This process would then amplify the entire process of asymmetrical rollback and back-arc opening. Asymmetrical rollback could also be facilitated by a density polarity in the subducting lithosphere, parallel to the trench axis. This density polarity could result from a variation in age of the subducting slab parallel to the trench or the presence of buoyant features on the subducting plate. With such a slab configuration, the denser part would have a tendency to roll back faster compared with the lighter part, thus promoting asymmetrical rollback.

5.4.1.2. Overriding plate segmentation

In natural arc systems, slab retreat does not result in the separation between the overriding and subducting plates along the trench. Instead, the overriding plate fails at some distance from the trench. In ocean-ocean subduction settings this often occurs along the volcanic arc, resulting in the formation of a remnant and active volcanic arc, separated by a back-arc basin [*Karig*, 1970, 1971a,b; *Kobayashi and Nakada*, 1979]. Examples include the Tonga-Kermadec Ridge, which was split from the Lau-Colville Ridge during formation of the Lau-Havre Basin. Another example is the Izu-Bonin arc - West Mariana Ridge in the Western Pacific, which was split from the Palau-Kyushu Ridge during formation of the Parece-Vela Basin. More recently, the active Mariana Ridge was split from the inactive West Mariana Ridge during formation of the Mariana Trough. In ocean-continent subduction settings, back-arc deformation is more diffuse. However, in a more advanced stage of deformation, retreat of the hinge-line can result in segmentation of the overriding plate, where a segment is being separated from the continent. One example is the Kuril arc, which separated from the Okhotsk microplate during opening of the Kuril Basin [*Maeda*, 1990]. Another example is the Ryukyu arc, which is presently being separated from East China, accompanied by extension in the Okinawa Trough [*Uyeda*, 1977]. Other examples include the Japan arc [*Uyeda and Miashiro*, 1974] and the South Shetland arc [*Lawver*, 1995].

A number of arguments can be given for the reason why the overriding plate separates at the arc and not at the trench. First of all, the strength of the overriding plate is at its lowest at

the arc due to thermal weakening and its relatively thick crust (Fig. 5-6). Also, the arc has the highest potential energy in the near vicinity of the subduction zone, further promoting separation along the arc. This excess potential energy results in a net push from the arc towards the overriding plate, which will therefore not allow separation between the overriding and subducting plate during rollback. Injection of asthenosphere material along the subduction boundary does not occur because of this push from the arc region to the subducting plate, the lithostatic pressure exerted by the overlying mass on the boundary and the net downward drag of material along the subduction boundary due to subduction of the slab.

In most experiments, no separation between the overriding plate and the retreating door occurred as well, even though the overriding plate was homogeneous throughout. This could be explained by the fact that in these experiments the buoyancy force was greater than the brittle strength of the overriding lithosphere, resulting in spreading of the overriding

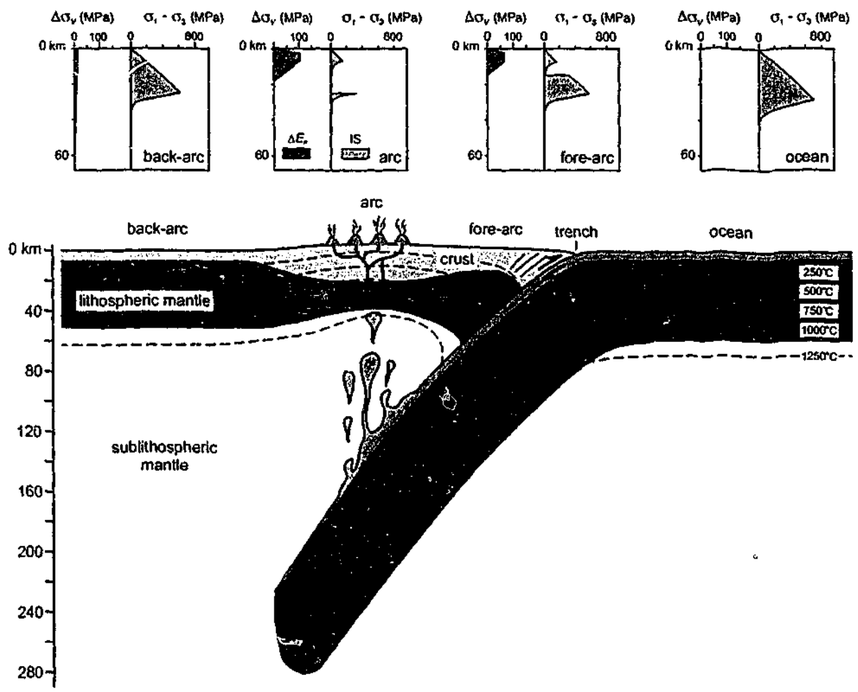

Fig. 5-6. Schematic sketch of ocean-ocean subduction system with inactive back-arc, demonstrating the mechanical weakness and high potential energy of the arc compared with the fore-arc region and the inactive back-arc region. This implies that during rollback of the subducting slab, the overriding plate is most likely to break up along the arc. Vertical stress difference profiles ($\Delta\sigma_v$) and strength profiles (σ_1-σ_3) for back-arc, arc, fore-arc and subducting lithosphere are plotted at the top. Vertical stress difference for each diagram with respect to the subducting lithosphere. Strength profiles are for extension. ΔE_p = potential energy difference; IS = integrated strength. Arc and fore-arc region have relatively high ΔE_p due to relatively thick crust, back-arc region has relatively low ΔE_p due to relatively thin crust. Arc has relatively low strength due to thick crust and warm geothermal gradient, while fore-arc and back-arc have relatively high strength due to cold geothermal gradient.

lithosphere over the glucose syrup in the space provided by the retreating door (Fig. 5-7). In an advanced stage of deformation, a ridge segment (i.e. arc) developed in between the retreating door and the principal zone of extension (PZE = zone which developed in an advanced stage of deformation and subsequently absorbed most or all of the extension during continuing retreat). The location of the PZE and the ridge (arc) could be related to lithospheric boudinage due to retreat of the door, where the silicone layer did not favour necking at the contact zone with the door, because this would result in high vertical shear stresses along the contact zone. Thus, it can be concluded that from pure mechanical reasons and even in a homogeneous overriding plate, rollback promotes extension to be localised at some distance from the subduction interface.

An interesting question that arises from experiment 5 (and also from experiment 7) is why the overriding plate did not immediately separate from the retreating boundary, but only did so after some considerable deformation of the overriding plate (Fig. 5-4a,b). One would not expect any deformation in the overriding lithosphere due to spreading, since the buoyancy force (between a column of glass beads lithosphere and a column of glucose syrup asthenosphere) in this experiment is a factor of ~ 8-9 smaller (see Table 6-2) than the integrated strength of the overriding lithosphere. Evidently, the retreating boundary can transmit deviatoric tensional stresses to the overriding lithosphere without any significant adhesion between the glass beads and the retreating door. A tentative explanation for this behaviour, based on the results of experiment 5, is sketched in Fig. 5-8. From an initial stage (Fig. 5-8a), retreat of the door over a short distance *dx* leads to the formation of a lithospheric

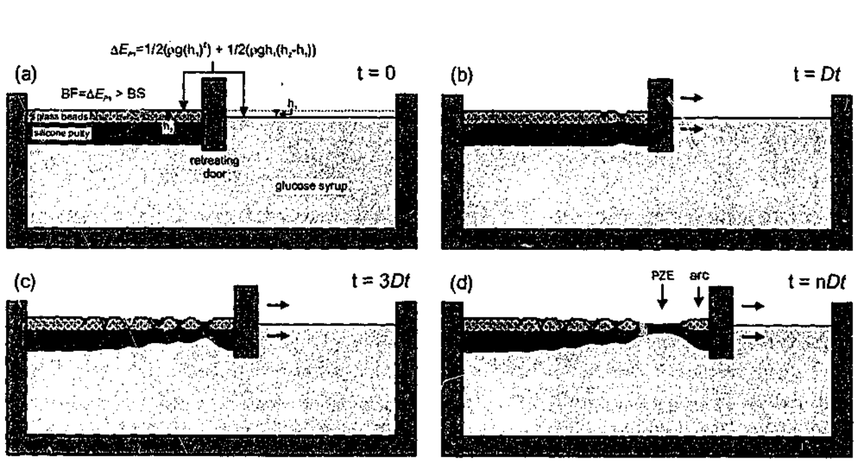

Fig. 5-7. Schematic sketches illustrating extension observed in experiments and the formation of a ridge (i.e. arc) along the retreating door. In most experiments the brittle strength (BS) of a column of lithosphere is smaller than the buoyancy force (BF = potential energy difference (ΔE_P) between column of model lithosphere (glass beads + silicone putty) and column of glucose syrup). This results in a gradual spreading of the overriding lithosphere during retreat of the door, where the spreading layer remains connected with the retreating door. (a) Initial stage. (b) Initial extension close to the retreating boundary. (c) Continuing retreat leads to a migration of the deformation front. (d) Formation of a principal zone of extension (PZE = zone absorbing most of the extension) and a ridge (arc), which is attached to the retreating boundary. The location of the PZE and arc could be related to the necking of the lithosphere due to retreat of the door, where the silicone layer is not allowed to neck at the contact zone with the door, because this would result in high vertical shear stresses.

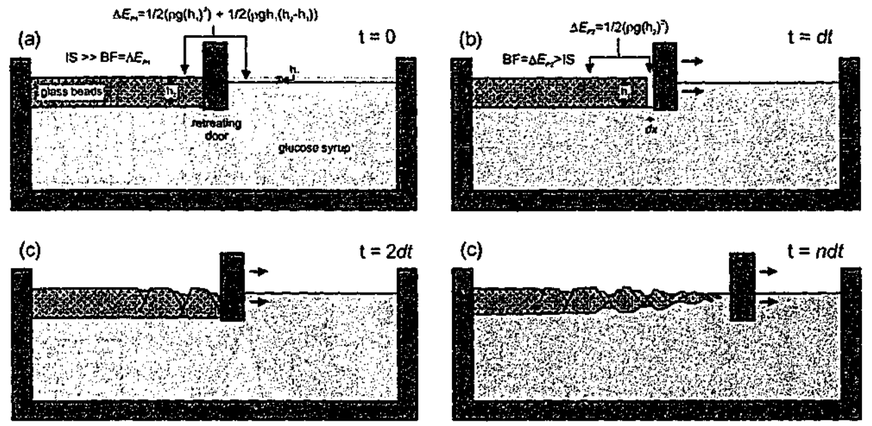

Fig. 5-8. Schematic sketches to explain extension observed in experiment 5 (Fig. 5-4b) (and also experiment 7 (Fig. 5-4a)), where the integrated strength (IS) of a column of glass beads is much greater than the buoyancy force (BF = potential energy difference (ΔE_P)) between column of glass beads and column of glucose syrup). (a) Initial stage. (b) Incremental retreat of the door over a distance *dx*. ΔE_P between column of glass beads and the gap created by the retreat of the door is greater than the integrated strength of a column of glass beads. (c) Collapse of the glass beads layer towards retreating door. (d) Continued retreat of the door may lead to separation of door from glass beads (e.g. experiment 5).

scale gap (Fig. 5-8b), which will not immediately be filled with glucose syrup. This will result in a large potential energy difference between the overriding lithosphere and the gap, leading to the failure and collapse of the overriding lithosphere into the gap (Fig. 5-8c). Extension continues until at some stage extension of the overriding lithosphere has reduced its thickness close to the retreating boundary resulting in the separation of the overriding lithosphere and the retreating boundary (Fig. 5-8d).

5.4.2. Natural examples of asymmetrical back-arc extension

Below, two natural examples of arc - back-arc systems displaying a structural asymmetry will be described. The first example is the Tonga arc from the Southwest Pacific and the second example is the Ryukyu arc from the Philippine Sea.

5.4.2.1. Tonga arc

The Tonga-Kermadec arc system is located in the Southwest Pacific, where the Pacific oceanic lithosphere is subducting westwards along the Tonga-Kermadec Trench underneath the Indo-Australian plate (Fig. 5-9). The Tonga arc is the northernmost half of the Tonga-Kermadec subduction zone, which is usually divided into two arc systems, based on the presence of the Louisville aseismic Ridge, located on the subducting Pacific plate. From west to east, the overriding plate consists of four distinct zones (Fig. 5-9):

(1) The South Fiji Basin, an Oligocene back-arc basin floured by oceanic crust [*Weissel*, 1981].

(2) The Lau-Colville Ridge, which is a remnant volcanic ridge [*Karig*, 1970].

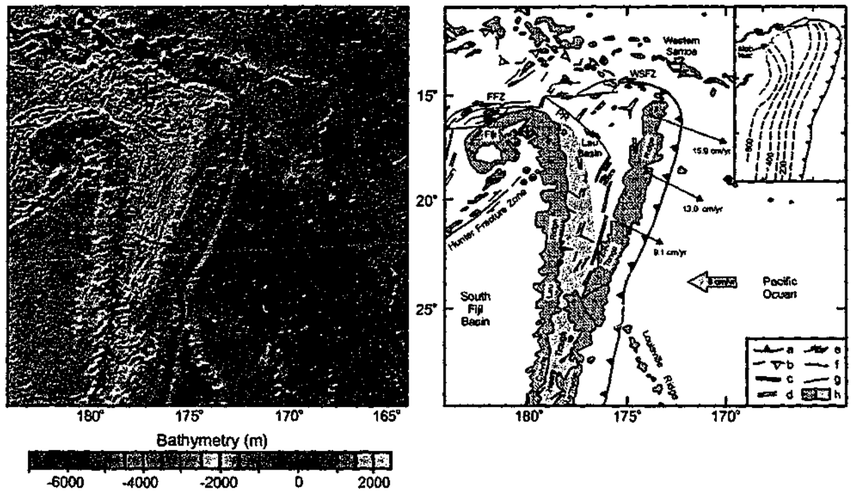

Fig. 5-9. (a) Bathymetric map of the Tonga arc region (from *Smith and Sandwell* [1997]). (b) Regional tectonic setting of (a) (compiled after *Wiedicke and Collier*, [1993], *Wiedicke and Habler*, [1993], *Sager et al.* [1994], *Bevis et al.* [1995], *Pelletier et al.* [1998] and *Fujiwara et al.* [2001]). GPS velocity (thin arrows) of Tonga arc relative to Australian plate (which includes Fiji block and Lau Ridge) (from *Bevis et al.* [1995]). Thick arrow represents relative convergence between Australian and Pacific plate (from *DeMets et al.* [1994]). Isobaths of Wadati-Benioff zone are shown in inset (100 km contours). a, trench (triangles on upper plate side); b, remnant trench; c, spreading axis; d, graben/trough; e, strike-slip fault; f, normal fault; g, fault (undifferentiated); h, main morphostructural feature on ocean floor (left) and extended crust in back-arc basin (right) (modified from *Parson and Hawkins* [1994]). FFZ = Fiji Fracture Zone, PR = Peggy Ridge, WSFZ = Western Samoa Fracture Zone.

(3) The Lau-Havre Basin, an active back-arc basin, which started extending at 7-6 Ma [*Parson and Hawkins*, 1994].
(4) The Tonga-Kermadec Ridge, which is the active volcanic ridge.

The Lau-Havre basin is a classical example of a back-arc basin in an ocean-ocean subducting setting, enclosed in between a remnant and an active volcanic arc [*Karig*, 1970]. The basin has formed due to eastward retreat of the subducting Pacific slab. Spreading started in the Lau Basin in the north at 5.5-4 Ma and has progressively migrated southward [*Parson and Hawkins*, 1994]. At present the spreading ridge has reached as far as 24° S [*Wiedicke and Collier*, 1993], which is the southern most part of the Lau Basin. The Havre Basin is still in an extensional phase [*Gamble and Wright*, 1995]. The extension is propagating south-southwestward, with intra-continental extension in the Taupo Volcanic Zone in New Zealand. Two models have been proposed to explain the wedge shaped geometry of the Lau Basin. In the first model the basin supposedly has progressively opened up from north to south (e.g. unzip model [*Hawkins*, 1995]). The second model is the so-called scissors or windscreen wiper model, where the rate of opening of the basin increases northwards [*Sager et al.*, 1994; *Bevis et al.*, 1995]. A GPS survey of the Tonga Ridge has revealed that the rate of opening increases from south to north and that the Tonga Ridge shows little or no arc-parallel deformation [*Bevis et al.*, 1995], indicating that the latter model is most applicable. Paleomagnetic data indicates that the Tonga Ridge has rotated ~ 20° during opening of the Lau Basin, comparable to the amount suggested by the wedge-shaped geometry of the basin

itself [*Sager et al.*, 1994]. In the scissors model, the hinge-point is defined by the Louisville Seamount chain located at the southern cusp of the arc. At the northern cusp of the arc, deformation is accommodated by the Western Samoa Fracture Zone. Here, the Tonga arc ends abruptly and the strike of the trench rotates some 90° from north-northeast to west-northwest. At depth, this corresponds to the vertical limit of the Tonga slab at ~ 15°S (Fig. 5-9), which seems to have formed due to tearing between the slab and the Pacific plate at the surface [e.g. *Millen and Hamburger*, 1998]. This tear could have formed due to asymmetric rollback of the Tonga slab, as schematically sketched in Fig. 5-2. Such asymmetric rollback and tearing would require sub-lithospheric mantle flow from the Pacific region around the tear towards the Lau Basin region and is evidenced by geochemical data from magmas erupted in the Lau Basin. Isotope data from these magmas indicate the presence of a Samoa mantle plume component for magmas in the northern part of the Lau Basin [*Wendt et al.*, 1997; *Turner and Hawkesworth*, 1998]. Seismic data, which indicate that arc-parallel southward shearing of the mantle is occurring beneath the Lau Basin [*Giardini and Woodhouse*, 1986], further support the tectonic model proposed above.

The Lau Basin has formed by two tectonic styles of extension. Initially, the western part of the basin formed by crustal extension and rifting, accompanied by magmatism that partly filled the rift basins [*Hawkins*, 1995]. This was followed by a phase of seafloor spreading [*Hawkins*, 1995] along spreading axes located more to the east. These spreading axes developed on rifts that started from a transform fault boundary [*Hawkins*, 1995].

The basin structures can best be compared with the model results presented in Fig. 5-4c, where extension is localised close to the retreating boundary. The model results show that initially extension is absorbed over a wider area, but is later accommodated entirely by a zone located just behind the rifted arc sliver. This is similar to the opening history of the Lau Basin. Furthermore, extensional structures in the basin are mainly parallel to the arc itself, as also observed in the model. This is most probably related to the early stage of opening of the basin. In a later stage of opening, one could expect arc-oblique and perpendicular spreading ridges to form near the hinge-point (i.e. near the Louisville Ridge). For instance, this is observed in the North Fiji Basin, which has opened up by ~ 40-50° of rotation of the New Hebrides arc [*Musgrave and Firth*, 1999]. In the basin, rift axes and spreading ridges near the northwestern cusp of the arc (i.e. hinge-point) are oriented at high angle to the arc, while rift axes and spreading ridges are oriented more parallel to the arc towards the southeast (Fig. 5-1) [*Schellart et al.*, 2002a].

5.4.2.2. Ryukyu arc

The Ryukyu arc is located along the South China active margin in an ocean-continent subduction setting. Here, the Philippine Sea plate is subducting northwestward along the Ryukyu Trench underneath the Ryukyu arc (Fig. 5-10). Two cusps define the lateral extent of the arc. The northeastern cusp is geographically linked to the Palau-Kyushu Ridge and the southwestern cusp to Taiwan. The Ryukyu arc is flanked on the northwestern side by the Okinawa Trough, an active back-arc basin, which has started extending since the Late Miocene [*Letouzey and Kimura*, 1985] and is at present still in a rifting stage. The Ryukyu arc itself has also experienced deformation from the Late Miocene to Present, with arc-parallel as well as arc-perpendicular extension [*Fournier et al.*, 2001]. The most recent stage of rifting (~ 1 Ma - Present [*Miki*, 1995]) in the Okinawa Trough occurs within a series of en echelon left-stepping grabens trending NE-SW in the north and ENE-WSW in the south (Fig. 5-10)

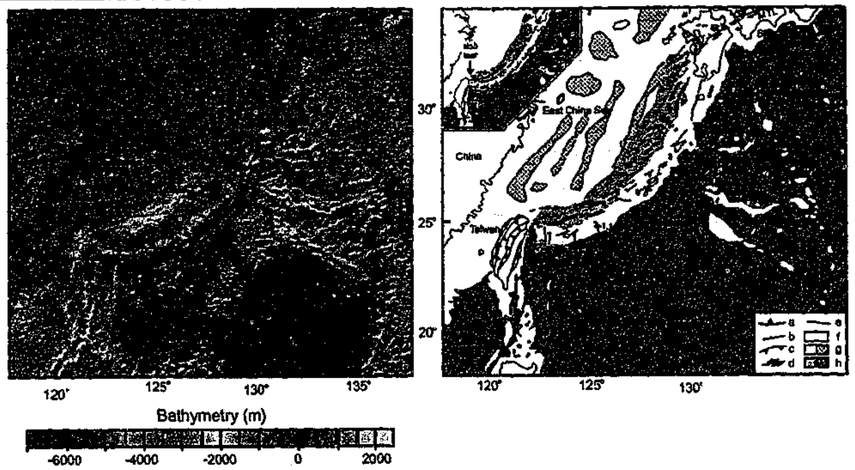

Fig. 5-10. (a) Bathymetric map of the Ryukyu arc and surrounding (from *Smith an Sandwell* [1997]). (b) Tectonic interpretation of (a) (compiled after *Sibuet et al.* [1987], *Kamata and Kodama* [1994] and *Lallemand et al.* [1999]). Horizontal GPS motions of the southern Ryukyu arc with respect to South China (thin arrows) are from *Imanishi et al.* [1996] and *Heki et al.* [1996]. The relative motion of the Philippine Sea plate with respect to Eurasia (thick arrow) is from *Seno et al.* [1993]. Isobaths (dashed lines) of the Wadati-Benioff zone (for 50, 100, 150 and 200 km) are shown in the inset (from *Eguchi and Uyeda* [1983]). a, trench (triangles on upper plate); b, normal fault; c, thrust fault; d, strike-slip fault; e, fault (undifferentiated); f, land; g, continental shelf/morphological feature on ocean floor (left) and depression in East China Sea (right) (modified from *Hsu et al.* [2001]); h, Okinawa Trough (left) and continental slope/ocean floor (right). MTL = Median Tectonic Line.

[*Sibuet et al.*, 1987]. In the north, the graben axes strike oblique to the main trend of the Okinawa Trough. The crustal thickness beneath the graben axis increases from 15-18 km in the southern part near Taiwan to 27-30 km in the northern part near Kyushu [*Iwasaki et al.*, 1990; *Sibuet et al.*, 1995].

Several models have been proposed to explain the opening of the Okinawa Trough, such as: opening of the Okinawa Trough as a consequence of the collision in Taiwan [*Letouzey and Kimura*, 1985]; opening in a pull-apart fashion due to India-Eurasia collision [*Fournier et al.*, 2001]; rollback of the subducting Philippine Sea plate towards the southeast [*Viallon et al.*, 1986]. It is suggested that the extension in the Okinawa Trough is best explained by rollback of the Philippine Sea plate towards the southeast. It is proposed that the most recent extension is the result of asymmetrical rollback, where the retreat rate increases from northeast to southwest, leading to asymmetrical extension in the overriding plate. Asymmetrical retreat could be explained by the presence of multiple buoyant features located on the subducting lithosphere along the northeastern part of the Ryukyu Trench (e.g. Palau-Kyushu Ridge, Amami Plateau, Daito Ridge, Oki-Daito Ridge). This would imply a higher average lithospheric density along the southwest of the trench compared with the northeast, resulting in a greater rollback velocity in the southwest. In addition, a vertical tear in the slab in the southwest of the arc would facilitate the lateral flow of asthenosphere material around the slab edge from underneath the slab towards the mantle wedge corner to accommodate rollback (e.g. Fig. 5-2c). This model could explain the en echelon pattern of the individual rift segments in the Okinawa Trough.

The analogue models show that the obliquity of individual rift systems increases towards the hinge. On a smaller scale, axes of individual rift segments, which are part of large-scale rift systems, are normally oriented oblique to the rift system itself and become progressively more oblique to the rift system towards the hinge. This is also observed for rift segments in the Okinawa Trough. From comparison, experiments 8 and 4 (Fig. 5-4c,e) show most resemblance with the Okinawa Trough. Experiment 4 show the development of a main extensional zone accommodating most of the extension (e.g. Okinawa Trough), located close to the retreating boundary with a narrow strip of material in between (i.e. comparable to the Ryukyu arc). In the early stages of the experiment extension also occurs along individual rift segments located further away from the retreating boundary, similar to extension observed in the East China Sea (Fig. 5-10). The extension in the north stopped after a through-going rift zone developed in experiment 4, similar to the extension in the East China Sea, which stopped after initiation of formation of the Okinawa Trough [*Hsu et al.*, 2001].

Another interesting analogy between model and nature is the presence of the Oita-Kumamoto Tectonic Line (Fig. 5-11a,b), a dextral strike-slip fault, which could be compared with the occurrence of dextral strike-slip faults near the hinge in most of the analogue experiments with a similar orientation compared with the trench (Fig. 5-11c,d). In most tectonic interpretations the Median Tectonic Line, located to the east of the Oita-Kumamoto Tectonic Line, has been interpreted as resulting from strain partitioning in the overriding plate due to oblique subduction of the Philippine Sea plate [*Tsukuda*, 1992; *Kamata and Kodama*, 1994]. This interpretation could correct for the Median Tectonic Line *sensu stricto*. However, in the light of the experiments presented here, its westernmost extension outcropping on Kyushu Island (Oita-Kumamoto Tectonic Line) could also be a mere effect of rotation of the arc segment located close to the hinge-point. Interestingly, *Kamata and Kodama* [1994] have noted the synchronous occurrence of dextral shearing along the Oita-Kumamoto Tectonic Line, anticlockwise rotation of the northeastern Ryukyu arc and the formation of rift segments striking oblique to the tectonic lineament.

The Wadati-Benioff zone of the subducting Philippine slab increases in depth from the northeast to the southwest, where it abruptly ends in the southwest just east of Taiwan (Fig. 5-10). This could imply a greater slab length (or at least a colder slab) in the southwest and therefore a greater negative buoyancy force, resulting in faster rollback in the southwest. This increase in retreat is facilitated in the southwest by the discontinuity of the slab, which allows asthenosphere material to flow horizontally around the slab edge. This is not possible in the northeast due to the continuity of the slab across the northeastern cusp. The increase in retreat velocity along the subduction zone is supported by recent GPS data from the southern Ryukyu arc (Fig. 5-10) [*Imanishi et al.*, 1996; *Heki et al.*, 1996] and could explain the southwestward decrease in crustal thickness of the Okinawa Trough. The abrupt ending of the slab in the southwest seems to represent a vertical tear, where the horizontal projection of this tear is oriented N-S and closely coincides with the steep N-S striking continental margin of eastern Taiwan. This leads to the tentative conclusion that whilst the Philippine slab is retreating towards the south to southeast, it is forming a tear between the buoyant (continental) part of the Philippine plate (Taiwan) and the dense (oceanic) part of the Philippine plate. Thus, the location of this tear would be triggered by the transition from continental to oceanic lithosphere.

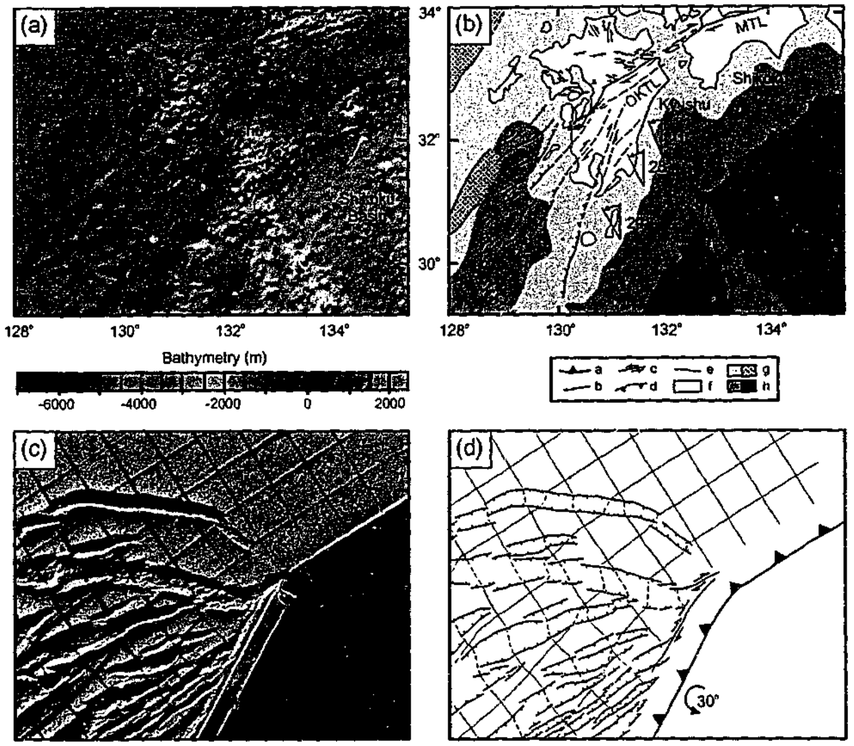

Fig. 5-11. Comparison between analogue results of experiment 8 and structures in the overriding plate around the Palau-Kyushu Ridge. (a) Bathymetric map surrounding the northeastern cusp of the Ryukyu arc (from *Smith an Sandwell* [1997]). (b) Tectonic interpretation of (a) (compiled after *Sibuet et al.* [1987] and *Kamata and Kodama* [1994]). Paleomagnetic declinations from *Kodama and Nakayama* [1993] and *Kodama et al.* [1995]. (c) Results of experiment after 30° rotation. (d) Interpretation of (c). a, trench (triangles on upper plate); b, normal fault; c, thrust fault; d, strike-slip fault; e, fault (undifferentiated); f, land; g, continental shelf/morphological feature on ocean floor (left) and depression in East China Sea (right) (modified from *Hsu et al.* [2001]); h, Okinawa Trough (left) and continental slope/ocean floor (right). MTL = Median Tectonic Line; OKTL = Oita-Kumamoto Tectonic Line.

5.4.2.3. Other examples

Another example of asymmetrical arc systems is the New Hebrides arc from the southwest Pacific ([*Schellart et al.*, 2002a], see also Chapter 7). This arc system is situated in an ocean-ocean subduction setting and is flanked by the North Fiji Basin, a wedge-shaped active back-arc basin, which developed since ~ 12-11 Ma [*Pelletier et al.*, 1993] due to asymmetrical clockwise opening (Fig. 5-1). In an initial stage of opening, back-arc spreading ridges had a strike ~ parallel to the arc (Fig. 5-1b), but in a later stage this pattern became more complicated with arc-oblique spreading ridges near the hinge-point (Fig. 5-1c). The most recent stage of development of the arc and back-arc basin has been complicated by subduction of the d'Entrecasteaux Ridge and the West Torres Plateau.

The Kuril arc system could also be regarded as a system that has developed to a large extent by asymmetrical rollback ([*Schellart et al.*, in review], see Chapter 6). The system is situated in an ocean-continent subduction setting and is flanked by the Kuril Basin and the Sea of Okhotsk, which developed by anticlockwise retreat of the Pacific slab from the Eocene until the Middle/Late Miocene. The back-arc region is characterised by diffuse deformation in the Sea of Okhotsk and a late stage opening of the wedge shaped Kuril Basin, which is thought to be underlain by oceanic crust.

5.5. Conclusions

Several back-arc basins display a geometry and internal structure that is asymmetric, i.e. where the amount of extension increases from one end of the arc to the other. A simple model has been presented to explain this geometry, where the opening is controlled by rollback of the hinge-line of the subducting lithosphere. The increase in extension is explained by the increase in retreat velocity of the subducting slab along the trench axis. This increase in velocity can be caused by an increase in lithospheric density along the trench axis and/or a vertical tear in the slab at the more rapidly retreating side of the retreating slab. Results of three-dimensional analogue models have been presented to simulate asymmetrical extension of an overriding lithosphere. In these models the initial rheology has been varied. The results show that with increasing lithospheric brittle to viscous strength (BS/VS), the fault density decreases, while the asymmetry in deformation pattern in the back-arc region increases. It is also shown that with decreasing brittle strength to buoyancy force ratio (BS/BF) the total area of surface deformation increases. The models and experimental results can be compared with several arc - back-arc systems, which display a relatively large amount of asymmetry along the arc and in the back-arc region (e.g. Tonga arc, Kuril arc, New Hebrides arc, Ryukyu arc) but a varying style of tectonic deformation. These differences are mainly the result of the stage of opening up of the back-arc basin and differences in rheology of the overriding lithosphere. The analogue results indicate that with an initially buoyant and weak overriding plate rheology, deformation can propagate inboard far from the retreating boundary, where the amount of propagation is comparable to the width of the retreating boundary.

FOREWORD CHAPTER 6

This chapter discusses a new tectonic model to explain the structure of the Kuril arc, Kuril Basin and Sea of Okhotsk, located in the Northwest Pacific. The conceptual model for the region was inspired by the geometry of the Kuril Basin and the asymmetric structures observed on published tectonic maps of the Kuril Basin - Sea of Okhotsk region [*Gnibidenko and Khvedchuk*, 1982; *Worrall et al.*, 1996].

The ideas and interpretations presented in this chapter are the sole work of the author. All the experimental work presented in this chapter is the sole work of the author. The clarity of ideas presented in this chapter benefited from discussion with Gordon Lister. Reviews of earlier versions of this chapter by Steve Boger, Anne Briais, Gideon Rosenbaum and Isabelle Manighetti are also acknowledged. The contents of this entire chapter has been submitted for publication to *Tectonics* and is currently in review. A reference can be found at the end of the thesis in the bibliography. Minor changes have been made to the text of the original paper in order to make the layout and spelling of this chapter consistent with the rest of the thesis.

CHAPTER 6

Asymmetric deformation in the back-arc region of the Kuril arc, Northwest Pacific: New insights from analogue modelling

Abstract

The tectonic evolution of the Kuril arc and back-arc region has been simulated with analogue experiments. The experiments simulate asymmetric deformation in the overriding plate due to anticlockwise rollback of the subducting Pacific plate. The results show the formation of a N-S to NE-SW-oriented dextral shear zone near the far edge of the retreating boundary analogous to the Sakhalin-Hokkaido dextral shear zone. Contemporaneously, normal faults and grabens form, striking parallel to the retreating boundary near the far edge but striking more oblique near the hinge-point and away from the retreating boundary. This is similar to extensional structures observed in the Kuril Basin and the Sea of Okhotsk. Furthermore, the model shows that the amount of extension progressively decreases away from the retreating boundary. This appears to have also happened in the Kuril - Okhotsk region, as evidenced by crustal thickness variation in the region. Finally, the model results show that extension is increasingly accommodated by the region close to the retreating boundary with progressive deformation. This can account for the Eocene - Early Miocene extension in the Sea of Okhotsk followed by Miocene spreading in the Kuril Basin.

6.1. Introduction

Back-arc basins are enigmatic features on Earth that develop in an overall convergent tectonic framework. Most back-arc basins develop by extension possibly followed by spreading, which seems rather contradictory with respect to the overall tectonic setting in which they develop. Examples are numerous in the Western Pacific and Mediterranean region and can be found in intra-oceanic subduction settings and along active continental subduction margins. The formation of such back-arc basins is often explained by the retreat of the hinge-line of the subducting lithosphere (rollback) and collapse and extension of the overriding plate towards the retreating hinge-line [*Elsasser*, 1971; *Molnar and Atwater*, 1978; *Garfunkel et al.*, 1986; *Royden*, 1993; *Lonergan and White*, 1997; *Wortel and Spakman*, 2000; *Faccenna et al.*, 2001a]. The physical concept behind the mechanism is rather simple. The subducting oceanic lithosphere is denser than the asthenosphere because it is colder. Therefore, the slab is pulled down by a negative buoyancy force, which results in sinking of the lithosphere, not only in a direction parallel to the slab dip but also perpendicular to it [*Elsasser*, 1971; *Molnar and Atwater*, 1978; *Lonergan and White*, 1997]. The physical validity of this concept has been verified in numerous physical and numerical experiments [*Kincaid and Olson*, 1987; *Olson and Kincaid*, 1991; *Guillou-Frottier et al.*, 1995; *Griffiths et al.*, 1995; *Christensen*, 1996; *Houseman and Gubbins*, 1997; *Faccenna et al.*, 1996, 1999; *Becker et al.*, 1999; *Faccenna et al.*, 2001b]. If slab rollback is either a driving agent of back-arc extension [*Elsasser*, 1971; *Molnar and Atwater*, 1978; *Le Pichon*, 1982; *Lonergan and White*, 1997] or is passively being pushed back [e.g. *Hatzfeld et al.*, 1997] remains a debate, but most geoscientists seem to favour the former view [*Taylor*, 1995]. Also, experimental insights into

this matter indicate that the negative buoyancy of the slab plays a more significant role in rollback than the buoyancy force resulting from potential energy contrast between the overriding plate and the subducting plate in ocean-continent subduction (e.g. Hellenic arc, Ryukyu arc, Kuril arc) [*Faccenna et al.*, 1996]. In an ocean-ocean setting, this buoyancy force would be even smaller (e.g. Mariana arc, Tonga arc, New Hebrides arc), pointing to a more prominent role of the negative buoyancy of the slab compared to the excess potential energy of the overriding plate with respect to the subducting plate.

In this chapter I will discuss the Kuril arc – back-arc region (Fig. 6-1), located in the Northwest Pacific, and in particular I will focus on the extensive deformation the region has undergone from the Eocene to the Middle/Late Miocene. Two popular models that exist for the structural development of the Kuril region are the extrusion tectonics model, where back-arc deformation is the result of collision between India and Eurasia [*Worrall et al.*, 1996], and the rollback model, resulting in collapse of the overriding plate towards the retreating hinge-line and extension in the back-arc region [*Maeda*, 1990]. It has also been suggested that both extrusion tectonics and rollback acted together to result in the deformation observed in the region [*Jolivet et al.*, 1990, 1994, 1999; *Fournier et al.*, 1994]. From these two models, it was suggested that the extrusion model is best in explaining the large-scale strike-slip structures observed on the islands of Sakhalin and Hokkaido, while the rollback model is best in explaining the opening up of the Kuril back-arc Basin. In this work, a simple tectonic model will be presented, which can explain the primary characteristic features of the region. The conceptual model will be supported with results from analogue experiments. In the experiments, deformation of the overriding plate has been modelled during asymmetric anticlockwise hinge-line retreat of the subducting lithosphere. Such anticlockwise retreat can be implied to have occurred from palaeomagnetic rotation along the Kuril arc and the asymmetric structures observed in the back-arc region, such as the wedge shaped geometry of the Kuril Basin. The first order structural and geometrical patterns in the model are similar to the characteristic features of the Kuril arc – back-arc region, supporting the validity of the conceptual tectonic model. The chapter is concluded with an evolutionary model of the Kuril arc - back-arc region for the past 65 Myr, which has been inspired by the results of the analogue experiments.

6.2. Geological Setting

The Kuril arc is located at the convergent plate boundary between the overriding Okhotsk microplate in the northwest and the subducting Pacific plate in the southeast (Fig. 6-1). The Okhotsk microplate is further outlined by diffuse intracontinental plate boundaries with the Eurasian plate to the west and the American plate to the northeast. These boundaries are defined by the Sakhalin-Hokkaido dextral shear zone and the Chersky Range sinistral shear zone, respectively [*Savostin et al.*, 1983; *Parfenov et al.*, 1988; *Riegel et al.*, 1993; *Seno et al.*, 1996]. The manifestation of the present tectonic setting, however, was accomplished quite recently (< 3 Ma [*Cook et al.*, 1986; *Imaev et al.*, 1990]) and has been preceded by a history of Palaeocene to Eocene accretion events and subsequent back-arc deformation. This included the collision and accretion of the Okhotsk block and several arc terranes to the N-S trending Sikhote - Alin and ENE-WSW trending Okhotsk -Chukotsk - Koryak palaeo-margins. At present, the accreted arc terranes are exposed on the Kamchatka peninsula and the Southern

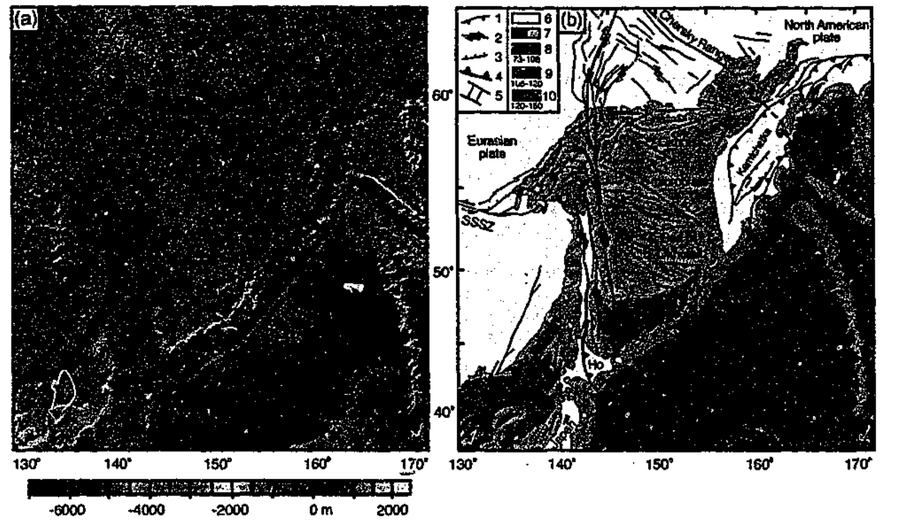

Fig. 6-1. (a) Topographic map of the Kuril Basin, the Sea of Okhotsk and surrounding (from *Smith and Sandwell* [1997]). (b) Regional tectonic setting of (a) (compiled after *Hilde et al.* [1977], *Gnibidenko and Khvedchuk* [1982], *Jolivet* [1987], *Hochstaedter et al.* [1994], *Worrall et al.* [1996], *Jolivet et al.* [1999] and *Konstantinovskaia* [2001]). For the Pacific plate, three different regions are indicated with different ages (in Ma) (from *Hilde et al.* [1977]). Ho, Hokkaido; KLZ, Kashevarov linear zone; KoB, Komandorsky Basin; Sa, Sakhalin; SR, Shirshov Ridge; SSSZ, Stanovoy sinistral shear zone. 1, reverse/thrust fault; 2, strike-slip fault; 3, normal fault; 4, subduction zone; 5 magnetic anomalies (thin lines) and transform faults (thick lines); 6, land; 7, sea, with basin/ocean floor (left) and continental shelf/morphological high on basin/ocean floor (right); 8-10, oceanic crust of the Pacific plate with age in Ma.

Siberian margin towards the east. Most of the Okhotsk block is underlying the Sea of Okhotsk and is composed of thinned continental crust [*Gnibidenko and Khvedchuk*, 1982; *Savostin et al.*, 1983; *Gnibidenko et al.*, 1995]. Small parts of the crust are exposed along the east coast of Sakhalin Island [*Rozhdestvenskiy*, 1982; *Fournier et al.*, 1994], the west coast of Kamchatka [*Parfenov et al.*, 1979; *Parfenov and Natal'in*, 1986] and at several sub-aqueous outcrops in the Sea of Okhotsk [*Gnibidenko and Khvedchuk*, 1982]. The crust is of Palaeozoic to Mesozoic age and has undergone Mesozoic metamorphism [*Fournier et al.*, 1994; *Gnibidenko et al.*, 1995].

The Okhotsk block has been extended during the Eocene to Early Miocene [*Gnibidenko and Khvedchuk*, 1982; *Worrall et al.*, 1996]. The thickness of its crust is up to 25 km beneath the basement rises and 15-20 km beneath the troughs [*Savostin et al.*, 1983]. Most of this extension is located beneath the Central Sea of Okhotsk, which is separated from the less extended Northern Sea of Okhotsk by the Kashevarov linear zone. This zone trends ~ NW-SE and has been interpreted as a southwest dipping normal fault zone [*Jolivet*, 1987]. The southern part of the Sea of Okhotsk is underlain by the wedge shaped Kuril back-arc Basin. This basin has an average depth of about 3300 m [*Maeda*, 1990] and is underlain by oceanic crust [*Gnibidenko and Khvedchuk*, 1982; *Gnibidenko and Svarichevsky*, 1984; *Savostin et al.*, 1983; *Gnibidenko et al.*, 1995] covered by some 3000-4000 m of undeformed sediments [*Gnibidenko and Svarichevsky*, 1984]. Initially, it has been suggested that the Kuril Basin

formed during the Late Oligocene to Early Miocene [*Kimura and Tamaki*, 1986a], based on heat flow, basement depth and sediment thickness. Later, *Maeda* [1990] has suggested that the Kuril Basin formed in the Middle Miocene between ~ 17-15 Ma, based on the southward migration of the northern terminus of subduction related arc magmatism on the islands of Sakhalin and Hokkaido. Such a fast opening would explain the rather uniform package of tectonically undisturbed sediments overlying the oceanic crust [*Gnibidenko et al.*, 1995]. This would suggest a very high but still realistic opening rate of the basin. With a maximum basin width of ~ 300 km and a time-span of 2 Myr, this results in a maximum opening rate of ~ 15 cm/yr. For comparison, the maximum present day GPS-determined opening rate of the Lau Basin (in its northernmost part) is 16 cm/yr [*Bevis et al.*, 1995]. Following similar arguments as *Maeda* [1990] but referring to a larger dataset, it has been suggested that the basin has opened up from the Early Miocene to Late Miocene (~ 23 - 9 Ma) [*Takeuchi et al.*, 1999 and references therein]. Also, it has been suggested by *Ikeda et al.* [2000] that the Kuril Basin continued opening until 7-9 Ma, based on similar aged basaltic rocks from northeast Hokkaido, which have a back-arc basin rift related affinity and have been related to the opening of the Kuril Basin. In any case, it is most likely that the Kuril Basin opened up in the Miocene and therefore postdates the extension in the Sea of Okhotsk. The northern and southern margins of the basin are rifted margins with normal faults dipping towards the depression [*Gnibidenko and Svarichevsky*, 1984; *Jolivet*, 1987]. From south along the Kuril arc to north on the Siberian mainland the strike of the normal fault structures in the back-arc region gradually changes from ~ southwest to ~ northeast [*Gnibidenko and Khvedchuk*, 1982; *Worrall et al.*, 1996].

The Kuril volcanic arc lies south of the Kuril Basin and is underlain by continental crust [*Gnibidenko and Khvedchuk*, 1982; *Gnibidenko et al.*, 1995]. The basin is at least of Late Cretaceous age, as indicated by the oldest volcanogenic sediments [*Gnibidenko and Khvedchuk*, 1982]. Palaeomagnetic data has indicated that the Nemuro Island region, located at the eastern end of Hokkaido in the western part of the Kuril arc, rotated anticlockwise some 29.4 ± 10.4° after the Early Eocene [*Tanaka and Uchimura*, 1989].

The Kuril Basin and the Sea of Okhotsk are bounded to the west by a regional system of ~ N-S trending dextral strike-slip faults (the Sakhalin-Hokkaido dextral shear zone) [*Rozhdestvenskiy*, 1982; *Fournier et al.*, 1994]. These faults formed in the Eocene and are still active [*Worrall et al.*, 1996]. Typical structures associated with the major strike-slip faults in the shear zone are NW-striking thrusts, steep reverse faults and en echelon folds, as well as a small amount of NE-striking normal faults and grabens filled with Paleogene - Neogene sediments [*Rozhdestvenskiy*, 1982]. All these associated structures point to a dextral sense of shear [*Rozhdestvenskiy*, 1982; *Fournier et al.*, 1994; *Worrall et al.*, 1996]. The shear zone has been described by *Fournier et al.* [1994] as a 2000 km long crustal-scale structure. However, estimates of dextral offset along the fault zone are in the order of at least 400 km [*Jolivet and Tamaki*, 1992], implying that the structure is most likely of lithospheric scale. Faults belonging to this system are exposed on the islands of Sakhalin and Hokkaido [*Rozhdestvenskiy*, 1982; *Jolivet and Huchon*, 1989; *Jolivet et al.*, 1992; *Fournier et al.*, 1994] and have also been interpreted to continue further northward to the Siberian mainland. These faults reactivated Late Cretaceous-Palaeocene shortening structures of the Sakhalin-Hokkaido accretionary complex, which formed due to collision of the Okhotsk block with the Eurasian active margin [*Rozhdestvensky*, 1986; *Jolivet and Huchon*, 1989; *Fournier et al.*, 1994; *Gnibidenko et al.*, 1995; *Worrall et al.*, 1996]. The dextral shear zone was mainly

transtensional from the Eocene to Early Miocene and transpressional from the Late Miocene to Present [*Worrall et al.*, 1996].

The Kuril arc exhibits two cusps. The northern cusp shows a spatial relationship with the Emperor Seamount Chain located on the subducting Pacific plate [*Vogt*, 1973]. The southern cusp seems to have no relationship with any topographic feature on the subducting plate. However, the southern cusp seems to be linked to the N-S striking Sakhalin-Hokkaido dextral shear zone located on the overriding plate, where the western part of the shear zone probably extends to the cusp [*Worrall et al.*, 1996].

6.3. Tectonic models

The structures of the Kuril arc, Kuril back-arc Basin and the Sea of Okhotsk have been explained by a variety of tectonic models including: extrusion tectonics along the eastern boundary of Asia, related to the India-Eurasia collision [*Worrall et al.*, 1996], in conjunction with rollback of the Pacific plate [*Jolivet et al.*, 1990, 1994, 1999; *Fournier et al.*, 1994]; retreat of the back-arc plate towards the north [*Savostin et al.*, 1983; *Kimura and Tamaki*, 1986b]; entrapment of oceanic lithosphere in the Okhotsk Sea region, followed by back-arc spreading in the Kuril Basin due to rollback [*Kimura*, 1994]; rollback of the Pacific plate towards the southeast [*Jolivet*, 1987; *Maeda*, 1990]. The shortcomings and errors of these models when applied to the Kuril region will be discussed in section 6.2.

A model will be presented to explain the structural and tectonic patterns in and around the Sea of Okhotsk and the Kuril Basin to test the hypothesis that rollback is responsible for the deformation observed in the area. In this model, asymmetric anticlockwise rollback of the hinge-line of the subducting plate is responsible for the wedge shaped opening of the Kuril Basin, asymmetric extension in the Sea of Okhotsk and anticlockwise rotation of the arc. Rollback of the hinge-line of the subducting lithosphere results in extension in the overriding lithosphere (i.e. back-arc extension), since the overriding lithosphere is not strong enough to sustain a potentially vacant region along the subduction boundary [*Elsasser*, 1971; *Lonergan and White*, 1997]. Therefore, the overriding plate collapses, extends and passively follows the retreating slab. Hinge-line migration most likely results from the negative buoyancy of the subducting lithosphere compared to the asthenosphere, resulting in sinking of the slab [*Elsasser*, 1971; *Molnar and Atwater*, 1978; *Lonergan and White*, 1997]. The asymmetric opening and extension in the Kuril Basin and the Sea of Okhotsk implies a northeast to southwest increase in hinge-retreat velocity along the Kuril trench during back-arc deformation in the Eocene to Middle Miocene. Similar conceptual models have been proposed for the formation of the North Fiji back-arc Basin bordering the New Hebrides arc [*Schellart et al.*, 2002a] and the Lau back-arc Basin bordering the Tonga arc [*Bevis et al.*, 1995]. Both basins have a wedge-shaped geometry and palaeomagnetic data support the idea of rotation of the arc. The amount and orientation of rotation [e.g. *Musgrave and Firth*, 1999; *Sager et al.*, 1994] is in both cases comparable to the amount one would expect with respect to the wedge-shaped geometry of the basin. In addition, GPS data for these arcs confirm the increase in back-arc spreading velocity from hinge-point towards the end [*Taylor et al.*, 1995; *Bevis et al.*, 1995].

The asymmetric retreat along the Kuril arc could be related to the increase in age (i.e. density) of the Pacific plate towards the south [*Hilde et al.*, 1977; *Clague and Dalrymple*, 1987] (Fig. 6-1b). However, the age polarity of the subducting Pacific plate along the Kuril

Trench might have been different during back-arc extension in the Eocene - Middle Miocene. If the age of the plate did indeed increase towards the southwest, this could result in a faster retreat velocity of the hinge-line in the southwest compared to the northeast. In this model, the Emperor Seamount Chain, a buoyant ridge located on the Pacific plate, could have defined the hinge-point at the northeastern cusp, although its location with respect to the trench is uncertain during extension of the Sea of Okhotsk and opening of the Kuril Basin (see also section 6.3). Deformation in the western part of the overriding plate could be accommodated by the N-S trending Sakhalin-Hokkaido dextral shear zone. Asymmetric slab retreat around a hinge-point located in the northeast would necessitate the formation of a (sub)vertical tear in the slab along the SW-side of the arc (cf. tear at northern extremity of the Tonga arc [*Millen and Hamburger*, 1998]). Such a tear would allow lateral asthenosphere flow around the slab edge from underneath the slab towards the mantle wedge and would further facilitate asymmetric rollback.

In this chapter I will describe the results of analogue experiments, with which I have investigated if asymmetric hinge-line retreat can explain the tectonic complexity observed in the Kuril back-arc region. Several analogue experiments have been executed with kinematic boundary conditions similar to the proposed boundary conditions for the overriding plate during the Eocene – Middle/Late Miocene. The new insights obtained from the experiments have been used to explain the structural framework of the Kuril back-arc region and to construct an evolutionary model of the region.

6.4. Analogue model

The scaling theory for analogue modelling of geological and tectonic processes has first been described by *Hubbert* [1937] and has later been discussed by *Horsfield* [1977], *Davy and Cobbold* [1991] and *Cobbold and Jackson* [1992]. In mechanical modelling, surface forces (stresses) should be properly scaled when compared to body forces (gravity). This implies that when the experiments are executed in a normal field of gravity, stresses should be scaled down as the product of density and length scales down [*Horsfield*, 1977; *Davy and Cobbold*, 1991]. In the experiments described here, a scale factor of ~ 2.5×10^{-7} (1 cm in experiment corresponds to ~ 40 km in nature) and a density factor of ~ 0.5 have been applied. Thus, stresses should be scaled down by ~ 1.25×10^{-7}. Both brittle and viscous rheologies have been used to simulate the natural behaviour of rocks. For brittle rocks, cohesion and friction coefficient are the most important parameters, as described by Coulomb's fracture criterion [*Coulomb*, 1776; *Handin*, 1969]. Since cohesion has the dimensions of Pascal (Pa), it should be scaled down in a similar fashion as stresses [*Davy and Cobbold*, 1991; *Cobbold and Jackson*, 1992]. The friction coefficient is dimensionless and should therefore have similar values in both model and nature. Finally, for viscous material, viscosity should scale down as the product of stresses and time scales down [*Davy and Cobbold*, 1991]. The experiments described here are executed in the normal field of gravity and the materials used in the experiments have been chosen as such, that they have been properly scaled to model the deformation of natural rocks.

The model that has been used consists of a three-layered system situated in a box (Fig. 6-2). On one side of the box a rotational sidewall is situated, which can rotate outwards in an anticlockwise fashion (Fig. 6-2a), simulating the progressive anticlockwise retreat of the

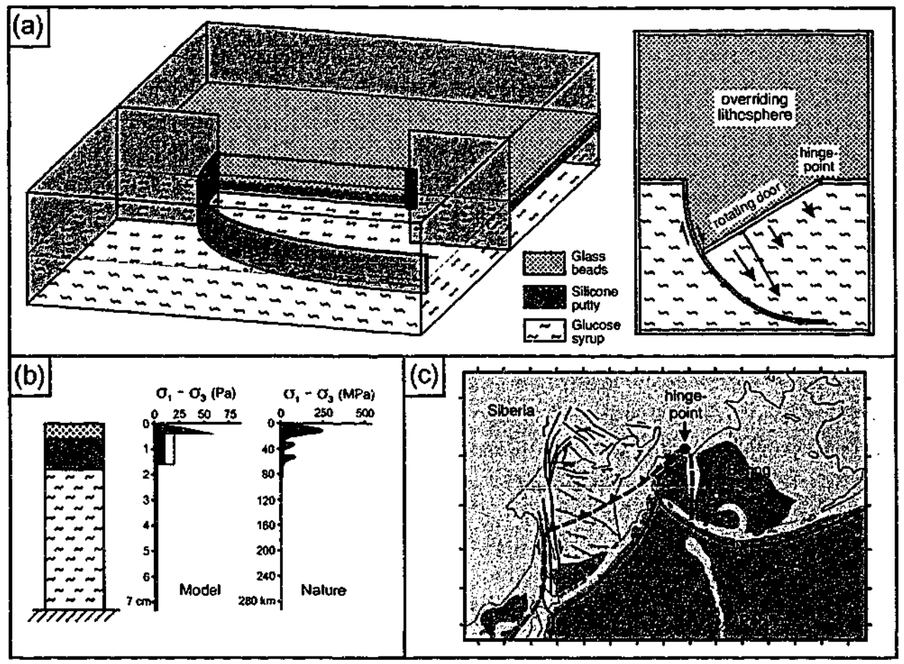

Fig. 6-2. (a) Three-dimensional view (left) and top view (right) of experimental apparatus to investigate asymmetric back-arc deformation of a two-layered brittle/ductile plate, simulating the overriding lithosphere (Okhotsk block), during opening of a door, simulating the asymmetric hinge-line retreat of the subducting lithosphere (Pacific plate). The model lithosphere is underlain by glucose syrup, simulating the asthenosphere, which gives the lithosphere isostatic support. (b) Strength profiles (for extension) for experiment 2 and natural prototype at the onset of deformation. Strength for silicone layer has been calculated for a strain rate of 10^{-3} s^{-1} (dashed line) and 5×10^{-4} s^{-1} (continues line). It should be noted that strain rate is highly variable in space and time in experiment due to asymmetry of applied boundary condition and will be smaller than 10^{-3} s^{-1} in most places. (c) Tectonic map of the Kuril region at the end of slab retreat (Middle or Late Miocene), superposed on which is the approximate location of the Kuril subduction zone (thick grey dashed line) at the start of slab retreat (Eocene). This illustrates the amount (~ 30°) and orientation (anticlockwise) of asymmetric retreat as well as the approximate location of the hinge-point.

hinge-line of the subducting Pacific plate with respect to the overriding plate (Fig. 6-2c). The Eocene position of the trench in Fig. 6-2c has been estimated from the amount of spreading (maximum of 300 km in the western Kuril Basin) and extension (500 - 700 km in the western Sea of Okhotsk) in the back-arc region, based on the crustal thickness map of *Gnibidenko et al.* [1995] and assuming a 40 km thick pre-extensional crust. The most important aspects of the retreating hinge-line is that it results in deviatoric tension along the boundary and that the retreating hinge-line does not separate from the overriding plate (since in nature the overriding plate never separates from the subducting plate along the trench). From an intuitive point of view, separation between a hinge-line and overriding plate would seem less likely for a dipping hinge than for a vertical hinge, since the overriding plate would partially rest on top of the hinge in the former case. However, in our model with the vertical hinge no separation occurred, so there was no need to make the dip of the hinge more realistic, which would unnecessarily complicate the construction of the model.

The uppermost two layers represent the overriding lithosphere. The lowermost layer represents the asthenosphere and gives the overlying lithosphere isostatic support. The uppermost brittle layer is made of fine-grained glass microspheres simulating the brittle upper lithosphere in nature, which show a Mohr-Coulomb type behaviour and are properly scaled to model brittle behaviour of rocks [*Schellart*, 2000]. The high viscosity middle layer is made of silicone putty (mixed with a dense filler) with a viscosity of ~ 2×10^4 Pa·s, simulating the viscous lower lithosphere in nature. The lower viscous layer is made of glucose syrup with a viscosity of ~ 100 Pa·s. Some physical properties of the individual experiments discussed in the text are given in Table 6-1.

The three-layered rheological stratification of the model has been adopted previously in arc – back-arc related analogue experiments (Fig. 6-2b) (e.g. *Hatzfeld et al.* [1997], *Gautier et al.* [1999] and *Martinod et al.* [2000]). The locus of extension in the Kuril Basin and the Sea of Okhotsk was most likely located on lithosphere previously thickened due to the collision of the Okhotsk block with the Sikhote-Alin and Okhotsk-Chukotsk palaeo-margins of Eurasia in the Early Tertiary [e.g. *Gnibidenko and Khvedchuk*, 1982; *Savostin*, 1983; *Zonenshain et al.*, 1990; *Gnibidenko et al.*, 1995]. Therefore, a two-layer representation of a continental lithosphere would be most realistic, since thermal relaxation would have diminished the strength of the upper mantle of the Okhotsk block, especially if the thermal relaxation time was sufficiently long. In this case, the strength of the lithosphere would reside almost entirely in the crust.

In the following experiments 1 hour corresponds to ~ 10 Myr in nature. With such a time scale factor, a viscosity of ~ 100 Pa·s (glucose syrup) and ~ 2×10^4 Pa·s (silicone mix) in the model are equivalent to a viscosity of ~ 7×10^{19} Pa·s and ~ 1.4×10^{22} Pa·s in nature, respectively. The first number is a reasonable approximation for the asthenosphere viscosity (~ 10^{19} - 10^{20} Pa·s [*Artyushkov*, 1983]) or the sub-lithospheric mantle viscosity (~ 10^{20} - 10^{21} Pa·s [*Ranalli*, 1995]). Furthermore, the viscosity contrast between the silicone mix and glucose syrup has a factor of ~ 200, which falls in the natural range for the lithosphere and sub-lithospheric mantle (~ 100-500 [*Faccenna et al.*, 2001a]). The progressive opening of the sidewall is driven by a step-motor. A passive grid (line spacing = 3 cm) and marker spheres have been laid on top of the brittle layer to monitor deformation. The progressive development of the model has been recorded by a camera from above, under oblique lightning of the top surface of the experiment to enhance the visibility of faults.

Experiment	Material	Rheology	Layer thickness (cm)	Opening rate (°/h)	Density (× 10^3 kg/m^3)
	Microspheres	Brittle	0.4		1.22
2	Silicone	Viscous (high)	1.2	12	1.22
	Glucose	Viscous (low)	5.5		1.42
	Microspheres	Brittle	0.6		1.22
3	Silicone	Viscous (high)	1.2	12	1.22
	Glucose	Viscous (low)	5.5		1.42
	Microspheres	Brittle	0.5		1.22
6	Silicone	Viscous (high)	1.2	12	1.22
	Glucose	Viscous (low)	5.5		1.42

Table 6-1. Some physical properties of experiments discussed in the text.

6.5. Results

Below follows the description of the results of experiment 2. Deformation begins close to the rotating boundary at the western side (Fig. 6-3a), slowly migrating towards the east and north (Fig. 6-3b). The earliest deformation is associated with the formation normal faults forming graben-like structures striking ~ parallel to the rotating boundary. New grabens that develop towards the east and northeast develop at more oblique angles to the rotating boundary, striking ~ WNW-ESE. Simultaneously, N-S to NE-SW trending dextral strike-slip faults develop at the western corner of the gate. These strike-slip faults propagate towards the north and northeast and are accompanied by conjugate strike-slip faults. In a later stage a relatively undeformed ~ 2 cm wide ridge develops along the entire length of the rotating boundary (i.e. the arc). This ridge increases in width from west to east (Fig. 6-3b). To the north of this ridge, a diffuse zone of extension has developed, which starts to accommodate most extension. In this region, normal faults strike NW-SE in the west and north and strike E-W to NE-SW in the centre and along the retreating boundary. To the north of the gate, a diffuse zone of conjugate transtensional strike-slip faults forms, where the dextral shears near the western side of the gate are best developed. In an advanced stage of deformation, dextral shearing of the spreading sheet along the curved boundary results in the formation of NW-SE striking en echelon right-stepping folds. Also, individual grabens form in the northernmost part of the deformation front in a late stage of deformation. At places of such graben formation, the

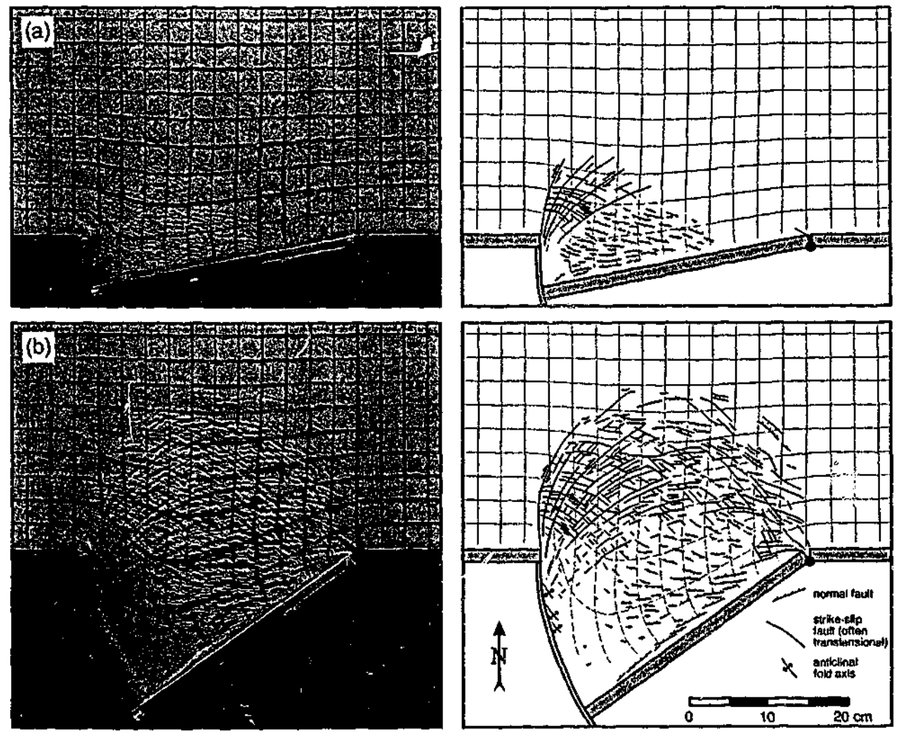

Fig. 6-3. Model results (left) and schematic interpretation (right) of experiment 2 (4 mm brittle layer and 12 mm viscous layer) with (a) after 1 hr (11°) and (b) after 3 hr (35°).

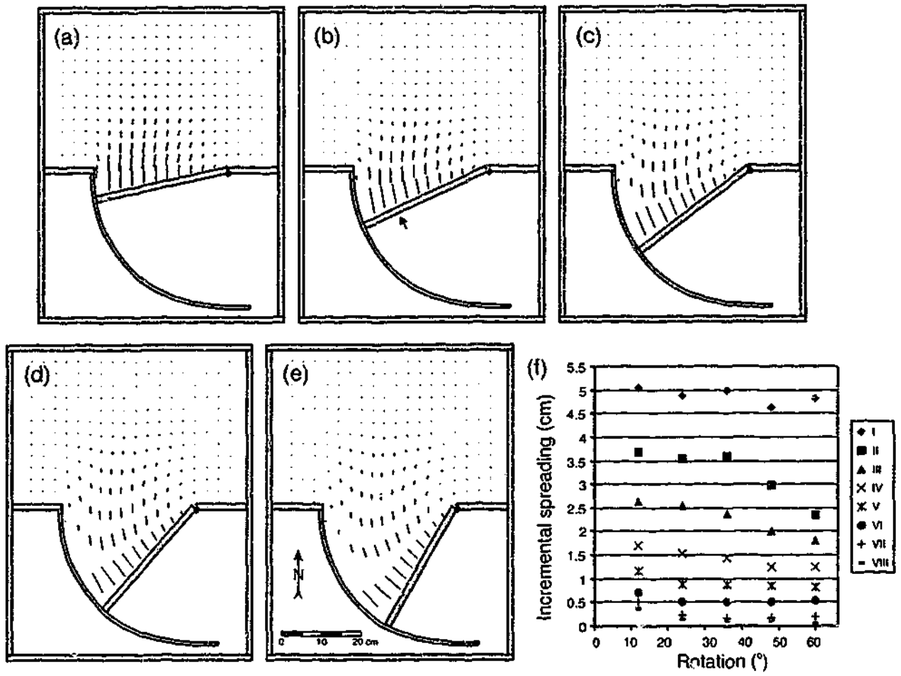

Fig. 6-4. (a-e) Displacement fields of experiment 2 between progressive stages of deformation. The increment of rotation used to determine the displacement vectors is 12°. (f) Diagram showing the amount of spreading for every 12° increment of rotation for eight successive spreading vectors located at grid intersection points of an initially N-S oriented grid line (see arrow in (b)). Here, I is the vector of the southernmost intersection point and VIII is the vector of the eighth intersection point (counting from south to north).

silicone layer has been thinned and has risen considerably due to the isostatic support of the brittle-ductile layer by the underlying glucose syrup. This isostatic support was also evident from small amounts of rift shoulder uplift (< 1 mm) for well-defined individual rift segments that developed in the north. The fault escarpments of such rift segments had a dip of ~ 60-80°. Interestingly, several strike-slip fault zones located close to the hinge-point, which were later reactivated as normal fault zones, had fault escarpments with a dip of only ~ 30-50°. This could be explained by the loss of cohesion of the granular material during strike-slip faulting [e.g. *Krantz*, 1991], making it incapable to support a steeply dipping escarpment.

The spreading pattern of experiment 2 has been plotted in Fig. 6-4 for 12° increments of rotation. It can be observed that the spreading velocity increases from the hinge-point towards the west. The spreading vectors close to the retreating boundary show a strong asymmetry, which decreases towards the north. The diagram in Fig. 6-4f shows that the length of the spreading vectors immediately north of the retreating boundary slightly decreases in magnitude during progressive opening, while the length of spreading vectors more to the north decreases considerably. This implies that the region close to the retreating boundary increasingly absorbs extension. This behaviour can also be observed in Fig. 6-5, where the incremental length increase (Δx) for several N-S trending grid-line segments has been plotted

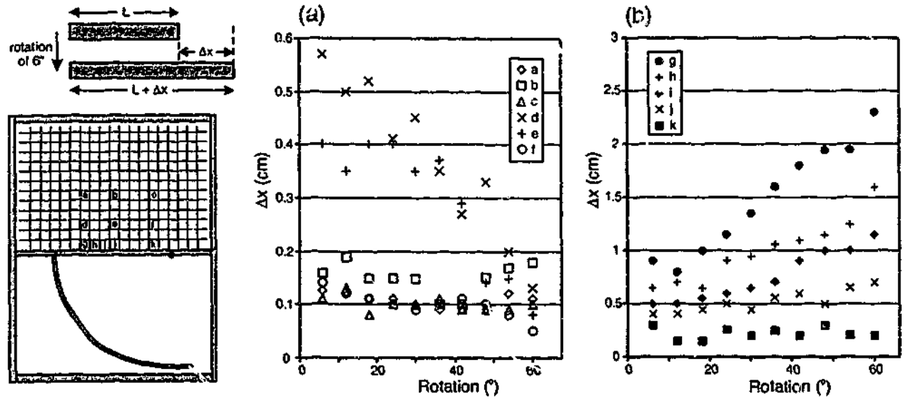

Fig. 6-5. Diagram illustrating increase in line length (Δx) in experiment 2 for every incremental increase in rotation of 6° for different segments of N-S oriented grid lines. Notice difference in scale for Δx in (a) and (b).

for an incremental rotation of 6°. In Fig. 6-5a, segments have been plotted, which are located at some distance from the retreating boundary. In Fig. 6-5b, segments have been plotted, which are located close to the retreating boundary. From the diagram in Fig. 6-5b, it can be concluded that Δx increases for segments g-j during progressive rotation. However, a decrease is observed for segments d-f in Fig. 6-5a, while segments a-c remain approximately constant. Thus, it can be concluded that the region close to the far end of the rotating boundary accommodates increasingly more of the total extension with progressive rotation at the expense of regions located further to the north. This behaviour can be explained from the velocity field in the early stage of the experiment (Fig. 6-4a), from which a decrease in strain rate from south to north can be deduced. Overriding plate extension due to continued retreat of the boundary will preferentially be absorbed by the region with the lowest integrated strength, i.e. the zone which has experienced maximum extensional strain.

The deformed surface grid and the amount of total horizontal extension of experiment 2 are illustrated in Fig. 6-6 after 30° of rotation. In general, the amount of extension decreases from the retreating boundary towards the north. The greatest amount of extension is found close to the far end of the retreating boundary. It can also be observed that the E-W asymmetry in extension close to the retreating boundary decreases towards the north (as observed in Fig. 6-4 and 6-5). Small amounts of shortening can be observed north of the corners of the gate.

Different experiments with different ratios of brittle to viscous strength (BS/VS) indicate that with increasing BS/VS ratio the deformation becomes more localised with fewer faults accommodating more deformation. Thus, the fault density decreases with increasing BS/VS ratio. This can be observed when the results of experiment 2 in Fig. 6-3b (BS/VS ≈ 0.12 N/m / 0.06 N/m) are compared with experiment 6 in Fig. 6-7a (BS/VS ≈ 0.18 N/m / 0.06 N/m) and experiment 3 in Fig. 6-7b (BS/VS ≈ 0.25 N/m / 0.06 N/m). Also, with increasing BS/VS ratio the structures in the interior of the box display a higher degree of asymmetry, where normal fault structures are better developed at the expense of strike-slip structures. For relatively high BS/VS ratios, deformation is mainly absorbed by strike-slip faulting near the far end corner and by normal faulting near the hinge-point corner. To the contrary, a diffuse zone of conjugate (transtensional) strike-slip faults develops for relatively low BS/VS ratios.

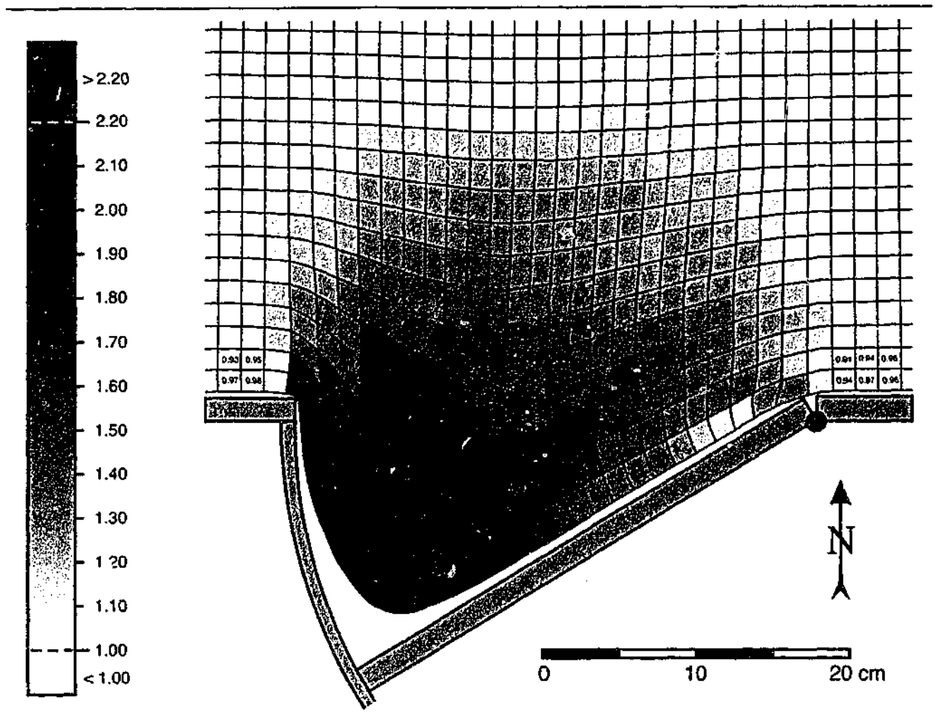

Fig. 6-6. Deformed surface grid of experiment 2 after 30° of rotation. Different greyscales indicate different factors of total horizontal surface stretch S ($S = A_F / A_O$, where A_F is final surface area and A_O is initial surface area).

6.6. Discussion

6.6.1. Comparison between model and nature

Out of seven experiments executed with a varying BS/VS ratio (ranging from ~ 1 - 25) and buoyancy force (BF = 0.03 - 0.27 N/m), experiment 2 (BS/VS ≈ 2, BF ≈ 0.21 N/m) gave the results most similar to the structures observed in the Kuril back-arc region, with relatively diffuse and widespread deformation in the back-arc region and the formation of a N-S to NE-SW striking dextral shear zone. This experiment had a relatively low BS/VS ratio and high BF number, corresponding to lithosphere with a relatively thick crust and warm geotherm. This probably corresponds to the rheological scenario for the Okhotsk block after it collided with the Eurasian margin in the Early Tertiary [e.g. *Gnibidenko and Khvedchuk*, 1982; *Savostin*, 1983; *Zonenshain et al.*, 1990; *Gnibidenko et al.*, 1995], where collision resulted in shortening and thickening of the crust, which itself led to an increased geothermal gradient.

One analogy between model and nature is the wedge shaped geometry of the Kuril Basin, which widens towards the southwest, and is located close to the retreating hinge-line of the subducting Pacific plate. In the model, most extension is observed close to the retreating door with maximum extension close to the far end of the retreating boundary (up to 300 % (exp. 2), 325 % (exp. 3) and 360 % (exp. 6) after 30° rotation). Such extension would probably be

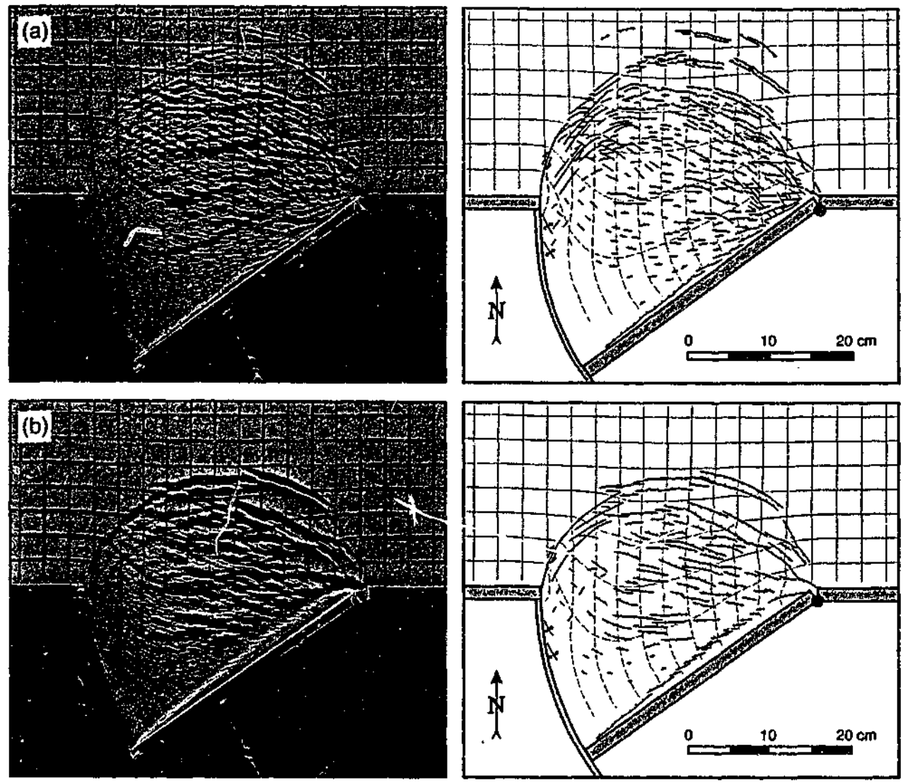

Fig. 6-7. Model results (left) and schematic interpretation (right) of (a) experiment 6 (5 mm brittle layer and 12 mm viscous layer) after 2 h 42 min (36°), and (b) experiment 3 (6 mm brittle layer and 12 mm viscous layer) after 2 h 54 min (35°).

sufficient to generate spreading in nature, since the continental crust just north of the Kuril Basin has experienced ~ 100 - 233 % extension (with a present crustal thickness of 15 - 20 km [*Gnibidenko et al.*, 1995] and assuming a pre-extension thickness of ~ 40 - 50 km). A difference between model and nature is that the Kuril Basin formed by spreading, while the zone of maximum extension in the model formed by extension, but this is simply explained by the limitation of the model, which is a mechanical model and not a thermo-mechanical model. Furthermore, the basin is bordered on the Pacific side by a thin strip of continental lithosphere (i.e. the Kuril arc) [*Gnibidenko et al.*, 1982, 1995; *Kimura and Tamaki*, 1986], which is considered to be at least Late Cretaceous in age [*Gnibidenko and Khvedchuk*, 1982; *Kimura*, 1986]. This strip was separated from the overriding plate during opening of the Kuril Basin [*Maeda*, 1990]. In the experiment, such a strip of relatively undeformed lithosphere developed as well (Figs. 6-3 and 6-7). Another analogy is the orientation of normal faults, which are oriented parallel to the arc close to the far end of the rotating boundary (southwest) and become progressively oblique to the arc towards the hinge-point (northeast) and away from the boundary (north to northwest). Extension is preferentially oriented towards the SW-corner due to the relative fast retreat of this corner with respect to the hinge-point. Pure strike-slip faults mainly formed near the far end of the retreating boundary striking N-S to NE-SW and had a dextral sense of shear, similar to the northernmost part of the Sakhalin-Hokkaido

dextral shear zone (northernmost part of Sakhalin until well into the Siberian mainland). This part of the shear zone shows a fanning pattern of dextral strike-slip faults changing strike from ~ N-S in the west of ~ NE-SW in the east. The southern part of the shear zone reflects a plate boundary remnant of the Late Cretaceous to Palaeocene Sakhalin-Hokkaido accretionary complex (Fig. 6-2c) [*Rozhdestvensky*, 1986; *Jolivet and Huchon*, 1989; *Fournier et al.*, 1994; *Gnibidenko et al.*, 1995; *Worrall et al.*, 1996] along which the western most part of the retreating slab migrated. Along this part of the shear zone numerous NW-striking en echelon folds and thrust have been reported [*Rozhdestvenskiy*, 1982; *Fournier et al.*, 1994; *Worrall et al.*, 1996], similar to the NW-striking right-stepping en echelon folds which developed along the curved boundary in the analogue model (Fig. 6-3b).

Both model and nature show that most extension is concentrated close to the arc (e.g. Kuril Basin, which is ~ 3300 m deep and underlain by oceanic crust) and decreases towards the north. North of the Kuril Basin, the extended Central Sea of Okhotsk is 1000-2000 m deep [*Maeda*, 1990], reflecting a relatively thin continental lithosphere [*Gnibidenko et al.*, 1995]. Further to the north lies the slightly extended Northern Sea of Okhotsk, which is 0-1000 m deep [*Maeda*, 1990]. In the northernmost part, subarial Southern Siberia attests to only marginal or no lithospheric extension. It is stressed that the N-S oriented strain gradient is best explained by a tensional boundary condition located south of the Kuril arc and would therefore be related to the subduction zone along the Kuril arc. Furthermore, spreading is greatest in the southwest of the Kuril Basin and extension in the Sea of Okhotsk is greatest just east of the Sakhalin-Hokkaido dextral shear zone and decreases further to the east, which is also observed in the model and indicates that retreat along the subduction zone must have been asymmetrical and anticlockwise. This anticlockwise retreat is supported by palaeomagnetic data from Nemuro Island (located along the Kuril arc just east of Hokkaido), which indicates that the region has rotated 29.4° ±10.4° anticlockwise after the Early Eocene [*Tanaka and Uchimura*, 1989], suggesting a similar amount of rotation for the entire Kuril arc. Finally, the model results show that extension is increasingly accommodated by the region close to the retreating boundary with progressive deformation (e.g. Fig. 6-4, 6-5). This can account for the late stage opening of the Kuril Basin in the Miocene [*Maeda*, 1990; *Takeuchi et al.*, 1999; *Ikeda et al.*, 2000], which was preceded by a prolonged period of extension in the Sea of Okhotsk from the Eocene - Early Miocene [*Worrall et al.*, 1996].

6.6.2. Comparison with other tectonic models

From the models, presented in section 1.2, the oceanic lithosphere entrapment model [*Kimura*, 1994] can be rejected, since the Sea of Okhotsk is underlain by thinned continental crust and not by oceanic crust [*Gnibidenko and Khvedchuk*, 1982; *Savostin et al.*, 1983; *Gnibidenko et al.*, 1995]. The model, which explains the structures in the region by northward retreat of the back-arc microplate [*Savostin et al.*, 1983] can be disregarded because there is no indication that extensive Eocene to Middle Miocene extension is being absorbed by comparable amounts of shortening north of the back-arc plate. Furthermore, there is no obvious driving mechanism present to drive such a back-arc microplate towards the north and at the same time create extension at its trailing southern end. A third point is that during the Eocene to Middle Miocene, there was no such thing as a "rigid" back-arc plate, since the entire region underwent extensive diffuse deformation.

Kimura and Tamaki [1986b] have suggested that the structures in the region have resulted from the India-Eurasia collision, which led to northward retreat and clockwise rotation of the

back-arc microplate due to dextral shear along the Sakhalin-Hokkaido dextral shear zone, resulting in opening of the Kuril Basin contemporaneous with shortening in Kamchatka. This model also does not explain the lack of extensive Eocene to Middle Miocene shortening north of the back-arc plate, as well as the observed widespread Eocene to Early Miocene extension in the Sea of Okhotsk region. Furthermore, palaeomagnetic data indicates that (at least part of) the Kuril arc has rotated some 30° anticlockwise after the Early Eocene [*Tanaka and Uchimura*, 1989], contrary to what the model of *Kimura and Tamaki* [1986b] would predict (e.g. no rotation of the Kuril arc but clockwise rotation of the Okhotsk region). Finally, the shortening structures observed in the Kamchatka region resulted from the accretion of several arc terranes to the overriding plate [*Bakhteev et al.*, 1997; *Konstantinovskaia*, 2001] and not from rotation of the supposed back-arc microplate as suggested by *Kimura and Tamaki* [1986b].

The extrusion model has first been proposed by *Molnar and Tapponnier* [1975] to explain the extensive intracontinental deformation of East and Northeast Asia as resulting from the India-Eurasia collision. This model was supported by analogue results of plane-strain experiments [*Tapponnier et al.*, 1982], which showed the sequential eastward extrusion of blocks along NE-SW oriented sinistral shear zones. This model was later refined by *Davy and Cobbold* [1988], who scaled their analogue experiments for gravity to incorporate buoyancy forces. In these more realistic experiments the importance of N-S trending dextral shear zones as conjugates to the NE-SW trending sinistral shear zones was discovered. This led Jolivet and co-workers to suggest that ~ N-S oriented dextral shear zones along the East Asian margin (such as the Sakhalin-Hokkaido dextral shear zone) resulted from extrusion tectonics while back-arc basin formation resulted from slab rollback along the East Asian margin [e.g. *Jolivet et al.*, 1990, 1994, 1999; *Fournier et al.*, 1994; *Worrall et al.*, 1996]. In addition, *Jolivet et al.* [1990, 1994] stated that without internal deformation of Asia due to collision with India, marginal basins along the East Asian margin would have opened in a symmetrical way. However, examples of asymmetric back-arc basins in the Southwest Pacific (North Fiji Basin and Lau Basin) confirm that back-arc basin can open up asymmetrically purely resulting from subduction related processes [*Bevis et al.*, 1995; *Schellart et al.*, 2002a]. Also, analogue modelling results of extrusion tectonics have shown that the ~ NE-oriented sinistral shear zones (cf. Stanovoy sinistral shear zone) are the major shear zones which accommodate relatively large amounts of shearing, while the conjugate ~ N-S oriented dextral shear zones are subsidiary (cf. Sakhalin-Hokkaido dextral shear zone) with relatively small amounts of offset [*Davy and Cobbold*, 1988; *Jolivet et al.*, 1990; *Jolivet et al.*, 1994]. In Northeast Asia, however, the opposite is observed. The amount of shearing along the Stanovoy shear zone can be estimated by estimating the amount of extension along the Baikal rift, which is (in the extrusion model) a releasing bend along the sinistral shear zone. Extension along the rift (and thus sinistral shearing) has been estimated at ~ 7 km based on structural mapping [*San'kov et al.*, 2000] and < 20 km based on crustal gravity modelling [*Zorin and Cordell*, 1991]. In stark contrast, dextral shearing along the Sakhalin-Hokkaido dextral shear zone has been estimated to be at least 400 km [*Jolivet and Tamaki*, 1992], based on the amount of opening of the Japan Sea. It is suggested, however, that the amount of shearing is even much higher (800 – 1000 km), based on the amount of extension in the western Sea of Okhotsk (500 – 700 km) and spreading in western Kuril Basin (300 km). Thus, it can be concluded that the N-S oriented Sakhalin-Hokkaido dextral shear zone did not result from the India-Eurasia collision. To finalise, timing could be invoked as an argument to support the connection between India-Eurasia collision (started in the Eocene [*Searle et al.*, 1987]) and back-arc deformation in the

Sea of Okhotsk (started in the Eocene). However, back-arc deformation in the Sea of Okhotsk region ended in the Early Miocene [*Gnibidenko and Khvedchuk*, 1982; *Worrall et al.*, 1996], and was subsequently followed by Miocene back-arc spreading in the Kuril Basin [*Maeda*, 1990; *Takeuchi et al.*, 1999; *Ikeda et al.*, 2000], while the India-Eurasia collision is active up to the Present. This timing of back-arc activity in the Kuril region closely coincides with the time of slow convergence between the Eurasian and Pacific Plates (Palaeocene - Middle Miocene) and faster convergence during the Cretaceous and Late Miocene - Present [*Northrup et al.*, 1995]. Therefore, it would seem more logical to connect the back-arc deformation with Pacific slab behaviour along the Kuril Trench.

As it is likely that the Okhotsk region was thickened due to collision with the Eurasian margin [e.g. *Gnibidenko and Khvedchuk*, 1982; *Savostin*, 1983; *Zonenshain et al.*, 1990; *Gnibidenko et al.*, 1995], one could invoke another mechanism for extension in the back-arc region, which is gravitational or extensional collapse [e.g. *Dewey*, 1988]. For instance, this scenario has been proposed for the formation of the Betic/Rif arc and Alboran back-arc region [*Platt and Vissers*, 1989] and the Hellenic arc and Aegean back-arc region [*Hatzfeld et al.*, 1997; *Gautier et al.*, 1999], with collapse of an overthickened orogenic wedge advancing over the subducting plate. For the Okhotsk region, however, not much is known about the extent of thickening of the region due to the Palaeocene collision. It could be that southward collapse of the thickened region played some role in extension of the region, but a prerequisite for this collapse to occur is southwestward retreat of the slab. Analogue and numerical modelling, and analytical insights into the role of collapse versus slab retreat indicate that slab retreat is the main driving agent of back-arc extension [*Le Pichon*, 1982; *Faccenna et al.*, 1996; *Meijer and Wortel*, 1997]. It could be that collapse played some role in the early stage of back-arc deformation, but this role would have diminished with time due to thinning of the region and decrease in excess potential energy of the region. Finally, one would expect collapse to result in extension perpendicular to the arc in alignment with the steepest potential energy gradient, while the extension in the back-arc region is highly asymmetrical and therefore not easily explained by collapse of a thickened lithosphere.

6.6.3. Evolutionary model

Below I will describe an evolutionary model proposed for the Kuril arc – back-arc region and surrounding regions, based on the model results and published geological an geophysical data. A conceptual scenario for the evolution since ~ 65 Ma is presented in Fig. 6-8. Although our model has not been intended to explain the structures that have formed in the region for the last few Myr, the final two diagrams of Fig. 6-8 at ~ 5 Ma and ~ 0 Ma have been included to offer a complete evolutionary scenario from ~ 65 Ma to Present.

~ 65 Ma (Fig. 6-8a): Oceanic lithosphere was subducted northwards [*Gordon and Jurdy*, 1986], accompanied by Late Cretaceous to Paleogene volcanism along the palaeo-margins of Sikhote Alin and Okhotsk-Chukotsk [*Worrall et al.*, 1996] and Late Cretaceous to Palaeocene volcanism along the Koryak and Beringian shelf [*Cooper et al.*, 1987a,b]. Oblique subduction in the Sikhote-Alin region caused sinistral shearing along arc-parallel strike-slip faults (Sikhote-Alin sinistral shear zone) [*Natal'in et al.*, 1986].

~ 55 Ma (Fig. 6-8b): During the Palaeocene the Okhotsk block was accreted to the Eurasian continent [*Gnibidenko and Khvedchuk*, 1982; *Zonenshain et al.*, 1990; *Worrall et al.*, 1996], followed by the accretion of the Valaginsky arc terrane during the latest

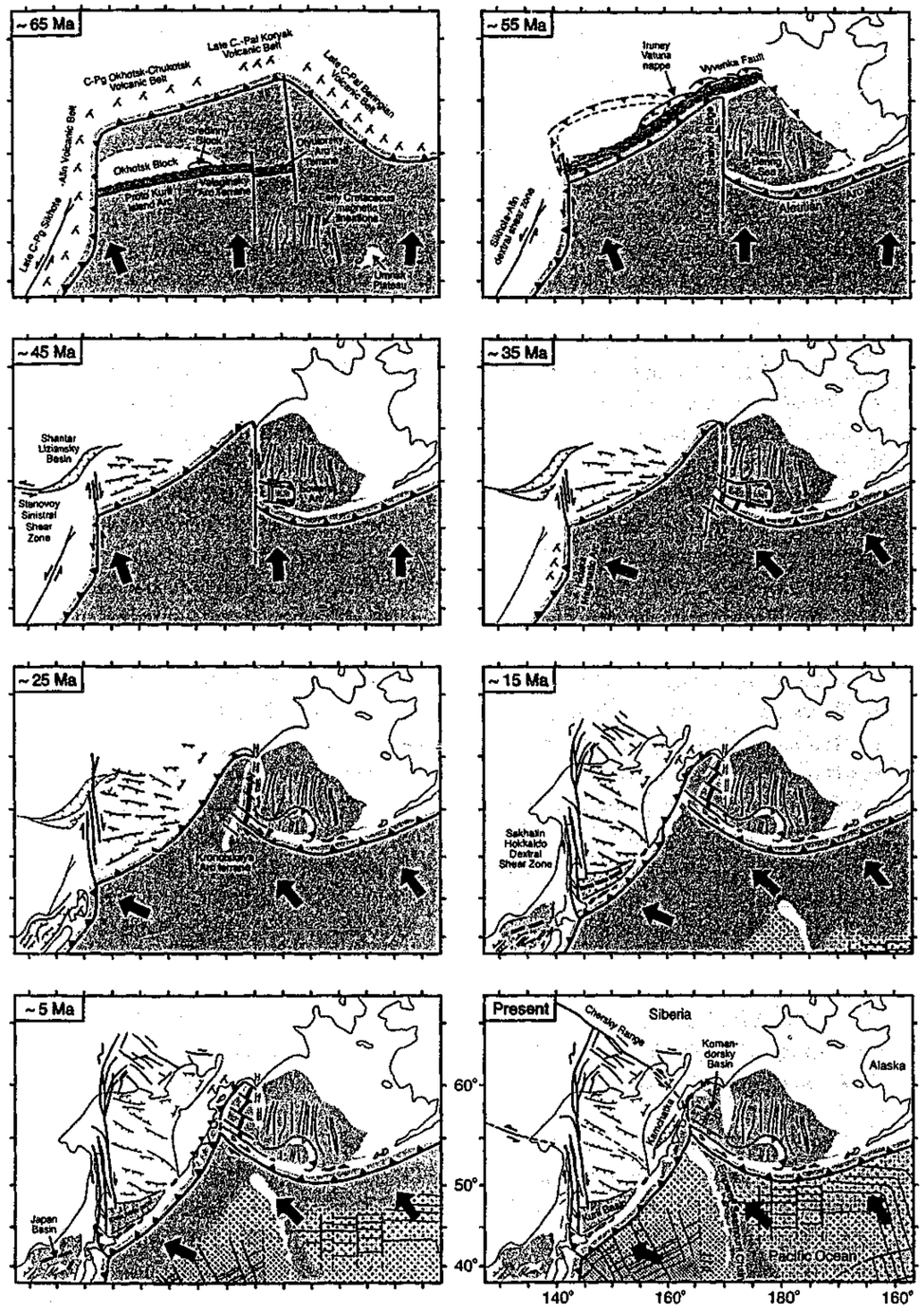

Fig. 6-8. Conceptual scenario for the evolution of the Kuril Arc, Kuril Basin, Sea of Okhotsk, Kamchatka Peninsula and surrounding for the past ~ 65 Myr. For explanation of the diagrams see text. For explanation of symbols see Fig. 1. The dot-patterns in the last three diagrams indicate the age of the subducting Pacific lithosphere, which is 120-150 Ma (fine pattern), 106-120 Ma (medium pattern), 73-106 Ma (coarse pattern) and 40-73 Ma (very coarse pattern).

Palaeocene - Early Eocene [*Konstantinovskaia*, 2001] and the accretion of the Olyutorsky terrane in the Early Eocene [*Worrall*, 1991; *Fedorchuk and Izvekov*, 1992]. After accretion of the Okhotsk block to Eastern Siberia, continued convergence was accommodated by a subduction zone located south of the Okhotsk block, i.e. the proto-Kuril Trench. It is proposed that the proto-Kuril Trench started to retreat southward asymmetrically somewhere in the Eocene akin to what is shown in the analogue models (Fig. 6-3 and 6-7), with deformation starting close to the retreating boundary and migration of the deformation front towards the north. Such retreat would lead to back-arc extension in the overriding plate and would explain the Eocene to (Early) Miocene extension in the Okhotsk region with sedimentary deposition into fault bound grabens [*Gnibidenko and Khvedchuk*, 1982; *Worrall et al.*, 1996]. Contemporaneously, the Sakhalin-Hokkaido dextral shear zone formed by reactivating shortening structures related to the Sikhote-Alin - Okhotsk block collision. Accretion of the Olyutorsky terrane and Umnak Plateau to the Koryak-Beringian margin stopped subduction along this active margin and resulted in a step-back of the subduction zone [e.g. *Karig*, 1974] towards the south. This resulted in the formation of the eastern part of the Aleutian arc and led to entrapment of Early Cretaceous oceanic lithosphere in the Bering Sea in between the newly formed arc and the Koryak-Beringian margin [*Cooper et al.*, 1976, 1992; *Ben-Avraham et al.*, 1981]. Rapid growth of the Central and Eastern Aleutian arc occurred as a consequence of voluminous magmatism between 55 - 37 Ma [*Scholl et al.*, 1970; *Marlow et al.*, 1973; *Hein and McLean*, 1980]. The Shirshov Ridge functioned as a transform ridge with a component of convergence in its early stages, possibly reactivating an older structure. Dredge samples from the Shirshov Ridge show both Late Cretaceous to Paleogene oceanic type rocks [*Bogdanov et al.*, 1983; *Tzukanov et al.*, 1984] and Late Eocene to Oligocene island arc type rocks [*Bogdanov*, 1988; *Cooper et al.*, 1987a,b].

~ 45 Ma (Fig. 6-8c): Retreat along the Kuril arc continued accompanied by back-arc extension and dextral shearing. The deformation front slowly migrated northward and eastward, akin to what is shown in the analogue model results. Somewhere during Early Tertiary times, the Shantar-Liziansky Basin formed west of the Siberia-Okhotsk block collision due to shearing along the Stanovoy sinistral shear zone and was filled with Eocene to Oligocene sediments [*Worrall et al.*, 1996]. Initiation of formation of the Bowers arc occurred with back-arc spreading in the back-arc region [*Scholl et al.*, 1975; *Cooper et al.*, 1987a,b, 1992].

~ 35 Ma (Fig. 6-8d): Retreat along the Kuril arc and the Bowers arc continued. At ~ 43-42 Ma a change in Pacific plate movement took place from ~ northward to ~ west-northwestward [*Dalrymple et al.*, 1977; *Engebretson et al.*, 1985; *Gordon and Jurdy*, 1986]. This change would have triggered WNW-ESE oriented extension in the Shirshov Ridge, which changed from a transform plate boundary to a transtensional plate boundary. Extension in the Shirshov Ridge has been reported to have started in Oligocene times and continued into the Miocene [*Baranov et al.*, 1991; *Cooper et al.*, 1992]. The change also caused expansion and growth of the Aleutian arc towards the northwest, resulting in the formation of a transform boundary, as has been suggested by *Cooper et al.* [1992]. This hypothesis is supported by the age of the oldest magmatic rocks which started to build up the western Aleutian arc and formed in a transtensional environment with a MORB affinity [*Yogodzinski et al.*, 1993]. Basaltic rocks of ~ 45 - 16 Ma are found on the Komandorsky islands in the westernmost part of the arc [*Tsvetkov*, 1991], while tholeiitic basalts of ~ 43 - 15 Ma occur on the Near islands more to the east [*Yogodzinski et al.*, 1993]. The extension of the Shirshov Ridge culminated in formation of and spreading in the Komandorsky Basin. Based on heat

flow data, *Baranov et al.* [1991] suggested that spreading in the basin began at ~ 30-25 Ma. In any case, spreading is older than ~ 9.3 ± 0.8 Ma, which is the age of MORB-like basalts from DSDP site 191 [*Rubenstone*, 1984]. Finally, *Maeda* [1990] has suggested that the change in convergence direction resulted in formation of the Hidaka magmatic arc from ~ 43 - 17 Ma due to a change from subduction at an acute angle to nearly perpendicular subduction. For the Kuril arc, the change in Pacific plate motion led to a change from NNW-directed subduction along a SW-oriented trench to WNW-directed subduction along a SW-oriented margin.

~ 25 Ma (Fig. 6-8e): Extension in the Shantar-Liziansky Basin ceased in the Late Oligocene or Early Miocene [*Worrall et al.*, 1996], while continued retreat of the Kuril arc caused the back-arc deformation front to migrate northward. This resulted in overprinting of the Sakhalin-Hokkaido dextral shear zone and E-W and NW-SE trending normal faults on top of the older structures of the Shantar-Liziansky Basin [e.g. *Worrall et al.*, 1996]. In the Bering Sea region, arc migration of the Bowers arc stopped [*Cooper et al.*, 1992]. Towards the southwest of the Kuril arc, rollback along the Japan arc resulted in the formation of the Japan Basin in the Late Oligocene (~ 30 Ma) [*Tamaki et al.*, 1992; *Jolivet et al.*, 1999].

~ 15 Ma (Fig. 6-8f): Opening and subsequent spreading in the Kuril Basin occurred from ~ 17 to 15 Ma [*Maeda*, 1990] or from ~ 23 to 8 Ma [*Takeuchi et al.*, 1999; *Ikeda et al.*, 2000]. Prior to and during opening of this basin, the Kronotskaya arc terrane (of Coniacian-Eocene age) collided with the Kamchatka peninsula and finally got accreted in the Late Miocene [*Bakhteev et al.*, 1997; *Konstantinovskaia*, 2001]. It is suggested that the arrival of such a buoyant fragment at the trench led to increased resistance to subduction of the Pacific plate along the Central Kamchatka subduction zone and retarded rollback, in a similar way as initiation of subduction of the West Torres Plateau along the northern New Hebrides Trench is retarding rollback there [e.g. *Schellart et al.*, 2002a]. This would have caused the hinge-point of opening of the Kuril back-arc region to move southwestward towards the southwest point of Kamchatka. However, active subduction continued along the northeast part of the Kamchatka Peninsula around 15 Ma, as indicated by subduction related volcanism in Northeast Kamchatka [*Hochstaedter et al.*, 1994].

~ 5 Ma (Fig. 6-8g): The Kuril Basin stopped opening at 15 Ma [*Maeda*, 1990] or ~ 8 Ma [*Takeuchi et al.*, 1999; *Ikeda et al.*, 2000]. This would imply that the Pacific slab stopped retreating during this time. The reason for such a halt in rollback are not immediately evident, since the Pacific slab continued to subduct along the Kuril trench. However, it could be that interaction of the slab tip with the upper-lower mantle transition zone retarded or even halted slab retreat. A similar scenario has been proposed by *Faccenna et al.* [2001a,b] for the Calabrian arc - back-arc system in the Central Mediterranean and has been supported by analogue experiments. The experiments show that slab retreat will first accelerate exponentially until the slab tip approaches the 670 km discontinuity, which will decelerate or might even halt rollback, possibly followed by a new phase of rollback. This might have happened along the Kuril Trench, where subduction zone rollback was relatively slow during the Eocene to Early Miocene extension of the Sea of Okhotsk and increased during the relatively rapid opening of the Kuril Basin in the Miocene and then suddenly came to a halt, as the slab tip might have approached the 670 km discontinuity. Extension in the Komandorsky basin continued with subduction along northern Kamchatka, while the Japan Sea stopped opening at ~ 10 Ma [*Jolivet et al.*, 1999].

Present (Fig. 6-8h): Active intra-arc extension is observed on the Kamchatka Peninsula, which might indicate that the Pacific slab is starting to retreat again. Active volcanism occurs along the entire Kuril arc. Spreading in the Komandorsky Basin has stopped and the only

active volcanism occurs in the southernmost part of the basin [*Yogodzinski et al.*, 1994]. Subduction and related spreading might have continued until ~ 1.3 Ma, which is the age of the youngest volcanic rocks in Northeastern Kamchatka [*Honthaas et al.*, 1995]. Subduction might have stopped due to the approach of buoyant fragments at the trench, which originated from the Shirshov Ridge but were split from it due to opening up of the Komandorsky Basin [*Yogodzinski et al.*, 1993].

At present, the Okhotsk microplate can be distinguished from the Eurasian plate to the west and the North American plate to the east and is moving towards the southeast with respect to the Eurasian plate. It is bounded to the west by the Sakhalin-Hokkaido dextral shear zone and in the northeast by the Chersky range sinistral shear zone [*Parfenov et al.*, 1988; *Riegel et al.*, 1993; *Seno et al.*, 1996]. The intracontinental plate boundaries are rather diffuse, however, and have been determined from a sparse amount focal mechanism data [*Parfenov et al.*, 1988; *Riegel et al.*, 1993; *Seno et al.*, 1996]. *Cook et al.* [1986] have suggested that the Okhotsk segment was attached to the North American plate but got separated in the past 3 Myr, when the regional stress pattern changed and the Okhotsk segment started to behave as an independent microplate.

From the reconstruction presented in Fig. 6-8 it can be concluded that the evolution of the Kuril-Aleutian cusp is complex and that its position changed through time. The cusp seems to have developed independently from the Emperor Seamount Chain and the spatial correlation between the cusp and the chain seems to be a coincidence rather then of tectonic significance, as was suggested earlier by *Vogt* [1973]. In addition, no signs of collision between the chain and the Kuril arc have been reported, possibly because the chain does not extend further to the northwest and therefore is now only starting to approach the trench. This idea is supported by the rapid decrease in topography of the chain at the northwestern extremity of the chain to ~ 3000 m below sea level. Also, the chain approaches the Kuril trench ~ 150 km south of the junction, again questioning the relevance of this chain with regards to the formation of the Kuril-Aleutian cusp.

6.7. Conclusions

Results of analogue experiments have been presented to simulate the structural and tectonic evolution of the Kuril arc and back-arc region. The results demonstrate that the first order structures in the region can be explained by asymmetric anticlockwise rollback of the Pacific slab and collapse of the overriding pate towards the retreating hinge-line. Similar models of asymmetric rollback and wedge-shaped back-arc opening have been proposed for the Tonga arc and New Hebrides arc in the Southwest Pacific [*Sager et al.*, 1994; *Bevis et al.*, 1995; *Musgrave and Firth*, 1999; *Schellart et al.*, 2002a], indicating that asymmetric slab retreat might be a fundamental type of slab behaviour. The analogue results show the progressive development of a N-S to NE-SW oriented dextral shear zone (cf. Sakhalin-Hokkaido dextral shear zone) near the far edge of the retreating boundary (cf. Kuril-Japan cusp), striking oblique to perpendicular to the boundary. Contemporaneously, normal faults and grabens form, striking parallel to the retreating boundary near the far edge but more oblique towards the hinge-point and towards the north. Similar structures are observed in the Kuril Basin and the Sea of Okhotsk, which developed contemporaneously with the Sakhalin-Hokkaido dextral shear zone. Furthermore, the model shows that the amount of extension progressively decreases away from the retreating boundary. Most likely, this has also happened in the Kuril

- Okhotsk region, where the crustal thickness increases from south to north [*Gnibidenko et al.*, 1995], probably reflecting the amount of thinning of previously relatively thick continental crust. Such a N-S oriented strain gradient implies that the Kuril - Okhotsk region has formed due to deviatoric tensional stresses along the Kuril Trench. It is concluded that the Sakhalin-Hokkaido dextral shear zone and extensional structures observed in the Kuril - Okhotsk region are not necessarily the far field effect of the India - Eurasia collision (e.g. extrusion model). Rather, they are better explained as to have resulted from anticlockwise retreat of the subducting Pacific slab and collapse of the overriding plate towards the retreating hinge-line.

FOREWORD CHAPTER 7

This chapter discusses a tectonic model and analogue modelling results to explain the asymmetric structures in the North Fiji Basin, located behind the New Hebrides arc in the Southwest Pacific. The conceptual model for the region was inspired by the geometry of the North Fiji Basin, the asymmetric structures observed on published tectonic maps of the region [*Auzende et al.*, 1988, 1994; *Pelletier et al.*, 1993, 1998; *Taylor et al.*, 1995; *Lagabrielle et al.*, 1996, 1997] and a reconstruction of the region from *Hathway* [1993].

The ideas and interpretations presented in this chapter are the sole work of the author. All the experimental work presented in this chapter is the sole work of the author. The clarity of ideas presented in this chapter benefited from discussion with Gordon Lister and Mark Jessell. Reviews of earlier versions of this chapter by Gideon Rosenbaum and Peter Betts are also acknowledged. The contents of this entire chapter has been published in *Geology*. A full reference can be found at the end of the thesis in the bibliography. Comments from the journal reviewers B. Pelletier and C. Talbot improved the contents of the paper. Minor changes have been made to the text of the original paper to make the layout and spelling of this chapter consistent with the rest of the thesis.

CHAPTER 7

Analogue modelling of arc and back-arc deformation in the New Hebrides arc and North Fiji Basin

Abstract

In most back-arc basins, extension is perpendicular to the arc. Thus individual spreading ridges run approximately parallel to the arc. In the North Fiji Basin, however, several ancient and active spreading ridges strike 70°-90° to the New Hebrides arc. These high-angle spreading ridges relocated southward during the asymmetric opening of the North Fiji Basin. The structural development of the North Fiji Basin and the New Hebrides arc have been simulated with scaled analogue models, where the results have inspired me to come to several tentative conclusions. The orientation of the high-angle spreading ridges is interpreted to be related to the asymmetric opening of the back-arc basin around a hinge, where they form close to the hinge. Relocation of these spreading ridges is most likely related to subduction of the West Torres Plateau along the New Hebrides Trench. This resulted in localised collision, retarded rollback of the subducting slab along the northwest corner of the trench and reduced extension and shearing in the northwest corner of the North Fiji Basin. Back-arc extension continued in the rest of the North Fiji Basin owing to continued rollback of the southern part of the subducting slab. Here, active extension was separated from the slightly or nonextending northwest corner by a zone striking at high angle to the New Hebrides arc, i.e., the Hazel Holme extensional zone. Moreover, impingement of the d'Entrecasteaux Ridge into the overriding plate led to local deformation and fragmentation of the arc.

7.1. Introduction

Back-arc basins are enigmatic features, which develop in an overall convergent plate-tectonic setting. Back-arc extension is often related to rollback of the hinge-line of the subducting plate and collapse of the adjacent overriding plate toward the retreating hinge-line. Here, rollback results from the negative buoyancy of the subducting slab compared to the surrounding asthenosphere, leading to sinking of the slab and retreat of the hinge-line [*Elsasser*, 1971; *Molnar and Atwater*, 1978]. Because the subducting plate provides the space, it also controls in which direction the upper plate is allowed to extend.

Back-arc extension in ocean-ocean subduction settings commonly results in relatively simple structures in the back-arc region (e.g., Mariana, Scotia, Lesser Antilles, Tonga, Kermadec and Izu-Bonin arc), where troughs and spreading ridges in the back-arc region run approximately parallel to the arc. This simplicity is in contrast with back-arc spreading in the North Fiji Basin adjacent to the New Hebrides arc (Fig. 7-1). Here, the rather complex pattern of spreading axes has yielded multiple spreading ridges in various orientations, including the active Hazel Holme extensional zone and South Pandora Ridge and the inactive 9°30' South Ridge and Tikopia Ridge, which strike at high angles (~70°-90°) to the strike of the New Hebrides arc (Fig. 7-1).

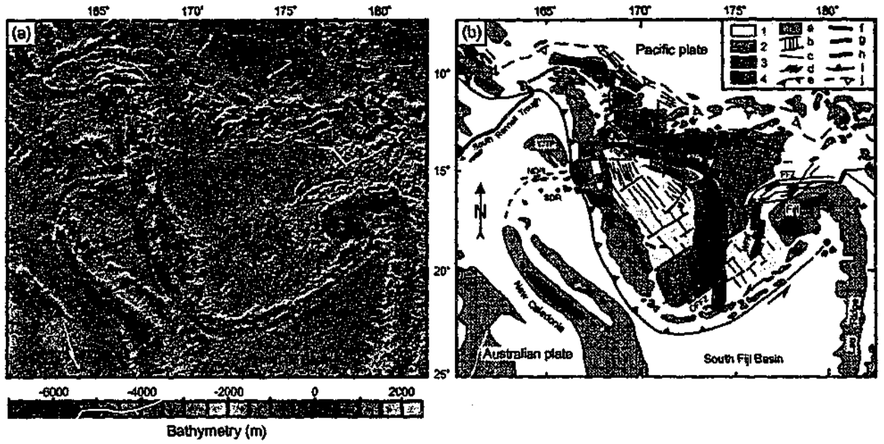

Fig. 7-1. (a) Bathymetric map of New Hebrides arc and North Fiji Basin. Arrows indicate GPS convergence rate between New Hebrides arc and Australian plate, which decreases northward (from ~12 cm/yr to ~4 cm/yr) (from *Taylor et al.* [1995]). (b) Regional tectonic setting of (a) (compiled from *Auzende et al.* [1988, 1994], *Pelletier et al.* [1993, 1998], *Taylor et al.* [1995], and *Lagabrielle et al.* [1996, 1997]). Four different phases of spreading are indicated by different gray scales: (1) 12-11 to 7 Ma, (2) 7 to 2.5 Ma, (3) 2.5 to 1.5-1 Ma, and (4) 1.5-1 Ma to Present [*Pelletier et al.*, 1993]. Features: a—main morphostructural feature, b—magnetic anomaly lineations and transforms, c—fault zone, d—strike-slip fault, e—thrust fault, f—spreading axis, g—remnant spreading axis, h—trough, i—trench (triangles on upper-plate side), j—possible remnant trench. 9°30'SR—9°30' South Ridge, CFFZ—Central Fiji Fracture Zone, CSR—Central Spreading Ridge, FFZ—Fiji Fracture Zone, HHEZ—Hazel Holme extensional zone, NDR—North d'Entrecasteaux Ridge, SDR—South d'Entrecasteaux Ridge, SPR—South Pandora Ridge, TiR—Tikopia Ridge, TR—Tripartite Ridge, WFR—West Fiji Ridge, and WTP—West Torres Plateau.

In this chapter I will focus on three questions: (1) Why do some ancient and active spreading ridges in the North Fiji Basin strike nearly perpendicular to the arc? (2) Why did the high-angle spreading ridges close to the arc relocate southward, as indicated by the inactive spreading ridges (i.e., 9°30' South Ridge, Tikopia Ridge) and magnetic anomalies located in the northwest of the North Fiji Basin (ca. 7 – 2.5 Ma), and the active Hazel Holme extensional zone (ca. 1 Ma – Present) to the south [*Pelletier et al.*, 1993]? (3) What is the influence of subduction and collision of ridges and plateaux, located on the subducting plate, on the structural evolution of the arc and the back-arc region of the overriding plate?

It is tested whether the complex pattern of back-arc spreading in the North Fiji Basin could be related to the asymmetric clockwise hinge-line retreat of the subducting plate [e.g., *Falvey*, 1978; *Auzende et al.*, 1988; *Hathway*, 1993]. This concept should result in a complex structural pattern in the North Fiji Basin that would be further complicated by the subduction of the d'Entrecasteaux Ridge and the West Torres Plateau along the New Hebrides Trench. The Hazel Holme extensional zone appears spatially and temporally linked with the approach of the North d'Entrecasteaux Ridge and the West Torres Plateau to the New Hebrides Trench. It has been argued that opening up along the Hazel Holme extensional zone did not commence before 1.5 - 1.0 Ma [*Pelletier et al.*, 1993], while subduction of the North d'Entrecasteaux Ridge and West Torres Plateau started between 1.89 - 1.58 Ma [*Greene and Collot*, 1994] and between ca. 0.7 - 1 Ma [*Meffre and Crawford*, 2000, 2001], respectively.

On the basis of these spatially and temporally related features, a series of scaled analogue experiments have been performed to test the hypothesis that asymmetric back-arc opening and collision of the North d'Entrecasteaux Ridge and West Torres Plateau with the New Hebrides arc can cause the tectonic complexity observed in the North Fiji Basin and the New Hebrides arc.

7.2. Analogue model

The scaling theory for analogue modelling of geologic processes has been described previously [*Davy and Cobbold*, 1991]. Here, the most important relationship is the one that relates surface forces (stresses) to body forces (gravity). The experiment described here was executed in a normal field of gravity. Therefore, stresses should be scaled down as the product of density and length scales down [*Davy and Cobbold*, 1991].

In the experiment 1 cm resembles 40 km in nature and a density factor of ~0.5 is applied. Furthermore, 20 minutes resemble ~1 Myr in nature. The model consists of a three-layered system confined in a box. The uppermost brittle layer is 0.6 cm thick, simulating the brittle upper lithosphere. It is made of fine-grained glass microspheres ($\rho \approx 1.22 \times 10^3$ kg/m^3), which are properly scaled to model brittle behaviour of rocks [*Schellart*, 2000]. The viscous middle layer is 1.2 cm thick, simulating the viscous lower lithosphere, and is made of silicone putty (mixed with a dense filler) with a viscosity of ~2×10^4 Pa·s ($\rho \approx 1.22 \times 10^3$ kg/m^3). The lowermost viscous layer is 5 cm thick, simulating the asthenosphere, and is made of glucose syrup with a viscosity of ~100 Pa·s ($\rho \approx 1.42 \times 10^3$ kg/m^3). A passive grid and black spheres have been laid on top of the brittle layer to monitor displacement and deformation. On one side of the box a rotational sidewall is situated, which can rotate outward in a clockwise fashion (~12°/h), simulating the progressive clockwise retreat of the Australian slab with respect to the Vitiaz Trench (Fig. 7-2). After ~30° of rotation, the spreading system collides with a rigid block (simulating the impingement of the North d'Entrecasteaux Ridge with the

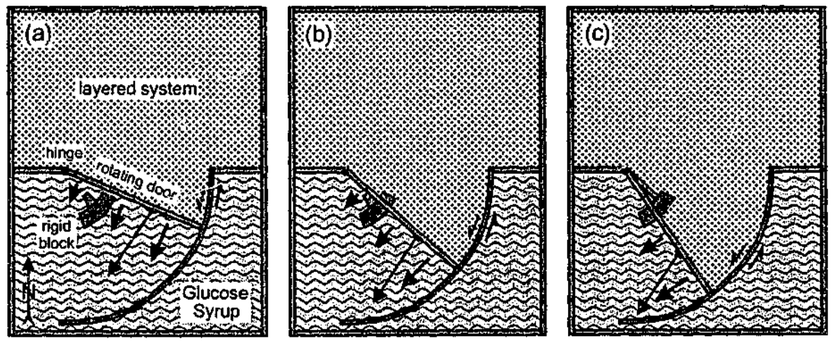

Fig. 7-2. Three stages of experiment to investigate asymmetrical back-arc opening. Layered system simulates overriding plate of North Fiji Basin; rotating door simulates progressive retreat of hinge-line of subducting Australian plate. (a) Initially, door opens smoothly and is unimpeded. (b) Collision of overriding plate with rigid block (e.g., North d'Entrecasteaux Ridge) takes place. (c) Northwest corner end of door is prevented from further opening (because of arrival of buoyant West Torres Plateau at trench).

New Hebrides arc) by opening a hatch in the sidewall, allowing the entrance for the rigid block. After another ~8° of rotation, the northern part of the rotating sidewall stops rotating, under continuing rotation of the southern part (simulating the arrival of the buoyant West Torres Plateau at the subduction zone, which retards rollback of the slab along the northwest part of the New Hebrides Trench).

7.3. Results

Deformation begins close to the rotating boundary at the eastern side (Fig. 7-3a), slowly migrating toward the west and north (Fig. 7-3b,c). Deformation starts with the formation of grabens striking parallel (east) but progressively more oblique (west) to the rotating boundary. Contemporaneously, sinistral strike-slip faults form at the eastern corner of the gate, propagating toward the northwest and north. In a later stage, grabens form near the hinge, striking at high angle to the rotating boundary (Fig. 7-3b). At this stage, a relatively undeformed 2 cm-wide ridge has developed along the entire length of the rotating boundary

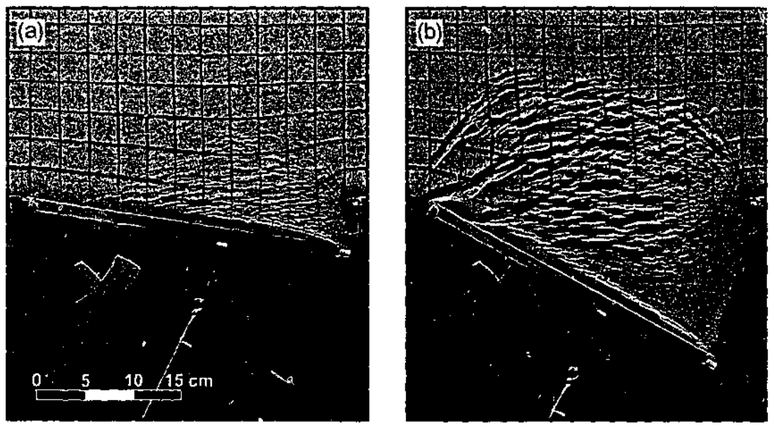

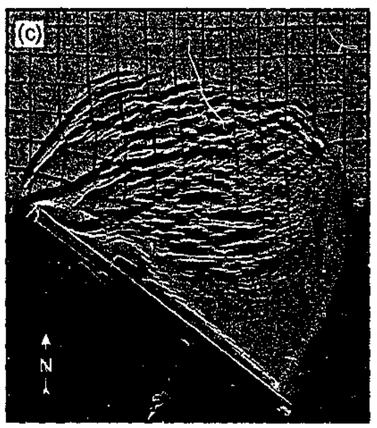

Fig. 7-3. Photographs of experiment 5 during different stages of deformation. (a) After 3/4 h (~2 Myr), (b) after 2 1/4 h (~7 Myr), and (c) after 3 h (~9 Myr).

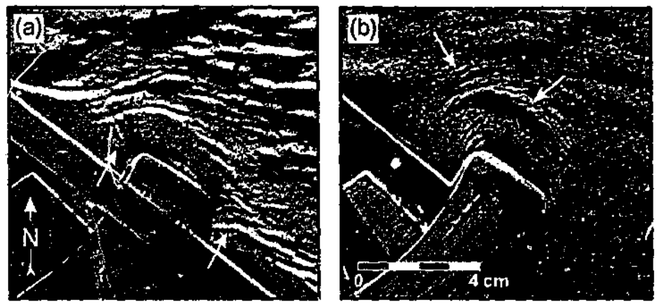

Fig. 7-4. (a) Enlargement of area in Fig. 7-3c around impinging block, showing strike-slip faults (arrows). (b) Enlargement of same area as in (a) but at end of experiment, showing top of silicone layer (after removal of brittle top layer) with small-scale folds (arrows) northeast of displaced arc segment.

(i.e. the arc). After 30° of rotation the arc collides with the rigid indenter (i.e., the North d'Entrecasteaux Ridge). This results in the fragmentation of the arc, where a relatively coherent segment is forced northeastward, bounded by slightly fanning strike-slip faults (Figs. 7-3c and 7-4a). The faults are sinistral at the northwest corner and dextral at the southeast corner of the block. Just northeast of the displaced segment shortening takes place. This can

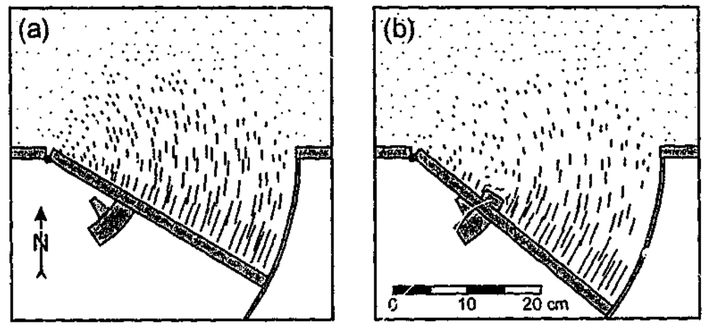

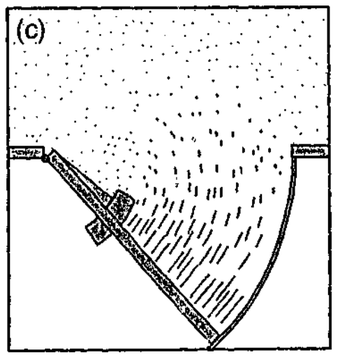

Fig. 7-5. Displacement fields of experiment 5. (a) Before block collision. (b) Between initiation and end of block collision. (c) After block collision (coinciding with stopping of rotation in northwest corner). For each illustrated stage, increment of rotation of door, used to define relative displacement vectors, was ~8°.

be observed in Fig. 7-4b, where the top of the silicone layer shows small-scale folds (wavelengths of ~1-3 mm) superimposed on thickened silicone, with fold axes striking parallel to the northeast boundary of the displaced arc segment. Collision of the block with the arc only has a regional influence on the spreading pattern of the overriding plate (cf. Figs. 7-5a and 7-5b). In a later stage, when the northwest part of the rotating boundary stops rotating, extension stops in the northwest corner of the back-arc region but continues elsewhere in the back-arc region (Fig. 7-5c). The result is the formation of a diffuse dextral transtensional shear zone striking ~ north-northeast, originating at the rigid block and separating nondeforming back-arc material in the northwest from spreading and extending back-arc material in the southeast.

7.4. Discussion

The age of the subducting lithosphere along the northern New Hebrides Trench has been estimated at ca. 30 Ma (Oligocene), and the South Rennell Trough (Fig. 7-1) has been interpreted as an inactive spreading ridge [*Larue et al.*, 1977]. If correct, then the South Rennell Trough was ca. 18 million years old and therefore relatively buoyant during initiation of subduction along the New Hebrides Trench and formation of the North Fiji Basin at ca. 12 Ma [*Pelletier et al.*, 1993]. Therefore, the South Rennell Trough might have acted as a buoyant hinge-zone resisting rollback during the first three spreading phases of back-arc opening (Fig. 7-1). The age of the subducting lithosphere along the southern New Hebrides Trench is ca. 50 Ma (early Eocene) and has tentatively been interpreted to become younger toward the south [*Weissel et al.*, 1982]. However, this interpretation is not supported by drilling data. Alternatively, the age of the subducting lithosphere might gradually increase southward. In this case, the lithospheric age (and therefore density) could increase southward along the entire length of the arc. Then, the slab would have a tendency to roll back faster in the south than in the north, which would explain the asymmetric opening of the North Fiji Basin [e.g. *Falvey*, 1978; *Auzende et al.*, 1988; *Hathway*, 1993]. However, this age polarity remains speculative.

During the past ~1-2 Myr, collision of the North d'Entrecasteaux Ridge and the West Torres Plateau with the New Hebrides arc led to a reorganisation of stresses along the subduction zone and the North Fiji Basin. This led to a reduction of convergence along the central New Hebrides Trench to ~4 cm/yr (Taylor et al., 1995). Rapid convergence along the southern trench continued, increasing from north (~4 cm/yr) to south (~12 cm/yr) [*Taylor et al.*, 1995; *Calmant et al.*, 1997]. This part of the arc is surrounded by the Australian plate, where the Lau-Fiji Ridge is relatively stable with respect to the Australian plate (Taylor et al. 1995). Therefore, convergence is largely absorbed by retreat of the hinge-line. In the northernmost part of the arc convergence is estimated to be greater [*Pelletier et al.*, 1998], but a large component of this convergence can be attributed to Australian-Pacific plate convergence. Thus, the remaining component of convergence related to rollback is then comparable in magnitude to ~4 cm/yr, measured in the central New Hebrides arc.

Lagabrielle et al. [1997] have argued that the occurrence of multiple spreading ridges in various orientations in the North Fiji Basin is related to an anomalous hot asthenosphere underlying it. It is argued that the occurrence of multiple spreading ridges might be a result of hot asthenosphere. However, the orientation of spreading ridges is better explained by the asymmetric opening of the basin and the localised impingement and collision of the North

d'Entrecasteaux Ridge and the West Torres Plateau with the New Hebrides arc as shown by the results of the analogue experiment.

As with all types of models, analogue models have their limitations, which have to be kept in mind. One major limitation is that analogue models are unable to take into account rheological modifications due to temperature variations during deformation [*Brun*, 1999], which can be important in highly extended regions such as the North Fiji Basin. Furthermore, no actual accretion of new oceanic crust occurs in the model. These limitations might explain why the model is not very successful in displaying the formation of actual spreading ridges and transforms, as are observed in the North Fiji Basin. The same limitations might explain why a clearly defined extensional zone (Hazel Holme extensional zone) formed in the basin after collision with the West Torres Plateau, whereas in the experiment at this stage only a diffuse transtensional shear zone developed (Fig. 7-5c). In the model the material in this equivalent region had been extended to such an extent that it could only deform in a ductile fashion. However, the model results do produce strain patterns that are similar to those in the North Fiji Basin to such an extent that they provide a dynamic framework of possible causes for the structures currently observed in the basin.

7.5. Conclusions

In this chapter, results from analogue experiments have been described in order to explain the large-scale structures observed in the North Fiji back-arc basin and the New Hebrides arc, located in the Southwest Pacific. The model suggests that back-arc deformation can be explained to a large extent by asymmetric clockwise back-arc opening due to asymmetric clockwise hinge-line retreat (rollback) of the subducting Australian lithosphere. This model explains the general orientation and mode of deformation, such as rifts and spreading ridges that strike oblique to perpendicular to the arc near the northwest corner of the basin (i.e., close to the hinge), but strike more parallel to the arc toward the southeast. Also, the model shows that deformation starts close to the arc with extensional structures parallel or slightly oblique to the arc (compare to phase 1, Fig. 7-1b), whereas in a later stage, extensional structures around the hinge strike oblique to perpendicular to the arc (compare to phase 2, Fig. 7-1b). In a later stage of deformation, the structures become modified owing to collision of the arc with the d'Entrecasteaux Ridge and later with the West Torres Plateau. The model shows that arc-ridge collision can lead to the fragmentation of the arc and displacement of an arc segment, under continuing opening of the back-arc basin. This results in formation of strike-slip structures at the corners of the ridge and shortening on the back-arc side of the arc segment (Figs. 7-3b,c, 7-4, 7-5b). Similar structures have also been proposed along the New Hebrides arc (Fig. 7-1b) [*Collot et al.*, 1985; *Louat and Pelletier*, 1989; *Taylor et al.*, 1995]. However, the results also indicate that collision with such a small indenter only results in local deformation but does not initiate southeastward relocation of the high-angle spreading ridges. However, a stop in hinge-line retreat along the northwest part of the arc (i.e., owing to initiation of subduction of the West Torres Plateau) stops back-arc opening in the northwest corner and results in the formation of a high-angle, transtensional shear zone in the back-arc region toward the southeast (Fig. 7-5c). In nature, this structure could be compared with the formation of the Hazel Holme extensional zone (Fig. 7-1), striking at high angle to the New Hebrides arc.

FOREWORD CHAPTER 8

This chapter discusses the widespread Cainozoic extensional and strike-slip deformation observed in East Asia. This deformation has previously been interpreted to have resulted from extrusion tectonics due to the India-Eurasia collision. In this chapter, an alternative model is proposed, relating the widespread deformation to eastward retreat of the lithosphere subducting along the East Asian active margin.

The ideas outlined in this chapter have solely resulted from the author and the experiments described in this chapter have been done by the author alone. Stimulating discussions with Jean Braun, Gideon Rosenbaum, Mark Harrison, Peter Betts, Gordon Lister and Mike Sandiford are acknowledged. Gideon Rosenbaum, Peter Betts and Gordon Lister are acknowledged for reviewing an early version of this chapter.

CHAPTER 8

New tectonic model for widespread deformation in East Asia

Abstract

East Asia is a region of widespread deformation, controlled by normal and strike-slip faulting. Deformation has been interpreted to result from extrusion tectonics related to the India-Eurasia collision [*Molnar and Tapponnier*, 1975, 1977], which started in the Early Eocene [*Searle et al.*, 1987; *Beck et al.*, 1995]. However, in East and Southeast China, deformation started earlier than the collision [*Northrup et al.*, 1995; *Ren et al.*, 2002] (latest Cretaceous to Palaeocene), suggesting that extrusion tectonics is not the only driving mechanism for East Asia deformation. It is shown that the East Asian active margin has influenced deformation in East Asia significantly. Along the margin, Cainozoic back-arc extension took place behind several arcs, implying rollback of the subducting slab and collapse of the overriding plate towards the retreating hinge-line [*Elsasser*, 1971; *Molnar and Atwater*, 1978]. It is shown that back-arc extension took place along a >7000 km long stretch of the East Asian margin. Physical models are described simulating back-arc extension, which reproduce the strain field of East Asia. For geometrical and rheological conditions scaled to represent East Asia, modelling shows that the active margin can be held responsible for deformation in East Asia as far west as the Baikal rift zone, located >3000 km from the margin.

8.1. Introduction

Back-arc basins develop in an overall convergent tectonic setting on the concave side of arcs. They are widely spread around the globe with numerous examples in the Western Pacific and Mediterranean. Back-arc basins result from extension, possibly followed by oceanic spreading, which seems counterintuitive to the overall convergent tectonic framework in which they develop. This has led to the development of a tectonic model in which subduction zone hinges are not static features but retreat during sinking of a lithospheric slab into the asthenosphere [*Elsasser*, 1971]. Such sinking would be driven by the slab's negative buoyancy compared with the asthenosphere (the slab is colder and therefore more dense than the asthenosphere) [*Elsasser*, 1971; *Molnar and Atwater*, 1978].

Back-arc basins develop in ocean-ocean and ocean-continent subduction settings. The style of extension in the overriding plate depends to a large extent on the overriding plate rheology, with deformation in a continental lithosphere resulting in more diffuse widespread deformation than in an oceanic lithosphere.

Back-arc basins are commonly viewed as narrow elongated features, with deformation occurring within a few hundred kilometres from the subduction zone. However, examples exist where rollback induced back-arc deformation occurs many hundreds of km inland from the adjacent retreating subduction zone. In the Aegean domain, back-arc deformation can be found inboard > 700 km from the Hellenic trench [*Gautier et al.*, 1999]. In the Sea of Okhotsk region, back-arc deformation can be observed >1500 km from the Kuril Trench [*Schellart et al.*, in review]. Results from numerical and physical modelling [*England and*

Houseman, 1988; *Hatzfeld et al.*, 1997; *Gautier et al.*, 1999; *Schellart et al.*, 2002a,b,c, in review] indicate that the distance of inboard propagation of the back-arc deformation front (D) primarily depends on the overriding plate rheology (buoyant, weak lithosphere promotes high D), on the width of the retreating boundary (W) (increase in W increases D) and on the amount of retreat (R) (increase in R increases D) (Fig. 8-1).

8.2. East Asia

East Asia is characterised by numerous arcs and back-arc basins along the East Asian active margin, widespread diffuse strike-slip and extensional deformation west of the margin, and shortening at the site of India-Eurasia collision (Fig. 8-2). In this tectonic framework, the Cainozoic collision of India with Eurasia is interpreted to be the cause for crustal shortening and thickening in the Himalayas and Tibet, as well as extension and strike-slip faulting northeast and east of Tibet [*Molnar and Tapponnier*, 1975, 1977]. The extension and strike-slip faulting has been explained by extrusion of continental blocks towards the east due to indentation of India into Eurasia [*Molnar and Tapponnier*, 1975, 1977].

The extrusion tectonics model has been simulated with analogue models [*Tapponnier et al.*, 1982; *Davy and Cobbold*, 1988]. In these models, a rigid indenter (India) collided with a homogeneous or stratified layer representing the overriding lithosphere (Eurasia). Extension was mainly interpreted as resulting from tension along releasing bends of major strike-slip faults (such as the Baikal rift and the South China Sea). The requirement for eastward extrusion of lithospheric blocks was the presence of a "free boundary" to the east [*Tapponnier et al.*, 1982; *Davy and Cobbold*, 1988], simulating the Pacific-Philippine subduction zone. The role of such a "free boundary" in the analogue models was essentially passive, to give the lithosphere lateral isostatic support, without being able to support any lateral deviatoric stresses.

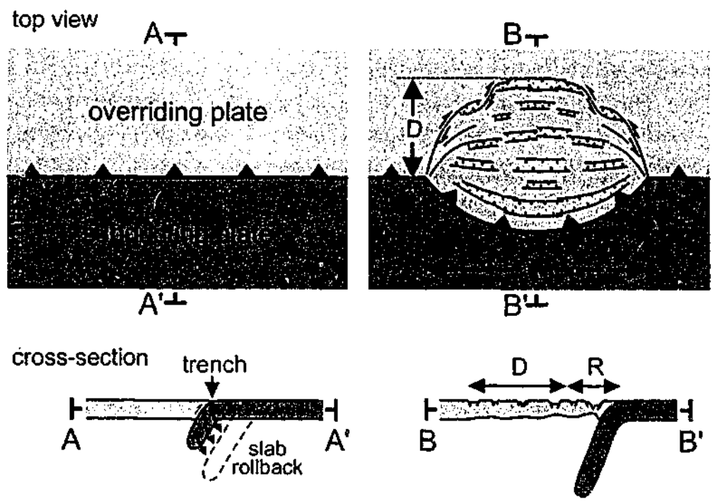

Fig. 8-1. Schematic diagram illustrating development of arc due to rollback of the subducting slab, accompanied by spreading and back-arc extension of the overriding plate. D = amount of propagation of deformation front; R = amount of retreat; W = width of retreating boundary.

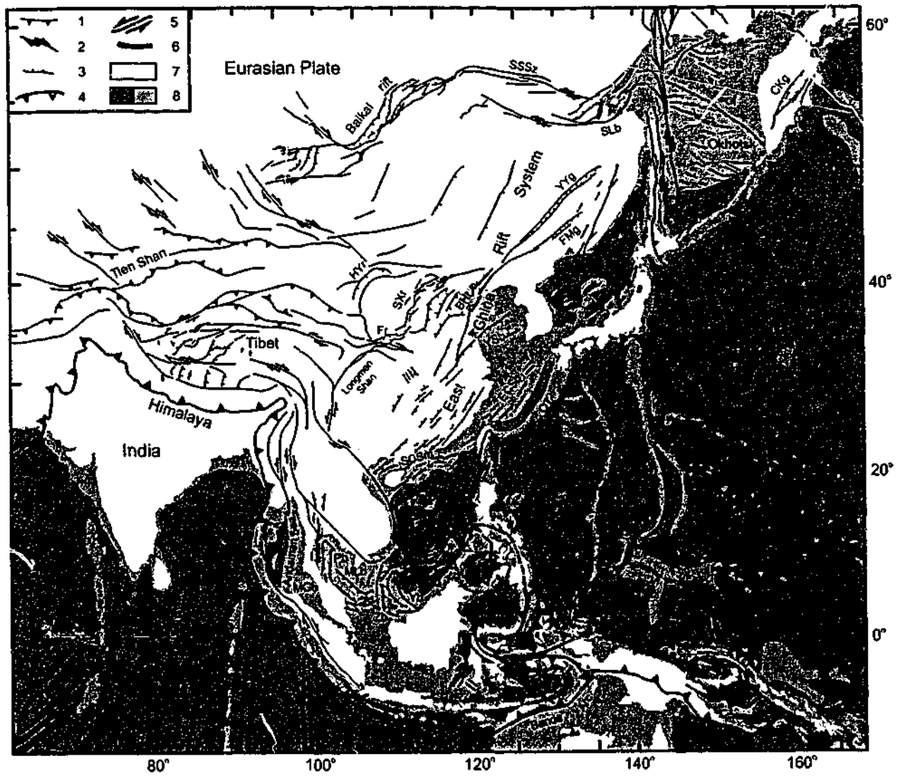

Fig. 8-2. Simplified tectonic map of East Asia and the western Pacific (modified from *Tapponnier* et al. [1982], *Ren et al.* [2002] and *Schellart et al.* [in review]). 1, 2 and 3 are major thrust, strike-slip and normal fault, respectively; 4, 5 and 6 are convergent (black triangles are for active and white triangles are for inactive boundary), transform and divergent plate boundary, respectively; 7 is land; and 8 is sea, with dark grey being basin / ocean floor and grey being continental shelf / morphological high on basin / ocean floor. BHb - Bohaiwan basin, BS - Banda Sea, CKg - Central Kamchatka graben, ECSb - East China Sea basin, FMr - Fushun-Meikehou graben, Fr - Fenwei rift, HYr - Hetao-Yinchuan rift, MGb - Mergui basin, MLb - Malay basin, MT - Mariana Trough, OT - Okinawa Trough, Pb - Pattani basin, SCSb - South China Sea basin, SCSm - South China Sea margin, SLb - Shantar-Liziansky basin, SSSz - Stanovoy Sinistral Shear zone, SXr - Shanxi rift, Yb - Yunqing basin, YSb - Yellow Sea basin, YYg - Yilang-Yitong graben, Zb - Zengmu basin, Zu - Zenghe uplift.

Alternatively, one could consider the active margin of East Asia to have played an active role in the deformation of East Asia, as has often been invoked on a smaller scale for the opening-up of back-arc basins [*Molnar and Atwater*, 1978; *Malinverno and Ryan*, 1986; *Royden*, 1993b; *Lonergan and White*, 1997; *Schellart et al.*, 2002a,b,c, in review]. In such a scenario, the subducting slab would be capable of extending the overriding lithosphere due to eastward rollback, causing widespread normal and strike-slip faulting in East Asia. This model is supported by the onset of extensional deformation in numerous places in East Asia close to the active margin, which preceded the India-Eurasia collision by 10-15 Myr [*Northrup et al.*, 1995; *Ren et al.*, 2002] (Fig. 8-3). Geological data indicate that ~ WNW-ESE oriented extension took place along most of the East Asian active margin during the

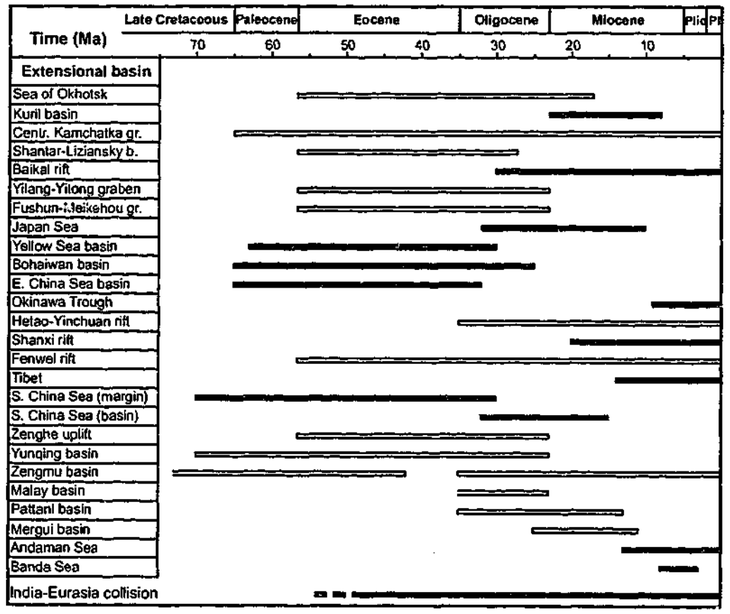

Fig. 8-3. Range chart of basin formation in East Asia during the latest Cretaceous to Present. Bars indicate duration of extension/spreading. Black bars indicate extension (timing is known in Ma), white bars indicate extension (timing is known in series name), and grey bars indicate spreading (timing is known in Ma). Compiled from numerous sources (see Table 8-1 (supplementary material) at the end of the chapter).

Cainozoic, stretching from the Zengmu basin in the SSW to the Sea of Okhotsk in the NNE (Fig. 8-2). This necessitates ESE-ward retreat along a ~7400 km long SSW-NNE striking subduction zone during most of the Cainozoic.

If the retreating boundary in question is ~7400 km long, then how far inboard of the retreating subduction zone does the overriding plate experience extension? The influence of W on (R+D) and D for a number of Cainozoic arcs in an ocean-continent subduction setting is shown in Fig. 8-4a. The diagram shows a positive correlation between W and the two other entities. Assuming that the Baikal rift resulted from the East Asian active margin, then (R+D) ≈ 3300 km, resulting in (R+D)/W ≈ 0.45. With R ≈ 600 km, this results in D/W ≈ 0.36. These non-dimensional ratios fall within the range for arcs plotted in Fig. 8-4a, with (R+D)/W ≈ 0.31 – 1.22 and D/W ≈ 0.24 - 0.65.

The spread in ratio numbers for the Cainozoic arcs is related to other parameters, mainly R and the brittle integrated strength to buoyancy force number (BIS/BF), estimated for each of these arcs at the onset of extension.

8.3. Physical experiments

To obtain a quantitative insight into the influence of R and BIS/BF on D, physical experiments scaled for gravity have been executed, simulating continental arc spreading and back-arc deformation (Fig. 8-5). The model consists of a two-layered brittle-ductile system

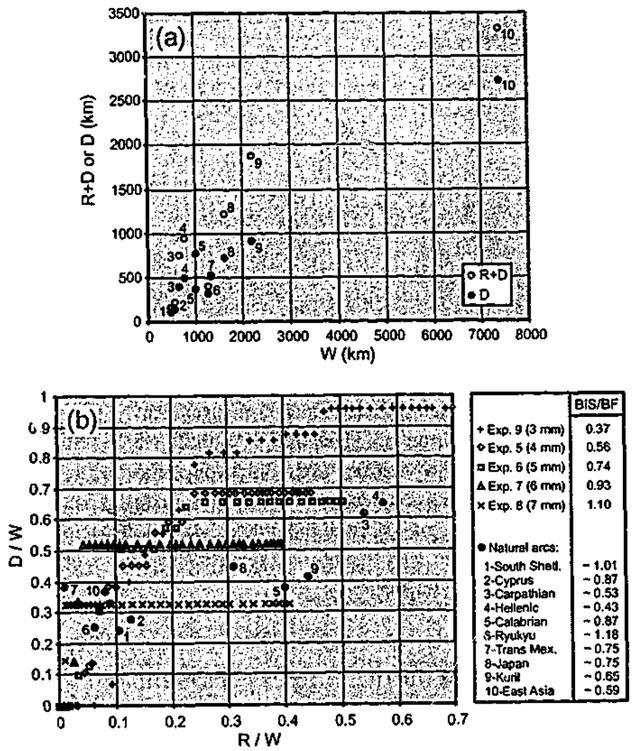

Fig. 8-4. (a) Diagram illustrating relationship between W (arc width) and R+D (R = arc migration and D = deformation front propagation), and between W and D for several Cainozoic arcs across the globe with an ocean-continent subduction setting. (b) Diagram illustrating non-dimensional relationship between R/W and D/W for several arc - back-arc spreading experiments and natural examples as plotted (a). For experiments, R/W and D/W increases with time due to forward migration of arc front and backward migration of deformation front. For experiments and natural examples, BIS/BF (integrated strength brittle layer / buoyancy force overriding plate) ratios have been given. Numbers between brackets indicate thickness of brittle top layer. For calculation of W, R and D, and calculation of BIS/BF for nature and experiment see Table 8-2, 8-3 and 8-4 (supplementary material) at the end of the chapter.

representing the overriding lithosphere, overlying a low viscosity layer simulating the asthenosphere for isostatic support. Spreading of the system through a gate over the low viscosity layer results from a potential energy gradient between the system and the low-viscosity front. Variation in the thickness of the brittle top-layer for each experiment results in a change in BIS/BF number for each experiment. More details about the modelling method and its application to arc formation and back-arc deformation are available elsewhere [*Schellart et al.*, 2002a,b,c, in review].

Results of experiments are shown with BIS/BF ranging between 0.37 and 1.10. At the start of each experiment, R = 0 and increases with progressive deformation. The model results show an increase in D with increasing R for all the experiments towards a maximum D-value (D(max)) (Fig. 8-4b). D(max) depends on the BIS/BF number, where an increase in BIS/BF results in a decrease in D(max). Also, the R-value belonging to D(max) decreases with increasing BIS/BF.

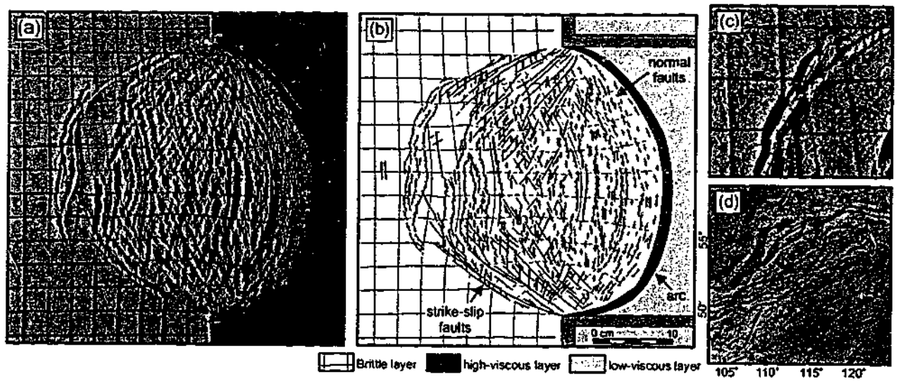

Fig. 8-5. (a) Top view photograph and (b) interpretation of experiment 5 (4 mm brittle layer, 12 mm high-viscous layer) after 6 hr, with gravity spreading of a brittle - high-viscous layer (simulating overriding lithosphere) towards a low-viscosity front (simulating retreating subducting lithosphere). Arc-parallel normal faults are located along and close to the arc, strike-slip faults are located towards the back and near the corners of the gate (sinistral in north and dextral in south), and strike-slip faults linking rift segments are located in the west (see box and (c)). (c) Enlargement of NW-corner of (a). (d) Tectonics of Baikal rift zone as a comparison to (c).

8.4. Comparison between nature and experiments

Comparison between experiments and nature shows agreement (Fig. 8-4b). Arcs with a low BIS/BF number (Hellenic and Carpathian arc) plot close to experiment 5 and 6. These are regions where extension initiated on thickened crust (~45-50 km thick). Arcs with a high BIS/BF number (South Shetland and Ryukyu arc) plot close to experiment 8. In these regions, extension initiated on relatively thin crust (~30-35 km thick). The average BIS/BF for East Asia is probably relatively low (~ 0.53-0.65) when assuming extensional brittle deformation down to 15 km (BIS $\approx 2.39 \times 10^{12}$ N/m) and a buoyancy force (~ 3.55×10^{12} N/m / ~ 4.52×10^{12} N/m) calculated between a pre-extensional crust of ~ 40-45 km thick ($\rho \approx 2750$ kg/m^3) and ocean lithosphere ($\rho \approx 3300$ kg/m^3). Thus, East Asia can best be compared with experiment 5 (BIS/BF ≈ 0.57). East Asia plots very close to values for experiment 5 with R/W ≈ 0.08. This non-dimensional comparison indicates that the retreat of the East Asian subduction zone is capable of driving extension in the Eurasian plate as far west as the Baikal rift.

Comparison between results of analogue models simulating arc formation and back-arc deformation with the extensional and strike-slip deformation in East Asia shows some structural, geometrical and kinematic similarities (Fig. 8-5). Normal faults in East Asia are predominantly located close to the subduction margin and strike ~ NNE-SSW, i.e. parallel to the subduction boundary [*Ren et al.*, 2002] (Fig. 8-2), in accordance with the analogue results (Fig. 8-5a,b). Further away from the subduction zone and in the NNE and SSW, deformation is accommodated by strike-slip faults, as also observed in the model (Fig. 8-5a,b). In the far west, strike-slip faults link up with rift segments (e.g. cf. Baikal rift, Shanxi Graben), similar to the model results (Fig. 8-5c,d). Finally, a decrease in extensional strain from east (close to the subduction zone) to west (far from the subduction zone) occurs in the model and can be implied for the East Asian region. Crustal thickness increases from east (back-arc basins (< 15 km) and margins (~ 15-30 km)) to centre (East China rift system (~ 25-40 km)) to west

(around Hetao-Yinchuan rift and Baikal rift (35-50 km)) [*Yu*, 1990; *Zorin and Cordell*, 1991; *Zai-Yi et al.*, 1992; *Gnibidenko et al.*, 1995].

8.5. Discussion and conclusions

The pattern of deformation along the East Asian margin is more complex than predicted by the experiments. This complexity can be related to the presence of irregularities on the subducting plates, such as aseismic ridges and continental blocks (i.e. Palau-Kyushu Ridge, Bonin Ridge, Emperor Seamount Chain, Taiwan block). If comparatively small, however, such irregularities will only have a local compressional effect on the overriding plate, but will not stop the overall pattern of extension in the back-arc region [*Schellart et al.*, 2002a].

In conclusion, it has been shown that back-arc extension can occur far from the subduction zone, provided that the width of the retreating boundary is sufficiently large. This was the case for East Asia during most of the Cainozoic (W ≈ 7400 km). The propagating distance further depends on the brittle integrated strength and buoyancy force of the overriding plate, as well as the amount of retreat of the boundary. Comparison of critical non-dimensional values for the East Asian region (BIS/BF ≈ 0.53 - 0.65 and R/W ≈ 0.08) with those for scaled physical experiments indicate that back-arc deformation can occur as far west as the Baikal rift zone, located some 3300 km from the subduction zone. The model results also demonstrate that deformation in the back-arc region is accompanied by the formation of an inter-linked pattern of rift and strike-slip structures, comparable to structures observed in East Asia. Therefore these structures did not necessarily result exclusively from extrusion tectonics caused by the India-Eurasia collision.

Region	Timing of extension and/or spreading	Timing of extension (Ma)	Ocean spreading	References
Sea of Okhotsk	Eocene - E. Miocene	~ 57 - 17	No	1
Kuril basin	M. Miocene	17/16 – 15	Yes	2a
	E.-L. Miocene	23 - 7	Yes	2b
Central Kamchatka graben	Palaeocene - Present	~ 65 - 0	No	3
Shantar-Liziansky basin	Eocene - L. Oligocene	~ 57 - 25	No	1
Baikal rift	L. Oligocene – Present	~ 30 – 0	No	4
Japan basin	L. Oligocene – L. Miocene	32 – 10	Yes	5
NE China rift system	E. Eocene – Pliocene/Present	~ 57 – 2 / 0	No	6
Yilan Yitong graben	Eocene - Oligocene	~ 57 - 23	No	7
Fushun Meikehou graben	Paleocene - Eocene	~ 65 - 35	No	8
	Early Tertiary	~ 65 - 23	No	9
Yellow Sea basin	Palaeocene – Early Oligocene	62 - ~ 31	No	9
Bohaiwan basin	Palaeocene - Oligocene	65 - 25	No	9
East China Sea	Palaeocene – Early Oligocene	65 - ~ 32	No	9
Okinawa Trough	L. Miocene – Present	9 – 0	No	10
Hetao-Yinchuan graben	Oligocene – Present	~ 35 - 0	No	11
Shanxi graben	Miocene – Present	~ 23 – 0	No	12
	Early Miocene – Present	~ 20 – 0	No	9
Fenwei rift	E. Eocene – Present	~ 57 – 0	No	13
Parece-Vela basin	L. Oligocene – M. Miocene	31 – 15	Yes	14
Bonin rift	Pleistocene – Present	2 – 0	No	15
Mariana Trough	L. Miocene – Present	10 – 0	Yes	16
S. China Sea (N. margin)	L. Cretaceous - E. Oligocene	~ 100 – 29	No	17a
	L. Cretaceous - Present	70 – 22	No	17b
S. China Sea (ocean basin)	E. Oligocene – M. Miocene	32 – 15	Yes	17c
Zenghe uplift	Eocene - Oligocene	~ 57 - 23	No	17b
Yunqing basin	L. Cret./Palaeocene - Oligocene	~ 70 - 23	No	17b
Zengmu basin	Cretaceous - M. Eocene	~ 80 - 42	No	18
	Oligocene - Recent	~ 35 - 0	No	18
Malay basin	Palaeocene - M. Miocene	~ 65 - 10	No	19a
	E. Oligocene - L. Oligocene	~ 35 - 23	No	19b
Pattani basin	Oligocene - Middle Miocene	~ 35 - 13	No	20
Mergui basin	L. Oligocene - ~ M. Miocene	~ 25 - ~ 11	No	21a
	E. Oligocene - ?	~ 35 - ?	No	21b
Andaman Sea	M. Miocene – Present	13 – 0	Yes	22
Banda Sea	L. Miocene - L. Pliocene	8 – 3	Yes	23
Tibet (north)	M. Pliocene – Present	3-4 – 0	No	24a
Tibet (south)	L. Miocene – Present	8 – 0	No	24b
Tibet	L. Miocene - Present	14 – 0	No	24c
India-Eurasia collision	Early Eocene – Present	~54 / 49 – 0	-	25

Table 8-1. Timing of latest Cretaceous and Cainozoic extension and spreading along the East Asian margin compared to India-Eurasia collision. References: 1—*Worrall et al.* [1996]; 2a—*Maeda* [1990]; 2b—*Takeuchi et al.* [1999] and *Ikeda et al.* [2000]; 3—*Maxwell and Chinakaye* [1999]; 4—*Delvaux et al.* [1997]; 5—*Tamaki et al.* [1992], *Ingle et al.* [1992] and *Jolivet et al.* [1999]; 6—*Zai-Yi et al.* [1992]; 7—*Zaiyi and Yonglin* [1987]; 8—*Chonglong et al.* [2000]; 9—*Ren et al.* [2002]; 10—*Letouzey and Kimura* [1985]; 11—*Hong et al.* [1987]; 12—*Xiwei et al.* [1993]; 13—*Jing-Ming* [1987]; 14—*Kobayashi and Nakada* [1979]; 15—*Taylor et al.* [1992]; 16—*Fryer* [1996]; 17a—*Yu* [1990]; 17b—*Zhou et al.* [1995]; 17c—*Briais et al.* [1993]; 18—*Shaoren et al.* [1994]; 19a—*Tapponnier et al.* [1986]; 19b—*Madon and Watts* [1998]; 20—*Morley* [2001]; 21a—*Polachan and Racey* [1994]; 21b—*Andreason et al.* [1997]; 22—*Curray et al.* [1979]; 23—*Honthaas et al.* [1998]; 24a—*Yin et al.* [1999], 24b—*Harrison et al.* [1995]; 24c—*Coleman and Hodges* [1995]; 25—*Searle et al.* [1987] and *Beck et al.* [1995].

Arc	Extent of W	Max. extent of extension	Reference	Estimated R (km)	Reference
South Shetland arc	Intersections with Hero and South Shackleton fracture zones	Southeast part of Bransfield Strait	1	~ 50 km (estimated from reconstructing trench in alignment with SW trench)	
Cyprus arc	Petheus trench to coast of Syria	Northernmost part of Cilicia basin	2	~ 70 km (estimated from reconstruction)	3
Carpathian arc	~ Vienna to ~ Kladovo	Zagreb (Sava basin)	4	~ 400 km (estimated from reconstruction)	5
Hellenic arc	Kephalonia fault to Pliny Trench (east of Rhodos)	Southern Bulgaria south of Balkanides	6	~ 445 km (355 km Aegean extension + 90 km Anatolia extrusion)	6
Calabrian arc	Allesandria (west Po plain) to Calabria	Southern Sardinia	7	~ 400 km (extension and spreading in Tyrrhenian region)	8
Ryukyu arc	East of Taiwan to Ryukyu-Japan cusp	Western margin of Okinawa trough	9	~ 80 km extension in Okinawa Trough	9
Trans Mexican arc	Golfo de Tehuantepec to Islas Marias	Cardonal fault in Mexico	10	< 15 km (estimate from < 3% extension in region)	10
Japan arc	Ryukyu -Japan cusp to Japan-Kuril cusp	East coast North Korea	11	~ 500 km (400 km from reconstruction and ~ 100 km estimate for extension of margin and arc)	12
Kuril arc	Japan-Kuril cusp to NE Komandorsky basin	NW Sea of Okhotsk and onshore Siberia	13, 14	~ 970 km (max. 300 km for Kuril Basin and 670 km for Sea of Okhotsk)	14
East Asia extensional margin	Zengmu basin to NE Komandors-ky basin	Baikal rift		~ 600 km (~ 500 km for Japan region and 100 km estimate for extension in East China and Baikal region)	

Table 8-2. Location of end points for W and D, and estimate for R for arcs plotted in Fig. 8-4. References: 1—*Gracia et al.* [1996]; 2—*Aksu et al.* [1992] and *Kempler and Ben-Avraham* [1987]; 3—*Payne and Robertson* [1995]; 4—*Royden et al.* [1983]; 5—*Wortel and Spakman* [2000]; 6—*Gautier et al.* [1999]; 7—*Carmignani et al.* [1994]; 8—*Faccenna et al.* [2001b]; 9—*Sibuet et al.* [1995]; 10—*Suter et al.* [2001]; 11—*Tamaki et al.* [1992] and *Tamaki* [1995]; 12—*Jolivet et al.* [1994]; 13—*Worrall et al.* [1996]; 14—*Schellart et al.* [in review].

Arc	BIS ($\times 10^{12}$ N/m)	Crustal thickness (km)	Estimate crustal thickness + reference	BF ($\times 10^{12}$ N/m)	BIS/BF
South Shetland	2.4	~ 32.5	Present crustal thickness of arc (1)	~ 2.4	1.01
Cyprus	2.4	~ 35	Estimate based on topographic elevation	~ 2.8	0.87
Carpathian	2.4	~ 45	Present crustal thickness of E. Alps and W. Dinarides (2)	~ 4.6	0.53
Hellenic	2.4	~ 50	Estimate from reference (3)	~ 5.6	0.43
Calabrian	2.4	~ 35	Present crustal thickness of Sardinia (4)	~ 2.8	0.87
Ryukyu	2.4	~ 30	Present crustal thickness of rift flanks (5,6)	~ 2.0	1.18
Trans Mexican	2.4	~ 37.5	Present crustal thickness (7)	~ 3.2	0.75
Japan	2.4	~ 37.5	Present crustal thickness NW Korea (5) and N, Japan (8)	~ 3.2	0.75
Kuril	2.4	~ 40	Present crustal thickness of around Sea of Okhotsk (9)	~ 3.7	0.65
East Asia	2.4	~ 40 - 45	Present crustal thickness west of Shanxi rift (5,10) and around Baikal rift (11)	~ 3.7 - 4.6	0.53 – 0.65

Table 8-3. Brittle integrated strength (BIS) and buoyancy force (BF) values for natural examples. Maximum depth of brittle deformation has been assumed to be ~ 15 km in all cases. Brittle integrated strength of overriding plate has been calculated by writing *Byerlee*'s [1978] law for extension in terms of principal stresses. Crustal thickness has been estimated for the time prior to extension. Buoyancy force between overriding and subducting plate has been calculated by assuming crustal density of 2750 kg/m^3 and oceanic lithospheric density of 3300 kg/m^3. References: 1—*Grad et al.* [1993]; 2—*Horváth* [1993]; 3—*Gautier et al.* [1999]; 4—*Gvirtzman and Nur* [2001]; 5—*Zai-Yi et al.* [1992]; 6—*Sibuet et al.* [1995]; 7—*Urrutia-Fucugauchi* [1986] 8—*Zhao et al.* [1990]; 9—*Gnibidenko et al.* [1995]; 10—*Hong et al.* [1987]; 11—*Zorin and Cordell* [1991].

Experiment	BIS (N/m)	Brittle layer thickness (mm)	BF (N/m)	BIS/BF
9	0.07	3	0.1894	0.37
5	0.12	4	0.2155	0.56
6	0.18	5	0.2433	0.74
7	0.25	6	0.2728	0.93
8	0.33	7	0.3040	1.10

Table 8-4. Brittle integrated strength (BIS) and buoyancy force (BF) values for experiments. Brittle integrated strength for extension has been calculated with values from *Schellart* [2000]. Thickness of high-viscous layer is 12 mm. Buoyancy force between brittle – high-viscous layer and low-viscous layer has been calculated with a brittle layer density of 1220 kg/m^3, a high-viscous layer density of 1220 kg/m^3, and a low-viscous layer density of 1420 kg/m^3.

FOREWORD CHAPTER 9

In this chapter, results of fluid dynamical experiments are presented to investigate the kinematics and dynamics of subduction, slab rollback and slab induced mantle convection. The model design that has been used in the experimental investigation was inspired by fluid dynamical experiments described in a paper from *Kincaid and Olson* [1987] and an abstract from *Funiciello et al.* [2000].

The ideas outlined in this chapter have solely resulted from the author and the experiments described in this chapter have been done by the author alone. Stimulating discussions with Jean Braun, Chris Kincaid, Ross Griffiths, Gordon Lister, Louis Moresi, Roberto Weinberg, David Giles and Mike Sandiford are acknowledged.

CHAPTER 9

Kinematic and dynamic behaviour of slabs in the upper mantle

Abstract

Results of fluid dynamical experiments are presented to model the kinematics and dynamics of lithospheric subduction in the upper mantle. The experiments model a dense high-viscosity plate (subducting lithosphere) overlying a less dense low-viscosity layer (upper mantle). The overriding lithosphere is not incorporated. Several important features of slab behaviour were investigated including the temporal variability of hinge-line migration, the kinematic behaviour of the slab and the slab induced upper mantle flow. Both a fixed and free trailing edge boundary condition of the subducting plate were investigated. Results show that hinge-line retreat is a natural consequence of subduction of a negatively buoyant slab. The migration rate increases during the free sinking of the slab until it approaches the 670 km discontinuity, resulting in a decrease in migration rate followed by a renewed increase and finally approaching a steady state. Slab retreat results in sub-lithospheric mantle flow from underneath the slab towards the mantle wedge. Experimental results indicate that all flow occurs laterally around the slab edges, forcing the hinge-line to attain a convex shape towards the direction of retreat. No signs for flow underneath the slab tip have been detected. For a fixed trailing edge, the slab does not sink vertically downward, but sinks at an angle in a regressive manner, in order to minimise deformation of the subducting plate. For a free trailing edge, slab sinking is oriented more vertically while the surface part of the subducting plate is dragged into the subduction zone.

9.1. Introduction

Wadati-Benioff zones and high seismic velocity zones in the Earth's interior indicate that oceanic lithosphere sinks into the mantle, attaining a wide variety of shapes. Focal mechanism data indicate that several slabs continue down to the upper-lower mantle boundary at ~ 670 km [*Isacks et al.*, 1968]. Tomographic data support this and also reveal that slabs may be horizontally draped over the discontinuity or penetrate into the lower mantle [*Spakman et al.*, 1988; *van der Hilst et al.*, 1991, *van der Hilst and Seno*, 1993; *Lucente et al.*, 1999; *Widiyantoro et al.*, 1999; *Wortel and Spakman*, 2000; *Fukao et al.*, 2001].

Geological and Geophysical data suggest that subducting slabs not only move in a downdip slab-parallel direction (e.g. wing-like sliding model [*Jacoby*, 1973]), but also in a slab-perpendicular backward direction, as has first been suggested by *Elsasser* [1971]. Such a slab-perpendicular backward component would result in regressive (oceanward) hinge-line migration of the subducting lithosphere (i.e. slab rollback). Regressive motion could then result in extension in the overriding plate (i.e. back-arc extension) due to collapse of the overriding plate towards the retreating hinge-line [*Elsasser*, 1971; *Molnar and Atwater*, 1978; *Lonergan and White*, 1997; *Schellart et al.*, 2002a]. Thus, back-arc extension seems to be a direct consequence of slab rollback. As evidenced by the episodic opening of back-arc basins [*Faccenna et al.*, 2001a,b] and the wide variety in shapes (from roughly symmetrical to highly asymmetrical) of arc - back-arc systems [*Schellart et al.*, 2002a,b,c], it is clear that slab

rollback is a transient three-dimensional process with significant trench-parallel variations in retreat velocity. This concept is supported by GPS-data for several arcs, indicating a variation in migration rate along the arc [i.e. *Bevis et al.*, 1995; *Taylor et al.*, 1995].

The process of subduction and slab retreat has been investigated with numerical and analogue models previously. In most of the numerical models, slab retreat was externally imposed as a boundary condition [*Garfunkel et al.*, 1986; *Christensen*, 1996; *Houseman and Gubbins*, 1997; *Olbertz et al.*, 1997; *Buiter et al.*, 2001; *Cízková et al.*, 2002] and therefore the self-consistent dynamical behaviour could not be investigated. Furthermore, the experiments were two-dimensional, therefore excluding lateral flow around slab edges to accommodate slab retreat, which is supposed to account for a significant part of slab induced mantle flow [*Dvorkin et al.*, 1993]. Most of the analogue experiments, however, were executed in three dimensions and the retreat was either imposed [*Guillou-Frottier et al.*, 1995; *Griffiths et al.*, 1995] or allowed to evolve naturally [*Jacoby*, 1973, 1976; *Kincaid and Olson*, 1987; *Becker et al.*, 1999; *Faccenna et al.*, 1996, 1999, 2001b; *Funiciello et al.*, 2000, 2002]. The analogue models were designed to investigate the influence of a stratified mantle on the subduction process [*Guillou-Frottier et al.*, 1995; *Griffiths et al.*, 1995; *Faccenna et al.*, 2001b; *Funiciello et al.*, 2000, 2002], to investigate subducting plate - overriding plate interaction [*Becker et al.*, 1999; *Faccenna et al.*, 1996, 1999], or to investigate hinge-migration of the subducting plate [*Jacoby*, 1973, 1976; *Faccenna et al.*, 2001b; *Funiciello et al.*, 2000, 2002].

In this chapter, attention is focussed on the kinematics and dynamics of subduction and slab induced mantle convection. In the experiments described in here, subduction and slab rollback were not kinematically imposed but were allowed to evolve naturally and were driven by buoyancy forces only, reflecting natural conditions. These models provide new insights into how the slab sinks into the mantle, and into the convection pattern resulting from subduction and slab rollback. The advantage of the analogue set-up used for the experiments described in this chapter is that it is designed to model in three-dimensional space and can therefore account for subduction and rollback induced lateral flow in the mantle. In addition, the influence of several physical parameters on hinge-line migration has been investigated, including the density of the slab, the boundary condition of the trailing edge of the slab and the width of the slab, to obtain insight into the optimal conditions for rapid slab rollback.

9.2. Fluid dynamic model

The models are made of a two-layered system with a high-viscosity layer (1.3-2.0 cm thick) overlying a low-viscosity layer (12 cm thick) comprised in a three-dimensional Cartesian model box, as adopted by other analogue modellers [*Kincaid and Olson*, 1987; *Griffiths et al.*, 1995; *Funicciello et al.*, 2000, 2002; *Faccenna et al.*, 2001b]. The model configuration is schematically plotted in Fig. 9-1 and was inspired by models from *Jacoby* [1973], *Kincaid and Olson* [1987] and *Funicciello et al.* [2000]. The upper layer is made of a filled silicone putty (density $\rho_{sp} = 1.48 - 1.56 \times 10^3$ kg/m^3), which is a visco-elastic material. With the strain rates in the order of 10^{-5} - 10^{-3} s^{-1}, the material behaves as a nearly Newtonian viscous material (viscosity $\eta_{sp} \approx 2.4 \times 10^4$ Pa·s). The silicone layer simulates a ~ 65-100 km thick oceanic lithosphere. The viscosity is homogeneous throughout the model lithosphere and therefore represent an average effective viscosity value for the entire lithosphere (e.g. thin viscous

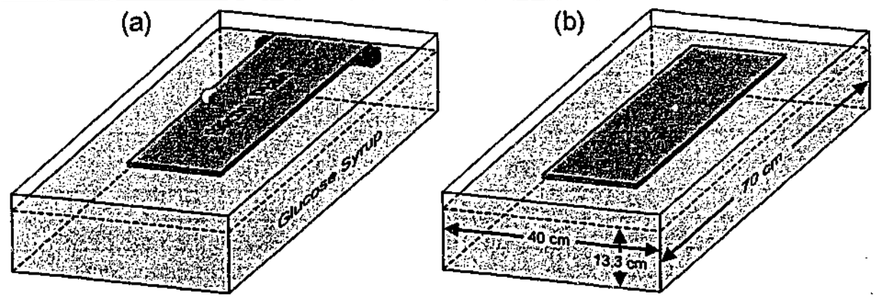

Fig. 9-1. Configuration of the modelling apparatus and experimental set-up for two different boundary conditions at the trailing edge of the plate, with (a) fixed trailing edge and (b) free trailing edge. For all experiments, a plate of silicone putty, representing oceanic lithosphere, is floating on top of glucose syrup, representing the sub-lithospheric upper mantle, down to the bottom of the box, representing the 670 km discontinuity. During an experiment, the first two cm of the tip of the silicone plate are depressed at an angle of 30° into the glucose syrup to initiate a subduction instability.

sheet approach [*Bird and Piper*, 1980; *Vilotte et al.*, 1982; *England and McKenzie*, 1982]). The viscous rheology is an appropriate first order approximation, since it has been supposed that a subducting lithosphere acts as a fluid of some sort over geological time scales [*Houseman and Gubbins*, 1997; *Becker*, 1999; *Faccenna et al.*, 2001b].

The lower layer is made of glucose syrup ($\eta_m \approx 1.3 \times 10^2$ Pa·s, $\rho_m \approx 1.42 \times 10^3$ kg/m^3) simulating some 600 km of low viscosity sub-lithospheric upper mantle where the base is in accordance with the 670 km discontinuity. The lateral edges of the model lithosphere are not attached to the sides of the box to avoid edge effects and to allow for lateral flow around the slab edges during subduction. The base is impenetrable and simulates the upper-lower mantle boundary. This boundary often (temporarily) halts subduction and therefore the simplification seems justified when investigating subduction processes in the upper mantle only. The effects of temperature or phase changes are not considered in the experiments. This approximation has been adopted before [*Becker et al.*, 1999; *Faccenna et al.*, 1996, 1999, 2001b; *Funiciello et al.*, 2000, 2002] and is justified to a first approximation, since the models are restricted to relatively rapid slab subduction in the upper mantle (corresponding to 2-14 cm/yr), in which the slab retains its thermal field to the first order [*Wortel*, 1982]. Some experimental parameters for the individual experiments discussed in this chapter are plotted in Table 9-1. The difference in viscosity between lithosphere and sub-lithospheric mantle in the model is a factor of ~ 185, which is close to effective viscosity difference values in nature estimated previously (~ 200 [*Houseman and Gubbins*, 1997], 50 – 200 [*Conrad and Hager*, 1999], ~ 100 [*Becker et al.*, 1999], 100-500 [*Faccenna et al.*, 2001a]). The timescale ratio between the analogue model and the natural prototype is $t^a / t^n \approx 3.81 \times 10^{-12}$ (1 hour in model represents ~ 30 Myr in nature). With such a time-scale ratio at hand one can calculate the upscaled sub-lithospheric upper mantle viscosity from the following scale relationship, which relates resistive viscous forces to the driving forces:

$$\frac{\eta^a}{\eta^n} = \frac{\sigma^a t^a}{\sigma^n t^n} \qquad (9\text{-}1)$$

Experiment Number	Slab density ($\times 10^3$ kg/m^3)	Slab width (cm)	Slab thickness (cm)	Trailing edge
4	1.480	20	1.3	Fixed
5	1.520	20	1.3	Fixed
6	1.560	20	1.3	Fixed
8	1.520	10	1.3	Fixed
9	1.520	15	1.3	Fixed
10	1.520	20	2.0	Fixed
11	1.520	15	1.3	Free
12	1.520	20	2.0	Free
20	1.505	15	1.3	Fixed
21	1.535	25	1.3	Fixed
22	1.520	5	1.3	Fixed
23	1.520	25	1.3	Fixed

Table 9-1. List of the experiments discussed in the text and their characteristic physical properties.

where superscript a denotes the analogue model and superscript n denotes the natural prototype; η indicates the viscosity and σ indicates the stresses. The driving force for deformation results from the density contrast $\Delta\rho$ between the subducting lithosphere and the sublithospheric mantle and therefore stresses scale as follows:

$$\frac{\sigma^a}{\sigma^n} = \frac{\Delta\rho^a g^a x^a}{\Delta\rho^n g^n x^n} \tag{9-2}$$

where g is the acceleration due to gravity and x indicates length. Since the experiments presented in this chapter are executed in the Earth's field of gravity, g in equation (9-2) can be omitted. Then, combining equation (9-1) and (9-2) results in:

$$\frac{\eta^a}{\eta^n} = \frac{\Delta\rho^a x^a t^a}{\Delta\rho^n x^n t^n} \tag{9-3}$$

With the aforementioned timescale ratio t^a / t^n is $\approx 3.81 \times 10^{-12}$, $\Delta\rho^a = 100$ kg/m^3, $\Delta\rho^n \approx 80$ kg/m^3, and $x^a / x^n = 2.0 \times 10^{-7}$ this results in an upscaled sub-lithospheric upper mantle viscosity of ~ 1.36×10^{20} Pa·s. This is similar to values of 10^{19} - 10^{21} Pa·s suggested for the natural prototype [*Artyushkov*, 1983, *Ranalli*, 1995], indicating that driving forces for subduction (e.g. due to gravity) are properly scaled with respect to the forces resisting subduction (e.g. viscous forces).

Several experiments have been executed with a different lithospheric density (1.48 - 1.56 $\times$ 10^3 kg/m^3, thus $\Delta\rho$ = 60 - 140 kg/m^3) to study the effect of increase in driving force. In addition, the effects of slab thickness and slab width have been investigated to gain insights into the influence of these parameters on the kinematics and dynamics of subduction. Passive markers were placed on top and in the side of the silicone layer and on top and in the glucose layer to track the kinematics of subduction and subduction induced convection. The experiments were recorded with three digital cameras. The first camera provided a top view perspective and the second camera provided a side view perspective. The third camera was installed as such to provide either a front view or a bottom view perspective. At the start of an experiment, the first 2 cm of the tip of the model lithosphere were submerged at an angle of ~

30° to create a subduction instability. This instability was enough to induce progressive subduction of the lithosphere without any externally imposed force or velocity. The overriding plate was not modelled to be able to track subduction induced mantle convection. However, the influence of the subducting plate on the state of stress at the trench can be deduced from the migration of the subduction hinge. Backward (i.e. oceanward) migration of the hinge would induce tensional stresses in the overriding plate and thus would promote extension in the overriding plate (i.e. back-arc extension). Forward migration of the hinge would induce compressional stresses in the overriding plate and would therefore promote shortening in the overriding plate. However, the omitting of the overriding plate does imply that the modelled retreat velocity is somewhat high, since the overriding plate is likely to suppress hinge-migration. Two boundary conditions were applied to the trailing edge of the slab: a fixed and a free trailing edge, simulating maximum and minimum resistance of the subducting plate to lateral movement. The influence of an applied velocity (e.g. ridge push) at the trailing edge of the subducting plate will be discussed in Chapter 10.

9.3. Results

9.3.1. Slab geometry and kinematics

The evolution of the slab during subduction has been illustrated in Fig. 9-2 and Fig. 9-3 for two experiments with different boundary conditions. Below, the evolution of these experiments will be briefly described.

For experiment 9 with a fixed trailing edge (Fig. 9-2a, 9-3a), the evolution of the slab geometry is relatively simple. The slab initially sinks and rolls back with an increasing slab-dip angle until it is approximately vertical. When the slab tip hits the bottom of the box, the slab folds backward and is subsequently draped over the horizontal discontinuity during slab rollback. During this stage the slab attains a relatively constant dip angle of ~ 60-65°. Extensional strain in the horizontal surface part of the plate is observed from displacement of passive white markers in the side and on top of the plate. This extension is oriented perpendicular to the trench and results from the slab's negative buoyancy (e.g. slab pull). In total, the extensional strain amounts to 6.2% from initiation of extension until the slab tip approached the bottom of the box. In addition, the slab part resting on top of the discontinuity is displaced forward, indicating that the slab exerts a push at its frontal part contemporaneously with pulling at the surface part of the plate. During rollback, the slab and trench-line attain a convex arcuate shape towards the direction of retreat (Fig. 9-3a), resulting from convection of the glucose syrup around the edges of the slab.

For experiment 11 with a free trailing edge (Fig. 9-2b, 9-3b), the evolution of the slab geometry is slightly more complicated. The slab initially sinks and rolls back with an increasing slab-dip angle until it is approximately vertical. When the slab tip hits the bottom of the box, the slab tip is slightly overturned, resulting in the formation of a recumbent fold. This is followed by backward folding of the slab and subsequent draping over the horizontal discontinuity during slab rollback. During this stage the slab attains a relatively steep dip angle of ~ 80°. During subduction, the slab pulls the horizontal surface part of the plate into the subduction zone, as evidenced by the displacement of the trailing edge of the plate (e.g. slab pull). No extension is observed in the horizontal surface part of the plate. To the

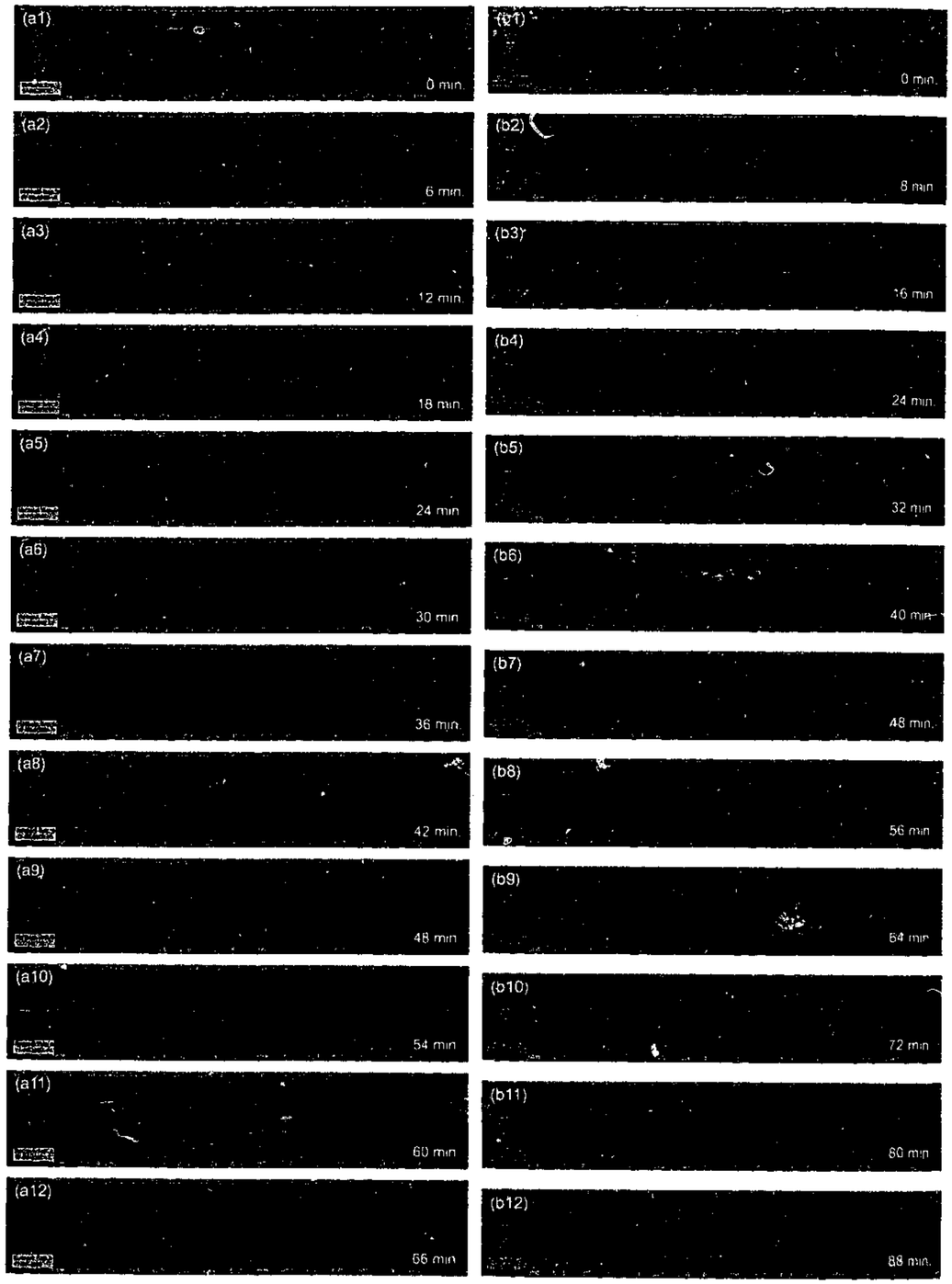

Fig. 2. Side view photographs showing geometrical evolution of slab during subduction for two experiments with different boundary conditions. (a) Experiment 9 with fixed trailing edge and (b) experiment 11 with free trailing edge. Box is 70 cm long.

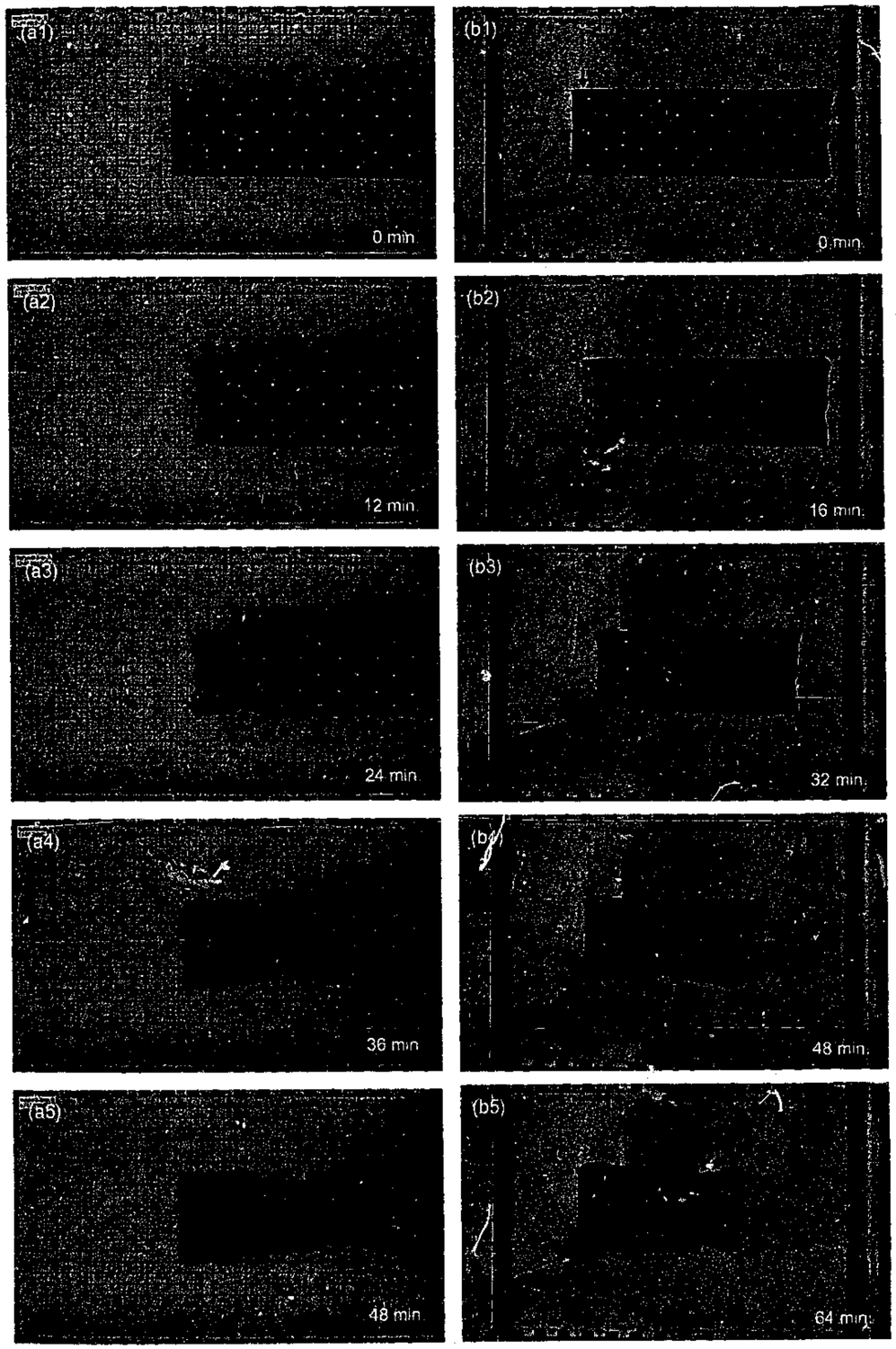

Fig. 3. Top view photographs of two experiments with different trailing edge boundary conditions showing geometrical evolution of slab during subduction. (a) Experiment 9 with fixed trailing edge and (b) experiment 11 with free trailing edge. Box is 70 cm long and 40 cm wide. Arrows indicate location of trench.

contrary, a slight shortening is observed in the plate, resulting from the buoyancy force between the glucose and the plate (~ 0.1% shortening strain from initiation of subduction until the slab tip hits the bottom of the box). In addition, the slab part resting on top of the discontinuity is displaced forward, indicating that the slab exerts a push at its frontal part. During rollback, the slab and trench-line attain a convex arcuate shape towards the direction of retreat (Fig. 9-3b), although not as well developed as in experiment 9, because the amount of slab retreat is much reduced in experiment 11.

The kinematics of the subduction process for experiment 9 and 11 has been plotted in Fig. 9-4a and 9-4c. In addition, results from experiment 10 (fixed trailing edge) and 12 (free

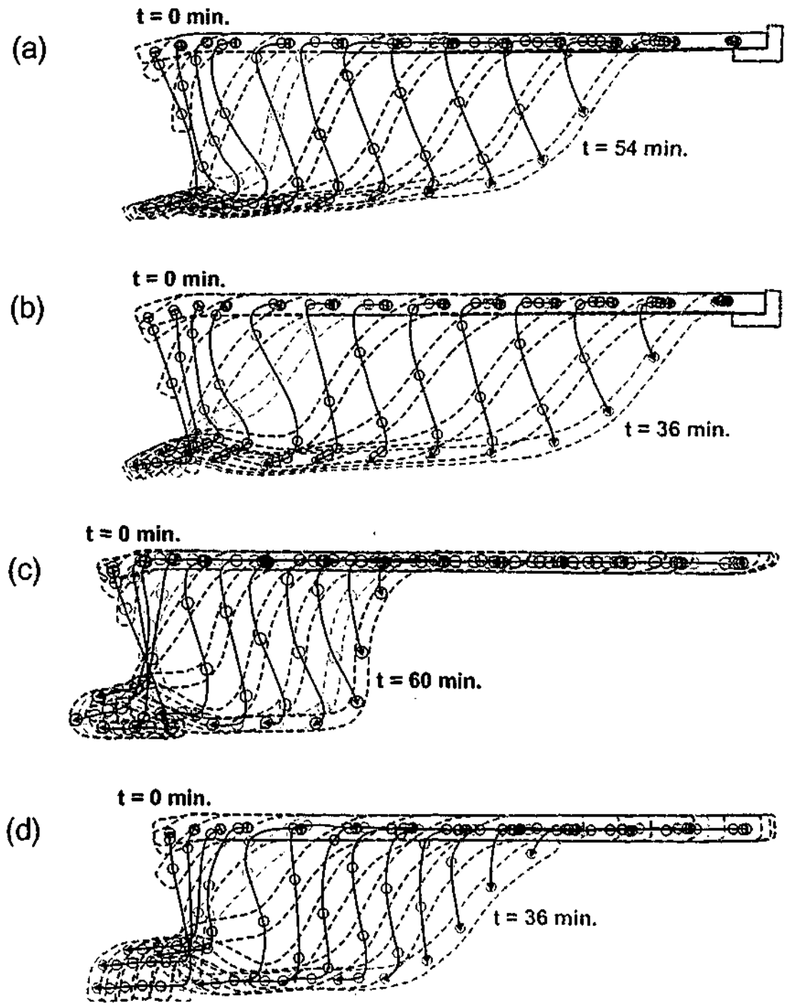

Fig. 9-4. Diagrams illustrating kinematic behaviour of slab and passive particles located on the side of the slab for four experiments with different trailing edge boundary condition and plate thickness. Time-step (Δt) between successive stages differs for experiments. (a) Experiment 9 with fixed trailing edge, plate thickness of 1.3 cm and Δt = 6 min., (b) experiment 10 with fixed trailing edge, plate thickness of 2.0 cm and Δt = 4 min., (c) experiment 11 with free trailing edge, plate thickness of 1.3 cm and Δt = 6 min., (d) experiment 12 with free trailing edge, plate thickness of 2.0 cm and Δt = 4 min.

trailing edge) have been plotted for which the plate is relatively thick (2.0 cm). In these plots, the displacement of passive markers in the side of the subducting plate has been traced during progressive stages of subduction. A difference between experiments with a fixed (experiment 9 and 10) and free trailing edge (experiment 11 and 12) can be observed. The experiments with a fixed trailing edge are dominated by backward sinking vectors (Fig. 9-4a,b), while the sinking vectors for the experiments with a free trailing are oriented more vertically, with a smaller component of regressive displacement (Fig. 9-4c,d). The difference is most evident for the free sinking stage, before the slab tip hits the lower discontinuity. This sinking behaviour can be explained in a purely geometrical way. Initially, vertical sinking is preferred simply because the gravitational force is oriented vertically downward. However, vertical sinking of the slab requires horizontal displacement of the surface part of the plate. In the fixed trailing edge experiments, the horizontal displacement is resisted significantly, although the plate does experience some extension, resulting in backward sinking. In the free trailing edge experiments, the horizontal displacement is resisted to a lesser extent (e.g. mantle drag-type resistive force) and the surface part of the subducting plate is dragged into the subduction zone, resulting in more vertically oriented sinking. If the mantle drag resistance would be reduced even more (e.g. reduction in viscosity of the mantle), one would expect the slab to sink vertical or possibly sink forward more parallel to the slab dip.

9.3.2. Hinge-migration

The hinge-migration of experiment 9 and 11 can be observed in Fig. 9-5a. Both experiments show an initial exponential increase in hinge-retreat with time, followed by a slowdown in retreat due to interaction of the slab tip with the discontinuity. Subsequently, the retreat velocity slightly increases and finally a steady state retreat is reached with a linear relation between retreat and time. The diagrams illustrate that hinge-migration is significantly

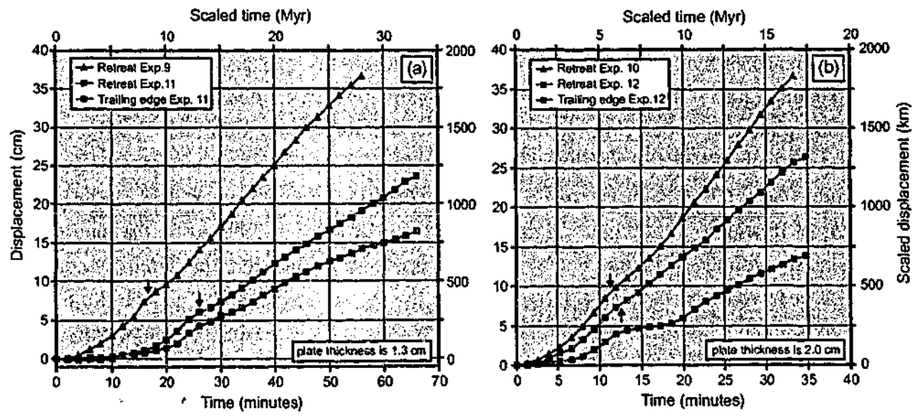

Fig. 9-5. Hinge-migration and trailing edge migration versus time for experiments with different plate thickness and trailing edge boundary condition. (a) Experiments with plate thickness of 1.3 cm, experiment 9 with fixed edge and experiment 11 with free edge. (b) Experiments with plate thickness of 2.0 cm, experiment 10 with fixed edge and experiment 12 with free edge. Arrows indicate time when slab tip hits discontinuity. For hinge-displacement, positive numbers point to hinge-retreat. Note that trailing edge displacement is opposite to direction of hinge-retreat, so displacement for trailing edge should actually be read as negative numbers.

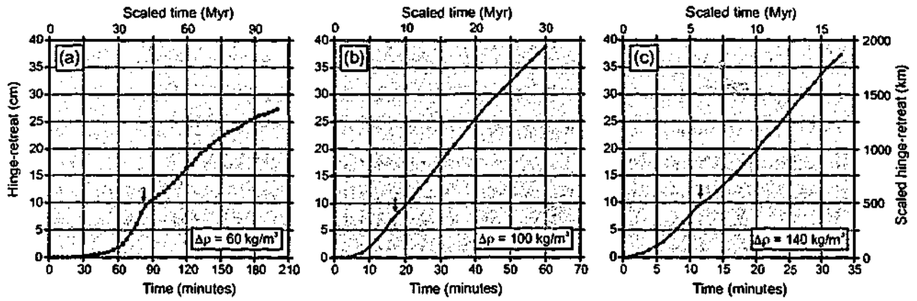

Fig. 9-6. Hinge-migration versus time for several experiments with different density difference ($\Delta\rho$) between slab and surrounding mantle. (a) Experiment 4, (b) experiment 5 and (c) experiment 6. Arrows indicate time when slab tip hits discontinuity. Note different scale on x-axis.

suppressed for a free trailing edge. For the free trailing edge experiment, the trailing edge displacement curve closely mimics the hinge-retreat curve, but the former has a smaller slope angle. The steady state retreat velocity is 46.3 cm/hr and 26.9 cm/hr for experiment 9 and 11 respectively, which scales to ~ 7.7 cm/yr and 4.5 cm/yr in nature respectively. It should be remembered that these values are somewhat on the high side, because several factors inhibiting fast rollback are not incorporated (e.g. no overriding plate).

The results of experiment 10 and 12 with a relatively thick slab (2.0 cm thick) have been plotted in Fig. 9-5b and show the same behaviour as experiment 9 and 11, but are retreating at a faster rate than the experiments with a relatively thin slab (experiment 9 and 11 with a 1.3 cm thick slab). The faster retreat is explained by the greater driving force resulting from the thicker slab. Evidently, the increase in driving force outweighs the increase in strength of the subducting plate due to the increase in plate thickness. The faster retreat in experiment 10 and 12 results in a more shallow dip during subduction (55° and 60-65° respectively during steady state retreat) compared to experiment 9 and 11 (60-65° and 80° respectively during steady state retreat).

The influence of slab density on the hinge-retreat velocity can be observed in Fig. 9-6. From the diagrams it is immediately clear that an increase in density contrast between subducting plate and underlying medium increases the hinge-migration rate. For the steady state part of the hinge-retreat, the average hinge-migration velocity (v_{hm}) increases from $v_{hm} \approx$ 12.6 cm/hr ($\Delta\rho$ = 60 kg/m^3) to $v_{hm} \approx$ 43.8 cm/hr ($\Delta\rho$ = 100 kg/m^3) to $v_{hm} \approx$ 81.8 cm/hr ($\Delta\rho \approx$ 140 kg/m^3). In addition, the hinge-migration rate is much more influenced by the interaction of the slab tip with the discontinuity for a low density contrast than for a high density contrast as can be observed from the clear defined kink in the curve in Fig. 9-6a. The slab dip during the steady state hinge-retreat was constant and decreased with increasing retreat velocity from ~ 80° ($v_{hm} \approx$ 12.6 cm/hr) to ~ 70° ($v_{hm} \approx$ 43.8 cm/hr) to ~ 60° ($v_{hm} \approx$ 81.8 cm/hr).

The influence of the slab width (W) on hinge-retreat has been plotted in Fig. 9-7 for five experiments with a width of 5, 10, 15, 20 and 25 cm and a constant thickness of 1.3 cm. These values result in slab width to thickness ratios (W/T) of 3.8, 7.7, 11.5, 15.4 and 19.2, respectively. The displacement curves all show a similar behaviour with an initial exponential increase in displacement, then a slowdown in displacement followed by a slight increase and then a steady state displacement. The highest retreat velocity is observed for experiment 8 with a steady state $v_{hm} \approx$ 66.0 cm/hr and W/T = 7.7. The slowest retreat velocity is observed

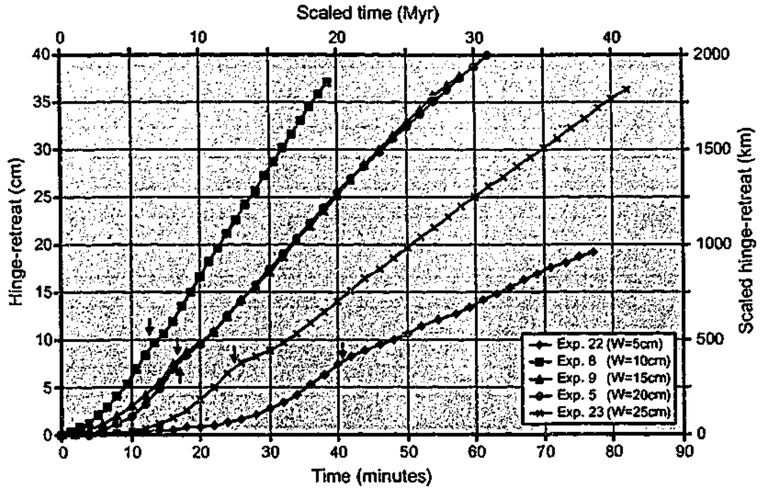

Fig. 9-7. Hinge-migration versus time for several experiments with different slab width. Arrows indicate time when slab tip hits discontinuity.

for experiment 22 with a steady state $v_{hm} \approx$ 19.3 cm/hr and W/T = 3.8. Although experiment 9 (W = 15 cm) and 5 (W = 20 cm) plot very close to each other, a decrease in hinge-retreat velocity with increasing slab width can also be observed. A reason for the nearly overlapping curves of experiment 9 and 5 might be that during rollback in experiment 5, the slab and arcuate trench were significantly curved and tightened, causing the effective slab width to be much smaller than 20 cm. In any case, the effect of the slab width on hinge-retreat velocity seems real and the hinge-retreat velocity is lowest for a W/T value somewhere between 3.8 and 11.5 close to 7.7.

The steady state retreat velocity has been plotted against steady state slab dip angle in Fig. 9-8 for a number of experiments (see also Table 9-2). The diagram suggests that there is a

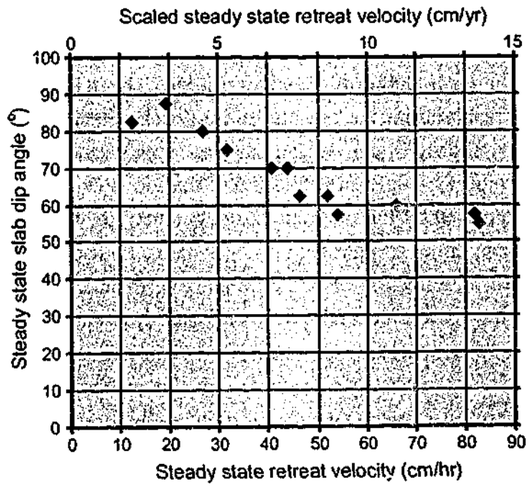

Fig. 9-8. Steady state retreat velocity plotted against steady state slab dip angle for experiments described in the text.

Experiment number	Steady state retreat velocity (cm/hr)	Scaled steady state retreat velocity (cm/yr)	Steady state slab dip
4	12.6	2.1	80-85°
5	43.8	7.3	70°
6	81.8	13.6	55-60°
8	66.0	11.0	60°
9	46.3	7.7	60-65°
10	82.8	13.8	55°
11	26.9	4.5	80°
12	52.1	8.7	60-65°
20	40.9	6.8	70°
21	54.1	9.0	55-60°
22	19.3	3.2	85-90°
23	31.9	5.3	75°

Table 9-2. List of some experimental results.

direct correlation between retreat velocity and slab dip angle, even if these different retreat velocities result from different physical parameters and boundary conditions. The data clearly suggest that an increase in retreat velocity is linked to a decrease in slab dip angle.

9.3.3. Slab induced mantle convection

Subduction and slab rollback induced convection were studied in the experiments by tracking passive markers randomly distributed inside and on top of the glucose syrup layer. The convection pattern for experiment 20 (fixed trailing edge) can be observed in Fig. 9-9. The flow is dominated by toroidal convection showing two elliptic convection cells with predominantly lateral flow from underneath the slab around the slab edges towards the mantle wedge. A small component of poloidal flow is also observed close to the subducting slab in the mantle wedge and underneath the slab due to shearing between the slab and the mantle resulting from the slab dip parallel component of displacement. No flow underneath the slab tip is observed during the entire duration of the experiment. The diagrams in Fig. 9-9 illustrate the side view and bottom view convection pattern before and just after the slab tip has hit the bottom of the box. Except for the magnitude of displacement vectors, the convection pattern in each diagram is very similar. The difference in magnitude of displacement vectors results from the reduction in rollback velocity after the slab tip has hit the box bottom. The similarity in convection patterns suggests that all slab rollback induced convection occurs around the edges of the slab and that no flow occurs underneath the slab tip. This is further supported by the orientation and geometry of the slab near the tip, which was close to vertical and either straight (Fig. 9-2a, 9-4a,b,d, 9-10b) or concave (Fig. 9-2b, 9-4c, 9-9, 9-10a) towards the direction of retreat in all experiments. If significant slab rollback induced flow would have occurred underneath the slab tip from the region under the slab towards the mantle wedge, the slab tip would have been convex towards the direction of retreat, as was observed for the lateral edges of the slab along which flow did occur (Fig. 9-3).

The convection pattern for experiment 11 (free trailing edge) can be observed in Fig. 9-10a. The flow pattern is more complex than in the fixed trailing edge experiments due to the large component of slab dip parallel displacement of the subducting plate. This results in a better

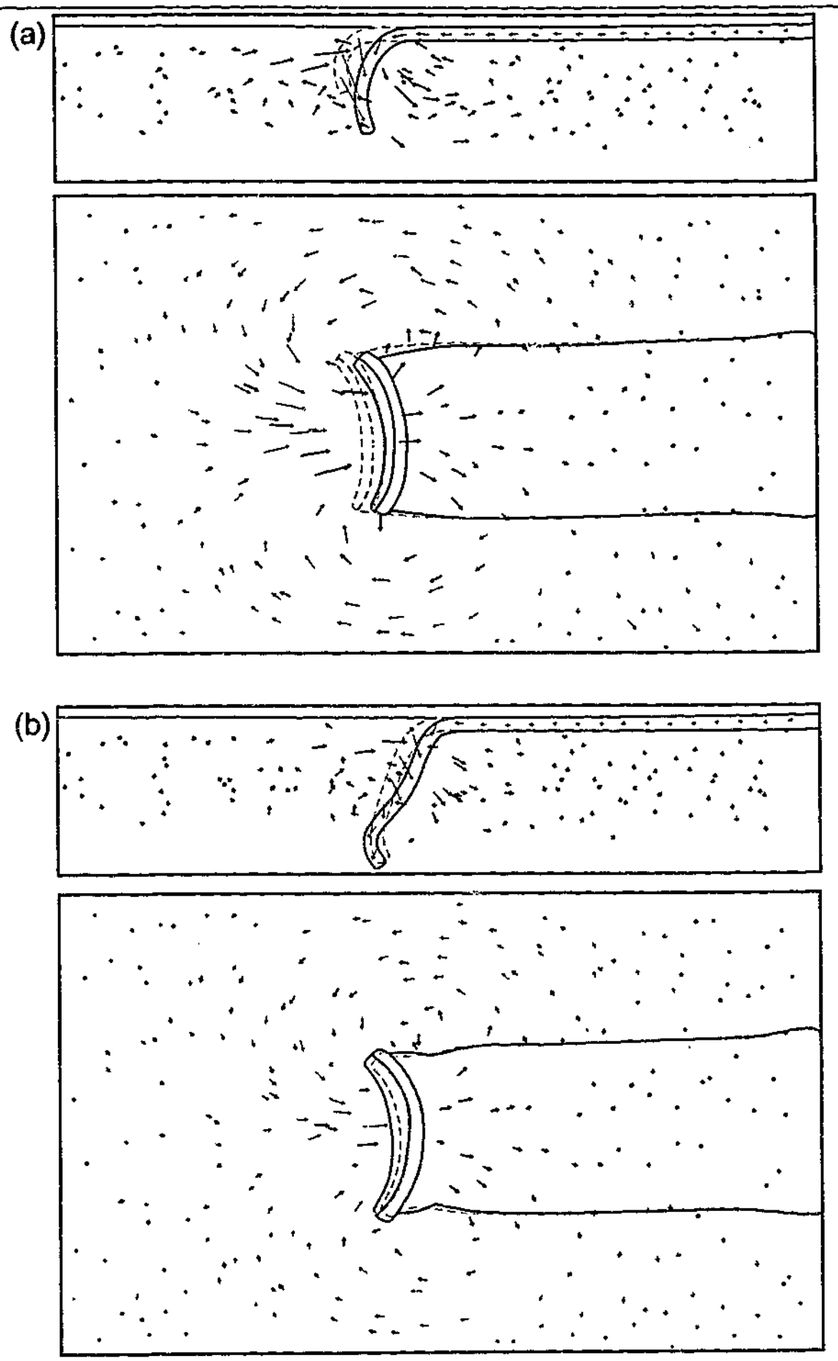

Fig. 9. Line drawings of side view and bottom view perspective of experiment 20 (fixed trailing edge) illustrating convection pattern in glucose syrup before and after slab tip hits bottom. (a) Before slab tip hits bottom between t = 22 min. and t = 26 min. and (b) after slab tip hits bottom between t = 30 min. and t = 34 min. Length of line-segment of vectors indicate amount of displacement while arrowhead indicates direction of displacement. Dots point to no displacement. Black vectors are for passive markers in the glucose syrup while grey vectors are for passive markers floating on top of the glucose syrup (bottom view) or passive markers in the side of subducting plate (side view). Light grey dashed lines and continuous dark grey lines illustrate subducting plate contours at the beginning and end of the time-lapse respectively.

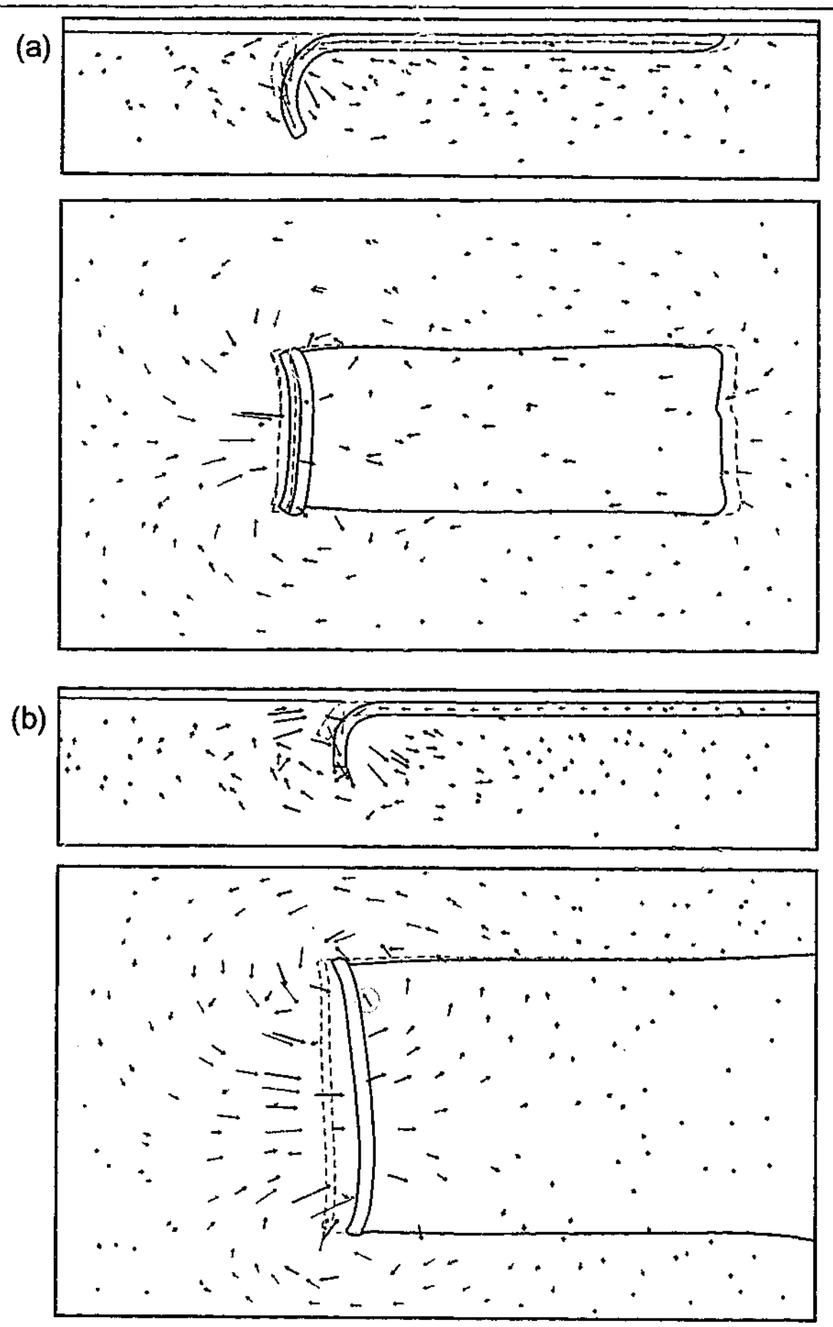

Fig. 10. Line drawings of side view and bottom view perspective of two experiments. (a) Experiment 11 (free trailing edge) illustrating convection pattern in glucose syrup before slab tip hits bottom between t = 19 min. 20 s and t = 23 min. 20 s. (b) Experiment 21 (fixed trailing edge) illustrating convection pattern in glucose syrup well before slab tip hits bottom between t = 9 min. and t = 14 min. Length of line-segment of vectors indicate amount of displacement while arrowhead indicates direction of displacement. Dots point to no displacement. Black vectors are for passive markers in the glucose syrup while grey vectors are for passive markers floating on top of the glucose syrup (bottom view) or passive markers in the side of the subducting plate (side view). Light grey dashed lines and continuous dark grey lines illustrate subducting plate contours at the beginning and end of the time-lapse respectively. Encircled vector in (b) points to small component of (oblique oriented) convection underneath slab tip.

defined poloidal component of flow with two convection cells divided by the slab, one located in the mantle wedge area and the other underneath the subducting plate. Horizontal displacement of the surface part of the subducting plate also produced two toroidal return flow convection cells on either side of the plate. Two toroidal convection cells are also observed akin to what was observed in experiment 20 with lateral flow around the edges of the slab. Again, no flow underneath the slab tip was observed for the entire duration of the experiment. The toroidal cells are not as well defined due to the reduced amount of slab rollback in experiment 11 and due to the interference with the convection pattern of the poloidal convection cells.

Only in two experiments (21 and 23) a small component of lateral flow underneath the slab tip was observed. This can be observed in Fig. 9-10b, which shows the convection pattern of experiment 21 in a stage well before the slab tip has hit the bottom of the box. The overall convection pattern is very similar to experiment 20 (Fig. 9-9a). However, near the slab tip close to one edge of the slab, the displacement vector of one particle (encircled) is oriented slightly towards the tip-line pointing to flow underneath the slab tip. It should be noted that for this experiment (as well as experiment 23), the penetration depth of the slab tip was not constant along the trench (e.g. slanting slab tip line) and the difference in penetration depth amounted up to 3-4 cm from the northernmost part of the tip-line towards the southernmost part of the tip-line. The small component of lateral flow underneath the slab tip was observed underneath the shallowest part of these slanting slab tips.

A schematic diagram illustrating the four dominant convection cells observed in both the fixed and free trailing edge experiments is illustrated in Fig. 9-11. The two toroidal convection cells on either side of the slab edge can be observed as well as the two poloidal convection cells, one located in the mantle wedge area and the other underneath the subducting plate.

A possible explanation for why slab rollback preferentially induces lateral flow around the slab edges and not flow underneath the slab tip has been illustrated in Fig. 9-12, showing two schematic cross-sections through a subduction experiment. The pressure in the glucose syrup in front and behind the slab is in equilibrium, while it is not underneath the slab, as indicated by the elevated isobars, due to sinking of the slab (Fig. 9-12a). Maximum elevation of the

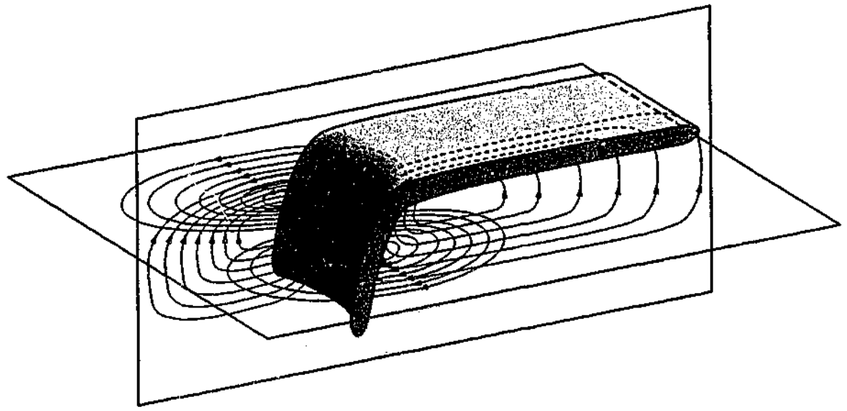

Fig. 9-11. Schematic sketch of subduction and slab rollback induced convection in the upper mantle. Slab dip parallel displacement induces two poloidal convection cells with one on each side of the slab. Slab rollback induces two toroidal convection cells with flow around the slab edges.

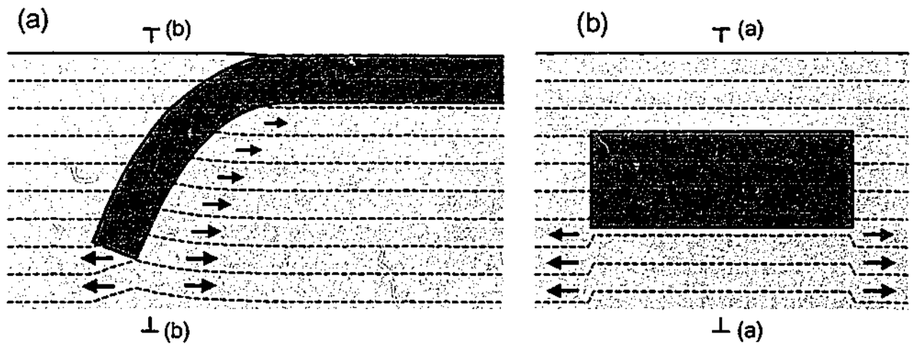

Fig. 9-12. Two schematic cross-sections for experiments to illustrate a possible explanation why flow in glucose is oriented only laterally around slab edges and not underneath slab tip. Dashed lines are isobars. Arrows indicate flow direction. (a) Cross-section perpendicular to the trench and (b) cross-section parallel to the trench.

isobars is located underneath the lowermost part of the slab tip, due to the maximum of slab material above this point. Left of this point, flow is directed towards the left, while right of this point, flow is directed towards the right (direction of slab retreat). Near the slab edges, the flow is directed outward from underneath the slab (Fig. 9-12b).

9.4. Discussion

9.4.1. Comparison with other dynamic models

9.4.1.1. Analogue models

Results of analogue experiments investigating subduction and rollback have been presented before [*Jacoby*, 1973, 1976; *Kincaid and Olson*, 1987; *Olson and Kincaid*, 1991; *Shemenda*, 1993; *Guillou-Frottier et al.*, 1995; *Griffiths et al.*, 1995; *Faccenna et al.*, 1996, 1999, 2001b; *Buttles and Olson*, 1998; *Becker et al.*, 1999; *Funiciello et al.*, 2000, 2002]. The results described by *Jacoby* [1973], *Kincaid and Olson* [1987], *Funiciello et al.* [2000, 2002] and *Faccenna et al.* [2001b] lend themselves best for comparison, since the model design in these papers is similar to the one presented in this chapter.

The results of the free trailing edge experiments can be compared with the model results from *Jacoby* [1973] and *Kincaid and Olson* [1987] with a similar experimental design. *Jacoby* [1973] reports subduction at a constant angle, displacement of the trailing edge and a stable hinge during subduction. However, as reported by the author, the stable hinge is merely related to the width of the model box, which was only slightly wider than the subducting plate and therefore inhibited lateral flow around the slab edges to accommodate rollback. Free trailing edge experiments from *Kincaid and Olson* [1987] were reported to show no sign of slab retreat during free sinking of the slab, but only slab retreat when the slab tip would interact with the upper-lower mantle discontinuity. This is in contrast with the results reported here, with significant slab retreat during free sinking of the slab contemporaneously with trailing edge advance, although slab retreat is suppressed with respect to fixed trailing edge

experiments. As suggested before, this might result from a smaller mantle drag force in the experiments of *Kincaid and Olson* [1987]. The viscosity that was used in their experiments for the upper mantle was 111 Pa·s, which is slightly lower than in the experiments described in here. If the trailing edge migration was also slower in their experiments, then this would have resulted in a smaller mantle drag force. However, no data of trailing edge migration versus time are given by *Kincaid and Olson* [1987], which therefore does not allow the drag force to be compared with the experiments described in here.

Comparison of the evolution of the slab geometry between the experiments with a fixed trailing edge reported in here and experiments with a similar experimental design reported elsewhere [*Kincaid and Olson*, 1987; *Faccenna et al.*, 2001; *Funiciello et al.*, 2002] show a good agreement. During free sinking of the slab, the slab sinks and rolls back with an increasing slab dip angle until it is subvertical. When the slab tip reaches the upper-lower mantle discontinuity, the slab is draped backward with a horizontal slab segment resting on top of the discontinuity. The slab continues to retreat but at a lower slab dip angle. *Faccenna et al.* [2001] and *Funiciello et al.* [2002] also reported an initial exponential increase in hinge-retreat during free sinking of the slab, followed by a slowdown during initial contact of the slab with the upper-lower mantle discontinuity, and finally a steady state retreat.

Buttles and Olson [1998] and *Funiciello et al.* [2002] concluded from physical experiments investigating slab rollback induced mantle convection that poloidal convection underneath the slab tip prevailed in the stage before the slab tip would reach the upper-lower mantle discontinuity. In addition, *Funiciello et al.* [2002] found that only when the slab tip would interact with the upper-lower mantle discontinuity, the toroidal component (lateral flow around the edges of the slab) would dominate. This is in disagreement with experimental results presented in this chapter. No poloidal component of slab induced convection underneath the slab tip from the region under the slab towards the mantle wedge region has been observed in any of the experiments either before or after the slab tip approached the upper-lower mantle discontinuity. Only in two experiments (21 and 23) a small component of lateral flow underneath the slab tip was observed. For these experiments, the penetration depth of the slab tip was not constant along the trench (e.g. slanting slab tip line) and the difference in penetration depth amounted up to 3-4 cm (simulating 150-200 km in nature). A small component of toroidal flow was observed underneath these slanting slab tips underneath the shallowest part of the tip.

The discrepancy with the results of *Buttles and Olson* [1998] can be explained by the difference in experimental design and boundary conditions. *Buttles and Olson* [1998] used a slab made of plexiglass and slab-dip parallel and perpendicular displacement of the slab were externally controlled. This could have possibly led to unrealistic flow patterns in the sub-lithospheric mantle, since the flow did not result from buoyancy-driven subduction forces of the slab as in nature, but from kinematic boundary conditions externally imposed on the slab.

Funiciello et al. [2002] describe slab induced convection patterns of experiments with slabs as wide as (laterally constrained) or half the width (laterally unconstrained) of the box. From the former design, it is not surprising that the forced flow would be directed underneath the slab tip, since it is effectively a two-dimensional experiment, comparable to *Garfunkel et al.* [1986]. *Garfunkel et al.* [1986] numerically investigated slab rollback induced mantle convection in a two-dimensional model box, in which displacement of the slab was externally imposed (Fig. 9-13). Only flow underneath the slab tip was observed due to the two-dimensional set-up of the model box. Surprisingly, the streamline pattern illustrating the flow

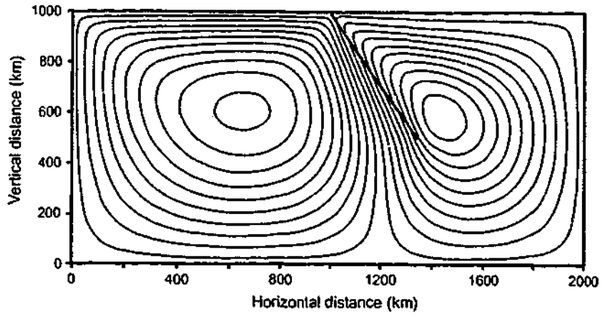

Fig. 9-13. Instantaneous slab-induced circulation pattern in a box of aspect ratio 2 during slab retreat (redrawn from *Garfunkel et al.* [1986]). The following velocity conditions have been applied: the left half of the top boundary moves with 8.0 cm/yr to the right; the right half of the top boundary moves with 2.0 cm/yr to the left; the trench and slab move with 2.0 cm/yr to the left.

underneath the slab tip drawn by *Funiciello et al.* [2002] (their Fig. 4b) is different from the streamline pattern from *Garfunkel et al.* [1986] (Fig. 9-13). Streamlines drawn by *Garfunkel et al.* [1986] intersect the slab at a steeper angle pointing to flow underneath the slab tip, while streamlines drawn by *Funicellio et al.* [2002] intersect the slab at a shallower angle. The discrepancy between the results reported in here and the laterally unconstrained experiments of *Funicellio et al.* [2002] is unclear, because the experimental design in both cases is very similar and the slab induced convection was in both cases driven entirely by the negative buoyancy of the subducting lithosphere.

From analogue and numerical experiments, *Becker et al.* [1999] and *Faccenna et al.* [2001a,b] found that the slab length $H(t)$ during free sinking of the slab (e.g. before interaction with the 670 km discontinuity) scales as follows:

$$H(t) = H_0 \exp\left(C \frac{\Delta\rho g r^3}{\eta_{sp} R^2} t \right) \qquad (9\text{-}4)$$

where H_0 is the initial slab length, C is a constant, $\Delta\rho$ is the density contrast between slab and mantle, r is the bending radius of the slab, R is the half thickness of the slab, and t is time. Equation (9-4) has been deduced under the assumption that the bending radius is constant during subduction and that viscous dissipation due to bending of the subducting lithosphere is the main force resisting subduction. The viscous dissipation would therefore be roughly equal to the potential energy dissipation of the subducted slab. Best fit curves for several fixed trailing edge experiments have been plotted in Fig. 9-14 using equation (9-4). For each experiment two curves have been plotted, one with a time dependent bending radius, as measured from the experiment (Fig. 9-15), and one with a constant bending radius (chosen as the minimum bending radius as observed in the experiment (see Fig. 9-15)). As can be observed in Fig. 9-14, a reasonable fit can be achieved with a constant bending radius and an optimised value for C. For the more realistic case of a time dependent bending radius, however, no satisfying fit can be achieved. This is mainly due to the fact that $H(t)$ in equation (9-4) is very sensitive to changes in r. The discrepancy between curve and data in the initial stage of the experiment could result from the fact that the initial bending radius is imposed

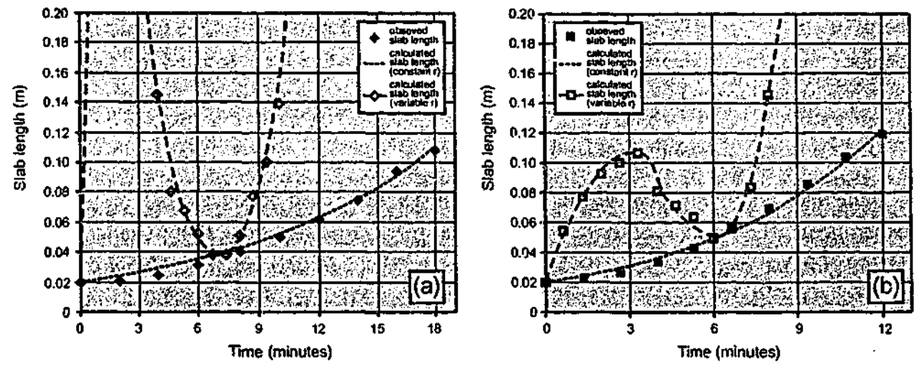

Fig. 9-14. Diagrams illustrating slab length during free fall into upper mantle (free fall stage is defined as the time frame between initiation of subduction and the moment when the slab tip hits the lower discontinuity). Observed slab length is compared with predicted slab length (calculated with equation (9-4)) for both a constant bending radius (minimum bending radius as observed in experiment (see Fig. 9-15)) and time dependent bending radius as observed in experiment (see Fig. 9-15). (a) Experiment 9 with C = 0.105 and minimum bending radius r = 0.025 m. (b) Experiment 10 with C = 0.037 and minimum bending radius r = 0.055 m.

rather then resulting from the dynamics of the system. Furthermore, part of the error between calculated and observed plot could follow from the initial assumption that the rapidity of subduction during the free fall stage is primarily controlled by the bending resistance. Calculations have shown that the bending resistance accounts for ~ 60% of resistance to subduction in the initial stage of subduction decreasing to ~ 30% just before the slab tip hits the lower discontinuity (see Chapter 11). The better fits between data and curves resulting from equation (9-4) obtained by *Faccenna et al.* [2001b] could be further explained by the larger viscosity of the slab ($\eta_{sp} = 1.6 \times 10^5$ Pa·s) and viscosity contrast between slab and upper mantle in their experiments (η_{sp}/η_m = 350-1000), compared to the experiments described in

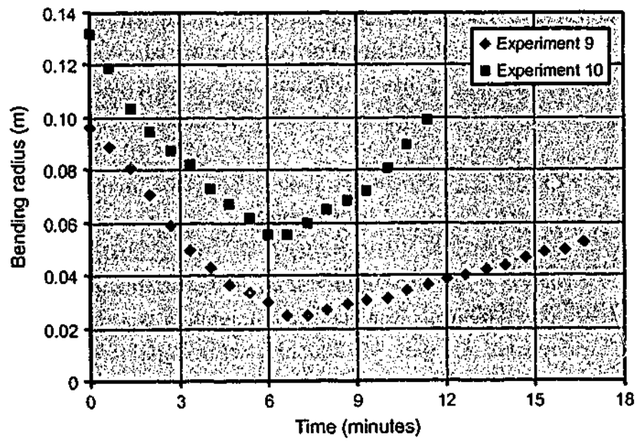

Fig. 9-15. Progressive development of bending radius r during the free fall stage of the slab into the upper mantle for two experiments (free fall stage is defined as the time frame between initiation of subduction and the moment when the slab tip hits the lower discontinuity).

here (η_{sp} = 2.4 × 10^4 Pa·s, η_{sp}/η_m = 185). These higher values could require a larger component of the driving force to be absorbed by the resistive force to bend the slab, rather than other resistive forces such as shear forces and rollback induced convection forces.

9.4.1.2. Numerical models

Numerical experiments on subduction and rollback have been conducted before, but these experiments were in most cases two-dimensional [i.e. *Garfunkel et al.*, 1986; *Giunchi et al.*, 1994; *Marotta and Sabadini*, 1995; *Christensen*, 1996; *Houseman and Gubbins*, 1997; *Olbertz et al.*, 1997; *Becker et al.*, 1999; *Buiter et al.*, 2001; *Cízková et al.*, 2002; *van Hunen et al.*, 2002]. The experimental results have demonstrated that lateral upper mantle flow around the slab edges is the dominant flow in the upper mantle to allow for slab rollback and no component of flow underneath the slab tip has been observed. The results demonstrate that two-dimensional investigations into slab rollback related processes such as hinge-retreat rates [e.g. *Giunchi et al.*, 1994], slab-induced mantle convection patterns [e.g. *Garfunkel et al.*, 1986] (Fig. 9-13) and the influence of these convection patterns on slab morphology [e.g. *Marotta and Sabadini*, 1995] could provide unreliable insights, because the boundary conditions enforced upon these models due to the two-dimensional approach will significantly and unrealistically influence the experimental outcomes. It could be argued that two-dimensional models of subduction and slab rollback could be representative for natural subduction settings for which the slab is relatively wide. However, even in the case of the South American subduction zone, which is at present the widest and most continuous subduction zone on Earth, shear wave splitting implies that mantle flow in the upper mantle underneath the subducting slab is predominantly oriented parallel to the trench [*Russo and Silver*, 1994, 1996]. This points to complex three-dimensional dynamic interaction between the slab and mantle, for which two-dimensional modelling approaches would not suffice.

The importance of slab width on hinge-retreat has been investigated analytically by *Dvorkin et al.* [1993]. Results indicate that a decrease in slab width increases the hinge-retreat velocity, because a limited slab allows for lateral flow from underneath the slab around the slab edges towards the mantle wedge. This flow reduces the mantle wedge suction force, which is a stabilising force for the dip of the slab. This is in agreement with the model results presented in this chapter, although the results also demonstrate that there is an optimum slab width value for a maximum retreat velocity. For very narrow slabs (with a W/T ratio close to and smaller than 3.8), the viscous shear resistance between slab and surrounding becomes increasingly important as the slab surface to volume ratio increases with decreasing slab width.

In a large number of models, a hinge-migration velocity was imposed on the subducting lithosphere as a boundary condition, rather then being investigated on its own [e.g. *Garfunkel et al.*, 1986; *Griffiths et al.*, 1995; *Guillou-Frottier et al.*, 1995; *Christensen*, 1996; *Houseman and Gubbins*, 1997; *Olbertz et al.*, 1997; *Buiter et al.*, 2001; *Cízková et al.*, 2002; *van Hunen et al.*, 2002]. From our results it is clear that hinge-migration is a transient process, as has been found by *Faccenna et al.* [1996, 1999, 2001b], *Becker et al.* [1999] and *Funiciello et al.* [2002]. Steady state retreat is only observed when interaction of the slab with the upper-lower mantle discontinuity results in horizontal draping of the slab over the discontinuity (see also *Funiciello et al.* [2002]).

9.4.2. Comparison with nature

The experimental results of the fixed trailing edge experiments (Fig. 9-2a) lend themselves particularly well for comparison with tomography images across the Calabrian arc [*Lucente et al.*, 1999] and Carpathian arc [*Wortel and Spakman*, 2000], because the horizontal velocity of the subducting plate in these arc systems was very low (~ 3 cm/yr at 30 Ma decreasing to ~ 1 cm/yr from 10 Ma to Present) [*Jolivet and Faccenna*, 2000]. In both examples, the slab signature has a relatively steep dip down to the upper-lower mantle discontinuity, where it is deflected horizontally (Fig. 9-16). The deflected part of the slab seems to rest on top of the discontinuity in both cases and continues as far west as the extent of the back-arc basins at the surface (northwest border of Liguro-Provencal Sea for Calabrian arc and southwest border of Pannonian Basin for Carpathian arc). The close resemblance between the slab geometry in nature and experiment would suggest that the slab geometry in both natural cases resulted from eastward slab rollback, which would explain the back-arc basins observed at the surface. The Calabrian arc encloses the Liguro-Provencal Sea and Tyrrhenian Sea, which both have a Cainozoic history of back-arc opening [e.g. *Malinverno and Ryan*, 1986; *Lonergan and White*, 1997]. The Carpathian arc encloses the Pannonian Basin, which also has a Cainozoic history of back-arc opening [e.g. *Royden et al.*, 1983].

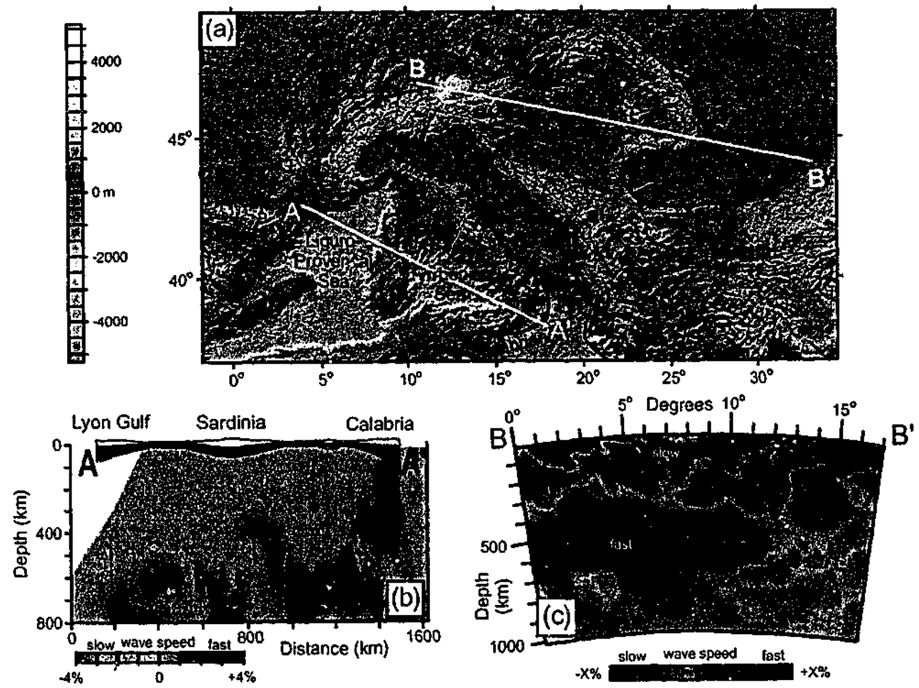

Fig. 9-16. Location map and cross-sections of tomographic images across the Calabrian and Carpathian arc. (a) Topographic map of the central Mediterranean and Carpathian regions (from *Smith and Sandwell* [1997]) showing major tectonic boundaries and location of cross-sections. (b) Tomographic image of the Ionian slab (from *Lucente et al.* [1999]) and lithospheric model of the overriding plate (from *Faccenna et al.* [2001b]). (c) Tomographic image and earthquakes of the Carpathian slab (from *Wortel and Spakman* [2000]).

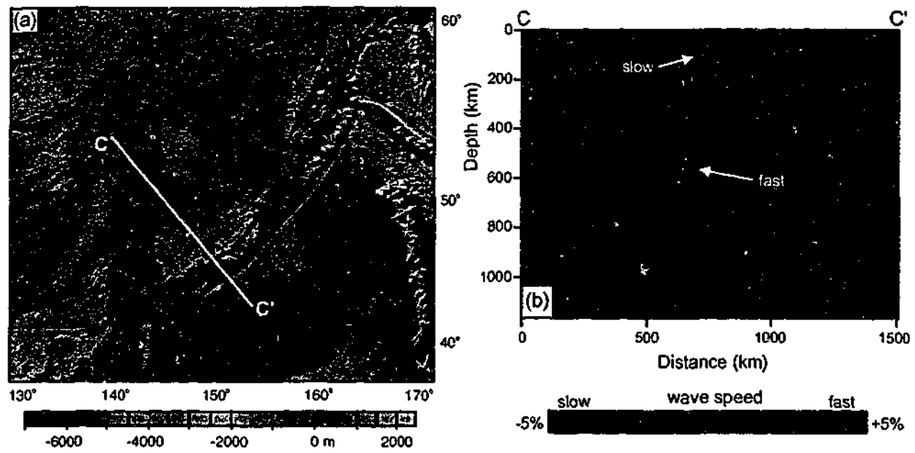

Fig. 9-17. Location map and cross-section of tomographic image across the Kuril arc. (a) Topographic map of the Kuril arc - back-arc region (from *Smith and Sandwell* [1997]) showing major tectonic boundaries and structures (from *Schellart et al.* [in review]) and location of cross-section. (b) Tomographic image and seismicity of the Pacific slab (from *van der Hilst et al.* [1991]).

Several tomographic images for subduction systems in the Western Pacific show a similar slab geometry including images across the Kuril arc [*van der Hilst et al.*, 1991] (Fig. 9-17) and across the Izu-Bonin arc [*van der Hilst and Seno*, 1993]. Again, the slab signature is deflected horizontally at the upper-lower mantle discontinuity. In both cases, the horizontal segment resting on top of the discontinuity underlies a back-arc basin at the surface, with a Cainozoic history of back-arc opening.

Slab width, or at least lateral continuity of the slab, seems to have a major influence on the hinge-retreat velocity in natural subduction systems. This is evidenced by the limited trench parallel extent of back-arc basins. A number of subduction systems, their lateral extent and their hinge-retreat velocity have been given in Table 9-3. Although the relation is not immediately straightforward, the data do show that the longest continuous subduction systems (Aleutian, Sunda and South American subduction systems) have the smallest retreat velocity. For the South American system, the slow retreat is probably mainly related to the ridge push exerted on the hinge by the overriding plate due to spreading at the South Atlantic mid-oceanic ridge [*Meijer and Wortel*, 1992] and to a lesser extent related to the negative buoyancy forces within the slab.

For the other subduction systems plotted in Table 9-3 there is no clear relation between slab width and hinge-retreat velocity. However, from the larger four of these systems (Ryukyu, Mariana, New Hebrides, Tonga-Kermadec), the largest retreat velocity is observed close to a pronounced vertical limit of the subducting slab (i.e. slab edge or tear). This would allow for sub-lithospheric mantle flow around the slab edge to accommodate slab rollback. Such rollback induced lateral flow around slab edges has been suggested for several subduction settings based on volcanic rock geochemistry in the arc or back-arc region (Calabrian arc [*Gvirtzman and Nur*, 1999]; Tonga arc [*Wendt et al.*, 1997; *Turner and Hawkesworth*, 1998]) and on seismic anisotropy (Kuril arc [*Peyton et al.*, 2001]). Thus it can be concluded that lateral slab discontinuities have a major influence on slab retreat in the sense that they facilitate rapid slab rollback.

Subduction system	Slab width (km)	Vertical tear location	Fastest retreat location	Retreat (cm/yr)	Slab dip angle	Overriding plate
Calabrian	~ 250	NE and SW	~ constant	6.0 since 5 Ma (1)	70°	Extension
Scotia	~ 600	N and S	~ constant	5.7 (2)	70°	Extension
Hellenic	~ 700	E?	~ constant	3.0 - 3.5 (3)	55°	Extension
Ryukyu	~ 1200	SW	SW	4.0 (SW) (4)	40-50°	Extension
				1.1 (Central SW) (4)	40-50°	
Mariana	~ 1400	S	S	3.0 - 4.3 (5)	80-90°	Extension
New Hebrides	~ 1500	SE	SE	11.8 (SE) (6)	55-60°	Extension
				4.2 (Centre) (6)	70-75°	
Tonga-Kermadec	~ 2500	NNE	NNE	15.9 (NNE) (7)	50°	Extension
				9.1 (Central NNE) (7)	55-60°	
				1.5 - 2.0 (SSW) (8)	70-80°	
Aleutian	~ 3000			-0.5 - 2.1 (9)		Neutral
Sunda	~ 3650			~ -0.3 - 1.1 (9)		Neutral
South America	~ 6500			~ 1.2 - 3.0 (9)		Shortening

Table 9-3. Slab width versus slab retreat. References: 1—*Faccenna et al.* [2001b]; 2—*Barker* [1995]; 3— *Kahle et al.* [1998] and *McClusky et al.* [2000]; 4—*Imanishi et al.* [1996] and *Heki et al.* [1996]; 5— *Martínez et al.* [2000]; 6—*Taylor et al.* [1995]; 7—*Bevis et al.* [1995]; 8—*Wright* [1993]; 9—*Jarrard* [1986].

From the experiments it can be concluded that the slab dip is dependent on the retreat velocity, with higher retreat velocities resulting in lower dip angles (Table 9-2, Fig. 9-8). This supports findings of previous experimental work of subduction and slab rollback [*Griffiths et al.*, 1995; *Guillou-Frottier et al.*, 1995]. The experimental results can be compared to several slabs in nature which are presently retreating (Table 9-3). The correlation between slab dip angle and hinge-retreat velocity are not immediately straightforward, probably because other physical factors then hinge-retreat velocity influence the slab dip angle. For example, the slab dip angle depends on several other factors including absolute velocity of the subducting plate (see Chapter 10), absolute velocity of the overriding plate and buoyancy of the slab [*van Hunen et al.*, 2002]. However, the Tonga-Kermadec subduction zone and the New Hebrides subduction zone do show a correlation between the two parameters. For these subduction zones, the absolute velocity and buoyancy of the plate is approximately constant along he trench. Both subduction zones show an increase in retreat velocity along the trench, which corresponds to a decrease in dip angle of the slab.

All arc-shaped subduction zones, which are or have recently been retreating (as evidenced by the activity in the back-arc region) are convex towards the direction of retreat. This has also been observed in the fluid dynamical models. In the models this resulted from lateral flow of glucose syrup from underneath the slab around the slab edges towards the mantle wedge, forcing the edges of the slab to bend towards the direction of flow. In nature, the convexity of slabs could also be explained in this manner, especially for arc systems, which are presently retreating. However, it should be kept in mind that other factors could also influence the arcuate shape of subduction zones, such as the presence of buoyant irregularities on the subducting plate [e.g. *Vogt*, 1973].

9.5. Conclusions

The experimental results oppose the view that subduction rollback can be regarded as a two-dimensional steady state process. To the contrary, rollback is a three-dimensional process in every aspect of its nature and demonstrates non-steady state behaviour. During subduction and rollback, the slab and trench attain an arc-shaped geometry, convex towards the direction of retreat, as also observed for arc - back arc systems in nature. Subduction and rollback produce a three-dimensional convection pattern with two types of convection cells. Slab dip parallel displacement produces two poloidal convection cells, one in the mantle wedge above the slab and one underneath the subducting plate. Slab perpendicular displacement produces two toroidal convection cells with lateral convection from underneath the slab around the slab edges towards the mantle wedge. No significant slab rollback induced convection underneath the tip of the slab is observed. The hinge-retreat velocity and dip of the slab change in time and in space from initiation of subduction until the slab is draped on top of the upper-lower mantle discontinuity. Only after the frontal segment of the slab has been horizontally draped over the discontinuity does the slab approach a steady state with a constant dip angle, constant sinking vectors and a constant retreat velocity. From the experimental results it can be concluded that the following factors retard slab rollback: (1) a decrease in density contrast between slab and sub-lithospheric mantle; (2) a relatively wide slab (~ > 750 km) or a very narrow slab (~ < 250 km); (3) a free trailing edge boundary condition for the subducting plate.

FOREWORD CHAPTER 10

In this chapter, the role of the horizontal velocity of the subducting lithosphere on the hinge-migration of the slab is investigated. The ideas, which initiated the research outlined in this chapter, were inspired by reading the papers from *Northrup et al.* [1995] and *Jolivet and Faccenna* [2000]. In these papers, it is suggested that a decrease in convergence velocity or absolute velocity of the subducting plate is responsible for the formation of back-arc basins.

The ideas outlined in this chapter have solely resulted from the author and the experiments described in this chapter have been done by the author alone. Stimulating discussions with Jean Braun, Chris Kincaid, Ross Griffiths, Gordon Lister, Louis Moresi, Roberto Weinberg and Mike Sandiford are acknowledged.

CHAPTER 10

Influence of the horizontal velocity of the subducting plate on the geometry and hinge-migration of the slab

Abstract

Geological observations indicate that several active continental margins (East Asia and Mediterranean) show major phases of extension synchronously with a reduction in velocity of the subducting plate. In this chapter, results of fluid dynamical experiments are presented to test the influence of the horizontal velocity of the subducting plate on the hinge-migration velocity, on the style of subduction and on the geometry of the slab. Results show that hinge-migration decreases with increasing horizontal velocity. In addition, phases of hinge-retreat alternate with phases of hinge-advance for relatively high horizontal velocities due to interaction of the slab with the bottom of the box, simulating the upper-lower mantle discontinuity. Such slab kinematics could explain the episodic behaviour of back-arc opening observed in convergent settings. The kinematics of slab subduction and the geometry of the slab are greatly influenced by the horizontal velocity of the subducting plate. Three subduction modes with accompanying slab geometry can be recognised. A relatively low applied horizontal velocity results in relatively fast hinge-retreat with backward sinking of the slab and a backward draping slab geometry. With increasing applied horizontal velocity hinge-migration is relatively small, resulting in subvertical oriented sinking of the slab and a folded slab geometry where the slab piles on top of itself. For a relatively high horizontal velocity the hinge migrates forward, resulting in forward oriented subduction vectors and a forward draping slab geometry.

10.1. Introduction

The influence of the horizontal velocity of the subducting lithosphere resulting from far field stresses (e.g. ridge push) on the hinge-migration of the subducting lithosphere is not straightforward. However, geological data indicate that several overriding plates in active continental margin settings (East Asia and Mediterranean) show major phases of extension (i.e. back-arc extension) coeval with a reduction in relative convergence velocity or absolute velocity of the subducting plate, implying hinge-retreat (Fig. 10-1). For instance, *Northrup et al.* [1995] argue that convergence between Eurasia and the Pacific plate slowed down from ~ 13 cm/yr in the Late Cretaceous to ~ 4 – 9 cm/yr during the Palaeocene – Middle Miocene. The convergence velocity increased again to over 10 cm/yr during the Late Miocene – Present. Since the absolute motion of Eurasia during this time interval was relatively low (~ 1 cm/yr) [*Jolivet and Faccenna*, 2000] this change in convergence velocity can be mainly regarded to have resulted from change in absolute velocity of the subducting Pacific plate. According to *Northrup et al.* [1995] the relatively low convergence rate coincided with phases of major extension along the East Asian active margin (e.g. Kuril Basin, Japan Sea, South China Sea) during the latest Cretaceous to Middle Miocene. According to *Northrup et*

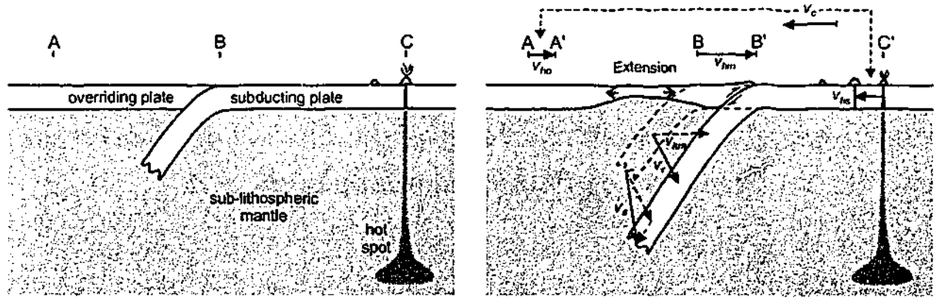

Fig. 10-1. Schematic representation of various kinematic vectors for subduction and rollback. Horizontal velocity of subducting plate is indicated by v_{hs}. Horizontal velocity of overriding plate is indicated by v_{ho}. The convergence velocity between the overriding and subducting plate is indicated by v_c and results from v_{ho} and v_{hs}. Hinge-migration (v_{hm}) is related to the backward sinking of the slab, as indicated by the vector v_r. Resultant sinking vector of the slab (v_s) results from v_r and v_{hs}. All vectors except v_c have the hot spot as a reference frame.

al. [1995] such a reduction in convergence velocity would result in a reduction of compressive stresses at the plate boundary, which could result in extension along the Eurasian margin. Nevertheless, a mere reduction in convergence velocity would still result in a net compressive stress across the subduction boundary, thus inhibiting extension to occur. However, a reduction in absolute velocity of the subducting plate could promote sinking and rollback of the subducting lithosphere. Such rollback would then enable the overriding plate to extend [e.g. *Elsasser*, 1971; *Lonergan and White*, 1997]. Similar ideas have recently been suggested by *Jolivet and Faccenna* [2000] for the relative timing of slowdown of absolute motion of the African plate and the opening of several back-arc basins in the Mediterranean region (Alboran Basin, Liguro-Provencal Basin, Tyrrhenian Basin, Pannonian Basin, Aegean Sea) at ~ 30 Ma.

In this chapter, results of fluid dynamical experiments are described to obtain quantitative insights into the influence of the horizontal velocity of the subducting plate (v_{hs}) on the hinge-migration velocity (v_{hm}). In each experiment a different horizontal velocity has been applied to the subducting plate to investigate the dependence of v_{hm} on v_{hs}. Physical experiments investigating subduction and rollback have been done before, but v_{hs} was in most cases set to zero [*Kincaid and Olson*, 1987; *Funiciello et al.*, 2000, 2002; *Faccenna et al.*, 2001b]. In some cases, v_{hs} was not applied but only resulted from slab pull forces [*Jacoby*, 1973; *Kincaid and Olson*, 1987]. In experiments by *Faccenna et al.* [1996] and *Becker et al.* [1999], v_{hs} was non-zero in the initial stage of the experiments to create a subduction instability and was later set to zero. In these experiments, rollback was mainly observed after setting v_{hs} to zero. In most of the numerical models, slab retreat was externally imposed as a boundary condition [e.g. *Garfunkel et al.*, 1986; *Christensen*, 1996; *Houseman and Gubbins*, 1997; *Olbertz et al.*, 1997; *Buiter et al.*, 2001; *Cízková et al.*, 2002; *van Hunen et al.*, 2002] and therefore the self-consistent dynamical behaviour of hinge-migration could not be investigated. In this investigation, the relation between v_{hm} and v_{hs} will be investigated quantitatively under an applied constant v_{hs}. In addition, v_{hm} is not externally imposed as a boundary condition but results only from the driving force resulting from the negative buoyancy of the slab, the viscous resistive forces and the applied v_{hs}, and thus closely reflects natural conditions.

10.2. Fluid dynamic model

The models consist of a layered system comprising a high-viscosity layer (1.3 cm thick) overlying a low-viscosity layer (12 cm thick) (Fig. 10-2). Similar designs have been adopted before to investigate subduction and slab rollback processes [*Kincaid and Olson*, 1987; *Griffiths et al.*, 1995; *Funiciello et al.*, 2000, 2002; *Faccenna et al.*, 2001b]. The upper layer is made of a Newtonian silicon putty with a viscosity $\eta_{sp} \approx 2.4 \times 10^4$ Pa·s and simulates a ~ 65 km thick oceanic lithosphere. The putty has been mixed with a dense filler (iron powder with a grain size < 150 μm) to obtain a slab density $\rho_{sp} \approx 1.52 \times 10^3$ kg/m^3. The lower layer is made of glucose syrup ($\eta_m \approx 1.3 \times 10^2$ Pa·s, $\rho_m \approx 1.42 \times 10^3$ kg/m^3) simulating some 600 km of sub-lithospheric upper mantle. The bottom of the box represents the 670 km discontinuity, which has been assumed to be impenetrable. This assumption is justified for a number of slabs, which are at least temporarily stalled at the 670 km discontinuity [*van der Hilst et al.*, 1991; *Lucente et al.*, 1999; *Widiyantoro et al.*, 1999; *Wortel and Spakman*, 2000; *Fukao et al.*, 2001]. The difference in viscosity between lithosphere and sub-lithospheric mantle in the model is a factor of ~ 185, which is close to the estimated effective viscosity difference in nature (~ 200 [*Houseman and Gubbins*, 1997], 50 – 200 [*Conrad and Hager*, 1999], ~ 100 [*Becker et al.*, 1999], 100-500 [*Faccenna et al.*, 2001a]). We have chosen the timescale ratio as follows: $t^a / t^n \approx 3.81 \times 10^{-12}$ (1 hour in model represents ~ 30 Myr in nature). With such a time-scale ratio at hand one can calculate the upscaled sub-lithospheric upper mantle viscosity from the following scale relationship (see Chapter 9):

$$\frac{\eta^a}{\eta^n} = \frac{\Delta\rho^a t^a g^a x^a}{\Delta\rho^n t^n g^n x^n} \qquad (10\text{-}1)$$

where superscript a denotes the analogue model and superscript n denotes the natural prototype; η indicates the viscosity; $\Delta\rho$ is the density difference between the subducting plate and the sub-lithospheric mantle, g is the acceleration due to gravity and x indicates length.

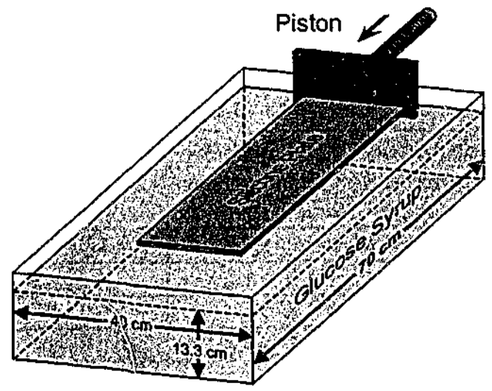

Fig. 10-2. Configuration of the modelling apparatus. A plate of silicone putty, representing oceanic lithosphere, floats on top of glucose syrup, representing the sub-lithospheric upper mantle. The bottom of the box simulates the 670 km discontinuity, assumed to be impenetrable. During an experiment, the tip of the silicone plate is depressed over a length of 2 cm at an angle of ~ 30° into the glucose syrup to initiate a subduction instability. The kinematic behaviour of the slab is investigated for a number of velocities of the piston.

Since the experiments presented in this chapter are executed in the Earth's field of gravity, equation (10-1) can be reduced to:

$$\frac{\eta^a}{\eta^n} = \frac{\Delta\rho^a t^a x^a}{\Delta\rho^n t^n x^n} \qquad (10\text{-}2)$$

From equation (10-2) and with the aforementioned timescale ratio $t^a / t^n \approx 3.81 \times 10^{-12}$, $\Delta\rho^a = 100$ kg/m^3, $\Delta\rho^n \approx 80$ kg/m^3, and $x^a / x^n = 2.0 \times 10^{-7}$ this results in an upscaled sub-lithospheric upper mantle viscosity of ~ 1.36×10^{20} Pa·s. This is similar to the natural prototype of 10^{19} - 10^{21} Pa·s [*Artyushkov*, 1983, *Ranalli*, 1995], indicating that driving forces for subduction (e.g. due to gravity) are properly scaled with respect to the forces resisting subduction (e.g. viscous forces). It would further result in an average oceanic lithosphere viscosity of 2.52×10^{22} Pa·s.

During an experiment, the high-viscosity layer is pushed by a piston at a constant rate (varying between 0 and 78 cm/hr) in a direction perpendicular to the trench. These applied velocity values can be compared with nature using the non-dimensional buoyancy number F [*Houseman and Gubbins*, 1997]:

$$F = (L^2 g \Delta\rho)/(v_{hs}\eta_{sp}) \qquad (10\text{-}3)$$

where L is the subducting plate thickness and η_{sp} is the average viscosity of the subducting plate. Characteristic buoyancy numbers for nature range somewhere between 0.415 and 0.028 with $L \approx 6.5 \times 10^4$ m, $g = 9.8$ m/s^2, $\Delta\rho \approx 80$ kg/m^3, $v_{hs} = 1$ - 15 cm/yr and $\eta_{sp} \approx 2.52 \times 10^{22}$ Pa·s. The greatest uncertainty in this number stems from the uncertainty of the lithosphere viscosity. Buoyancy numbers for the experiments and for nature for a number of v_{hs}-values are presented in Table 10-1. Here it can be observed that 1 cm/yr and 13 cm/yr in nature correspond to 6 cm/hr and 78 cm/hr in the experiments, respectively.

Before the experiment was started, some 2 cm of the tip of the lithosphere was submerged at an angle of ~ 30° to create a subduction instability. The overriding plate has not been incorporated in these experiments. However, the influence of the subducting plate on the state of stress at the contact between the overriding plate and the subducting plate can be deduced

Experiment Number	Horizontal velocity v_{hs} for experiments (cm/hr)	Buoyancy number F for experiments	Horizontal velocity v_{hs} for nature (cm/yr)	Buoyancy number F for nature
9	0	∞	1	0.415
	3	0.828	2	0.207
	6	0.414	3	0.138
	9	0.276	5	0.083
19	11	0.228	7	0.059
13	26	0.096	9	0.046
15	42	0.060	11	0.038
17	63	0.040	13	0.032
18	78	0.032	15	0.028

Table 10-1. Individual properties for experiments discussed in the text and comparison to nature.

from the migration of the hinge. Backward migration of the hinge would induce tensional stresses in the overriding plate and thus would promote extension in the overriding plate (i.e. back-arc extension). Forward migration of the hinge would induce compressional stresses in the overriding plate and would therefore promote shortening in the overriding plate.

10.3. Results

10.3.1. Slab geometry during sinking

Diagrams showing the evolution of the slab during subduction for various experiments with a different applied horizontal velocity have been plotted in Fig. 10-3. Below the evolution of each experiment plotted in Fig. 10-3 will be briefly described.

For experiment 9 with $v_{hs} = 0$ cm/hr (Fig. 10-3a), the evolution of the slab geometry is relatively simple. The slab initially sinks and rolls back with an increasing slab-dip angle until it is approximately vertical. When the slab tip hits the horizontal discontinuity (the bottom of the box), the slab folds backward and is subsequently draped over the horizontal discontinuity during slab rollback. During this stage the slab attains a relatively constant dip angle of ~ 60-65°.

For experiment 19 with a low horizontal velocity ($v_{hs} = 11$ cm/hr) (Fig. 10-3b), the slab sinks with an increasing dip-angle and shows hinge-advance during the first five minutes of the experiment followed by hinge-retreat. When the slab-tip reaches the bottom, the tip is overturned, resulting in the formation of a recumbent fold. This is followed by the backward draping of the slab over the discontinuity at a slab dip angle of ~ 70°.

For experiment 13 with an intermediate horizontal velocity ($v_{hs} = 26$ cm/hr) (Fig. 10-3c), the slab sinks with an increasing dip-angle and shows hinge-advance during the first six minutes of the experiment followed by hinge-retreat. When the slab-tip reaches the bottom, the tip is overturned, resulting in the formation of a recumbent fold. This is followed by the draping of the slab over the discontinuity and the formation of another recumbent fold in a late stage. The average slab dip angle is ~ 80-90°.

For experiment 17 with a high horizontal velocity ($v_{hs} = 63$ cm/hr) (Fig. 10-3d), the slab sinks with an increasing dip-angle and shows hinge-advance during the first seven minutes of the experiment followed by hinge-retreat. Phases of hinge-retreat are interchanged with phases of hinge-advance. This results in the horizontal piling and folding of the slab on top of itself. The average slab dip angle is ~ 80-100°.

For experiment 18 with a very high horizontal velocity ($v_{hs} = 78$ cm/hr) (Fig. 10-3e), the slab sinks with an increasing dip-angle, which becomes overturned. The hinge is mainly advancing and is being draped forward over the discontinuity. The average slab dip angle is ~ 80-100°.

From the experiments, three different subduction modes with accompanying slab geometry can be recognised: (1) slow to intermediate v_{hs} resulting in fast to intermediate hinge-retreat and a backward draping slab geometry (experiment 9 and 19); (2) fast v_{hs} resulting in slow hinge-migration or stable hinge and a slab piling geometry (experiment 17); (3) very fast v_{hs} resulting in hinge-advance and a forward draping slab geometry (experiment 18).

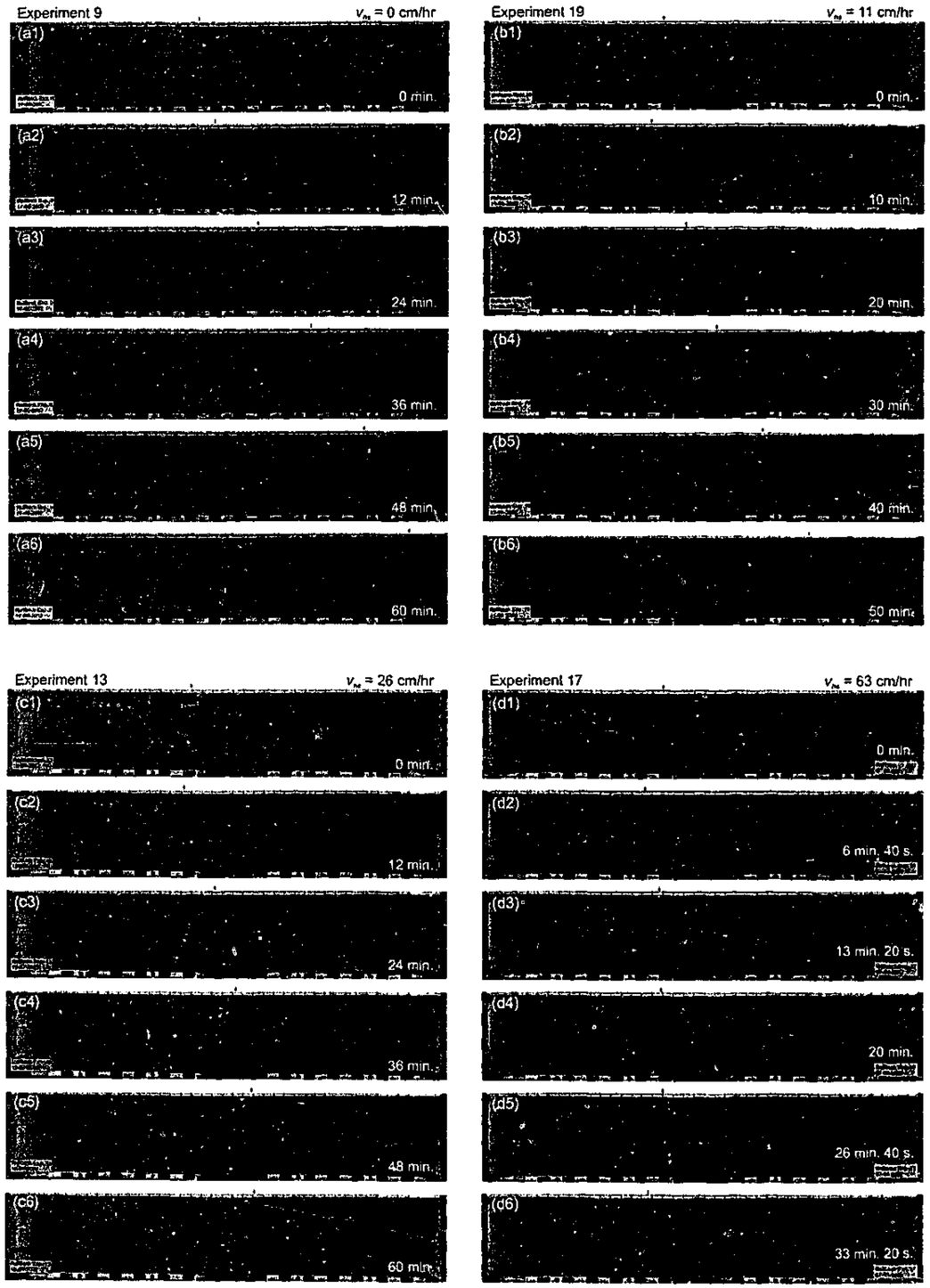

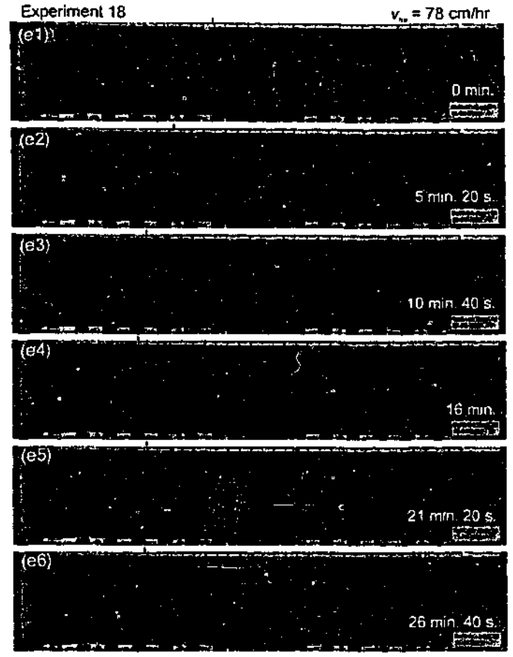

Fig. 10-3 (previous page and above). Cross-section photographs showing geometrical evolution of slab during subduction for five experiments with different applied horizontal velocity (v_{bs}). (a) Experiment 9, (b) experiment 19, (c) experiment 13, (d) experiment 17 and (e) experiment 18. Box length is 70 cm for scale. Black ticks indicate location of hinge.

10.3.2. Slab kinematics

The kinematics of subduction for the experiments discussed in the previous section has been illustrated in Fig. 10-4. For experiments 9 and 19, the kinematics is dominated by backward oriented sinking vectors (Fig. 10-4a,b). In addition, one can observe the differential displacement of passive particles in the horizontal surface part of the subducting plate with increasing horizontal displacement from right to left (this can best observed in Fig. 10-4a). This indicates that the surface part of the plate is being extended and pulled into the subduction zone by the sloping part of the slab. Contemporaneously, the subhorizontal part of the slab resting on top of the discontinuity is also being displaced horizontally, indicating that it is being pushed by the sloping part of the slab. Thus, at the same time that the surface part of the plate is pulled into the subduction zone, the part resting on top of the discontinuity is pushed forward. For experiment 13, the sinking vectors are oriented slightly backward to subvertical (Fig. 10-4c). For experiment 17, the kinematics is dominated by vertically oriented sinking vectors (Fig. 10-4d). The subhorizontal part resting on top of the discontinuity for experiment 13 and 17 appears to be stable. For experiment 18, the kinematics is dominated by forward oriented sinking vectors subparallel to the slab (Fig. 10-4e). The subhorizontal part resting on top of the discontinuity is moving backward, with displacement vectors oriented subhorizontal and parallel to the slab. In this experiment, the slab appears to be part of a convection cell, in which the slab part resting on top of the discontinuity is part of the return flow.

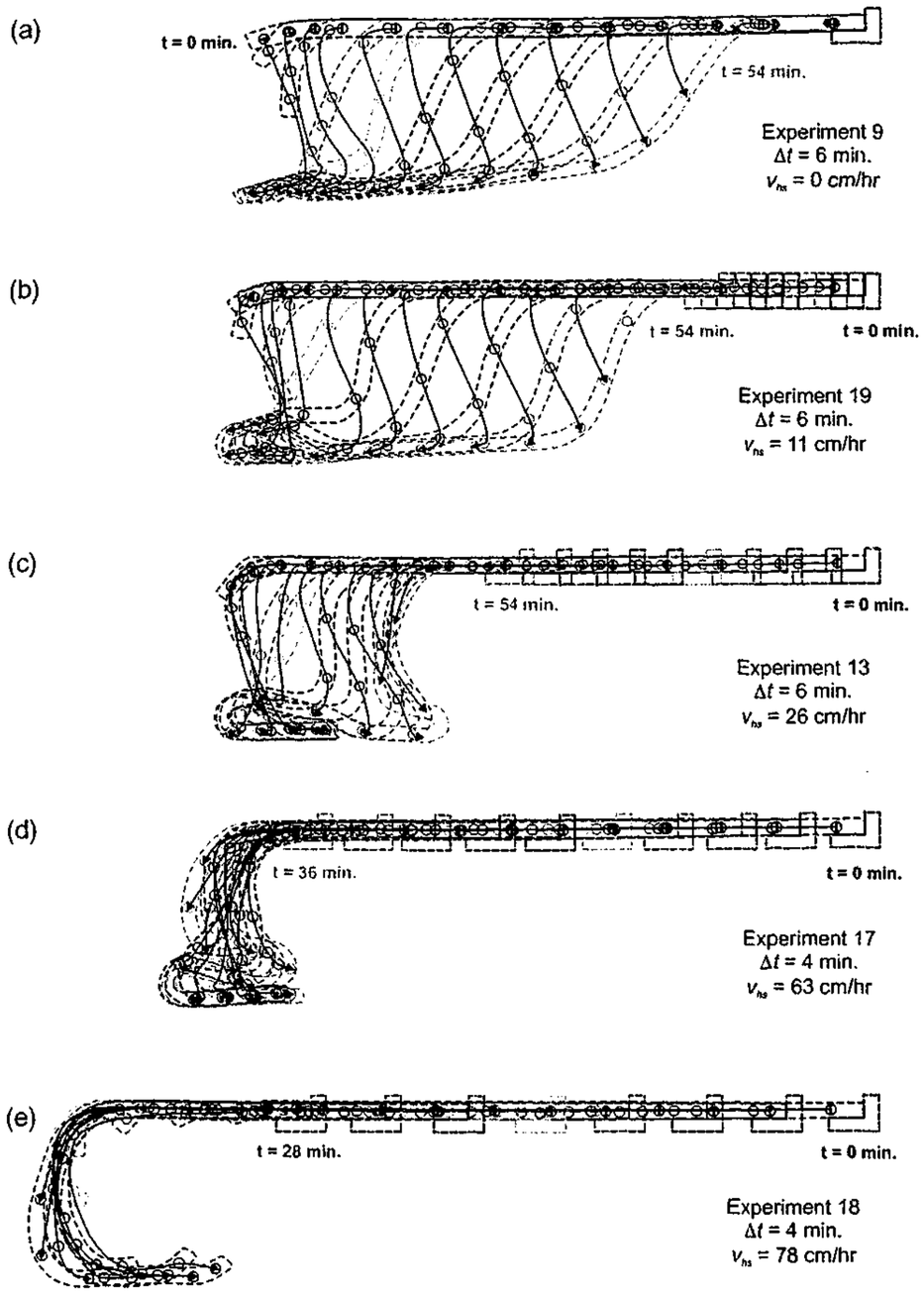

Fig. 10-4. Diagrams illustrating kinematic behaviour of slab and passive particles located on the side of the slab for five experiments with different applied horizontal velocity. Time-step (Δt) between successive stages differs for experiments.

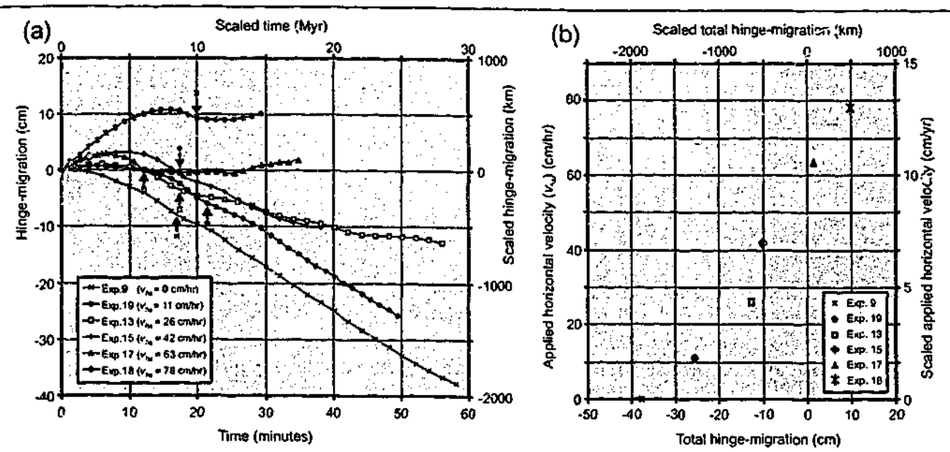

Fig. 10-5. (a) Hinge-migration versus time for six experiments with different applied horizontal velocities. Arrows indicate time when slab tip hits discontinuity. Positive sloping curve indicates hinge-advance, while negative sloping curve indicates hinge-retreat. (b) Total hinge-migration observed in experiments versus applied horizontal velocity for six experiments. The data suggest that hinge-retreat decreases with increasing applied horizontal velocity.

10.3.3. Hinge-migration during subduction

The hinge-migration for six experiments with different applied horizontal velocity is plotted in Fig. 10-5a. A negative sloping curve points to hinge-retreat. From this diagram it appears that the horizontal velocity suppresses hinge-migration. All experiments except experiment 9 show an initial stage of hinge-advance followed by hinge-retreat. Experiment 13, 15 and 17 show the most complicated hinge-migration curves owing to the interaction between the slab and the lower discontinuity with several phases of folding of the slab on top of the discontinuity. A folding event at the lower discontinuity generally coincides with a distinct reduction in retreat velocity. With a relatively low v_{hs} (experiment 9 and 19), the hinge-migration is rather smooth with initially an exponential increase in hinge-migration until the slab tip hits the bottom of the box, followed by a decrease, and then a slight increase towards a steady-state linear retreat. With an intermediate v_{hs}, the hinge-migration is more episodic in behaviour with periods of fast and slow hinge-retreat, a stable hinge or hinge-advance (experiment 13, 15, 17). For a relatively high v_{hs}, the hinge is mainly advancing with an intermittent period of hinge-retreat (experiment 18). The total hinge-migration has been plotted against the applied horizontal velocity in Fig. 10-5b, indicating that the total hinge-retreat decreases with increasing applied horizontal velocity.

10.3.4. Hinge-migration versus strain rate in the surface part of the plate

In Fig. 10-6 the strain rate in the surface part of the subducting plate has been plotted and compared to the hinge-migration for two experiments. For both experiments, the shape of the strain rate curve is similar and the point of maximum strain rate coincides with the point when the slab tip reaches the bottom of the box, i.e. the point of maximum hinge-retreat velocity. For experiment 13, this maximum strain rate is an extensional strain rate, while for

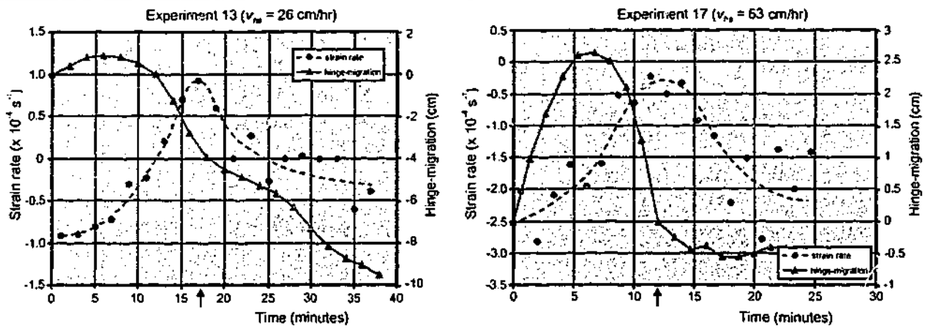

Fig. 10-6. Diagrams illustrating strain rate in the surface part of subducting plate and hinge-migration for two experiments. Positive strain rate points to extension. Negative sloping hinge-migration curve points to hinge-retreat. Arrows indicate time when slab tip hits discontinuity.

experiment 17, this is still a shortening strain rate. The difference in maximum and minimum strain rate for both experiments is in the order of ~ 2×10^{-4} s^{-1}.

The increase in strain rate in the initial stage of the experiments can simply be explained by the increase in length of the slab during subduction, which results in an increase in slab pull. The difference in maximum strain rate between both experiments is simply explained by the difference in applied horizontal velocity, which induces shortening and compression in the plate. This velocity is higher for experiment 17 and therefore suppresses the slab pull force, which would induce tension and extension in the horizontal part of the plate. Interestingly, the experiments show that hinge-retreat does not imply a tensional state of stress in the surface part of the plate, since the strain rate is negative (shortening) for the entire duration of experiment 17. Also, for experiment 13, between 6 and 12 minutes, hinge-retreat coincides with a shortening stain rate.

10.4. Discussion

10.4.1. Comparison with nature

10.4.1.1. v_{hs} versus v_{hm}

Northrup et al. [1995] argued that the convergence velocity decreased from 13 cm/yr in the Late Cretaceous to a minimum of 4 cm/yr in the Middle Eocene and that the timing of slow convergence roughly coincided with periods of back-arc extension in the overriding plate. For the following argumentation it will be assumed that a reduction of convergence velocity can be mainly accredited to a reduction in v_{hs} of the Pacific plate (since the absolute velocity of the Eurasian plate was very low [*Jolivet and Faccenna*, 2000]). The velocities 13 cm/yr and 4 cm/yr in nature correspond to ~ 78 cm/hr and ~ 29 cm/hr in the experiments respectively, and are thus comparable to experiments 18 and 13 respectively. Experiment 18 was dominated by hinge-advance, promoting shortening in the overriding plate. In contrast, experiment 13 was dominated by hinge-retreat, promoting extension in the overriding plate. Thus, the experimental results support the hypothesis that a reduction in convergence velocity along the

East Asian margin from the Late Cretaceous to Middle Eocene could have facilitated slab retreat, which would have caused the onset back-arc extension in the Eurasian plate.

For the Mediterranean region, the African absolute motion decreased from ~ 3 cm/yr before ~ 30 Ma to a minimum of ~ 1 cm/yr since 10 Ma [*Jolivet and Faccenna*, 2000]. According to *Jolivet and Faccenna* [2000], this slowdown in absolute motion would have initiated rollback of the subducting African plate in the Mediterranean region, which resulted in back-arc extension and formation of several basins in the Mediterranean. The absolute velocities of Africa correspond to ~ 22 cm/hr and ~ 7 cm/hr in the experiments, respectively. Experiments with velocities close to these are experiment 9, 13 and 19. All three experiments are dominated by hinge-retreat, although experiment 13 and 19 do show a stage of hinge-advance during the initial stage of subduction. Thus, our experiments do not support the idea of *Jolivet and Faccenna* [2000] that a slowdown of the absolute motion of Africa would have been responsible for the formation of the Mediterranean back-arc basins. A more likely cause for the initiation of hinge-retreat and back-arc extension in the Mediterranean region can be found in the behaviour of the hinge during progressive subduction, as has been observed for experiment 13 and 19 (Fig. 10-5a). Slab rollback during convergence can be initiated only after a considerable amount of slab has been subducted to create a substantial negative buoyancy force to pull down the slab and to cause rapid slab retreat. Similar ideas have also been suggested by *Faccenna et al.* [2001a].

10.4.1.2. Slab dip angle

The experiments indicate that the slab dip angle increases with decreasing hinge-retreat and increasing v_{hs} (Table 10-2). A similar relation can also be implied for several actively retreating slabs in nature (as can be implied from the opening up of their adjoining back-arc basins) (Table 10-3). Subducting plates with a relatively low v_{hs} and relatively high hinge-retreat velocity have a relatively low slab dip angle, such as the Hellenic slab with $\alpha \approx 55°$ and the Ionian slab with $\alpha \approx 70°$. In contrast, subducting plates with a relatively high v_{hs} and relatively low hinge-retreat velocity have a relatively high slab dip angle, such as the Pacific slab subducting along the Mariana arc with $\alpha \approx$ 80-90°. Another interesting example is the Tonga-Kermadec arc, along which the retreat velocity increases dramatically from south (~ 2 cm/yr) to north (~ 16 cm/yr). This seems to correlate with the slab dip angle, which decreases from south with $\alpha \approx$ 70-80° to north with $\alpha \approx 50°$. Obviously, there are other factors that have

Experiment Number	Total hinge-migration (cm)	Average hinge-migration velocity v_{hm} (cm/hr)	Hinge-migration number *HM*	Average slab dip angle
9	- 37.8	-39.1	0.085	60-65°
19	- 25.7	-31.2	0.068	70°
13	- 12.8	-13.7	0.030	80-90°
15	- 10.2	-16.1	0.035	80-90°
17	1.6	2.8	-0.006	80-100°
18	9.9	20.1	-0.044	80-100°

Table 10-2. Some experimental results. Note that average hinge-migration velocity has been calculated by dividing the total hinge-migration (Fig. 10-5b) by the duration of the experiment. The resulting values are somewhat misleading, since the hinge-migration velocity changed significantly during the duration of each experiment (see Fig. 10-5a). Negative hinge-migration indicates hinge-retreat.

Arc	v_{hs} (cm/yr)	F	v_{hm} (cm/yr)	HM	Average slab dip angle
Hellenic arc	~ 1.3 (1)	~ 0.319	~ -3.0 - -3.5 (2)	~ 0.039 - 0.046	55° (3)
Calabrian arc	~ 1.3 (1)	~ 0.319	~ -6 from 5-0 Ma (4)	~ 0.078	70° (5)
Scotia arc	~ 2.2 (6,7)	~ 0.188	~ -5.7 (8)	~ 0.074	70° (9)
Tonga-Kermadec arc	~ 10 (7)	~ 0.041	~ -15.9 in north (10)	~ 0.207	~ 50° (9)
			~ -9.1 in central north (10)	~ 0.118	~ 55-60° (9)
			~ -1.5- -2.0 in south (11)	~ 0.020 - 0.026	~ 70-80° (9)
Mariana arc	~ 10 (7)	~ 0.041	~ -3.0 - -4.3 (12)	~ 0.039 - 0.056	80-90° (9,13)

Table 10-3. Hinge-retreat velocity versus convergence velocity and horizontal velocity of the subducting plate. Hinge-migration has been deduced from rate of back-arc opening. References: 1—*Jolivet and Faccenna* [2000]; 2—*Kahle et al.* [1998] and *McClusky et al.*, [2000]; 3— *Spakman et al.* [1988]; 4—*Faccenna et al.* [2001b]; 5—*Lucente et al.* [1999]; 6—*Minster and Jordan* [1978]; 7—*Gripp and Gordon* [1990]; 8—*Barker* [1995]; 9—*Yamaoka et al.* [1986]; 10—*Bevis et al.* [1995]; 11—*Wright* [1993]; 12—*Martínez et al.* [2000]; 13— *Katsumata and Sykes* [1969].

an important control on the slab dip angle, such as the buoyancy of the slab and the velocity of the overriding plate [*van Hunen et al.*, 2002] (for example along the South American subduction zone), which have not been investigated in this study.

10.4.1.3. Slab geometry

From the experiments, three different slab geometries have been recognised: (1) the backward draping slab geometry (experiment 9 and 19); (2) the slab piling geometry (experiment 17); and (3) the forward draping slab geometry (experiment 18). These three slab geometries can also be recognised in nature. The backward draping slab geometry seems to be fairly common in nature and can be observed underneath the Kuril arc (Fig. 9-17) and underneath the Izu-Bonin arc [*van der Hilst*, 1991], as well as underneath the Calabrian and Carpathian arcs (Fig. 9-16) [*Wortel and Spakman*, 2000]. The slab geometry of the Ionian slab subducting underneath the Calabrian arc can be observed in Fig. 10-7a, which seems to have been draped on top of the upper-lower mantle discontinuity and shows a resemblance with experiment 9 and 19 (Fig. 10-3a,b). As in the experiments, $|v_{hm}| >> v_{hs}$, while v_{hs} is very low and v_{hm} is negative (retreating hinge) and relatively high (see Table 10-3). Tomographic images for the Mariana region show a subvertical slab signature, possibly folded and piled up on top of and partly penetrating the upper-lower mantle discontinuity (Fig. 10-7b). For the Mariana slab, $v_{hs} > |v_{hm}|$ and v_{hs} is relatively high, while the hinge is slowly retreating (see Table 10-3). This image resembles the slab piling geometry as observed in an advanced stage of experiment 17 (Fig. 10-3d). The similarity would probably have been more striking if the upper-lower mantle boundary in the experiments would not have been as rigid but more gradual in order to allow for partial penetration of the slab. Note, that in this slab configuration the slab would be most likely to penetrate through the upper-lower mantle discontinuity, due to concentration of buoyancy stresses [e.g. *Guillou-Frottier et al.*, 1995]. Finally, a tomographic image of the Tethyan slab, which subducted along the Eurasian

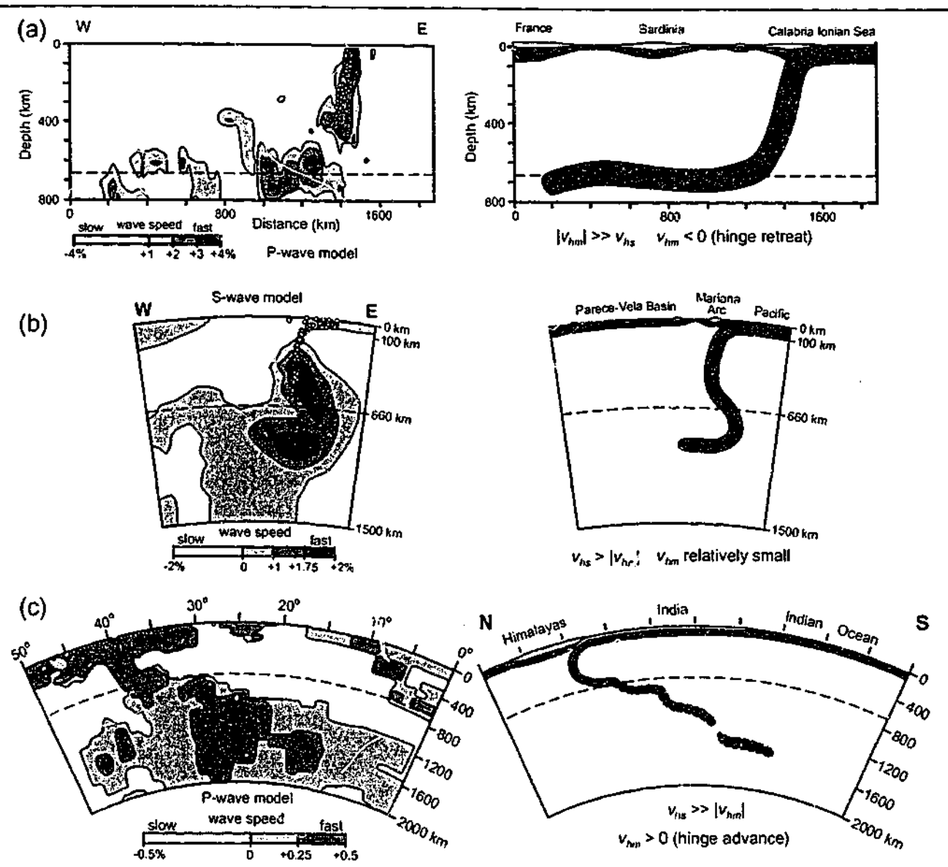

Fig. 10-7. Cross-sections of tomographic images (left) and their interpretation (right) across several subduction zones showing difference in slab geometry. (a) Image of the Ionian lithosphere subducting underneath the Calabrian arc in the Mediterranean (tomography simplified from *Lucente et al.* [1999]), showing a westward dipping slab, which is deflected horizontally near the upper-lower mantle discontinuity (compare to experiment 9 (Fig. 10-3a)). (b) Image of the Mariana subduction zone (tomography simplified from *Widiyantoro et al.* [1999]), showing a near vertical slab signature in the upper mantle and possible large-scale folding of the slab across the upper-lower mantle discontinuity (compare to experiment 17 (Fig. 10-3d)). (c) Image of the Tethyan slab subducting underneath the Himalayas (tomography simplified from *Van der Voo et al.* [1999]), showing a rollover slab structure (compare to experiment 18 (Fig. 10-3e)).

margin during India-Asia convergence, shows it has been draped forward (Fig. 10-7c), resembling the forward draping slab geometry as observed in experiment 18 (Fig. 10-3e). Interestingly, the hinge of the subducting Tethyan plate is one of the few examples which has been advancing instead of retreating during closure of the Tethys ocean [*Patriat and Achache*, 1984; *Kincaid and Olson*, 1987], as also observed during most of experiment 18. This hinge-advance might be mainly related to the high plate velocity of the Indian lithosphere (decreasing from 15-20 cm/yr in the Late Cretaceous to ~ 4.5 cm/yr at Present) [*Patriat and Achache*, 1984], which would promote hinge-advance instead of hinge-retreat, as also observed in experiment 18.

10.4.1.4. Episodic nature of hinge-migration

The experiments show that hinge-migration is not a steady state process due to interaction of the slab with the upper-lower mantle discontinuity. For relatively slow horizontal velocities, hinge-retreat is relatively steady. With increasing horizontal velocity, the hinge-migration becomes more episodic and phases of hinge-retreat alternate with phases of hinge-stability or hinge-advance. Such slab behaviour could explain the episodic nature of some back-arc basins, which stopped opening up for unclear reasons. In the Western Mediterranean, the opening of the Liguro-Provencal Basin from 30 to 16 Ma was followed by a period of tectonic quiescence in the back-arc region. Back-arc opening resumed during opening of the Tyrrhenian Basin from 10 Ma to Present [*Faccenna et al.*, 2001b]. In the Western Pacific, opening of the Parece-Vela Basin from 31 to 15 Ma [*Kobayashi and Nakada*, 1979] was followed by a period of tectonic quiescence in the back-arc region. Overriding plate extension resumed during opening of the Mariana Trough from 10 Ma to Present [*Fryer*, 1996] and rifting in the Izu-Bonin arc from 2 Ma to Present [*Taylor et al.*, 1992]. One of the most striking examples of episodic opening of back-arc basins is the Southwest Pacific region East of Australia. Here, a sequence of no less than five individual back-arc basins can be recognised, which can all be thought of as to have resulted from progressive eastward retreat of the Pacific slab during the latest Cretaceous to present. From west to east, these basins and adjoining bounding ridges are: the East Australian margin, the Tasman Sea, the Lord Howe Rise, the New Caledonia Basin, the Norfolk Ridge, the Norfolk Basin, the Three Kings Ridge, the South Fiji Basin, the Colville Ridge, the Havre Trough and the Kermadec-Tonga Ridge. The relation between slab interaction with the upper-lower mantle discontinuity and episodic hinge-migration has been suggested before for a fixed subducting plate (v_{hs} = 0) [*Funiciello et al.*, 2000, 2002; *Faccenna et al.*, 2001b]. As suggested from the work presented in here, the episodic behaviour of the hinge is dramatically amplified for $v_{hs} > 0$ (e.g. compare experiment 9 with other experiments in Fig. 10-5a).

10.4.2. Comparison with other dynamic models

The influence of hinge-migration on the geometry of the slab has been investigated previously in fluid dynamical laboratory experiments [*Griffiths et al.*, 1995; *Guillou-Frottier et al.*, 1995]. The experimental results with a single mantle layer design of *Griffiths et al.* [1995] and *Guillou-Frottier et al.* [1995] show that for a stationary hinge, the slab attains a vertical dip angle and is folded on top of itself at the base of the experimental box as observed for experiment 17 (Fig. 10-3d). The authors also concluded that the slab dip increases with decreasing hinge-retreat rate, similar to the experimental results described here (Table 10-2). If a hinge-migration number HM is defined, then this will allow a comparison between experiments with a non-stationary hinge (modified from *Griffiths et al.* [1995]):

$$HM = -(v_{hm}\eta_m)/(L^2 g \Delta\rho) \qquad (10\text{-}4)$$

It should be remembered, though, that the hinge-migration rate in the experiments described by *Griffiths et al.* [1995] and *Guillou-Frottier et al.* [1995] was constant and pre-imposed instead of allowed to evolve naturally as for the experiments described in this chapter. The experiments presented in here show that the hinge-migration rate is highly variable through time (Fig. 10-5a). Only a steady state retreat velocity was obtained in experiment 9 and 19

after the slab tip had hit the bottom of the box. To obtain the HM numbers for the experiments, the average hinge-retreat velocity (see Table 10-2) has been used in equation (10-4). This is somewhat misleading, since the hinge-migration velocity has been shown to be highly variable. However, at least it gives an indication of HM for each experiment.

With $HM < 0.12$ (small hinge-retreat velocity), *Griffiths et al.* [1995] concluded that the motion is stable with a constant slab dip-angle of 45-70° and horizontal draping of the slab over the bottom of the box. All the experiments presented in here belong to this category. Observed slab dips were higher from 60-90°. For $HM > 0.12$ (high hinge-retreat velocity), *Griffiths et al.* [1995] concluded that the motion is unstable, with oscillation of the slab dip during retreat up to ~ 25°. No experiments were conducted which resulted in $HM > 0.12$. Experiment 9 with the highest retreat velocity and v_{hs} = 0 cm/hr had a $HM \approx 0.085$.

Comparison of the experimental results with numerical simulations is somewhat more difficult, since most of these simulations are performed in two-dimensional space. For example, *Gurnis and Hager* [1988] conducted numerical simulations of subduction in a two-dimensional box. The subduction hinge was allowed to migrate by applying a periodic boundary condition at the sides of the box, such that the fluid could flow out of one side of the box and into the other. Although it can be questioned if such a boundary condition is realistic when compared to flow in the Earth's mantle, the numerical results did show similarities to the experiments presented in this chapter. The slab dip angle increased during the initial stage of subduction up to 90°, followed by bending of the slab near the upper-lower mantle discontinuity and a decrease in slab dip angle, as also observed in the analogue experiments.

The results of two-dimensional numerical simulations by *Houseman and Gubbins* [1997] are somewhat different from the results presented in here, related to the difference in boundary conditions. The mantle surrounding the slab entered the calculations only through the boundary conditions on the slab ends and its upper and lower surface. This resulted in a subvertical slab in all their experiments, in contrast with the experiments presented in here. In most experiments, a v_{hs} was applied and in a small number of experiments an additional v_{hm} was applied, which was 25% of v_{hs}. The experiments including hinge-retreat produced a horizontal slab segment resting on top of the upper-lower mantle boundary, as observed in experiment 9. A stable hinge produced either a folded pile on top of the discontinuity, in agreement with the results from experiment 17, but also a forward folded slab, as observed in experiment 18. In experiment 18, however, the hinge was allowed to migrate and migrated forward.

10.4.3. Kinematic models of subduction

The kinematics of subduction has been debated since the advent of the theory of plate tectonics. Five models can be thought of for the sinking kinematics of the slab into the sub-lithospheric mantle (Fig. 10-8). These include the forward sinking model with an advancing hinge, the slab-parallel sinking model with a stable hinge [e.g *Jacoby*, 1973], the forward sinking model with a retreating hinge, the vertical sinking model with a retreating hinge [e.g. *Dvorkin*, 1993] and the backward sinking model with a retreating hinge [e.g. *Elsasser*, 1971]. From geometry alone, it can be concluded that the first four of these models require either slab parallel extension or horizontal displacement of the surface part of the subducting lithosphere. In the last model, such extension or displacement is not required if the slab sinking vector sinks at an angle $\beta = (180° - \alpha) / 2$ (where α is the subduction angle).

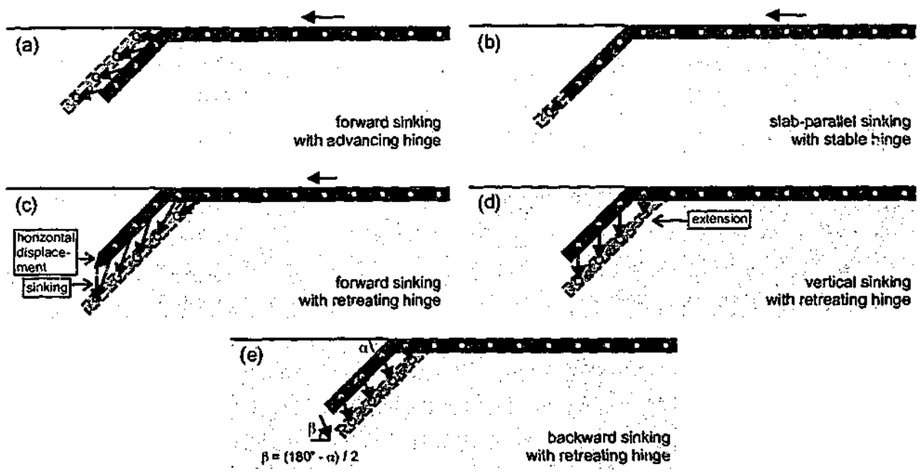

Fig. 10-8. Simplified diagrams showing five possible scenarios for slab subduction kinematics. In (a) the hinge is advancing, in (b) the hinge is stable and in (c), (d) and (e) the hinge is retreating. (a) Forward sinking model with advancing hinge, (b) slab-parallel sinking model (inspired by *Jacoby* [1973]), (c) forward sinking model with retreating hinge, (d) vertical sinking model (inspired by *Dvorkin* [1993]), and (e) backward sinking model (inspired by *Elsasser* [1971]). Scenarios (a), (b), (c) and (d) require either slab-parallel extension or horizontal displacement of the horizontal part of the subducting plate to accommodate slab-parallel component of displacement. Examples of horizontal displacement of the subducting plate are shown in (a), (b) and (c), while example of extension is shown in (d). Backward sinking at an angle $\beta = (180° - \alpha) / 2$ as shown in (e) does not require any slab parallel extension or horizontal displacement of the surface part of the subducting plate.

The experiments indicate that all five of these models might be applicable to the kinematics of subduction, depending on the magnitude of v_{hm} and v_{hs}. For a relatively low v_{hs} (experiment 9 and 19, Fig. 10-4a,b) the hinge is retreating and backward sinking is dominant (Elsasser model, Fig. 10-8e). The sinking vector was dipping ~ 70° in experiment 9 (Fig. 10-4a) and ~ 65° in experiment 19 (Fig. 10-4b), which is close but a little on the high side compared to the one predicted from their average dip angle with $\beta \approx 60°$ (experiment 9, $\alpha \approx 60°$) and 55° (experiment 19, $\alpha \approx 70°$). This discrepancy results from extension of the surface part of the plate in experiment 9 and the applied piston push in experiment 19. The Elsasser scenario is for example most likely for the slabs subducting underneath the Hellenic arc, Calabrian arc and Scotia arc. In these settings, the absolute motion of the subducting plate is relatively small compared to the hinge-migration rate (Table 10-3) and F and HM numbers are comparable to the numbers for experiments 9 and 19 (Table 10-2). For an intermediate to high v_{hs} and a smaller hinge-migration (experiment 13 and 17, Fig. 10-4c,d) the vertical sinking model is more applicable, with sinking vectors oriented subvertical (Fig. 10-8d). This scenario is probably applicable to the Mariana subduction zone. With a very high v_{hs} (experiment 18, Fig, 4e) the slab sinking vectors are oriented forward, subparallel to the dip of the slab (Fig. 10-8a,b). This scenario could be applicable to the Tethyan slab subducting underneath the Himalayas.

10.5. Conclusions

In this chapter, fluid dynamical experiments have been presented to shed new light on the influence of the absolute velocity of the subducting plate on the hinge-migration velocity, the mode of subduction and the slab geometry. Results show that an increase in applied horizontal velocity results in a decrease in total hinge-migration. In addition, phases of hinge-retreat alternate with phases of hinge-stability or hinge-advance for relatively high horizontal velocities due to interaction of the slab with the upper-lower mantle discontinuity. Such slab behaviour could explain the episodic nature of some back-arc basins, which stopped opening for unclear reasons.

Three different subduction modes with accompanying slab geometry can be recognised from the experimental results: (1) Slow to intermediate v_{hs} (corresponding to ~ 0 - 2 cm/yr in nature), which results in fast to intermediate hinge-retreat, backward sinking vectors and a backward draping slab geometry. (2) Fast v_{hs} (corresponding to ~ 3 - 11 cm/yr), which results in slow hinge-migration or a stable hinge, subvertical sinking vectors and a slab piling geometry. With increasing horizontal velocity the hinge-retreat decreases and the slab becomes increasingly folded on top of the discontinuity. At a relatively high v_{hs} (corresponding to ~ 11 cm/yr in nature) hinge-migration is suppressed to such an extent that the average hinge-migration is close to zero, and the slab forms a folded pile on top of the upper-lower mantle discontinuity. (3) Very fast v_{hs} (corresponding to ~ $\geq$ 13 cm/yr in nature), which results in hinge-advance, forward oriented sinking vectors and a forward draping slab geometry.

It can be concluded that forward hinge-migration of an oceanic lithosphere would require a very high absolute velocity of the subducting plate. Most plates are currently moving at a lower velocity, except for the Cocos plate (~ 14.3 cm/yr in a hotspot reference frame [*Gripp and Gordon*, 1990]). This could explain why most subduction zones are currently either stable or retreating [e.g. *Garfunkel et al.*, 1986]. However, it should be kept in mind that other physical factors also play an important role in determining the nature of the hinge, including slab width, slab density and slab thickness (see also Chapter 9).

FOREWORD CHAPTER 11

In this chapter, the role of the lithospheric slab in transmitting tensional stresses to the horizontal surface part of the subducting plate is investigated. The ideas, which initiated the research outlined in this chapter, were inspired by the results of experiments presented in Chapter 9. In these experiments, it was observed that the horizontal surface part of the subducting plate is pulled into the subduction zone by the lithospheric slab.

The ideas outlined in this chapter have solely resulted from the author and the experiments described in this chapter have been done by the author alone. Stimulating discussions with Jean Braun, Chris Kincaid, Ross Griffiths, Gordon Lister, Louis Moresi, Roberto Weinberg and Mike Sandiford are acknowledged.

CHAPTER 11

Quantifying the effective slab pull force as a driving mechanism for plate tectonics

Abstract

In plate tectonics, the main driving forces are though to be the ridge push force and the slab pull force. The ridge push force is relatively easy to quantify from the excess potential energy of mid-oceanic ridges. To the contrary, the slab pull force resulting from the negative buoyancy of the subducted slab compared to the surrounding mantle is difficult to quantify since an unknown part of this force is being absorbed by shearing resistance in the mantle. Although it has been proposed that the lithosphere can act as a stress guide, it is unclear how much of the slab pull force can be transmitted towards the horizontal part of the subducting lithosphere. Therefore, fluid dynamical experiments have been executed to quantify the effective slab pull force (F_{ESP}) with respect to the total negative buoyancy force of the slab (F_{BF}). The experiments investigate the kinematic and dynamic evolution of a dense, high-viscosity plate (representing a subducting oceanic lithosphere) subducting into a less dense low-viscosity layer (representing the sub-lithospheric upper mantle). The results show that F_{ESF} increases with increase in slab length and subduction angle. It can constitute up to ~ 8 % of F_{BF}. Most of F_{BF} is used to displace sub-lithospheric mantle due to slab retreat, for bending of the subducting lithosphere near the trench and for shearing between the subducting plate and the surrounding mantle.

11.1. Introduction

Plate tectonic theory provides explanations for numerous large-scale features on Earth, such as mid-oceanic ridges, trenches and mountain chains. In this theory, new oceanic crust is created at mid-oceanic ridges, is transported away from the ridges and is subsequently destroyed at trenches, where the oceanic crust subducts underneath the overriding plate back into the mantle [*McKenzie*, 1969]. The theory of plate tectonics is well established and accepted by most geoscientists, but it is only a kinematic theory. Considerable debate remains about the driving forces of the tectonic plates and their relative importance. Some important forces that have been proposed are the slab pull force, the ridge push force, the trench suction force and the mantle drag force (Fig. 11-1) [*Elsasser*, 1967; 1969; 1971; *Forsyth and Uyeda*, 1975; *Chapple and Tullis*, 1977]. It is generally thought that the main driving forces for plate tectonics are the ridge push force resulting from the excess potential energy of mid oceanic ridges and the slab pull force resulting from the negative buoyancy of the subducted slab compared to the surrounding mantle [*Forsyth and Uyeda*, 1975]. The ridge push force is relatively easy to quantify and is though to be in the order of 2-3 $\times$ 10^{12} N/m [*Harper*, 1975; *Lister*, 1975; *Parsons and Richter*, 1980; *Meijer and Wortel*, 1992; *Bott*, 1993]. To the contrary, the slab pull force is difficult to quantify since an unknown part of this force is being absorbed by shearing resistance in the mantle, in which the slab is subducting [*Forsyth and Uyeda*, 1975; *Chapple and Tullis*, 1977; *Richardson*, 1992]. Although it has been proposed that the lithosphere can act as a stress guide [*Elsasser*, 1967, 1969, 1971], it is not

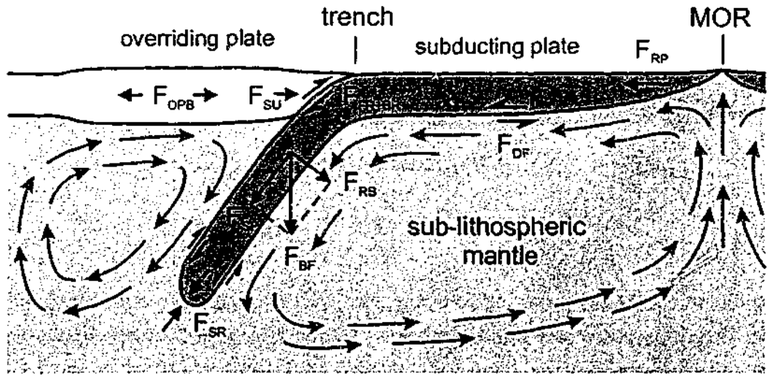

Fig. 11-1. Several forces acting on lithospheric plates. Some forces act as driving agents of plate motion (F_{BF}, F_{RP}, F_{SU} and F_{OPB}) and others resist plate motion (F_{DF}, F_{SR}, F_{FR+BR}, F_{TF}). F_{BF} = buoyancy force slab, F_{SP} = slab pull force, F_{RB} = rollback force, F_{RP} = ridge push, F_{SU} = trench suction, F_{OPB} = overriding plate buoyancy force, F_{SR} = slab resistance to subduction, F_{DF} = drag force, F_{SR+BR} = shear resistance subduction boundary and bending resistance, F_{TF} = transform fault resistance. F_{TF} not shown in diagram.

immediately clear how and how much of the slab pull force can be transmitted across the subduction hinge towards the horizontal part of the subducting lithosphere.

To gain better insights into the driving forces of plate tectonics, various physical, analytical and numerical modelling techniques have been used to investigate specific aspects of plate tectonics. In this chapter, results of three-dimensional fluid dynamical experiments are presented to quantify the contribution of lithosphere subduction in driving tectonic plates and mantle convection. The experiments simulate subduction of oceanic lithosphere into the upper mantle. With these experiments, the magnitude of the effective slab pull force (part of slab pull force that is transmitted from the sinking slab across the subduction hinge towards the horizontal surface part of the subducting lithosphere) is quantified and compared with the total negative buoyancy force of the slab. Other forces resisting subduction, including the inertial force, the bending force, the shearing force and the rollback induced convection force are also investigated and quantified.

11.2. Fluid dynamical model

The model consists of a high-viscosity high-density layer (silicone putty, ρ_{sp} = 1520 kg/m^3, Newtonian viscosity with $\eta_{sp} \approx 2.4 \times 10^4$ Pa·s) overlying a low-viscosity lower-density layer (glucose syrup, ρ_m = 1420 kg/m^3, Newtonian viscosity with $\eta_m \approx 1.3 \times 10^2$ Pa·s), comprised in a rectangular box (Fig. 11-2). The upper layer is 1.3-2.0 cm thick and simulates a ~ 65-100 km thick subducting oceanic lithosphere. The lower layer is ~ 12 cm thick and simulates ~ 600 km of sub-lithospheric upper mantle. The viscosity ratio $\eta_{sp} / \eta_m \approx 185$ and $\Delta\rho$ = 100 kg/m^3, which is similar to values suggested for the natural prototype [*Cloos*, 1993; *Houseman and Gubbins*, 1997; *Conrad and Hager*, 1999; *Becker et al.*, 1999; *Faccenna et al.*, 2001a]. The applied timescale ratio t(model) / t (nature) is ~ 3.81 x 10^{-12} (1 hour in model represents ~ 30 Myr in nature). With such a time-scale ratio at hand, and the scale relationship (see Chapter 9, section 9.2):

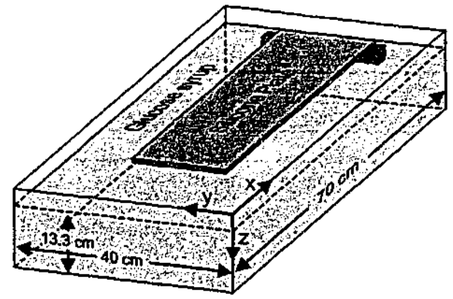

Fig. 11-2. Configuration of the modelling apparatus and experimental set-up with a fixed trailing edge boundary condition. For the experiments, a plate of silicone putty, representing oceanic lithosphere, is floating on top of glucose syrup, representing the sub-lithospheric upper mantle, down to the bottom of the box, representing the 670 km discontinuity. During an experiment, the first two cm of the tip of the silicone plate are depressed at an angle of 30° into the glucose syrup to initiate a subduction instability.

$$\frac{\eta^a}{\eta^n} \approx \frac{\Delta\rho^a t^a x^a}{\Delta\rho^n t^n x^n} \qquad (11\text{-}1)$$

this results in an upscaled sub-lithospheric upper mantle viscosity of 1.36 × 10^{20} Pa·s, which is similar to the natural prototype of 10^{19} - 10^{21} Pa·s [*Artyushkov*, 1983, *Ranalli*, 1995]. Thus, it can be concluded that gravitational forces and viscous forces are properly scaled with respect to each other and closely reflect the force balance present in the natural prototype.

The overriding lithosphere is effectively removed from the model in order to track the convection in the syrup enforced by the subducting plate. To visualise this forced convection, passive neutrally buoyant particles have been randomly distributed in the syrup. To visualise deformation in the subducting plate, passive markers have been placed at regular intervals at the side and on the top surface of the silicone slab. The experiments are isothermal. Although this is a rough simplification, it has been argued that the thermal field of the slab is attained to the first order during subduction into the upper mantle [*Wortel*, 1982].

At the start of the experiment, a subduction instability is produced at the tip of the slab. The system is then allowed to evolve naturally. The trailing edge of the plate is fixed to the sidewall of the box (Fig. 11-2). Some physical properties of the experiments discussed in the text are plotted in Table 11-1.

11.3. Results

The results of experiment 9 will be briefly described. For a more complete description see Chapter 9. Results show that hinge-line migration for the entire duration of experiment 9 is regressive (Fig. 9-2a, 9-3a). The sinking of the slab and the hinge-retreat increase exponentially during the free sinking of the slab (Fig. 11-3a,c), with a gradual increase in slab dip up to ~ 90°. The retreat velocity and sinking velocity increase approximately linearly with time (Fig. 11-3b,d). The total velocity of the slab also increases approximately linearly with time (Fig. 11-3e). Thus, it can be concluded that slab displacement is dependent on time to the power two. The acceleration of the slab is constant and can be deduced from the slope of the velocity curve. Subsequently, the migration slows down when the slab tip hits the

Experiment number	Slab density ($\times 10^3$ kg/m^3)	Slab width (cm)	Slab thickness (cm)	Trailing edge
8	1.52	10	1.3	Fixed
9	1.52	15	1.3	Fixed
10	1.52	20	2.0	Fixed

Table 11-1. Physical properties of experiments discussed in the text.

discontinuity, followed by a renewed increase until a steady state is reached (see Chapter 9). The slab geometry is relatively simple with a horizontal slab segment draped over the bottom of the box (670 km discontinuity) (Fig. 9-2a, 9-3a).

Slab retreat results in forced convection of sub-lithospheric mantle from underneath the slab towards the mantle wedge. The experimental results show that flow underneath the slab tip is

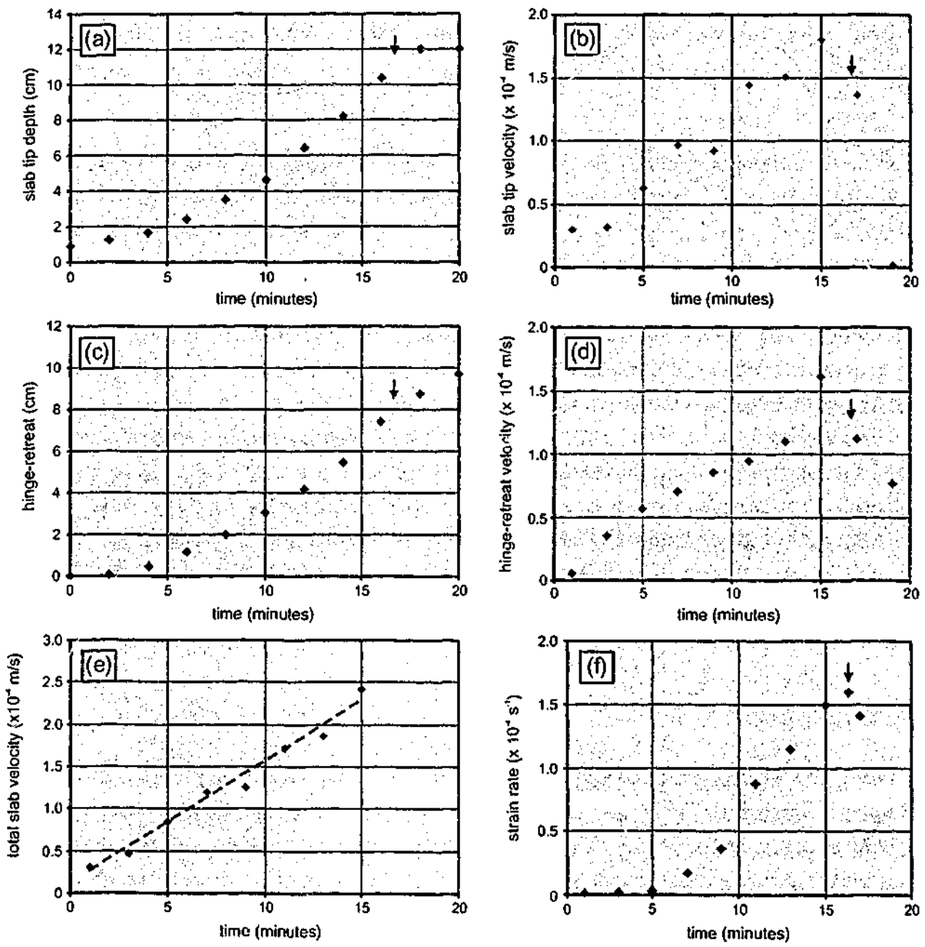

Fig. 11-3. Some results of experiment 9 for the first stage of subduction (from initiation of subduction until the slab tip hits the lower discontinuity). (a) Sinking displacement of the slab tip, (b) sinking velocity, (c) hinge-retreat, (d) hinge-retreat velocity, (e) total slab velocity (deduced from the sinking velocity and the hinge-retreat velocity), and (f) extensional strain rate in the horizontal surface part of the subducting plate. Arrow indicates time when the slab tip hits the lower discontinuity.

negligible and almost all flow occurs laterally around the edges of the slab. This lateral flow forces the hinge-line of the subducting lithosphere to attain a convex shape towards the direction of retreat. During the free sinking of the slab, it transmits tensional stresses to the horizontal part of the subducting lithosphere as can be deduced from the observed extensional strain in the surface part of the lithosphere (for example, see differential horizontal displacement of passive markers in surface part of subducting plate in Fig. 9-4a,b). The strain rate in the surface part of the lithosphere has been plotted versus time in Fig. 11-3f.

11.4. Force balance

11.4.1. Driving force

The driving force for subduction, slab deformation and subduction induced convection in the experiments results entirely from the negative buoyancy force of the slab (F_{BF}) due to the density contrast between the slab and sub-lithospheric mantle. This can be expressed as follows:

$$F_{BF} = V_s(\rho_{sp} - \rho_m)g \qquad (11\text{-}2)$$

where V_S is the slab volume, ρ_{sp} is the density of the subducting plate, ρ_m is the mantle density and g is the acceleration due to gravity. F_{BF} can only be calculated for the time from initiation of subduction until the time when the slab tip hits the bottom of the box. From this stage onwards, the negative buoyancy of the slab is partly supported by the bottom of the box, the magnitude of which is unknown. The magnitude of the buoyancy force has been plotted in Fig. 11-4a. The total slab pull force (F_{SP}) is the component of the F_{BF} parallel to the slab dip [*Forsyth and Uyeda*, 1975]:

$$F_{SP} = F_{BF}\sin(\alpha) \qquad (11\text{-}3)$$

where α is the slab dip angle.

11.4.2. Resistive forces

The driving force is balanced by the resistive forces. These include the inertial force (F_I) (due to accelerated sinking of the slab), the viscous shear friction force between the subducting plate and surrounding mantle (F_{SH}) (resulting from plate parallel displacement), the bending force (F_{Be}) (to bend subducting plate into the subduction zone), the corrected extension force (F_{CE}) (to extend the horizontal part of plate) and the forced convection force (F_C) (to drive convection in the mantle resulting from rollback of the slab). The force balance can be expressed as follows:

$$F_{BF} = F_I + F_{SH} + F_{Be} + F_{CE} + F_C \qquad (11\text{-}4)$$

11.4.2.1. Inertial force

From the resistive forces, the inertial force (F_I) for the slab can be expressed as follows:

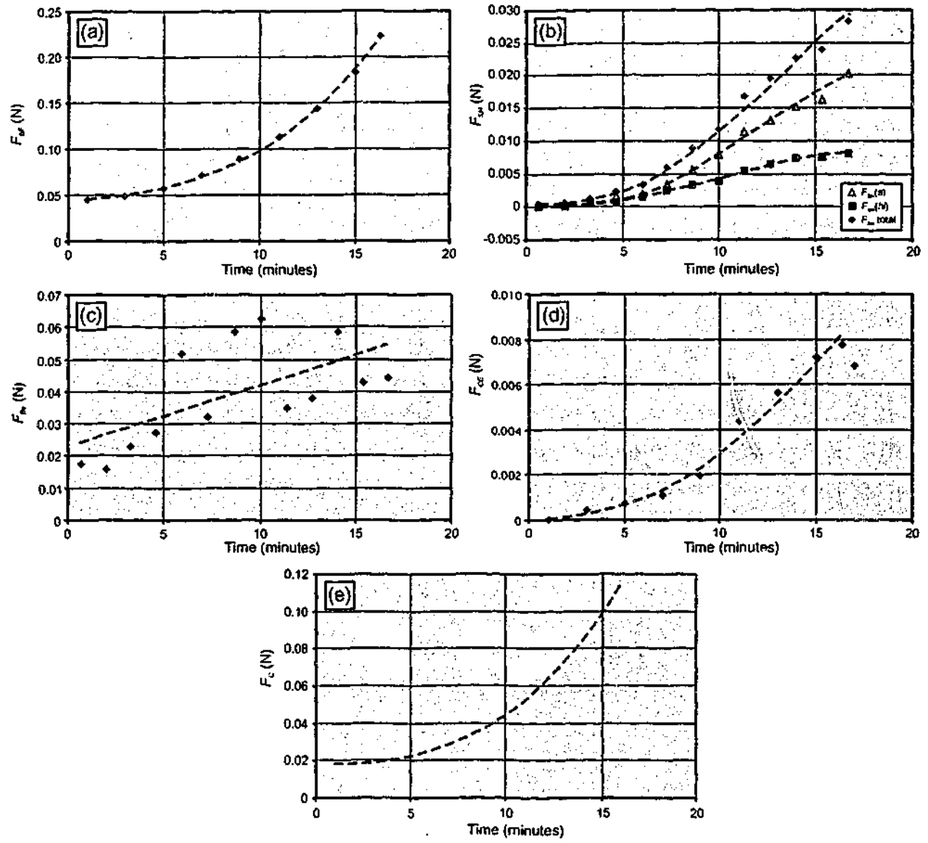

Fig. 11-4. Diagrams illustrating the development of the most important driving and resistive forces in experiment 9, with (a) buoyancy force of the slab (F_{BF}), (b) shear force between the subducting plate and surrounding mantle material (F_{SH}), (c) bending force of the subducting plate (F_{Be}), (d) corrected extension force in the surface part of the subducting plate (F_{CE}), and (e) slab induced convection force (F_C). Note that the plot for F_C did not result from direct measurements but was quantified indirectly from the four other forces.

$$F_I = V_s \rho_{sp} a_s \tag{11-5}$$

where a_s is the acceleration of the slab, which can be expressed as:

$$a_s = \sqrt{\left(\frac{d^2x}{dt^2}\right)^2 + \left(\frac{d^2z}{dt^2}\right)^2} \tag{11-6}$$

where x is oriented horizontal and z is vertical. The horizontal component can be deduced from the hinge-retreat velocity (Fig. 11-3d), while the vertical component can be deduced from the sinking velocity of the slab tip (Fig. 11-3b). The resulting acceleration of the slab can be deduced from the slope of the curve plotted in Fig. 11-3e. Comparison between the magnitude of a_s (~ 2.4×10^{-7} m/s^2) in equation (11-5) and the magnitude of g (9.8 m/s^2) in equation (11-2) indicates that F_{BF} is ~ 2.7×10^6 times larger than F_I and therefore negligible.

Even if it is realised that subduction of the slab also accelerates the surrounding glucose syrup which should also be incorporated to quantify the total inertial force, F_I remains negligible with respect to F_{BF}. For example, if an upper estimate is made for the volume of glucose syrup accelerated by the slab of ~ $25 \times V_s$, then the difference between F_{BF} and F_I is still ~ 1.1×10^5. Thus, it can be concluded that the inertial force can be neglected in this force balance calculation.

11.4.2.2. Shear friction force

The shear friction force (F_{SH}) results from shearing between the subducting plate and the sub-lithospheric mantle due to displacement parallel to the subducting plate. F_{SH} can be expressed as follows (modified from *Jacoby* [1973]):

$$F_{SH} = \eta_m A_s \frac{d}{d\zeta}\left(\frac{d\xi}{dt}\right) + \eta_m A_{hl} \frac{d}{d\zeta}\left(\frac{d\xi}{dt}\right) \tag{11-7}$$

where η_m is the viscosity of the sub-lithospheric mantle; A_s is the surface area of the slab; ζ indicates a direction in the xz-plane; everywhere perpendicular to the subducting plate; ξ indicates a direction in the xz-plane, everywhere parallel to the subducting plate; and A_{hl} is the surface area of the horizontal surface part of the lithosphere in contact with the glucose syrup. The first part of equation (11-7) ($F_{SH}(s)$) quantifies the shear force between the slab and the surrounding mantle, while the second part ($F_{SH}(hl)$) quantifies the shear force between the horizontal surface part of the subducting plate and the underlying mantle. $F_{SH}(hl)$ contributes to a part of the effective slab pull force F_{ESP}. The magnitude of $F_{SH}(s)$ and $F_{SH}(hl)$ as well as the total shear force F_{SH} have been plotted in Fig. 11-4b. It can be observed that the most of the total shear force results from the slab, because the $d\xi/dt$ component of displacement is largest for this part. The $d\xi/dt$ component of displacement is relatively small in the surface part of the plate and only results from the extension in this part of the plate.

11.4.2.3. Bending force

The bending force (F_{Be}) results from the resistance of the subducting plate to bend into the subduction zone and can be calculated from the observed strain rate in the slab due to bending:

$$F_{Be} = \eta_{sp} \dot{\varepsilon}_s W_{sp} T_{sp} \tag{11-8}$$

where η_{sp} is the subducting plate viscosity; $\dot{\varepsilon}_s$ is the strain rate in the slab due to bending; W_{sp} is the plate width; and T_{sp} is the plate thickness. During bending, the outer convex part of the slab experiences extension while the inner concave part experiences shortening. Both regions are divided by a neutral surface. From the maximum extensional strain rate at the top surface and a maximum shortening strain rate at the bottom surface, an average strain rate for the thickness of the slab has been estimated, from which F_{Be} has been calculated. F_{Be} has been plotted in Fig. 11-4c. Although the development of F_{Be} through time is not as straightforward as for most of the other forces in Fig.11-4, the data do suggest that F_{Be} increases with time, possibly linearly.

11.4.2.4 Corrected extension force

Part of the effective slab pull force (F_{ESP}) can be attributed to the extension force (F_E), which can be deduced from the extensional strain rate in the surface part of the subducting plate. The tensional stress in the plate can be expressed as follows [*Benes and Davy*, 1996]:

$$\sigma_1 - \sigma_3 = \eta_{sp}\dot{\varepsilon}_h \tag{11-9}$$

where σ_1 is the maximum principal stress; σ_3 is the minimum principal stress; and $\dot{\varepsilon}_h$ is the strain rate in the horizontal surface part of the subducting lithosphere. From equation (11-9) F_E can be deduced and can be expressed as follows:

$$F_E = \eta_{sp}\dot{\varepsilon}_h W_{sp} T_{sp} \tag{11-10}$$

The magnitude of F_E has been plotted for experiment 8, 9 and 10 in Fig. 11-5. In order to obtain the true extensional force in the surface part of the subducting plate, F_E has to be corrected for the compression resulting from the buoyancy force between the glucose syrup and the silicone plate (F_{BG}). This compression was evident from shortening observed in the early stage of the development for the experiments plotted in Fig. 11-5 and would reduce the extensional strain rate in the horizontal part of the plate. This buoyancy force could be expressed as follows:

$$F_{BG} = W_{sp}\Delta E_p \tag{11-11}$$

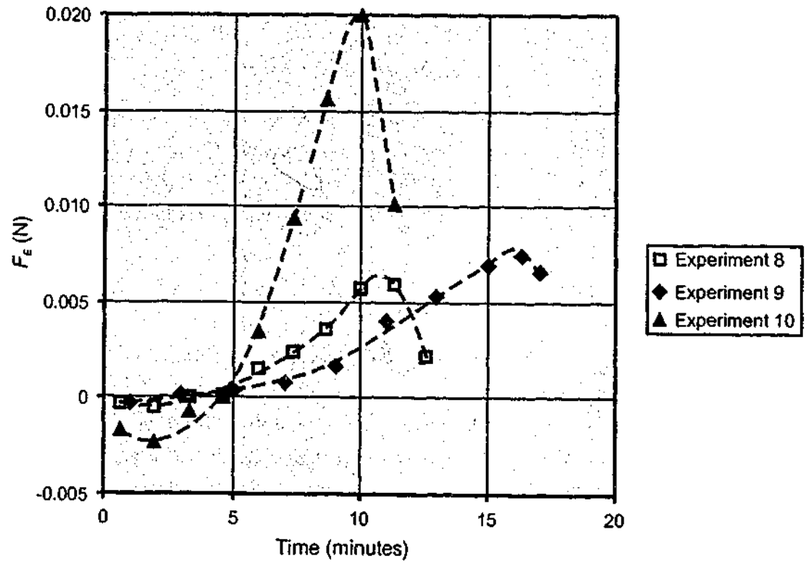

Fig. 11-5. Diagram illustrating development of extensional force in the surface part of the subducting plate (F_E) for three experiments. In all three experiments, density of silicone plate and glucose mantle are the same (1520 kg/m^3 and 1420 kg/m^3 respectively). In experiment 8, the plate is 1.3 cm thick and 10 cm wide. In experiment 9, the plate is 1.3 cm thick and 15 cm wide. In experiment 10, the plate is 2.0 cm thick and 20 cm wide.

with:

$$\Delta E_p = \frac{\rho_{sp}}{2\rho_m} g (T_{sp})^2 (\rho_{sp} - \rho_m) \tag{11-12}$$

where ΔE_p is the potential energy difference between the glucose syrup and the silicone plate. For the appropriate values for experiment 9 one would calculate $W_{sp}\Delta E_p \approx 0.0133$ N. This should result in a shortening strain rate of $W_{sp}\Delta E_p / \eta_{sp} W_{sp} T_{sp} \approx 2.9 \times 10^{-4}$ s^{-1} in the surface part of the subducting plate. This is a relatively high shortening strain rate (compare for instance with strain rates plotted in Fig. 11-3f) and is not observed, not even in the earliest stage of the experiments. It is more likely that F_{BG} is much smaller in magnitude due to a slight surface tension in the glucose syrup, which keeps the silicone plate floating higher than would be predicted from the density contrast alone. The F_{BG} for experiment 9 plotted in Fig. 11-5 has been estimated from the shortening strain rate in the early stage of the experiment. The corrected extensional force (F_{CE}) for experiment 9 has been plotted in Fig. 11-4d.

11.4.2.5. Forced convection force

The forced convection force (F_C) is the most difficult force to quantify, since the convection pattern due to slab retreat is rather complex and the flow velocity in the mantle with respect to depth is unknown. It can be quantified indirectly from equation (11-4), since all the other components in this equation are at least roughly known. The resulting graph has been plotted in Fig. 11-4e. From this graph it can be seen that F_C increases in a similar fashion as F_{BF}, F_{SH} and F_{CE}. This is not surprising, since the volume of mantle participating in convection probably increases in close correlation with the increase in depth of penetration of the slab tip (see Fig. 11-3a).

11.4.3. Effective slab pull force

The effective slab pull force (F_{ESP}) can be calculated for experiment 9 from the corrected extension force (F_{CE}) and the shear friction force at the base of the horizontal surface part of the subducting plate ($F_{SH}(hl)$). F_{ESP} can be expressed as follows:

$$F_{ESP} = F_{CE} + F_{SH}(hl) \tag{11-13}$$

F_{ESP} has been plotted in Fig. 11-6a. The F_{ESP} / F_{BF} ratio has been plotted in Fig. 11-6b to compare the magnitude between the two forces. It can be observed that F_{ESP} increases exponentially with time. The F_{ESP} / F_{BF} ratio increases exponentially with time until ~ 7 minutes, when slope of the curve decreases and reaches a maximum value at ~ 11 minutes and then remains constant. The maximum for F_{ESP} / F_{BF} is approximately equal to 0.08 at a subduction depth of ~ 5.6 cm (corresponding to ~ 310 km in nature).

11.5. Discussion and conclusions

From experiments with a fixed and free trailing edge it can be concluded that the subducting slab can transmit tensional stresses to the horizontal part of the lithosphere (see also Chapter 9). Thus, the lithosphere acts as a stress guide and effectively drags the surface

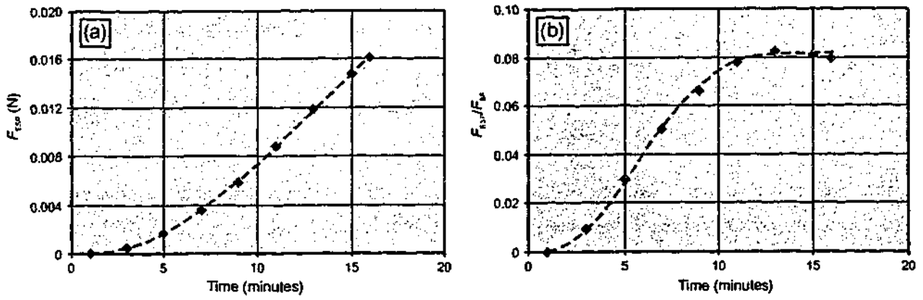

Fig. 11-6. Diagrams illustrating (a) the development of the effective slab pull force (F_{ESP}) and (b) the development of the effective slab pull force to buoyancy force ratio (F_{ESP} / F_{BF}).

part of the subducting lithosphere into the subduction zone, as predicted earlier [*Elsasser*, 1967, 1969, 1971]. Quantification of the effective slab pull force shows that it constitutes up to ~ 8% of the total negative buoyancy force of the slab. If this would be related to nature, with a relatively steeply dipping slab ~ 700 km long and 100 km thick, with a density contrast between slab and surrounding mantle of $\Delta\rho \approx$ 80 kg/m^3, then the effective slab pull force would be up to ~ 4.4 × 10^{12} N/m. This makes the effective slab pull force comparable in magnitude but somewhat larger with respect to the ridge push force (~ 2-3 × 10^{12} N/m), as already suggested by torque-balance calculations for global plate tectonic motions [*Forsyth and Uyeda*, 1975; *Richardson*, 1992] and empirical relationships between plate boundaries (boundary type, plate age and type) and plate velocity [*Forsyth and Uyeda*, 1975]. These two forces are both thought to be the main driving mechanisms in plate tectonics [*Forsyth and Uyeda*, 1975].

In addition, the results also indicate that the maximum 8% of stress transmission is only reached after the slab has reached a depth of ~ 310 km. Thus, for subducting slabs with a small subduction depth, the effective slab pull force might be considerably smaller than the ridge push force, since both the effectiveness of stress transmission and the total negative buoyancy force of the slab are smaller. From the remainder of the negative buoyancy force of the slab, a large part is dissipated in the mantle due to slab rollback induced mantle convection. The magnitude of this force increases with respect to the total negative buoyancy force from ~ 40% in the early stage of subduction to ~ 54% just before the slab starts to interact with the upper-lower mantle discontinuity. The rest is dissipated in bending forces to bend the subducting plate into the subduction zone (decreasing from ~ 59% to ~ 28% of the negative buoyancy force) and in shear forces between the slab and the surrounding mantle (increasing from ~ 1% to ~ 10% of the negative buoyancy force).

CHAPTER 12

Conclusions

12.1. Introduction

In this thesis, the processes of subduction rollback, arc formation and back-arc extension have been investigated by means of analogue models (scaled physical laboratory experiments). The conclusions that can be drawn from the research outlined in this thesis are manifold. First and foremost it is concluded that subduction rollback, arc formation and back-arc extension are truly three-dimensional processes. This stems from the fact that the slabs, which play a primary role in these processes, are segmented structures with a limited lateral extent. During rollback of a slab segment with a limited lateral extent, this results in arc-shaped subduction zones and back-arc basins with a limited extent along the trench axes. The slab rollback induced deformation pattern in the back-arc region and the convection pattern in the sub-lithospheric mantle are complex and vary significantly along the trench-line. Thus, to investigate the kinematics and dynamics of subduction rollback, arc formation and back-arc extension in physical and numerical models, it is of primary importance to do experiments in three-dimensional space.

All the experiments described in this thesis have been executed in three-dimensional space. The results demonstrate that even in these simplified models, the geometries, structures and flow patterns that result in these experiments are complex and intrinsically three-dimensional. In the back-arc extension experiments, the change in geometry of the spreading boundary from initially rectilinear to progressively more arc-shaped resulted in arc-parallel changes in structural style in the overriding plate. In the subduction experiments, rollback of slabs with a limited lateral extent induced complex three-dimensional convection patterns in the mantle with lateral convection around the slab edges. This flow forced the slab into an arcuate shape, convex towards the direction of retreat.

12.2. Reflection on key questions

In the first chapter of this thesis, three key questions were formulated, which have played a central role in the research undertaken. These questions have been addressed in theoretical, experimental and regional studies outlined in the thesis. Below I will briefly summarise the answers to each of these three questions as can be concluded from the research presented in this thesis.

(1) *What is the influence of slab rollback and the formation of arc-shaped subduction zones on the overriding plate?*

It is concluded that the formation of arc-shaped subduction zones imposes significant strain on the overriding plate, resulting in back-arc extension. The style and localisation of deformation in the overriding plate depend to a large extent on the kinematic evolution of the subduction zone interface. Symmetrical boundary conditions such as radial and unidirectional arc migration result in symmetrical deformation in the overriding plate. Asymmetrical boundary conditions result in asymmetrical deformation in the overriding plate, with normal faults and graben structures striking at high angle to the strike of the arc. In addition, the

rheology and buoyancy force of the overriding plate have a significant influence on the deformation style of the overriding plate. A high buoyancy force and low brittle strength favour distributed deformation over a large area dominated by strike-slip faulting near the arc corners and in the back and normal faulting close to the arc. A low buoyancy force and high brittle strength favour localised deformation over a small area dominated by normal faulting close to the arc.

(2) *What drives rollback of the subducting slab and the formation of arc-shaped subduction zones?*
It is concluded that rollback can be driven by the negative buoyancy of the slab compared to the asthenosphere. Slab rollback was observed with a slab-upper mantle density contrast $\Delta\rho$ between 60 and 140 kg/m^3. Natural values for $\Delta\rho$ range between ~ 50 and ~ 100 kg/m^3. Slab rollback might be possible for smaller density contrasts, but this has not been investigated. Arc-shaped subduction zones can evolve from rectilinear subduction zones due to lateral flow of mantle material from underneath the slab around the slab edges towards the mantle wedge. Such flow forces the slab to attain a convex shape towards the direction of retreat and results in an arc-shaped trench at the surface. Density anomalies could also influence the formation of arc-shaped subduction zones, as evidenced by the spatial correlation between several buoyant irregularities on the subducting slab (such as aseismic ridges and buoyant plateaux) and arc cusps (for example the Caroline ridge and the Marcus-Necker ridge for the Mariana arc). This could lead to faster rollback of the denser part of the slab compared to the buoyant irregularities. However, this has not been investigated in this thesis but could be investigated in future research.

(3) *Which physical factors enhance subduction rollback?*
It is concluded that slab rollback is enhanced by an increase in density contrast between slab and sub-lithospheric mantle. Slab rollback is also enhanced for a relatively narrow slab, which facilitates flow of sub-lithospheric mantle material around slab edges. However, for a very narrow slab, shear stresses between the slab and the sub-lithospheric mantle slow down rollback. Slab rollback is also enhanced when the trailing edge of the subducting plate is stationary or moving relatively slow. Although not investigated in this thesis, slab rollback can be enhanced by the decrease in effective viscosity of the lithosphere and sub-lithospheric mantle. It is also suggested that the ease with which the retreating slab will tear from the surface part of the subducting plate will also influence the subduction rollback process.

12.3. Drawbacks of analogue models

In the research outlined in this thesis, conceptual models were tested with scaled analogue laboratory experiments. An advantage of this technique is that it can be readily applied in three-dimensional space. The three-dimensional approach in this research project was proven to be critical in investigating the processes of subduction rollback, arc formation and back-arc extension, because the experimental results are highly evolved in three-dimensional space. Trench-parallel continuity of structures or patterns across a particular model was not observed in any of the experiments.

All the modelling described in this thesis was purely mechanical. Difference in rheological behaviour of rocks due to change in temperature with depth was only incorporated by building models with an initially stratified set-up with layers with different rheological

properties. No thermal readjustment occurred during deformation in the experiments, which would influence the mechanical behaviour of the materials affected by these temperature changes. Such thermal readjustment does occur in nature and is important for large-scale processes such as rifting, back-arc spreading and subduction. Thus, some caution is warranted when applying the model results to natural examples.

12.4. Future perspective

In future research, it would be of significant value to do numerical simulations of subduction rollback, arc formation and back-arc extension with a similar design as the analogue simulations in order to compare the experimental results of both modelling techniques. An advantage of numerical simulations is that they are better suited to provide quantitative insights into specific geological problems compared to laboratory simulations. For example, the influence of the slab width on subduction rollback could be investigated more quantitatively for a large number of slab widths. A disadvantage, however, is that the resolution for numerical experiments executed in three-dimensional space is much reduced compared to physical experiments. For example, this might be a problem when investigating the structural evolution in the back-arc region during back-arc extension, for which the individual structures are relatively small when compared to the size of the back-arc basin itself. In any case, simulations of a particular process with both the numerical and physical modelling technique will provide a powerful tool to obtain new insights into the processes under investigation. In an initial stage of the investigation, three-dimensional mechanical simulations could be executed with a particular numerical code to see if there is a qualitative and quantitative agreement between the physical and numerical experiments. In a later stage of investigation, thermomechanical numerical experiments could be executed to make the models better scaled when applied to nature. However, this requires numerical codes to be able to cope with deformation in three-dimensions and still provide reasonable resolution. It might still be some time away before such numerical experiments provide outcomes with a resolution comparable to analogue experiments.

APPENDIX I

Scaling Theory

A I-1. Introduction

Analogue or scaled physical experiments are subjected to specific scaling rules. The theory of these rules for geological processes was first introduced by *Hubbert* [1937] and later also discussed by *Hubbert* [1951], *Ramberg* [1967], *Horsfield* [1977], *Shemenda* [1983], *Davy and Cobbold* [1991] and *Cobbold and Jackson* [1992]. According to *Hubbert* [1937], there are three similarity criteria, which have to be fulfilled, in order for the model to be properly scaled. These criteria include geometric similarity, kinematic similarity and dynamic similarity. An analogue model and a natural prototype are geometrically similar if all the corresponding lengths are proportional and all the corresponding angles within the bodies are equal. For kinematic similarity, the geometrically similar model and natural example have to undergo similar changes of shape and/or position, where the time required for any change in the model is proportional to the corresponding change in the prototype [*Ramberg*, 1967]. Dynamic similarity requires a similar distribution of driving forces (tectonic), body forces (gravitational) and resistive forces (frictional, viscous). This requires a similar distribution of density and rheology in both experiment and nature. In this thesis, the Earth's lithosphere and sub-lithospheric mantle have been simulated with brittle and viscous materials. Brittle behaviour of rocks has been simulated with dry granular material, which shows a Mohr-Coulomb type behaviour similar to rocks. The scaling rules for brittle material will be discussed in section A I-2. Viscous behaviour of rocks has been simulated with Newtonian viscous materials, which have a constant viscosity for the strain rates applied in the experiments. The scaling rules for viscous material will be discussed in section A I-3.

A I-2. Brittle material

Cauchy's equation of motion for a continuous medium, describing the balance of linear momentum is expressed by the following equation:

$$\rho \frac{D^2 x_i}{Dt^2} = \frac{\partial \sigma_{ij}}{\partial x_j} + \rho g_i \qquad (i,j = 1,2,3) \qquad \text{(aI-1)}$$

where ρ is the density, x is the position vector, t is the time, σ is Cauchy's stress tensor and g is the acceleration due to gravity. The suffixes refer to Cartesian vector and tensor components in a fixed spatial frame.

For slow motions, the only forces to be considered are body forces (due to gravity) and surface forces (stresses). Therefore, we neglect inertial forces, and the second derivative of x to time t in equation (aI-1) can be put to zero. Rearrangement of equation (aI-1) results in:

$$\partial \sigma_{ij} = -\rho g_i \partial x_j \qquad \text{(aI-2a)}$$

Integration of equation (aI-2a), with the boundary condition $\sigma_{ij} = 0$ at $x_j = 0$ (for lithospheric scaling, normal and shear stresses at the Earth's surface are negligible compared to stresses at depth) leads to:

$$\sigma_{ij} = -\rho g_i x_j \qquad \text{(aI-2b)}$$

Writing equation (aI-2b) for both the analogue model (superscript a) and the natural prototype (superscript n), and dividing the first by the last one leads to:

$$\frac{\sigma_{ij}^a}{\sigma_{ij}^n} = \frac{\rho^a g_i^a x_j^a}{\rho^n g_i^n x_j^n} \qquad \text{(aI-3)}$$

When the experiments are executed in a normal field of gravity, then gravity is the same for both the natural prototype and the model, and equation (aI-3) becomes:

$$\frac{\sigma_{ij}^a}{\sigma_{ij}^n} = \frac{\rho^a x_j^a}{\rho^n x_j^n} \qquad \text{(aI-4a)}$$

For the description of scaling rules for analogue experiments executed in an artificial field of gravity (e.g. centrifuge experiments), the reader is referred to *Ramberg* [1967] and *Peltzer* [1988]. When the density ratio is very close to unity equation (aI-4a) can be written as:

$$\frac{\sigma_{ij}^a}{\sigma_{ij}^n} = \frac{x_j^a}{x_j^n} \qquad \text{(aI-4b)}$$

Thus, for equation (aI-4b) stresses scale down by the same ratio as lengths. When natural rocks and model materials are considered to show frictional plastic behaviour, their principal stresses have to satisfy Coulomb's yield criterion [*Coulomb*, 1776]:

$$\tau = C + \mu\sigma_n = C + \tan(\phi)\sigma_n \qquad \text{(aI-5)}$$

or:

$$C - \tau = -\sigma_n \tan(\phi) \qquad \text{(aI-6)}$$

where τ is the shear stress, C is the cohesion, σ_n is the normal stress and ϕ is the angle of internal friction. Again, writing equation (aI-6) for both the analogue model and the natural prototype, and dividing the first by the last one results in:

$$\frac{C^a - \tau^a}{C^n - \tau^n} = \frac{\sigma_n^a \tan(\varphi^a)}{\sigma_n^n \tan(\varphi^n)} \qquad \text{(aI-7)}$$

Assuming that ϕ is the same in both the natural prototype and the model (which it should be if we want the strain in the model to resemble the strain in nature), equation (aI-7) can be written as:

$$\frac{C^a - \tau^a}{C^n - \tau^n} = \frac{\sigma_n^a}{\sigma_n^n} \qquad \text{(aI-8)}$$

Rewriting this equation:

$$C^a - \tau^a = (C^n - \tau^n)\frac{\sigma_n^a}{\sigma_n^n} \quad \Leftrightarrow \quad C^a = (C^n - \tau^n)\frac{\sigma_n^a}{\sigma_n^n} + \tau^a$$

$$\Leftrightarrow \quad C^a = C^n \frac{\sigma_n^a}{\sigma_n^n} - \tau^n \frac{\sigma_n^a}{\sigma_n^n} + \tau^a$$

Dividing by C^n leads to:

$$\frac{C^a}{C^n} = \frac{\sigma_n^a}{\sigma_n^n} - \frac{\tau^n \sigma_n^a}{C^n \sigma_n^n} + \frac{\tau^a}{C^n} \qquad \text{(aI-9)}$$

This leads to:

$$\frac{C^a}{C^n} = \frac{\sigma_n^a}{\sigma_n^n} \qquad \text{(aI-10)}$$

because:

$$-\frac{\tau^n \sigma_n^a}{C^n \sigma_n^n} + \frac{\tau^a}{C^n} = -\frac{\tau^n \sigma_n^a}{\sigma_n^n} + \tau^a = 0$$

This is true, because shear stresses scale down by the same ratio as normal stresses:

$$\frac{\tau^a}{\tau^n} = \frac{\sigma_n^a}{\sigma_n^n} \qquad \text{(aI-11)}$$

One can easily prove relationship (aI-11) by writing the stress tensor in matrix form:

$$\sigma_{ij} = \begin{pmatrix} \sigma_{11} & \sigma_{12} & \sigma_{13} \\ \sigma_{21} & \sigma_{22} & \sigma_{23} \\ \sigma_{31} & \sigma_{32} & \sigma_{33} \end{pmatrix} = \begin{pmatrix} \sigma_{11} & 0 & 0 \\ 0 & \sigma_{22} & 0 \\ 0 & 0 & \sigma_{33} \end{pmatrix} + \begin{pmatrix} 0 & \sigma_{12} & \sigma_{13} \\ \sigma_{21} & 0 & \sigma_{23} \\ \sigma_{31} & \sigma_{32} & 0 \end{pmatrix} = \sigma_n + \tau$$

Combining this with equation (aI-4a):

$$\frac{\sigma_{ij}^a}{\sigma_{ij}^n} = \frac{\rho^a x_j^a}{\rho^n x_j^n} = K \quad \Leftrightarrow \quad \sigma_{ij}^a = K\sigma_{ij}^n \qquad \text{(aI-12)}$$

where K is a constant.

$$\begin{pmatrix}\sigma_{11} & 0 & 0\\ 0 & \sigma_{22} & 0\\ 0 & 0 & \sigma_{33}\end{pmatrix}^a + \begin{pmatrix}0 & \sigma_{12} & \sigma_{13}\\ \sigma_{21} & 0 & \sigma_{23}\\ \sigma_{31} & \sigma_{32} & 0\end{pmatrix}^a = K\begin{pmatrix}\sigma_{11} & 0 & 0\\ 0 & \sigma_{22} & 0\\ 0 & 0 & \sigma_{33}\end{pmatrix}^n + K\begin{pmatrix}0 & \sigma_{12} & \sigma_{13}\\ \sigma_{21} & 0 & \sigma_{23}\\ \sigma_{31} & \sigma_{32} & 0\end{pmatrix}^n$$

This relation can only hold if:

$$\frac{\sigma_n^a}{\sigma_n^n} = K \;\wedge\; \frac{\tau^a}{\tau^n} = K \qquad \text{(aI-13)}$$

and therefore, equation (aI-11) is valid.
Combining (aI-12) and (aI-13) leads to:

$$\frac{\sigma_{ij}^a}{\sigma_{ij}^n} = \frac{\sigma_n^a}{\sigma_n^n} = \frac{\tau^a}{\tau^n} \qquad \text{(aI-14)}$$

Combining equation (aI-4a), (aI-10), and (aI-14) leads to:

$$\frac{\sigma_{ij}^a}{\sigma_{ij}^n} = \frac{\rho^a x_j^a}{\rho^n x_j^n} = \frac{C^a}{C^n} \qquad \text{(aI-15)}$$

From equation (aI-15) it can be observed that cohesion has to be scaled down with the same factor as stresses and the product of density and length scale down.

Cohesive strengths of sedimentary rocks in natural settings in the uppermost km's of the crust are typically ~5 MPa [*Horsfield*, 1977]. With a similar density in model and nature, and a length ratio of $x^a / x^n = 10^{-5}$ (1 cm in the model represents 1 km in nature) this would result in a cohesive strength for the material used in the models of $C^a \approx 50$ Pa. These values approximate the amount of cohesion of dry granular materials which can range between 0 Pa and ~100 - 250 Pa, depending on the amount of normal stress and the type of material [*Schellart*, 2000]. For lithospheric modelling, length ratios normally vary between 10^{-6} - 10^{-7} (1 cm in the model represents 10 - 100 km in nature). Values for cohesion of crustal and upper lithospheric rocks vary somewhere between 30 and 110 MPa, depending on the type of rock. Downscaling of these values, assuming a similar density in both the model and nature, leads to a downscaled cohesion of 30 - 110 Pa ($x^a / x^n = 10^{-6}$) to 3 - 11 Pa ($x^a / x^n = 10^{-7}$). Again, these values approximate values of cohesion for dry granular materials, experimentally determined by *Schellart* [2000], although the cohesion for the modelling materials (especially material with a high degree of angularity and a low degree of sphericity) is on the high side. Since dry granular materials display frictional plastic behaviour, which is comparable with the behaviour of rocks in nature, these materials are good analogues for analogue modelling of brittle deformation in the earth's crust and lithosphere.

A I-3. Viscous material

When viscous material is used in analogue modelling, the experiments become time-dependent. Therefore, time has to be properly scaled as well. Most of the viscous material used in analogue experiments (silicon putty and glucose syrup) have an (almost) Newtonian rheology, and therefore their dynamic behaviour can be described by the following equation [*Benes and Davy*, 1996]:

$$\sigma'_{ij} = \eta\dot{\varepsilon}_{ij} \qquad \text{(aI-16)}$$

where σ'_{ij} is the deviatoric stress tensor, η is the dynamic viscosity and $\dot{\varepsilon}_{ij}$ is the strain rate tensor. Writing equation (aI-16) for the analogue model and the natural situation and dividing the first by the last one results in:

$$\frac{\sigma'^a_{ij}}{\sigma'^n_{ij}} = \frac{\eta^a\dot{\varepsilon}^a_{ij}}{\eta^n\dot{\varepsilon}^n_{ij}} \qquad \text{(aI-17)}$$

Since strain rate is basically a velocity gradient over a length, it can be rewritten as follows [*Houseman and Molnar*, 1997]:

$$\dot{\varepsilon}_{ij} = \frac{1}{2}\left[\frac{\partial U_i}{\partial x_j} + \frac{\partial U_j}{\partial x_i}\right] \qquad \text{(aI-18a)}$$

where U is the velocity vector. For scaling purposes, equation (aI-18a) can be simplified by the following equation:

$$\dot{\varepsilon}_{ij} = \frac{\partial U_i}{\partial x_j} \qquad \text{(aI-18b)}$$

Rewriting equation (aI-18b) results in:

$$\dot{\varepsilon}_{ij}\partial x_j = \partial U_i \qquad \text{(aI-18c)}$$

Integration of equation (aI-18c) leads to the following:

$$\dot{\varepsilon}_{ij}x_j = U_i + C_1 \qquad \text{(aI-18d)}$$

where C_1 is a constant. At $x_j = 0$, the left hand side of equation (aI-18d) is zero and therefore the constant $C_1 = 0$. This has been illustrated graphically in Fig. aI-1. Here a slab is illustrated with length L at $t = 0$ and length $2L$ at $t = 1$. From this diagram it is clear that the velocity U increases linearly. Since velocity (U) and position (x) both increase linearly, the strain rate is constant along the entire length of the slab. Rewriting equation (aI-18d) yields the result:

$$\dot{\varepsilon}_{ij} = \frac{U_i}{x_j} \qquad \text{(aI-19)}$$

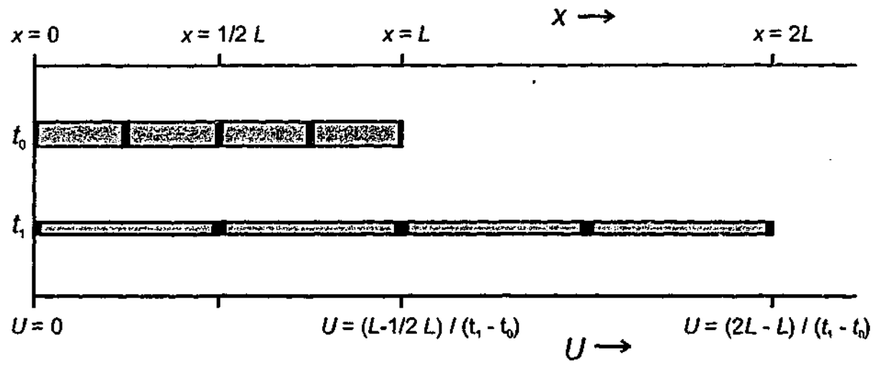

Fig. aI-1. Increase in length of a slab with length L at $t(0)$ to length $2L$ at $t(1)$.

Substitution of equation (aI-19) in equation (aI-17) leads to:

$$\frac{\sigma'^{a}_{ij}}{\sigma'^{n}_{ij}} = \left(\frac{\eta^a U^a_j}{\eta^n U^n_j}\right)\left(\frac{x^n_j}{x^a_j}\right) \qquad \text{(aI-20)}$$

By writing the stress tensor in a matrix form, one can prove that deviatoric stresses scale down by the same ratio as the total stresses, as well as the non-deviatoric stresses:

$$\sigma_{ij} = \begin{pmatrix} \sigma_{11} & \sigma_{12} & \sigma_{13} \\ \sigma_{21} & \sigma_{22} & \sigma_{23} \\ \sigma_{31} & \sigma_{32} & \sigma_{33} \end{pmatrix} = \begin{pmatrix} \sigma_{11}-\overline{\sigma}_n & \sigma_{12} & \sigma_{13} \\ \sigma_{21} & \sigma_{22}-\overline{\sigma}_n & \sigma_{23} \\ \sigma_{31} & \sigma_{32} & \sigma_{33}-\overline{\sigma}_n \end{pmatrix} + \begin{pmatrix} \overline{\sigma}_n & 0 & 0 \\ 0 & \overline{\sigma}_n & 0 \\ 0 & 0 & \overline{\sigma}_n \end{pmatrix} = \sigma'_{ij} + \sigma^*_{ij}$$

with:

σ^*_{ij} = non-deviatoric stress tensor

$$\overline{\sigma}_n = \frac{\sigma_{11}+\sigma_{22}+\sigma_{33}}{3}$$

Combining this with equation (AI-4a):

$$\frac{\sigma^a_{ij}}{\sigma^n_{ij}} = \frac{\rho^a x^a_j}{\rho^n x^n_j} = K \quad \Leftrightarrow \quad \sigma^a_{ij} = K\sigma^n_{ij} \qquad \text{(aI-21)}$$

where K is a constant. This leads to:

$$\begin{pmatrix} \sigma_{11}-\overline{\sigma}_n & \sigma_{12} & \sigma_{13} \\ \sigma_{21} & \sigma_{22}-\overline{\sigma}_n & \sigma_{23} \\ \sigma_{31} & \sigma_{32} & \sigma_{33}-\overline{\sigma}_n \end{pmatrix}^a + \begin{pmatrix} \overline{\sigma}_n & 0 & 0 \\ 0 & \overline{\sigma}_n & 0 \\ 0 & 0 & \overline{\sigma}_n \end{pmatrix}^a$$

$$= K\begin{pmatrix} \sigma_{11}-\overline{\sigma}_n & \sigma_{12} & \sigma_{13} \\ \sigma_{21} & \sigma_{22}-\overline{\sigma}_n & \sigma_{23} \\ \sigma_{31} & \sigma_{32} & \sigma_{33}-\overline{\sigma}_n \end{pmatrix}^n + K\begin{pmatrix} \overline{\sigma}_n & 0 & 0 \\ 0 & \overline{\sigma}_n & 0 \\ 0 & 0 & \overline{\sigma}_n \end{pmatrix}^n$$

This relation can only hold if:

$$\frac{\sigma'^{a}_{ij}}{\sigma'^{n}_{ij}} = K \;\wedge\; \frac{\sigma^{*a}_{ij}}{\sigma^{*n}_{ij}} = K \qquad \text{(aI-22)}$$

Combining (aI-21) and (aI-22) leads to:

$$\frac{\sigma^a_{ij}}{\sigma^n_{ij}} = \frac{\sigma'^{a}_{ij}}{\sigma'^{n}_{ij}} = \frac{\sigma^{*a}_{ij}}{\sigma^{*n}_{ij}} \qquad \text{(aI-23)}$$

Combining equation (aI-4a) and (aI-20) with equation (aI-23) results in:

$$\frac{\sigma^a_{ij}}{\sigma^n_{ij}} = \left(\frac{\eta^a U^a_i}{\eta^n U^n_i}\right)\left(\frac{x^n_j}{x^a_j}\right) = \frac{\rho^a x^a_j}{\rho^n x^n_j} \qquad \text{(aI-24)}$$

Rewriting equation (a-I-24) in terms of viscosity leads to:

$$\frac{\eta^a}{\eta^n} = \frac{\rho^a U^n_i \left(x^a_j\right)^2}{\rho^n U^a_i \left(x^n_j\right)^2} \qquad \text{(aI-25)}$$

Equation (aI-25) shows that the viscosity of analogue material compared to rocks in nature should be scaled down as the product of density, velocity and the square of length scale down. When velocity is replaced with distance over time then equation (aI-25) can also be written as:

$$\frac{\eta^a}{\eta^n} = \frac{\rho^a\left(x^n_i / t^n\right)\left(x^a_j\right)^2}{\rho^n\left(x^a_i / t^a\right)\left(x^n_j\right)^2} = \frac{\rho^a x^n_i t^a \left(x^a_j\right)^2}{\rho^n x^a_i t^n \left(x^n_j\right)^2} \quad \Rightarrow \quad \frac{\eta^a}{\eta^n} \approx \frac{\rho^a t^a x^a}{\rho^n t^n x^n} \qquad \text{(aI-26)}$$

Equation (aI-26) shows that the viscosity of analogue material compared to rocks in nature should be scaled down as the product of density, time and length scale down.

Examples of viscosity values for rocks are salt with $\eta \approx 10^{16}$ - 10^{19} Pa·s [*Odé*, 1965], asthenosphere with $\eta \approx 10^{19}$ - 10^{20} Pa·s [*Artyushkov*, 1983], sub-lithospheric mantle with $\eta \approx 10^{20}$ - 10^{21} Pa·s [*Ranalli*, 1995], and mantle with $\eta \approx 10^{19}$- 10^{24} [*Carter and Tsenn*, 1987].

APPENDIX II

Rheological equations

A II-1. Introduction

The mechanical response of the lithosphere to stresses results form a combination of rheological properties of rocks, including brittle, viscous, plastic and elastic behaviour. The way that rocks deform depends on a variety of physical conditions of the rocks, such as pressure, temperature, strain rate, and rock composition. For long-term (millions of year) large-scale (lithospheric scale) investigations, the mechanical behaviour of the lithosphere and mantle can be approximated with a stratification of brittle and viscous rheologies. From such stratified profiles and accompanying rheological equations one can calculate the integrated strength of the lithosphere. Combining the brittle strength of rocks and the viscous strength of rocks leads to the well-known strength profiles for lithospheric columns [*Goetze and Evans*, 1979; *Brace and Kohlstedt*, 1980; *Kirby*, 1983; *Ranalli and Murphy*, 1987; *Stephenson and Cloetingh*, 1991]. The integrated strength of the lithosphere at a specific strain rate can then be calculated by integrating the differential stress over the appropriate depth range [*Sonder and England*, 1986; *Ranalli*, 1987]. In the following sections, the rheological equations for brittle and viscous material will be discussed for both the natural prototype and the analogue models, which were used throughout the thesis to calculate the integrated strength of the lithosphere in nature and experiment.

A II-2. Brittle behaviour

A II-2.1 Brittle behaviour of rocks

In the Coulomb Fracture Criterion the relationship between shear stress and normal stress is described as follows [*Coulomb*, 1776]:

$$\tau = C + \mu\sigma_n \qquad \text{(aII-1)}$$

where τ is the shear stress, C is the cohesion, μ is the friction coefficient, and σ_n is the normal stress. The algebraic expressions of normal and shear stress in terms of principal stresses can be described as follows [*Mohr*, 1882,1900]:

$$\sigma_n = \left[\frac{\sigma_1 + \sigma_3}{2}\right] + \left[\frac{\sigma_1 - \sigma_3}{2}\right]\cos(2\theta) \qquad \text{(aII-2a)}$$

$$\tau = \left[\frac{\sigma_1 - \sigma_3}{2}\right]\sin(2\theta) \qquad \text{(aII-2b)}$$

where σ_1 is the maximum principal stress, σ_3 is the minimum principal stress, and θ_f is the fracture angle. Using the equations:

$$2\theta_f = 90 + \phi \qquad \text{(aII-3a)}$$

$$\mu = \tan(\phi) \qquad \text{(aII-3b)}$$

then combining equation (aII-3a) and (aII-3b) leads to:

$$\mu = \tan(2\theta_f - 90) = \frac{\sin(2\theta_f - 90)}{\cos(2\theta_f - 90)} = -\frac{\cos(2\theta_f)}{\sin(2\theta_f)} \qquad \text{(aII-4)}$$

Substitution of equation (aII-2) and (aII-4) into equation (aII-1) leads to:

$$\left[\frac{\sigma_1 - \sigma_3}{2}\right]\sin(2\theta_f) = -\frac{\cos(2\theta_f)}{\sin(2\theta_f)}\left(\left[\frac{\sigma_1 + \sigma_3}{2}\right] + \left[\frac{\sigma_1 - \sigma_3}{2}\right]\cos(2\theta_f)\right) + C \qquad \text{(aII-5)}$$

With some algebra and using some trigonometric relations this leads to:

$$[\sigma_1 - \sigma_3]\sin^2(2\theta_f) = -[\sigma_1 + \sigma_3]\cos(2\theta_f) - [\sigma_1 - \sigma_3]\cos^2(2\theta_f) + 2C\sin(2\theta_f)$$

$$[\sigma_1 - \sigma_3]\left(\sin^2(2\theta_f) + \cos^2(2\theta_f)\right) = -[\sigma_1 + \sigma_3]\cos(2\theta_f) + 2C\sin(2\theta_f)$$

$$\sigma_1\left(1 + \cos(2\theta_f)\right) = 2C\sin(2\theta_f) + \sigma_3\left(1 - \cos(2\theta_f)\right)$$

This can be rewritten in the following equation:

$$\sigma_1 = \frac{2C\sin(2\theta_f)}{1 + \cos(2\theta_f)} + \frac{1 - \cos(2\theta_f)}{1 + \cos(2\theta_f)}\sigma_3 \qquad \text{(aII-6)}$$

The Coulomb Fracture Criterion in terms of principal stresses is then:

$$\sigma_1 = S + K\sigma_3 \qquad \text{(aII-7)}$$

where:

$$S = \frac{2C\sin 2\theta_f}{1 + \cos 2\theta_f} \qquad K = \frac{1 - \cos 2\theta_f}{1 + \cos 2\theta_f} \qquad \text{(aII-8)}$$

Here S is normally called the fracture strength under uniaxial compression and zero confining pressure.

A II-2.1.1 Extension

During extensional tectonics, the first principal stress is approximately equal to the overburden pressure (σ_v) minus the pore fluid pressure (p_f):

$$\sigma_1 = \sigma_v - p_f = \sigma_v - \lambda\sigma_v = \sigma_v(1 - \lambda) = \rho gz(1 - \lambda) \qquad \text{(aII-9)}$$

where λ is the pore fluid factor, ρ is the density of rock, g is the acceleration due to gravity, and z is the depth. For complete saturation of the rock:

$$\lambda = \frac{P_f}{\sigma_v} = \frac{\rho_{water} gz}{\rho_{rock} gz} = \frac{\rho_{water}}{\rho_{rock}} \qquad \text{(aII-10)}$$

This relationship suggests that λ can not exceed an approximate value of about 0.3 - 0.4 (ρ_{water} = 1.0 x 10^3 kg/m^3 and ρ_{rock} ~ 2.5 -3.3 x 10^3 kg/m^3). This is however not always the case and λ can reach values approaching 1. This is due to the fact that for the relationship to hold, the rock in which the water is present should be permeable from the surface down to the specific depth. If the rock is impermeable, fluid pressure can build up and reach values larger than 0.4. Substituting equation (aII-9) in equation (aII-7) leads to:

$$\rho gz(1 - \lambda) = S + K\sigma_3 \qquad \text{(aII-11)}$$

Rearrangement leads to:

$$\sigma_3 = \frac{\rho gz(1 - \lambda) - S}{K} \qquad \text{(aII-12)}$$

Subtraction of the third principal stress from the first principal stress leads to:

$$\sigma_1 - \sigma_3 = \rho gz(1 - \lambda) - \frac{\rho gz(1 - \lambda) - S}{K} = \frac{K - 1}{K}\rho gz(1 - \lambda) + \frac{S}{K} \qquad \text{(aII-13)}$$

The integrated strength for extension of a brittle material defined by equation (aII-13) is the integration of equation (aII-13) over its depth range from $z = 0$ to $z = z_b$:

$$\int_0^{z_b}(\sigma_1 - \sigma_3)dz = \int_0^{z_b}\left(\frac{K - 1}{K}\rho gz(1 - \lambda) + \frac{S}{K}\right)dz = \frac{K - 1}{2K}\rho g(z_b)^2(1 - \lambda) + \frac{S}{K}z_b \qquad \text{(aII-14)}$$

A II-2.1.2. Shortening

During shortening tectonics, the first principal stress lies in the horizontal plane. The third principal stress is equal to the vertical stress:

$$\sigma_3 = \sigma_v - p_f = \sigma_v - \lambda\sigma_v = \sigma_v(1 - \lambda) = \rho gz(1 - \lambda) \qquad \text{(aII-15)}$$

Substituting equation (aII-15) in equation (aII-7) results in:

$$\sigma_1 = S + K\rho gz(1 - \lambda) \qquad \text{(aII-16)}$$

Subtraction of the third principal stress from the first principal stress leads to:

$$\sigma_1 - \sigma_3 = K\rho gz(1 - \lambda) - \rho gz(1 - \lambda) + S = (K - 1)\rho gz(1 - \lambda) + S \qquad \text{(aII-17)}$$

The integrated strength for shortening of a brittle material defined by equation (aII-17) is the integration of this equation over its dept range from $z = 0$ to $z = z_b$:

$$\int_0^{z_b}(\sigma_1-\sigma_3)dz=\int_0^{z_b}\left((K-1)\rho g z(1-\lambda)+S\right)dz=\frac{K-1}{2}\rho g(z_b)^2(1-\lambda)+Sz_b \qquad \text{(aII-18)}$$

A II-2.2. Brittle behaviour of granular material

The brittle behaviour of granular material can be approximated by the following equation [*Schellart*, 2000]:

$$\tau=\left(\frac{C'}{\sigma_n^*}+\mu\right)\sigma_n \qquad \text{for} \qquad 0\,\text{Pa} \le \sigma_n < \sigma_n^* \qquad \text{(aII-19a)}$$

$$\tau=C'+\sigma_n \qquad \text{for} \qquad \sigma_n \ge \sigma_n^* \qquad \text{(aII-19b)}$$

where C' is the maximum extrapolated cohesion, and σ_n^* is the critical normal stress, below which the relation between σ_n and τ is non-linear but can be approximated with equation (aII-19a). Equation (aII-19a) can be written in terms of principal stresses by substitution of equation (aII-2a), (aII-2b), and (aII-4) in equation (aII-19a):

$$\left[\frac{\sigma_1-\sigma_3}{2}\right]\sin(2\theta_f)=\left(\frac{C'}{\sigma_n^*}-\frac{\cos(2\theta_f)}{\sin(2\theta_f)}\right)\left(\left[\frac{\sigma_1+\sigma_3}{2}\right]+\left[\frac{\sigma_1-\sigma_3}{2}\right]\cos(2\theta_f)\right) \qquad \text{(aII-20)}$$

Rewriting the equation and multiplying both sides with $2\sin(2\theta_f)$ leads to:

$$[\sigma_1-\sigma_3]\sin^2(2\theta_f)=-[\sigma_1+\sigma_3]\cos(2\theta_f)-[\sigma_1-\sigma_3]\cos^2(2\theta_f)+[\sigma_1+\sigma_3]\frac{C'}{\sigma_n^*}\sin(2\theta_f)$$
$$+[\sigma_1-\sigma_3]\frac{C'}{\sigma_n^*}\sin(2\theta_f)\cos(2\theta_f)$$

Rewriting in terms of σ_1 and σ_3 leads to:

$$\sigma_1\left(1+\cos(2\theta_f)-\frac{C'}{\sigma_n^*}\sin(2\theta_f)-\frac{C'}{\sigma_n^*}\sin(2\theta_f)\cos(2\theta_f)\right)$$
$$=\sigma_3\left(1-\cos(2\theta_f)+\frac{C'}{\sigma_n^*}\sin(2\theta_f)-\frac{C'}{\sigma_n^*}\sin(2\theta_f)\cos(2\theta_f)\right)$$

This can be rewritten in the following equation:

$$\sigma_1=\frac{\left(1-\cos(2\theta_f)\right)\left(1+\frac{C'}{\sigma_n^*}\sin(2\theta_f)\right)}{\left(1+\cos(2\theta_f)\right)\left(1-\frac{C'}{\sigma_n^*}\sin(2\theta_f)\right)}\sigma_3 \qquad \text{(aII-21)}$$

This finally leads to the following equations:

$$\sigma_1=K^*\sigma_3 \qquad \text{for} \qquad 0\,\text{Pa} \le \sigma_n < \sigma_n^* \qquad \text{(aII-22a)}$$

$$\sigma_1=S'+K\sigma_3 \qquad \text{for} \qquad \sigma_n \ge \sigma_n^* \qquad \text{(aII-22b)}$$

with:

$$K'=\frac{\left(1-\cos(2\theta_f)\right)\left(1+\frac{C'}{\sigma_n^*}\sin(2\theta_f)\right)}{\left(1+\cos(2\theta_f)\right)\left(1-\frac{C'}{\sigma_n^*}\sin(2\theta_f)\right)} \qquad S'=\frac{2C'\sin(2\theta_f)}{1+\cos(2\theta_f)} \qquad \text{(aII-22c)}$$

A II-2.2.1. Extension

For extension in granular material, the same principals are valid as described in section A II-2.1.1. For the low stress regime described by equation (aII-22a), equation (aII-12) can be rewritten by simply replacing K by K' and putting S to zero. Also, $\lambda = 0$, since only dry granular material has been used in the analogue experiments. For the high stress regime described by equation (aII-22b), equation (aII-12) can be rewritten by simply replacing S by S'. This leads to the following equations:

$$\sigma_1-\sigma_3=\frac{K'-1}{K'}\rho g z \qquad \text{for} \qquad 0\,\text{Pa} \le \sigma_n < \sigma_n^* \qquad \text{(aII-23a)}$$

$$\sigma_1-\sigma_3=\frac{K-1}{K}\rho g z+\frac{S'}{K} \qquad \text{for} \qquad \sigma_n \ge \sigma_n^* \qquad \text{(aII-23b)}$$

The integrated strength for extension of a brittle material defined by equations (aII-23a) and (aII-23b) is the integration of these equations over their depth range from $z = 0$ to $z = z_b$:

$$\int_0^{z^*}(\sigma_1-\sigma_3)dz=\frac{K'-1}{2K'}\rho g(z^*)^2 \qquad \text{for } 0 \le z < z^* \qquad \text{(aII-24a)}$$

$$\int_{z^*}^{z_b}(\sigma_1-\sigma_3)dz=\frac{K-1}{2K}\rho g\left((z_b)^2-(z^*)^2\right)+\frac{S'}{K}(z_b-z^*) \qquad \text{for } z \ge z^* \qquad \text{(aII-24b)}$$

where z^* is the depth at which $\sigma_n = \sigma_n^*$ (i.e. the intersection of the curves of equation (aII-23a) and equation (aII-23b)).

A II-2.2.2. Shortening

For shortening in granular material, the same principals are valid as described in section A II-2.1.2. For the low stress regime described by equation (aII-22a), equation (aII-16) can be rewritten by simply replacing K by K' and putting S to zero. Also, $\lambda = 0$, since only dry granular material has been used in the analogue experiments. For the high stress regime described by equation (aII-22b), equation (aII-16) can be rewritten by simply replacing S by S'. This leads to the following equations:

$$\sigma_1 - \sigma_3 = (K' - 1)\rho g z \qquad \text{for} \qquad 0\ \text{Pa} \le \sigma_n < \sigma_n^* \qquad \text{(aII-25a)}$$

$$\sigma_1 - \sigma_3 = (K - 1)\rho g z + S' \qquad \text{for} \qquad \sigma_n \ge \sigma_n^* \qquad \text{(aII-25b)}$$

The integrated strength for extension of a brittle material defined by equations (aII-25a) and (aII-25b) is the integration of these equations over their depth range:

$$\int_0^{z^*} (\sigma_1 - \sigma_3)dz = \tfrac{1}{2}(K' - 1)\rho g (z^*)^2 \qquad \text{for } 0 \le z < z^* \qquad \text{(aII-26a)}$$

$$\int_{z^*}^{z_b} (\sigma_1 - \sigma_3)dz = \tfrac{1}{2}(K - 1)\rho g\left((z_b)^2 - (z^*)^2\right) + S'(z_b - z^*) \qquad \text{for } z \ge z^* \qquad \text{(aII-26b)}$$

where z^* is the depth at which $\sigma_n = \sigma_n^*$ (i.e. the intersection of the curves of equation (aII-25a) and equation (aII-25b)).

A II-3. Viscous behaviour

A II-3.1. Temperature dependent viscous behaviour

At depths below ~ 10-15 km, the temperature of the rocks becomes so high that they start to deform in a viscous manner. The algebraic expression for this type of deformation is [*Twiss and Moores*, 1992]:

$$\sigma_1 - \sigma_3 = K\dot{\varepsilon}^{\frac{1}{n}} e^{\frac{Q}{nRT}} \qquad \text{(aII-27)}$$

where $\dot{\varepsilon}$ is the steady state incremental strain rate, K, A and n are material constants, Q is the activation energy, R is the universal gas constant, and T is the temperature (in Kelvin).
K can be expressed as:

$$K = \left[\frac{1}{A}\right]^{\frac{1}{n}} \qquad \text{(aII-28)}$$

Therefore, equation (aII-27) can be written as:

$$\sigma_1 - \sigma_3 = \left|\frac{\dot{\varepsilon}}{A}\right|^{\frac{1}{n}} e^{\frac{Q}{nRT}} \qquad \text{(aII-29)}$$

Temperature increase in the lithosphere can be approximated by a linear geotherm:

$$T = T_0 + \frac{z}{z_l}(T_1 - T_0) \qquad 0 \le z \le z_l \qquad \text{(aII-30)}$$

where T_0 is the temperature at $z = 0$ and T_l is the temperature at $z = z_l$. Combining equation (aII-30) with equation (aII-29) leads to:

$$\sigma_1 - \sigma_3 = \left|\frac{\dot{\varepsilon}}{A}\right|^{\frac{1}{n}} e^{\frac{Q}{nR\left(T_0 + z/z_l(T_1 - T_0)\right)}} \qquad \text{(aII-31)}$$

Integration of equation (aII-31) over its depth range from $z = z_b$ to $z = z_v$ can be expressed as follows:

$$\int_{z_b}^{z_v} (\sigma_1 - \sigma_3)dz = \int_{z_b}^{z_v} \left(\left|\frac{\dot{\varepsilon}}{A}\right|^{\frac{1}{n}} e^{\frac{E^*}{nR(T_0 + z/z_l(T_1 - T_0))}} \right) dz \qquad \text{(aII-32)}$$

With equation (aII-32) one can calculate the integrated strength of viscous parts of the lithosphere, such as the lower crust and lower lithospheric mantle.

A II-3.2. Newtonian viscous behaviour with constant temperature

The rheological behaviour of Newtonian viscous material with a constant temperature can be described in terms of principal stresses [*Benes and Davy*, 1996]:

$$\sigma_1 - \sigma_3 = \eta\dot{\varepsilon}_{ij} \qquad \text{(aII-33)}$$

The strain rate can be approximated by dividing the velocity of shortening/extension by the length of the shortened/extended part of the viscous layer [*Benes and Davy*, 1996].
The integrated strength for shortening/extension of a Newtonian viscous material is defined by integration of equation (aII-33) over its depth range $z = z_b$ to $z = z_v$:

$$\int_{z_b}^{z_v} (\sigma_1 - \sigma_3)dz = \int_{z_b}^{z_v} (\eta\dot{\varepsilon}_{ij})dz = \eta\dot{\varepsilon}_{ij}(z_v - z_b) \qquad \text{(aII-34)}$$

Equation (aII-34) can be applied to calculate the integrated strength of Newtonian viscous materials such as silicone putties used in analogue experiments, when the experiment is isothermal.

FOREWORD APPENDIX III

This appendix discusses the physical properties of granular materials, which are frequently used in analogue models of geological processes. The ideas presented in this appendix were inspired by reading a paper from *Krantz* [1991] and realising that there seemed to be a lack of knowledge on the mechanical behaviour of granular materials for very low normal stresses (~ 0 - 1000 Pa). Such low normal stresses are dominant in analogue experiments.

The ideas and interpretations presented in this appendix are the sole work of the author. All the experimental work presented in this appendix are the sole work of the author. I would like to thank Gordon Lister for useful discussions and suggestions to improve the contents of this appendix. Furthermore, the comments of Greg Houseman and Terence Barr on an early version of the manuscript were very helpful. Also, I would like to thank Andrew Kos, who helped with recording of some of the experiments. The contents of this entire appendix has been published in *Tectonophysics*. A full reference can be found at the end of the thesis in the bibliography. Minor changes have been made to the text of the original paper in order to make the layout and spelling of this appendix consistent with the rest of the thesis. Finally, I would like to thank the journal reviewers R. W. Krantz and P. R. Cobbold for reviewing the paper.

APPENDIX III

Shear test results of cohesion and friction coefficients for different granular materials: Scaling implications for their usage in analogue modelling

Abstract

Laboratory tests have been made on dry granular materials such as quartz sand, glass microspheres and sugar with different grain size, rounding and sphericity. The measurements have been made with a simple shear test machine for different values of normal stress (~ 50 - 900 Pa). Shear stress has been plotted against normal stress in order to determine the cohesion and coefficient of internal friction for the investigated materials.

Resulting values of cohesion and coefficient of internal friction are mainly dependent on rounding and sphericity, while grain size has a less significant influence. Further, the behaviour of the materials for very small normal stresses (~ 0 - 400 Pa) is more complex than previously assumed. The fracture envelopes for all materials investigated are convex-outward for this small range and converge towards a straight failure envelope with increasing normal stress. Finally, in extensional faulting experiments there is no significant change in fault dip with increasing depth. Therefore, the non-linear behaviour for small normal stresses is best described as a dependence of the cohesion on the normal stress and not as a dependence of the coefficient of internal friction on the normal stress. Values for cohesion increase from ~ 0 Pa (±15 Pa) at zero normal stress to 137 - 247 Pa (± 15 Pa) for normal stresses greater than ~ 250 - 400 Pa. The results show that well rounded, spherical material is better suited to model brittle behaviour of rocks in crustal and lithospheric scale analogue models than less well rounded material, since it has a smaller cohesion and a coefficient of internal friction, which comes closer to values of natural rocks.

A III-1. Introduction

Dry granular materials such as sand have been previously used in many analogue models of structural and tectonic processes [*Hubbert*, 1951; *Horsfield*, 1977; *Naylor et al.*, 1986; *Vendeville et al.*, 1987; *Davy and Cobbold*, 1988; *McClay*, 1990; *Davy and Cobbold*, 1991; *Ratschbacher et al.*, 1991a; *Richard*, 1991; *Richard and Krantz*, 1991; *Richard et al.*, 1991; *Lallemand et al.*, 1992; *Nieuwland and Walters*, 1993; *Brun et al.*, 1994; *Richard et al.*, 1995; *Faccenna et al.*, 1996; *Bonini et al.*, 1997; *Hatzfeld et al.*, 1997; *Keep and McClay*, 1997; *Basile and Brun*, 1998; *Faccenna et al.*, 1999]. In most of these papers the cohesion of these materials has been assumed to be negligible and the coefficient of internal friction to be ~ 0.58. However, shear test measurements done by *Krantz* [1991] pointed out that the cohesion of sand is probably in the order of 300 - 520 Pa (depending on the physical handling technique), which is certainly not negligible. Further, the coefficient of internal friction is in the order of 0.58 - 1.00. These values could however be subject to an error due to extrapolation of data towards very small normal stresses (0 - 600 Pa), as has been suggested by *Krantz* [1991] and *Richard and Krantz* [1991]. Recently, *Cobbold and Castro* [1999] did

shear tests for normal stresses ranging from 300 - 1600 Pa. They obtained an extrapolated cohesion of 85 Pa for the material and a coefficient of internal friction of 0.57. *Cobbold and Castro* [1999] also did shear tests with upward fluid flow through the material, leading to effective normal stresses of 0 -1600 Pa. To the data resulting from these experiments they also fitted straight lines. However, it would have been possible to fit more complex envelopes to these data sets, especially near the origin.

Analogue experiments are subject to specific scaling rules, which were introduced to geology by *Hubbert* [1937]. According to these scaling rules, an analogue model is representative of a natural prototype if both systems are dynamically similar. This means that in both experiment and nature, similar distributions of stresses, densities and rheologies should be present. In analogue modelling of structural and tectonic processes, cohesion should scale down in a similar way that stresses scale down [*Horsfield*, 1977; *Davy and Cobbold*, 1988; *Cobbold and Jackson*, 1992]. When analogue experiments are executed in a normal field of gravity, stresses should be scaled down as the product of density and length vectors scale down:

$$\frac{C^a}{C^n} = \frac{\sigma_{ij}^a}{\sigma_{ij}^n} = \frac{\rho^a x_j^a}{\rho^n x_j^n} \qquad \text{(aIII-1)}$$

where superscript a denotes the analogue model and superscript n the natural prototype; C is the cohesion; σ_{ij} are the stresses; ρ is the density; and x_j is a length vector.

If a scale factor of 5 x 10^{-7} is applied to stresses (with a density ratio of 1/2 and a length ratio of 1 cm / 10 km), the implied cohesion values in the natural system are in the range of 600 – 1040 MPa. That is of course, when the values for cohesion of *Krantz* [1991] are correct. These upscaled values are extremely high and unrealistic values for natural rocks. Uniaxial compressive strength tests and shear strength tests on natural rocks have indicated that values for cohesion of intact rocks range between ~ 20 - 110 MPa. Some values of cohesion and coefficient of internal friction for intact sedimentary and igneous rocks can be observed in Table aIII-1.

Rock Type	μ	ϕ	C (MPa)	Reference
Granite	0.64	32.6	31	1
Gabbro	0.66	33.4	38	1
Trachyte	0.68	34.2	41	1
Serpentinised olivine	0.65	33.0	90	2
Sandstone	0.51	26.6	28	1
Berea sandstone	0.49	26.1	24	3
Weber sandstone	0.60	31.0	70	3
Tennessee sandstone	0.84	40.0	50	4
Lueders limestone	0.53	27.9	15	4
Solnhofen limestone	0.53	27.9	105	4
Marble	0.75	36.9	110	1
Blair dolomite	1.00	45.0	45	4

Table aIII-1. Values of μ (coefficient of internal friction), ϕ (angle of internal friction) and C (cohesion) for different rock types. References: 1 - *Jaeger and Cook* [1976]; 2 - *Raleigh and Paterson* [1965]; 3 - *Twiss and Moores* [1992]; 4 – *Handin* [1969].

As most rocks are broken by numerous joints, faults and fractures, at least on a larger scale compared to the test specimens investigated in these tests [*Hubbert*, 1951], the cohesion of natural rocks will probably be even lower than the values given in Table aIII-1.

Also, in lithospheric modelling some people assume that the cohesion for the upper (brittle) part of the lithosphere is negligible, since they apply the following equation for this brittle behaviour [*Sibson*, 1974]:

$$\sigma_1 - \sigma_3 \geq \beta\rho g z(1-\lambda) \qquad \text{(aIII-2a)}$$

where σ_1 and σ_3 are the maximum and minimum principal stress, respectively; β is a parameter depending on the type of faulting (3, 1.2 and 0.75 for thrust, strike-slip and normal faulting respectively); g is the acceleration due to gravity; z is the depth below the surface; and λ is the pore fluid factor.

This assumption of negligible cohesion is mainly based on the idea that the upper part of the crust is criss-crossed by discontinuities of every shape and size [*Ranalli and Murphy*, 1987]. This statement could be true for the continental lithosphere, which normally has experienced major deformation events. However, this statement is probably less valid for the oceanic lithosphere, where intensive deformation is absent and the only major faults are transform faults offsetting different mid oceanic ridge segments.

Another equation that is often used for plots of lithospheric strength profiles is the one proposed by *Byerlee* [1978]:

$$\tau = 0.85\sigma_n \qquad \text{for } \sigma_n < 200 \text{ MPa} \qquad \text{(aIII-2b)}$$

$$\tau = 60 \text{ MPa} + 0.6\sigma_n \qquad \text{for } 200 < \sigma_n < 1700 \text{ MPa} \qquad \text{(aIII-2c)}$$

where τ is the shear stress and σ_n is the normal stress.

When equation (aIII-2b) and (aIII-2c) are rewritten in terms of principal stresses [*Kirby*, 1983] this leads to:

$$\sigma_1 - \sigma_3 = 3.9\sigma_3 \qquad \text{for } \sigma_3 < 120 \text{ MPa} \qquad \text{(aIII-2d)}$$

$$\sigma_1 - \sigma_3 = 210 \text{ MPa} + 2.1\sigma_3 \qquad \text{for } \sigma_3 > 120 \text{ MPa} \qquad \text{(aIII-2e)}$$

The equations of *Byerlee* [1978] have been empirically determined from numerous experiments on shear strength along fracture planes of various types of prefractured rocks. From equation (aIII-2b) it can be observed that prefractured rocks have essentially no cohesion along their fracture planes for this small stress range. However, for increasing normal pressure, equation (aIII-2c) shows prefractured rocks do have a cohesion of 60 MPa. According to *Byerlee* [1978] this difference is related to different physical mechanisms involved in the sliding of rock at various pressures. At low normal stresses the surfaces can move with respect to one another by lifting over the interlocked irregularities, while at high normal stresses this effect is suppressed and the surfaces then slide by shearing through the irregularities.

However, since analogue models of the crust and lithosphere have been made, where the (upper) brittle part of the crust has been simulated with pure sand [*Brun et al.*, 1994; *Bonini et al.*, 1997; *Basile and Brun*, 1998], or sand mixed with a certain amount of ethyl cellulose [*Davy and Cobbold*, 1988; *Davy and Cobbold*, 1991; *Ratschbacher et al.*, 1991a; *Cobbold*

and Jackson, 1992; *Faccenna et al.*, 1996; *Hatzfeld et al.*, 1997], the cohesion of these materials could have a major affect on the strength profiles through the model crusts and lithospheres. The inclusion of cohesion in the analogue models may lead to integrated strengths, which are too large for the brittle upper part of the lithosphere. The lithospheric strength can be plotted by the following formula, which is a form of Coulomb's fracture criterion [*Coulomb*, 1773] rewritten in terms of principal stresses:

$$\sigma_1 - \sigma_3 = (K-1)\rho g z(1-\lambda) + S \qquad \text{(shortening)} \qquad \text{(aIII-3a)}$$

$$\sigma_1 - \sigma_3 = \frac{(K-1)}{K}\rho g z(1-\lambda) + \frac{S}{K} \qquad \text{(extension)} \qquad \text{(aIII-3b)}$$

with:

$$S = \frac{2C\sin 2\theta_f}{1+\cos 2\theta_f} \qquad K = \frac{1-\cos 2\theta_f}{1+\cos 2\theta_f} \qquad \text{(aIII-3c)}$$

and:

$$2\theta_f = 90 + \phi \qquad \mu = \tan\phi \qquad \text{(aIII-3d)}$$

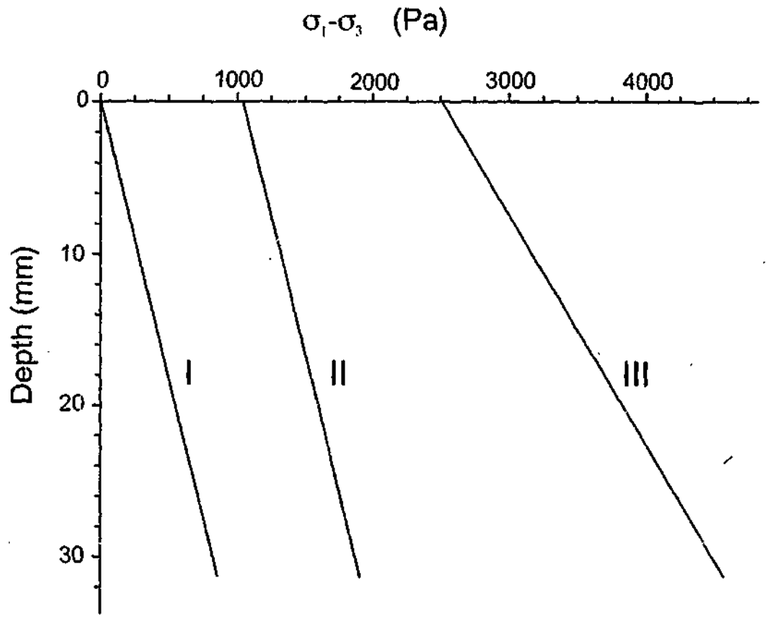

Fig. aIII-1. Brittle failure curves of dry granular materials for shortening. All 3 curves are for material with a frictional plastic behaviour, with a pore fluid factor $\lambda = 0$. For convenience, a constant density (ρ) of 1400 kg/m^3 for all three curves has been chosen. Curves with different values for K (related to the coefficient of internal friction μ) and S (related to cohesion C and μ) have been plotted. For curve I, the fracture strength $S = 0$ Pa and $K = 3.00$, for curve II $S = 1042$ Pa and $K = 3.00$ and for curve III $S = 2511$ Pa and $K = 5.83$. The 3 different curves clearly indicate that cohesion as well as coefficient of internal friction have a major influence on the strength of the material and therefore on the integrated strength profiles for lithospheric analogue models.

where K is a parameter depending on the fracture angle; S is the fracture strength under uniaxial compression with zero confining pressure; θ_f is the fracture angle; ϕ is the angle of internal friction; and μ is the coefficient of internal friction.

A strength curve for sand (shortening) can be plotted, using equation (aIII-3a) with a coefficient of internal friction $\mu = 0.58$ and a cohesion $C = 0$ Pa, as assumed by most analogue crustal scale and lithospheric modellers [*Davy and Cobbold*, 1988; *Davy and Cobbold*, 1991; *Ratschbacher et al.*, 1991a; *Cobbold and Jackson*, 1992; *Brun et al.*, 1994; *Faccenna et al.*, 1996; *Bonini et al.*, 1997; *Basile and Brun*, 1998]. When this is compared with a strength curve for poured sand with $C = 300$ Pa and $\mu = 0.58$ and sprinkled sand with $C = 520$ Pa and $\mu = 1.00$ (as deduced by *Krantz* [1991]), the difference in integrated strength is very large (Fig. aIII-1).

For the first 10 mm the integrated strength for curve I is ~ 1.4 N/m and for curve III ~ 28.4 N/m, which differ by a factor 20. The integrated strength for the first 20 mm for curve I is ~ 5.5 N/m and for curve III ~ 63.5 N/m, which is still a factor 11 in difference. This indicates that if the calculated values for cohesion and angle of internal friction of *Krantz* [1991] are correct, than the integrated strength of sand does not scale properly to represent the lithosphere, at least when a scaling factor $< 5 \times 10^{-6}$ is applied to the analogue model.

However, since the experiments of *Krantz* [1991] have been executed with normal stresses varying somewhere between 600 and 3500 Pa and his data have been extrapolated to normal stresses of 0 – 600 Pa, this extrapolation might lead to errors and therefore incorrect strength curves. Normally, sand layers used in lithospheric analogue models have thicknesses smaller than a few cm, leading to vertical normal stresses of up to only a few hundred Pa. Therefore, shear test experiments reported here have been executed for very low normal stresses (50 - 900 Pa). The aim of these experiments is to get a better picture of the dynamic behaviour of sand and other granular materials in this low normal stress range and to investigate which material is most suitable for future analogue modelling of the lithosphere.

A III-2. Measurements

For a frictional plastic material (such as pure sand and glass microspheres) it is important to know its cohesion, since its inherent shear strength is dependent on it. This dependence can be observed in Coulomb's fracture criterion [*Coulomb*, 1773]:

$$\tau = C + \mu\sigma_n \qquad \text{(aIII-4)}$$

To determine the cohesion from a granular material (which probably has a very small or even zero cohesion) it is important to measure the relationship between the shear stress (which leads to fracturing) and the normal stress when the normal stress is as small as possible, to minimise the uncertainty of extrapolations to zero normal stress.

Shear strengths can be measured using a Hubbert-type apparatus [*Hubbert*, 1951]. Here, an upper ring is suspended above a fixed lower ring, with a small gap in between (Fig. aIII-2). The lower and upper rings are filled with the material under investigation to a desired depth (h). On the upper suspended ring an increasing shear load is applied until failure occurs in the material, which results in a significant displacement of the upper ring. This displacement was limited by a mechanical stop to approximately 4 mm.

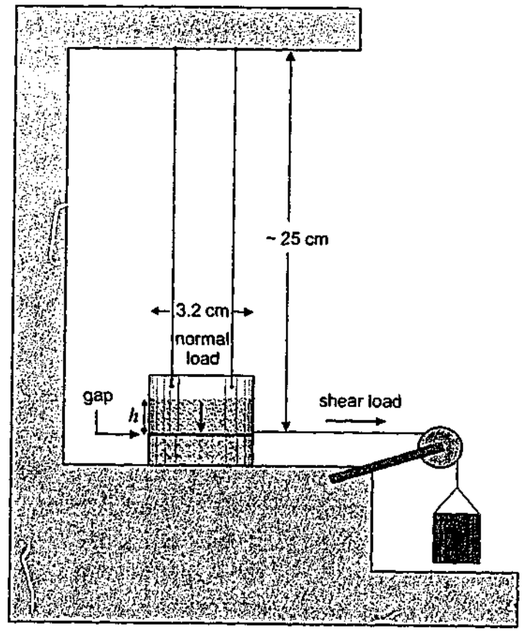

Fig. aIII-2. Sketch of shear test apparatus. The upper ring is suspended above a fixed lower ring with a gap of ~ 0.3 mm in between. After filling the rings to a desired depth (h), measured from the gap (the future fault zone), an increasing shear load is applied by a mass hanging over a pulley until failure occurs. This mass is essentially an empty bucket, which can be filled gradually with sand.

A few modifications to this apparatus have been applied, as have been done by *Krantz* [1991]. The first one is that the suspension of the upper ring was nearly 25 cm in length (or about 8 times the diameter of the rings), to reduce friction of the apparatus itself. The second one is that the normal stress on the horizontal fault surface was determined only by the thickness of the overlying sandpack (h).

Further, a modification on the apparatus of *Krantz* [1991] has been applied. This modification is that the rings that have been used have a much smaller diameter (3.2 cm) than the rings in his apparatus (14 cm). This has been done in order to be able to make the sediment thickness in the upper ring as small and as constant as possible. With this experimental set-up it was possible to execute experiments with normal stresses in the range of 50 - 900 Pa.

A few things should be taken into consideration in order to minimise errors in the measurements. First of all, the friction of the pulley and the suspended ring should be taken into consideration. The friction of the total system has been measured by investigating the amount of mass needed to significantly displace the upper suspended (empty) ring. It has been found that a shear stress as small as 3.0 Pa was sufficient to displace the upper suspended ring some 3mm. The error in shear stress induced by this friction is thus in the order of only a few Pa and since the shear stresses in the experiments range between 100 - 1000 Pa this leads to a maximum error of a few percent.

Further, the friction between the sediment and the upper suspended ring should be taken into consideration. If this force is very large, than it will inhibit the grains to fall freely and therefore it will reduce the normal stress of the sediment load. This possible influence of such a force has been checked by weighing the mass of the sediment, while supported by the

suspended upper ring and comparing it with the mass of the sediment, when the suspended ring was removed. It has been found that this force was less than 0.5 %.

Also, it is important to prepare the material for every experiment with a uniform method, since density and coefficient of internal friction of the material are dependent on the physical handling technique [*Krantz*, 1991]. The experiments of *Krantz* [1991] revealed that density, cohesion and coefficient of internal friction increase significantly when granular material is sprinkled instead of rapidly poured. In all the following shear test experiments, the test material has been slowly poured from a uniform height of ~ 10 cm.

Finally, with a very small sediment thickness it is important that the fault plane in the sediment does run according to the plane defined by the gap between the two rings. In most experiments with a very small sediment thickness (~ < 0.5 cm) the fault plane had an inclined angle to the horizontal (small thrust fault). The results from experiments where thrust faults developed have been rejected.

The shear stress is related to the mass of the shear load and the area of the fault plane, the normal stress is related to the thickness of the sandpack (h) and the density of the material. The shear stress and the normal stress have been calculated with the following equations:

$$\tau = \frac{mg}{A} \qquad \text{(aIII-5a)}$$

$$\sigma_n = \rho g h \qquad \text{(aJII-5b)}$$

where m, A and h are the mass of shear load, the area of the fault surface and thickness of the sandpack (with respect to the gap), respectively.

By plotting the shear stress, necessary to induce horizontal faulting, versus different normal stresses (by varying the height h of the sediment column) a curve can be obtained. Here, the intersection of this curve with the shear stress axis (σ_n = 0 Pa) is the cohesion of the material and the slope tangent of the curve is the coefficient of internal friction.

With a ring diameter of 3.2 cm, the area of the future fault surface is ~ 8.0 x 10^{-4} m^2. The acceleration due to gravity g has been taken as 9.8 m/s^2. For each material at least 70 shear tests have been done, with values for the height of the sediment column (h) in the range of 0.5 - 5.0 cm. Also, a few experiments have been recorded with a digital video camera, in order to investigate the experiments at different increments of time during shearing. The camera shot 25 images per second, where every image was shot over a time lapse of one millisecond.

A III-3. Materials

In the shear tests, only dry granular materials have been examined. Dry granular materials such as sand exhibit frictional plastic behaviour and fail according to the Mohr-Coulomb failure criterion [*Hubbert*, 1951, *Mandl et al.*, 1977]. Dry sand (S), glass microspheres (GM) and caster sugar (CS) with different grain size have been examined. The materials that have been investigated and some of their physical properties (density, grain size, roundness, sphericity) are given in Table aIII-2. The roundness of the materials has been classified using the classification of *Powers* [1953]. Sphericity has been determined by dividing the shortest axis of the grain by its longest axis. Where most grains had numbers smaller than 0.5, the sphericity has been classified as low, for numbers between 0.5 and 0.8, the sphericity has been classified as intermediate and for numbers higher than 0.8 the sphericity has been classified as high.

Material	Density (kg/m³)	grain size (μm)	Roundness	Sphericity
S I	1731	< 400	(sub)angular	intermediate
S II	1674	90 - 180	(sub)angular	intermediate
GM I	1905	400 - 600	very well rounded	very high
GM II	1609	90 - 180	well rounded	high
CS	1044	< 355	Angular	Low

Table aIII-2. Material properties of materials used in the shear test experiments, where "S" stands for sand, "GM" for glass microspheres and "CS" for caster sugar. The error in density is ± 2%.

The grain size has been determined by using sieves with different mesh sizes. The density of the materials has been determined by measuring the mass of known volumes of the material with an electronic balance.

The mass has been determined for five different volumes in the upper suspended ring, with a thickness (h) increasing from 1 to 5 cm. This has been done to examine if there would be any increase in density for increasing thickness of the sediment column due to compaction. For the materials investigated, the measurements gave almost perfectly linear results (Fig. aIII-3), suggesting that compaction in this range due to increasing normal stress is absent, as has also been recovered by *Cobbold and Castro* [1999].

A III-4. Results

The results of the shear tests have been plotted in Fig. aIII-4a. Approximate best-fit lines for the data have been plotted in Fig. aIII-4b. Here, it can be observed that, if no data were present for normal stresses, lower than 400 Pa, extrapolation of the data would lead to

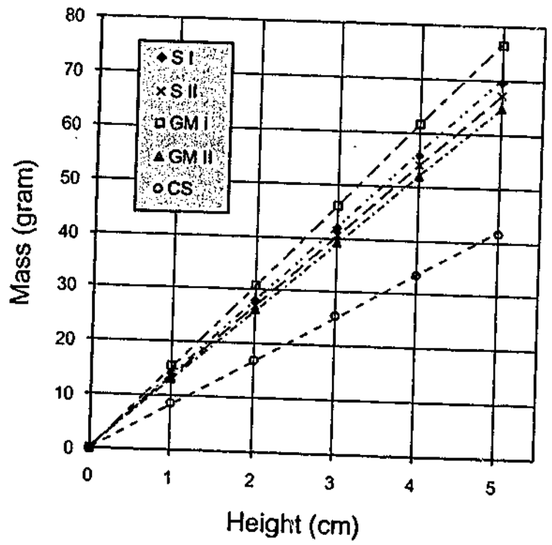

Fig. aIII-3. Plot of data displaying the relationship between increase in mass and increase in height of the sediment column (h) for the investigated materials. Dashed lines are best-fit straight lines for the data. From these results it can be seen that compaction does not influence density significantly for such small sediment thicknesses.

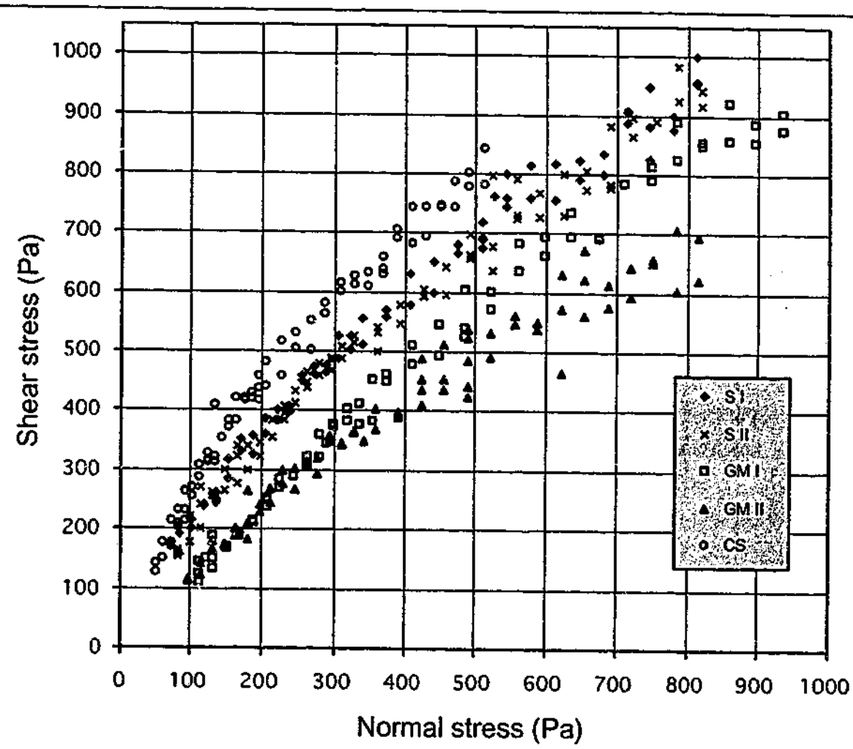

Fig. aIII-4a. Shear stress plotted as a function of normal stress for different dry granular materials. Material properties for the different materials have been given in Table aIII-2.

estimated values for cohesion, which would be much too high for the normal stress range of 0 - 400 Pa. Further it can be observed that sphericity and rounding seem to have more effect on the shape and position of the curve than grain size.

The data sets for each material strongly suggest convex-outward envelopes for normal stresses below ~ 250 - 400 Pa and shear stresses below ~ 300 - 550 Pa, with a non-linear relationship between τ and σ_n (Fig. aIII-4a). Above these values, the relationship between τ and σ_n shows normal Coulomb behaviour, as defined by equation (aIII-4). Approximate values of μ, ϕ and C' (maximum extrapolated cohesion) for the data in the range $\sigma_n >$ 250 - 400 Pa are given in Table aIII-3. Further it can be observed that for $\sigma_n <$ 250 - 400 Pa the data converge towards the origin, indicating that at zero normal stress the cohesion of all the granular materials is 0 Pa (± 15 Pa), as has been suggested earlier by *Richard and Krantz* [1991].

From the individual experiments and careful investigation of some of the experiments, recorded with a video camera, it has been observed that rupture (which led to a significant displacement of more than 3 mm) was preceded by one or two microslips. These microslips were most evident for experiments with S I, S II and CS and least evident with GM I. In most recorded experiments the first microslip was smaller (~ 0.1 - 0.2 mm) than the second one (~ 0.2 - 0.3 mm).

Further, dilatancy of the fault zones has been observed during and after the experiments, as mentioned by *Mandl et al.* [1977] and *Mandl* [1988]. After rupture, the sediment in the upper

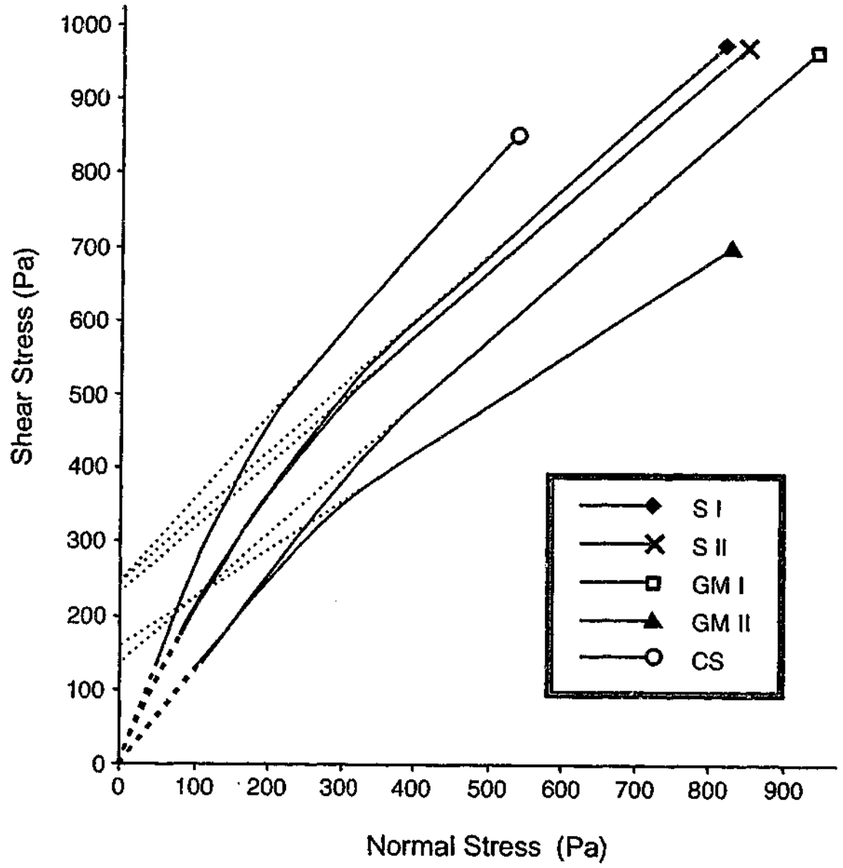

Fig. aIII-4b. Approximate best fit envelopes for the data of the materials plotted in Fig. aIII-4a. Continuous lines are for regions, where data is present, dashed lines are extrapolated for very low normal stresses (< 50 - 100 Pa) and stippled lines are extrapolated lines, when no data for normal stresses lower than ~ 250 - 400 Pa is included. The intersection of these stippled lines with the shear stress axis gives the maximum extrapolated cohesion C'.

suspended ring was uplifted with respect to this ring, compared to the stage before rupture. This uplift was maximum and approximately 1 mm for small sediment columns ($h \approx 0.5$-0.6 cm) and decreased gradually to 0 mm for larger sediment columns ($h \approx 1.3$-2.0 cm). This decrease in uplift is probably related to the increase in normal stress on the fault plane and therefore dilatancy of fault zones in dry granular materials probably decreases with increasing depth. It has also been observed that the uplift decreases with decreasing grain size, uplift values for S II and GM II being approximately half as large as those for S I, GM I and CS. The decrease in dilatancy of the shear zones with increasing normal stress could be related to the convex-outward behaviour of the envelopes at low normal stresses, since the normal stresses, where this dilatancy becomes negligible (250 - 350 Pa), coincide approximately with the normal stresses at the point where the envelopes become more or less straight (250 -400 Pa). A possible explanation for the decrease in dilatancy in these shear zones is that different physical mechanisms operate at different normal stresses. For low normal stresses, the individual grains in a shear zone can move over one another, leading to dilatation of the shear

Material	μ	ϕ	C' (Pa)
S I	0.89	41.7	245
S II	0.88	41.3	230
GM I	0.87	41.0	137
GM II	0.65	33.0	160
CS	1.14	48.8	247

Table aIII-3. Values for μ (coefficient of internal friction), ϕ (angle of internal friction) and C' (maximum extrapolated cohesion), all for the linear part of the failure envelopes for the investigated materials. Errors in the data are in the order of 5 %.

zone and uplift of the sediment column. For high normal stresses, this effect is suppressed and the individual grains have to slide through the irregularities. This concept has already been proposed by *Byerlee* [1978], for shearing along fracture planes in rocks.

Finally, from the recorded experiments, there were strong indications that during the major shear events, the shears grew from the back of the ring towards the front, because the uplift of the sediment column started in the back and progressively migrated towards the front of the ring (where the ring is attached to the shear load). The development of these shears normally took approximately 0.05 - 0.1 s.

When starting at the origin, with increasing normal stress, the failure envelopes are convex-outward and converge towards the straight curve until they reach a critical point x^*, which is defined by its critical normal and shear stress (σ_n^*, t^*). From this critical point, with increasing normal stress, the curve is more or less straight. The non-linear behaviour below this critical point x^* could be described as a dependence of C on σ_n and/or μ on σ_n:

$$C = f(\sigma_n) \qquad \text{and/or} \qquad \mu = g(\sigma_n) \tag{aIII-6}$$

Before investigating which of these factors influences the behaviour of the curves below x^*, we will transform these curves in terms of principal stresses and burial depth (a standard σ_1 - σ_3 versus burial depth (z) plot). This transformation has been executed both for shortening and extension. The resulting curves for S I and GM II are plotted in Fig. aIII-5. Here it can be observed that the critical point has a much higher z value in extension than in shortening.

Dependence of the critical depth z on the type of deformation (shortening or extension) can be explained by plotting a Mohr circle, which makes contact with the envelope at the critical point x^* (Fig. aIII-6). For shortening, σ_1 is the horizontal stress and σ_3 the vertical stress. For extension it is just the opposite. Since vertical stress is approximated by the following equation:

$$\sigma_{vertical} = \rho g z \tag{aIII-7}$$

Then for shortening at the critical point:

$$\sigma_{vertical} = \sigma_3 = \rho g z_1 \tag{aIII-8a}$$

And for extension at the critical point:

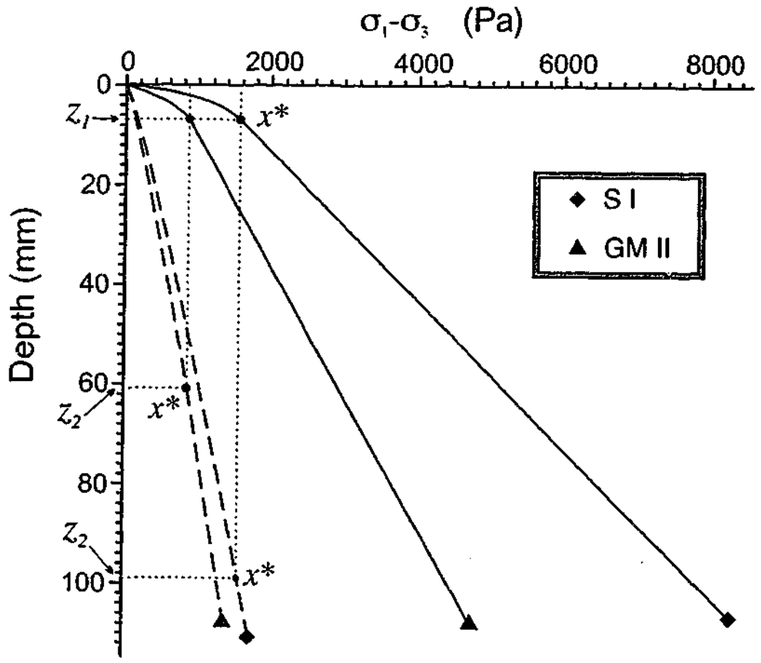

Fig. aIII-5. Brittle failure curves of S I and GM II for shortening (continuous lines) and extension (dashed lines). From the curves it is evident that the critical point x^* has a much greater critical depth value in extension (z_2) than in shortening (z_1). Further it can be seen that the stress value for x^* ($\sigma_1 - \sigma_3$) is the same in both cases, as would be suspected from Fig. aIII-6.

$$\sigma_{vertical} = \sigma_1 = \rho g z_2 \qquad \text{(aIII-8b)}$$

Dividing equation (aIII-8a) by equation (aIII-8b) leads to:

$$\frac{\sigma_3}{\sigma_1} = \frac{\rho g z_1}{\rho g z_2} = \frac{z_1}{z_2} \quad \begin{matrix}\text{(shortening)}\\ \text{(extension)}\end{matrix} \qquad \text{(aIII-9)}$$

since gravity and density are the same in both cases. From this relation it is clear that the depth of x^* in extension (z_2) is greater than its depth in shortening (z_1).

We will now return to the question of which factor in equation (aIII-6) influences the non-linear behaviour of the envelope. If μ is a function of σ_n, then the angle of internal friction ϕ should decrease with depth. In an extensional setting (where σ_1 is vertical), this would lead to a decreasing dip angle of normal faults with depth. For example, for the material S I this would lead to a dip angle of ~ 80° in the uppermost few cm, decreasing progressively to ~ 66° at $z \geq z_2$.

The possible dependence of μ on σ_n has been investigated in a small number of extensional experiments. The experiments have been performed in laterally unconfined piles of sediment for the materials S I and GM II, since lateral confinement increases fault dips at the edges due to extra frictional resistance [*Hubbert*, 1951; *Krantz*, 1991]. The sediment piles rested on a flat basal plate with, on one side, a thin plastic sheet in between the sediment pile and the

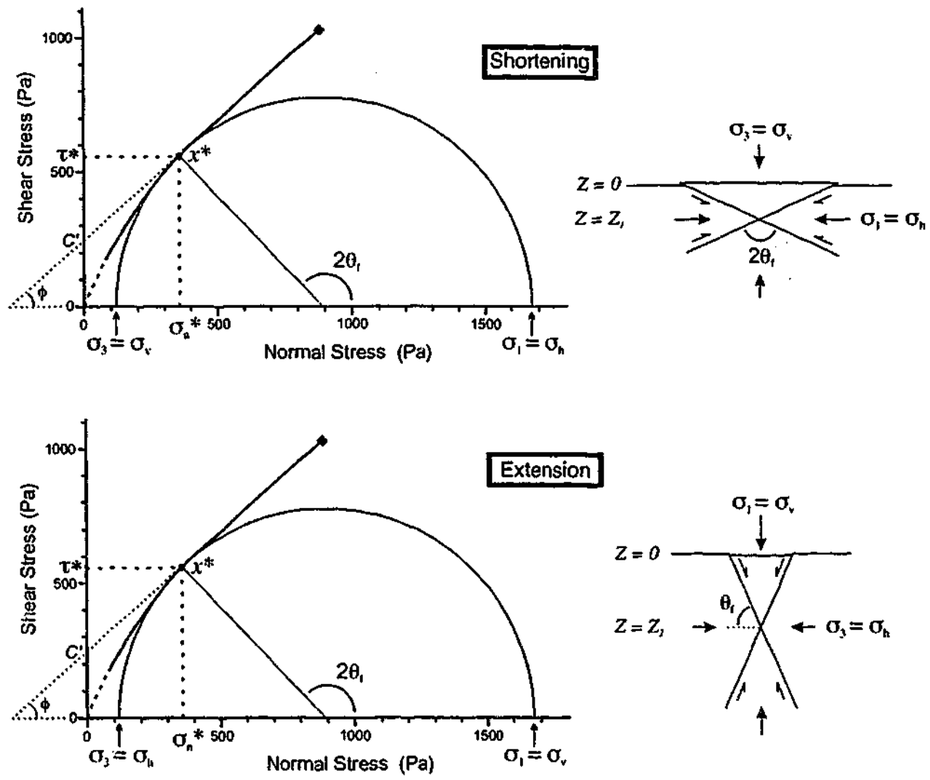

Fig. aIII-6. Mohr diagram and failure envelope for S I. Failure occurs at the critical point x^*, for a critical normal stress and shear stress, with accessory values for σ_1 and σ_3. For shortening, the critical point will be reached at a depth z_1 and for extension, the critical point will be reached at a depth z_2, with $z_1 < z_2$.

basal plate. During an experiment the plastic sheet was moved laterally outward, perpendicular to its straight edge, where the lateral displacement was no bigger than required to produce a visible fault scarp. To investigate the possible dependence of μ with respect to the burial depth, the thickness of the sediment pack was varied (2, 4, 6, 8 and 10 cm). For instance, this results in a normal stress range along the fault plane of 0 Pa to ~ 31 Pa (S I) or 0 Pa to ~ 72 Pa (GM II) for a 2 cm thick sediment pack. For a 10 cm thick sediment pack, this results in a normal stress range along the fault plane of 0 Pa to ~ 365 Pa (S I) or 0 Pa to ~ 580 Pa (GM II). Measurements have been done both for rapidly poured and sprinkled sediment.

During every experiment, a symmetric graben developed, where a synthetic and an antithetic fault developed simultaneously. The fault scarps were approximately of constant strike.

The fault dip has been determined by taking the inverse tangent of the thickness of the sediment pack, divided by half the width of the graben, assuming that it is constant with depth. Since the maximum principal stress in these extensional experiments is vertical, the relationship between the dip of the fault plane, the fracture angle (θ_f) and the angle of internal friction (ϕ) can be written as follows:

$$\text{fault dip} = \theta_f = 45° + \frac{\phi}{2} \qquad \text{(aIII-10)}$$

The fault dips obtained from the experiments and the calculated angles of internal friction are given in Table aIII-4. The dip angles in Table aIII-4 validate the assumption of constant dip with increasing depth and therefore indicate that there is no dependence of μ on the burial depth, at least for this small range. Thus, there is no indication of a dependence of μ on σ_n. Therefore, the non-linear behaviour of the failure envelopes for very small normal stresses is best described as a dependence of the cohesion C on σ_n. From Table aIII-4 it can also be observed that using a different physical handling technique to deposit the sediment piles has a major influence on the angle of internal friction, as has been noted earlier by *Krantz* [1991].

The calculated values for ϕ in Table aIII-3 lie somewhere in between the obtained values for ϕ for pouring and sprinkling of the sediment in Table aIII-4. This could be related to the slight difference in physical handling technique of the sediment in the shear test experiments or to the inexact approximation of the normal and shear stress in these shear tests by using equation (aIII-5a) and (aIII-5b).

A III-5. Discussion

The shear tests pointed to non-linear convex-outward behaviour in normal versus shear stress diagrams for all granular materials investigated, for normal stresses smaller than ~ 250 - 400 Pa and approximate linear behaviour for higher normal stresses (Fig. aIII-4a,b). The values of cohesion for all the investigated materials are approximately 0 Pa (± 15 Pa) for σ_n = 0 Pa and gradually increase to 137 - 247 Pa (± 15 Pa) for σ_n > 250 - 400 Pa.

This non-linear behaviour of the envelopes below some critical normal stress is not the result of a dependence of the coefficient of internal friction μ on σ_n, but may be represented as a dependence of the cohesion C on σ_n. This conclusion has been drawn, because no change in fault dip with increasing burial depth (and thus increasing normal stress) has been observed in the extensional experiments (Table aIII-4).

The obtained envelopes for the investigated materials may be represented by the following equations:

Thickness (cm)	Fault dip angle				Angle of internal friction (ϕ)			
	S I		GM II		S I		GM II	
	poured	*sprinkled*	*poured*	*sprinkled*	*poured*	*Sprinkled*	*poured*	*Sprinkled*
2	59.9	69.8	58.8	65.9	29.9	49.6	27.6	41.8
4	59.5	70.3	60.0	65.5	28.9	50.5	30.0	41.1
6	58.3	70.8	59.0	66.2	26.5	51.7	27.9	42.4
8	60.9	69.5	60.1	66.0	31.8	49.0	30.1	42.0
10	61.4	70.0	60.5	67.3	32.8	50.0	31.0	44.5

Table aIII-4. Fault dip angles and angles of internal friction ϕ for different thicknesses of the sediment packs for the materials S I and GM II (for both pouring and sprinkling of the sediment). From these results it is clear that there is little or no dependence of μ on σ_n. The error in fault dip angle is ± 3°.

$$\tau = f(\sigma_n) + \mu\sigma_n \qquad \text{for} \qquad 0\,\text{Pa} \le \sigma_n < \sigma_n^* \qquad \text{(aIII-11a)}$$

$$\tau = C' + \mu\sigma_n \qquad \text{for} \qquad \sigma_n \ge \sigma_n^* \qquad \text{(aIII-11b)}$$

An approximate representation of the curves for 0 Pa < σ_n < σ_n* might be a straight line. This results in:

$$\tau = \frac{\sigma_n}{\sigma_n^*} C' + \mu\sigma_n \qquad \text{for} \qquad 0\,\text{Pa} \le \sigma_n < \sigma_n^* \qquad \text{(aIII-12a)}$$

$$\tau = C' + \mu\sigma_n \qquad \text{for} \qquad \sigma_n \ge \sigma_n^* \qquad \text{(aIII-12b)}$$

These equations show a close resemblance to the equations (aIII-2b) and (aIII-2c) of *Byerlee* [1978]. However, caution should be taken since his equations are deduced from experiments on prefractured rocks, while equation (aIII-12a) and (aIII-12b) are representative for undeformed (dry granular) material.

Plotting curves for equation (aIII-12a) and (aIII-12b) in a diagram would show 2 straight intersecting lines with different slopes. Here, the slope of the line for equation (aIII-12b) equals the angle of internal friction, but the slope of the line for equation (aIII-12a) does not equal the angle of internal friction. This is, because the slope is dependent both on the angle of internal friction and on the gradual increase of cohesion with increasing normal stress.

The shear tests have profound implications for strength profiles of lithospheric models, where dry granular material has been used to simulate brittle behaviour of rocks in the lithosphere. In Fig. aIII-7 brittle failure curves (for shortening) have been plotted.

First of all, 3 curves have been plotted for sand (Ia,b and III), which are the same curves as plotted in Fig. aIII-1, except for their densities. These curves have been plotted by using equation (aIII-3a). For curve Ia, ρ = 1325 kg/m^3, for curve Ib, ρ = 1650 kg/m^3 and for curve III, ρ = 1780 kg/m^3. For curve Ia,b the densities have been chosen according to the scaling theory (with a density ratio of 1/2 for the analogue model / natural prototype), where curve Ia is the analogue for the continental (granitic) crust and Ib is the analogue for the upper oceanic (serpentinised olivine) lithosphere. The densities for granite and serpentinised olivine have been taken to be 2650 kg/m^3 and 3300 kg/m^3, respectively. The density for curve III is for sprinkled sand from *Krantz* [1991].

Further, curves have been plotted for the investigated materials S I, S II, GM I, GM II and CS, again by using equation (aIII-3a).

Finally, 2 curves have been plotted (Granite and Serpentinite), which are downscaled analogue curves for a granitic crust for a continental lithosphere and a serpentinised olivine upper lithosphere for an oceanic lithosphere. The curves have been scaled down with a length factor of 10^{-6} (which is often used in analogue lithospheric models) and a density factor of 0.5. These curves represent the scaled down curves (for these scaling factors) to which an ideal brittle analogue material should show a perfect match. Curve Granite has been calculated using equation (aIII-2d) and (aIII-2e) and Serpentinite has been calculated using equation (aIII-3a). This choice of equations has been made, since a continental crust is criss-crossed by discontinuities of every shape and size [*Ranalli and Murphy*, 1987], while an oceanic lithosphere is less deformed compared to a continental lithosphere, because the

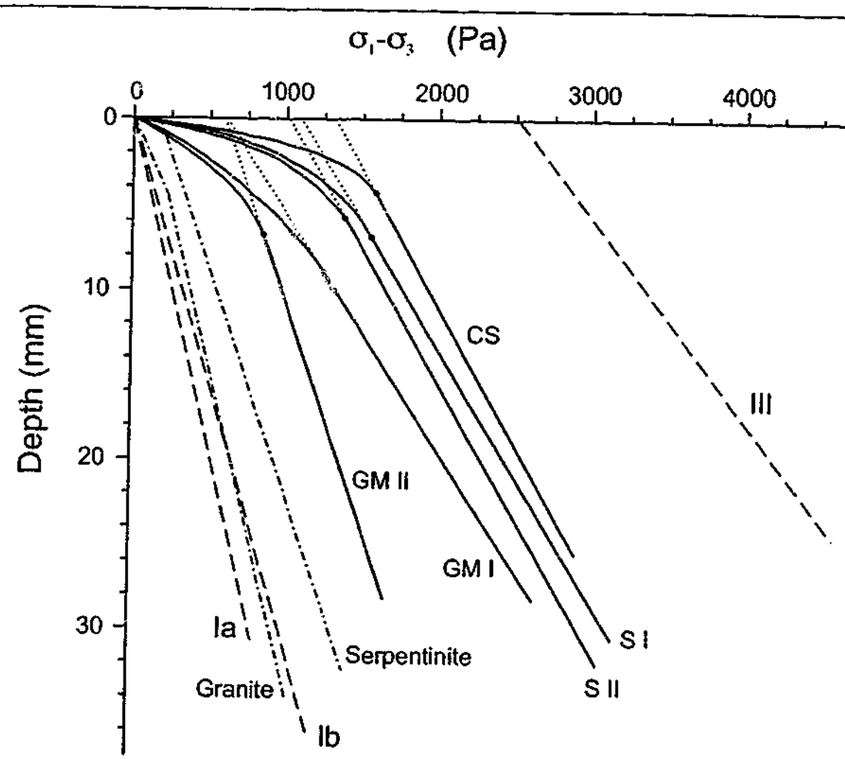

Fig. aIII-7. Brittle failure curves for shortening. The curves numbered Ia,b and III are the same curves as plotted in Fig. aIII-1, only that their densities have been changed. For curve Ia ρ = 1325 kg/m^3, for curve Ib ρ = 1650 kg/m^3 and for curve III ρ = 1780 kg/m^3. Further, the curves for the investigated materials, S I, S II, GM I, GM II and CS can be seen. Finally, 2 curves have been plotted (Granite and Serpentinite), which are downscaled analogue curves for a granitic crust for a continental lithosphere and a serpentinised olivine upper lithosphere for an oceanic lithosphere. All the curves have been plotted by using equation (aIII-3a), except for Granite, which has been plotted by using equation (aIII-2d) and (aIII-2e). For all the curves the pore fluid factor is 0. From these curves it can be seen that the strength profiles for the investigated materials are more complex than previously suggested and that their integrated strengths take a position between the two extremes of curves Ia,b and III.

formation and vertical growth of oceanic lithosphere is related to thermal cooling and normally an oceanic upper lithosphere has undergone less intensive deformation than continental crust, which grows by intrusions, collision, accretion and underplating. Therefore, the strength of upper continental crust is related to shear resistance of rocks on existing fracture planes, while for upper oceanic lithosphere cohesion plays a more significant role in its strength. For Serpentinite the values of μ and C have been obtained from Table aIII-1. The density of granite and serpentinised olivine has been taken to be 2650 kg/m^3 and 3300 kg/m^3, respectively. Pore fluid pressure has been assumed to be zero in both cases.

From the curves of Fig. aIII-7 it is clear that the integrated strengths for the investigated materials take a position between curves Ia,b and III. The integrated strengths for the curves plotted in Fig. aIII-7 have been given in Table aIII-5 for several thicknesses. Here it can be seen that the integrated strength increases with increasing thickness. Further it can be observed that the integrated strength of material GM II shows most resemblance with the

Material	Integrated strength (N/m)		
	10 mm	20 mm	30 mm
Ia	1.31	5.23	11.77
Ib	1.63	6.51	14.65
III	29.32	67.90	113.23
S I	~ 12	~ 33	~ 61
S II	~ 11	~ 31	~ 57
GM I	~ 8	~ 25	~ 49
GM II	~ 7	~ 19	~ 34
CS	~14	~37	~65
Granite	2.11	7.06	14.60
Serpentinite	3.57	9.29	18.83

Table aIII-5. Integrated strengths for the curves plotted in Fig. aIII-7.

integrated strength of curve Ia,b and more important, shows most resemblance with the ideal analogue curves. Especially, curve Serpentinite, with a downscaled cohesion of 45 Pa, shows resemblance with this analogue material, although the integrated strength of GM II is still too high. However, to a first approximation, it could be a good analogue material to model the upper oceanic lithosphere. For bigger scale factors other materials (like S I and S II) might also be appropriate to model brittle behaviour of the upper lithosphere. However, a disadvantage of these bigger scale factors is that the analogue models become extremely large.

A III-6. Conclusions

From the shear tests and normal faulting experiments on various dry granular materials presented above, the following conclusions can be drawn:

1. The coefficient of internal friction and cohesion of the investigated materials are mainly dependent on sphericity and rounding of the individual grains and less dependent on grain size.
2. For normal stresses below a critical value (~ 250 - 400 Pa), failure curves are convex-outward. Above the critical value, failure curves are straight (coulomb-type behaviour).
3. The convex shapes of the failure envelopes are associated with a gradual increase of cohesion of the material with increasing normal stress and not with a gradual decrease in coefficient of internal friction, since extensional experiments revealed that there is no significant decrease in fault dip with increasing depth (and thus increasing normal stress on the fault plane).
4. The obtained curves resemble those obtained by *Byerlee* [1978]. The different physical mechanisms operating at different normal stresses, resulting in convex-outward shaped curves for low normal stresses and straight lines for higher normal stresses, are probably comparable with the different physical mechanisms resulting in the two equations (aIII-2b and aIII-2c) from *Byerlee* [1978].
5. Values of cohesion for the investigated materials increase from 0 Pa (± 15 Pa) at σ_n = 0 Pa to 137 - 247 Pa (± 15 Pa) for $\sigma_n \geq \sigma_n^*$.

6. The material GM II (fine grained glass microspheres) is probably the best material to model brittle deformation in the lithosphere, since its integrated strength shows most resemblance with downscaled values of integrated strengths of natural prototype lithospheres (for a length factor of 10^{-6} and a density factor of 1/2). Also, the coefficient of internal friction for GM II (μ = 0.65) is (almost) the same as for granite and serpentinised olivine (μ = 0.64 and μ = 0.65, respectively). Another advantage is that for fine-grained material the width of fault zones and their dilatancy are much more reduced when compared with coarse-grained material and therefore it is probably better scaled. Since fine-grained material also provides more structural detail than coarse-grained material, it makes it a better analogue to model brittle behaviour of rocks.

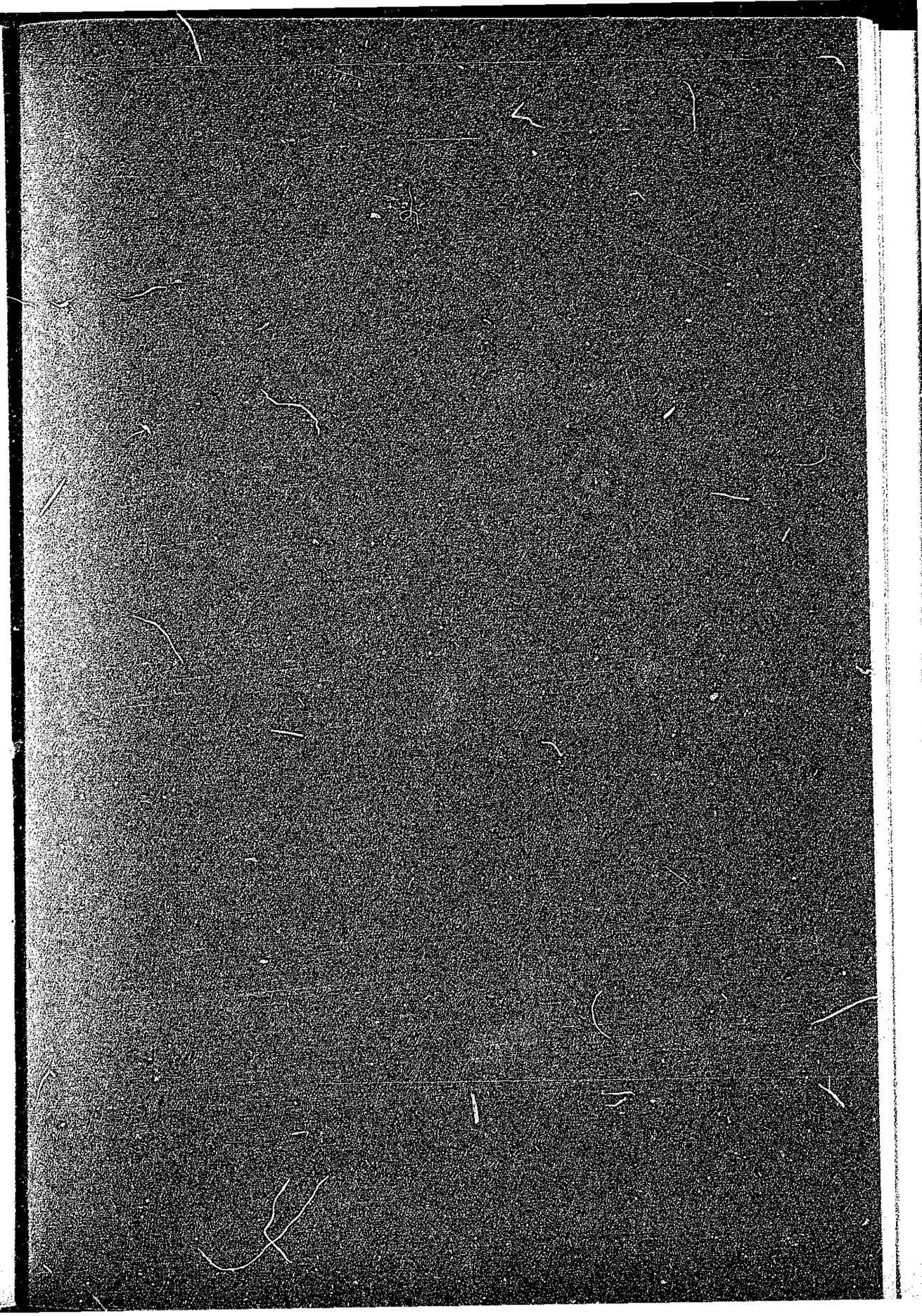

APPENDIX IV

Viscous analogue materials

A IV-1. Introduction

In analogue modelling of large scale tectonic processes basically two types of viscous materials have been used which both have a more or less Newtonian viscosity: high viscosity silicone putties (silicone oils) and any kind of (low viscosity) sugar solution (honey, glucose syrup, corn syrup, golden syrup, sugar solution, sucrose solution). In the experiments described in this thesis, I have used glucose syrup (manufactured by Colonial Farms, Australia) as a relatively low viscosity material (~ 1×10^2 Pa·s) and a silicone putty (Rhodorsil Gum FB, manufactured by Rhodia, France) as a relatively high viscosity material (~ 2×10^4 Pa·s).

A IV-2. Silicone Putty

The common name for this material is silicone putty or silicone oil, its chemical name is polydimethylsiloxane and its industry name is Rhodorsil Gum FB.

The rheological behaviour of the material has been tested by a commercial company for strain rates between 10^{-4} and 10^{-2} s^{-1} at temperatures of 20, 60, and 90° C. The average strain rate for the various experiments varied within the range of 10^{-5} to 10^{-2} s^{-1}. From these measurements it was concluded that the silicone putty is Newtonian in behaviour for these strain rates and temperatures. The following consecutive equation applies for this material:

$$\eta = Ae^{(E_a / RT)} \qquad \text{(aIV-1)}$$

where η is the viscosity; A is a material constant; E_a is the activation energy; R is the gas constant; and T is the temperature in Kelvin. Here, A = 17.812 Pa·s, E_a = 17048 J mol^{-1} and R = 8.31434 $J \cdot K^{-1}$ mol^{-1}. From equation (aIV-1) it can be concluded that at a temperature of ~ 20° C (293.15° K), the silicone putty has a viscosity of ~ 1.94×10^4 Pa·s.

The silicone putty is transparent and it is a cohesive material. The density of the silicone putty is 970 kg/m^3. The density of the silicone putty can be varied by mixing the putty with a dense filler. In all the experiments finegrained iron powder has been used as filler (grainsize of 0-150 μm). With this method, the density of the silicone putty has been increased to 1200 – 1500 kg/m^3 without changing the viscosity of the material significantly [e.g. *Wijermars*, 1986]. The new viscosity of the silicone – iron powder mix can be approximated with the following equation [*Wijermars*, 1986]:

$$\eta_{mix} = \eta_s (1 - c\frac{V_i}{V_s})^{-2.5} \qquad \text{(aIV-2)}$$

where η_{mix} is the viscosity of the silicone – iron powder mix; η_s is the viscosity of the pure silicone; c is a constant depending on the roundness and grain size distribution of the powder (1 for spherical material with a large variety in grain size); V_i is the volume of powder in the

mix; and V_s is the volume of the silicone in the mix. For calculations of η_{mix}, c has been assumed to be 1.

The addition of filler to the silicone putty makes the mix opaque. After addition of the filler, the mix has to be spread out on a table to let it settle and allow the air bubbles to escape.

Some of the advantages of the silicone putty are that it is relatively easy and clean to work with, and that its density can be varied according to the needs of the experimenter without changing its mechanical properties significantly. Furthermore, it can be moulded into sheets with a desired geometry, the material can be recycled and it is save to work with in experiments. Although the price at which this material has been obtained in Australia was relatively cheap (AU$ 13,- a kg at Rhodia, VIC, Australia), these prices may vary significantly in different countries. Unfortunately the material (as any other high viscosity silicone putty) is not easily obtainable, since several main producers of silicone putties have stopped with the production line some years ago [*P.R. Cobbold*, pers. comm.].

A IV-3. Glucose syrup

The glucose syrup is a Newtonian viscous material. Its viscosity has been determined with a rotary viscometer ($\eta \approx 1\text{-}2 \times 10^2$ Pa·s at 20°C). Viscosity has also been measured with a Stokes viscometer (falling rigid ball in fluid) [e.g. *Weijermars*, 1986]. The viscosity can be determined with the following equation:

$$\eta_f = \frac{2gR^2(\rho_b - \rho_f)\Delta t}{9L} \qquad \text{(aIV-2)}$$

where η_f is the dynamic viscosity of the fluid; g is the acceleration due to gravity; R is the radius of the ball; ρ_b is the density of the ball; ρ_f is the density of the fluid; Δt is the time lapse for the ball to travel a distance L.

The viscosity can be changed significantly by changing its water content (addition of water will decrease its viscosity) or by changing its temperature (decreasing the temperature will increase its viscosity). It has a density of ~ 1420 kg/m^3. Some of the advantages of glucose syrup is that its viscosity is a factor of ~ 200 smaller than the viscosity of the silicone putty, it is (semi)transparent, a harmless chemical, cheap and easily available in large quantities (~ AU$ 50,- for a 25 kg drum, Colonial Farms, NSW, Australia). Furthermore, although it is relatively sticky material, it dissolves in warm water. One disadvantage is that it attracts large quantities of ants, which means that after every experiment, the lab has to be thoroughly cleaned.

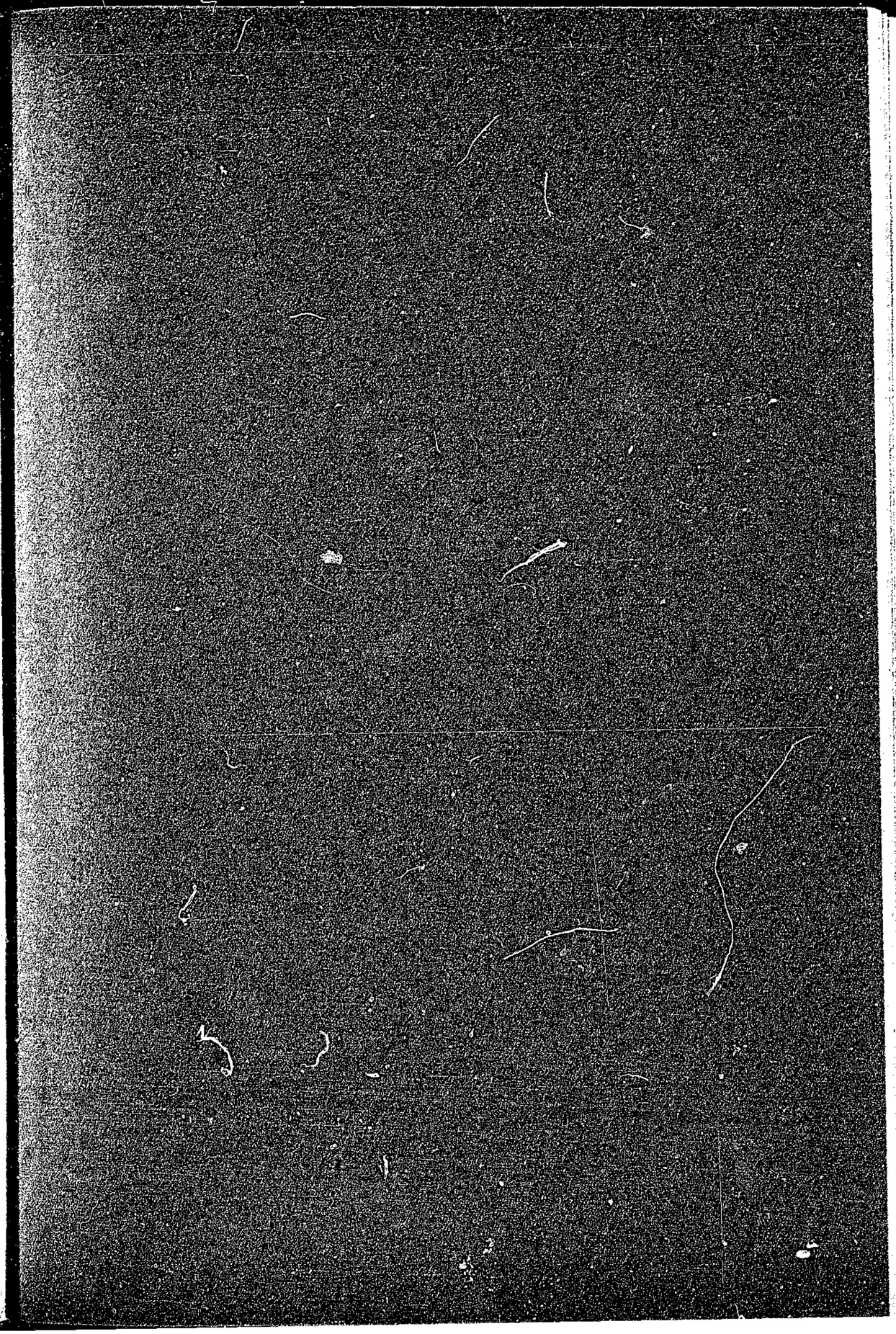

REFERENCES

Aksu, A.E., A. Ulug, D.J.W. Piper, Y.T. Konuk, and S. Turgut, Quaternary sedimentary history of Adana, Cilicia and Iskenderun basins; Northeast Mediterranean Sea, *Marine Geology, 104*, 55-71, 1992.

Alvarez, W., Geological evidence for the geographical pattern of mantle return flow and the driving mechanism of plate tectonics, *Journal of Geophysical Research, 87*, 6697-6710, 1982.

Ampferer, O., Über das Bewegungsbild von Faltengebirgen, *Geol. Reichsanst. Vienna Jahrb., 56*, 539-622, 1906.

Andreason, M.W., B. Mudford, and J.E.S. Onge, Geologic evolution and petroleum system of Thailand Andaman Sea Basins., in *Proceedings of the International Conference on Petroleum Systems of SE Asia and Australia, Indonesian Petroleum Association*, edited by J.V.C. Howes, and R.A. Noble, pp. 337-350, 1997.

Angelier, J., N. Lyberis, X. Le Pichon, E. Barrier, and P. Huchon, The tectonic development of the Hellenic Arc and the Sea of Crete; a synthesis, *Tectonophysics, 86*, 159-196, 1982.

Armijo, R., B. Meyer, G.C.P. King, A. Rigo, and D. Papanastassiou, Quaternary evolution of the Corinth Rift and its implications for the late Cenozoic evolution of the Aegean, *Geophysical Journal International, 126*, 11-53, 1996.

Artyushkov, E.V., Stresses in the Lithosphere Caused by Crustal Thickness Inhomogeneities, *Journal of Geophysical Research, 78*, 7675-7708, 1973.

Artyushkov, E.V., *Geodynamics*, 312 pp., Elsevier, Amsterdam, 1983.

Auzende, J.-M., Y. Lafoy, and B. Marsset, Recent geodynamic evolution of the North Fiji Basin (Southwest Pacific), *Geology, 16*, 925-929, 1988.

Auzende, J.-M., B. Pelletier, and Y. Lafoy, Twin active spreading ridges in the North Fiji Basin (Southwest Pacific), *Geology, 22*, 63-66, 1994.

Bada, G., F. Horvath, P. Gerner, and I. Fejes, Review of the present-day geodynamics of the Pannonian Basin; progress and problems, *Journal of Geodynamics, 27*, 501-527, 1999.

Bakhteev, M.K., O.A. Morozov, and S.R. Tikhomirova, Structure of the eastern Kamchatka ophiolite-free collisional suture, Grechishkin Thrust, *Geotectonics, 31*, 236-246, 1997.

Baranov, B.V., N.I. Seliverstov, A.V. Murav'ev, and E.L. Muzurov, The Komandorsky Basin as a product of spreading behind a transform plate boundary, *Tectonophysics, 199*, 237-269, 1991.

Barker, P.F., The Cenozoic subduction history of the Pacific margin of the Antarctic Peninsula; ridge crest-trench interactions, *Journal of the Geological Society of London, 139*, 787-801, 1982.

Barker, P.F., Tectonic framework of the East Scotia Sea, in *Backarc basins: tectonics and magmatism*, edited by B. Taylor, pp. 281-314, Plenum Press, New York, 1995.

Barker, P.F., Scotia Sea regional tectonic evolution; implications for mantle flow and palaeocirculation, *Earth-Science Reviews, 55*, 1-39, 2001.

Basile, C., and J.P. Brun, Transtensional faulting patterns ranging from pull-apart basins to transform continental margins; an experimental investigation, *Journal of Structural Geology, 21*, 23-37, 1998.

Beck, R.A., D.W. Burbank, W.J. Sercombe, G.W. Riley, J.K. Barndt, J.R. Berry, J. Afzal, A.M. Khan, H. Jurgen, J. Metje, A. Cheema, N.A. Shafique, R.D. Lawrence, and M.A. Khan, Stratigraphic evidence for an early collision between Northwest India and Asia, *Nature, 373*, 55-58, 1995.

Becker, T.W., C. Faccenna, R.J. O'Connell, and D. Giardini, The development of slabs in the upper mantle; insights from numerical and laboratory experiments, *Journal of Geophysical Research, 104*, 15207-15226, 1999.

Ben-Avraham, Z., A. Nur, D. Jones, and A. Cox, Continental accretion; from oceanic plateaus to allochthonous terranes, *Science, 213*, 47-54, 1981.

Benes, V., and P. Davy, Modes of continental lithospheric extension; experimental verification of strain localization processes, *Tectonophysics, 254*, 69-87, 1996.

Bevis, M., F.W. Taylor, B.E. Schutz, J. Recy, B.L. Isacks, S. Helu, R. Singh, E. Kendrick, J. Stowell, B. Taylor, and S. Calmant, Geodetic observations of very rapid convergence and back-arc extension at the Tonga Arc, *Nature, 374*, 249-251, 1995.

Bird, P., Lateral extrusion of lower crust from under high topography, in the isostatic limit, *Journal of Geophysical Research,, 96*, 10275-10286, 1991.

Bird, P., and K. Piper, Plane-stress finite-element models of tectonic flow in southern California, *Physics of the Earth and Planetary Interiors, 21*, 158-175, 1980.

Bogdanov, N.A., Geology of the Komandorsky deep basin, *Journal of Physics of the Earth, 36*, S65-S71, 1988.

Bogdanov, N.A., V.S. Vishnevskaya, and A.N. Suchov, Upper Cretaceous deposits from the Shirshov Ridge (Bering Sea), *Dokl. Akad. Nauk SSSR, 273*, 1183-1187 (in Russian), 1983.

Bonini, M., T. Souriot, M. Boccaletti, and J.-P. Brun, Successive orthogonal and oblique extension episodes in a rift zone; laboratory experiments with application to the Ethiopian Rift, *Tectonics, 16*, 347-362, 1997.

Bott, M.H.P., Modelling the plate-driving mechanism, *Journal of the Geological Society of London, 150*, 941-951, 1993.

Boutelier, D., and A. Chemenda, Continental subduction and exhumation of HP rocks: first experience of physical thermomechanical modelling, *Journal of the Virtual Explorer, 7*, 61-65, 2002.

Brace, W.F., and D.L. Kohlstedt, Limits on lithospheric stress imposed by laboratory experiments, *Journal of Geophysical Research, 85*, 6248-6252, 1980.

Briais, A., P. Patriat, and P. Tapponnier, Updated interpretation of magnetic anomalies and seafloor spreading stages in the South China Sea; implications for the Tertiary tectonics of Southeast Asia, *Journal of Geophysical Research, 98*, 6299-6328, 1993.

Brun, J.-P., D. Sokoutis, and J. van den Driessche, Analogue modeling of detachment fault systems and core complexes, *Geology, 22*, 319-322, 1994.

Brun, J.P., Narrow rifts versus wide rifts; inferences for the mechanics of rifting from laboratory experiments, *Royal Society. Mathematical, Physical and Engineering Sciences, 357*, 695-712, 1999.

Brune, J.N., and M.A. Ellis, Structural features in a brittle-ductile wax model of continental extension, *Nature, 387*, 67-70, 1997.

Buck, W.R., Modes of continental lithospheric extension, *Journal of Geophysical Research, 96*, 20161-20178, 1991.

Bucky, B.P., The use of models for hte study of mining problems, *Technical Publication, American Institure of Mining Engineers, 425*, 1931.

Buiter, S.J.H., R. Govers, and M.J.R. Wortel, A modelling study of vertical surface displacements at convergent plate margins, *Geophysical Journal International, 147*, 415-427, 2001.

Burg, J.-P., D. Sokoutis, and M. Bonini, Model-inspired interpretation of seismic structures in the Central Alps: Crustal wedging and buckling at mature stage of collision, *Geology, 30*, 643-646, 2002.

Burke, K., Tectonic evolution of the Caribbean, *Annual Review of Earth and Planetary Sciences, 16*, 201-230, 1988.

Buttles, J., and P. Olson, A laboratory model of subduction zone anisotropy, *Earth and Planetary Science Letters, 164*, 245-262, 1998.

Byerlee, J., Friction of rocks, *Pure and Applied Geophysics, 116*, 615-626, 1978.

Cadell, H.M., Experimental researches in mountain building, *Transactions of the Royal Society of Edinburgh, 1*, 339-343, 1889.

Calmant, S., B. Pelletier, R. Pillet, M. Regnier, P. Lebellegard, D. Maillard, F. Taylor, M. Bevis, and J. Recy, Interseismic and coseismic motions in GPS series related to the M (sub s) 7.3 July 13, 1994, Malekula earthquake, central New Hebrides subduction zone, *Geophysical Research Letters, 24*, 3077-3080, 1997.

Carmignani, L., S. Barca, L. Disperati, P.L. Fantozzi, A. Funedda, G. Oggiano, and S. Pasci, Tertiary compression and extension in the Sardinian basement, *Bollettino di Geofisica Teorica ed Applicata, 36*, 45-62, 1994.

Carmignani, L., and R. Kligfield, Crustal extension in the Northern Apennines; the transition from compression to extension in the Alpi Apuane core complex, *Tectonics, 9*, 1275-1303, 1990.

Carter, N.L., and M.C. Tsenn, Flow properties of continental lithosphere, *Tectonophysics, 136*, 27-63, 1987.

Catalano, R., C. Doglioni, and S. Merlini, On the Mesozoic Ionian Basin, *Geophysical Journal International, 144*, 49-64, 2001.

Channel, J.E.T., Palaeomagnetism and continental collision in the Alpine Belt and the formation of late-tectonic extensional basins, in *Collision tectonics*, edited by M.P. Coward, and A.C. Ries, pp. 261-184, 1986.

Chapple, W.M., and T.E. Tullis, Evaluation of the forces that drive the plates, *Journal of Geophysical Research, 82*, 1967-1984, 1977.

Chemenda, A.I., J.-P. Burg, and M. Mattauer, Evolutionary model of the Himalaya-Tibet system; geopoem based on new modelling, geological and geophysical data, *Earth and Planetary Science Letters, 174*, 397-409, 2000.

Chemenda, A.I., M. Mattauer, and A.N. Bokun, Continental subduction and a mechanism for exhumation of high-pressure metamorphic rocks; new modelling and field data from Oman, *Earth and Planetary Science Letters, 143*, 173-182, 1996.

Chemenda, A.I., M. Mattauer, J. Malavieille, and A.N. Bokun, A mechanism for syn-collisional rock exhumation and associated normal faulting; results from physical modelling, *Earth and Planetary Science Letters, 132*, 225-232, 1995.

Chemenda, A.I., R.K. Yang, C.H. Hsieh, and A.L. Groholsky, Evolutionary model for the Taiwan collision based on physical modelling, *Tectonophysics, 274*, 253-274, 1997.

Chemenda, A.I., R.K. Yang, J.F. Stephan, E.A. Konstantinovskaya, and G.M. Ivanov, New results from physical modelling of arc-continent collision in Taiwan; evolutionary model, *Tectonophysics, 333*, 159-178, 2001.

Chonglong, W., Y. Qi, Z. Zuoduo, L. Gang, and L. Xing, Thermodynamic analysis and simulation of coal metamorphism in the Fushun Basin, China, *International Journal of Coal Geology, 44*, 149-168, 2000.

Christensen, U.R., The influence of trench migration on slab penetration into the lower mantle, *Earth and Planetary Science Letters, 140*, 27-39, 1996.

Cízková, H., J. van Hunen, A.P. van den Berg, and N.J. Vlaar, The influence of rheological weakening and yield stress on the interaction of slabs with the 670 km discontinuity, *Earth and Planetary Science Letters, 199*, 447-457, 2002.

Clague, D.A., and G.B. Dalrymple, The Hawaiian-Emperor volcanic chain; Part I, Geologic evolution, in *Volcanism in Hawaii*, edited by R.W. Decker, T.L. Wright, and P.H. Stauffer, pp. 5-54, U. S. Geological Survey Professional Paper 1350, Denver, 1987.

Cloos, E., Experimental analysis of fracture patterns, *Geological Society of America Bulletin, 66*, 241-256, 1955.

Cloos, M., Lithospheric buoyancy and collisional orogenesis: Subduction of oceanic plateaus, continental margins, island arcs, spreading ridges and seamounts, *Geological Society of America Bulletin, 105*, 715-737, 1993.

Cobbold, P.R., A biaxial press for model deformation and rheological tests, *Tectonophysics, 26*, T1-T5, 1975.

Cobbold, P.R., and L. Castro, Fluid pressure and effective stress in sandbox models, *Tectonophysics, 301*, 1-19, 1999.

Cobbold, P.R., and M.P.A. Jackson, Gum rosin (colophony); a suitable material for thermomechanical modelling of the lithosphere, *Tectonophysics, 210*, 255-271, 1992.

Coleman, M., and K. Hodges, Evidence for Tibetan plateau uplift before 14 Myr ago from new minimum age for east-west extension, *Nature, 374*, 49-52, 1995.

Collot, J.Y., J. Daniel, and R.V. Burne, Recent tectonics associated with the subduction/collision of the d'Entrecasteaux Zone in the central New Hebrides, *Tectonophysics, 112*, 325-356, 1985.

Conrad, C.P., and B.H. Hager, Effects of plate bending and fault strength at subduction zones on plate dynamics, *Journal of Geophysical Research*, *104*, 17551-17571, 1999.

Cook, D.B., K. Fujita, and C.A. McMullen, Present-day plate interactions in Northeast Asia; North American, Eurasian, and Okhotsk plates, *Journal of Geodynamics*, *6*, 33-51, 1986.

Cooper, A.K., M.S. Marlow, and D.W. Scholl, Mesozoic magnetic lineations in the Bering Sea marginal basin, *Journal of Geophysical Research*, *81*, 1916-1934, 1976.

Cooper, A.K., M.S. Marlow, and D.W. Scholl, Geologic framework of the Bering Sea crust, in *Geology and resource potential of the continental margin of western North America and adjacent ocean basins, Beaufort Sea to Baja California*, edited by D.W. Scholl, A. Grantz, and J.G. Vedder, pp. 73-102, 1987a.

Cooper, A.K., M.S. Marlow, D.W. Scholl, and A.J. Stevenson, Evidence for cenozoic crustal extension in the Bering Sea region, *Tectonics*, *11*, 719-731, 1992.

Cooper, A.K., D.W. Scholl, and M.S. Marlow, Structural framework, sedimentary sequences, and hydrocarbon potential of the Aleutian and Bowers basins, Bering Sea, in *Geology and resource potential of the continental margin of western North America and adjacent ocean basins, Beaufort Sea to Baja California*, edited by D.W. Scholl, A. Grantz, and J.G. Vedder, pp. 473-502, 1987b.

Coulomb, C.A., Sur une application des régles maximis et minimis a quelques problèmes de statique, relatifs à l'architecture, *Mémoires de Mathématique et de Physique, Académie Royale des Sciences*, *7*, 343-382, 1776.

Csontos, L., and A. Nagymarosy, The Mid-Hungarian line; a zone of repeated tectonic inversions, *Tectonophysics*, *297*, 51-71, 1998.

Csontos, L., G. Tari, F. Bergerat, and L. Fodor, Evolution of the stress fields in the Carpatho-Pannonian area during the Neogene, *Tectonophysics*, *199*, 73-91, 1991.

Curray, J.R., D.G. Moore, L.A. Lawver, F.J. Emmel, R.W. Raitt, M. Henry, and R. Kieckhefer, Tectonics of the Andaman Sea and Burma, in *Geological and geophysical investigations of continental margins. AAPG Memoir*, edited by J.S. Watkins, L. Montadert, and P.W. Dickerson, pp. 189-198, 1979.

Dalrymple, G.B., D.A. Clague, and M.A. Lanphere, Revised age for Midway Volcano, Hawaiian volcanic chain, *Earth and Planetary Science Letters*, *37*, 107-116, 1977.

Daubre, A., *Etudes synthétiques de géologie expérimentale*, 828 pp., Dunod, pt. 1 Paris, 1879.

Davies, R., P. England, B. Parsons, H. Billiris, D. Paradissis, and G. Veis, Geodetic strain of Greece in the interval 1892-1992, *Journal of Geophysical Research*, *102*, 24571-24588, 1997.

Davis, G.H., *Structural geology of rocks and regions*, 492 pp., John Wiley and Sons, New York, 1984.

Davy, P., and P.R. Cobbold, Indentation tectonics in nature and experiment. 1. Experiments scaled for gravity, *Bulletin of the Geological Institutions of the University of Uppsala, New Series*, *14*, 129-141, 1988.

Davy, P., and P.R. Cobbold, Experiments on shortening of a 4-layer model of the continental lithosphere, *Tectonophysics*, *188*, 1-25, 1991.

De Fazio, T.L., Island-arc and underthrust-plate geometry, *Tectonophysics*, *23*, 149-154, 1974.

De Sausurre, H.B., *Voyages dans les Alpes, Vol II, III*, Fauche, Neuchâtel, 1784 until 1796.

De Sausurre, H.B., *Voyages dans les Alpes, Vol IV*, Fauche-Borel, Neuchâtel, 1796.

Delvaux, D., R. Moeys, G. Stapel, C. Petit, K.G. Levi, A. Miroshnichenko, V.V. Ruzhich, and V. San'kov, Paleostress reconstructions and geodynamics of the Baikal region, Central Asia; Part 2, Cenozoic rifting, *Tectonophysics*, *282*, 1-38, 1997.

DeMets, C., R.G. Gordon, D.F. Argus, and S. Stein, Effect of recent revisions to the geomagnetic reversal time scale on estimates of current plate motions, *Geophysical Research Letters*, *21*, 2191-2194, 1994.

Dennis, J.G., *Orogeny*, 379 pp., Hutchinson Ross Publishing Company, Stroudsburg, 1982.

Descartes, R., *Principia Philosophiae*, 310 pp., Elsevier, Amsterdam, 1644.

Dewey, J.F., Episodicity, sequence, and style at convergent plate boundaries, in *The continental crust and its mineral deposits*, edited by D.W. Strangway, pp. 553-573, Toronto, ON, Canada, 1980.

Dewey, J.F., Extensional collapse of orogens, *Tectonics*, *7*, 1123-1139, 1988.

Dietz, R.S., Continent and ocean basin evolution by spreading of the sea floor, *Nature*, *190*, 854-857, 1961.

Diraison, M., P.R. Cobbold, D. Gapais, E.A. Rossello, and C. Le Corre, Cenozoic crustal thickening, wrenching and rifting in the foothills of the southernmost Andes, *Tectonophysics*, *316*, 91-119, 2000.

Dixon, J.M., A new method of determining finite strain in models of geological structures, *Tectonophysics*, *24*, 99-114, 1974.

Dixon, J.M., Finite strain and progressive deformation in models of diapiric structures, *Tectonophysics*, *28*, 89-124, 1975.

Dixon, J.M., and J.M. Summers, Recent developments in centrifuge modelling of tectonic processes; equipment, model construction techniques and rheology of model materials, *Journal of Structural Geology*, *7*, 83-102, 1985.

Doglioni, C., E. Gueguen, P. Harabaglia, and F. Mongelli, On the origin of west-directed subduction zones and applications to the western Mediterranean, in *Mediterranean basins; Tertiary extension within the Alpine Orogen*, edited by B. Durand, L. Jolivet, F. Horvath, and M. Seranne, pp. 541-561, Cergy-Pontoise, France, 1999b.

Doglioni, C., P. Harabaglia, S. Merlini, F. Mongelli, A. Peccerillo, and C. Piromallo, Orogens and slabs vs. their direction of subduction, *Earth-Science Reviews*, *45*, 167-208, 1999a.

Duermeijer, C.E., W. Krijgsman, C.G. Langereis, and J.H. ten Veen, Post-early Messinian counterclockwise rotations on Crete; implications for late Miocene to Recent kinematics of the southern Hellenic Arc, *Tectonophysics*, *298*, 177-189, 1998.

Dutton, On some of the greater problems of physical geology, *Philosophical Society Washington Bulletin*, *12*, 51-64, 1889.

Dvorkin, J., A. Nur, G. Mavko, and Z. Ben-Avraham, Narrow subducting slabs and the origin of backarc basins, *Tectonophysics*, *227*, 63-79, 1993.

Eguchi, T., and S. Uyeda, Seismotectonics of the Okinawa Trough and Ryukyu Arc, in *Chung Kuo Ti Ch'ih Hsueh Hui Chuan Kan = Memoir of the Geological Society of China*, pp. 189-210, 1983.

Elsasser, W.M., Convection and stress propagation in the upper mantle, *Princeton University Technical Report*, *5*, 1967.

Elsasser, W.M., Convection and stress propagation in the upper mantle, in *the application of modern physics to the Earth and planetary interiors*, edited by S.K. Runcorn, pp. 223-246, Wiley-Interscience, Lodon, 1969.

Elsasser, W.M., Sea-floor spreading as thermal convection, *Journal of Geophysical Research*, *76*, 1101-1112, 1971.

Engebretson, D.C., A. Cox, and R.G. Gordon, Relative motions between oceanic and continental plates in the Pacific Basin, *Special Paper - Geological Society of America*, *206*, 1-59, 1985.

England, P., and G. Houseman, Finite strain calculations of Continental Deformation 2. Comparison with the India-Asia collision zone, *Journal of Geophysical Research*, *91*, 3664-3676, 1986.

England, P., and D. McKenzie, A thin viscous sheet model for continental deformation, *Geophysical Journal of the Royal Astronomical Society*, *70*, 295-321, 1982.

England, P., and D. McKenzie, Correction to; A thin viscous sheet model for continental deformation, *Geophysical Journal of the Royal Astronomical Society*, *73*, 523-532, 1983.

England, P.C., Diffuse continental deformation; length scales, rates and metamorphic evolution, *Philosophical Transactions of the Royal Society of London, Series A: Mathematical and Physical Sciences*, *321*, 3-22, 1987.

England, P.C., and G. Houseman, Extension during continental convergence, with application to the Tibetan Plateau, *Journal of Geophysical Research*, *94*, 17561-17579, 1989.

England, P.C., and G.A. Houseman, The mechanics of the Tibetan Plateau, *Philosophical Transactions of the Royal Society of London, Series A: Mathematical and Physical Sciences*, *326*, 301-320, 1988.

England, P.C., and A.B. Thompson, Pressure-temperature-time paths of regional metamorphism; I. Heat transfer during the evolution of regions of thickened continental crust, *Journal of Petrology*, *25*, 894-928, 1984.

Escher, B.G., and P.H. Kuenen, Experiments in connection with salt domes, *Leidsche Geologische Mededeelingen*, *3*, 151-182, 1929.

Ewing, M., and B. Heezen, Some problems of Antarctic submarine geology, *Geophysical Monograph*, *1* (462), 75-81, 1956.

Faccenna, C., T.W. Becker, F.P. Lucente, L. Jolivet, and F. Rossetti, History of subduction and back-arc extension in the Central Mediterranean, *Geophysical Journal International*, *145*, 809-820, 2001a.

Faccenna, C., P. Davy, J.-P. Brun, R. Funiciello, D. Giardini, M. Mattei, and T. Nalpas, The dynamics of back-arc extension; an experimental approach to the opening of the Tyrrhenian Sea, *Geophysical Journal International*, *126*, 781-795, 1996.

Faccenna, C., F. Funiciello, D. Giardini, and P. Lucente, Episodic back-arc extension during restricted mantle convection in the Central mediterranean, *Earth and Planetary Science Letters*, *187*, 105-116, 2001b.

Faccenna, C., D. Giardini, P. Davy, and A. Argentieri, Initiation of subduction at Atlantic-type margins; insights from laboratory experiments, *Journal of Geophysical Research*, *104*, 2749-2766, 1999.

Falvey, D.A., Analysis of palaeomagnetic data from the New Hebrides, *Australian Society of Exploration Geophysicists Bulletin*, *9*, 117-123, 1978.

Faugere, E., and J.P. Brun, Modelisation experimentale de la distention continentale; Experimental models of a stretched continental crust, *Comptes-Rendus des Seances de l'Academie des Sciences, Serie 2: Mecanique-Physique, Chimie, Sciences de l'Univers, Sciences de la Terre*, *299*, 365-370, 1984.

Favre, A., Archives des Sciences Physique et Naturelles,, *No. 246*, 1878.

Fedorchuk, A.V., and I.N. Izvekov, New Data on the geology of the northern Sredinny Range (Kamchatka), *Transactions USSR Academy of Sciences, Geological Series*, *10*, 147-151 (in Russian), 1992.

Ferrari, L., C.M. Petrone, and L. Francalanci, Generation of oceanic-island basalt-type volcanism in the western Trans-Mexican volcanic belt by slab rollback, astehnosphere infiltration, and variable flux melting, *Geology*, *29*, 507, 2001.

Fisher, O., *Physics of the Earth's crust*, 299 pp., Macmillan, London, 1881.

Forsyth, D.W., and S. Uyeda, On the relative importance of the driving forces of plate motion, *The Geophysical Journal of the Royal Astronomical Society*, *43*, 163-200, 1975.

Fournier, M., O. Fabbri, J. Angelier, and J.-P. Cadet, Regional Seismicity and on-land deformation in the Ryukyu arc: Implications for the kinematics of opening of the Okinawa Trough, *Journal of Geophysical Research*, *106*, 13751-13768, 2001.

Fournier, M., L. Jolivet, P. Huchon, K.F. Sergeyev, and L.S. Oscorbin, Neogene strike-slip faulting in Sakhalin and the Japan Sea opening, *Journal of Geophysical Research*, *99*, 2701-2725, 1994.

Frank, F.C., Curvature of island arcs, *Nature*, *220*, 363, 1968.

Frisch, W., J. Kuhlemann, I. Dunkl, and A. Bruegel, Palinspastic reconstruction and topographic evolution of the Eastern Alps during late Tertiary tectonic extrusion, *Tectonophysics*, *297*, 1-15, 1998.

Fryer, P., Geology of the Mariana Trough, in *Backarc Basins; Tectonics and Magmatism*, edited by B. Taylor, pp. 237-279, Plenum, New York, 1995.

Fryer, P., Evolution of the Mariana convergent plate margin system, *Reviews of Geophysics*, *34*, 89-125, 1996.

Fryer, P., and D.M. Hussong, Seafloor spreading in the Mariana Trough; results of Let 60 drill site selection surveys, *Initial Reports of the Deep Sea Drilling Project*, *60*, 45-55, 1982.

Fujiwara, T., T. Yamazaki, and M. Joshima, Bathymetry and magnetic anomalies in the Havre Trough and southern Lau Basin; from rifting to spreading in back-arc basins, *Earth and Planetary Science Letters*, *185*, 253-264, 2001.

Fukao, Y., S. Widiyantoro, and M. Obayashi, Stagnant slabs in the upper and lower mantle transition region, *Reviews of Geophysics*, *39*, 291-323, 2001.

Funiciello, F., C. Faccenna, D. Giardini, and P. Lucente, Episodic back-arc extension during restricted mantle convection in the Central Mediterranean, *Eos, Transactions, American Geophysical Union*, *81* (48), 1081-1082, 2000.

Funiciello, F., C. Faccenna, D. Giardini, G. Morra, and K. Regenauer-Lieb, Dynamics of retreating slabs: laboratory and numerical experiments, *Bolletino di Geofysica Teorica ed Applicata*, *42 (suppl. 1/2)*, 170-173, 2002.

Gamble, J.A., and I.C. Wright, The Southern Havre Trough geological structure and magma petrogenesis of an active backarc rift complex, in *Backarc basins: tectonics and magmatism*, edited by B. Taylor, pp. 29-62, Plenum Press, New York, 1995.

Garfunkel, Z., C.A. Anderson, and G. Schubert, Mantle circulation and the lateral migration of subducted slabs, *Journal of Geophysical Research*, *91*, 7205-7223, 1986.

Gaudemer, Y., C. Jaupart, and P. Tapponnier, Thermal control on post-orogenic extension in collision belts, *Earth and Planetary Science Letters*, *89*, 48-62, 1988.

Gautier, P., J.-P. Brun, R. Moriceau, D. Sokoutis, J. Martinod, and L. Jolivet, Timing, kinematics and cause of Aegean extension; a scenario based on a comparison with simple analogue experiments, *Tectonophysics*, *315*, 31-72, 1999.

Gelabert, B., F. Sàbat, and A. Rodríguez-Perea, A new proposal for the late Cenozoic geodynamic evolution of the western Mediterranean, *Terra Nova*, *14*, 93-100, 2002.

Ghisetti, F., and L. Vezzani, Different styles of deformation in the Calabrian Arc (southern Italy); implications for a seismotectonic zoning, *Tectonophysics*, *85*, 149-165, 1982.

Giardini, D., and J.H. Woodhouse, Horizontal shear flow in the mantle beneath the Tonga arc, *Nature*, *319*, 551-555, 1986.

Giunchi, C., P. Gasperini, R. Sabadini, and G. D'Agostino, The role of subduction on the horizontal motions in the Tyrrhenian Basin; a numerical model, *Geophysical Research Letters*, *21*, 529-532, 1994.

Glazner, A.F., and J.M. Bartley, Evolution of lithospheric strength after thrusting, *Geology*, *13*, 42-45, 1985.

Gnibidenko, H.S., T.W.C. Hilde, E.V. Gretskaya, and A.A. Andreyev, Kuril (South Okhotsk) backarc basin, in *Backarc Basins: Tectonics and Magmatism*, edited by B. Taylor, pp. 421-449, Plenum Press, New York, 1995.

Gnibidenko, H.S., and I.I. Khvedchuk, The tectonics of the Okhotsk Sea, *Marine Geology*, *50*, 155-197, 1982.

Gnibidenko, H.S., and A.S. Svarichevsky, Tectonics of the South Okhotsk deep-sea basin, *Tectonophysics*, *102*, 225-244, 1984.

Goetze, C., and B. Evans, Stress and temperature in the bending lithosphere as constrained by experimental rock mechanics, *Geophysical Journal of the Royal Astronomical Society*, *59*, 463-478, 1979.

Gordon, R.G., and D.M. Jurdy, Cenozoic global plate motions, *Journal of Geophysical Research*, *91*, 12389-12406, 1986.

Gracia, E., M. Canals, M.-L. Farran, M.J. Prieto, J. Sorribas, J. Acosta, J. Baraza, P. Bart, A.M. Calafat, J.L. Casamor, M. De Batist, G. Ercilla, G. Frances, E. Ramos, J.L. Sanz, and A. Tassone, Morphostructure and evolution of the central and eastern Bransfield basins (NW Antarctic Peninsula), *Marine Geophysical Researches*, *18*, 429-448, 1996.

Grad, M., A. Guterch, and T. Janik, Seismic structure of the lithosphere across the zone of subducted Drake Plate under the Antarctic Plate, West Antarctica, *Geophysical Journal International*, *115*, 586-600, 1993.

Greene, H.G., and J.-Y. Collot, Ridge-arc collision: timing and deformation determined by Leg 134 drilling, central New Hebrides island arc, *Proceedings of the Ocean Drilling Program, Scientific Results, 134*, 2841-2853, 1994.

Griffiths, R.W., R.I. Hackney, and R.D. van der Hilst, A laboratory investigation of effects of trench migration on the descent of subducted slabs, *Earth and Planetary Science Letters, 133*, 1-17, 1995.

Griggs, D.T., A theory of mountain building, *American Journal of Science, 237*, 611-650, 1939.

Gripp, A.E., and R.G. Gordon, Current plate velocities relative to the hotspots incorporating the NUVEL-1 global plate motion model, *Geophysical Research Letters, 17*, 1109-1112, 1990.

Guillou-Frottier, L., J. Buttles, and P. Olson, Laboratory experiments on the structure of subducted lithosphere, *Earth and Planetary Science Letters, 133*, 19-34, 1995.

Gurnis, M., and B.H. Hager, Controls of the structure of subducted slabs, *Nature, 335*, 317-321, 1988.

Gvirtzman, Z., and A. Nur, The formation of Mount Etna as the consequence of slab rollback, *Nature, 401*, 782-785, 1999.

Gvirtzman, Z., and A. Nur, Residual topography, lithospheric structure and sunken slabs in the central Mediterranean, *Earth and Planetary Science Letters, 187*, 117-130, 2001.

Hafkenscheid, E., S.J.H. Buiter, M.J.R. Wortel, W. Spakman, and H. Bijwaard, Modelling the seismic velocity structure beneath Indonesia: a comparison with tomography, *Tectonophysics, 333*, 35-46, 2001.

Hall, J., On the vertical position and convolutions of certain strata and their relationship with granite, *Transactions of the Royal Society of Edinburgh, 7*, 79-108, 1815.

Hamilton, W., Tectonics of the Indonesian region, in *U. S. Geological Survey Professional Paper*, pp. 345, 1979.

Handin, J., On the Coulomb-Mohr failure criterion, *Journal of Geophysical Research, 74*, 5343-5348, 1969.

Harper, J.F., On the Driving Forces of Plate Tectonics, *The Geophysical Journal of the Royal Astronomical Society, 40*, 465-474, 1975.

Harrison, T.M., P. Copeland, W.S.F. Kidd, and O.M. Lovera, Activation of the Nyainqentanghla shear zone; implications for uplift of the southern Tibetan Plateau, *Tectonics, 14*, 658-676, 1995.

Hathway, B., The Nadi Basin; Neogene strike-slip faulting and sedimentation in a fragmented arc, western Viti Levu, Fiji, *Journal of the Geological Society of London, 150*, 563-581, 1993.

Hatzfeld, D., J. Martinod, G. Bastet, and P. Gautier, An analog experiment for the Aegean to describe the contribution of gravitational potential energy, *Journal of Geophysical Research, 102*, 649-660, 1997.

Hawkins, J.W., The geology of the Lau Basin, in *Backarc basins: tectonics and magmatism*, edited by B. Taylor, pp. 63-138, Plenum Press, New York, 1995.

Hein, J.R., and H. McLean, Paleogene sedimentary and volcanogenic rocks from Adak Island, central Aleutian Islands, Alaska, *U. S. Geological Survey Professional Paper*, E1-E16, 1980.

Heki, K., Horizontal and vertical crustal movements from three-dimensional very long baseline interferometry kinematic reference frame; implication for the reversal timescale revision, *Journal of Geophysical Research, 101*, 3187-3198, 1996.

Hess, H.H., History of ocean basins, in *Petrologic studies: A volume in honor of A. F. Buddington*, pp. 599-620, Geological Society of America, 1962.

Hilde, T.W.C., N. Isezaki, and J.M. Wageman, Mesozoic Sea-Floor Spreading in the North Pacific, in *The Geophysics of the Pacific Ocean Basin and its Margin*, edited by G.H. Sutton, M.H. Manghnani, and R. Moberly, pp. 205-226, American Geophysical Union, Washington D.C., 1977.

Hochstaedter, A.G., P.K. Kepezhinskas, M.J. Defant, M.S. Drummond, and H. Bellon, On the tectonic significance of arc volcanism in northern Kamchatka, *Journal of Geology, 102*, 639-654, 1994.

Holmes, A., Radioactivity and the earth movements, *Transaction Geological Society Glasgow, 18*, 559-606, 1928.

Hong, Y., Z. Botao, and M. Fungying, The Cenozoic tectonic evolution of the Great North China: two types of rifting and crustal necking in the Great North China and their tectonic implications, *Tectonophysics, 133*, 217-227, 1987.

Honthaas, C., H. Bellon, P.K. Kepezhinskas, and R.C. Maury, Nouvelles datations (super 40) K- (super 40) Ar du magmatisme Cretace a Quaternaire du Kamchatka du nord (Russie), *Comptes Rendus de l'Academie des Sciences, Serie II. Sciences de la Terre et des Planetes, 320*, 197-204, 1995.

Honthaas, C., J.-P. Rehault, R.C. Maury, H. Bellon, C. Hemond, J.-A. Malod, J.-J. Cornee, M. Villeneuve, J. Cotten, S. Burhanuddin, H. Guillou, and N. Arnaud, A Neogene back-arc origin for the Banda Sea basins; geochemical and geochronological constraints from the Banda ridges (East Indonesia), *Tectonophysics, 298*, 297-317, 1998.

Hopkins, W., Researches in physical geology, part 1, *Philosophical Transactions of the Royal Society of London (for 1839)*, 381-432, 1839.

Horsfield, W.T., An experimental approach to basement-controlled faulting, *Geologie en Mijnbouw, 56*, 363-370, 1977.

Horváth, F., Towards a mechanical model for the formation of the Pannonian Basin, *Tectonophysics, 226*, 333-357, 1993.

Houseman, G., and P. England, Crustal thickening versus lateral expulsion in the Indian-Asian continental collision, *Journal of geophysical research, 98*, 12233-12249, 1993.

Houseman, G.A., and P.C. England, Finite strain calculations of continental deformation; 1, Method and general results for convergent zones, *Journal of Geophysical Research, 91*, 3651-3663, 1986.

Houseman, G.A., and D. Gubbins, Deformation of subducted oceanic lithosphere, *Geophysical Journal International, 131*, 535-551, 1997.

Houseman, G.A., D.P. McKenzie, and P. Molnar, Convective instability of a thickened boundary layer and its relevance for the thermal evolution of continental convergent belts, *Journal of Geophysical Research, 86*, 6115-6132, 1981.

Houseman, G.A., and P. Molnar, Gravitational (Rayleigh-Taylor) instability of a layer with non-linear viscosity and convective thinning of continental lithosphere, *Geophysical Journal International, 128*, 125-150, 1997.

Hsu, S.-K., J.C. Sibuet, and C.T. Shyu, Magnetic inversion in the East China Sea and Okinawa Trough: tectonic implications, *Tectonophysics, 333*, 111-122, 2001.

Hsui, A.T., Application of fluid mechanic principles to the study of geodynamic processes at trench-arc-back arc systems, *Pure and Applied Geophysics, 128*, 661-681, 1988.

Hsui, A.T., and S. Youngquist, A dynamic model of the curvature of the Mariana Trench, *Nature, 318*, 455-457, 1985.

Hubbert, M.K., Theory of scale models as applied to the study of geologic structures, *Geological Society of America Bulletin, 48*, 1459-1520, 1937.

Hubbert, M.K., Mechanical basis for certain familiar geologic structures, *Geological Society of America Bulletin, 62*, 355-372, 1951.

Hutton, J., Theory of the Earth, *Transactions of the Royal Society of Edinburgh, 1*, 109-304, 1788.

Ikeda, Y., R.J. Stern, H. Kagami, and C.-H. Sun, Pb, Nd, and Sr isotopic constraints on the origin of Miocene basaltic rocks from northeast Hokkaido, Japan: Implications for opening of the Kurile back-arc basin, *The Island Arc, 9*, 161-172, 2000.

Imaev, V.S., L.P. Imaeva, and B.M. Koz'min, *Active faults and seismotectonics of Northeastern Yakutia (in Russian)*, 138 pp., Yakutskii Nauchnyi Tsentr, Yakutsk, 1990.

Imanishi, M., F. Kimata, N. Inamori, R. Miyajima, T. Okuda, K. Takai, K. Hirahara, and T. Kato, Horizontal displacements by GPS measurements at the Okinawa-Sakishima Islands (1994-1995), *Zisin = Jishin, 49*, 417-421, 1996.

Ingle, J.C., Subsidence of the Japan Sea; stratigraphic evidence from ODP sites and onshore sections, *Proceedings of the Ocean Drilling Program, Scientific Results, 127-128*, 1197-1218, 1992.

Isacks, B., J. Oliver, and L.R. Sykes, Seismology and the new global tectonics, *Journal of Geophysical Research, 73*, 5855-5899, 1968.

Isacks, B.L., and M. Barazangi, Geometry of Benioff zones: lateral segmentation and downwards bending of the subducted lithosphere, in *Island Arcs, Deep Sea Trenches and Back-Arc Basins*, edited by M. Talwani, and W.C. Pitman, pp. 99-114, American Geophysical Union, Washington D.C., 1977.

Iwasaki, T., N. Hirata, T. Kanazawa, J. Melles, K. Suyehiro, T. Urabe, L. Moeller, J. Makris, and H. Shimamura, Crustal and upper mantle structure in the Ryukyu Island Arc deduced from deep seismic sounding, *Geophysical Journal International*, *102*, 631-657, 1990.

Jacoby, W.R., Model experiment of plate movements, *Nature (Physical Science)*, *242*, 130-134, 1973.

Jacoby, W.R., Paraffin model experiment of plate tectonics, *Tectonophysics*, *35*, 103-113, 1976.

Jaeger, J.C., and N.G.W. Cook, *Fundamentals of rock mechanics*, 585 pp., Chapman and Hall, John Wiley & Sons, New York, 1976.

Jarrard, R.D., Relations among subduction parameters, *Reviews of Geophysics*, *24*, 217-284, 1986.

Jing-Ming, W., The Fenwei rift and its recent periodic activity, *Tectonophysics*, *133*, 257-275, 1987.

Jolivet, L., America-Eurasia plate boundary in eastern Asia and the opening of marginal basins, *Earth and Planetary Science Letters*, *81*, 282-288, 1987.

Jolivet, L., P. Davy, and P. Cobbold, Right-lateral shear along the Northwest Pacific margin and the India-Eurasia collision, *Tectonics*, *9*, 1409-1419, 1990.

Jolivet, L., and C. Faccenna, Mediterranean extension and the Africa-Eurasia collision, *Tectonics*, *19*, 1095-1106, 2000.

Jolivet, L., C. Faccenna, N. D'Agostino, M. Fournier, and D. Worrall, The kinematics of back-arc basins, examples from the Tyrrhenian, Aegean and Japan seas, in *Continental tectonics*, edited by C. Mac Niocaill, and P.D. Ryan, pp. 21-53, 1999.

Jolivet, L., M. Fournier, P. Huchon, V.S. Rozhdestvenskiy, K.F. Sergeyev, and L.S. Oscorbin, Cenozoic intracontinental dextral motion in the Okhotsk-Japan Sea region, *Tectonics*, *11*, 968-977, 1992.

Jolivet, L., and P. Huchon, Crustal-scale strike-slip deformation in Hokkaido, northern Japan, *Journal of Structural Geology*, *11*, 509-522, 1989.

Jolivet, L., and K. Tamaki, Neogene kinematics in the Japan Sea region and volcanic activity of the Northeast Japan Arc, *Proceedings of the Ocean Drilling Program, Scientific Results*, *127-128*, 1311-1331, 1992.

Jolivet, L., K. Tamaki, and M. Fournier, Japan Sea, opening history and mechanism; a synthesis, *Journal of Geophysical Research*, *99*, 22237-22259, 1994.

Kahle, H.-G., C. Straub, R. Reilinger, S. McClusky, R. King, K. Hurst, G. Veis, K. Kastens, and P. Cross, The strain rate field in the eastern Mediterranean region, estimated by repeated GPS measurements, *Tectonophysics*, *294*, 237-252, 1998.

Kamata, H., and K. Kodama, Tectonics of an arc-arc junction; an example from Kyushu Island at the junction of the Southwest Japan Arc and the Ryukyu Arc, *Tectonophysics*, *233*, 69-81, 1994.

Karig, D.E., Ridges and basins of the Tonga-Kermadec island arc system, *Journal of Geophysical Research*, *75*, 239-254, 1970.

Karig, D.E., Origin and development of marginal basins in the western Pacific, *Journal of Geophysical Research*, *76*, 2542-2561, 1971.

Karig, D.E., Structural history of the Mariana island arc system, *Geological Society of America Bulletin*, *82*, 323-344, 1971.

Karig, D.E., Evolution of arc systems in the western Pacific, *Annual Review of Earth and Planetary Sciences*, *2*, 51-75, 1974.

Katsumata, M., and L.R. Sykes, Seismicity and tectonics of the western Pacific; Izu-Mariana-Caroline and Ryukyu-Taiwan regions, *Journal of Geophysical Research*, *74*, 5923-5948, 1969.

Kearey, P., and F.J. Vine, *Global tectonics*, 333 pp., Blackwell Science, Oxford, 1996.

Keep, M., Models of lithospheric-scale deformation during plate collision; effects of indentor shape and lithospheric thickness, *Tectonophysics*, *326*, 203-216, 2000.

Keep, M., and K.R. McClay, Analogue modelling of multiphase rift systems, *Tectonophysics*, *273*, 239-270, 1997.

Kempler, D., and Z. Ben-Avraham, The tectonic evolution of the Cyprean arc, *Annales Tectonicae*, *1*, 58-71, 1987.

Kimura, G., Oblique subduction and collision: Forearc tectonics of the Kuril arc, *Geology*, *14*, 404-407, 1986.

Kimura, G., The latest Cretaceous-early Paleogene rapid growth of accretionary complex and exhumation of high-pressure series metamorphic rocks in northwestern Pacific margin, *Journal of Geophysical Research*, *99*, 22147-22164, 1994.

Kimura, G., and K. Tamaki, Tectonic framework of the Kuril Arc since its initation, in *Advances in earth and planetary sciences; formation of active ocean margins*, edited by N. Nasu, K. Kobayashi, S. Uyeda, I. Kushiro, and H. Kagami, pp. 641-676, Terra Sci. Publ. Co, Tokyo, Japan, 1986a.

Kimura, G., and K. Tamaki, Collision, rotation, and back-arc spreading in the region of the Okhotsk and Japan seas, *Tectonics*, *5*, 389-401, 1986b.

Kincaid, C., and P. Olson, An experimental study of subduction and slab migration, *Journal of Geophysical Research*, *92*, 13832-13840, 1987.

Kirby, S.H., Rheology of the lithosphere, *Reviews of Geophysics and Space Physics*, *21*, 1458-1487, 1983.

Kissel, C., and C. Laj, The Tertiary geodynamical evolution of the Aegean arc; a paleomagnetic reconstruction, *Tectonophysics*, *146*, 183-201, 1988.

Kobayashi, K., and M. Nakada, Magnetic anomalies and tectonic evolution of the Shikoku inter-arc basin, in *Geodynamics of the Western Pacific*, edited by S. Uyeda, R. Murphy, and K. Kobayashi, pp. 391-402, Jpn. Sci. Soc. Press, Tokyo, 1979.

Kodama, K., and K.-i. Nakayama, Paleomagnetic evidence for post-late Miocene intra-arc rotation of South Kyushu, Japan, *Tectonics*, *12*, 35-48, 1993.

Kodama, K., H. Tashiro, and T. Takeuchi, Quaternary counterclockwise rotation of South Kyushu, Southwest Japan, *Geology*, *23*, 823-826, 1995.

Konstantinovskaia, E.A., Arc-continent collision and subduction reversal in the Cenozoic evolution of the Northwest Pacific: an example from Kamchatka (NE Russia), *Tectonophysics*, *333*, 75-94, 2001.

Koyi, H., Experimental modeling of role of gravity and lateral shortening in Zagros mountain belt, *AAPG Bulletin*, *72*, 1381-1394, 1988.

Koyi, H., Analogue modelling; from a qualitative to a quantitative technique; a historical outline, *Journal of Petroleum Geology*, *20*, 223-238, 1997.

Koyi, H.A., and A. Skelton, Centrifuge modelling of the evolution of low-angle detachment faults from high-angle normal faults, *Journal of Structural Geology*, *23*, 1179-1185, 2001.

Krantz, R.W., Measurements of friction coefficients and cohesion for faulting and fault reactivation in laboratory models using sand and sand mixtures, *Tectonophysics*, *188*, 203-207, 1991.

Kuenen, P.H., The negative isostatic anomalies in the East Indies (with experiments), *Leidsche Geologische Mededeelingen*, *8*, 1936.

Kuenen, P.H., and L.U. de Sitter, Experimental investigation into the mechanism of folding, *Leidse Geologische Mededelingen*, 217-239, 1938.

Kusznir, N.J., and D.H. Matthews, Deep seismic reflections and the deformational mechanics of the continental lithosphere, *Journal of Petrology, Special Lithosphere Issue*, 63-87, 1988.

Lagabrielle, Y., J. Goslin, H. Martin, J.-L. Thirot, and J.-M. Auzende, Multiple active spreading centres in the hot North Fiji Basin (Southwest Pacific): a possible model for Archaean seafloor dynamics?, *Earth and Planetary Science Letters*, *149*, 1-13, 1997.

Lagabrielle, Y., E. Ruellan, M. Tanahashi, J. Bourgois, G. Buffet, G. de Alteriis, J. Dyment, J. Goslin, E. Gracia-Mont, Y. Iwabuchi, P. Jarvis, M. Joshima, A.-M. Karpoff, T. Matsumoto, H. Ondreas, B. Pelletier, and O. Sardou, Active oceanic spreading in the northern North Fiji Basin: Results of the NOFI cruise of R/V L'Atalante (Newstarmer Project), *Marine Geophysical Researches*, *18*, 225-247, 1996.

Lallemand, S., C.-S. Liu, S. Dominguez, P. Schnuerle, and J. Malavieille, Trench-parallel stretching and folding of forearc basins and lateral migration of the accretionary wedge in the southern Ryukyus; a case of strain partition caused by oblique convergence, *Tectonics*, *18*, 231-247, 1999.

Lallemand, S.E., J. Malavieille, and S. Calassou, Effects of oceanic ridge subduction on accretionary wedges; experimental modeling and marine observations, *Tectonics*, *11*, 1301-1313, 1992.

Larue, B., J. Daniel, C. Jouannic, and J. Recy, The South Rennell Trough: evidence for a fossil spreading zone, in *International symposium on the geodynamics of the South-West Pacific*, pp. 51-61, Editions Technip, Paris, 1977.

Lawver, L.A., R.A. Keller, M.R. Fisk, and J.A. Strelin, Bransfield strait, Antarctic Peninsula: active extension behind a dead arc, in *Backarc basins: tectonics and magmatism*, edited by B. Taylor, pp. 315-342, Plenum Press, New York, 1995.

Le Pichon, X., Sea-floor spreading and continental drift, *Journal of Geophysical Research*, *73*, 3661-3697, 1968.

Le Pichon, X., Landlocked ocean basins and continental collision: the Eastern Mediterranean as a case example, in *Mountain Building Processes*, edited by K. Hsu, pp. 201-211, Academic Press, London, 1982.

Letouzey, J., and M. Kimura, Okinawa Trough genesis; structure and evolution of a backarc basin developed in a continent, *Marine and Petroleum Geology*, *2*, 111-130, 1985.

Link, T.A., Experiments relating to salt-dome structures, *Bulletin of the American Association of Petroleum Geologists*, *14*, 483-508, 1930.

Linzer, H.-G., Kinematics of retreating subduction along the Carpathian Arc, Romania, *Geology*, *24*, 167-170, 1996.

Linzer, H.-G., W. Frisch, P. Zweigel, R. Girbacea, H.-P. Hann, and F. Moser, Kinematic evolution of the Romanian Carpathians, *Tectonophysics*, *297*, 133-156, 1998.

Lister, C.R.B., Gravitational drive on oceanic plates caused by thermal contraction, *Nature*, *257*, 663-665, 1975.

Lister, G.S., G. Banga, and A. Feenstra, Metamorphic core complexes of Cordilleran type in the Cyclades, Aegean Sea, Greece, *Geology*, *12*, 221-225, 1984.

Liu, M., and K.P. Furlong, Crustal shortening and Eocene extension in the southeastern Canadian Cordillera; some thermal and rheological considerations, *Tectonics*, *12*, 776-786, 1993.

Liu, M., and Y. Shen, Crustal collapse, mantle upwelling, and Cenozoic extension in the North American Cordillera, *Tectonics*, *17*, 311-321, 1998.

Liu, S., and J.M. Dixon, Centrifuge modelling of thrust faulting: structural variation along strike in fold-thrust belts, *Tectonophysics*, *188*, 39-62, 1991.

Lonergan, L., and N. White, Origin of the Betic-Rif mountain belt, *Tectonics*, *16*, 504-522, 1997.

Lonsdale, P., Segmentation and disruption of the East Pacific Rise in the mouth of the Gulf of California, *Marine Geophysical Researches*, *17*, 323-359, 1995.

Louat, R., and B. Pelletier, Seismotectonics and present-day relative plate motions in the New Hebrides-North Fiji Basin region, *Tectonophysics*, *167*, 41-55, 1989.

Lucente, F.P., C. Chiarabba, G.B. Cimini, and D. Giardini, Tomographic constraints on the geodynamic evolution of the Italian region, *Journal of Geophysical Research*, *104*, 20307-20327, 1999.

Madon, M.B., and A.B. Watts, Gravity anomalies, subsidence history and the tectonic evolution of the Malay and Penyu Basins (offshore Peninsular Malaysia), *Basin Research*, *10*, 375-392, 1998.

Madsen, J.A., D.J. Fornari, M.H. Edwards, D.G. Gallo, and M.R. Perfit, Kinematic framework of the Cocos-Pacific plate boundary from 13°N to the Orozco transform fault: results from an extensive magnetic and SeaMarc II survey, *Journal of Geophysical Research*, *97*, 7011-7024, 1992.

Maeda, J.i., Opening of the Kuril Basin deduced from the magmatic history of central Hokkaido, North Japan, *Tectonophysics*, *174*, 235-255, 1990.

Malahoff, A., R.H. Feden, and H.S. Fleming, Magnetic anomalies and tectonic fabric of marginal basins north of New Zealand, *Journal of Geophysical Research*, *87*, 4109-4125, 1982.

Malinverno, A., and W.B.F. Ryan, Extension in the Tyrrhenian Sea and shortening in the Apennines as result of arc migration driven by sinking of the lithosphere, *Tectonics*, *5*, 227-245, 1986.

Mandl, G., L.N.J. de Jong, and A. Maltha, Shear zones in granular material; an experimental study of their structure and mechanical genesis, *Rock Mechanics*, *9*, 95-144, 1977.

Mandl, G., and H.J.e. Zwart, *Mechanics of tectonic faulting; models and basic concepts*, 407 pp., Elsevier, Amsterdam, 1988.

Mantovani, E., D. Albarello, D. Babbucci, and C. Tamburelli, Recent/present tectonic processes in the Italian region and their relation with seismic and volcanic activity, *Annales Tectonicae*, *11*, 27-57, 1997b.

Mantovani, E., D. Albarello, C. Tamburelli, D. Babbucci, and M. Viti, Plate convergence, crustal delamination, extrusion tectonics and minimization of shortening work as main controlling factors of the recent Mediterranean deformation pattern, *Annali di Geofisica*, *40*, 611-643, 1997a.

Mantovani, E., M. Viti, D. Albarello, C. Tamburelli, D. Babbucci, and N. Cenni, Role of kinematically induced horizontal forces in Mediterranean tectonics; insights from numerical modeling, *Journal of Geodynamics*, *30*, 287-320, 2000.

Mantovani, E., M. Viti, D. Babbucci, C. Tamburelli, and D. Albarello, Back Arc Extension: Which Driving Mechanism?, *Journal of the Virtual Explorer*, *3*, 17-44, 2001.

Mareschal, J.-C., Thermal regime and post-orogenic extension in collision belts, *Tectonophysics*, *238*, 471-484, 1994.

Marlow, M.S., D.W. Scholl, E.C. Buffington, and T.R. Alpha, Tectonic History of the Central Aleutian Arc, *Geological Society of America Bulletin*, *84*, 1555-1574, 1973.

Marotta, A.M., and R. Sabadini, The style of the Tyrrhenian subduction, *Geophysical Research Letters*, *22*, 747-750, 1995.

Martínez, F., P. Fryer, and N. Becker, Geophysical characteristics of the southern Mariana Trough, 11 degrees 50'N-13 degrees 40'N, *Journal of Geophysical Research*, *105*, 16591-16607, 2000.

Martinod, J., D. Hatzfeld, J.P. Brun, P. Davy, and P. Gautier, Continental collision, gravity spreading, and kinematics of Aegea and Anatolia, *Tectonics*, *19*, 290-299, 2000.

Marton, E., and L. Fodor, Combination of palaeomagnetic and stress data; a case study from North Hungary, *Tectonophysics*, *242*, 99-114, 1995.

Maxwell, R., and R. Chinakayev, Potential outlined for Kamchatka back-arc basin, Far East Russia, *The Oil and Gas Journal*, *97*, 98-101, 1999.

McCabe, R., Implications of paleomagnetic data on the collision related bending of island arcs, *Tectonics*, *3*, 409-428, 1984.

McClay, K.R., Deformation mechanics in analogue models of extensional fault systems, in *Deformation mechanisms, rheology and tectonics*, edited by R.J. Knipe, and E.H. Rutter, pp. 445-453, 1990.

McClusky, S., S. Balassanian, A. Barka, C. Demir, S. Ergintav, I. Georgiev, O. Gurkan, M. Hamburger, K. Hurst, H. Kahle, K. Kastens, G. Kekelidze, R. King, V. Kotzev, O. Lenk, S. Mahmoud, A. Mishin, M. Nadariya, A. Ouzounis, D. Paradissis, Y. Peter, M. Prilepin, R. Reilinger, I. Sanli, H. Seeger, A. Tealeb, M.N. Toksoz, and G. Veis, Global positioning system constraints on plate kinematics and dynamics in the eastern Mediterranean and Caucasus, *Journal of Geophysical Research*, *105*, 5695-5719, 2000.

McKenzie, D., Active tectonics in the Mediterranean region, *Geophysical Journal of the Royal Astronomical Society*, *30*, 109-185, 1972.

McKenzie, D., Active tectonics of the Alpine-Himalayan belt; the Aegean Sea and surrounding regions, *Geophysical Journal of the Royal Astronomical Society*, *55*, 217-254, 1978.

McKenzie, D.P., Speculations on the consequences and causes of plate motions, *The Geophysical Journal of the Royal Astronomical Society*, *18*, 1-32, 1969.

McKenzie, D.P., and R.L. Parker, The north Pacific; an example of tectonics on a sphere, *Nature*, *216*, 1276-1280, 1967.

McQuarrie, N., and C.G. Chase, Raising the Colorado Plateau, *Geology*, *28*, 91-94, 2000.

Mead, W.J., Notes on the mechanics of geologic structures, *Journal of Geology, 28*, 505-523, 1920.

Meffre, S., and A.J. Crawford, Collision tectonics in the New Hebrides Arc (Vanuatu), *The Island Arc, 10*, 33-50, 2001.

Meffre, S., and T. Crawford, Ridge subduction in the New Hebrides intra-oceanic island arc: implications for the recognition of collision events in ancient arc-related sequences, *Geological Society of Australia, Abstracts, 59*, 341, 2000.

Meijer, P.T., and M.J.R. Wortel, The dynamics of motion of the South American Plate, *Journal of Geophysical Research, 97*, 11915-11931, 1992.

Meijer, P.T., and M.J.R. Wortel, Present-day dynamics of the Aegean region: a model analysis of the horizontal pattern of stress and deformation, *Tectonics, 16*, 879-895, 1997.

Menard, H.W., Sea floor relief and mantle convection, *Physics and Chemistry of the Earth, 6*, 315-364, 1965.

Mercier, J.L., Extensional-compressional tectonics associated with the Aegean Arc; comparison with the Andean Cordillera of South Peru-North Bolivia, *Philosophical Transactions of the Royal Society of London, Series A: Mathematical and Physical Sciences, 300*, 337-355, 1981.

Merle, O., Strain models within spreading nappes, *Tectonophysics, 165*, 57-71, 1989.

Meulenkamp, J.E., M.J.R. Wortel, W.A. van Wamel, W. Spakman, and E. Hoogerduyn Strating, On the Hellenic subduction zone and the geodynamic evolution of Crete since the late middle Miocene, *Tectonophysics, 146*, 203-215, 1988.

Miki, M., Two-phase opening model for the Okinawa Trough inferred from paleomagnetic study of the Ryukyu Arc, *Journal of Geophysical Research, 100*, 8169-8184, 1995.

Millen, D.W., and M.W. Hamburger, Seismological evidence for tearing of the Pacific Plate at the northern termination of the Tonga subduction zone, *Geology, 26*, 659-662, 1998.

Minster, J.B., and T.H. Jordan, Present-day plate motions, *Journal of Geophysical Research, 83*, 5331-5354, 1978.

Mohr, O., Ueber die Darstellung des Spannungzustandes eines Körperelementes, *Civiling., 28*, 113-156, 1882.

Mohr, O., Welche Umstände bedingen die Elastizitätsgrenze und den Bruch eines Materiales?, *Zeits. Ver. Deutsch. Ing., 44*, 1524-1530, 1572-1577, 1900.

Molnar, P., and T. Atwater, Interarc spreading and Cordilleran tectonics as alternates related to the age of subducted oceanic lithosphere, *Earth and Planetary Science Letters, 41*, 330-340, 1978.

Molnar, P., and H. Lyon-Caen, Some simple physical aspects of the support, structure, and evolution of mountain belts, in *Processes in continental lithospheric deformation*, pp. 179-207, 1988.

Molnar, P., and D. Qidong, Faulting associated with large earthquakes and the average rate of deformation in central and eastern Asia, *Journal of Geophysical Research, 89*, 6203-6227, 1984.

Molnar, P., and P. Tapponnier, Cenozoic tectonics of Asia; effects of a continental collision, *Science, 189*, 419-426, 1975.

Molnar, P., and P. Tapponnier, Relation of the tectonics of eastern China to the India-Eurasia collision; application of slip-line field theory to large-scale continental tectonics, *Geology, 5*, 212-216, 1977.

Molnar, P., and P. Tapponnier, Active tectonics of Tibet, *Journal of Geophysical Research, 83*, 5361-5375, 1978.

Moore, G.W., Westward Tidal Lag as the Driving Force of Plate Tectonics, *Geology, 1*, 99-100, 1973.

Morgan, W.J., Rises, trenches, great faults, and crustal blocks, *Journal of Geophysical Research, 73*, 1959-1982, 1968.

Morgan, W.J., Deep Mantle Convection Plumes and Plate Motions, *The American Association of Petroleum Geologists Bulletin, 56*, 203-213, 1972.

Morley, C.K., Combined escape tectonics and subduction rollback-back arc extension; a model for the evolution of Tertiary rift basins in Thailand, Malaysia and Laos, *Journal of the Geological Society of London, 158*, 461-474, 2001.

Musgrave, R.J., and J.V. Firth, Magnitude and timing of New Hebrides Arc rotation; paleomagnetic evidence from Nendo, Solomon Islands, *Journal of Geophysical Research, 104*, 2841-2853, 1999.

Natal'in, B.A., L.M. Parfenov, A.A. Vrublevsky, L.P. Karsakov, and V.V. Yushmanov, Main fault systems of the Soviet Far East, *Philosophical Transactions of the Royal Society of London, Series A: Mathematical and Physical Sciences, 317*, 267-275, 1986.

Naylor, M.A., G. Mandl, and C.H.K. Sijpesteijn, Fault geometries in basement-induced wrench faulting under different initial stress states, *Journal of Structural Geology, 8*, 737-752, 1986.

Nelson, T.H., and P.G. Temple, Mainstream Mantle Convection; A Geologic Analysis of Plate Motion, *The American Association of Petroleum Geologists Bulletin, 56*, 226-246, 1972.

Nettleton, L.L., and T.A. Elkins, Geologic models made from granular materials, *Transactions - American Geophysical Union, 28*, 451-466, 1947.

Ni, J., and J.E. York, Late Cenozoic tectonics of the Tibetan Plateau, *Journal of Geophysical Research, 83*, 5377-5384, 1978.

Nieuwland, D.A., and J.V. Walters, Geomechanics of the South Furious Field; an integrated approach towards solving complex structural geological problems, including analogue and finite-element modelling, *Tectonophysics, 226*, 143-166, 1993.

Northrup, C.J., L.H. Royden, and B.C. Burchfiel, Motion of the Pacific Plate relative to Eurasia and its potential relation to Cenozoic extension along the eastern margin of Eurasia, *Geology, 23*, 719-722, 1995.

Ode, H., Viscous properties and creep of salt, *Bulletin of the American Association of Petroleum Geologists, 49*, 354-355, 1965.

Oertel, G., A progress report on stress, strain and fracture in clay models of geologic deformation, *Geotimes, 6*, 26-31, 1962.

Olbertz, D., M.J.R. Wortel, and U. Hansen, Trench migration and subduction zone geometry, *Geophysical Research Letters, 24*, 221-224, 1997.

Olson, P., and C. Kincaid, Experiments on the interaction of thermal convection and compositional layering at the base of the mantle, *Journal of Geophysical Research, 96*, 4347-4354, 1991.

Otofuji, Y.-i., T. Itaya, and T. Matsuda, Rapid rotation of Southwest Japan; palaeomagnetism and K-Ar ages of Miocene volcanic rocks of Southwest Japan, *Geophysical Journal International, 105*, 397-405, 1991.

Parfenov, L.M., B.M. Koz'min, O.V. Grinenko, V.S. Imaev, and L.P. Imaeva, Geodynamics of the Chersky seismic belt, *Journal of Geodynamics, 9*, 15-37, 1988.

Parfenov, L.M., and B.A. Natal'in, Mesozoic tectonic evolution of northeastern Asia, *Tectonophysics, 127*, 291-304, 1986.

Parfenov, L.M., I.P. Voinova, B.A. Natal'in, and D.F. Semenov, Geodynamics of northeastern Asia in the Mesozoic and Cenozoic and the nature of the volcanic belt, *Journal of Physics of the Earth, 26 (supplement)*, S503-S526, 1979.

Parker, T.J., and A.N. McDowell, Model studies of salt-dome tectonics, *Bulletin of the American Association of Petroleum Geologists, 39*, 2384-2470, 1955.

Parson, L.M., and J.W. Hawkins, Two-stage ridge propagation and the geological history of the Lau backarc Basin, *Proceedings of the Ocean Drilling Program, Scientific Results, 135*, 819-828, 1994.

Parsons, B., and F.M. Richter, A relation between the driving force and geoid anomaly associated with mid-ocean ridges, *Earth and Planetary Science Letters, 51*, 445-450, 1980.

Patriat, P., and J. Achache, India-Eurasia collision chronology has implications for crustal shortening and driving mechanism of plates, *Nature, 311*, 615-621, 1984.

Payne, A.S., and A.H.F. Robertson, Neogene supra-subduction zone extension in the Polis graben system, West Cyprus, *Journal of the Geological Society of London, 152*, 613-628, 1995.

Pelletier, B., S. Calmant, and R. Pillet, Current tectonics of the Tonga-New Hebrides region, *Earth and Planetary Science Letters, 164*, 263-276, 1998.

Pelletier, B., Y. Lafoy, and F. Missegue, Morphostructure and magnetic fabric of the northwestern North Fiji Basin, *Geophysical Research Letters, 20*, 1151-1154, 1993.

Peltzer, G., Centrifuged experiments of continental scale tectonics in Asia, *Bulletin of the Geological Institutions of the University of Uppsala, New Series, 14*, 115-128, 1988.

Peltzer, G., and P. Tapponnier, Formation and evolution of strike-slip faults, rifts, and basins during the India-Asia collision; an experimental approach, *Journal of Geophysical Research*, *93*, 15085-15117, 1988.

Peyton, V., V. Levin, J. Park, M. Brandon, J. Lees, E. Gordeev, and A. Ozerov, Mantle flow at a slab edge; seismic anisotropy in the Kamchatka region, *Geophysical Research Letters*, *28*, 379-382, 2001.

Plafker, G., Tectonic deformation associated with the 1964 Alaska earthquake, *Science*, *148*, 1675-1687, 1965.

Platt, J.P., and P.C. England, Convective removal of lithosphere beneath mountain belts; thermal and mechanical consequences, *American Journal of Science*, *294*, 307-336, 1994.

Platt, J.P., and R.L.M. Vissers, Extensional collapse of thickened continental lithosphere; a working hypothesis for the Alboran Sea and Gibraltar Arc, *Geology*, *17*, 540-543, 1989.

Polachan, S., and A. Racey, Stratigraphy of the Mergui Basin, Andaman Sea; implications for petroleum exploration, *Journal of Petroleum Geology*, *17*, 373-406, 1994.

Powers, M.C., A new roundness scale for sedimentary particles, *Journal of Sedimentary Petrology*, *23*, 117-119, 1953.

Raleigh, C.B., and M.S. Paterson, Experimental deformation of serpentinite and its tectonic implications, *Journal of Geophysical Research*, *70*, 3965-3985, 1965.

Ramberg, H., Natural and experimental boudinage and pinch-and-swell structures, *Journal of Geology*, *63*, 512-526, 1955.

Ramberg, H., Model experimentation of the effect of gravity on tectonic processes, *The Geophysical Journal of the Royal Astronomical Society*, *14*, 307-329, 1967.

Ramberg, H., Model studies in relation to intrusion of plutonic bodies, in *Mechanism of igneous intrusion*, edited by G. Newall, and N. Rast, pp. 261-286, 1970.

Ramberg, H., *Gravity, deformation and the Earth's crust*, Academic Press, London, 1981.

Ranalli, G., *Rheology of the Earth; deformation and flow processes in geophysics and geodynamics*, 366 pp., Allen and Unwin, Boston, 1987.

Ranalli, G., *Rheology of the Earth*, 413 pp., Chapman and Hall, London, 1995.

Ranalli, G., and D.C. Murphy, Rheological stratification of the lithosphere, *Tectonophysics*, *132*, 281-295, 1987.

Ratschbacher, L., W. Frisch, H.-G. Linzer, and O. Merle, Lateral extrusion in the Eastern Alps; Part 2, Structural analysis, *Tectonics*, *10*, 257-271, 1991b.

Ratschbacher, L., W. Frisch, F. Neubauer, S.M. Schmid, and J. Neugebauer, Extension in compressional orogenic belts; the Eastern Alps, *Geology*, *17*, 404-407, 1989.

Ratschbacher, L., O. Merle, P. Davy, and P. Cobbold, Lateral extrusion in the Eastern Alps; Part 1, Boundary conditions and experiments scaled for gravity, *Tectonics*, *10*, 245-256, 1991a.

Ren, J., K. Tamaki, L. Sitian, and Z. Junxia, Late Mesozoic and Cenozoic rifting and its dynamic setting in Eastern China and adjacent areas, *Tectonophysics*, *344*, 175-205, 2002.

Richard, P., Experiments on faulting in a two-layered cover sequence overlying a reactivated basement fault with oblique-slip, *Journal of Structural Geology*, *13*, 459-469, 1991.

Richard, P., and R.W. Krantz, Experiments on fault reactivation in strike-slip mode, *Tectonophysics*, *188*, 117-131, 1991.

Richard, P., B. Mocquet, and P.R. Cobbold, Experiments on simultaneous faulting and folding above a basement wrench fault, *Tectonophysics*, *188*, 133-141, 1991.

Richard, P.D., M.A. Naylor, and A. Koopman, Experimental models of strike-slip tectonics, *Petroleum Geoscience*, *1*, 71-80, 1995.

Richardson, R.M., Ridge forces, absolute plate motions, and the intraplate stress field, *Journal of Geophysical Research*, *97*, 11739-11748, 1992.

Richter, F.M., Convection and the Large-Scale Circulation of the Mantle, *Journal of Geophysical Research*, *78*, 8735-8745, 1973.

Riedel, W., Zur Mechanik geologischer Brucherscheinungen, *Centralblat für Mineralogie, Geologie, und Paleontologie, B*, 354-368, 1929.

Riegel, S.A., K. Fujita, B.M. Koz'min, V.S. Imaev, and D.B. Cook, Extrusion tectonics of the Okhotsk plate, Northeast Asia, *Geophysical Research Letters*, *20*, 607-610, 1993.

Rixon, L.K., Clay modelling of the Fitzroy Graben, *BMR Journal of Australian Geology and Geophysics*, *3*, 71-76, 1978.

Rom, J., A new forerunner for continental drift, *Nature*, *367*, 407-408, 1994.

Rosenbaum, G., G.S. Lister, and C. Duboz, Relative motions of Africa, Iberia and Europe during Alpine orogeny, *Tectonophysics*, *359*, 117-129, 2002a.

Rosenbaum, G., G.S. Lister, and C. Duboz, Reconstruction of the tectonic evolution of the western Mediterranean since the Oligocene, *Journal of the Virtual Explorer*, *8*, 107-130, 2002b.

Rossetti, F., C. Faccenna, G. Ranalli, and F. Storti, Convergence rate-dependent growth of experimental viscous orogenic wedges, *Earth and Planetary Science Letters*, *178*, 367-372, 2000.

Rossetti, F., G. Ranalli, and C. Faccenna, Rheological properties of paraffin as an analogue material for viscous crustal deformation, *Journal of Structural Geology*, *21*, 413-417, 1999.

Rossi, D., Use of hollow granular materials to simulate detachment folding and deformation partitioning in sandbox thrust wedges, *Bolletino di Geofysica Teorica ed Applicata*, *42 (suppl. 1/2)*, 222-223, 2002.

Royden, L., F. Horvath, and J. Rumpler, Evolution of the Pannonian Basin system; 1, Tectonics, *Tectonics*, *2*, 63-90, 1983.

Royden, L., E. Patacca, and P. Scandone, Segmentation and configuration of subducted lithosphere in Italy; an important control on thrust-belt and foredeep-basin evolution, *Geology*, *15*, 714-717, 1987.

Royden, L.H., The tectonic expression of slab pull at continental convergent boundaries, *Tectonics*, *12*, 303-325, 1993a.

Royden, L.H., Evolution of retreating subduction boundaries formed during continental collision, *Tectonics*, *12*, 629-638, 1993b.

Royden, L.H., B.C. Burchfiel, R.W. King, E. Wang, C. Zhiliang, S. Feng, and L. Yuping, Surface deformation and lower crustal flow in eastern Tibet, *Science*, *276*, 788-790, 1997.

Rozhdestvenskiy, V.S., The role of wrench-faults in the structure of Sakhalin, *Geotectonics*, *16*, 323-332, 1982.

Rozhdestvensky, V.S., Evolution of the Sakhalin fold system, *Tectonophysics*, *127*, 331-339, 1986.

Rubenstone, J.L., Geology and geochemistry of early Tertiary submarine volcanic rocks of the Aleutian Islands, and their bearing on the development of the Aleutian Island arc, PhD thesis, Cornell University, Ithaca, New York, 1984.

Runcorn, S.K., Towards a theory of continental drift, *Nature*, *193*, 311-314, 1962.

Russo, R.M., and P.G. Silver, Trench-parallel flow beneath the Nazca Plate from seismic anisotropy, *Science*, *263*, 1105-1111, 1994.

Russo, R.M., and P.G. Silver, Cordillera formation, mantle dynamics, and the Wilson cycle, *Geology*, *24*, 511-514, 1996.

Sager, W.W., C.J. Macleod, and N. Abrahamsen, Paleomagnetic constraints on Tonga Arc tectonic rotation from sediments drilled at sites 840 and 841, *Proceedings of the Ocean Drilling Program, Scientific Results*, *135*, 763-783, 1994.

San'kov, V., J. Deverchere, Y. Gaudemer, F. Houdry, and A. Filippov, Geometry and rate of faulting in the North Baikal Rift, Siberia, *Tectonics*, *19*, 707-722, 2000.

Savostin, L.A., L. Zonenshain, and B. Baranov, Geology and plate tectonics of the Sea of Okhotsk, in *Geodynamics of the western Pacific-Indonesian region*, edited by T.W.C. Hilde, and S. Uyeda, pp. 189-221, 1983.

Schardt, H., Geological Studies in the Pays-D'Enhant Vaudois, *Bull. de le Soc. Vaudois des Sci. Nat.*, *xx*, 143-146, 1884.

Schellart, W.P., Shear test results for cohesion and friction coefficients for different granular materials: scaling implications for their usage in analogue modelling, *Tectonophysics*, *324*, 1-16, 2000.

Schellart, W.P., M.W. Jessell, and G.S. Lister, Asymmetric deformation in the back-arc region of the Kuril arc, Northwest Pacific: New insights from analogue modeling, *Tectonics*, in review.

Schellart, W.P., G.S. Lister, and M.W. Jessell, Analogue modeling of arc and backarc deformation in the New Hebrides arc and North Fiji Basin, *Geology*, *30*, 311-314, 2002a.

Schellart, W.P., G.S. Lister, and M.W. Jessell, Analogue modelling of asymmetrical back-arc extension, *Journal of the Virtual Explorer*, *7*, 25-42, 2002b.

Schellart, W.P., G.S. Lister, and M.W. Jessell, Some experimental insights into arc formation and back-arc extension, *Bollettino di Geofisica Teorica ed Applicata*, *42 (suppl. 1/2)*, 85-91, 2002c.

Scholl, D.W., E.C. Buffington, and M.S. Marlow, Plate tectonics and the structural evolution of the Aleutian-Bering Sea region, *Special Paper - Geological Society of America*, *151*, 1-31, 1975.

Scholl, D.W., H.G. Greene, and M.S. Marlow, Eocene age of the Adak 'Paleozoic(?)' rocks, Aleutian islands, Alaska, *Geological Society of America Bulletin*, *81*, 3583-3591, 1970.

Schwinner, R., Vulkanismus und Gebirgsbildung, *Zeitschrift fur Volkanologie*, *5*, 176-230, 1920.

Searle, M.P., B.F. Windley, M.P. Coward, D.J.W. Cooper, A.J. Rex, D. Rex, L. Tingdong, X. Xuchang, M.Q. Jan, V.C. Thakur, and S. Kumar, The closing of Tethys and the tectonics of the Himalaya, *Geological Society of America Bulletin*, *98*, 678-701, 1987.

Sébrier, M., J.L. Mercier, F. Megard, G. Laubacher, and E. Carey-Gailhardis, Quaternary normal and reverse faulting and the state of stress in the Central Andes of South Peru, *Tectonics*, *4*, 739-780, 1985.

Seno, T., T. Sakurai, and S. Stein, Can the Okhotsk plate be discriminated from the North American plate?, *Journal of Geophysical Research*, *101*, 11305-11315, 1996.

Seno, T., S. Stein, and A.E. Gripp, A model for the motion of the Philippine Sea Plate consistent with NUVEL-1 and geological data, *Journal of Geophysical Research*, *98*, 17941-17948, 1993.

Shaoren, J., Z. Xiaozhong, H. Ciliu, and X. Kanyuan, The stratigraphy, structure and evolution of Zengmu Basin, *Tectonophysics*, *235*, 51-62, 1994.

Shemenda, A.I., Similarity criteria in mechanical modeling of tectonic processes, *Soviet Geology and Geophysics*, *24*, 8-16, 1983.

Shemenda, A.I., Horizontal lithosphere compression and subduction; constraints provided by physical modeling, *Journal of Geophysical Research*, *97*, 11097-11116, 1992.

Shemenda, A.I., Subduction of the lithosphere and back arc dynamics; insights from physical modeling, *Journal of Geophysical Research*, *98*, 16167-16185, 1993.

Shemenda, A.I., *Subduction; insights from physical modeling*, 215 pp., Kluwer Academic Publishers, Dordrecht, 1994.

Shemenda, A.I., and A.L. Grocholsky, Physical modelling of lithosphere subduction in collision zones, *Tectonophysics*, *216*, 273-290, 1992.

Shemenda, A.I., and A.L. Grocholsky, Physical modeling of slow seafloor spreading, *Journal of Geophysical Research*, *99*, 9137-9153, 1994.

Sibson, R.H., Frictional constraints on thrust, wrench and normal faults, *Nature*, *249*, 542-544, 1974.

Sibuet, J.-C., S.-K. Hsu, C.-T. Shyu, and C.-S. Liu, Structural and kinematic evolutions of the Okinawa Trough backarc Basin, in *Backarc Basins: Tectonics and Magmatism*, edited by B. Taylor, pp. 343-379, Plenum Press, New York, 1995.

Sibuet, J.-C., J. Letouzey, F. Barbier, J. Charvet, J.-P. Foucher, T.W.C. Hilde, M. Kimura, C. Ling-Yun, B. Marsset, C. Muller, and J.-F. Stephan, Back arc extension in the Okinawa Trough, *Journal of Geophysical Research*, *92*, 14041-14063, 1987.

Smith, W.H.F., and D.T. Sandwell, Global sea floor topography from satellite altimetry and ship depth soundings, *Science*, *277*, 1956-1962, 1997.

Sonder, L.J., and P.C. England, Vertical averages of rheology of the continental lithosphere; relation to thin sheet parameters, *Earth and Planetary Science Letters*, *77*, 81-90, 1986.

Sonder, L.J., P.C. England, B.P. Wernicke, and R.L. Christiansen, A physical model for Cenozoic extension of western North America, in *Continental extensional tectonics*, edited by M.P. Coward, J.F. Dewey, and P.L. Hancock, pp. 187-201, 1987.

Spakman, W., M.J.R. Wortel, and N.J. Vlaar, The Hellenic subduction zone: A tomographic image and its geodynamic implications, *Geophysical Research Letters*, *15*, 60-63, 1988.

Stephenson, R.A., and S.A.P.L. Cloetingh, Some examples and mechanical aspects of continental lithospheric folding, *Tectonophysics*, *188*, 27-37, 1991.

Stüwe, K., and T.D. Barr, On the relationship between surface uplift and gravitational extension, *Tectonics*, *19*, 1056-1064, 2000.

Suess, E., *Die Entstehung der Alpen*, 168 pp., Braumüller, Vienna, 1875.

Suess, E., *Antlitz der Erde, Vol. 1*, 778 pp., Tempsky, Prague, 1885.

Suter, M., M.L. Martínez, O.Q. Legorreta, and M.C. Martínez, Quarternary intra-arc extension in the central Trans-Mexican volcanic belt, *Geological Society of America Bulletin*, *113*, 693-703, 2001.

Sykes, L.R., The seismicity and deep structure of island arcs, *Journal of Geophysical Research*, *71*, 2981-3006, 1966.

Takeuchi, T., K. Kodama, and T. Ozawa, Paleomagnetic evidence for block rotations in central Hokkaido-south Sakhalin, Northeast Asia, *Earth and Planetary Science Letters*, *169*, 7-21, 1999.

Talbot, C.J., Inclined and asymmetric upward-moving gravity structures, *Tectonophysics*, *42*, 159-181, 1977.

Tamaki, K., Opening tectonics of the Japan Sea, in *Backarc Basins: Tectonics and Magmatism*, edited by B. Taylor, pp. 407-420, Plenum Press, New York, 1995.

Tamaki, K., K. Suyehiro, J. Allan, J.C. Ingle, Jr., and K.A. Pisciotto, Tectonic synthesis and implications of Japan Sea ODP drilling, *Proceedings of the Ocean Drilling Program, Scientific Results*, *127-128*, 1333-1348, 1992.

Tanaka, H., and H. Uchimura, Tectonics of Hokkaido deduced from paleomagnetic study, *Chikyu Monthly*, *11*, 298-306 (in Japanese), 1989.

Tapponnier, P., G. Peltzer, and R. Armijo, On the mechanics of the collision between India and Asia, in *Collision tectonics*, edited by M.P. Coward, and A.C. Ries, pp. 115-157, London, United Kingdom, 1986.

Tapponnier, R., G. Peltzer, A.Y. Le Dain, R. Armijo, and P. Cobbold, Propagating extrusion tectonics in Asia; new insights from simple experiments with plasticine, *Geology*, *10*, 611-616, 1982.

Taylor, B., Preface, in *Backarc basins: tectonics and magmatism*, edited by B. Taylor, pp. IX-XI, Plenum Press, New York, 1995.

Taylor, B., K. Fujioka, T.R. Janecek, J.C. Aitchison, S.M. Cisowski, A. Colella, P.A. Cooper, K.A. Dadey, P.K. Egeberg, J.V. Firth, J.B. Gill, Y. Herman, R.N. Hiscott, M. Isiminger-Kelso, K. Kaiho, A. Klaus, M. Koyama, H. Lapierre, M.A. Lovell, K.M. Marsaglia, A. Nishimura, P.A. Pezard, K.S. Rodolfo, R.N. Taylor, K. Tazaki, and P. Torssander, Rifting and the volcanic-tectonic evolution of the Izu-Bonin-Mariana Arc, *Proceedings of the Ocean Drilling Program, Scientific Results*, *126*, 627-651, 1992.

Taylor, F.W., M.G. Bevis, B.E. Schutz, D. Kuang, J. Recy, S. Calmant, D. Charley, M. Regnier, B. Perin, M. Jackson, and C. Reichenfeld, Geodetic measurements of convergence at the New Hebrides island arc indicate arc fragmentation caused by an impinging aseismic ridge, *Geology*, *23*, 1011-1014, 1995.

ten Veen, J.H., and P.T. Meijer, Late Miocene to Recent tectonic evolution of Crete (Greece); geological observations and model analysis, *Tectonophysics*, *298*, 191-208, 1998.

Tovish, A., and G. Schubert, Island arc curvature, velocity of convergence and angle of subduction, *Geophysical Research Letters*, *5*, 329-332, 1978.

Tsvetkov, A.A., Magmatism of the westernmost (Komandorsky) segment of the Aleutian island arc, *Tectonophysics*, *199*, 289-317, 1991.

Turcotte, D.L., Mechanisms of crustal deformation, *Journal of the Geological Society of London*, *140*, 701-724, 1983.

Turcotte, D.L., and E.R. Oxburgh, Mantle convection and the new global tectonics, *Annual Review of Fluid Mechanics*, *4*, 33-68, 1972.

Turcotte, D.L., and G. Schubert, Structure of the olivine-spinel phase boundary in the descending lithosphere, *Journal of Geophysical Research*, *76*, 7980-7987, 1971.

Turcotte, D.L., and G. Schubert, *Geodynamics; applications of continuum physics to geological problems*, 456 pp., Cambridge University Press, Cambridge, 2002.

Turner, S., and C. Hawkesworth, Using geochemistry to map mantle flow beneath the Lau Basin, *Geology*, *26*, 1019-1022, 1998.

Twiss, R.J., and E.M. Moores, *Structural geology*, 532 pp., W.H. Freeman and Company, New York., 1992.

Tzukanov, N.V., V.S. Vishnevskaya, G. Kazarina, and D.I. Vitukhin, Composition and age of deep-sea cherts from the Shirshov Ridge (Bering Sea), *Izv. Akad. Nauk SSSR, Ser. Geol.*, *11*, 80-85 (in Russian), 1984.

Urrutia-Fucugauchi, J., Crustal thickness, heat flow, arc magmatism, and tectonics of Mexico - preliminary report, *Geofisica Internacional*, *25*, 559-573, 1986.

Uyeda, S., Some basic problems in the trench-arc-back arc system, in *Island arcs, deep sea trenches and back-arc basins, Maurice Ewing Series*, edited by M. Talwani, and W.C. Pitman, pp. 1-14, Harriman, New York, 1977.

Uyeda, S., and H. Kanamori, Back-arc opening and the mode of subduction, *Journal of Geophysical Research*, *84*, 1049-1061, 1979.

Uyeda, S., and A. Miyashiro, Plate Tectonics and the Japanese Island; A Synthesis, *Geological Society of America Bulletin*, *85*, 1159-1170, 1974.

van der Hilst, R., and T. Seno, Effects of relative plate motion on the deep structure and penetration depth of slabs below the Izu-Bonin and Mariana island arcs, *Earth and Planetary Science Letters*, *120*, 395-407, 1993.

van der Hilst, R.D., R. Engdahl, W. Spakman, and G. Nolet, Tomographic imaging of subducted lithosphere below Northwest Pacific island arcs, *Nature*, *353*, 37-43, 1991.

van der Linden, W.J.M., Looping the loop; geotectonics of the Alpine-Mediterranean region, *Geologie en Mijnbouw*, *64*, 281-295, 1985.

Van der Voo, R., W. Spakman, and H. Bijwaard, Tethyan subducted slabs under India, *Earth and Planetary Science Letters*, *171*, 7-20, 1999.

van Dijk, J., and M. Okkes, Neogene tectonostratigraphy and kinematics of Calabrian basins; implications for the geodynamics of the central Mediterranean, *Tectonophysics*, *196*, 23-60, 1991.

van Hunen, J., A.P. van den Berg, and N.J. Vlaar, On the role of subducting oceanic plateaus in the development of shallow flat subduction, *Tectonophysics*, *352*, 317-333, 2002.

Vendeville, B., P.R. Cobbold, P. Davy, J.P. Brun, and P. Choukroune, Physical models of extensional tectonics at various scales, in *Continental extensional tectonics*, edited by M.P. Coward, J.F. Dewey, and P.L. Hancock, pp. 95-107, 1987.

Vening Meinesz, F., *Gravity expeditions at sea, 1923-1932*, 208 pp., Netherlands Geodetic Commision, Delft, 1934.

Vening Meinesz, F.A., Thermal convection in the earth's mantle, in *Continental drift*, edited by S.K. Runcorn, pp. 145-176, Academic Press, New York, 1962.

Viallon, C., P. Huchon, and E. Barrier, Opening of the Okinawa Basin and collision in Taiwan; a retreating trench model with lateral anchoring, *Earth and Planetary Science Letters*, *80*, 145-155, 1986.

Vilotte, J.P., M. Daignieres, and R. Madariaga, Numerical modelling of intraplate deformation: simple mechanical models of continental collision, *Journal of Geophysical Research*, *87*, 10709-10728, 1982.

Vine, F.J., and D.H. Matthews, Magnetic anomalies over oceanic ridges, *Nature*, *199*, 947-949, 1963.

Vogt, P.R., Subduction and aseismic ridges, *Nature*, *241*, 189-191, 1973.

Walcott, C.R., and S.H. White, Constraints on the kinematics of post-orogenic extension imposed by stretching lineations in the Aegean region, *Tectonophysics*, *298*, 155-175, 1998.

Watts, A.B., J.H. Bodine, and M.S. Steckler, Observations of flexure and the state of stress in the oceanic lithosphere, *Journal of Geophysical Research*, *85*, 6369-6376, 1980.

Watts, A.B., J.R. Cochran, and G. Selzer, Gravity anomalies and flexure of the lithosphere: A three-dimensional study of the Great Meteor Seamount, Northeast Atlantic, *Journal of Geophysical Research*, *80*, 1391-1398, 1975.

Wegener, A., Die Entestehung der kontinente, *Geologische Rundschau*, *3*, 276-292, 1912.

Wegener, A., *Die Entstehung der Kontinente und Ozeane*, 108 pp., Vieweg, Braunschweig, 1915.

Weijermars, R., Flow behaviour and physical chemistry of bouncing putties and relates polymers in view of tectonic laboratory applications, *Tectonophysics*, *124*, 325-358, 1986.

Weissel, J.K., Magnetic lineations in marginal basins of the western Pacific, *Philosophical Transactions of the Royal Society of London, Series A: Mathematical and Physical Sciences*, *300*, 223-247, 1981.

Weissel, J.K., A.B. Watts, and A. Lapouille, Evidence for late Paleocene to late Eocene seafloor in the southern New Hebrides Basin, *Tectonophysics*, *87*, 243-251, 1982.

Wendt, J.I., M. Regelous, K.D. Collerson, and A. Ewart, Evidence for a contribution from two mantle plumes to island-arc lavas from northern Tonga, *Geology*, *25*, 611-614, 1997.

Widiyantoro, S., B.L.N. Kennett, and R.D. van der Hilst, Seismic tomography with P and S data reveals lateral variations in the rigidity of deep slabs, *Earth and Planetary Science Letters*, *173*, 91-100, 1999.

Widiyantoro, S., and R. van der Hilst, Structure and evolution of lithospheric slab beneath the Sunda arc, Indonesia, *Science*, *271*, 1566-1570, 1996.

Wiedicke, M., and J. Collier, Morphology of the Valu Fa spreading ridge in the southern Lau Basin, *Journal of Geophysical Research*, *98*, 11769-11782, 1993.

Wilcox, R.E., T.P. Harding, and D.R. Seely, Basic Wrench Tectonics, *The American Association of Petroleum Geologists Bulletin*, *57*, 74-96, 1973.

Willis, B., Part 2; The mechanics of Appalachian structure, *United States Geological Survey Annual Report*, *13, Part 2*, 211-281, 1893.

Wilson, J.T., A new class of faults and their bearing on continental drift, *Nature*, *207*, 343-347, 1965.

Worrall, D.M., Tectonic history of the Bering Sea and the evolution of Tertiary strike-slip basins of the Bering shelf, *Special Paper - Geological Society of America*, *257*, pp. 120, 1991.

Worrall, D.M., V. Kruglyak, F. Kunst, and V. Kuznetsov, Tertiary tectonics of the Sea of Okhotsk, Russia: Far-field effects of the India-Eurasia collision, *Tectonics*, *15*, 813-826, 1996.

Wortel, M.J.R., and W. Spakman, Structure and dynamics of subducted lithosphere in the Mediterranean region, *Proceedings of de Koninklijke Nederlandse Akademie van Wetenschappen*, *95*, 325-347, 1992.

Wortel, M.J.R., and W. Spakman, Subduction and slab detachment in the Mediterranean-Carpathian region, *Science*, *290*, 1910-1917, 2000.

Wortel, R., Seismicity and rheology of subducted slabs, *Nature*, *296*, 553-556, 1982.

Wright, I.C., Pre-spread rifting and heterogeneous volcanism in the southern Havre Trough back-arc basin, *Marine Geology*, *113*, 179-200, 1993.

Xiwei, X., M. Xingyuan, and D. Qidong, Neotectonic activity along the Shanxi rift system, China, *Tectonophysics*, *219*, 305-325, 1993.

Yamaoka, K., Y. Fukao, and M. Kumazawa, Spherical shell tectonics: Effects of sphericity and inextensibility on the geometry of the descending lithosphere, *Reviews of Geophysics*, *24*, 27-53, 1986.

Yin, A., P.A. Kapp, M.A. Murphy, C.E. Manning, T.M. Harrison, M. Grove, D. Lin, D. Xiguang, and W. Cunming, Significant late Neogene east-west extension in northern Tibet, *Geology*, *27*, 787-790, 1999.

Yogodzinski, G.M., J.L. Rubenstone, S.M. Kay, and R.W. Kay, Magmatic and tectonic development of the western Aleutians; an oceanic arc in a strike-slip setting, *Journal of Geophysical Research*, *98*, 11807-11834, 1993.

Yogodzinski, G.M., O.N. Volynets, A.V. Koloskov, N.I. Seliverstov, and V.V. Matvenkov, Magnesian andesites and the subduction component in a strongly calc-alkaline series at Piip Volcano, far western Aleutians, *Journal of Petrology, 35*, 163-204, 1994.

Yokokura, T., On subduction dip angles, *Tectonophysics, 77*, 63-77, 1981.

Yu, H.-S., The Pearl River Mouth Basin: A rift basin and its geodynamic relationship with the southeastern Eurasian margin, *Tectonophysics, 183*, 177-186, 1990.

Zai-Yi, T., H. Ping, and X. Ke-Ding, The Mesozoic-Cenozoic East China rift system, *Tectonophysics, 208*, 341-363, 1992.

Zaiyi, T., and D. Yonglin, Formation and evolution of the Yilan-Yitong graben, *Tectonophysics, 133*, 165-173, 1987.

Zhao, D., S. Horiuchi, and A. Hasegawa, 3-D seismic velocity structure of the crust and the uppermost mantle in the northeastern Japan Arc, *Tectonophysics, 181*, 135-149, 1990.

Zhou, D., K. Ru, and H. Chen, Kinematics of Cenozoic extension on the South China Sea continental margin and its implications for the tectonic evolution of the region, *Tectonophysics, 251*, 161-177, 1995.

Zonenshain, L.P., M.I. Kuzmin, and L.M. Natapov, Geology of the USSR; a plate-tectonic synthesis, in *Geodynamics Series*, edited by B.M. Page, pp. 242, 1990.

Zorin, Y.A., and L.E. Cordell, Crustal extension in the Baikal rift zone, *Tectonophysics, 198*, 117-121, 1991.

BIBLIOGRAPHY

The work presented in individual chapters in this thesis has resulted in several publications, from which some have been published or are in press, some are still in the reviewing process and some are intended to be submitted to journals for publications. Below I have listed the papers that are either published, in press, in review or have been submitted.

Publications

Schellart, W.P., Shear test results for cohesion and friction coefficients for different granular materials: scaling implications for their usage in analogue modelling. *Tectonophysics* **324**, 1-16, 2000.

Schellart, W.P., G.S. Lister and M.W. Jessell, Analogue modeling of arc and backarc deformation in the New Hebrides arc and North Fiji Basin. *Geology* **30**, 311-314, 2002.

Schellart, W.P., Analogue modelling of large-scale tectonic processes: An introduction. In: Analogue modelling of large-scale tectonic processes, edited by W.P. Schellart and C. Passchier. *Journal of the Virtual Explorer* **7**, 1-6, 2002.

Schellart, W.P., G.S. Lister and M.W. Jessell, Analogue modelling of asymmetrical back-arc extension. In: Analogue modelling of large-scale tectonic processes, edited by W.P. Schellart and C. Passchier. *Journal of the Virtual Explorer* **7**, 25-42, 2002.

Schellart, W.P., G.S. Lister and M.W. Jessell, Some experimental insights into arc formation and back-arc extension. *Bollettino di Geofisica Teorica ed Applicata* **42** (suppl. 1/2), 85-91, 2002.

Schellart, W.P., M.W. Jessell and G.S. Lister, Asymmetric extension in the back-arc region of the Kuril Arc, Northwest Pacific: Some insights from analogue modelling. *Tectonics* (in review).

Schellart, W.P. and G.S. Lister, Tectonic models for the formation of arc-shaped convergent zones and back-arc basins. *Special Paper - Geological Society of America* (submitted).

Publications not related to thesis

Schellart, W.P., Alpine deformation at the Western Termination of the Axial Zone, Southern Pyrenees. In: Reconstruction of the evolution of the Alpine-Himalayan orogeny, edited by G. Rosenbaum and G.S. Lister. *Journal of the Virtual Explorer* **8**, 35-56, 2002.

Schellart, W.P. and D.A. Nieuwland, 3D evolution of a pop-up structure above a double basement strike-slip fault: Some insights from analogue modelling. *Geological Society Special Publications* **212** (in press).

Nevertheless, mindful of my insignificance, I affirm nothing.

.....

Nor would I wish anyone to believe anything except what he is convinced of by clear and irrefutable reason.

René Descartes